Physics of the Solid State, Vol. 46, No. 10, 2004, pp. 1785–1791. Translated from Fizika Tverdogo Tela, Vol. 46, No. 10, 2004, pp. 1729–1734.

METALS AND SUPERCONDUCTORS

Critical Temperature of Disordered *d*-Wave Superconductors with Small Coherence Length

I. A. Semenikhin

Institute of Physical Technology, Russian Academy of Sciences, Nakhimovskiĭ pr. 34, Moscow, 117218 Russia

e-mail: isemenihin@mail.ru

Received January 12, 2004

Abstract—The critical temperature of *d*-wave superconductors with a small coherence length is studied numerically as a function of atomic disorder. Calculations are performed using the Bogolyubov–de Gennes method with inclusion of spatial nonuniformity of the superconducting order parameter. This approach allowed us to explain why the experimentally observed critical transition temperature decreases more slowly with increasing disorder than that predicted from the Abrikosov–Gor'kov theory. The quasilinear dependence of the critical temperature on the concentration of defects is also explained. © *2004 MAIK "Nauka/Interperiodica".*

1. INTRODUCTION

It is not completely clear yet exactly how impurities and defects influence high-temperature superconductors (HTSCs) with an anisotropic superconducting order parameter $\Delta(\mathbf{k})$ ($\mathbf{k}$ is the wave vector). There is a well-known relation between the critical temperature T_c and the carrier relaxation time due to nonmagnetic impurities and defects τ for superconductors with an arbitrary symmetry of $\Delta(\mathbf{k})$. This relation was derived using the BCS approximation in the framework of the Abrikosov–Gor'kov theory [1] and has the form

$$\ln\left(\frac{T_{c0}}{T_c}\right) = \chi\left[\Psi\left(\frac{1}{2}+\frac{1}{4\pi T_c\tau}\right)-\Psi\left(\frac{1}{2}\right)\right], \qquad (1)$$

where T_{c0} is the value of T_c in the absence of impurities, Ψ is the digamma function, $\chi = 1 - \langle\Delta(\mathbf{k})\rangle_{FS}^2/\langle\Delta^2(\mathbf{k})\rangle_{FS}$ characterizes anisotropy of the order parameter, and $\langle\ldots\rangle_{FS}$ denotes averaging over the Fermi surface. In the case of isotropic *s*-wave pairing symmetry, we have $\Delta(\mathbf{k}) = \text{const}$; hence, $\langle\Delta(\mathbf{k})\rangle_{FS}^2 = \langle\Delta^2(\mathbf{k})\rangle_{FS}$ and $\chi = 0$. For a superconductor with *d*-wave symmetry, we have $\chi = 1$, because $\langle\Delta(\mathbf{k})\rangle_{FS} = 0$. In the cases of anisotropic *s*-wave and mixed (*s* + *d*)-wave symmetry, χ varies from 0 to 1; the higher the anisotropy of $\Delta(\mathbf{k})$, the closer χ to unity. It should be noted that finding the actual symmetry of $\Delta(\mathbf{k})$ of an HTSC is a very important problem in itself, because its solution may help elucidate the nature of the high-temperature superconductivity. At present, it has been established that $\Delta(\mathbf{k})$ is highly anisotropic in HTSCs, in contrast to that in ordinary, low-temperature superconductors. Though it is widely assumed that $\Delta(\mathbf{k})$ has *d*-wave symmetry in HTSCs [2], there are experimental data (in particular, those obtained by phase-sensitive techniques) that indicate anisotropic *s*-wave symmetry of $\Delta(\mathbf{k})$ [3]. It is also reasonable to consider mixed (*s* + *d*)-wave symmetry; in this case, the proportion of *s*-wave and *d*-wave components in $\Delta(\mathbf{k})$ is of special interest.

Dependences of T_c/T_{c0} on $1/\tau T_{c0}$ calculated from Eq. (1) for various values of χ are presented in Fig. 1. Note that impurities do not affect T_c in the case of isotropic *s*-wave pairing symmetry ($\chi = 0$), whereas at $\chi = 1$ (*d*-wave pairing symmetry) T_c vanishes at a critical value of τ_c, which is defined by the equation $1/\tau T_{c0} = 4\pi\exp(-\Psi(1/2)) \approx 1.76$. Over the range $0 < \chi < 1$, T_c falls off steadily with increasing $1/\tau T_{c0}$ and the falloff becomes progressively steeper with increasing χ.

However, Eq. (1) contradicts experimental data (see, e.g., [4] and references in [5]), which show a much weaker effect of impurities on T_c of *d*-wave superconductors than that predicted by Eq. (1). In experiments, T_c

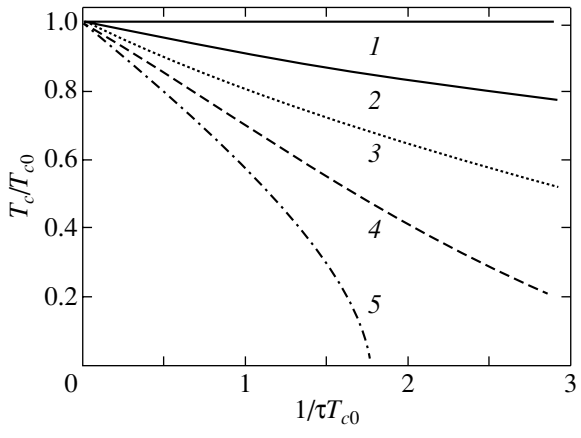

Fig. 1. Reduced critical temperature T_c/T_{c0} as a function of $1/\tau T_{c0}$ calculated from Eq. (1) for various values of χ: (*1*) 0, (*2*) 0.25, (*3*) 0.5, (*4*) 0.75, and (*5*) 1.0. T_{c0} is the critical temperature in the absence of disorder.

1063-7834/04/4610-1785$26.00 © 2004 MAIK "Nauka/Interperiodica"

decreases almost linearly with increasing defect concentration (which is proportional to $1/\tau$) [4, 6], whereas it follows from Eq. (1) that the dependence of T_c/T_{c0} on $1/\tau T_{c0}$ should have a negative curvature for *d*-wave superconductors (Fig. 1). According to Eq. (1), such a relatively slow decrease in T_c should be exhibited by superconductors with anisotropic *s*-wave or mixed (*s* + *d*)-wave symmetry of $\Delta(\mathbf{k})$. Several ways to settle this inconsistency between theory and experiment have been suggested. For example, it was shown in [5] that the contradiction can be resolved in the framework of the Abrikosov–Gor'kov theory by assuming $\chi < 1$ and the presence of magnetic impurities in the sample. In [6], effects of phase fluctuations were assumed to be responsible for changes in T_c in samples subjected to electron irradiation. According to [7], the influence of nonmagnetic impurities on T_c of *d*-wave superconductors can be weakened if there is a singularity in the density of states.

In the present paper, we suggest another way to reconcile theory and experiment. As is well known, Eq. (1) was derived with no consideration for spatial nonuniformity of the order parameter, which exists in a superconductor with impurities. This approximation is valid for superconductors with a large coherence length ξ_0. In this case, many different patterns of impurities exist on the length scale of variations in Δ and it is possible to use variables averaged over impurity configurations, as is done in deriving the equation for T_c in the Abrikosov–Gor'kov theory. However, in a superconductor with a small ξ_0, as in HTSCs, it becomes vitally important to take into account spatial nonuniformity of Δ, since, as shown in [8] for *s*-wave superconductors, this nonuniformity can qualitatively change the behavior of T_c with increasing disorder. According to [9, 10], the effect of impurities on T_c of *d*-wave superconductors becomes less pronounced if nonuniformity of Δ is taken into account.

Our goal here is to study in detail the influence of disorder on the critical temperature of superconductors with a small coherence length. We study extensively how the effect of impurities on T_c varies as one goes from superconductors with a large ξ_0 (low values of T_{c0}) to superconductors with a small ξ_0 (HTSCs). We use the Bogolyubov–de Gennes approach and take into account spatial nonuniformity of the order parameter.

2. MODEL

To study the influence of disorder on the critical temperature of a *d*-wave superconductor, we use the model Hamiltonian

$$H = -t\sum_{\langle i,j\rangle,\sigma} a^+_{i\sigma}a_{j\sigma} - \mu\sum_{i,\sigma} n_{i\sigma} + \sum_{i,\sigma}\varepsilon_i n_{i\sigma} + \sum_{i,j} V_{i,j} n_{i\uparrow}n_{j\downarrow}, \quad (2)$$

where $a^+_{i\sigma}$ and $a_{i\sigma}$ are the creation and annihilation operators, respectively, for an electron with spin σ at site i on a square lattice; $n_{i\sigma} = a^+_{i\sigma}a_{i\sigma}$; t is the hopping matrix element characterizing the kinetic energy of electrons; $\langle\ldots\rangle$ stands for a sum over nearest neighbors; and μ is the chemical potential. The diagonal impurity potential ε_i is assumed to be distributed uniformly over the range $(-W/2, W/2)$. The diagonal Anderson disorder introduced by ε_i represents nonmagnetic impurities and defects. The matrix elements $V_{i,j}$ are given by

$$V_{i,j} = \begin{cases} V_0, & i = j \\ V_1, & i \text{ and } j \text{ are nearest neighbors} \\ 0, & \text{otherwise.} \end{cases} \quad (3)$$

The potential $V_0 > 0$ gives the repulsion of electrons positioned on the same site, and the potential $V_1 < 0$ is the attraction of electrons placed on adjacent sites.

It should be noted that Eq. (2) with this choice of $V_{i,j}$ differs from a generalized Hubbard model [10, 11] (often used for modeling HTSCs) only in that the Hamiltonian (2) takes into account interaction only between electrons with opposite spins. We use this approximation because only such electrons form Cooper pairs; this simplification is not critical but reduces the computational effort. It can be shown that, in the mean-field theory, terms of the form $n_{i\uparrow}n_{j\uparrow}$ and $n_{i\downarrow}n_{j\downarrow}$ change the Hartree–Fock energy only. As follows from the discussion below, the inclusion of such terms does not affect our conclusions.

In the framework of the Bogolyubov–de Gennes approach [12], the problem with Hamiltonian (2) is described by the effective Hamiltonian

$$H_{\text{eff}} = -t\sum_{\langle i,j\rangle,\sigma} a^+_{i\sigma}a_{j\sigma} + \sum_{i,\sigma}(\varepsilon_i + U(\mathbf{r}_i) - \mu)n_{i\sigma} + \sum_i [\Delta(\mathbf{r}_i,\mathbf{r}_j)a^+_{i\uparrow}a^+_{j\downarrow} + \Delta^*(\mathbf{r}_i,\mathbf{r}_j)a_{j\downarrow}a_{i\uparrow}], \quad (4)$$

where

$$\Delta(\mathbf{r}_i,\mathbf{r}_j) = V_{i,j}\langle a_{i\downarrow}a_{j\uparrow}\rangle \text{ and } U(\mathbf{r}_i) = \frac{1}{2}\sum_j V_{i,j}n_j \quad (5)$$

are the superconducting order parameter and the Hartree–Fock energy at the site i, respectively, and n_i is the mean electron number at the site i. The Hamiltonian

H_{eff} can be diagonalized by the Bogolyubov transformation

$$a_{i\uparrow} = \sum_n u_n(\mathbf{r}_i)\gamma_{n\uparrow} - v_n^*(\mathbf{r}_i)\gamma_{n\downarrow}^+,$$
$$a_{i\downarrow} = \sum_n u_n(\mathbf{r}_i)\gamma_{n\downarrow} + v_n^*(\mathbf{r}_i)\gamma_{n\uparrow}^+. \quad (6)$$

Here, γ_n^+ and γ_n are new quasiparticles operators and amplitudes $u_n(\mathbf{r}_i)$ and $v_n(\mathbf{r}_i)$ are obtained from the equation

$$\begin{pmatrix} \hat{H}^N & \hat{\Delta} \\ \hat{\Delta}^* & -(\hat{H}^N)^* \end{pmatrix}\begin{pmatrix} u_n(\mathbf{r}_i) \\ v_n(\mathbf{r}_i) \end{pmatrix} = E_n\begin{pmatrix} u_n(\mathbf{r}_i) \\ v_n(\mathbf{r}_i) \end{pmatrix}, \quad (7)$$

where E_n is the energy of quasiparticle excitations,

$$\hat{H}^N u_n(\mathbf{r}_i) = -t\sum_\delta u_n(\mathbf{r}_i + \delta) + (\varepsilon_i + U(\mathbf{r}_i) - \mu)u_n(\mathbf{r}_i), \quad (8)$$

$$\hat{\Delta} v_n(\mathbf{r}_i) = \sum_j \Delta(\mathbf{r}_i, \mathbf{r}_j) v_n(\mathbf{r}_j), \quad (9)$$

and $\delta = \pm\hat{x}, \pm\hat{y}$ are vectors corresponding to the nearest neighbors of the site i.

The quantities $\Delta(\mathbf{r}_i, \mathbf{r}_j)$ and $U(\mathbf{r}_i)$ should satisfy the self-consistency conditions

$$\Delta(\mathbf{r}_i, \mathbf{r}_j) = -V_{i,j}\sum_n u_n(\mathbf{r}_i)v_n^*(\mathbf{r}_j)(1 - f_n) - v_n^*(\mathbf{r}_i)u_n(\mathbf{r}_j)f_n, \quad (10)$$

$$U(\mathbf{r}_i) = \sum_j V_{i,j}\sum_n |u_n(\mathbf{r}_j)|^2 f_n + |v_n(\mathbf{r}_j)|^2(1 - f_n), \quad (11)$$

where $f_n = 1/(1 + \exp(E_n/T))$ is the Fermi–Dirac distribution function (here and henceforth, the Boltzmann constant is set equal to unity). The chemical potential can be derived from the following equation for the electron density:

$$n_e = \sum_i n_i/N = 2\sum_{n,i}[|u_n(\mathbf{r}_i)|^2 f_n + |v_n(\mathbf{r}_i)|^2(1 - f_n)]/N. \quad (12)$$

The temperature T_c can be found using the method described in detail in [8]. In a linear approximation with respect to Δ (which is valid at $T \longrightarrow T_c$), it follows from Eqs. (7) and (10) that

$$\Delta(\mathbf{r}_i, \mathbf{r}_j) = -\frac{V_{i,j}}{2} \times \sum_{i_1, j_1}\Delta(\mathbf{r}_{i_1}, \mathbf{r}_{j_1})\sum_{n,m} u_n(\mathbf{r}_i)u_m(\mathbf{r}_j)u_m^*(\mathbf{r}_{i_1})u_n^*(\mathbf{r}_{j_1}) \times \frac{\tanh(E_n/2T) + \tanh(E_m/2T)}{E_n + E_m}, \quad (13)$$

where $u(\mathbf{r}_i)$ and E_n are solutions to Eqs. (7), (10), and (11) for the normal state, i.e., solutions to the equation

$$\hat{H}^N u_n(\mathbf{r}_i) = E_n u_n(\mathbf{r}_i), \quad (14)$$

the self-consistency condition

$$U(\mathbf{r}_i) = \frac{1}{2}\sum_j V_{i,j}n_j = \sum_{n,j} V_{i,j}|u_n(\mathbf{r}_j)|^2 f_n \quad (15)$$

and the corresponding equation for the chemical potential. The quantity $\Delta(\mathbf{r}_i, \mathbf{r}_j)$ and the amplitudes $u_n(\mathbf{r}_i)$ can be assumed to be real in the absence of current and magnetic field. The temperature T_c is defined as the maximum temperature at which uniform equation (13) has a nonzero solution.

If we neglect nonuniformity of $\Delta(\mathbf{r}_i, \mathbf{r}_j)$, then the averaged values of the diagonal (Δ_0) and off-diagonal (Δ_1) components of the order parameter are given by

$$\Delta_0 = \sum_i \Delta(\mathbf{r}_i, \mathbf{r}_i)/N, \quad (16)$$

$$\Delta_1 = \sum_i (\Delta(\mathbf{r}_i, \mathbf{r}_i + \hat{x}) \mp \Delta(\mathbf{r}_i, \mathbf{r}_i + \hat{y}) + \Delta(\mathbf{r}_i, \mathbf{r}_i - \hat{x}) \mp \Delta(\mathbf{r}_i, \mathbf{r}_i - \hat{y}))/4N, \quad (17)$$

where $\hat{x}$ and $\hat{y}$ are the vectors corresponding to the nearest neighbors along the **x** and **y** axes, respectively. In Eq. (17), the plus sign corresponds to the *s*-wave symmetry of $\Delta(\mathbf{k})$ and the minus sign, to the *d*-wave symmetry. This difference in the definition of Δ_1 is due to the fact that the matrix elements $\Delta(\mathbf{r}_i, \mathbf{r}_i \pm \hat{x})$ and $\Delta(\mathbf{r}_i, \mathbf{r}_i \pm \hat{y})$ have opposite signs for a *d*-wave superconductor, in contrast to an *s*-wave one. Within the approximation made above, we obtain well-known expressions for the order parameter in the quasi-momentum representation: $\Delta(\mathbf{k}) = \Delta_0 + 2\Delta_1(\cos(k_x) + \cos(k_y))$ for the *s*-wave symmetry of Δ and $\Delta(\mathbf{k}) = 2\Delta_1(\cos(k_x) - \cos(k_y))$ for the *d*-wave symmetry. In the case where Δ is uni-

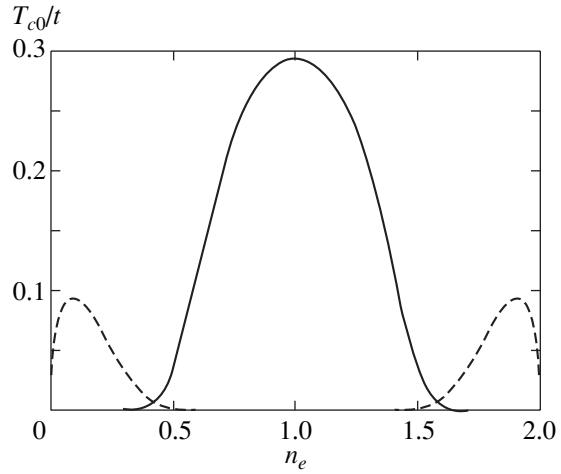

Fig. 2. Critical temperature T_{c0} as a function of the relative electron density n_e calculated for *d*-wave (solid line) and anisotropic *s*-wave (dash line) symmetry of the order parameter in the case of no atomic disorder ($W = 0$) for $V_0 = 0$ and $V_1 = -1.6t$.

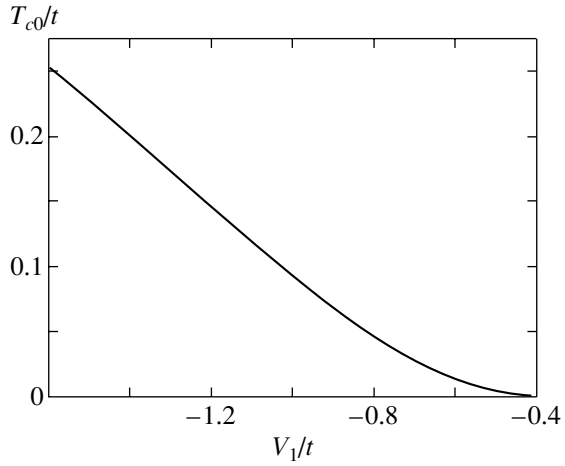

Fig. 3. Critical temperature T_{c0} as a function of potential V_1 for *d*-wave symmetry of the order parameter in the case of no atomic disorder ($W = 0$) for $n_e = 0.8$.

form over space, Eq. (13) reduces to the following equations for Δ_0 and Δ_1 in the vicinity of T_c:

$$\Delta_0 = -\frac{V_0}{2N}\sum_n(\Delta_0 + \Delta_1 a_{n,n})\frac{\tanh(E_n/2T)}{E_n},$$

$$\Delta_1 = -\frac{V_1}{8N}\sum_{n,m} a_{n,m}(\Delta_0\delta_{n,m} + \Delta_1 a_{m,n}) \qquad (18)$$

$$\times\frac{\tanh(E_n/2T) + \tanh(E_m/2T)}{E_n + E_m},$$

where $a_{n,m} = \sum_i u_n(\mathbf{r}_i)(u_m(\mathbf{r}_i + \hat{x}) \mp u_m(\mathbf{r}_i + \hat{y}) + u_m(\mathbf{r}_i - \hat{x}) \mp u_m(\mathbf{r}_i - \hat{y}))$, $\delta_{n,m}$ is the Kronecker delta, and the plus and minus signs correspond to superconductors with *s*-wave and *d*-wave symmetry of Δ, respectively. From the first of Eqs. (18), it follows that, in the case of *d*-wave superconductors, the diagonal component Δ_0 is always zero if $V_0 > 0$. It is interesting that, in this approximation, the critical temperature of a *d*-wave superconductor is independent of the magnitude of the potential V_0 describing on-site electron repulsion. In the case of anisotropic *s*-wave symmetry, an increase in V_0 brings about a decrease in T_c. We will use Eqs. (18) to determine T_c in the approximation of spatially uniform Δ.

In order to compare the results obtained for the case of a spatially nonuniform order parameter with the results based on Eq. (1), we need to know the dependence of T_c on $1/\tau$. However, Eq. (13) gives us the dependence of T_c on W. Hence, we have to find the $\tau(W)$ dependence. In this case, our problem will become simpler, because when dealing with $T_c(1/\tau)$ instead of $T_c(W)$ we need not take the Hartree–Fock potential $U(\mathbf{r}_i)$ into account explicitly. To calculate $T_c(W)$ and $\tau(W)$, we assume $\varepsilon_i' = \varepsilon_i + U(\mathbf{r}_i)$ to be a new impurity distribution, which is defined in much the same way as ε_i, and then calculate T_c and τ in the usual way, thus obtaining $T_c(1/\tau)$ without explicit use of $U(\mathbf{r}_i)$.

3. RESULTS AND DISCUSSION

First, we choose the electron density n_e for calculations. The dependence of T_c on n calculated in the absence of disorder is shown in Fig. 2. It can be seen that, in the case of $n_e \approx 1$ (half-filled band), *d*-wave symmetry of Δ is realized, while at low electron (hole) concentrations the superconductor has anisotropic *s*-wave symmetry of Δ. The following point is of interest.

Near the crossing point of graphs of the critical temperature for *d*-wave and anisotropic *s*-wave superconductors, let us choose a value of n_e such that the critical temperature for the *d*-wave superconductor is slightly higher than that for the *s*-wave superconductor. In this case, the symmetry of the order parameter can change over from the *d*-wave to anisotropic *s*-wave type with increasing impurity concentration, because suppression of T_c by impurities is stronger for superconductors with *d*-wave symmetry of Δ (Fig. 1). Since we intend to study superconductors with *d*-wave symmetry of Δ, we should choose $n_e \approx 1$. However, the value of n_e should not be chosen very close to unity, because the mean-field theory for a two-dimensional lattice may fail at half-filling [11]. For this reason, we performed calculations for $n_e = 0.8$.

Now, we are to select the potential V_1. At low values of $|V_1|$, the critical temperature decreases exponentially

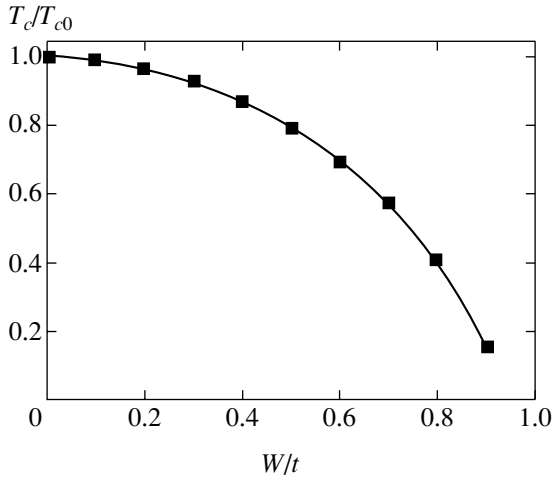

Fig. 4. T_c/T_{c0} as a function of the degree of disorder W for a d-wave superconductor calculated neglecting spatial nonuniformity of the order parameter for an arbitrarily chosen disorder configuration on a square lattice of $N = 50 \times 50$ sites at $V_0 = 0$, $V_1 = -0.8t$, and $n_e = 0.8$.

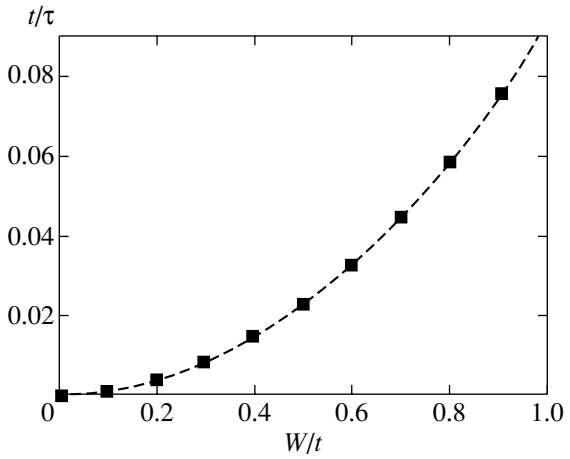

Fig. 5. Inverse carrier relaxation time due to impurities $1/\tau$ as a function of the degree of disorder W obtained by comparing the calculated dependence of T_c/T_{c0} on W and the dependence of T_c/T_{c0} on $1/\tau T_{c0}$, see Eq. (1). These calculation data are obtained for one arbitrarily chosen disorder configuration on a square lattice of $N = 50 \times 50$ sites at $V_0 = 0$, $V_1 = -0.8t$, and $n_e = 0.8$.

as $|V_1|$ grows (Fig. 3) and, accordingly, ξ_0 increases. Since ξ_0 should be smaller than the linear dimension of the system, $|V_1|$ is limited from below. On the other hand, at high $|V_1|$, the mean-field theory fails [11]. Therefore, we performed calculations for V_1 values in the range from $-0.8t$ to $-1.6t$. The case of $|V_1| > t$, where ξ_0 is of the order of several lattice constants, corresponds to HTSCs.

Figure 4 shows the dependence of T_c/T_{c0} on the degree of disorder W for a d-wave superconductor calculated neglecting spatial nonuniformity of the order parameter in the same way as Eq. (1) was derived in [1]. By comparing this relation with Eq. (1) at $\chi = 1$ (Fig. 1), one can obtain the dependence of τ on W shown in Fig. 5. As expected, $1/\tau \sim W^2$. The proportionality factor is about 0.1 and depends on the disorder configuration only slightly. The dependence of τ on W is calculated separately for each disorder configuration. Knowing $\tau(W)$, we can find the dependence of T_c/T_{c0} on $1/\tau T_{c0}$ with allowance for the spatial nonuniformity of Δ. The dependences of T_c/T_{c0} on $1/\tau T_{c0}$ calculated for $V_0 = 0$, $n_e = 0.8$, and various values of V_1 are presented in Fig. 6. The dashed line in Fig. 6 is calculated for the pure d-wave symmetry from Eq. (1) with $\chi = 1$.

As already mentioned, the approximations made in deriving Eq. (1) are valid for large values of ξ_0, i.e., for low values of $|V_1|$, which corresponds to the weak coupling BCS limit. Therefore, for low $|V_1|$, the dependences of T_c/T_{c0} on $1/\tau T_{c0}$ calculated with and without inclusion of spatial nonuniformity of Δ should be close to each other. Indeed, as seen from Fig. 6, the curve calculated for nonuniform Δ at $V_1 = -0.8t$ is very close to the curve for the uniform order parameter plotted according to Eq. (1). As $|V_1|$ grows and, accordingly, ξ_0 decreases, spatial nonuniformity of Δ becomes important. The dependence of T_c/T_{c0} on $1/\tau T_{c0}$ is seen to differ more and more from that calculated from Eq. (1). We

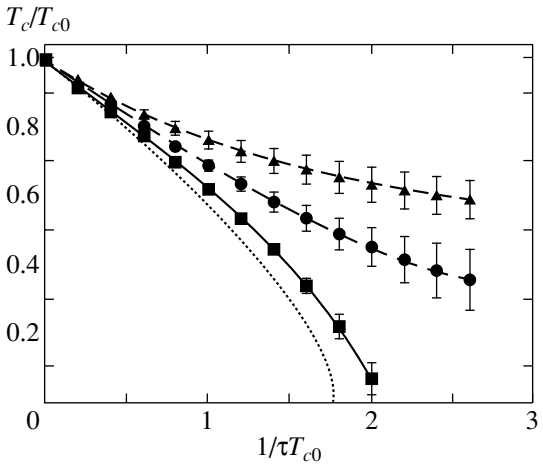

Fig. 6. T_c/T_{c0} as a function of $1/\tau T_{c0}$ calculated for several values of V_1 with inclusion of spatial nonuniformity of the order parameter. Calculations are performed for $V_1 = -0.8t$ and $N = 50 \times 50$ (squares); $V_1 = -1.2t$ and $N = 28 \times 28$ (circles); and $V_1 = -1.6t$ and $N = 28 \times 28$ (triangles). In all cases, $V_0 = 0$ and $n_e = 0.8$. Averaging is performed over 20 different configurations of disorder in the case of a lattice of $N = 50 \times 50$ sites and over 40 configurations in the case of a lattice of $N = 28 \times 28$ sites. The dashed line is plotted according to Eq. (1) for $\chi = 1$ (d-wave symmetry). Vertical lines represent rms deviation of T_c/T_{c0} due to variations in T_c for different disorder configurations.

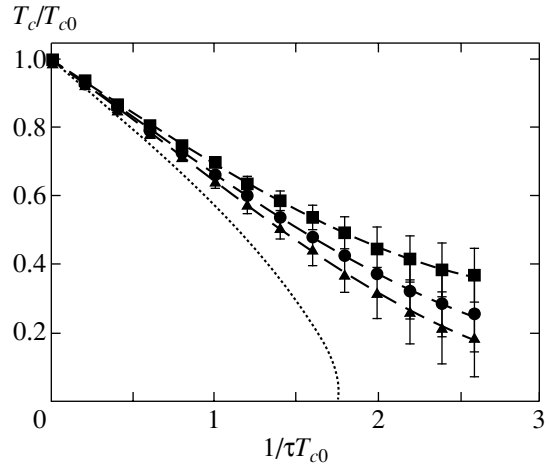

Fig. 7. T_c/T_{c0} as a function of $1/\tau T_{c0}$ for various values of V_0 in the case of a spatially nonuniform order parameter. Calculations are performed for $V_0 = 0$ (squares), $V_0 = 1.2t$ (circles), and $V_0 = 2.4t$ (triangles). In all cases, $N = 28 \times 28$, $V_1 = -1.2t$, and $n_e = 0.8$. Averaging is performed over 40 different disorder configurations. The dashed line is plotted according to Eq. (1) for $\chi = 1$ (*d*-wave symmetry).

note that, with an increase in disorder, T_c/T_{c0} decreases much more slowly than it follows from Eq. (1). Similar behavior was observed for T_c in experiments [4, 6]. It should also be noted that, as $|V_1|$ grows, the curvature of the T_c/T_{c0} versus $1/\tau T_{c0}$ curve changes from negative to positive. At $|V_1| \approx t$, the dependence of T_c/T_{c0} on $1/\tau T_{c0}$ is close to an experimentally observed linear dependence [4, 6]. Thus, the critical temperature of a *d*-wave superconductor with impurities calculated with consideration of nonuniformity of the order parameter agrees qualitatively with experimental data.

Up to this point, we limited ourselves to the case where there is no electron on-site repulsion ($V_0 = 0$) and, therefore, the pure *d*-wave symmetry of the order parameter persists under disordering, since the matrix elements $\Delta(\mathbf{r}_i, \mathbf{r}_i)$ responsible for the *s*-wave component remain zero. Hence, in the $\mathbf{k}$ representation, $\Delta(\mathbf{k})$ is always equal to $2\Delta_1(\cos(k_x) - \cos(k_y))$, where Δ_1 is the average of $\Delta(\mathbf{r}_i, \mathbf{r}_j)$ over all sites calculated from Eq. (17).

Thus, in the case of $V_0 = 0$, we have $\Delta(\mathbf{r}_i, \mathbf{r}_i) = 0$ for all sites *i* and spatial nonuniformity of Δ does not cause the *d*-wave symmetry of Δ to break under the influence of disorder. However, $\Delta(\mathbf{r}_i, \mathbf{r}_i) \neq 0$ in the case of $V_0 > 0$. At first glance, this result can be seen as evidence in favor of mixed (*s* + *d*)-wave symmetry. However, according to numerical calculations, $\Delta(\mathbf{r}_i, \mathbf{r}_i)$ is an alternating function of $\mathbf{r}_i$ and, on the average, $\Delta_0 = \langle\Delta(\mathbf{r}_i, \mathbf{r}_i)\rangle \approx 0$.[1] Therefore, in the case of $V_0 > 0$, the *d*-wave symmetry of the order parameter is also probably preserved under disordering.

The dependence of T_c/T_{c0} on $1/\tau T_{c0}$ for various values of V_0 is presented in Fig. 7. It is seen that an increase in V_0 causes T_c to decrease faster with increasing disorder. Variations in V_0 also change the curvature of the T_c/T_{c0} versus $1/\tau T_{c0}$ curve. Hence, a linear dependence of T_c/T_{c0} on the impurity concentration, similar to those observed in experiments, can be obtained for a whole range of parameters V_0 and V_1. The fact that, as in the case of $V_0 = 0$ (Fig. 6), the dependence of T_c/T_{c0} on $1/\tau T_{c0}$ for *d*-wave superconductors is not universal, in contrast to the predictions from the Abrikosov–Gor'kov theory [see Eq. (1), Fig. 1], is due to spatial nonuniformity of Δ. This may be a key to understanding of diverse behaviors of T_c/T_{c0} in different HTSCs under disordering.

4. CONCLUSIONS

To summarize, we make the following conclusions.

(1) The critical transition temperature of a *d*-wave superconductor with a small coherence length decreases with disordering more slowly than the Abrikosov–Gor'kov theory predicts. The smaller the coherence length, the weaker the influence of disorder on the critical temperature and the larger the discrepancy between theoretical curves calculated with and without inclusion of spatial nonuniformity of the order parameter. This fact may well be the reason behind known contradictions between predictions from the Abrikosov–Gor'kov theory and experimental data on the influence of impurities and radiation defects on the critical temperature of HTSCs.

(2) For *d*-wave superconductors with a small coherence length, the reduced critical temperature T_c/T_{c0} is not a universal function of parameter $1/\tau T_{c0}$, which explains the diverse behavior of T_c/T_{c0} in different HTSCs under disordering.

(3) The experimentally observed linear dependence of the critical temperature on the concentration of impurities can be explained if spatial nonuniformity of the order parameter is taken into account.

ACKNOWLEDGMENTS

The author is grateful to L.A. Openov for discussions and valuable comments.

This work was supported by the Ministry of Industry, Science, and Technology of the Russian Federation (contract no. 40.012.1.1.1357).

[1] Because of the finite size of the lattices used in the calculations, we do not reach the strict equality $\Delta_0 = 0$. Nevertheless, the ratio Δ_0/Δ_1 is very small (for example, $\Delta_0/\Delta_1 < 10^{-3}$ for $N = 28 \times 28$, $W = 2.0t$, $V_1 = -1.2t$, and $V_0 = 2.4t$) and decreases with increasing lattice size.

REFERENCES

1. A. A. Abrikosov, Physica C (Amsterdam) **214** (1–2), 107 (1993).
2. C. C. Tsuei and J. R. Kirtley, Rev. Mod. Phys. **72** (4), 969 (2000).
3. G.-M. Zhao, cond-mat/0305483.
4. V. F. Elesin, K. É. Kon'kov, A. V. Krasheninnikov, and L. A. Openov, Zh. Éksp. Teor. Fiz. **110** (2), 731 (1996) [JETP **83**, 395 (1996)].
5. L. A. Openov, Phys. Rev. B **58** (14), 9468 (1998).
6. F. Rullier-Albenque, H. Alloul, and R. Tourbot, Phys. Rev. Lett. **91**, 047 001 (2003).
7. I. Grosu, J. Supercond. **13** (1), 141 (2000).
8. I. A. Semenikhin, Fiz. Tverd. Tela (St. Petersburg) **45** (9), 1545 (2003) [Phys. Solid State **45**, 1622 (2003)].
9. M. E. Zhitomirsky and M. B. Walker, Phys. Rev. Lett. **80** (24), 5413 (1998).
10. M. Franz, C. Kallin, A. J. Berlinsky, and M. I. Salkola, Phys. Rev. B **56** (13), 7882 (1997).
11. R. Micnas, J. Ranninger, and S. Robaszkiewicz, Rev. Mod. Phys. **62** (1), 113 (1990).
12. P. G. de Gennes, *Superconductivity of Metals and Alloys* (Benjamin, New York, 1966; Mir, Moscow, 1968).

Translated by G. Tsydynzhapov

Physics of the Solid State, Vol. 46, No. 10, 2004, pp. 1792–1797. Translated from Fizika Tverdogo Tela, Vol. 46, No. 10, 2004, pp. 1735–1739.

METALS AND SUPERCONDUCTORS

Crossover from the "Clean" Limit to the "Dirty" Limit in a Network of *S–N–S* Weak Links in $Y_{3/4}Lu_{1/4}Ba_2Cu_3O_7 + BaPb_{1-x}Sn_xO_3$ ($0 \le x \le 0.25$) Composites

M. I. Petrov, D. A. Balaev, D. M. Gokhfel'd, K. A. Shaĭkhutdinov, S. V. Ospishchev, and K. S. Aleksandrov

Kirensky Institute of Physics, Siberian Division, Russian Academy of Sciences, Akademgorodok, Krasnoyarsk, 660036 Russia
e-mail: smp@iph.krasn.ru

Received February 5, 2004

Abstract—Composites with a network of "superconductor–normal metal–superconductor" (*S–N–S*) weak links are prepared from a $Y_{3/4}Lu_{1/4}Ba_2Cu_3O_7$ high-temperature superconductor and $BaPb_{1-x}Sn_xO_3$ ($0 \le x \le 0.25$) metal oxides. It is found that an increase in the tin content x in the nonsuperconducting component of the composite leads to an increase in the electrical resistivity ρ and, hence, to a decrease in the mean free path l of charge carriers. The temperature dependences of the electrical resistivity $\rho(T)$ and critical current $j_C(T)$ of the composites are analyzed in the framework of the de Gennes theory of *S–N–S* junctions. It is demonstrated that the network of weak links in the composites is characterized by a crossover from the "clean" limit ($l \ge L$) to the "dirty" limit ($l \le L$) (where L is the effective thickness of *N* interlayers between high-temperature superconductor grains). © *2004 MAIK "Nauka/Interperiodica".*

1. INTRODUCTION

It has been universally accepted that, in high-temperature superconducting ceramics, natural grain boundaries forming a Josephson-type weak-link network are responsible for the transport properties of polycrystals. Taking into account disagreement among authors regarding the nature of boundaries (metallic, dielectric, etc.) in polycrystalline high-temperature superconductors [1–12], the inference can be made that their conductivity is governed by technological factors. In our earlier works [5, 10–12], we analyzed the transport properties of polycrystalline high-temperature superconductors with a 1–2–3 structure and conclusively proved that the standard procedure of synthesizing these materials leads to the formation of natural grain boundaries of metallic nature. However, systematic investigations into the preparation and transport properties of polycrystalline high-temperature superconductors with a network of "superconductor–normal metal–superconductor" (*S–N–S*) weak links have been undertaken neither in the "clean" limit (when the mean free path l of charge carriers in the normal metal is greater than the geometric thickness L of N interlayers; i.e., $l \ge L$ [13]) nor in the "dirty" limit ($l \le L$ [13]). In composites based on high-temperature superconductors, the nonsuperconducting component is a material forming boundaries between superconducting grains [6–12, 14–18]. The transport properties of the composite as a whole are governed by the type of nonsuperconducting component (metal [6, 8, 9, 16–18] or dielectric [14, 15]).

Earlier [11], we studied the transport properties of $Y_{3/4}Lu_{1/4}Ba_2Cu_3O_7 + BaPbO_3$ composites. It was shown that these composites have a network of *S–N–S* weak links and that the transport properties of the composites are determined by an *N* interlayer whose effective thickness L depends on the volume content of the metal. It was established that the experimental temperature dependences of the critical current $j_C(T)$ for the composites are in good agreement with the theoretical dependences $j_C(T)$ for clean *S–N–S* junctions [19]. This made it possible to estimate the effective thickness of *N* interlayers in the composites under investigation. It turned out that the effective thickness L of *N* interlayers monotonically increases (in proportion to $V^{1/3}$, where V is the volume content of the nonsuperconducting component) from ~40 Å for the composite with 4 vol % $BaPbO_3$ to ~125 Å for the composite with 45 vol % $BaPbO_3$ [9]. These values of L were used in the present work to make a comparison with the mean free path of charge carriers in the nonsuperconducting component of the composite.

Investigations into the current–voltage characteristics [16] and the critical current [17] of YBCO + $BaPbO_3$ and YBCO + $BaPb_{0.9}Sn_{0.1}O_3$ composites and their analysis in terms of the theory of *S–N–S* junctions [20–23] gave grounds to assert that the network of *S–N–S* junctions is formed in the clean limit for composites containing $BaPbO_3$ and in the effectively dirty limit for composites with $BaPb_{0.9}Sn_{0.1}O_3$. In the authors' opinion, it is of interest to investigate a crossover from the clean limit to the dirty limit in a "high-temperature superconductor + $BaPb_{1-x}Sn_xO_3$" composite by decreasing

the conductivity of the $BaPbO_3$ metal oxide through partial replacement of lead by tin ($0 \le x \le 0.25$). In this work, we compared the transport properties of composites with the same volume content of the $BaPb_{1-x}Sn_xO_3$ component but with different tin contents x. All the composites were simultaneously prepared according to the same procedure. Therefore, the size distribution of N interlayers can be considered to be identical for all composites of the same series and all changes in the transport properties of the composites thus prepared can be explained by the evolution of the physical properties (in particular, electrical resistance) of the $BaPb_{1-x}Sn_xO_3$ nonsuperconducting component, which is responsible for the formation of weak links between high-temperature superconductor grains.

2. SAMPLE PREPARATION AND EXPERIMENTAL TECHNIQUE

2.1. Synthesis and Electrical Resistivity of $BaPb_{1-x}Sn_xO_3$ Compounds

Compounds $BaPb_{1-x}Sn_xO_3$ at different tin contents x were prepared by solid-phase synthesis from BaO_2, PbO, and SnO_2 oxides at a temperature of 950°C for 160 h with 13 intermediate millings. According to Mössbauer investigations [17], these conditions provide a uniform distribution of tin atoms in the $BaPbO_3$ perovskite structure. The ^{119}Sn Mössbauer spectra of $BaPb_{1-x}Sn_xO_3$ compounds at a tin content $x = 0.1$ are given in [17]. In our experiments, we synthesized a series of samples at tin contents $x = 0$, 0.037, 0.125, and 0.250. The choice of these values of x will be explained below. All the samples were prepared simultaneously. The x-ray powder diffraction patterns of the metal oxides contain only the reflections corresponding to the $BaPbO_3$ structure. The table presents the electrical resistivities ρ of the $BaPb_{1-x}Sn_xO_3$ compounds at temperatures of 5 and 77 K.

An increase in the tin content from 0 to 25 at. % leads to an increase in the electrical resistivity ρ by almost one order of magnitude. Since the structure of the $BaPb_{1-x}Sn_xO_3$ compounds in this case remains virtually unchanged, the electrical resistivity increases as the result of a decrease in the mean free path l of charge carriers [24]. For a $BaPbO_3$ single crystal, the mean free path $l = 220$ Å was obtained by Kitazawa *et al.* [25] from the classical expression

$$l = 3^{1/3}\pi^{2/3}\hbar e^{-2}\rho^{-1}n^{-2/3}, \quad (1)$$

where $\hbar$ is the Planck constant, e is the elementary charge, and n is the carrier density. It is known that, in $Ba(Pb_{1-x}Bi_x)O_3$ polycrystals, charge scattering by grain boundaries brings about an additional increase in the magnitude of the electrical resistivity ρ [26–28]. Most likely, this increase is the reason why substituting the resistivities ρ of our samples into formula (1) gives underestimated mean free paths (smaller than the lattice constant). In our opinion, it is expedient to calculate the effective mean free path l_{eff}, which depends on the most probable distance r between tin impurity atoms in the structure of the $BaPb_{1-x}Sn_xO_3$ compounds. Taking into account that the mean free path in a polycrystal is shorter than the mean free path in a single crystal, the value of l_{eff} can be calculated from the relationship

$$l_{eff}^{-1} = l^{-1} + r^{-1}. \quad (2)$$

Here, $l = 220$ Å for $BaPbO_3$ [25] and the most probable distance r is determined from the formula $r = ax^{-1/3}$ (where x is the atomic fraction of tin; and $a = 4.268$ Å is the lattice constant, which is determined from the x-ray powder diffraction patterns and agrees with the data obtained in [29]). The most probable distances r and the effective mean free paths l_{eff} calculated from the above expressions are listed in the table.

Parameters of $BaPb_{1-x}Sn_xO_3$ nonsuperconducting components of the studied composites

x	ρ(5 K), Ω cm	ρ(77 K), Ω cm	Designation	r, Å	l_{eff}, Å
0	0.0069	0.0057	Sn0	–	220
0.037	0.0085	0.0068	Sn0.037	12.8	12.1
0.125	0.0130	0.0130	Sn0.125	8.5	8.2
0.25	0.0590	0.0537	Sn0.25	4.3	4.2

Note: ρ is the electrical resistivity, r is the most probable distance between Sn atoms, and l_{eff} is the effective mean free path calculated from relationship (2).

2.2. Preparation of Composites Based on a High-Temperature Superconductor and $BaPb_{1-x}Sn_xO_3$ Compounds

The $Y_{3/4}Lu_{1/4}Ba_2Cu_3O_7$ high-temperature superconductor was prepared using the standard procedure. The synthesis of the $BaPb_{1-x}Sn_xO_3$ compounds was described above. The composites were synthesized according to the following procedure, which we called the rapid sintering technique. Powder components of the composite to be synthesized were taken in required proportions, mixed thoroughly in an agate mortar, and pressed into pellets. Then, the pressed pellets in preheated boats were placed in a furnace heated to 930°C and were allowed to stand for 5 min. After high-temperature sintering, the samples were placed in another furnace, held at 400°C for 6 h, and cooled to room temperature together with the furnace. These conditions ensured the recovery of the initial oxygen stoichiometry of high-temperature superconductors with a 1–2–3 structure, because oxygen losses due to sintering are quite probable [30]. By this means, we prepared composites with volume contents $V = 7.5$, 15.0, 30.0, 37.5, and 45.0 vol % $BaPb_{1-x}Sn_xO_3$. Note that the samples with different x and identical V were sintered and satu-

rated with oxygen at the same time. In this work, the composite samples are designated as $S + V\mathrm{Sn}x$. Here, Snx stands for the nonsuperconducting component (see table). The volume content of the $Y_{3/4}Lu_{1/4}Ba_2Cu_3O_7$ high-temperature superconductor is equal to $100\% - V$. The x-ray powder diffraction patterns of the composites prepared exhibit only the reflections attributed to the two phases of the initial components. According to electron microscopy, the mean size of high-temperature superconductor grains is approximately equal to 1.5 μm. The superconducting transition temperature determined for the composites from magnetic measurements is equal to 93.5 K. This temperature corresponds to the temperature T_C for the $Y_{3/4}Lu_{1/4}Ba_2Cu_3O_7$ initial high-temperature superconductor.

2.3. Measurements of Transport Properties

The temperature dependences of the electrical resistance $R(T)$ were measured by the standard four-point probe method. These measurements were performed with samples $1.5 \times 1.5 \times 12$ mm in size. The distance between the potential contacts was approximately equal to 10 mm. The electrical resistivity corresponding to the superconducting transition was measured accurate to within $\sim 10^{-6}$ Ω cm. The critical current j_C was determined from the initial portion of the current–voltage characteristic according to a standard criterion of 1 μV/cm [23].

3. RESULTS AND DISCUSSION

3.1. Transport Properties of High-Temperature Superconductor + $BaPb_{1-x}Sn_xO_3$ Composites

Figure 1 shows the temperature dependences of the electrical resistance $R(T)$ of the composites under investigation. The dependences are normalized to the resistance R at $T = 93.5$ K. At this temperature, which coincides with the temperature T_C determined from the magnetic measurements, the electrical resistance exhibits a jump corresponding to the superconducting transition in high-temperature superconductor grains. The second (smooth) portion of the dependence $R(T)$ reflects the transition of weak links to the superconducting state. The temperature T_{C0} at which the electrical resistance disappears strongly depends on the measuring current j. This is characteristic of a weak superconductivity. The influence of the transport current on the dependence $R(T, j)$ was previously studied for other composites prepared by the rapid sintering technique [25–27]. The dependences $R(T)$ shown in Fig. 1 were measured at the current $j = 5$ mA/cm^2 (this current was chosen according to a reasonable signal-to-noise ratio). At weaker currents j, the resistance R does not depend on j. The current–voltage characteristics of all the studied composites, including the $S + 45\mathrm{Sn}0.25$ composite, are nonlinear in the temperature range from T_{C0} to T_C. This is typical of Josephson junctions. The $S + 45\mathrm{Sn}x$ composites are in a resistive state even at a temperature of 4.2 K. The shift in the threshold of percolation through the superconducting component toward higher superconductor contents in the composites synthesized by the rapid sintering technique was considered in [30, 31].

In [9, 28], it was demonstrated that an increase in the volume content of a metal oxide (in our case, $BaPb_{1-x}Sn_xO_3$) leads to a decrease in the temperature T_{C0} due to an increase in the effective length of metallic weak links. The results of measurements of the electrical resistance at different tin contents x are presented in Fig. 1 in the corresponding panels for each volume content of $BaPb_{1-x}Sn_xO_3$. The influence of the distribution over the geometric parameters of *S–N–S* junctions in the composites on the electrical resistance is assumed to be identical due to the preparation procedure being the same. Consequently, the decrease in the temperature T_{C0} and variations in the dependences $R(T)$ for a given series of samples depend only on the change in the conductivity of the nonsuperconducting component (or, eventually, on the change in the mean free path of charge carries in the material of *N* interlayers between high-temperature superconductor grains).

In the $S + 37.5\mathrm{Sn}x$ composites, an increase in the tin content in the metal oxide to the highest content ($x = 0.25$) leads to a change in the temperature T_{C0} by ~ 70 K. For composites at a lower content of the metal oxide, the temperature T_{C0} varies over narrower ranges: ~ 30 K for $S + 30\mathrm{Sn}x$, ~7 K for $S + 15\mathrm{Sn}x$, and ~5 K for $S + 7.5\mathrm{Sn}x$. It is known that, with a decrease in the thickness of *N* interlayers in *S–N–S* junctions, the effect of their transparency on the superconducting current becomes weaker [13, 19, 23]. This circumstance clearly manifests itself in the temperature dependences of the electrical resistance of the composites.

3.2. Analysis of the Temperature Dependences of the Critical Current for Composites

The nature of weak links can be judged from the temperature dependence of the critical current in a better way than, for example, from the magnitude of the critical current even for a single junction [13, 23, 32, 33] and, especially, for a random network of weak links. The processing of the experimental data for *S–N–S* junctions in terms of the de Gennes theory [22] makes it possible to evaluate indirectly their physical parameters, such as the mean free path of charge carriers and the geometric thickness of an *N* interlayer [8, 17, 33–37]. It is expedient to apply this approach to the composites studied in the present work.

At temperatures not far from T_C, the critical current through an *S–N–S* junction within the de Gennes theory is described by the relationship [22, 23, 35–37]

$$j_C(T) = k(1 - T/T_C)^2 \frac{L/\xi_N}{\sinh(L/\xi_N)}, \qquad (3)$$

where k is a constant determined in [22, 23, 35–37]. For a network of *S–N–S* junctions, the constant k plays the

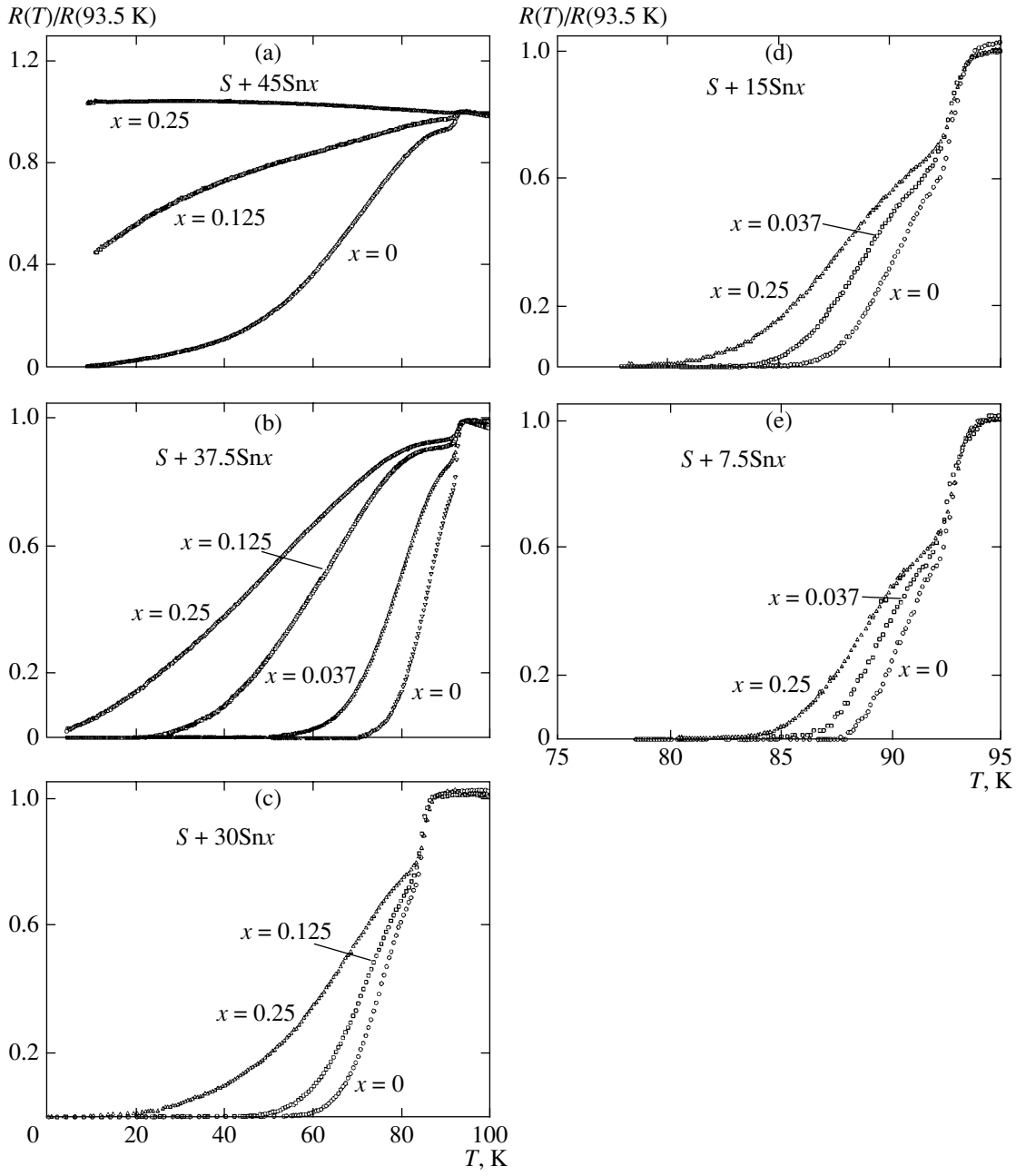

Fig. 1. Temperature dependences of the electrical resistance (normalized to the resistance R at T = 93.5 K) for the $S + V$Snx composites at volume contents V = (a) 45.0, (b) 37.5, (c) 30.0, (d) 15.0, and (e) 7.5%.

role of a normalizing factor. In relationship (3), the coherence length ξ_N for a normal metal is determined by the following expressions [35–37]:

$$\xi_N = \hbar V_F / 2\pi k_B T \quad (4)$$

for a clean N interlayer and

$$\xi_N = (\hbar V_F l / 6\pi k_B T)^{1/2} \quad (5)$$

for a dirty N interlayer. In expressions (4) and (5), k_B is the Boltzmann constant and V_F is the Fermi velocity in the normal metal. For $BaPb_{1-x}Sn_xO_3$ compounds, the Fermi velocity V_F was obtained from the relationship $V_F = \hbar 3^{1/3}\pi^{2/3}n^{1/3}m^{-1}$ (where m is the electron mass) at $n = 1.4 \times 10^{20}$ cm^{-3} with the use of the data taken from [25]. In [11], the effective thickness of N interlayers for the 85 vol % $Y_{3/4}Lu_{1/4}Ba_2Cu_3O_7$ + 15 vol % $BaPbO_3$ composite was estimated as $L \sim 100$ Å. These parameters were used to describe the experimental dependences $j_C(T)$, because the composites studied in [11] and in this work were prepared according to the same

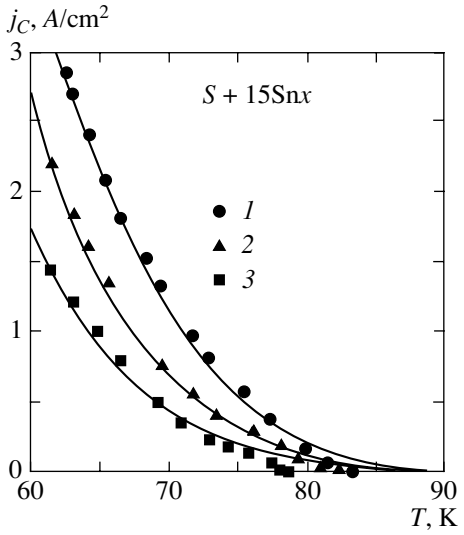

Fig. 2. Experimental temperature dependences of the critical current for the S + 15Snx composites at x = (*1*) 0, (*2*) 0.037, and (*3*) 0.25. Solid lines are the results of the best fitting to the de Gennes theory with the use of formulas (3)–(5) for the effective thickness L = 100 Å and mean free paths l = (*1*) 220, (*2*) 11, and (*3*) 4.2 Å.

procedure. As a result, apart from the normalizing factor, relationship (3) involves a single fitting parameter l.

Figure 2 depicts the experimental temperature dependences of the critical current $j_C(T)$ for S + 15Snx composites and the corresponding curves obtained by fitting to the de Gennes theory. The dependence $j_C(T)$ for the S + 15Sn0 composite in the temperature range 60–80 K was calculated from expressions (3) and (4). The use of expression (4) for the coherence length ξ_N in the case of a composite containing 15 vol % $BaPbO_3$ without impurities is justified because the quantities l (220 Å for $BaPbO_3$ [25]) and L (~100 Å) satisfy the condition for the clean S–N–S junction: $l \geq L$. The solid curves in Fig. 2 approximate the experimental dependences $j_C(T)$ for the S + 15Sn0.037 and S + 15Sn0.25 composites fairly well and represent the results of the best fitting to the de Gennes theory with the use of formulas (3) and (5) for mean free paths l = 11 ± 3 and 4.2 ± 1 Å, respectively. These values are close to the calculated effective mean free paths l_{eff} for $BaPb_{1-x}Sn_xO_3$ compounds (see table). For S + 7.5Snx composites, the experimental dependences $j_C(T)$ are also in good agreement with the theoretical curves calculated from expression (4) for the coherence length $\xi_N(T)$ of the clean N interlayer in the S + 7.5Sn0 sample at L = 80 Å and from expression (5) for the coherence length $\xi_N(T)$ of the dirty N interlayer in the S + 7.5Sn0.25 sample at l = 4.2 ± 1 Å. Therefore, the results of processing of the experimental dependences $j_C(T)$ in terms of the de Gennes theory at temperatures close to T_C indirectly confirm the mean free paths determined above for the $BaPb_{1-x}Sn_xO_3$ compounds (see Subsection 2.1 and table). It can be seen that the inequality $l_{\text{eff}} < L$ (L ~ 80–125 Å) holds for composites with $BaPb_{1-x}Sn_xO_3$ compounds even at x = 0.037. The more strict inequality $l_{\text{eff}} \ll L$ (the diffusive limit [38, 39]) is satisfied at $x \geq 0.125$. Thus, the crossover from the clean limit to the dirty limit in the network of S–N–S weak links in $Y_{3/4}Lu_{1/4}Ba_2Cu_3O_7$ + $BaPb_{1-x}Sn_xO_3$ composites is observed with an increase in the tin content x from 0 to 0.25. In the near future, the results obtained will be described in terms of the theories developed for current–voltage characteristics of S–N–S weak links with a variable mean free path in an N interlayer.

ACKNOWLEDGMENTS

We are grateful to A.D Vasil'ev and A.F. Bovina for performing the x-ray diffraction analysis, O.A. Bayukov for Mössbauer investigations, L.I. Kveglis for electron microscopic examination of the samples, N.I. Kirienko for the assistance in performing the experiments, and S.A. Satsuk and S.I. Popkov for their participation in discussions of the results. M.I. Petrov, and D.M. Gokhfel'd would like to thank R. Kümmel (Universität Würzburg, Germany) for helpful discussions regarding the problem of crossover in S–N–S junctions.

This work was supported in part by the Siberian Division of the Russian Academy of Sciences in the framework of the Lavrent'ev Competition of Research Projects of Young Scientists (2002).

REFERENCES

1. J. Mannhart, P. Chaudhary, D. Dimos, C. C. Tsuei, and T. R. McGuire, Phys. Rev. Lett. **61** (21), 2476 (1988).
2. R. Nicolsky, Cryogenics **29** (3), 388 (1989).
3. J. W. C. De Vries, G. M. Stolmann, and M. A. M. Gijs, Physica C (Amsterdam) **157**, 406 (1989).
4. R. Gross, P. Chaudhari, D. Dimos, A. Gupta, and G. Koren, Phys. Rev. Lett. **64** (2), 228 (1990).
5. M. I. Petrov, S. N. Krivomazov, B. P. Khrustalev, and K. S. Aleksandrov, Solid State Commun. **82** (6), 453 (1992).
6. Z. Damm, T. S. Orlova, B. I. Smirnov, and V. V. Shpeĭzman, Fiz. Tverd. Tela (St. Petersburg) **36** (8), 2465 (1994) [Phys. Solid State **36**, 1341 (1994)].
7. Yu. F. Revenko, A. I. D'yachenko, O. V. Grigut', and V. M. Svistunov, Pis'ma Zh. Tekh. Fiz. **14** (22), 2094 (1988) [Sov. Tech. Phys. Lett. **14**, 909 (1988)].
8. J. J. Calabrese, M. A. Dubson, and J. C. Garland, J. Appl. Phys. **72** (7), 2958 (1992).
9. J. Jung, M. A.-K. Mohamed, I. Isaak, and L. Friedrich, Phys. Rev. B **49** (17), 12188 (1994).
10. M. I. Petrov, D. A. Balaev, B. P. Khrustalev, and K. S. Aleksandrov, Physica C (Amsterdam) **235–240**, 3043 (1994).
11. M. I. Petrov, D. A. Balaev, S. V. Ospishchev, K. A. Shaihutdinov, B. P. Khrustalev, and K. S. Aleksandrov, Phys. Lett. A **237**, 85 (1997).
12. M. I. Petrov, D. A. Balaev, D. M. Gokhfel'd, K. A. Shaĭkhutdinov, and K. S. Aleksandrov, Fiz. Tverd. Tela (St.

Petersburg) **44** (7), 1179 (2002) [Phys. Solid State **44**, 1229 (2002)].

13. K. K. Likharev, Rev. Mod. Phys. **51** (1), 101 (1979).
14. D. Berling, B. Loegel, A. Mehdaouli, S. Regnier, C. Cananoni, and J. Marfaing, Supercond. Sci. Technol. **11**, 1292 (1998).
15. H. Nadifi, A. Ouali, C. Grigoresqu, H. Faqir, O. Monneraau, L. Tortet, G. Vacquier, and C. Boulesteix, Supercond. Sci. Technol. **13**, 1174 (2000).
16. M. I. Petrov, D. A. Balaev, D. M. Gonfeld, S. V. Ospishchev, K. A. Shaihutdinov, and K. S. Aleksandrov, Physica C (Amsterdam) **314**, 51 (1999).
17. M. I. Petrov, D. A. Balaev, S. V. Ospishchev, and K. S. Aleksandrov, Fiz. Tverd. Tela (St. Petersburg) **42** (5), 791 (2000) [Phys. Solid State **42**, 810 (2000)].
18. D. A. Balaev, S. V. Ospishchev, M. I. Petrov, and K. S. Aleksandrov, Supercond. Sci. Technol. **16** (1), 60 (2003).
19. U. Gunsenheimer, U. Schüssler, and R. Kümmel, Phys. Rev. B **49** (9), 6111 (1994).
20. R. Kümmel, U. Gunsenheimer, and R. Nicolsky, Phys. Rev. B **42** (7), 3992 (1990).
21. L. A. A. Pereira and R. Nicolsky, Physica C (Amsterdam) **282–287**, 2411 (1997).
22. P. G. de Gennes, Rev. Mod. Phys. **36**, 225 (1964).
23. A. Barone and J. Paterno, *Physics and Application of the Josephson Effect* (Wiley, New York, 1982; Mir, Moscow, 1984).
24. T. Tsakudo, H. Uwe, T. Suzuki, J. Fujita, J. Shiozawa, and M. Isobe, J. Phys. Soc. Jpn. **55** (1), 314 (1986).
25. K. Kitazawa, A. Katsui, A. Toriumi, and S. Tanaka, Solid State Commun. **52** (4), 459 (1984).
26. Y. Enomoto, M. Suzuki, T. Murakami, T. Inukai, and T. Inamura, Jpn. J. Appl. Phys. **20** (9), L661 (1981).
27. T. D. Thanh, A. Koma, and S. Tanaka, Appl. Phys. **22**, 205 (1980).
28. A. M. Gabovich and D. P. Moiseev, Usp. Fiz. Nauk **150** (4), 599 (1986) [Sov. Phys. Usp. **29**, 1135 (1986)].
29. A. W. Sleight, J. L. Gillson, and P. E. Bierstedt, Solid State Commun. **17** (1), 27 (1975).
30. M. I. Petrov, D. A. Balaev, K. A. Shaihutdinov, and K. S. Aleksandrov, Supercond. Sci. Technol. **14**, 798 (2001).
31. K. A. Shaihutdinov, D. A. Balaev, D. M. Gokhfeld, S. I. Popkov, and M. I. Petrov, J. Low Temp. Phys. **130** (3–4), 347 (2003).
32. U. Schüssler and R. Kümmel, Phys. Rev. B **47**, 2754 (1993).
33. E. Polturak, G. Koren, D. Cohen, E. Aharoni, and G. Deutscher, Phys. Rev. Lett. **67** (21), 3038 (1991).
34. J. Niemeyer and G. von Minngerode, Z. Phys. B **36**, 57 (1979).
35. L. Antogonazza, S. J. Berkowittz, T. H. Geballe, and K. Char, Phys. Rev. B **51** (13), 8560 (1995).
36. K. Char, Physica C (Amsterdam) **282–287**, 419 (1997).
37. L. Antogonazza, B. H. Moeckly, T. H. Geballe, and K. Char, Phys. Rev. B **52** (6), 4559 (1995).
38. V. Barzykin and A. M. Zagoskin, Superlattices Microstruct. **25** (5/6), 797 (1999).
39. P. Dubos, H. Courtois, B. Pannetier, F. K. Wihelm, A. D. Zaikin, and G. Shon, Phys. Rev. B **63**, 064502 (2001).

Translated by O. Borovik-Romanova

Physics of the Solid State, Vol. 46, No. 10, 2004, pp. 1798–1804. Translated from Fizika Tverdogo Tela, Vol. 46, No. 10, 2004, pp. 1740–1745.

METALS AND SUPERCONDUCTORS

Penetration of a Magnetic Field into the $YBa_2Cu_3O_{7-\delta}$ High-Temperature Superconductor: Magnetoresistance in Weak Magnetic Fields

V. V. Derevyanko, T. V. Sukhareva, and V. A. Finkel'

Kharkov Institute of Physics and Technology, National Scientific Center, ul. Akademicheskaya 1, Kharkov, 61108 Ukraine
e-mail: finkel@kipt.kharkov.ua

Received February 10, 2004

Abstract—The penetration of a magnetic field into superconducting grains and weak links of $YBa_2Cu_3O_{7-\delta}$ ceramic high-temperature superconductors is investigated using measurements of the transverse and longitudinal magnetoresistances at $T = 77.3$ K and $0 \le H \le \sim 500$ Oe as a function of the transport current in the range $\sim 0.01 \le I/I_c \le \sim 0.99$. The effects associated with the complete penetration of Josephson vortices into weak links of the high-temperature superconductor in magnetic fields H_{c2J}, the onset of penetration of Abrikosov vortices into superconducting grains in magnetic fields H_{c1A}, and the first-order transition from the Bragg glass phase to the vortex glass phase in fields H_{BG-VG} are revealed and interpreted. The I–H phase diagrams of the $YBa_2Cu_3O_{7-\delta}$ high-temperature superconductors are constructed for $\mathbf{I} \perp \mathbf{H}$ and $\mathbf{I} \parallel \mathbf{H}$. © *2004 MAIK "Nauka/Interperiodica".*

1. INTRODUCTION

In recent years, considerable interest has been expressed by researchers in the study of the effects associated with the penetration of magnetic flux vortices into high-temperature superconductors in a magnetic field H, the formation and evolution of the vortex structure, pinning of the magnetic flux, melting of the vortex lattice, etc. In our previous work [1], the resonance and magnetic properties of $YBa_2Cu_3O_{7-\delta}$ ceramic high-temperature superconductors in the superconducting state were studied in weak magnetic fields ($T = 77.3$ K, $0 \le H \le 600$ Oe). We revealed correlations between the field dependences of the parameters of the internal friction spectra (logarithmic damping decrement Q^{-1}, resonance frequency f) and the trapped magnetic flux ΔM and determined the boundaries of the regions corresponding to different magnetic states of superconducting grains.

Unfortunately, investigations of the resonance and magnetic properties and critical currents (see, for example, [2]), as a rule, cannot provide information regarding the penetration of a magnetic field into quasi-two-dimensional intergranular contacts (Josephson weak links) in high-temperature superconductors. For these links, the critical temperatures T_c and the lower (H_{c1}) and upper (H_{c2}) critical fields are considerably less than those for superconducting grains (see, for example, [3]): $T_{cJ} \le T_{cA}$, $H_{c1J} \ll H_{c1A}$, and $H_{c2J} \ll H_{c2A}$ (the superscripts J and A refer to weak links and superconducting grains, i.e., Josephson and Abrikosov media, respectively). It is evident that the penetration of a magnetic field into weak links and superconducting grains of ceramic high-temperature superconductors can be more effectively studied using a more sensitive method based on measurements of the magnetoresistance in weak magnetic fields.

It should be noted that, despite the great potential of this method for studying fundamental parameters of superconductivity (such as the lower H_{c1} and upper H_{c2} critical fields (see review [4])) and the dynamics of magnetic vortices (see reviews [5–7]), the magnetoresistance measurements occupy a relatively modest place in investigations of "vortex matter" in high-temperature superconductors (as compared, for example, with measurements of critical currents). The main advantage of magnetoresistance investigations (measurements of V–H characteristics at I = const) over investigations of critical currents (measurements of V–I characteristics at H = const) is the possibility of performing measurements at very small currents $I \ll I_c$ (where I_c is the critical current), i.e., when the magnetic fields induced by transport currents are relatively weak.

Analysis of the experimental data on the magnetoresistance of high-temperature superconductors is rather complicated, because the orientational dependence $\frac{\Delta\rho}{\rho}(H)$ is described by a fourth-rank tensor [8]. For this reason, when interpreting the experimental dependences $\frac{\Delta\rho}{\rho}(H, T)$ for granular high-temperature superconductors, the object of investigation is usually treated as a continuous medium consisting of a mixture of superconducting and normal phases [9–13]. In some cases, the effective-medium approximation [14], as applied to granular high-temperature superconductors

in combination with the percolation theory used for solving the problem of charge transfer in a superconducting–normal medium [15], appears to be highly efficient for interpreting the experimental data.

In this work, we investigated the penetration of magnetic vortices into superconducting grains and weak links of the $YBa_2Cu_3O_{7-\delta}$ granular (ceramic) high-temperature superconductor and the evolution of the vortex structure in the magnetic field. For this purpose, we measured the field dependences of the longitudinal (**I** ∥ **H**) and transverse (**I** ⊥ **H**) magnetoresistances $\frac{\Delta\rho}{\rho}(H)$ at T = 77.3 K in the range of magnetic field strengths $0 \le H \le$ ~500 Oe, which covers the critical fields H_{c1J}, H_{c2J}, and H_{c1A}.

2. SAMPLE PREPARATION AND EXPERIMENTAL TECHNIQUE

Samples of the $YBa_2Cu_3O_{\sim 6.95}$ high-temperature superconductor were synthesized according to the standard ceramic technique [16]. For measurements, we used samples 20 × 3 × 2 mm in size. Low-resistance current and potential silver contacts were applied to samples with a conducting silver-based adhesive. The samples were characterized using x-ray diffraction and measurements of the critical temperature T_c of the superconducting transition and the critical currents I_c (T = 77.3 K, H = 0).

The samples prepared had a nearly single-phase composition. According to the x-ray diffraction data, the crystal structure was weakly pronounced and resembled the texture of the (001) basal plane of an orthorhombic lattice [17, 18]. This structure is most likely formed at the stage of uniaxial pressing of the powders prior to the final synthesis stage (sintering in an oxidizing atmosphere). For all samples, the temperature $T_c^{1/2}$ at the midpoint of the superconducting transition range was 92.6 K and the temperature range of the transition was determined to be ΔT_c = 0.4 K. The critical current I_c varied over a rather wide range. Since the critical currents in the samples differed significantly and the resistances $R_{273\,K}$ of the samples in the normal state were also somewhat different (typical values: $\rho_{273\,K} \sim 100$ μΩ cm, $j_c \sim 100$ A/cm^2), we considered the relative currents I/I_c and the relative resistivities $\rho/\rho_{273\,K}$. Running a little ahead, it should be noted that, when the results are presented in this way, the data obtained for different samples appear to be in rather good agreement.

In the experiments, the electrical resistance of the $YBa_2Cu_3O_{\sim 6.95}$ samples was precisely measured at a constant temperature T = 77.3 K as a function of the magnetic field **H**. As was noted above, the measurements were performed for two orientations of the magnetic field **I** ⊥ **H** and **I** ∥ **H**. The distinctive feature of the present work is that the *V–H* characteristics were measured by varying the measuring (transport) current over a wide range ~$0.01 \le I/I_c \le$ ~0.99.

In order to measure the *V–H* characteristics at I = const, we devised a special setup on the basis of an IBM PC 386 computer [2]. The setup consisted of a unit controlling the current I_{sol} of a magnetic field source (a solenoid) and a unit controlling the measuring (transport) current I_{meas} passing through the sample. A Dewar vessel (filled with liquid nitrogen) with a rotation gear (a sample holder) was placed in the solenoid. The angle between the sample and solenoid axes could be specified accurate to within ~2° with the use of the rotation gear.

All the measurements were carried out in automatic mode: at a specified transport current I_{meas}, the solenoid current I_{sol} was gradually increased to a value corresponding to a specified maximum strength of the magnetic field H_{max}. The data obtained in the form of the dependence $R(H)$ at I = const were recorded on computer. [The error in the measurement of the relative magnetoresistance $\partial R/\partial R(H)$ did not exceed 10^{-2}%.] Then, the transport current was switched off, the sample was heated to $T > T_c$, the next value of current I_{meas} was specified, and the measurement cycle was repeated.

3. RESULTS

*3.1. Transverse Magnetoresistance (**I** ⊥ **H**)*

The typical dependences of the transverse magnetoresistance $\Delta\rho/\rho_{273\,K}(H)$ of the $YBa_2Cu_3O_{\sim 6.95}$ high-temperature superconductor on the magnetic field strength in the range $0 \le H \le 500$ Oe at **I** ⊥ **H** are plotted in Fig. 1.

The characteristic features of the dependences $\Delta\rho/\rho_{273\,K}(H)$ are as follows. For all the transport currents used (~$0.01 \le I/I_c \le$ ~0.99), the magnetoresistance arises in sufficiently weak magnetic fields (the corresponding critical field is designated as H^1). A further increase in the field strength leads to an increase in the resistance R. The dependences $\Delta\rho/\rho_{273\,K}(H)$ exhibit pronounced kinks at $H = H^2$, even though it is very difficult to determine the kink positions precisely. In magnetic fields $H_{jump} \gg H^1$, the resistance R increases jumpwise (or, more exactly, over a very narrow range of field strengths H). Note also that the dependences $\Delta\rho/\rho_{273\,K}(H)$ obtained at low densities of the transport current ($I/I_c \ge$ ~0.3) are characterized by maxima at $H > H_{jump}$.

An increase in the transport current I is attended by the following regularities: (i) the total magnetoresistance $\Delta\rho/\rho_{273\,K}$ increases, (ii) the critical field H^1 decreases drastically, (iii) the jump $\Delta\rho_{jump}/\rho_{273\,K}$ in the dependences $\Delta\rho/\rho_{273\,K}(H)$ decreases and then disappears almost completely (see inset to Fig. 1), (iv) the maxima in the dependences $\Delta\rho/\rho_{273\,K}(H)$ are flattened and then disappear completely, and (v) the critical fields H^2 and H_{jump} do not depend on the current to within the experimental error.

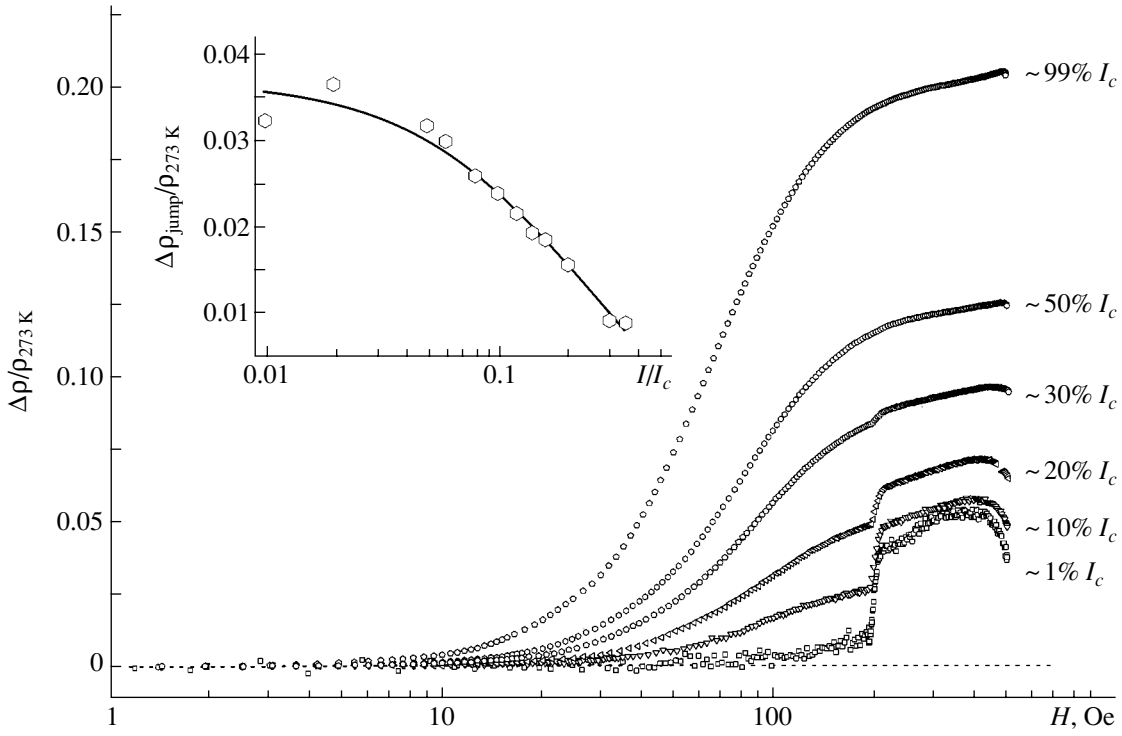

Fig. 1. Dependences of the transverse magnetoresistance of the $YBa_2Cu_3O_{\sim 6.95}$ high-temperature superconductor (**I** ⊥ **H**) on the magnetic field strength at different transport currents. The inset shows the dependence of the magnetoresistance jump on the transport current at $H = H_{jump}$.

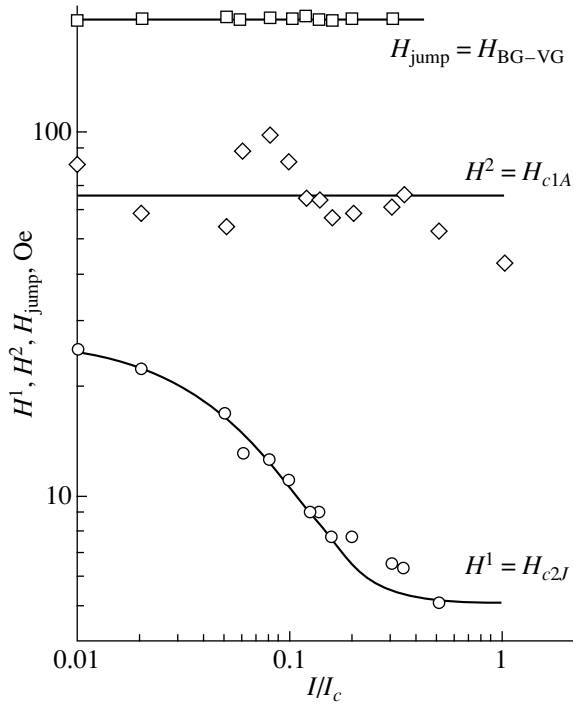

Fig. 2. Dependences of the critical fields H^1 (H_{c2J}), H^2 (H_{c1A}), and H_{jump} (H_{BG-VG}) on the transport current for the $YBa_2Cu_3O_{\sim 6.95}$ high-temperature superconductor. Transverse magnetoresistance (**I** ⊥ **H**).

The corresponding *I–H* phase diagram is depicted in Fig. 2.

*3.2. Longitudinal Magnetoresistance (**I** ∥ **H**)*

The evolution of the dependence of the longitudinal magnetoresistance $\Delta\rho/\rho_{273\,K}(H)$ at **I** ∥ **H** on the magnetic field strength for the $YBa_2Cu_3O_{\sim 6.95}$ high-temperature superconductor with a variation in the transport current is shown in Fig. 3.

Although the dependences $\Delta\rho/\rho_{273\,K}(H)$ for the longitudinal magnetoresistance are qualitatively similar to those depicted in Fig. 1, there are significant quantitative differences:

(i) On the whole, the magnetoresistance at **I** ∥ **H** is slightly less than that at **I** ⊥ **H**.

(ii) The critical fields H^1 at **I** ∥ **H** are somewhat stronger than those at **I** ⊥ **H**.

(iii) The jumps in the dependences $\Delta\rho/\rho_{273\,K}(H)$ in fields H_{jump} at **I** ∥ **H** are considerably less than those at **I** ⊥ **H**.

(iv) As the transport current increases, the magnetoresistance jump in the field H_{jump} at **I** ∥ **H** increases (see inset to Fig. 3) rather than decreases, as is the case with **I** ⊥ **H**. For $I/I_c > \sim 0.4$, no jumps are observed in the dependences $\Delta\rho/\rho_{273\,K}(H)$.

(v) The dependences $\Delta\rho/\rho_{273\,K}(H)$ exhibit no maxima over the entire range of transport currents *I*.

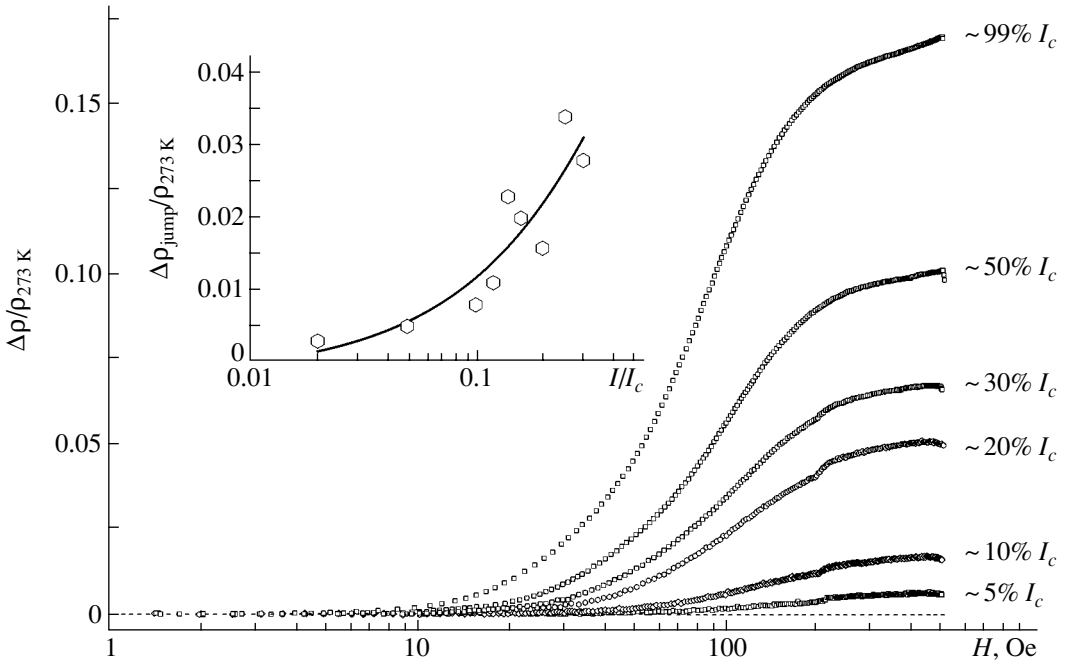

Fig. 3. Dependences of the longitudinal magnetoresistance of the $YBa_2Cu_3O_{\sim 6.95}$ high-temperature superconductor (**I** ∥ **H**) on the magnetic field strength at different transport currents. The inset shows the dependence of the magnetoresistance jump on the transport current at $H = H_{jump}$.

As in the case when **I** ⊥ **H**, the critical fields H^2 and H_{jump} at **I** ∥ **H** do not depend on the transport current. Moreover, the critical fields H^2 and H_{jump} at **I** ⊥ **H** and **I** ∥ **H** coincide to within the limits of experimental error.

The corresponding *I–H* phase diagram is depicted in Fig. 4.

4. DISCUSSION

We will discuss the following experimental results obtained in this work:

(1) the appearance of the magnetoresistance of the $YBa_2Cu_3O_{7-\delta}$ ceramic high-temperature superconductors in the vicinity of the critical fields H^1,

(2) the dependence of the critical field H^1 on the density of the transport current,

(3) the orientational dependence of the critical field H^1,

(4) the appearance of anomalies in the field dependences of the magnetoresistance in the vicinity of the critical fields H^2, and

(5) the appearance of magnetoresistance jumps in magnetic fields H_{jump} and the dependence of these jumps on the density of the transport current and on the mutual orientation of the vectors **H** and **I**.

4.1. Magnetoresistance in the Vicinity of the Critical Fields H_{c2J}

Judging from the critical fields H^1, which are of the order of 20 Oe at the lowest densities of the transport current (Figs. 2, 4), the appearance of nonzero magnetoresistance of the $YBa_2Cu_3O_{7-\delta}$ ceramic high-temperature superconductors cannot be attributed to the onset of the penetration of the magnetic field into weak links, because the critical fields H_{c1J} are very weak at liquid-nitrogen temperature (see, for example, [3, 19]). Note that, in measurements at considerably lower temperatures [20] (when the critical fields H_{c1J} are substantially stronger), the magnetoresistance of the $YBa_2Cu_3O_{7-\delta}$ high-temperature superconductors in weak magnetic fields remained zero.

On the other hand, the critical fields H^1 determined for weak transport currents I are rather close to the critical fields H_{c2J} for complete penetration of the magnetic flux into weak links in the $YBa_2Cu_3O_{7-\delta}$ high-temperature superconductors according to the data obtained by magnetic (and other) methods [3, 21, 22]. Thus, there are strong grounds to believe that $H^1 \equiv H_{c2J}$.

4.2. Dependence of the Critical Field H_{c2J} on the Transport Current

The considerable decrease observed in the upper critical fields H_{c2J} of weak links and the increase in the magnetoresistance with an increase in the transport current I (Figs. 1–4) are obviously associated with the transition of weak links to the resistive state due to the elec-

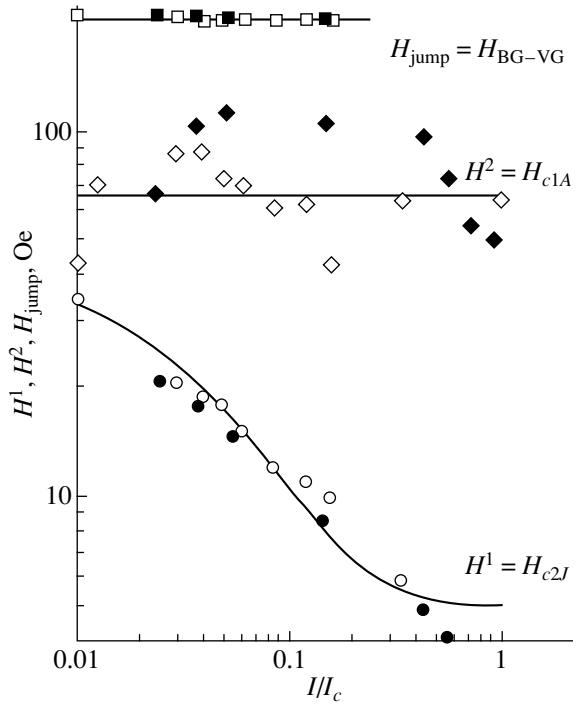

Fig. 4. Dependences of the critical fields H^1 (H_{c2J}), H^2 (H_{c1A}), and H_{jump} (H_{BG-VG}) on the transport current for the $YBa_2Cu_3O_{\sim 6.95}$ high-temperature superconductor. Longitudinal magnetoresistance (**I** || **H**). Open and closed symbols indicate the experimental data obtained for two samples with different resistances $R_{273\,K}$ and critical currents I_c.

trical current [23]. According to the existing notions [20], the conditions for the transition of an individual weak link to the resistive state are completely determined by the local magnetic field H_{local} and the local current density j_{local}. The local magnetic field H_{local} is a superposition of the demagnetizing fields H_{demagn} induced by adjacent superconducting grains and the external magnetic field H_{ext} and can be substantially stronger than the external field.

The dependence of the local current density on the local magnetic field strength can be written in the form [20]

$$j_{local} = j_{local,\,0}\frac{H_0}{\pi H_{local}}, \qquad (1)$$

where $j_{local,\,0}$ is the local current density in the absence of a magnetic field and H_0 is a parameter dependent on the microstructure of a granular superconductor.

It is obvious that we have the equality $H_{local} = H_{c2J}$. In this case, from relationship (1), we obtain

$$H_{c2J}(j_{local}) = H_0\frac{j_{local,\,0}}{\pi j_{local}}. \qquad (2)$$

On the whole, the behavior of the dependences $H_{c2J}(I)$, namely, a sharp decrease in the critical field with an increase in the transport current (Figs. 2, 4), is in agreement with the results of solving Eq. (2). The deviation from the hyperbolic dependence is most likely associated with the fact that the condition $I \sim j_{local}$ providing this dependence can be satisfied only for a normal distribution of local current densities in $YBa_2Cu_3O_{7-\delta}$ ceramic samples, whereas the distribution of local currents in ceramic materials according to [24] is described by a power function.

4.3. Orientational Dependence of the Critical Field H_{c2J}

The orientational dependence of the critical field H_{c2J}, i.e., $H_{c2J}(\mathbf{I} \perp \mathbf{H}) \neq H_{c2J}(\mathbf{I} \parallel \mathbf{H})$ (Figs. 2, 4), can be caused by a number of factors. These include a substantial difference in the demagnetizing fields for different experimental geometries (it is well known that these fields for ceramic high-temperature superconductors can be taken into account quantitatively only in the simplest cases [25]), a significant difference between the longitudinal and transverse sizes of grains in $YBa_2Cu_3O_{7-\delta}$ ceramic samples, the presence of a texture, etc.

It seems likely that the anisotropy of the critical fields H_{c2J} in weak links is predominantly governed by the crystallographic texture (i.e., the different orientation of the magnetic vector **H** with respect to weak links), the difference in the critical parameters of weak links depending on their orientation relative to superconducting grains ("the hierarchy of weak links" [3]), the orientational dependence of the current density j_{local}, etc. In order to reveal the contributions of different factors to the anisotropy of the critical fields H_{c2J}, it is necessary to measure the magnetoresistance of the $YBa_2Cu_3O_{7-\delta}$ high-temperature superconductor at different angles between the vectors **I** and **H** (such measurements are currently being performed at our laboratory).

4.4. Anomalies of Magnetoresistance in the Vicinity of the Critical Fields H_{c1A}

A change in the behavior of the dependences $\Delta\rho/\rho_{273\,K}(H)$ in the vicinity of the critical fields H^2, namely, the appearance of kinks in the dependences above which the curves tend to flatten out (Figs. 1, 3), indicates that a new magnetoresistance mechanism comes into play. Most likely, this mechanism is associated with the onset of the penetration of the magnetic flux into $YBa_2Cu_3O_{7-\delta}$ superconducting grains, i.e., the formation of Abrikosov vortices in the superconductor [26]. To put it differently, we can make the inference that $H^2 \equiv H_{c1A}$.

It is important that the critical fields H_{c1A} depend neither on the transport current I nor on the mutual orientation of the vectors **I** and **H** (Figs. 2, 4). Note that, although the kink positions in the dependences $\Delta\rho/\rho_{273\,K}(H)$ are determined with low accuracy, the above inference is significant statistically. On the other

hand, as is well known, direct measurements of the critical field H_{c1A} for $YBa_2Cu_3O_{7-\delta}$ high-temperature superconductors demonstrate that this field is characterized by a strong anisotropy [27–30]. It is evident that, in measurements of the magnetoresistance, the kinks in the dependence $\Delta\rho/\rho_{273\,K}(H)$ correspond to the minimum critical fields H_{c1A}, i.e., the weaker critical fields H_{c1A}^{ab} of superconducting grains in the **ab** basal plane of the orthorhombic lattice. Recall that, when the critical field H_{c1A} is measured from a change in the critical current I_c, the field H_{c1A}^{ab} also corresponds to the point at which the dependence $I_c(H)$ begins to deviate from I_c = max [2, 18, 21, 31]. It should also be noted that the critical field H_{c1A}^{ab} obtained in the present work is very close to the field determined in our earlier works [2, 18] for $YBa_2Cu_3O_{7-\delta}$ high-temperature superconductors similar to those studied in this work.

4.5. Magnetoresistance Jumps

The anomalies (apparently revealed for the first time) in the field dependences of the magnetoresistance $\Delta\rho/\rho_{273\,K}(H)$ for the $YBa_2Cu_3O_{7-\delta}$ ceramic high-temperature superconductors at $H_{jump} > H_{c1A}$ (i.e., a jumpwise change in the transport properties in magnetic fields) primarily suggest that a first-order phase transition is induced by the magnetic field. Note that, in the I/I_c range corresponding to these jumps, the maxima in the dependences $\Delta\rho/\rho_{273\,K}(H)$ are observed in fields $H > H_{jump}$ at least for the orientation $\mathbf{I} \perp \mathbf{H}$ (Fig. 1). It seems likely that both of the aforementioned effects are associated with the change in the vortex structure in superconducting grains. It should be remembered that these effects are observed for ceramic samples with a defect crystal lattice and, at $H_{jump} > H_{c1A}$, with an imperfect vortex lattice (the Bragg glass (BG) state [32–35]).

It can be assumed that the magnetoresistance jumps for the $YBa_2Cu_3O_{7-\delta}$ ceramic high-temperature superconductors in weak magnetic fields are caused by the change in the vortex structure, namely, by the melting of a vortex lattice or the first-order transition from a Bragg glass phase to a vortex glass (VG) phase (BG–VG transition) [36–39]. The change in the kinetic properties upon BG–VG transition (a jumpwise decrease in the critical current I_c along the **c** axis and a drastic increase in the critical current I_c in the **ab** basal plane) was predicted by Hernández and Domínguez [36]. The critical magnetic fields for the melting of a vortex lattice in ceramic high-temperature superconductors $Bi_2Sr_2CaCu_2O_{8\pm\delta}$ [37] and $HgBa_2CuO_{4\pm\delta}$ [40] are close to the critical fields H_{jump} obtained in the present work for the $YBa_2Cu_3O_{7-\delta}$ high-temperature superconductor. The appearance of a maximum of the magnetoresistance (transforming into a plateau at high densities of the transport current) in the dependences $\Delta\rho/\rho_{273\,K}(H)$ at $H > H_{jump}$ can be associated with the decrease in the pinning force due to the formation of the vortex glass phase.

Therefore, we can draw the inference that $H_{jump} \equiv H_{BG-VG}$.

The behavior of the field dependences of the magnetoresistance upon the BG–VG first-order phase transition is consistent with the predictions made from theory in [36] (see insets to Figs. 1, 3). Note that the lines of the BG–VG phase transitions in the *I–H* diagrams terminate at $I/I_c > \sim 0.3$–0.4 (Figs. 2, 4) and the magnetoresistance jumps at $\mathbf{I} \perp \mathbf{H}$ decrease considerably with an increase in the ratio I/I_c. These circumstances show that the differences between the Bragg glass and vortex glass phases become smoother with an increase in the current and that the BG–VG phase transition is completed at a critical point.

REFERENCES

1. V. M. Arzhavitin, N. N. Efimova, M. B. Ustimenkova, and V. A. Finkel', Fiz. Tverd. Tela (St. Petersburg) **42** (8), 1361 (2000) [Phys. Solid State **42**, 1398 (2000)].
2. V. A. Finkel' and V. V. Derevyanko, Fiz. Nizk. Temp. **26** (2), 128 (2000) [Low Temp. Phys. **26**, 92 (2000)].
3. N. N. Efimova, Yu. A. Popkov, M. B. Ustimenkova, and V. A. Finkel', Fiz. Nizk. Temp. **20** (4), 343 (1994) [Low Temp. Phys. **20**, 273 (1994)].
4. E. Z. Meĭlikhov and V. G. Shapiro, Sverkhprovodimost: Fiz., Khim., Tekh. **4**, 1437 (1991).
5. G. Blatter, M. V. Feigel'man, V. D. Geshkenbein, A. I. Larkin, and V. M. Vinokur, Rev. Mod. Phys. **66**, 1125 (1994).
6. E. H. Brandt, Rep. Prog. Phys. **58**, 1465 (1995).
7. Y. Yeshurun, A. Shaulov, and A. P. Malozemoff, Rev. Mod. Phys. **68**, 911 (1996).
8. H. Kontani, J. Phys. Soc. Jpn. **70** (7), 1873 (2001); Phys. Rev. Lett. **89** (23), 237 003 (2002).
9. C. A. M. dos Santos and A. J. S. Machado, Physica C (Amsterdam) **354**, 213 (2001).
10. G. L. Olivera, C. A. M. dos Santos, C. Y. Shigue, and A. J. S. Machado, IEEE Trans. Appl. Supercond. **12** (1), 1272 (2002).
11. Y. Schlesinger, L. Burlachkov, and E. Mogilko, Physica C (Amsterdam) **307**, 291 (1998).
12. E. Mogilko, L. Burlachkov, Y. M. Strelniker, Y. Schlesinger, and S. Havlin, Physica B (Amsterdam) **329–333**, 150 (2003).
13. L. Burlachkov, E. Mogilko, Y. Schlesinger, Y. M. Strelniker, and S. Havlin, Phys. Rev. B **67**, 104509 (2003).
14. R. Juretschke, R. Landauer, and J. A. Swanson, J. Appl. Phys. **27**, 838 (1956).
15. J. P. Clerc, G. Giraud, J. M. Laugier, and J. M. Luck, Adv. Phys. **39**, 191 (1990).
16. V. A. Finkel', V. M. Arzhavitin, A. A. Blinkin, V. V. Derevyanko, and Yu. Yu. Razdovskii, Physica C (Amsterdam) **235–240**, 303 (1994).
17. A. S. Kapcherin, I. I. Papirov, P. I. Stoev, V. V. Toryanik, V. A. Finkel', V. A. Shkuropatenko, and T. I. Bukharova, Sverkhprovodimost: Fiz., Khim., Tekh. **5**, 113 (1992).

18. V. A. Finkel' and V. V. Toryanik, Funct. Mater. **3**, 190 (1996).
19. C. Y. Lee, L. W. Song, and Y. H. Kao, Physica C (Amsterdam) **191**, 429 (1992).
20. D. Daghero, P. Mazzetti, A. Stepanescu, P. Tura, and A. Masoero, Phys. Rev. B **66**, 184514 (2002).
21. E. Altshuler, S. Garcia, and J. Barroso, Physica C (Amsterdam) **177**, 61 (1991).
22. Q. H. Lam and C. D. Jeffries, Physica C (Amsterdam) **194**, 37 (1992).
23. Y. S. Hascicek and L. B. Testardi, IEEE Trans. Magn. **27** (2), 1186 (1991).
24. E. Z. Meĭlikhov, Usp. Fiz. Nauk **163** (3), 27 (1993) [Phys. Usp. **36**, 129 (1993)].
25. M. N. Kunchur and T. R. Askew, J. Appl. Phys. **84**, 6763 (1998).
26. C. A. M. dos Santos, M. S. da Luz, B. Ferreira, and A. J. S. Machado, Physica C (Amsterdam) **391** (4), 345 (2003).
27. A. F. Hebard, A. T. Fiory, and D. R. Harshman, Phys. Rev. Lett. **62**, 2885 (1989).
28. S. Sridhar, Dong-Ho Wu, and W. Kennedy, Phys. Rev. Lett. **63**, 1873 (1989).
29. L. Krusin-Elbaum, A. P. Malozemoff, Y. Yeshurun, D. C. Cronemeyer, and F. Holtzberg, Phys. Rev. B **39**, 2936 (1989).
30. Ch. Heinzek, Ch. Neumann, and P. Ziemann, Europhys. Lett. **13**, 531 (1990).
31. A. A. Zhukov, D. A. Komarkov, and G. T. Karapetov, Physica B (Amsterdam) **169**, 661 (1991).
32. T. Giamarchi and P. Le Doussal, Phys. Rev. Lett. **72**, 1530 (1994).
33. T. Nattermann and S. Sheidl, Adv. Phys. **49**, 607 (2000).
34. T. Klein, I. Joumard, S. Blanchard, R. Cubitt, T. Giamarchi, and P. Le Doussal, Nature **413**, 404 (2001).
35. D. Domínguez, Phys. Rev. Lett. **82**, 181 (1999).
36. A. D. Hernández and D. Domínguez, cond-mat/0308511, V. 1 (2003).
37. N. Avraham, B. Khaykovich, Y. Myasoedov, M. Rappaport, H. Shtrikman, D. E. Feldman, E. Zeldov, T. Tamegai, P. H. Kes, M. Li, M. Konczykowski, and K. van der Beek, Physica C (Amsterdam) **369**, 36 (2002).
38. A. van Otterlo, R. T. Scaletter, and G. T. Zimányi, Phys. Rev. Lett. **81**, 1497 (1998).
39. C. J. Olson, C. Reichhardt, R. T. Scalettar, G. T. Zimányi, and N. Grønbech-Jensen, Phys. Rev. B **67**, 184523 (2003).
40. D. Stamopoulos and M. Pissas, Phys. Rev. B **65**, 134524 (2002).

Translated by O. Borovik-Romanova

Physics of the Solid State, Vol. 46, No. 10, 2004, pp. 1805–1809. Translated from Fizika Tverdogo Tela, Vol. 46, No. 10, 2004, pp. 1746–1750.

SEMICONDUCTORS AND DIELECTRICS

Bound-Exciton Cathodoluminescence in ZnSe Crystals and Two-Phonon Resonance

A. A. Klyukanov*, K. D. Sushkevich*, M. V. Chukichev, and V. Gurau***

**Moldova State University, ul. Mateevicha 60, Chisinau, MD-2009 Moldova*

e-mail: klukanov@cinf.usm.md

***Moscow State University, Vorob'evy gory, Moscow, 119899 Russia*

Received August 11, 2003

Abstract—A study has been made of the cathodoluminescence of ZnSe crystals annealed in vacuum [ZnSe(Vac)], in vacuum and, subsequently, in antimony melt [(ZnSe(Vac)(Sb)], or in a zinc melt with subsequent annealing in antimony [ZnSe(Zn)(Sb)]. The emission of all samples contained the $I_1^{s,d}$–nLO series. The LO-phonon replicas of the emission line I_1^s observed in ZnSe(Vac) samples are accompanied by single-plasmon satellites. The plasmon energy determining the replica separation is $\hbar\omega_p \cong 10$ meV. The emission lines of ZnSe(Zn)(Sb) samples have the smallest half-width. We report the first observation of anomalous broadening of the zero-phonon line I_1^s in ZnSe(Vac) samples caused by a high zinc vacancy content. A theory on the shape of the emission spectrum under two-phonon resonance is developed including bound-exciton interaction with mixed plasmon–phonon vibrational modes. It is shown that the splitting of the I_1^d line at $T \cong 2$ K may originate from resonance exciton–phonon interaction between exciton–impurity complexes. © *2004 MAIK "Nauka/Interperiodica".*

1. INTRODUCTION

The emission line I_1^d in ZnSe crystals forms in recombination of an exciton bound to a neutral acceptor, which may be either a zinc vacancy (V_{Zn}) or a copper atom substituting for zinc (Cu_{Zn}) [1–7]. Because annealing ZnSe crystals in liquid zinc makes the I_1^d line disappear and annealing in vacuum brings about an increase in Zn vacancy concentration and, accordingly, an increase in the intensity of this line, the close relation of Zn vacancies to the I_1^d line is unquestionable. As for the involvement of copper in the formation of the I_1^d line, we believe this problem remains open. The high-purity ZnSe crystals studied in [1] were first annealed in saturated selenium vapor (which led to the formation of V_{Zn}) and then doped with copper by diffusion in argon vapor. It was natural to expect that after this procedure the emission spectrum would contain the I_1^d line due to V_{Zn}, and this was corroborated by experiment [1]. Subsequent annealing in zinc should have excluded the effect of V_{Zn} on the spectrum. Because the I_1^d–nLO line remained in the emission spectrum after low-temperature annealing, it was decided in [1] that this could be only the Cu_{Zn}-based exciton–impurity complex series. In our opinion, the experimental data from [1] can also be explained by an incomplete disappearance of zinc vacancies in such low-temperature annealing.

Another argument for the existence of two centers based on V_{Zn} and Cu_{Zn} is the shift of the I_1^d line to shorter wavelengths with increasing Cu concentration [1]. However, I_1^d was observed in [4] to shift to longer wavelengths after ZnSe crystals were doped by copper. As in [1], this shift was accounted for by the existence of two lines originating from two different complexes based on V_{Zn} and Cu_{Zn}. One sees that shifts of the I_1^d line in opposite directions may be caused by the interaction of a bound exciton with an electron–hole plasma. Indeed, the bound-exciton energy reckoned from the conduction band bottom

$$E_n = \langle n|\hat{H}|n\rangle - \frac{1}{2}\sum_k V_k\left|(\rho_k)_{nn}\right|^2\left\{1 - \frac{\varepsilon_\infty}{\varepsilon(k,0)}\right\} \approx \langle n|\hat{H}|n\rangle - N_+\hbar\omega_+ - N_-\hbar\omega_- \quad (1)$$

depends on the plasma concentration through its dependence on the static-screening factor $1 - \varepsilon_\infty/\varepsilon(k, 0)$. Hence, the position of the I_1^d spectral line can depend on the sample and the excitation level. The Hamilton operator $\hat{H}$ in Eq. (1) is the sum of the Hamilton operator of a free exciton and of its interaction with an impurity center. The other notation here and in what follows is the same as in [8–10].

1063-7834/04/4610-1805$26.00 © 2004 MAIK "Nauka/Interperiodica"

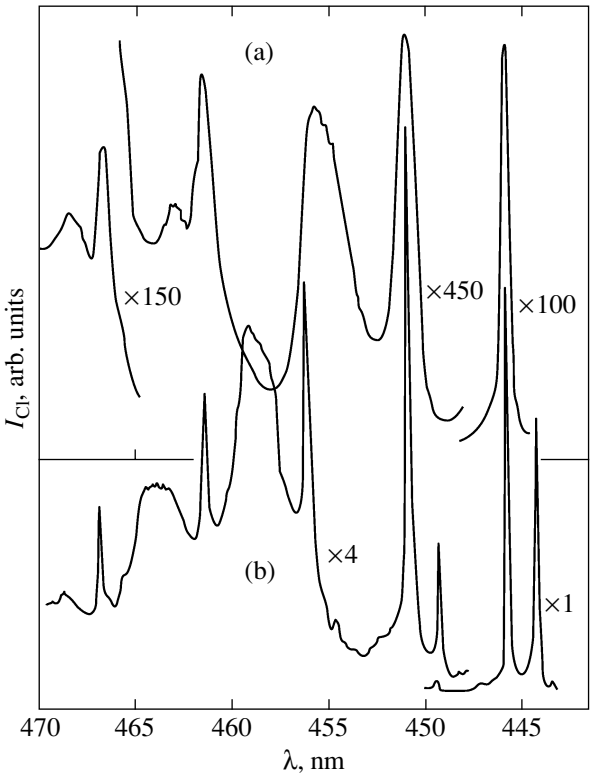

Fig. 1. Cathodoluminescence spectra of ZnSe crystals measured at 4.2 K: (a) ZnSe(Vac) and (b) ZnSe(Zn)(Sb) samples.

The frequency dependence of the spontaneous recombination rate of a bound exciton interacting with $\omega_\pm$ vibrational modes [11] can be written as

$$r(\omega) = r_0\left(1 + \frac{\omega_+}{\omega_g}x\right)\sum_{n=0}^{\infty}\sum_{m=-\infty}^{\infty}\frac{N_+^n}{n!}I_m(z_-)e^{-\beta_+\left(x+n+\frac{1}{2}mb\right)} \times \frac{\gamma_{nm}}{(x+n+bm)^2+\gamma_{nm}^2}. \quad (2)$$

As seen from Eq. (2), at low temperatures, the intensities of phonon replicas obey the Poisson distribution. Our theory [8–10] provides an explanation for many of the fine features observed in experiment. For instance, the I_1^d and I_1^d–LO lines exhibit additional sidebands on the long-wavelength side in some samples [7, 9, 10]. These sidebands are assigned in [7] to the involvement of acoustic phonons in the emission. In other samples, however, no such sidebands are observed. Hence, the totality of the data cannot be explained as due only to the interaction of bound excitons with acoustic phonons. The shape of the emission spectrum calculated using Eq. (2) agrees with experiment only if these sidebands are assumed to be plasmon replicas of the I_1^d and I_1^d–LO lines at low plasma concentrations. In the case where plasmons are not elementary excitations, Coulomb interaction of a bound exciton with plasma in inelastic collisions gives rise to the formation of a sideband on the long-wavelength side of the spectrum.

Based on the deviation of the intensity distribution of I_1^d-line LO-phonon replicas from a Poisson profile at $T = 4.2$ K, we put forward the assumption [9] that there is a new spectral line I_1^s that coincides in position (at plasma concentrations $N \cong 10^{17}$ cm^{-3}) with the second LO-phonon replica of the I_1^d line. It might seem that the deviation from the Poisson distribution could be related to the presence of two centers, V_{Zn} and Cu_{Zn} (which are responsible for the I_1^d line), if the coupling with LO phonons is considered weak for one center and strong for the other. This assumption does not, however, find experimental support, because either in copper-doped or in pure crystals the first LO-phonon replica should have been stronger than the I_1^d line, which is not observed in practice [1, 4]. Direct experimental evidence for the existence of the I_1^s–*n*LO–*m*P1 series was furnished in [10]. At low electron–hole plasma concentrations ($\leq 10^{16}$ cm^{-3}), superposition of the I_1^s and I_1^d–2LO lines is fairly obvious [10, Fig. 1]. We consider here new experimental features in the $I_1^{s,d}$–*n*LO series and analyze the conditions fostering resonance interaction of excitonic complexes.

2. EXPERIMENTAL RESULTS AND DISCUSSION

Cathodoluminescence in ZnSe crystals was excited at $T = 4.2$ K by an electron beam with an energy of 40 keV. The pulse repetition frequency was 200 Hz, and the pulse duration was 40 μs. The radiation was analyzed with a DFS-12 monochromator in the wavelength range 400–800 nm. ZnSe crystals grown from the vapor phase were first annealed in vacuum [ZnSe(Vac)] (their emission spectrum is shown in Fig. 1a) and then in an antimony melt [ZnSe(Vac)(Sb)]. We also studied ZnSe(Zn)(Sb) samples, the spectrum of one of which (Fig. 1b) consists of $I_1^{s,d}$ and I_1^x lines and their LO-phonon replicas. The Poisson distribution for phonon satellite intensities in the I_1^x–*n*LO series is met with $N_{LO} \cong 0.1$. As seen from Fig. 1b, the dominant spectral line is I_1^d, for which the average number of LO phonons per photon is $N_{LO} \cong 0.25$, if N_{LO} is derived from the intensity ratio of the first I_1^d–LO replica to the zero-phonon I_1^d line. In the region of the second LO-phonon replica, however, the Poisson distribution breaks down. At $\lambda = 456.2$ nm, the I_1^s and I_1^d–2LO lines become superposed. For the I_1^s–*n*LO series, the constant $N_{LO} \cong 1.5$. The emission spectrum of ZnSe(Vac)(Sb) crystals is similar in shape to the one presented in Fig. 1b. The most significant distinctions are that the

dominant line here is I_1^x and the lines of the $I_1^{s,d}$–nLO series have a larger half-width and are somewhat weaker in intensity. For the I_1^s–nLO series measured in ZnSe(Vac)(Sb) samples, the constant $N_{LO} \cong 1$. In both cases, the I_1^s–nLO series turns out to be superposed, as is evident from Fig. 1b, on the donor–acceptor pair emission band. Spectra of ZnSe(Vac) crystals exhibit substantial differences (Fig. 1a). The I_1^x line is almost not at all seen. The I_1^d line and its first LO-phonon replica are broadened, and a broad structureless band is observed near $\lambda = 455$ nm. Each of the first several LO-phonon replicas of the I_1^s–nLO series ($n = 1, 2, 3, 4$) is accompanied by the first plasmon satellite. The plasmon energy as derived from the line separation is $\hbar\omega_p \cong 10$ meV. The low emission intensity, the absence of the I_1^x line, and the large linewidth in the $I_1^{s,d}$–nLO series should be assigned to strong interaction of the bound exciton with V_{Zn}, whose concentration here is substantially higher than in the ZnSe(Zn)(Sb) samples. The high concentration of the I_1^s centers responsible for the I_1^s–nLO series (we believe these centers to be actually complexes including V_{Zn} and the selenium vacancy [9]) follows from analyzing the emission spectra. As seen from Fig. 1a, the intensity of the I_1^s line is slightly weaker than that of the I_1^d line. The matrix element

$$M_n = \langle n|\delta(\bar{r}_e - \bar{r}_h)|\rangle = \iint \Psi_n^*(\bar{r}_e, \bar{r}_h)\delta(\bar{r}_e - \bar{r}_h)d\bar{r}_e d\bar{r}_h, \quad (3)$$

which determines the probability of finding an electron and a hole within one unit cell, is less for the I_1^s center than for I_1^d, because one of the carriers is localized near the I_1^s center and the other is far away. Hence, the comparatively high intensity of the I_1^s line can be due only to the high concentration of the corresponding centers.

Consider an I_1^s center with a localized exciton and a nearby unoccupied center of the same type, which is separated from the first one by a potential barrier. The exciton tunneling from one center to the other will result in energy level splitting. At high impurity concentrations, the split levels merge to form a miniband similar to the impurity band. Because interaction of a bound exciton with an adjacent center weakens the coupling with the center to which the exciton is bound, the miniband will extend from the level of an isolated center toward the conduction band bottom. Recombination of bound excitons from this miniband broadens the I_1^s emission line. This broadening, rather than being symmetric relative to the I_1^s line, will extend from it toward shorter wavelengths. The electron and the hole residing in bound-exciton states belonging to the miniband have large radii of states, which are approximately equal in magnitude. As a result, the coupling of these excitons with LO phonons and plasmons is weak and the miniband excitons recombine without involving phonons and plasmons in optical transitions. Phonon replicas appear only when excitons of comparatively distant I_1^s centers recombine. It is these features that we do indeed observe in the emission spectrum of vacuum-annealed ZnSe crystals in the wavelength region $\lambda \geq 455$ nm (Fig. 1a).

3. TWO-PHONON BOUND-EXCITON RESONANCE

Excitons bound to a center can interact not only with centers of the same type. Interaction of an exciton bound to an I_1^d center with an empty I_1^s center is, however, of a different resonance character. Indeed, the binding energies of excitons bound to I_1^s and I_1^d centers differ from each other by an amount $\approx 2\hbar\omega_{LO}$. As soon as the distance between the electronic energy levels becomes equal to the energy of one or several vibrational quanta, strong interaction with lattice vibrations characteristic of electron–phonon resonance arises [12–16]. Under resonance pinning conditions [12–15], the perturbation splits the degenerate energy level. In our case, the state of an exciton at the lowest level $E_m = E_1^s$ with two phonons and the state of an exciton at the top level $E_n = E_1^d$ without phonons belong to the same twofold degenerate energy level of the electron–phonon system, which is split by the interaction of the electron with the phonon subsystem. In this case, in addition to the Hamilton operator of the free exciton, its interaction with the I_1^d and I_1^s centers should be included in the Hamilton operator $\hat{H}$. The exciton can be localized near either of these centers. The standard perturbation theory is invalid here, because it yields diverging results. Consider the problem of radiative recombination of bound excitons under resonance conditions, $E_n - E_m - 2\hbar\omega_0 \approx 0$, where the highest plasmon–phonon vibrational mode of frequency ω_+ falls in resonance.

Invoking the calculation technique developed in [8–10], the bound-exciton contribution to the rate of spontaneous emission of light in a semiconductor can be found to be

$$r(\omega) = \frac{4\omega}{3\pi\hbar v_g}\left(\frac{eP_{cv}}{m_0 c}\right)^2 e^{-\frac{\hbar\omega}{k_0 T}} \times \sum_n N_n |M_n|^2 \mathrm{Re}\int_0^\infty e^{i(\omega-\omega_g)t} I_{nn}(t)dt. \quad (4)$$

Here, ω and v_g are the frequency and group velocity of light, respectively; e and m_0 are the electronic charge

and mass; k_0 is the Boltzmann constant, T is the crystal temperature, $\hbar\omega_g = E_g$ is the crystal band-gap width, N_n is the number of bound excitons in the nth quantum state per unit volume of the semiconductor, and n symbolizes the set of quantum numbers of a bound exciton. The generating function of the emission spectrum shape can be written as

$$I_{nn}(t) = \left\langle n \left| \exp\left\{ -\frac{i}{\hbar}\int_0^t \hat{H}(s)ds - \hat{g}(t) \right\} \right| n \right\rangle, \qquad (5)$$

where $|n\rangle = \Psi_n(\bar{r}_e, \bar{r}_h)$ is the bound-exciton wave function and $\hat{H}$ is the bound-exciton Hamilton operator (not containing interaction with lattice vibrations) in the Heisenberg representation, $\hat{H}(s) = e^{\frac{i}{\hbar}\hat{\hat{H}}s}\hat{H}e^{-\frac{i}{\hbar}\hat{\hat{H}}s}$. Interaction with phonons and plasmons leads to retarded self-interaction of the exciton $\hat{g}(t)$ given by

$$\hat{g}(t) = \frac{1}{\pi\hbar}\sum_k V_k \int_0^t ds \int_0^s ds_1 \hat{\rho}_k(s)\hat{\rho}_{-k}(s_1)K(s-s_1), \qquad (6)$$
$$\rho_k = e^{i\mathbf{k}\mathbf{r}_n} - e^{i\mathbf{k}\mathbf{r}_e}.$$

Here, $\mathbf{r}_e$ and $\mathbf{r}_h$ are the position vectors of the electron and the hole, respectively. The frequencies of the vibrational modes of the crystal (including plasma vibrations) with which the exciton interacts are derived from the condition of vanishing of the dielectric function $\varepsilon(k, \Omega)$.

$$K(t) = \int_0^\infty T_\Omega^*(t)\mathrm{Im}\left\{\frac{\varepsilon_\infty}{\varepsilon^*(k,\Omega)}\right\}d\Omega, \qquad (7)$$
$$T_\Omega(t) = n(\Omega)e^{-i\Omega t} + (n(\Omega)+1)e^{i\Omega t}.$$

The state vectors $|n\rangle$ of a bound exciton are eigenfunctions of operator $\hat{\hat{H}}$, and $\tilde{E}_n$ are its eigenvalues. Operator $\hat{\hat{H}}$ differs from operator $\hat{H}$ in the presence of instantaneous interaction mimicking the retarded interaction (6). The parameters of this conventional operator should be determined self-consistently. When calculating the expectation value in Eq. (5), two-phonon processes can be included using the approximation of the second semi-invariant employed in the method of Kubo [17], $\langle e^{\hat{A}}\rangle \approx e^{\langle\hat{A}\rangle + \frac{1}{2}(\langle\hat{A}^2\rangle - \langle\hat{A}\rangle^2)}$. Taking into account resonant two-quanta processes of spontaneous emission of the ω_+ vibrational modes [11], the self-consistent equation for the upper level energy of a bound exciton can be cast as

$$\tilde{E}_n = E_n + \frac{F_{nm}}{\tilde{E}_n - E_m - 2\hbar\omega_+},$$

$$F_{nm} = \left(\frac{C_+}{2}\right)^2 \sum_{k',k} V_k V_{k'} \sum_{l,p} (\rho_k)_{nl}(\rho_{k'})_{lm}$$
$$\times [(\rho_{-k})_{mp}(\rho_{-k'})_{pn} + (\rho_{-k'})_{mp}(\rho_{-k})_{pn}]\frac{1}{\omega_{np}-\omega_+}\frac{1}{\omega_{nl}-\omega_+}. \qquad (8)$$

Here, E_n is the bound-exciton energy defined by Eq. (1), the summation in Eq. (8) is preformed over the states of the bound-exciton discrete spectrum, and the levels n and m are assumed to be in resonance. At low temperatures, the splitting of the lowest level can be neglected. The upper level splits into two sublevels, which can be found [by solving the quadratic equation (8)] to be

$$\tilde{E}_n = \frac{E_n + E_m + 2\hbar\omega}{2} \pm \frac{1}{2}\hbar\tilde{\Omega},$$

$$\hbar\tilde{\Omega} = \left\{(E_n - E_m - 2\hbar\omega_+)^2 + \left(\frac{2}{\hbar}\right)^2 F_{nm}\right\}^{\frac{1}{2}}. \qquad (9)$$

Here, $\tilde{\Omega}$ is the phonon counterpart of the Rabi frequency. The interaction of an exciton with the wave forming in vibrations is a resonant periodic perturbation acting on the exciton subsystem. We thus come to the well-known quantum-mechanical problem [18] in which a periodic perturbation transforms functions Ψ_n and Ψ_m into functions $a_n\Psi_n + a_m\Psi_m$. If at $t = 0$ the exciton was in the state Ψ_n, then the probability for observing it in the state Ψ_m will vary periodically from zero to $\frac{\tilde{\Omega}^2 - \Delta^2}{\tilde{\Omega}^2}$ with a period $2\pi/\tilde{\Omega}$, where $\Delta = \frac{E_n - E_m}{\hbar} - \omega$ is the resonance detuning. The relative intensity of the components of the zero-phonon doublet produced in exciton recombination from the doublet state with energies $\tilde{E}_n$ given by Eq. (9) is defined by the relation $\frac{I_1}{I_2} = \frac{\tilde{\Omega} - \Delta}{\tilde{\Omega} + \Delta}$ and can be either larger or smaller than unity, depending on the magnitude and sign of the resonance detuning Δ. At an exact resonance, we have $\Delta = 0$ and $I_1/I_2 = 1$.

Pinning in a magnetic field is observed by changing Δ through varying the field strength [12–15]. For rare-earth ions, Δ has a fixed value and no pinning is observed. The zero-phonon line exhibits a splitting [16]. In the case of bound excitons, as follows from Eq. (1), the energy E_n depends on the electron–hole

plasma concentration; hence, Δ can be changed by properly varying the pump level. The positions of the doublet components and their relative intensities can vary with plasma concentration irrespective of whether or not the plasma is in equilibrium. Therefore, the splitting pattern will have all the features of pinning. We believe that it is such a doublet structure with different relative component intensities of the I_1^d zero-phonon emission line (a feature characteristic of pinning) that was observed in [1, 7] at temperatures $T \approx 2$ K. The I_1/I_2 ratio in the doublet varied in magnitude from greater than to smaller than unity [1, 7]. At $T = 4.2$ K, however, the structure smoothens out and the resonant exciton–phonon interaction brings about only a broadening of the I_1^d line [4, 9, 10]. If the I_1^d and I_1^s centers are far from one another, so that the wave functions of their bound excitons do not overlap, then $(\rho_k)_{nm} = 0$ and no splitting is observed. The centers closest together provide the major contribution to the splitting of the I_1^d zero-phonon line. If the number of such pairs in the crystal is large enough, splitting will be observable. If the magnitude of the splitting depends strongly on the center separation, splitting of the energy level of the I_1^d center will give rise only to inhomogeneous broadening of the emission line, much like what is seen in Fig. 1a.

We note in conclusion that interaction can involve not only two levels belonging to different centers and separated by an energy equal to an integral multiple of a vibrational quantum but also levels of the same center.

REFERENCES

1. S. Huang, J. Nozne, and K. Igaki, Jpn. J. Appl. Phys. **22** (7), 1420 (1983).
2. P. J. Dean, D. C. Herbert, C. J. Werkhoven, and R. N. Bhargava, Phys. Rev. B **23** (10), 4888 (1981).
3. P. J. Dean, A. P. Pitt, M. S. Skolnick, P. J. Wright, and B. Ceckayne, J. Cryst. Growth **59** (12), 301 (1982).
4. V. Z. Bolboshenko, G. N. Ivanova, I. Kalmykova, I. A. Kasiyan, D. D. Nedeoglo, and B. V. Novikov, Fiz. Tekh. Poluprovodn. (Leningrad) **24** (11), 1929 (1990) [Sov. Phys. Semicond. **24**, 1200 (1990)].
5. H. Roppisher, J. Jacobs, and B. V. Novikov, Phys. Status Solidi A **27** (1), 123 (1975).
6. G. N. Ivanova, D. D. Nedeoglo, B. V. Novikov, and V. G. Talalaev, Fiz. Tverd. Tela (Leningrad) **23** (9), 2693 (1981) [Sov. Phys. Solid State **23**, 1579 (1981)].
7. J. L. Merz, H. Kukimoto, K. Nassau, and J. W. W. Shiever, Phys. Rev. B **6** (2), 545 (1972).
8. A. A. Klyukanov, N. A. Loiko, I. V. Babushkin, and V. Gurau, Proc. SPIE **4748**, 301 (2002); A. A. Klyukanov, N. A. Loiko, and I. V. Babushkin, Laser Phys. **11** (3), 318 (2001).
9. V. S. Vavilov, A. A. Klyukanov, K. D. Sushkevich, M. V. Chukichev, A. Z. Avavdekh, and R. R. Rezvanov, Fiz. Tverd. Tela (St. Petersburg) **41** (7), 1176 (1999) [Phys. Solid State **41**, 1070 (1999)].
10. V. S. Vavilov, A. A. Klyukanov, K. D. Sushkevich, M. V. Chukichev, A. Z. Avavdekh, and R. R. Rezvanov, Fiz. Tverd. Tela (St. Petersburg) **43** (5), 776 (2001) [Phys. Solid State **43**, 808 (2001)].
11. P. M. Platzman and P. A. Wolff, *Waves and Interactions in Solid State Plasmas* (Academic, New York, 1973; Mir, Moscow, 1975).
12. E. J. Johnson and D. M. Larsen, Phys. Rev. Lett. **16** (15), 655 (1966); K. L. Ngai and E. J. Johnson, Phys. Rev. Lett. **29** (24), 1607 (1972).
13. V. I. Ivanov-Omskiĭ and E. M. Sheregiĭ, Fiz. Tverd. Tela (Leningrad) **16** (1), 238 (1974) [Sov. Phys. Solid State **16**, 153 (1974)]; V. I. Golubev, V. I. Ivanov-Omskiĭ, and E. M. Sheregiĭ, Fiz. Tverd. Tela (Leningrad) **17** (1), 185 (1975) [Sov. Phys. Solid State **17**, 108 (1975)].
14. D. H. Dickei, E. J. Johnson, and D. M. Larsen, Phys. Rev. Lett. **18** (10), 539 (1967); K. Nagasaca, Phys. Rev. B **15** (4), 2273 (1977).
15. A. A. Klyukanov, V. N. Gladilin, and C. H. Wu, Ukr. Fiz. Zh. **25** (6), 937 (1980); A. A. Klyukanov, E. P. Pokatilov, V. N. Gladilin, and Tr. H. Wu, Phys. Status Solidi B **87** (1), K159 (1978).
16. Yu. E. Perlin, A. A. Kaminskiĭ, V. N. Enakiĭ, and D. N. Vylegzhanin, Pis'ma Zh. Éksp. Teor. Fiz. **30** (7), 426 (1979) [JETP Lett. **30**, 398 (1979)]; V. N. Enachi, A. Lupei, V. Lupei, C. Presura, and V. E. Ciobu, Proc. SPIE **3405**, 570 (1998).
17. R. Kubo, J. Phys. Soc. Jpn. **17** (7), 1100 (1962).
18. L. D. Landau and E. M. Lifshitz, *Course of Theoretical Physics*, Vol. 3: *Quantum Mechanics: Non-Relativistic Theory*, 3rd ed. (Nauka, Moscow, 1963; Pergamon, Oxford, 1977).

Translated by G. Skrebtsov

Physics of the Solid State, Vol. 46, No. 10, 2004, pp. 1810–1814. Translated from Fizika Tverdogo Tela, Vol. 46, No. 10, 2004, pp. 1751–1755.

SEMICONDUCTORS AND DIELECTRICS

Effect of Current on the Electroluminescence of Defects Produced by High-Temperature Post-Implantation Annealing of Si : (Er,O) Structures in a Chlorine-Containing Environment

A. M. Emel'yanov and E. I. Shek

Ioffe Physicotechnical Institute, Russian Academy of Sciences, Politekhnicheskaya ul. 26, St. Petersburg, 194021 Russia
e-mail: emelyanov@mail.ioffe.ru

Received November 26, 2003

Abstract—The forward-current dependence of defect-related electroluminescence (EL) in silicon structures produced by erbium and oxygen implantation into silicon single crystals with subsequent annealing in a chlorine-containing ambient at 1100°C has been studied. At 80 K, an increase in the current was observed to cause the photon energies corresponding to the maxima of two defect-related EL peaks to increase from 0.807 and 0.87 eV to 0.85 and 0.92 eV, respectively. The increase in the current was also accompanied by an increase in the half-width and intensity of the EL peaks. To explain the observed effects, a model that was proposed earlier for the defect-related EL in plastically deformed silicon is developed further; this model assumes the possible generation of inverse population involving four energy levels. *© 2004 MAIK "Nauka/Interperiodica".*

1. INTRODUCTION

Interest in studies of the luminescence of single-crystal silicon (*c*-Si) stems from both the wide use this material enjoys in semiconductor technology and the potential of the *c*-Si electroluminescence (EL) in optoelectronics. One of the kinds of luminescence observed in silicon is that related to defects in the wavelength region $\lambda \sim 1.2$–1.6 μm [1–11], more specifically, the so-called *D* peaks, which are usually assigned to dislocations and oxygen precipitates present in silicon. The best studied of them are the four *D* luminescence lines (*D*1, *D*2, *D*3, *D*4), which are located at the following energies at sufficiently low temperatures (for instance, ≤80 K) [6]: $E_m \cong 0.807$, 0.87, 0.95, and 0.99 eV, respectively (E_m is the photon energy at the maximum of the wavelength distribution). Such EL and photoluminescence (PL) peaks have been observed, for example, in plastically deformed silicon. Two PL peaks near the positions of the *D*1 and *D*2 lines indicated above were observed in silicon structures obtained by implantation of the rare-earth element Er, followed by annealing in a chlorine-containing ambient (CCA) at 1100°C [3–5, 7]. The positions of the luminescence intensity maxima in such structures not only differ sometimes from those of the *D*1 and *D*2 lines but also depend on the preparation technology [4, 7]. Defect-related PL was not seen if argon was employed in place of CCA. Studies of the Si : Er structures [3–5, 7] have shown that the observed defect PL correlates with the presence of pure edge dislocations.

This communication reports on a continuation of an investigation into the defect-related luminescence in the wavelength interval $\lambda \sim 1.2$–1.6 μm observed in erbium-implanted silicon structures annealed in CCA at 1100°C. In particular, we report here on the first study of the effect of forward current on the defect EL.

2. EXPERIMENTAL TECHNIQUE

Samples needed for the EL studies (samples 1) were prepared in the following way. Erbium ions with energies of 2.0, 1.6, 1.2, and 0.8 MeV were implanted to a dose $D = 1 \times 10^{13}$ cm^{-2} into Czochralski-grown, (100)-oriented, polished *n*-silicon plates with an electrical resistivity of 15 Ω cm. To increase the probability of formation of oxygen-containing defects, oxygen ions were coimplanted (0.28, 0.22, 0.17, 0.11 MeV; $D = 1 \times 10^{14}$ cm^{-2}) into the front face of the plates. To produce optically active centers, the samples were annealed at $T = 1100$°C (for 3 h) in CCA, which was a flow of oxygen with an addition of 1 vol % carbon tetrachloride. Ions of boron (60 keV, $D = 5 \times 10^{15}$ cm^{-2}) and phosphorus (100 keV, $D = 5 \times 10^{15}$ cm^{-2}) were implanted into the front and back faces of the plates, respectively, to produce heavily doped p^+ and n^+ layers. To reduce the density of the defects created by boron and phosphorus implantation, the samples were annealed in CCA at 1000°C for 30 min. Mesa diodes with an operating *p*–*n* junction area of 1.5 mm^2 were prepared by conventional technology involving thermal deposition of aluminum. The EL was excited by square current pulses 3-ms long at a frequency of 33 Hz. The structure luminescence was focused by a lens system onto the entrance slit of an MDR-23 monochromator, with its

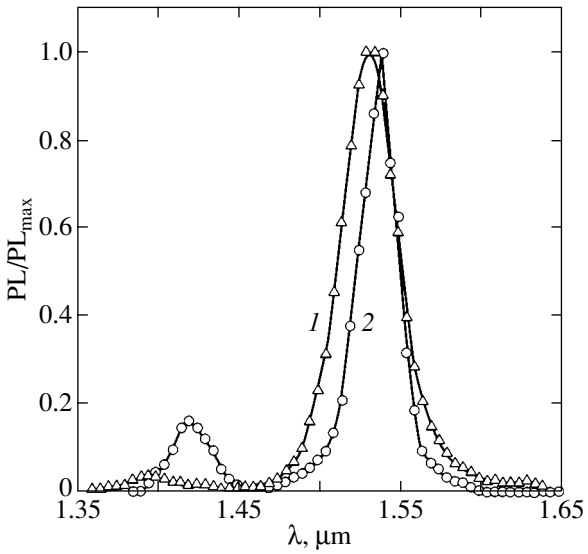

Fig. 1. PL intensity normalized to its maximum level, PL_{max}, vs. wavelength graphs obtained under illumination of sample 2 from (*1*) the front and (*2*) back sides at 80 K.

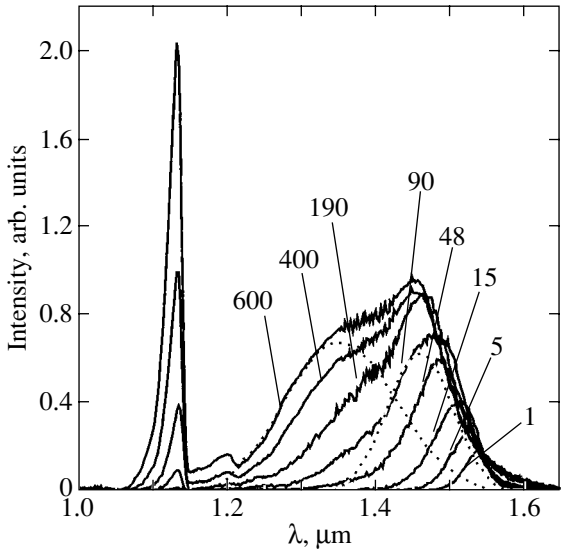

Fig. 2. EL spectra of sample 1 measured at 80 K and different currents (indicated in milliamperes by adjoining figures) (solid curves). Dashed curves are Gaussians fitting the defect-related EL spectrum at a current of 600 mA.

output measured by an uncooled InGaAs diode (7-nm resolution at $\lambda = 1.0$–1.65 μm). In studies of the PL, the samples were illuminated by visible light from a halogen lamp through a band-pass filter. A mechanical chopper interrupted the beam with a frequency of 36 Hz. The radiation power was about 50 mW. The luminescence spectra were corrected for the spectral response of the photodetector and the entire optical train. The samples intended for PL studies described below (samples 2) were prepared as follows. Erbium ions with an energy of 1.0 MeV were implanted to a dose $D = 1 \times 10^{13}$ cm^{-2} into the front face of Czochralski-grown (Cz-Si) (100)-oriented, polished *p*-silicon plates with an electrical resistivity of 20 Ω cm. To obtain optically active centers, annealing at $T = 1100$°C (for 1 h) was employed in CCA. After the annealing, a ~10-μm-thick silicon layer was etched off the back side of the plate. The structural defects produced in sample 2 by ion implantation and annealing were studied earlier and described in [3].

3. EXPERIMENTAL RESULTS AND DISCUSSION

Figure 1 presents PL spectra of sample 2 obtained under illumination from the front (curve *1*) and back (curve *2*) sides at 80 K and normalized to the maximum intensity. The maxima in the PL spectra obtained under sample illumination from the back side lie at 0.8065 and 0.873 eV; i.e., they practically coincide in position with the *D*1 and *D*2 lines quoted in the literature. When illuminated from the front side, the maxima shift toward shorter wavelengths (0.810 and 0.89 eV, respectively) and the peaks broaden from ~25 to ~40 nm. Broadening of the *D*1 peak and the shortward shift of the maximum were already observed in plastically deformed Cz-Si single crystals in [2] and assigned to an increase in the luminescence excitation intensity. When Si : Er structures are illuminated from the back side, the carrier concentration in the defected, optically active layer is substantially smaller than in the case of illumination from the front. The concentration difference is larger, the smaller the exciton diffusion length. The results of this PL study and those reported in [2] suggest the conclusion that, in the Si : Er structures, the above different positions and half-widths of the *D*1 and *D*2 peaks, as well as their dependence on the preparation technology employed [4, 7], may also be associated with different concentrations of carriers responsible for the luminescence and with specific properties of the defects accounting for the formation of these peaks. The results of EL studies made on Si : (Er,O) structures and presented below support this conclusion.

Figure 2 shows EL spectra of sample 1 measured at 80 K and different currents. The spectra contain EL peaks with maxima at wavelengths of ~1.13 and ~1.2 μm, which are presently believed to originate primarily from phonon-mediated radiative recombination of free excitons. For currents ≤15 mA, the EL spectra featured only one defect-related EL peak of Gaussian shape. For higher currents (for instance, ≥90 mA), the defect EL spectrum could be fitted by two Gaussian curves. Decomposition of an experimental EL curve obtained at a current of 600 mA into two Gaussian peaks is illustrated in Fig. 2 by dotted curves. Figure 3 plots the forward-current dependences of the photon energies that correspond to the maxima of the Gaussians describing the experimental spectra of defect-related EL. As is evident from Fig. 3, the structures studied reveal a consid-

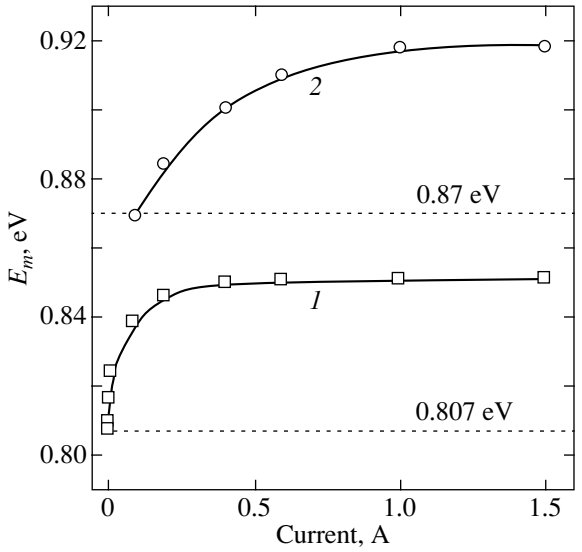

Fig. 3. Forward-current dependence of photon energies E_m corresponding to the maxima of the Gaussians fitting the defect-related EL spectra at 80 K.

erable growth of these photon energies with increasing current. It is only at relatively small currents that the peaks agree with the commonly accepted positions of the *D*1 and *D*2 lines. Figure 4 displays the current dependences of the half-widths *W* of the Gaussian peaks. These curves characterize the EL peak broadening. The variation of the integrated EL intensity of the *D*1 and *D*2 peaks can be characterized by the current dependence of the product of the EL intensity at the Gaussian maximum (EL_m) multiplied by the half-width *W*. Such dependences are depicted in Fig. 5. A comparison of the results of the experiments presented in Figs. 2–5 suggests the following conclusions. Both EL peaks exhibit a monotonic growth of E_m, *W*, and EL_m with increasing current. At high enough currents, the above parameters practically stop growing and the maxima of the two broad Gaussian peaks of the defect EL are positioned at $E_{m1} \cong 0.85$ eV and $E_{m2} \cong 0.92$ eV. These positions differ from the commonly accepted and given above positions of the *D*1 and *D*2 peaks by ~40–50 meV.

When the diode operating temperature was increased to 300 K, the spectral region under study contained, in addition to the interband EL peak, one defect-related EL peak with a maximum at $\lambda \approx 1.59$ μm (Fig. 6). For comparison, Fig. 6 also shows an EL spectrum measured for the same current but at 80 K. The maximum of the defect EL peak coincides in position with that of the *D*1 luminescence peak obtained at 300 K in silicon samples in which dislocations were created by treating the crystal with radiation from a high-power argon laser [10].

Note that the increase in E_m and *W* with increasing luminescence excitation intensity observed in [2] in plastically deformed silicon relates to the *D*1 peaks only (the *D*2 peak was not observed). Furthermore, the shift of the *D*1 peak maximum to shorter wavelengths measured in [2] at 80 K and at a current density of 400 mA/mm^2 is substantially smaller than that obtained in this study. Indeed, the maximum value of E_m for the *D*1 peak quoted in [2] was only ~0.83 eV. Because the current density at which the energy $E_{m1} = 0.85$ eV was reached by us for the *D*1 peak practically coincides with the maximum current density in [2], this difference could be assigned to the minority carrier lifetimes τ_p reached in [2] having been shorter than those attained

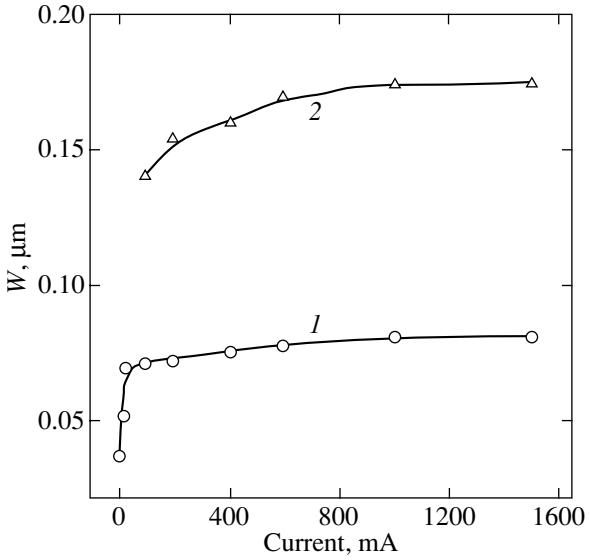

Fig. 4. Forward-current dependence of half-width *W* of the Gaussians fitting the defect-related EL spectra at 80 K. Curve numbers are the same as in Fig. 3.

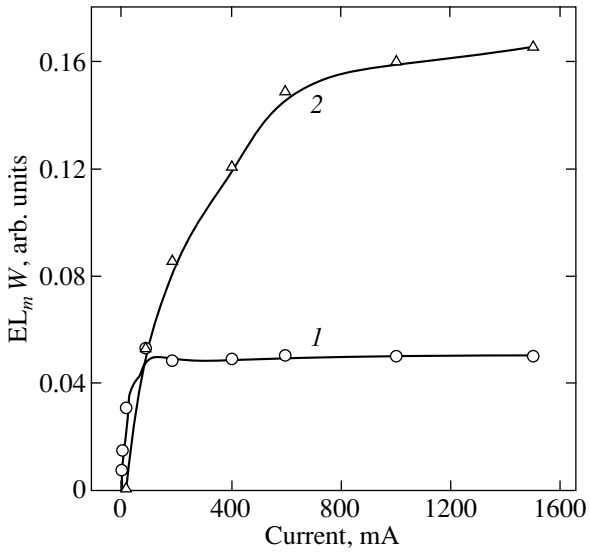

Fig. 5. Product of the EL intensity EL_m at the maximum of the Gaussian curve multiplied by its half-width *W* plotted vs. forward current. Curve numbers are the same as in Fig. 3.

in the present work. Indeed, a decrease in τ_p, with all other conditions being equal, entails a decrease in the density of minority carriers generated by light or injection from the *p–n* junction region. The above reasoning suggests that the smaller shift of the EL peak *D*1 with increasing current and the absence of any mention of observation of the *D*2 peak in the same sample in [2] are due to the fact that the carrier concentrations in the diode base reached in [2] were not as high as those in our samples.

An explanation for the above increase in E_{m1} and *W* with current was put forward in [2]. It builds on the idea that radiative transitions do not occur between the defect band in the silicon band gap and one of the allowed (conduction or valence) bands but rather between defect levels themselves, which form bands in the silicon band gap. At relatively low luminescence excitation intensities, only the levels farthest from the valence band top in the defect band nearest to the valence band are occupied by holes. Therefore, the emitted photons have the lowest energy in this case. One may conceive of a case where a similar effect is caused by electrons filling only the deepest levels in the defect band closest to the conduction band. We note that, at high enough luminescence excitation intensities, the energy level diagram described in [2] is similar to the well-known four-level system in which inverse population can be readily realized. This fact suggests that the class of light-emitting structures considered here might turn out to be among the most promising for achieving the laser effect in silicon. No results obtained in this study argue against the explanation put forward in [2] for the observed effects. At the same time, our present measurements and those reported in [11] permit us to complement these model concepts. The study reported in [11] compared defect PL spectra of *c*-Si plates with different oxygen contents but similar dislocation densities that were plastically deformed in clean conditions. At 4.2 K, the maxima of the *D*1 and *D*2 PL peaks in samples with a lower oxygen concentration (Fz-Si) were found to lie at 0.807 and 0.873 eV, respectively. In samples with a higher oxygen concentration (Cz-Si), the maxima of the *D*1 and *D*2 peaks were measured to lie at 0.825 and 0.877 eV, respectively. The *D*1 and *D*2 peaks in Cz-Si were broader and weaker in intensity than those in Fz-Si. These results suggest that the broadening and shortward shift of the *D*1 and *D*2 peaks are due to the *D*1 and *D*2 centers interacting with oxygen. This results in the defect levels lying at different energies (depending on the extent of this interaction). Therefore, for some defects, the emitted photons gain in energy relative to those in the case of weak defect interaction with oxygen. For other defects, interaction with oxygen can cause the *D*1 and *D*2 defects in silicon not to emit. The above model concepts allow us to conclude that the difference in the effect of current density on the *D*1 and *D*2 luminescence peaks in Si : (Er,O) structures and plastically deformed Cz-Si [2] may be related not only to a difference in τ_p but also to different oxygen contents in the defect region.

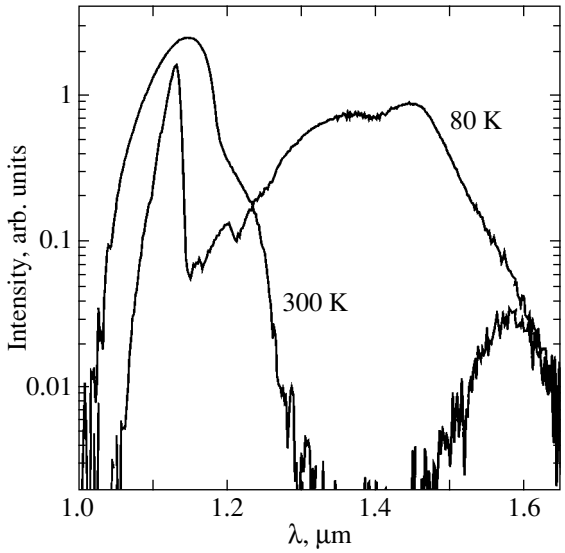

Fig. 6. EL spectra measured at a current of 500 mA at temperatures of 300 and 80 K.

4. CONCLUSIONS

Cz-Si : Er and Cz-Si : (Er,O) structures at ~80 K exhibit a growth of E_m and *W* with increasing luminescence excitation intensity for two defect-related luminescence peaks. At low excitation levels, the values of E_m are ~0.807 and ~0.87 eV, which coincides with the commonly accepted positions of the *D*1 and *D*2 peak maxima. When sufficiently strong currents are passed through the Si : (Er,O) diodes, the maximum values of E_m are ~0.85 and ~0.92 eV. The increase in E_m and *W* is similar to that for the *D*1 peak with increasing luminescence excitation intensity in plastically deformed Cz-Si [2]. This similarity indicates that the defects responsible for the *D*1 luminescence peak in plastically deformed silicon and in the structures studied by us are of the same nature. A comparison of our results with literature data suggests that the large width of the EL spectra may originate from different interaction of the *D*1 and *D*2 defects with oxygen.

ACKNOWLEDGMENTS

The authors are indebted to N.A. Sobolev for organizational help in preparing the samples.

This study was supported in part by the Russian Foundation for Basic Research (project no. 02-02-16374) and INTAS (project no. 2001-0194).

REFERENCES

1. R. Sauer, J. Weber, and J. Stolz, Appl. Phys. A **36**, 1 (1985).

2. V. V. Kveder, E. A. Steinman, S. A. Shevchenko, and H. G. Grimmeiss, Phys. Rev. B **51** (16), 10520 (1995).
3. N. A. Sobolev, O. B. Gusev, E. I. Shek, V. I. Vdovin, T. G. Yugova, and A. M. Emel'yanov, Appl. Phys. Lett. **72** (25), 3326 (1998).
4. N. A. Sobolev, O. B. Gusev, E. I. Shek, V. I. Vdovin, T. G. Yugova, and A. M. Emel'yanov, J. Lumin. **80**, 357 (1998).
5. N. A. Sobolev, E. I. Shek, A. M. Emel'yanov, V. I. Vdovin, and T. G. Yugova, Fiz. Tekh. Poluprovodn. (St. Petersburg) **33** (6), 656 (1999) [Semiconductors **33**, 610 (1999)].
6. S. Pizzini, M. Guzzi, E. Grilli, and G. Borionetti, J. Phys.: Condens. Matter **12**, 10131 (2000).
7. N. A. Sobolev, A. M. Emel'yanov, E. I. Shek, V. I. Vdovin, T. G. Yugova, and S. Pizzini, J. Phys.: Condens. Matter **14**, 13241 (2002).
8. S. A. Shevchenko and A. N. Izotov, Fiz. Tverd. Tela (St. Petersburg) **45** (2), 248 (2003) [Phys. Solid State **45**, 259 (2003)].
9. S. Pizzini, E. Leoni, S. Binetti, M. Acciarri, A. Le Donne, and B. Pichaud, in *Proceedings of 10th International Autumn Meeting on Gadest 2003* (Germany, 2003), p. 273.
10. E. Ö. Sveinbjörnsson and J. Weber, Appl. Phys. Lett. **69** (18), 2686 (1996).
11. M. Acciarri, S. Binetti, O. V. Feklisova, E. A. Steinman, and E. B. Yakimov, in *Proceedings of 10th International Autumn Meeting on Gadest 2003* (Germany, 2003), p. 453.

Translated by G. Skrebtsov

Physics of the Solid State, Vol. 46, No. 10, 2004, pp. 1815–1821. Translated from Fizika Tverdogo Tela, Vol. 46, No. 10, 2004, pp. 1756–1762.

SEMICONDUCTORS AND DIELECTRICS

Amplitude-Phase Reflectance Spectra of Amorphous Silicon–Based Bragg Structures

V. G. Golubev, A. A. Dukin, A. V. Medvedev, A. B. Pevtsov, A. V. Sel'kin, and N. A. Feoktistov

Ioffe Physicotechnical Institute, Russian Academy of Sciences, Politekhnicheskaya ul. 26, St. Petersburg, 194021 Russia

e-mail: dookin@gvg.ioffe.ru

Received February 9, 2004

Abstract—Amplitude-phase spectra of light reflection from distributed Bragg reflectors and Fabry–Pérot microcavities based on *a*-Si : H/*a*-SiO_x : H thin films have been studied. The frequency dependence of the phase difference between the amplitude *p*- and *s*-light reflection coefficients within the photonic band gap is measured. The phase spectrum exhibits predominantly a monotonic, close-to-linear frequency behavior, except for spectral regions near the stop band edges and near the singularities related to the microcavity eigenmodes. The experimental spectra are compared with theoretical calculations based on the transfer matrix method and approximate analytical relations. A method based on analyzing amplitude-phase reflectance spectra is proposed for structural characterization of multilayer microcavity systems. *© 2004 MAIK "Nauka/Interperiodica".*

1. INTRODUCTION

Propagation of an electromagnetic field in layered periodic media, with which Bragg structures can be classed, is accompanied by a number of optical phenomena of fundamental nature widely used in modern optoelectronics [1]. Of particular interest are solid-state structures made up of distributed Bragg reflectors (DBRs) and an active layer sandwiched between them, the so-called Fabry–Pérot microcavities (MCs). An MC permits controllable quantization of a photon field with a wavelength on the order of the cavity active-region thickness. As the microcavity *Q* factor increases, there can occur a number of novel quantum-electrodynamic effects, in particular, enhancement or suppression of spontaneous emission bands [2, 3] (with the corresponding energy shifts [4]) and Rabi splitting [5, 6]. The MCs have considerable application potential for a new generation of optoelectronics devices, including low-threshold lasers and light-emitting diodes capable of operating in both the visible and IR spectral ranges [7, 8].

While many studies have dealt with the optical properties of MCs, they focused primarily on measuring the energy parameters of the light flux interacting with the structures of interest [9–11]. However, in addition to energy parameters, an electromagnetic wave has phase characteristics, whose measurement offers additional information on the properties of the object under study. When light is reflected from the DBRs present in a microcavity structure, the phase of the reflected wave undergoes a change relative to that of the incident wave because of the specific properties of a periodic system in the spectral region where propagating photonic modes are not excited in a DBR [photonic band gap region (PBG)]. Note that the phase spectrum of the amplitude reflectance is closely related to the geometric and optical parameters of a system, in particular, with the *Q* factor [12].

The importance of spectral ellipsometric studies of MCs and DBRs has been pointed out several times [13–17]. Until recently, however, no systematic studies of amplitude-phase spectra of the reflectance of DBRs and MCs in the PBG region (including a comparison of theory with experiment) had been carried out.

It thus appeared of interest to perform direct experimental measurements of the phase characteristics of light reflection coefficients from both single DBRs and MCs, to work out theoretical approaches for analyzing such systems, and to develop methods for their structural characterization with due account of the specific features of their amplitude-phase spectra.

2. EXPERIMENT

We used multilayer planar systems grown on glass substrates as the objects of our investigation. The samples consisted of alternating *a*-Si : H and *a*-SiO_x : H layers and were made up only of DBRs in one case and of MCs in another. A description of the fabrication technology employed and the results obtained in studies of the intensity reflectance and transmittance spectra of such systems can be found in [18–20].

An important feature of a DBR based on *a*-Si : H and *a*-SiO_x : H thin films is its high optical contrast (ratio of the refractive indices, larger to smaller, of the layers making up a DBR), which is substantially greater than that for structures fabricated from III–V compounds [21]. Therefore, by using amorphous silicon as a base material, one can prepare DBRs with a high reflectance and a large PBG spectral width for a

1063-7834/04/4610-1815$26.00 © 2004 MAIK "Nauka/Interperiodica"

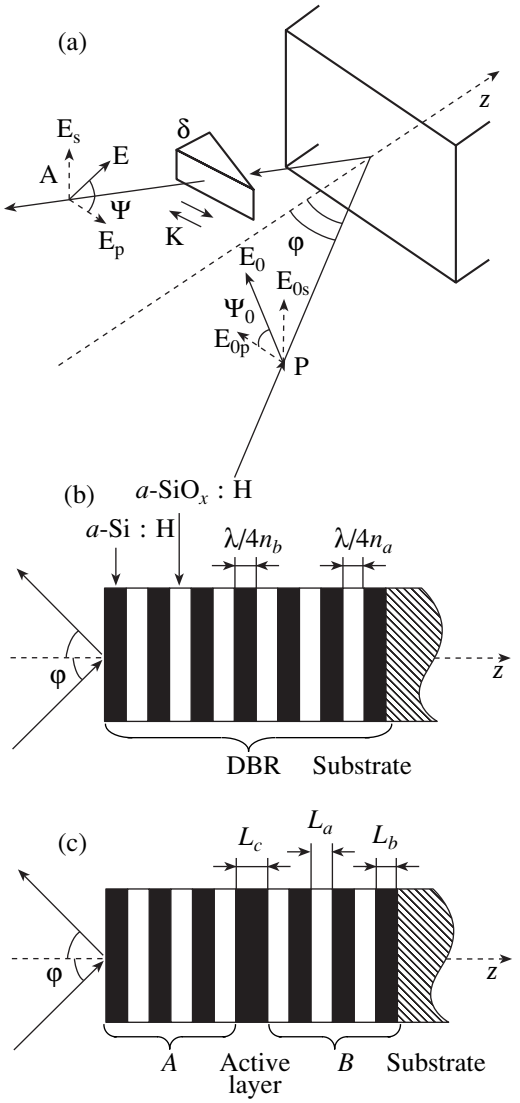

Fig. 1. (a) Geometry of phase measurements in studies of microcavity reflectance spectra. φ is the angle of incidence of light; Ψ_0 and Ψ are the azimuthal angles of polarizer P and analyzer A, respectively, reckoned from the plane of incidence; K is the phase-shifting wedge introducing an additional phase shift δ between the *p* and *s* components of the amplitudes of the reflected light; and the *z* axis is perpendicular to the surface and layers of the structure. (b) Distributed Bragg reflector DBR (schematic). The sample was grown on a glass substrate and consists of 13 quarter-wave *a*-SiO_x : H and *a*-Si : H layers with refraction indices n_a and n_b, respectively. (c) Microcavity (schematic). The sample consists of two DBRs [(*A*) top and (*B*) bottom DBRs made up of six layers each]; L_a and L_b are the thicknesses of quarter-wave DBR layers with low (n_a) and high (n_b) refractive indices, respectively, and L_c is the thickness of the active layer.

comparatively small number of layers in each reflector. This makes the technology of growing of DBRs based on thin *a*-Si : H and *a*-SiO_x : H films more promising than that based on III–V semiconductors.

The DBR reported on here consisted of 13 alternating *a*-Si : H and *a*-SiO_x : H quarter-wave layers. The layer thicknesses were chosen such that the PBG lied completely within the sensitivity band of the photodetector used (InGaAs-based photodiode) and was entirely accessible for measurements. The microcavity structure contained two (top and bottom) DBRs, which sandwiched a half-wave ($\lambda/2n_c$) *a*-Si : H active layer of thickness L_c, with a refractive index $n_c = 3.31$ (Fig. 1). The top (*A*) and bottom (*B*) DBRs are identical and include three pairs of quarter-wave ($\lambda/4n_{a,b}$) layers of *a*-SiO_x : H (thickness L_a, refractive index $n_a = 1.46$) and *a*-Si : H (thickness L_b, refractive index $n_b = 3.31$) each. The values of n_a and n_b were preliminarily measured with an LÉF-3M ellipsometer at a wavelength of 632.8 nm and reduced to the 1.5 μm region, with allowance made for dispersion of the refractive indices of *a*-SiO_x : H and *a*-Si : H films.

The geometric parameters of the structure were monitored interferometrically during its growth, which allowed us to estimate the thickness of individual layers to within about 10%. The microcavity parameters were chosen such that the MC eigenmode under normal incidence of light lied in the region of 1.5 μm, which corresponds to the TELECOM standard for optical fiber communication lines.

The phase measurements were performed using the technique developed by us earlier [22], which allows one to determine the phase difference $\Delta = \Delta^p - \Delta^s$ of complex amplitude reflectances $r^p = |r^p|\exp(i\Delta^p)$ and $r^s = |r^s|\exp(i\Delta^s)$ for the *p*- and *s*-light polarization components, respectively. The frequency response $\Delta(\omega)$ was found using an optical setup (Fig. 1a) that allowed measurement of the intensity reflectance spectra $R_\delta(\Psi_0, \varphi, \Psi)$ under oblique incidence of light at an angle φ to the surface normal (the *z* axis in Fig. 1). Ψ_0 and Ψ are the azimuths of the polarizer (P) and analyzer (A), respectively, reckoned clockwise from the plane of incidence if looking along the direction of light propagation, and δ is an additional controllable phase shift (introduced by the phase-shifting quartz wedge K) between the *p* and *s* components of the electric field amplitudes of reflected light. The output signal from the measuring circuit was proportional to the intensity reflectance, which depends on the actual properties of the structure under study and parameters δ, Ψ_0, and Ψ:

$$R_\delta(\Psi_0, \varphi, \Psi) = \left|r^p \exp(i\delta)\cos(\Psi)\cos(\Psi_0) + r^s \sin(\Psi)\sin(\Psi_0)\right|^2.$$

The $R_\delta(\Psi_0, \varphi, \Psi)$ spectra were obtained at $\Psi_0 = 45°$ in four configurations corresponding to $\Psi = \pm 45°$ and $\delta = 0$ and $-\pi/2$, and the relation [22]

$$\Delta(\omega) = \arctan\frac{R_{-\pi/2}(45°, \varphi, 45°) - R_{-\pi/2}(45°, \varphi, -45°)}{R_0(45°, \varphi, 45°) - R_0(45°, \varphi, -45°)} \quad (1)$$

was used to derive the spectral response of the relative phase $\Delta(\omega)$.

To exclude the effect of dispersion in the refractive indices of the optical components of the setup, the phase-shifting wedge was adjusted during the measurements in order to maintain the values $\delta = 0$ and $-\pi/2$ constant within the spectral interval under study.

3. THEORY

Prior to switching to an analysis of the microcavity structure, let us consider the reflection of light from a single DBR bounded by air on one side and by a semi-infinite substrate on the other. At a given angle of incidence φ (Fig. 1b; the source of radiation is located in air to the left of the DBR), the frequency response of the phase Δ^σ_{DBR} of the amplitude reflectance $r^\sigma_{DBR} = \sqrt{R^\sigma_{DBR}}\exp(i\Delta^\sigma_{DBR})$ for a DBR can be approximated in the spectral region near the PBG center by a linear function [23, 24]:

$$\Delta^\sigma_{DBR} = \alpha^\sigma_{DBR}(\omega - \omega^\sigma_{DBR}), \quad (2)$$

where $\sigma = p, s$ is an index indicating the polarization of incident light; R^σ_{DBR} is the intensity reflectance; α^σ_{DBR} is a coefficient independent of frequency ω; and ω^σ_{DBR} is the phase compensation frequency ($\Delta^\sigma_{DBR} = 0$ for $\omega = \omega^\sigma_{DBR}$), which assumes different values for different polarization states σ in the case of oblique incidence.

The phase difference (relative phase) $\Delta_{DBR} = \Delta^p_{DBR} - \Delta^s_{DBR}$ of the p and s coefficients of reflection from a DBR can also be considered a linear function of frequency in the central part of the PBG:

$$\Delta_{DBR} = \alpha_{DBR}(\omega - \omega_{DBR}), \quad (3)$$

where $\alpha_{DBR} = \alpha^p_{DBR} - \alpha^s_{DBR}$ and ω_{DBR} is the phase compensation frequency for the relative phase ($\Delta_{DBR} = 0$ for $\omega = \omega_{DBR}$).

From direct numerical calculations performed using the transfer matrix method, it follows that $\omega_{DBR} \approx \omega^p_{DBR} \approx \omega^s_{DBR}$ for the DBRs studied here for angles of incidence that are not very large ($\varphi < 40°$). Therefore, we will not differentiate between the phase compensation frequencies ω_{DBR} and ω^σ_{DBR} in our subsequent approximate analytical estimations.

Turning now to an analysis of light reflection from an MC, we note that the amplitude reflectance r^σ_{MC} of the microcavity structure as a whole (Fig. 1c; light strikes the structure from air from the left) can be expressed in terms of the amplitude reflectances $\tilde{r}^\sigma_A$ and r^σ_B for the light incident from the active layer onto the A and B DBRs, respectively, as

$$r^\sigma_{MC} = \frac{r^\sigma_A[1 - r^\sigma_B\Phi^2/\tilde{r}^{\sigma *}_A]}{1 - \tilde{r}^\sigma_A r^\sigma_B\Phi^2}, \quad (4)$$

where r^σ_A is the amplitude reflectance of the A DBR for light falling from the outer medium (air), $\Phi = \exp(ik_0 n_{cz} L_c)$ is the phase delay experienced by the light wave in propagating through an active layer of thickness L_c, $k_0 = \omega/c$, $n_{cz} = \sqrt{n_c^2 - n_x^2}$, $n_x = \sqrt{\varepsilon_V}\sin\varphi$, ε_V is the permittivity of the outer medium, and c is the velocity of light in free space. The tilde indicates that the projection of the wave vector of incident light on the z axis is negative. By virtue of approximations (2), the phase of the MC reflectance in the PBG region (just as in the case of a single DBR) depends almost linearly on frequency, with the exception of a narrow region of resonance singularities associated with the MC eigenmodes.

Using Eqs. (2) and (4), one can easily show that the spectral response of the complex amplitude reflectance of an MC near an eigenmode frequency ω^σ_m can be cast as

$$r^\sigma_{MC} \approx \exp[i\alpha^\sigma_A(\omega - \omega^\sigma_A)]\frac{\omega - (\omega^\sigma_m + iC^\sigma\Gamma^\sigma\sqrt{R^\sigma_{min}}/2)}{\omega - (\omega^\sigma_m - i\Gamma^\sigma/2)}, \quad (5)$$

where Γ^σ is the eigenmode broadening parameter originating from the finite radiative lifetime of the mode because of the limited number of DBR layers and absorption in the MC layers, R^σ_{min} is the intensity reflectance of an MC at the minimum of the resonance reflectance line, $C^\sigma = \mathrm{sgn}(R^\sigma_B - \tilde{R}^\sigma_A|\Phi(\omega^\sigma_m)|^4)$, $R^\sigma_B = |r^\sigma_B|^2$, and $\tilde{R}^\sigma_A = |\tilde{r}^\sigma_A|^2$. The shape of the resonance line given as a dip in the reflectance spectrum allows approximate description by a Lorentzian profile:

$$R^\sigma_{MC} \equiv |r^\sigma_{MC}|^2 \approx 1 - \frac{1 - R^\sigma_{min}}{1 + (x^\sigma)^2}, \quad (6)$$

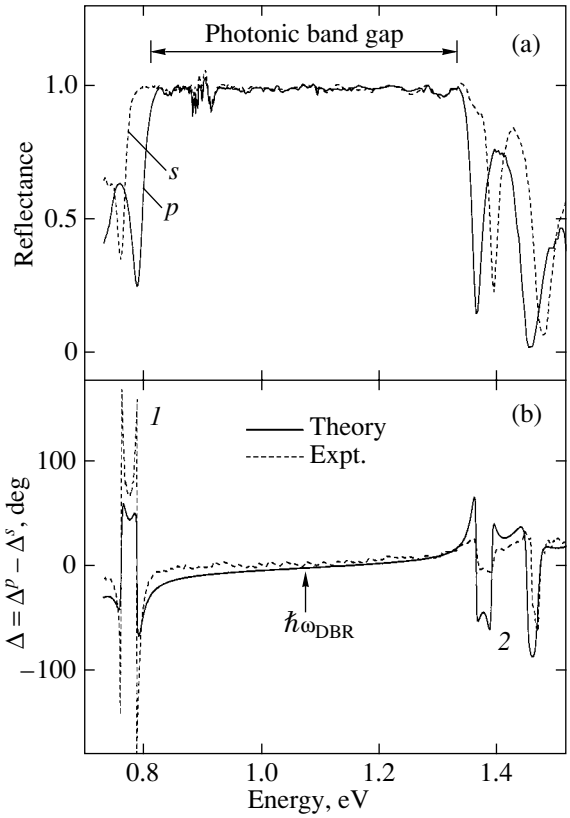

Fig. 2. (a) Experimental spectra of light reflection from a distributed Bragg reflector in the region of the photonic band gap obtained for *p* and *s* polarizations at an angle of incidence φ = 30°. (b) (*1*) Experimental and (*2*) theoretical spectra of the relative phase shift Δ obtained in the region of the photonic band gap for an angle of incidence φ = 30°; ω_{DBR} is the frequency at which the *p* and *s* reflectances coincide in phase.

where $x^\sigma = 2(\omega - \omega_m^\sigma)/\Gamma^\sigma$ and the phase of the amplitude reflectance $\Delta_{MC}^\sigma = \arg r_{MC}^\sigma$ can be written as

$$\Delta_{MC}^\sigma \approx \alpha_A^\sigma(\omega - \omega_A^\sigma) + \arctan\frac{(\sqrt{R_{min}^\sigma}C^\sigma + 1)x^\sigma}{\sqrt{R_{min}^\sigma}C^\sigma - (x^\sigma)^2}. \quad (7)$$

The frequency dependence of Δ_{MC}^σ contains a background linear contribution determined only by the phase of the coefficient of reflection of the *A* DBR. The effect of the *B* DBR manifests itself only in the last term of Eq. (7), which is nonlinear in frequency.

The parameters Γ^σ and R_{min}^σ are determined by the reflectances of the *A* and *B* DBRs and coefficients of extinction in the active layer and also depend on the values of $\tilde{\alpha}_A^\sigma$, α_B^σ, and $\alpha_c \equiv 2L_c\mathrm{Re}(n_{cz})/c$ as

$$\Gamma^\sigma = \frac{1 - \sqrt{\tilde{R}_A^\sigma R_B^\sigma}\left|\Phi(\omega_m^\sigma)\right|^2}{\sqrt[4]{\tilde{R}_A^\sigma R_B^\sigma}\left|\Phi(\omega_m^\sigma)\right|}\frac{2}{(\alpha_c + \tilde{\alpha}_A^\sigma + \alpha_B^\sigma)}, \quad (8)$$

$$R_{min}^\sigma = \left(\frac{\sqrt{\tilde{R}_A^\sigma} - \sqrt{R_B^\sigma}\left|\Phi(\omega_m^\sigma)\right|^2}{1 - \sqrt{\tilde{R}_A^\sigma R_B^\sigma}\left|\Phi(\omega_m^\sigma)\right|^2}\right)^2. \quad (9)$$

If the active-layer material is transparent (which is typical of the MCs under study), one should set $\left|\Phi(\omega_m^\sigma)\right| = 1$ in the above equations.

The relations obtained above reveal clearly which factors affect the formation of resonance singularities in the MC mode states and in what way. A comparison of experimental spectra with calculations made using Eqs. (5)–(9) affords the possibility of placing additional constraints on the DBR parameters that determine the values of the internal reflectances $\tilde{R}_A^\sigma$ and R_B^σ of the structure under study.

In the experiments, one measures the relative phase of reflection from an MC, $\Delta_{MC} = \Delta_{MC}^p - \Delta_{MC}^s$. In a region of PBG not containing mode singularities, this phase is a linear function of frequency,

$$\Delta_{MC} \approx \Delta_b \equiv (\alpha_A^p - \alpha_A^s)(\omega - \omega_{MC}), \quad (10)$$

where $\omega_{MC} = (\alpha_A^p\omega_A^p - \alpha_A^s\omega_A^s)/(\alpha_A^p - \alpha_A^s)$ is the frequency of phase compensation for the MC.

4. RESULTS AND DISCUSSION

The DBR reflectance spectra $R_\delta(\Psi_0, \varphi, \Psi)$ were measured at an angle of incidence φ = 30° in six experimental configurations: $R_0(45°, \varphi, \pm45°)$, $R_{-\pi/2}(45°, \varphi, \pm45°)$, $R_0(0°, \varphi, 0°) \equiv R^p$, and $R_0(90°, \varphi, 90°) \equiv R^s$. The spectra obtained for *p*- and *s*-polarized light are displayed in Fig. 2a and exhibit a well-pronounced band of nearly total reflection originating from the PBG, with a sharp drop in reflectance observed in the long- and short-wavelength wings of this band (at ~0.8 and ~1.35 eV, respectively). The series of narrow lines near 0.9 eV is due to light absorption by water vapor present in the air. The spectral dependence of the phase difference Δ(ω) (Fig. 2b) was obtained using Eq. (1) and experimental spectra $R_\delta(\Psi_0, \varphi, \Psi)$. This dependence is close to linear over a broad frequency region within the PBG. At $\hbar\omega_{DBR}$ = 1.08 eV, the reflectance phases for the *p* and *s* polarizations coincide and are approximately zero. Outside the PBG, the DBR reflectance spectra exhibit a complex interference structure (Fig. 2a).

To compare theory with experiment, the DBR spectral response Δ(ω) was calculated using the transfer

matrix method [25]. The theoretical spectrum, on the whole, fits well with the experimental data in the region of PBG and the spectral positions of the singularities at its edges if the DBR layer thicknesses are taken to be L_a = 208 and L_b = 88 nm. Some quantitative discrepancies in the phase (particularly at the PBG edges) may be due to our having neglected the effects associated with DBR layer thickness fluctuations in the calculation.

Figure 3 presents the following experimental MC amplitude-phase reflectance spectra needed to construct the spectral response of Δ: (a) R^p and R^s, (b) $R_0(45°, 30°, \pm 45°)$, and (c) $R_{-\pi/2}(45°, 30°, \pm 45°)$. For $\hbar\omega < 0.95$ eV, a band of nearly total reflection corresponding to the PBG is observed (Figs. 3a, 3b). The short-wavelength PBG edge manifests itself clearly for $\hbar\omega > 0.95$ eV in a noticeable decrease in reflectance toward shorter wavelengths. Part of the MC reflectance spectrum deriving from the long-wavelength PBG edge (unlike the DBR spectrum in Fig. 2) lies beyond the region of sensitivity of the photodetector used and, hence, is not presented in Fig. 3. It should be pointed out that the PBG of the MC fabricated by us (Fig. 3) is shifted to longer wavelengths relative to the corresponding PBG for a single DBR (Fig. 2), which should be assigned to the difference in the DBR layer thicknesses in our structures. In contrast to the spectra obtained from a single DBR (Fig. 2), the MC spectra clearly reveal resonance singularities at the energies $\hbar\omega_m^p = 0.834$ and $\hbar\omega_m^s = 0.843$ eV, which correspond to MC eigenmode excitation in the *p* and *s* polarizations and exhibit a noticeable polarization mode splitting [12].

The spectral response of the relative phase shift Δ calculated from Eq. (1) using experimental spectra (Figs. 3b, 3c) is displayed in Fig. 3d. The experimental Δ(ω) dependence is close to linear in the PBG spectral region (0.72–0.92 eV), except for the region of mode-state resonance singularities. This dependence can be approximated, in the greater part of the PBG, by a straight line (dashed line Δ_b in Fig. 3d), whose slope is related to the thicknesses of the microcavity structure layers. At an energy of 0.736 eV (the phase compensation frequency ω_{MC} in Fig. 3d), the phases of the *p*- and *s*-polarized light reflectance are the same. In the spectral region corresponding to excitation of the MC eigenmodes, the Δ(ω) phase undergoes an abrupt change.

Note that the polarization splitting of mode states for the *p* and *s* polarizations in the MC under study is larger than the resonance line width (Fig. 3a). This makes it possible to observe the resonance character of variation of each of the Δ^p and Δ^s phases in the difference spectrum $\Delta = \Delta^p - \Delta^s$ near the frequencies ω_m^p and ω_m^s.

Figure 4 gives MC reflectance spectra for the *p* and *s* polarizations (Fig. 4a) and spectra of the relative phase shift Δ (Fig. 4b) obtained in the resonance region of eigenmode states. The experimental spectra are presented by points. The solid lines were calculated numerically using the transfer matrix method, and the dashed lines were constructed using approximate analytical expressions for R^σ_{MC} [Eq. (6); Fig. 4a] and $\Delta_{MC} = \Delta^p_{MC} - \Delta^s_{MC}$ [Eq. (7); Fig. 4b].

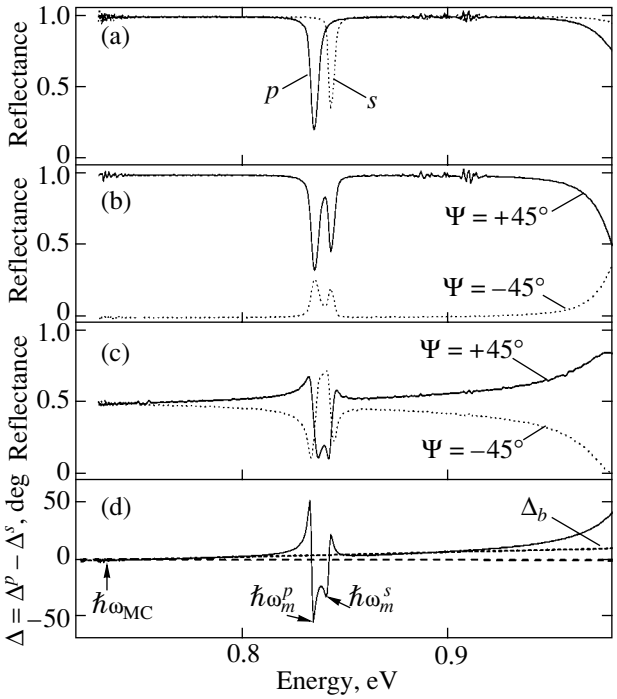

Fig. 3. Experimental spectra of (a–c) the reflectance $R_\delta(\Psi_0, \varphi, \Psi)$ and (d) the relative phase shift Δ for a microcavity structure obtained in the region of the photonic band gap at an angle of incidence φ = 30°. (a) $\Psi_0 = \Psi = 0°$ for *p* polarization and $\Psi_0 = \Psi = 90°$ for *s* polarization; (b) δ = 0 and $\Psi_0 = \Psi = 45°$, or δ = 0, $\Psi_0 = 45°$, and $\Psi = -45°$; (c) $\delta = -\pi/2$ and $\Psi_0 = \Psi = 45°$, or $\delta = -\pi/2$, $\Psi_0 = 45°$, and $\Psi = -45°$. (d) The spectrum of Δ is calculated from Eq. (1) using the amplitude-phase spectra (b) and (c); ω_{MC} is the phase compensation frequency (the *p* and *s* reflectance phases are zero); ω_m^p and ω_m^s are the microcavity eigenmode frequencies in *p* and *s* polarizations, respectively; and straight line Δ_b is a linear approximation of the relative phase shift in the region of the photonic band gap.

The calculations involving analytical formulas (6) and (7) were carried out by varying the resonance frequencies, broadening parameters, and R^σ_{min} in order to obtain the best fit of the theoretical to experimental curves. The parameters of the linear background contribution Δ_b [given by Eq. (10)] to the relative phase Δ of MC reflectance were derived from experiment: $d\Delta_b/d(\hbar\omega) = (\alpha_A^p - \alpha_A^s)/\hbar = 0.8$ rad/eV and $\hbar\omega_{MC} = 0.736$ eV. The theoretical calculation reproduces the basic qualitative features well, both in the intensity reflectance spectra and in the spectral response of the phase shift, provided one uses the following numerical

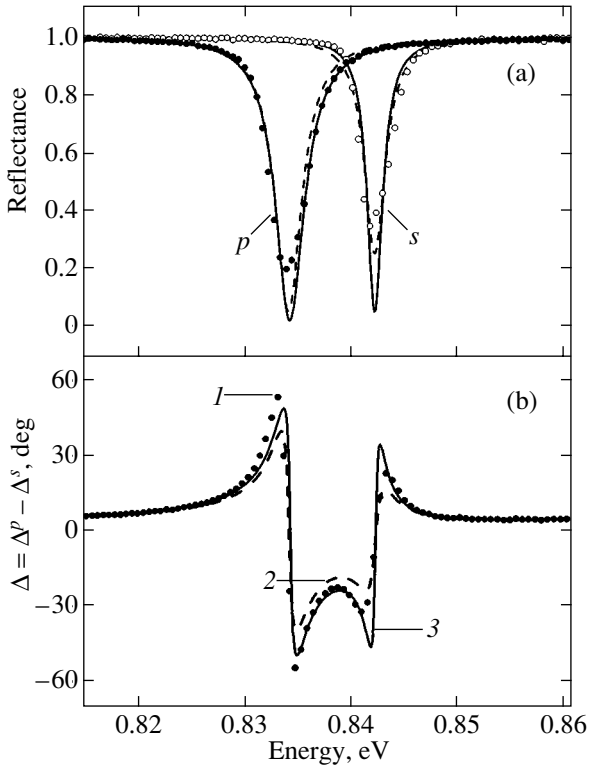

Fig. 4. (a) Reflectance spectra of a microcavity structure in the region of mode states for *p* and *s* polarizations: points are experimental data, dashed lines are calculated in the approximation of Lorentzian profiles using Eq. (6), and solid lines are calculated using the transfer matrix method. (b) Spectrum of the relative phase shift Δ: (*1*) experimental data, (*2*) calculation using Eq. (7), and (*3*) transfer matrix calculation.

values of the parameters: $\hbar\Gamma^p = 3.1$ meV, $\hbar\Gamma^s = 2.4$ meV, $R^p_{\min} = 0.05$, and $R^s_{\min} = 0.25$. The discrepancy between the experiment and theory (just as in the case of Fig. 2 for a single DBR) should apparently be assigned to the inhomogeneous broadening of the mode states, which is neglected in the theoretical model and arises as a result of microscopic fluctuations in the layer thickness, particularly in that of the active layer [12].

As already mentioned, the interferometric method employed by us to measure the layer thicknesses in periodic structures during the growth process provides only a limited accuracy. Using the thicknesses derived by this method causes the theoretical curves to deviate noticeably from the experimental amplitude-phase reflectance spectra for the MCs. However, an analysis reveals that one can determine the MC layer thicknesses (L_c, L_a, L_b) independently by making use of the experimental $\Delta(\omega)$ graph. For this purpose, one can employ three independent equations relating these parameters. The frequency derivatives of Eqs. (7) (for $\sigma = p, s$) in the region where the $\Delta(\omega)$ dependence is linear define the equation

$$\alpha^p_A(L_a, L_b) - \alpha^s_A(L_a, L_b) = \frac{d\Delta_b(\omega)}{d\omega}. \qquad (11)$$

The relations for the eigenmode frequencies in *p* and *s* polarizations yield two more equations:

$$\omega^\sigma_m = \frac{2\pi + \tilde{\alpha}^\sigma_A(L_a, L_b)\tilde{\omega}^\sigma_A(L_a, L_b) + \alpha^\sigma_B(L_a, L_b)\omega^\sigma_B(L_a, L_b)}{\alpha_c(L_c) + \tilde{\alpha}^\sigma_A(L_a, L_b) + \alpha^\sigma_B(L_a, L_b)}. \qquad (12)$$

The experimental values of $\hbar\omega^p_m$ and $\hbar\omega^s_m$ derived from the spectrum in Fig. 3a were given above. Because our MC consists of two DBRs (*A*, *B*) with similar parameters, we have $\tilde{\alpha}^\sigma_A \approx \alpha^\sigma_B$ and $\tilde{\omega}^\sigma_A \approx \omega^\sigma_B$. Therefore, for practical estimates, one can assume that $\alpha^\sigma_{\mathrm{DBR}} = \tilde{\alpha}^\sigma_A = \alpha^\sigma_B$ and $\omega^\sigma_{\mathrm{DBR}} = \tilde{\omega}^\sigma_A = \omega^\sigma_B$. The quantities $\omega^\sigma_{\mathrm{DBR}}$ and $\alpha^\sigma_{\mathrm{DBR}}$ can be expressed analytically through the thicknesses L_a and L_b of the DBR layers and their refractive indices [23]. By solving the coupled equations (11) and (12) for the parameters L_a, L_b, and L_c, we find $L_a = 296$, $L_b = 130$, and $L_c = 205$ nm with a relative error of no greater than 2%.

The numerical values of L_a, L_b, and L_c thus found were used to calculate the resonance spectra of reflectances R^p and R^s and the relative phase shift Δ by using the transfer matrix method (solid curves in Fig. 4). As seen from Fig. 4, the approach based on the more accurate transfer matrix method yields results that are in good agreement with the experimental data and are close to those obtained from approximate analytical expressions (6) and (7).

An important characteristic of MC quality is the *Q* factor, which is experimentally found as the ratio of the frequency of a resonance line to its half-width, $\omega_m/\Delta\omega$. Inclusion of the spectral responses of the DBR reflectance phases is needed to calculate the *Q* factor of an MC. The *Q* factor can be calculated as [18]

$$Q^\sigma_{\mathrm{theor}} = \frac{\sqrt[4]{\tilde{R}^\sigma_A R^\sigma_B}\left|\Phi(\omega^\sigma_m)\right|}{1 - \sqrt{\tilde{R}^\sigma_A R^\sigma_B}\left|\Phi(\omega^\sigma_m)\right|^2}\frac{(\alpha_c + \tilde{\alpha}^\sigma_A + \alpha^\sigma_B)\omega^\sigma_m}{2}. \qquad (13)$$

In the case of a transparent active layer under consideration here, one may assume $\left|\Phi(\omega^\sigma_m)\right| = 1$. The numerical values of L_a, L_b, and L_c obtained by solving the coupled equations (11) and (12) permit one to determine the other quantities entering into Eq. (13) and to find the *Q* factor for any angle of incidence and polarization of light. The quality factor found experimentally for *p* polarization and the angle of incidence $\varphi = 30°$ is $Q^p_{\mathrm{exp}} = 245$, and the theoretical factor Q^p_{theor} derived

from Eq. (13) is 257. We see that Q^p_{exp} and Q^p_{theor} are in good agreement, thus confirming the correctness of the choice of the parameters of the MC used in this study.

5. CONCLUSIONS

Amplitude-phase reflectance spectra of distributed Bragg reflectors and Fabry–Pérot microcavities based on *a*-Si : H/*a*-SiO_x : H thin films have been studied. The spectral response of the reflectance phase for a light wave incident on a distributed Bragg reflector and a planar microcavity structure has been measured for the first time. It was shown that the frequency dependence of the phase is close to linear over a broad spectral interval within the photonic band gap, with the exception of its edges and of the singularities associated with the microcavity eigenmodes. Approximate analytical expressions describing the spectral response of the microcavity reflectance phase near the MC eigenmode states were derived. A method based on analyzing the amplitude-phase reflectance spectra is proposed for determining the thicknesses of Bragg mirror layers and of the microcavity active layer. The theoretical calculations performed are in good agreement with experimental data. The proposed approach to investigating Bragg structures, which makes use of amplitude-phase reflectance spectra, demonstrates new attractive aspects of the spectral characterization of layered periodic media in the optical range.

ACKNOWLEDGMENTS

This study was supported by the Ministry of Industry, Sciences, and Technology of the Russian Federation under the program "Physics of Solid-State Nanostructures" (project no. 01.40.01.09.03) and by NATO (grant PST.CLG 980399).

REFERENCES

1. A. Yariv and P. Yeh, *Optical Waves in Crystals* (Wiley, New York, 1984; Mir, Moscow, 1987).
2. P. Goy, J. M. Raimond, M. Gross, and S. Haroche, Phys. Rev. Lett. **50** (24), 1903 (1983).
3. R. G. Hulet, E. S. Hilfer, and D. Kleppner, Phys. Rev. Lett. **55** (20), 2137 (1985).
4. V. Sandoghdar, C. Sukenik, E. Hinds, and S. Haroche, Phys. Rev. Lett. **68** (23), 3432 (1992).
5. F. Bernardot, P. Nussenzveig, M. Brune, J. M. Raimond, and S. Haroche, Europhys. Lett. **17** (1), 33 (1991).
6. M. Lipson and L. C. Kimerling, Appl. Phys. Lett. **77** (8), 1150 (2000).
7. Y. Yamamoto and R. Slusher, Phys. Today **46** (6), 66 (1993).
8. M. S. Skolnick, T. A. Fisher, and D. M. Whittaker, Semicond. Sci. Technol. **13** (7), 645 (1998).
9. H. Benisty, C. Weisbuch, and V. M. Agranovich, Physica E (Amsterdam) **2** (1–4), 909 (1998).
10. W. Heiss, T. Schwarzl, and G. Springholz, Phys. Status Solidi A **188** (3), 929 (2001).
11. M. S. Skolnick, V. N. Astratov, D. M. Whittaker, A. Armitage, M. Emam-Ismael, R. M. Stevenson, J. J. Baumberg, J. S. Roberts, D. G. Lidzey, T. Virgili, and D. D. C. Bradley, J. Lumin. **87–89**, 25 (2000).
12. A. A. Dukin, N. A. Feoktistov, V. G. Golubev, A. V. Medvedev, A. B. Pevtsov, and A. V. Sel'kin, Phys. Rev. E **67** (4), 046602 (2003).
13. G. Jungk, Thin Solid Films **313**, 594 (1998).
14. G. Jungk, M. Ramsteiner, and R. Hey, Nuovo Cimento D **17** (11–12), 1519 (1995).
15. B. Rheinlander, J. Kovac, J.-D. Hecht, J. Borgulova, F. Uherek, J. Waclawek, V. Gottschalch, and P. Barna, Thin Solid Films **313**, 599 (1998).
16. M. Patrini, M. Galli, M. Belotti, L. C. Andreani, G. Guizzetti, G. Pucker, A. Lui, P. Bellutti, and L. Pavesi, J. Appl. Phys. **92** (4), 1816 (2002).
17. G. Jungk, Philos. Mag. B **70** (3), 493 (1994).
18. V. G. Golubev, A. A. Dukin, A. V. Medvedev, A. B. Pevtsov, A. V. Sel'kin, and N. A. Feoktistov, Fiz. Tekh. Poluprovodn. (St. Petersburg) **35** (10), 1266 (2001) [Semiconductors **35**, 1213 (2001)].
19. A. A. Dukin, N. A. Feoktistov, V. G. Golubev, A. V. Medvedev, A. B. Pevtsov, and A. V. Sel'kin, Appl. Phys. Lett. **77** (19), 3009 (2000).
20. A. A. Dukin, N. A. Feoktistov, V. G. Golubev, A. V. Medvedev, A. B. Pevtsov, and A. V. Sel'kin, J. Non-Cryst. Solids **299–302**, 694 (2002).
21. *Semiconductor Quantum Optoelectronics: from Quantum Physics to Smart Devices: Proceedings of 50th Scottish Universities Summer School in Physics, St. Andrews, 1998*, Ed. by A. Miller, M. Ebrahimzadeh, and D. M. Finlayson (Inst. of Physics, Bristol, 1999).
22. A. B. Pevtsov and A. V. Sel'kin, Fiz. Tverd. Tela (Leningrad) **23** (9), 2814 (1981) [Sov. Phys. Solid State **23**, 1644 (1981)].
23. G. Panzarini, L. C. Andreani, A. Armitage, D. Baxter, M. S. Skolnick, V. N. Astratov, J. S. Roberts, A. V. Kavokin, M. R. Vladimirova, and M. A. Kaliteevski, Fiz. Tverd. Tela (St. Petersburg) **41** (8), 1337 (1999) [Phys. Solid State **41**, 1223 (1999)].
24. V. Savona, L. C. Andreani, P. Schwendimann, and A. Quattropani, Solid State Commun. **93** (9), 733 (1995).
25. M. Born and E. Wolf, *Principles of Optics*, 4th ed. (Pergamon, Oxford, 1969; Nauka, Moscow, 1970).

Translated by G. Skrebtsov

Physics of the Solid State, Vol. 46, No. 10, 2004, pp. 1822–1824. Translated from Fizika Tverdogo Tela, Vol. 46, No. 10, 2004, pp. 1763–1765.

SEMICONDUCTORS AND DIELECTRICS

Quantum Oscillations of Hall Resistance in Bismuth Bicrystals with Twist Low-Angle Internal Boundaries

F. M. Muntyanu*, Yu. A. Dubkovetskiĭ*, and A. Gilevski**

** Institute of Applied Physics, Academy of Sciences of Moldova, Academiei 5, Chisinau, MD 2028 Moldova*
e-mail: CSA@moldnet.md
*** International Laboratory of Strong Magnetic Fields and Low Temperatures, Wroclaw, 53-421 Poland*
Received February 16, 2004

Abstract—Quantum oscillations of the Hall resistance $\rho_{ij}(B)$ of bismuth bicrystals are investigated in magnetic fields up to 35 T. It is found that the twist low-angle internal boundary possesses *n*-type conductivity and comprises a central part and two adjacent layers, which are characterized by the specific features of the Fermi surface of electrons. © *2004 MAIK "Nauka/Interperiodica".*

1. INTRODUCTION

The internal boundary (CI) in bicrystals is considered a two-dimensional defect separating two physically identical phases (monoblocks) with different spatial orientations of the crystallographic axes. This boundary can compare in degree of perfection only with a surface cleaved under high vacuum. As a rule, the crystal lattice of the twist internal boundary is strongly distorted and differs significantly from the structure of monoblocks. The twist boundary is characterized by the angle of misorientation Θ_1 with respect to the plane of the internal boundary and by the angle of rotation Θ_2 of crystallites about the normal to this plane (Fig. 1) [1].

Detailed investigations of the Shubnikov–de Haas effect in strong magnetic fields have revealed considerable changes in the electron energy spectrum of twist high-angle internal boundaries of bismuth crystals. For example, in our earlier work [2], it was shown that the Fermi surface of the internal boundary with a misorientation angle $\Theta_i > 22°$ consists of one general hole ellipsoid that is elongated along the bisecting axis of individual parts of the bicrystal. This ellipsoid is appreciably larger than the hole ellipsoid of revolution of rhombohedral bismuth (the hole part of the Fermi surface of bismuth is elongated along the trigonal axis, and the hole density p in this part is approximately equal to 3.015×10^{23} m^{-3}). It was revealed [2, 3] that, at low temperatures, the twist high-angle internal boundaries contain superconducting inclusions (single-crystal bismuth is not a superconductor!) with $T_c \approx 8.5$ K (for some bicrystals, $T_{\text{onset}} \approx 16$ K). On the other hand, the twist low-angle boundaries of bismuth ($\Theta_i < 6°$) do not exhibit superconducting properties, even though these boundaries are characterized by a higher degree of perfection and a lower dislocation density as compared to internal boundaries with a misorientation angle $\Theta_i > 22°$.

In this work, we studied the quantum oscillations of the Hall resistance $\rho_{ij}(B)$ in bismuth bicrystals in static (up to 18 T) and pulsed (up to 35 T) magnetic fields. The quantum oscillations of the Hall resistance $\rho_{ij}(B)$ were examined both in a magnetic field aligned with the principal crystallographic directions and under the conditions where the magnetic field rotates in the bisecting trigonal and bisecting binary planes. In our experiments, we used four bicrystal samples with an internal boundary width in the range $170 \le L \le 250$ nm.

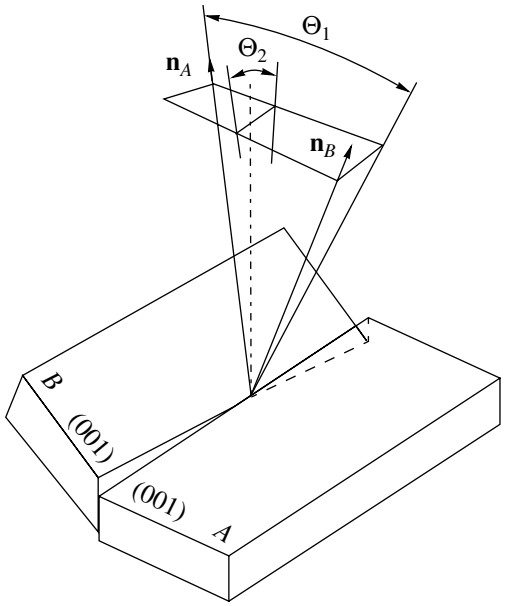

Fig. 1. Schematic drawing of the bicrystal with a twist internal boundary.

1063-7834/04/4610-1822$26.00 © 2004 MAIK "Nauka/Interperiodica"

2. SAMPLE PREPARATION AND EXPERIMENTAL TECHNIQUE

Bismuth bicrystals were grown through zone recrystallization with a double seed. For measurements, bicrystal samples were prepared in the form of parallelepipeds. Contacts were spark-welded to the internal boundary. The measurements were carried out at the International Laboratory of Strong Magnetic Fields and Low Temperatures (Wroclaw, Poland). The quantum oscillations of the Hall resistance were investigated in Bitter, superconducting, and pulsed magnets. The experimental setups used made it possible to record the curves $\rho_{ij}(B)$ in the forward and backward fields, to compensate for the monotonic component, to determine the frequencies of the components of the oscillation curves from Fourier analysis, etc.

3. RESULTS AND DISCUSSION

The orientation of the magnetic field $B \parallel C_3$ (C_3 is the trigonal axis of the crystallites) is best suited to investigate the structure of the internal boundary of bismuth bicrystals with the use of quantum-oscillation effects. As is known [4], single-crystal bismuth in a magnetic field of this orientation exhibits Shubnikov–de Haas oscillations. These oscillations are characterized by periods corresponding to a small cross section ($S_h \approx 6.76 \times 10^{-52}$ kg m s^{-1}) of the hole ellipsoid located at the T point of the Brillouin zone and a cross section ($S_e \approx 8.98 \times 10^{-52}$ kg m s^{-1}) of three equivalent electron ellipsoids (the isoenergetic surfaces of L electrons are elongated along the directions [C_1, axis 1] ≈ 6.23°). In a magnetic field $B \parallel C_3$, the oscillations of holes of the Fermi surface make the main contribution to the Shubnikov–de Haas effect, whereas the contribution from electrons predominantly manifests itself in quantum oscillations of the Hall resistance.

According to Hiruma and Miura [5], the magnetoresistance of single-crystal bismuth in a magnetic field $B \parallel C_3$ monotonically increases to 45 T. However, the Shubnikov–de Haas oscillations disappear in magnetic fields $B > 10$ T. On the other hand, quantum oscillations of the Hall resistance of bicrystals also manifest themselves in magnetic fields $B > 10$ T for the same orientation [1], but their frequencies are not characteristic of the Fermi surface of single-crystal bismuth. For example, the harmonic of quantum oscillations of the Hall resistance $\rho_{ij}(B)$ from the cross sections of the Fermi surface, which exceed the extreme cross sections of the Fermi surface of single crystals by a factor of approximately 5, was revealed in the low-angle bismuth bicrystals with a tilt internal boundary [1]. For bicrystals with a twist internal boundary, the frequency of these oscillations corresponds to even larger (~25%) cross sections of the Fermi surface [1]. As a rule, the oscillations of the Hall resistance at this frequency manifest themselves in magnetic fields $B \geq 2$–2.5 T. According to estimates, the diameter of cyclotron orbits d_{cycl} of charge carriers in these fields correlates with the thickness of the boundary layer between the monoblocks, which was determined using electron microscopy. In addition to this harmonic of oscillations of the Hall resistance $\rho_{ij}(B)$, a second component, whose frequency is higher by a factor of approximately 2, is observed for bismuth bicrystals with a twist internal boundary in magnetic fields $B \geq 10$ T (Fig. 2). The diameter of the cyclotron orbit of charge carriers d_{cycl} ~ 70–90 nm, which corresponds to the field of the disappearance of the second harmonic (in the low-field range), determines the width of the central part of the intercrystalline boundary. Therefore, the experimental results indicate that the twist internal boundary in low-angle bismuth bicrystals consists of a central part with a high density of states and two adjacent layers from which the space-charge region propagates into the crystal bulk.

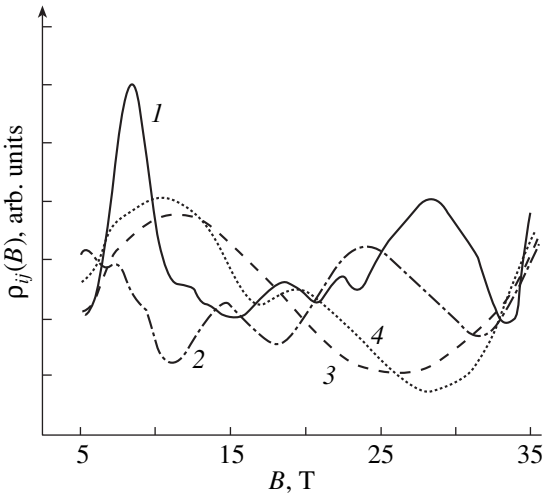

Fig. 2. Quantum oscillations of the Hall resistance $\rho_{ij}(B)$ in the bismuth bicrystal with a twist boundary and misorientation angles $\Theta_1 = 5°$ and $\Theta_2 = 5.5°$ for different orientations of the magnetic field at different temperatures: (*1*) $B \parallel$ CI $\parallel C_3$, $T = 1.5$ K; (*2*) $B \parallel$ CI $\parallel C_1$, $T = 4.2$ K; (*3*) [B, CI] ~ 10°, $T = 4.2$ K; and (*4*) $B \perp$ CI $\perp$ I, $T = 4.2$ K.

The cyclotron masses of charge carriers for different directions of the magnetic field B were estimated from the temperature dependences of the oscillation amplitude. In particular, we obtained $m_3 \approx 0.085m_0$ for $B \parallel$ CI $\parallel C_3$ and $m_1 \approx 0.1m_0$ for $B \parallel$ CI $\parallel C_1$, where C_1 is the bisecting axis of the single crystal. These estimates demonstrate that the periodic change in the density of states in a magnetic field at the internal boundary of the bicrystal is predominantly determined by electrons.

Judging from the frequencies of quantum oscillations of the Hall resistance $\rho_{ij}(B)$, the electron density is equal to ~1.5×10^{20} m^{-2} in the central part of the internal boundary and ~0.67×10^{20} m^{-2} in the adjacent layers. These values are three orders of magnitude higher than those for bismuth films of approximately the same size [6].

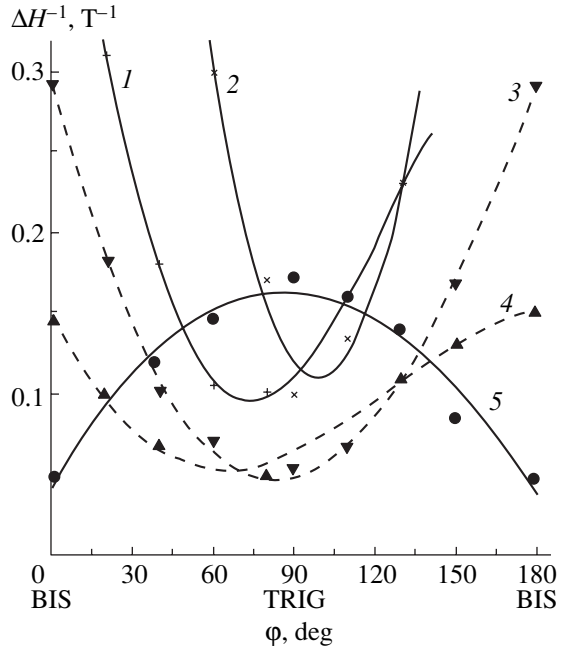

Fig. 3. Angular dependences of the periods of quantum oscillations of the Hall resistance upon rotation of the magnetic field in the bisecting trigonal plane of the bismuth bicrystal: (*1*, *2*, *5*) monoblocks and (*3*, *4*) adjacent layers of the internal boundary of the bicrystal.

The use of magnetic fields up to 35 T in the experiments made it possible to determine the frequencies of quantum oscillations of the Hall resistance $\rho_{ij}(B)$ in different field ranges. These frequencies characterize the Fermi surface of monoblocks, adjacent layers, and the central part of the internal boundary.

Figure 3 shows the angular dependences of the periods of quantum oscillations of the Hall resistance in bismuth bicrystals. It can be seen from Fig. 3 that the structure of the electron part of the Fermi surface in the adjacent layers is similar to that of the monoblocks (three electron surfaces localized at the *L* points of the Brillouin zone and rotated through an angle of 120° relative to each other). However, the isoenergetic surfaces are less anisotropic and are oblate in the bisecting trigonal plane. Their volume considerably exceeds the volume of the electron quasi-ellipsoids of the monoblocks. It is found that the ratio between the axes of the electron quasi-ellipsoid in the adjacent layers of the crystals studied is 1 : 1.34 : 12.6. (Note that, for rhombohedral bismuth, this ratio is 1 : 1.40 : 14.8 [4].) Therefore, not only the electron density increases in low-angle internal boundaries of bismuth bicrystals (as, for example, upon doping of bismuth with Se or Te donor impurities) but also the shape of the Fermi surface and the *A*7 Bi crystal lattice transforms (the internal displacement *u* and the trigonal angle α increase) [7].

Quantum oscillations of the Hall resistance from the central layer of the internal boundary of bismuth bicrystals, which are associated with the Fermi surface of electrons, were clearly observed only when the magnetic field was oriented along the plane of the internal surface. As the magnetic field deviated by an angle $\varphi > 10°$, the quantum oscillations disappeared. Nonetheless, the results obtained indicate that the electron density in the central part of the internal boundary is considerably higher than that in the adjacent layers (i.e., the Fermi surface extends). This means that the low-angle internal boundaries of bismuth bicrystals exhibit a more pronounced tendency to metallization of bonds as compared to the crystal bulk.

4. CONCLUSIONS

Thus, we investigated the quantum oscillations of the Hall resistance of bismuth bicrystals and established that the twist internal boundary consists of a central part and two adjacent layers. The Fermi surface of the layers significantly increases in volume. The extension of the Fermi surface of electrons is caused by structural transformations of the bismuth lattice (towards metallization of bonds) and by the formation of regions with a high density of states of unsaturated bonds between monoblocks of the bicrystal.

ACKNOWLEDGMENTS

We would like to thank Ya. Klyamut, V. Nizhankovskiĭ, and T. Palevskiĭ for their assistance in performing the measurements at the International Laboratory of Strong Magnetic Fields and Low Temperatures (Wroclaw, Poland).

REFERENCES

1. F. M. Muntyanu, M. I. Onu, and V. G. Kistol, Phys. Status Solidi B **158**, 301 (1990).
2. F. M. Muntyanu and N. I. Leporda, Fiz. Tverd. Tela (St. Petersburg) **37** (2), 549 (1995) [Phys. Solid State **37**, 298 (1995)].
3. D. V. Gitsu, A. D. Groav, V. G. Kistol, N. I. Leporda, and F. M. Muntyanu, Pis'ma Zh. Éksp. Teor. Fiz. **55** (7), 398 (1992) [JETP Lett. **55**, 403 (1992)].
4. V. S. Edelman, Adv. Phys. **25**, 555 (1976).
5. K. Hiruma and N. Miura, J. Phys. Soc. Jpn. **52**, 2118 (1983).
6. J. A. van Hulst, H. M. Jaeger, and S. Radelaar, Phys. Rev. B **52** (8), 5953 (1995).
7. A. B. Shick, B. Ketterson, D. L. Novikov, and A. J. Freeman, Phys. Rev. B **60** (23), 15 484 (1999).

Translated by N. Korovin

Physics of the Solid State, Vol. 46, No. 10, 2004, pp. 1825–1829. Translated from Fizika Tverdogo Tela, Vol. 46, No. 10, 2004, pp. 1766–1769.

SEMICONDUCTORS AND DIELECTRICS

Experimental Determination of the Constants of Absolute Volume Deformation Potentials at Band Edges in Semiconductors

M. I. Daunov, I. K. Kamilov, and S. F. Gabibov

Institute of Physics, Dagestan Scientific Center, Russian Academy of Sciences, ul. 26 Bakinskikh Komissarov 94, Makhachkala, 367003 Dagestan, Russia

e-mail: kamilov@datacom.ru

Received November 16, 2003; in final form, February 24, 2004

Abstract—A method is proposed for determining the constants of absolute volume deformation potentials at edges of the conduction and valence bands in semiconductors. This method is based on (i) the volume-concentration effect, (ii) the concept that the energy of deep-lying strongly localized impurity centers does not depend on the hydrostatic pressure, and (iii) the use of experimental data on the electrical resistivity and Hall coefficient. For Ge, GaAs, InAs, and InSb semiconductors, the constants of absolute volume deformation potentials at edges of the conduction and valence bands are determined from our results and data available in the literature.

1. INTRODUCTION

Determining the constants of absolute volume deformation potentials at band edges in semiconductors, i.e., the individual constants of deformation potentials at edges of the conduction band $a_{Ci} = (dE_{Ci}/dP)B$ (where i stands for Γ, L, and X) and the valence band $a_V = (dE_V/dP)B$ (where B is the bulk modulus), is a complex theoretical problem [1, 2]. It should be noted that, in general, the constants of the volume deformation potential, which characterize the change in the energy of charge carries under hydrostatic pressure, do not coincide with the constants of the deformation potential, which describe the interaction of charge carries with acoustic phonons. The difference between the constants of the deformation potentials can be explained by the fact that the strain induced by an acoustic wave is universally inhomogeneous. However, these parameters of the deformation potentials can be determined from the results of investigations into the electron-transfer phenomena and optical properties of samples under hydrostatic pressure.

In this work, we proposed an experimental method for estimating the constants of absolute volume deformation potentials at edges of the conduction and valence bands in semiconductors under hydrostatic pressure from data on the electrical resistivity and Hall coefficient. This method is based on the concept postulated in our previous papers [3–5], according to which the energy of deep-lying strongly localized states does not depend on the hydrostatic pressure. Moreover, the proposed approach allows for the volume-concentration effect [6].

2. THEORETICAL BACKGROUND

Let us consider a heavily doped degenerated semiconductor with a single type of charge carriers in the impurity region. It is assumed that the Hall coefficient does not depend on the temperature and the strength of the magnetic field. For this semiconductor, we can write the following relationships:

$$N = n\Omega, \tag{1}$$

$$\frac{d\Omega}{\Omega} = \alpha\frac{db}{b}, \tag{2}$$

$$V_R = \frac{RIH}{b} = -\frac{\Omega IH}{Neb}, \tag{3}$$

$$\frac{d\Omega}{\Omega} \cong \frac{\alpha}{\alpha - 1}\frac{dV_R}{V_R}. \tag{4}$$

Here, V_R is the Hall potential difference; R is the Hall coefficient; I is the current intensity; H is the strength of the magnetic field; b is the thickness of the sample; Ω is the volume of the crystal; N is the total number of free charge carriers in volume Ω; n is the concentration of charge carriers; e is the elementary charge; $d\Omega$ and dV_R are the changes in the quantities Ω and V_R under hydrostatic pressure P, respectively; and $\alpha = \theta/\chi$ is the ratio of the isothermal coefficients of the volume compressibility θ and linear compressibility χ. In the isotropic approximation, the relationship $\alpha \cong 3$ is satisfied to within small quantities. For anisotropic crystals, the quantity α is determined by the crystallographic orientation of the sample with thickness b.

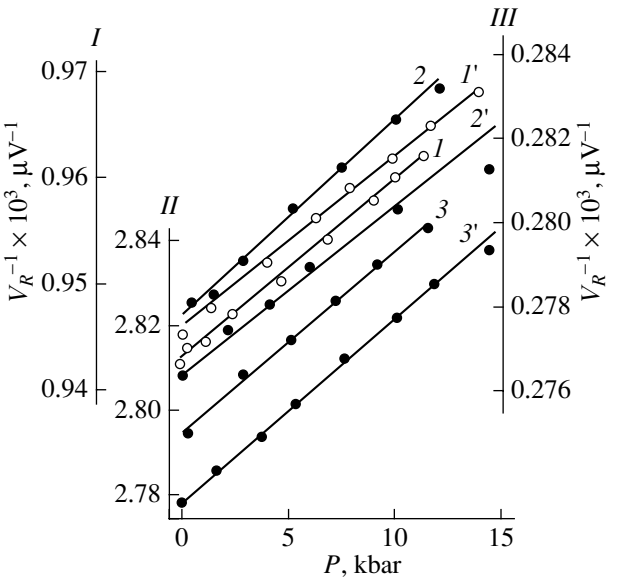

Fig. 1. Dependences of the inverse Hall potential difference on the hydrostatic pressure for *n*-InSb and *n*-$CdSnAs_2$ semiconductors: (*1*, *1*') $n = 10^{18}$ cm^{-3} for *n*-InSb (scale *I*), (*2*, *2*') $n = 6.25 \times 10^{17}$ cm^{-3} for *n*-$CdSnAs_2$ (scale *III*), and (*3*, *3*') $n = 1.8 \times 10^{18}$ cm^{-3} for *n*-$CdSnAs_2$ (scale *II*). Temperature *T*, K: (*1*–*3*) 77 and (*1*'–*3*') 300.

Relationship (3) holds for a sample in the form of a rectangular parallelepiped. Expression (4) immediately follows from relationship (3). It is evident that, upon compression of the crystal, a decrease in the volume Ω is accompanied by an increase in the charge carrier concentration n [see formula (1)] and a decrease in the quantities R and V_R [see relationship (3)]. Since the increase in the charge carrier concentration is caused by compression of the semiconductor, the phenomenon under consideration is referred to as the volume-concentration effect.

It follows from expression (4) that the bulk modulus B and the Hall potential difference V_R can be represented in the form

$$B = P\frac{V_R}{V_{R0} - V_R}\frac{\alpha - 1}{\alpha}, \quad (5)$$

$$\frac{1}{V_R} = \frac{1}{V_{R0}}\frac{\alpha - 1}{\alpha}B^{-1}P + \frac{1}{V_{R0}}, \quad (6)$$

where the subscript $R0$ indicates the unstrained state of the sample.

3. RESULTS AND DISCUSSION

Analysis of the experimental data obtained for 11 crystals of *n*-InSb and *n*-$CdSnAs_2$ semiconductors with an electron concentration ranging from 10^{17} to 10^{18} cm^{-3} at temperatures of 77 and 300 K revealed that, in all cases, the dependences $V_R^{-1}(P)$ at pressures up to P = 1.5 GPa exhibit a linear behavior in accordance with relationship (6) (Fig. 1). From these data and relationship (6), we determined the following values of the bulk modulus for the InSb compound: B = 43.7 GPa at 77 K and B = 46.0 GPa at 300 K. For the $CdSnAs_2$ compound, averaging over a series of unoriented crystals led to the following values: B = 37.0 GPa at 77 K and B = 43.5 GPa at 300 K. It turned out that, for all the studied crystals of the aforementioned two compounds, the bulk modulus determined at 300 K is 5–10% greater than that obtained at 77 K.

For the InSb semiconductor, the bulk modulus obtained with the use of the volume-concentration effect is in satisfactory agreement with the values estimated by other methods. In particular, the value of B calculated from elastic constants at room temperature [2, 7] is equal to 45 ± 1.8 GPa, whereas the bulk modulus calculated from the relationship $B = (a_{C\Gamma} - a_V)/(d\varepsilon_g/dP)$ (where ε_g is the band gap) according to the data presented in [2] is found to be 49 GPa.

However, when estimating the constants of absolute volume deformation potentials at edges of the conduction and valence bands in semiconductors, it is necessary to know not only the bulk modulus but also the second factor, namely, the pressure coefficient for the band edges. In order to determine this coefficient, it is expedient to use the experimental data for the derivative of the difference between the energies at the band edge and at the impurity level with respect to the pressure. Moreover, the calculation should be performed considering that the energy of deep-lying strongly localized impurity centers does not depend on the hydrostatic pressure. This concept was postulated in our recent papers [3–5] on the basis of analyzing and generalizing the results obtained in our earlier works [3, 4, 8–10], experimental data published by other authors in [11–16], and theoretical inferences made in [17, 18].

It should be noted that the pressure dependence of the energy of deep-lying impurity centers (measured from the vacuum level) is negligible within the limits of the experimental error. Therefore, the wave functions of these centers should be constructed throughout the Brillouin zone. In this case, the effect of pressure on the energy of a deep-lying impurity center is determined by the evolution of the band structure as a whole rather than by the nearest one or two bands. In this respect, mention should be made of the simplified models proposed in [19–21]. These models have often been used to predict the pressure coefficients for energy gaps between the band edges and the energy levels of deep-lying impurity centers. In particular, Hong *et al.* [20] made the inference that the pressure coefficients for a number of deep-lying levels in IV, III–V, and II–VI semiconductors vary in the range from –30 to +30 meV/GPa (depending on the location of the energy level in the band gap). Chadi and Chang [21] derived a relationship between the pressure coefficient for a deep-lying level of donor impurity centers and the pressure coefficients for the Γ, L, and X

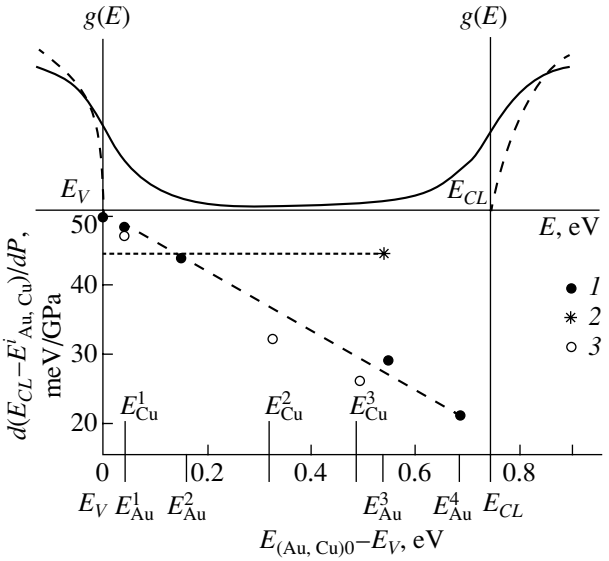

Fig. 2. Density of states $g(E)$ in a heavily doped compensated semiconductor (germanium) and pressure coefficients for gold and copper impurity levels according to the data taken from (*1*) [9] (gold impurity levels), (*2*) [2] (gold impurity levels), and (*3*) [22] (copper impurity levels).

valleys with respect to the valence band top. It is pertinent to note that, in contrast to the trivial case of shallow-lying acceptor and donor impurities, "the theory of charged defects, regardless of their origin, is still in a primitive stage of development …, and the models proposed fall far short of reality" [17].

The above assumption that the energy of deep-lying impurity centers (measured from the vacuum level) does not depend on pressure is convincingly supported by experimental data. Analysis of the experimental data obtained in this work and those available in the literature demonstrates that, in Ge : Au (Fig. 2) and InSb (Fig. 3), the energy separation between the levels of deep-lying impurity centers located at different distances from the band edges does not depend on pressure [3, 11, 13, 22, 23].

The experimental data on the pressure coefficients for energy levels of deep-lying impurity centers of gold [3, 11] and copper [24] in germanium are presented in the table and Fig. 2. A detailed analysis of these data was performed earlier in [3]. In the present paper, we will dwell briefly on only two factors responsible for the decrease in the pressure coefficients $\gamma_{CL} = d(E_{CL} - E_i)/dP$ and $\gamma_V = d(E_i - E_V)/dP$ in *n*- and *p*-regions, respectively. First and foremost, it is necessary to use the Gibbs statistics, which was not correctly included in the analysis carried out by Pel' *et al.* [24]. Holland and Paul [11] took into account the Gibbs statistics and, moreover, measured the pressure dependence of the electrical resistivity in Ge : Au at low temperatures with the aim of obtaining more reliable results. However, slightly soluble impurities (such as Au, Hg, and Cu) in doped and compensated germanium can form clusters with a

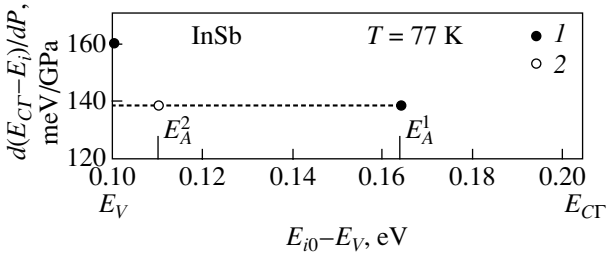

Fig. 3. Pressure coefficients for deep-lying levels of acceptor impurity centers in InSb according to the data taken from (*1*) [11] and (*2*) [21].

high probability. As the temperature decreases and the pressure increases, the concentration of free charge carriers decreases and the amplitude of a random potential and, correspondingly, the degree of fluctuation bending of energy bands increase. In this situation, if an energy level of a deep-lying impurity center is located in the band gap, there can occur a transition to a state similar to that of a heavily doped, completely compensated semiconductor [25]. This must necessarily lead to a decrease in the pressure coefficients for the energy gaps calculated from the pressure dependence of the charge carrier concentration, which is confirmed by the data presented in Fig. 2 and in the table. It is also evident that the effect of the random potential increases with a decrease both in the temperature and in the energy separation between the level of the deep-lying impurity center and the edge of the intrinsic band (see Fig. 2 and table).

Figure 3 presents the pressure coefficients for two energy levels of deep-lying acceptor impurity centers in InSb [13, 22], which were calculated from the pressure dependences of the electrical resistivity and Hall coefficient. It can be seen from Fig. 3 that, in the InSb semiconductor, the energy separation between the levels does not depend on the pressure and the pressure coefficients calculated with respect to the band edges coincide, as is the case with the Ge : Au semiconductor.

Pressure coefficients for four Au impurity levels in germanium [9] according to the data obtained from the pressure dependences of the electrical resistivity in the range up to 0.7 GPa [9]

Level	Type	$E_C - E_i$, eV	$d(E_{CL} - E_i)/dP$, meV/GPa	T, K
E_4	Acceptor	0.043	21	45–49.3
E_3	"	0.19	29(44)	112–194
E_2	"	0.60	44	170–273
E_1	Donor	0.71	49	49.5
E_V	"	0.75	50	

Note: The parenthetic value of $d(E_{CL} - E_i)/dP$ was obtained from the pressure dependences of the electrical resistivity and Hall coefficient in the range up to 0.7 GPa at 300 K [2].

Thus, when determining the pressure coefficients for extrema of the conduction band γ_{Ci} (i is Γ or L) and the valence band γ_V, we took into account that $E_i/dP \approx 0$. As a result, the following values of the pressure coefficients γ_{Ci} and γ_V and the corresponding constants of absolute volume deformation potentials for Ge, GaAs, InAs, and InSb were determined from the data obtained in [2, 12, 15, 26] and in this work.

Ge: $\gamma_{CL} = 44$ meV/GPa, $\gamma_V = -6$ meV/GPa,

$a_{CL} = 3.4$ eV, $a_V = -0.47$ eV;

GaAs: $\gamma_{C\Gamma} = 100$ meV/GPa, $\gamma_V = -16$ meV/GPa,

$a_{C\Gamma} = 7.5$ eV, $a_V = -1.2$ eV;

InAs: $\gamma_{C\Gamma} = 90$ meV/GPa, $\gamma_V = -8$ meV/GPa,

$a_{C\Gamma} = 5.22$ eV, $a_V = -0.46$ eV;

InSb: $\gamma_{C\Gamma} = 140$ meV/GPa, $\gamma_V = -20$ meV/GPa,

$a_{C\Gamma} = 6.7$ eV, $a_V = -0.95$ eV.

The bulk moduli for the InSb semiconductor are given above. For the other semiconductors, the bulk moduli B are as follows: $B = 78.7$ GPa [27] for Ge, $B = 75$ GPa [28] for GaAs, and $B = 58$ GPa [2] for InAs.

In the aforementioned semiconductors and in CdTe [12], the top of the valence band (Γ_{25}, Γ_{15}) and the bottom of the X valley are displaced in a nearly identical manner when the crystal lattice is subjected to isotropic compression.

Yu and Cardona [2] discussed the available data on the constants of volume deformation potentials for germanium, silicon, III–V, and II–VI semiconductors. It was noted that, in optical experiments under hydrostatic pressure, it is possible to measure only the relative volume constants of deformation potentials ($a_C - a_V$) between the conduction band and the valence band. In [2, Table 3.1], the constants of absolute volume deformation potentials are given only for GaAs ($a_{C\Gamma} = 8.6$ eV, $a_V = -0.4$ eV) and InP ($a_{C\Gamma} = 7.0$ eV, $a_V = 0.6$ eV). The value of $a_{C\Gamma}$ for GaAs seems to be overestimated, because, for $a_C - a_V = 9.0$ eV, we obtain $d\varepsilon_g/dP = 120$ meV/GPa. However, according to [26], we have $d\varepsilon_g/dP \leq 116$ meV/GPa. As regards the estimates obtained for InP, the positive value of a_V is at variance with the above values of a_V for Ge, GaAs, InAs, InSb, and CdTe.

4. CONCLUSIONS

From the above discussion, it follows that reliable estimates of the pressure coefficients for energy gaps and, correspondingly, the constants of absolute volume deformation potentials (in particular, from the results of investigations into the electron-transfer phenomena) requires comprehensive analysis and adequate quantitative interpretation of a concrete situation. In order to suppress the adverse effect of the random potential, it is necessary to perform the experiments at sufficiently high temperatures and moderate pressures, because variations in the statistics of charge carriers lead to a change in the amplitude of the random potential. Furthermore, the effect of hybridization of the resonance deep-lying energy levels located in the band continuum must be taken into account. Under resonant conditions, the mobility of charge carriers in the impurity energy band approaches the mobility of charge carriers in the intrinsic band; i.e., the charge carriers undergo a partial delocalization to the extent that there occurs a crossover to quasi-metallic conduction. As a result, the ratio of the charge carrier mobilities reaches several units and, hence, in quantitative analysis, allowance must be made for at least two types of charge carriers [25, 29]. Under pressure, the bands become widely separated and the impurity band is displaced into the band gap. The charge carriers are localized at impurity centers, and the effective mobility of impurity states tends to zero. Ignoring this circumstance can lead to substantially overestimated values of the pressure coefficient (by approximately 50%), as was the case, for example, in *n*-CdTe [30] and *n*-InAs [31] with resonance donor impurity levels.

It should also be noted that, when determining the pressure coefficients for energy gaps, it is necessary to analyze thoroughly the optical and other properties of semiconductors (tails of the density of states at band edges, hybridization of resonance states with states of the band continuum, etc.). Let us adduce only one example. In-Hwan Choi and Yu [18, 32] obtained underestimated values of the pressure coefficient for the band gap in I–III–VI_2 and II–IV–V_2 ($CdGeP_2$) chalcopyrite semiconductors from the results of studies of the optical properties: for $CdGeP_2$, $d\varepsilon_g/dP = 65$ meV/GPa in [32] and $d\varepsilon_g/dP = 97$ meV/GPa in [9].

The proposed method for estimating the constants of absolute volume deformation potentials in semiconductors from experimental data on the electrical conductivity and Hall coefficient is based on the volume-concentration effect and the concept postulated in [3–5], according to which the energy of deep-lying impurity centers does not depend on pressure. This method is relatively simple and can be used to determine the constants of absolute volume deformation potentials in IV, III–V, and II–VI semiconductors.

The results reported in this paper were presented in part at the Joint 19th AIRAPT–41st EHPRG International Conference "High Pressures in Science and Technology," Bordeaux, France, 2003 [33].

ACKNOWLEDGMENTS

This work was supported by the Russian Foundation for Basic Research, project no. 02-02-17888.

REFERENCES

1. K. Kosaka and K. Takarabe, Phys. Status Solidi B **235** (2), 423 (2003).
2. P. Y. Yu and M. Cardona, *Fundamentals of Semiconductors* (Springer, Berlin, 1996; Fizmatlit, Moscow, 2002).

3. M. I. Daunov, I. K. Kamilov, and S. F. Gabibov, Fiz. Tekh. Poluprovodn. (St. Petersburg) **35** (1), 58 (2001) [Semiconductors **35**, 59 (2001)].
4. M. I. Daunov, I. K. Kamilov, S. F. Gabibov, and R. Rh. Akchurin, Phys. Status Solidi B **223** (1–2), 529 (2001).
5. M. I. Daunov, I. K. Kamilov, R. K. Arslanov, S. F. Gabibov, and D. M. Daunova, in *Abstracts of XXXIX European High-Pressure Research Group Meeting* (Spain, 2001), p. 34.
6. M. I. Daunov, A. B. Magomedov, and A. E. Ramazanova, Fiz. Tekh. Poluprovodn. (Leningrad) **19** (5), 936 (1985) [Sov. Phys. Semicond. **19**, 577 (1985)].
7. P. I. Baranskiĭ, V. P. Klochkov, and I. V. Potykevich, *Semiconductor Electronics: Handbook* (Naukova Dumka, Kiev, 1975) [in Russian].
8. M. I. Daunov, I. K. Kamilov, A. B. Magomedov, and A. Sh. Kirakosyan, Fiz. Tekh. Poluprovodn. (St. Petersburg) **33** (1), 58 (1999) [Semiconductors **33**, 51 (1999)].
9. M. I. Daunov, A. B. Magomedov, and A. E. Ramazanova, Izv. Vyssh. Uchebn. Zaved., Fiz., No. 8, 98 (1986).
10. M. I. Daunov, A. B. Magomedov, and V. I. Danilov, Fiz. Tekh. Poluprovodn. (Leningrad) **25** (3), 467 (1991) [Sov. Phys. Semicond. **25**, 282 (1991)].
11. M. G. Holland and W. Paul, Phys. Rev. **128** (1), 43 (1962).
12. W. Paul, in *Proceedings of the 9th International Conference on Semiconductors* (Moscow, 1968), Vol. 1, p. 51.
13. V. V. Popov, M. L. Shubnikov, S. S. Shalyt, and V. V. Kosarev, Fiz. Tekh. Poluprovodn. (Leningrad) **11** (10), 1914 (1977) [Sov. Phys. Semicond. **11**, 1120 (1977)].
14. A. Plitrikas, A. Krotkus, L. A. Balagurov, and E. M. Omel'yanovskiĭ, Fiz. Tekh. Poluprovodn. (Leningrad) **14** (12), 2123 (1980) [Sov. Phys. Semicond. **14**, 1262 (1980)].
15. M. Holtz, T. Saungy, T. Dallas, M. Seon, C. P. Palsule, S. Gangopadhyay, and S. Massie, Phys. Status Solidi B **198** (1), 199 (1996).
16. N. B. Brandt and E. P. Skipetrov, Fiz. Nizk. Temp. **22** (8), 870 (1996) [Low Temp. Phys. **22**, 665 (1996)].
17. V. A. Telezhkin and K. B. Tolpygo, Fiz. Tekh. Poluprovodn. (Leningrad) **16** (8), 1337 (1982) [Sov. Phys. Semicond. **16**, 857 (1982)].
18. In-Hwan Choi and P. Y. Yu, Phys. Status Solidi B **211** (1), 143 (1999).
19. V. Iota and A. Weinstein, Phys. Status Solidi B **211** (1), 91 (1999).
20. R.-D. Hong, D. W. Jenkins, S. Y. Ren, and J. Dow, Phys. Rev. B **38** (15), 12549 (1988).
21. D. J. Chadi and K. J. Chang, Phys. Rev. Lett. **61** (9), 873 (1988).
22. M. I. Daunov, I. K. Kamilov, S. F. Gabibov, and A. B. Magomedov, Phys. Status Solidi B **235** (2), 297 (2003).
23. P. Kordos, Phys. Status Solidi **33** (2), K129 (1969).
24. E. G. Pel', V. I. Fistul', A. Yagshigel'dyev, and A. G. Yakovenko, Fiz. Tekh. Poluprovodn. (Leningrad) **14** (6), 1220 (1980) [Sov. Phys. Semicond. **14**, 721 (1980)].
25. I. K. Kamilov, M. I. Daunov, V. A. Elizarov, and A. B. Magomedov, Zh. Éksp. Teor. Fiz. **104** (1), 2436 (1993) [JETP **77**, 92 (1993)].
26. M. D. Frogley and D. J. Dunstan, Phys. Status Solidi B **211** (1), 17 (1999).
27. M. Shashkov, *Metallurgy of Semiconductors* (GNTI, Moscow, 1960) [in Russian].
28. E. G. Moroni, W. Wolf, J. Hafner, and R. Podloucky, Phys. Rev. B **59** (20), 12 860 (1999).
29. I. K. Kamilov, M. I. Daunov, V. A. Elizarov, and A. B. Magomedov, Pis'ma Zh. Éksp. Teor. Fiz. **54** (10), 589 (1991) [JETP Lett. **54**, 594 (1991)].
30. A. G. Foyt, R. E. Halsted, and W. Paul, Phys. Rev. Lett. **16** (1), 55 (1966).
31. M. I. Daunov, A. Yu. Mollaev, R. K. Arslanov, L. A. Saĭpulaeva, and S. F. Gabibov, Izv. Vyssh. Uchebn. Zaved., Fiz., No. 9 (1996); Available from VINITI, No. 2038-B96 (1996).
32. In-Hwan Choi and P. Y. Yu, Phys. Status Solidi B **235** (2), 307 (2003).
33. M. I. Daunov, I. K. Kamilov, S. F. Gabibov, and A. B. Magomedov, in *Abstracts of Joint 19th AIRAPT–41st EHPRG International Conference on High Pressures in Science and Technology* (Bordeaux, France, 2003), p. 153.

Translated by O. Borovik-Romanova

Physics of the Solid State, Vol. 46, No. 10, 2004, pp. 1830–1835. Translated from Fizika Tverdogo Tela, Vol. 46, No. 10, 2004, pp. 1770–1775.

SEMICONDUCTORS AND DIELECTRICS

Standardless XPS Method for Determining the Chemical Composition of Multiphase Compounds and Its Application to Studies of InP Plasma Oxide Nanofilms

V. M. Mikushkin, S. E. Sysoev, and Yu. S. Gordeev

Ioffe Physicotechnical Institute, Russian Academy of Sciences, Politekhnicheskaya ul. 26, St. Petersburg, 194021 Russia

Received February 26, 2004

Abstract—A modified version of x-ray photoelectron spectroscopy (XPS) is proposed for analysis of the phase chemical composition of substances. In contrast to the well-known XPS method of Siegbahn, the proposed version is standardless and permits determination of the chemical composition of complex multiphase compounds with high accuracy and reliability. In addition to the chemical composition, the method yields the core-level binding energies of atoms in the chemical phases of a studied compound, which have had to be determined in separate experiments on reference samples. The main idea underlying the proposed approach consists in self-consistent unfolding of photoelectron lines of two or more elements. The binding energies act as fitting parameters in this decomposition. The requirement that the contents of like chemical phases derived from the decomposition of spectra of two or more elements be identical makes the solution of the problem unique. This method was used to study the chemical composition of nanofilms of the InP plasma oxide containing several chemical phases. It is shown that, in order to improve the quality of a film and of the interface, the oxidizable surface should be enriched by phosphorus. *© 2004 MAIK "Nauka/Interperiodica".*

1. INTRODUCTION

X-ray photoelectron spectroscopy (XPS), proposed by K. Siegbahn in the 1960s for chemical analysis of matter [1–3], became a major method for establishing the chemical state of elements in a solid in the decades following, and photoelectron spectrometers needed for this purpose are now available at practically all large centers involved in research and technology. The sensitivity to a layer only 1–3 nm thick makes this method indispensable in the development of nanotechnologies. The method consists essentially in irradiating a sample for study with monochromatic x rays and measuring the photoelectron spectra, and it is based on the chemical shift of photoelectron lines, i.e., on the change in the core-electron binding energy induced by a change in the chemical state of the atom. Determination of the chemical composition of a material reduces to solving the problem of decomposing an experimental photoelectron spectrum into primary constituents corresponding to the various chemical states of the atoms. The chemical composition to be found is derived from the contributions of these constituents, with due account made of the stoichiometry of the chemical phases.

The problem of spectral decomposition is solved easily, reliably, and accurately if the primary constituents of the spectrum are single (resolved) lines, i.e., if their widths are less than the chemical shifts. Otherwise, these constituents merge to form one line of the experimental spectrum, thus making the problem much more complicated. This case becomes, however, increasingly more typical with the advent of new multielement and multiphase materials, such as the cuprate HTSCs, solid solutions, and oxides. Determination of the chemical composition becomes a particularly complex problem in the development of technologies of materials production, a process entailing the formation of additional undesirable chemical phases, which give rise to an increase in the number of unresolved lines. In such unfavorable cases, the solution is searched for by minimizing the error functional between the experimental photoelectron spectrum and the envelope of a set of model primary lines, with the intensities of the lines being fitting parameters. For this solution to be unique, one has to set in advance the possible number of lines (number of chemical states), as well as the corresponding values of the binding energies E_b and of the errors of their determination δE_b. The binding energies are derived from measurements performed with reference materials. Most of the applied research is done with the use of published data. The accuracy and even reliability of determination of the binding energies E_b turn out frequently to be inadequate because of the complexity or impossibility of preparing reference samples in pure form and of preventing surface degradation and contamination. A noticeable contribution to the error δE_b derives from uncontrollable systematic errors, which are different in experiments with different references. Therefore, the problem of separating unresolved lines is solved unreliably or inaccurately. The costly process of monochromatization of x rays from standard sources does not always successfully solve the problem of unfolding an experimental spectral line,

because this procedure usually improves the spectrometer resolution by only a factor of 2 (from 0.8–0.7 to 0.5–0.3 eV) while decreasing the x-ray fluxes by more than an order of magnitude and, thus, decreasing the sensitivity of the method. Further improvement of the resolution by using highly monochromatic synchrotron radiation is generally pointless because of the finite natural width of a photoelectron line.

We propose a modification of the method that is free of the above shortcomings; i.e., it makes possible reliable and fairly accurate determination of the chemical phase composition of multiphase substances. The proposed method does not require experiments with reference samples but does make it possible to determine (simultaneously with the chemical composition) the binding energies E_b in the chemical compounds that make up the substance under study with a substantially higher accuracy than in experiments with reference samples. The characteristics of the new method are described in considerable detail in [4]. The method was tested in solving the comparatively simple problem of establishing the part played by atomic oxygen in the formation of CuO films [5].

2. FORMATION OF NANOFILMS OF A NATIVE OXIDE ON THE InP SURFACE

The shortcomings of the commonly used method and specific features of the proposed approach are illustrated in the present communication through the specific example of the formation of a thermodynamically stable and dielectrically strong InP native plasma oxide with a low density of states of the interface with the InP surface [6]. The advantages of the III–V semiconductors over silicon are known to be counterbalanced to a considerable extent by the poor dielectric properties of their native oxides (NatO), i.e., by the absence of a good and technologically compatible insulator, which is provided by the silicon oxide SiO_2 in silicon-based electronics. Indeed, the InP interface with a multiphase NatO layer usually exhibits a fairly high density of states and poor thermodynamic and temporal stability of its parameters. Nevertheless, the technological compatibility of native oxides with semiconductor material stimulated in the 1980s–1990s an active search for ways to improve the quality of insulating oxide layers and of their interfaces with the use of various diagnostics, including XPS [6–16]. Out of the various methods of oxidation, including thermal, chemical, electrochemical, anode, and plasma oxidation, the last two yield sufficiently good results [6, 7]. The major factor determining the interface quality was found to be the chemical composition of the oxide layer: the lower the fraction of the In_2O_3 oxide and the higher that of the $InPO_4$ and $In(PO_3)_3$ oxides, the lower the density of surface states of the interface and the higher its stability. Thus, the development of adequate diagnostics for the chemical composition of the InP native oxides is an urgent problem in the formation of NatO–InP/InP structures. Determination of the phase composition of NatO–InP has remained an urgent problem over recent years. Considerable efforts were devoted to methods of chemical cleaning of an oxidized InP surface [17] and thermal [18, 19], anode [20, 21], and plasma [22–24] oxidation of InP with the purpose of obtaining MOSFET structures and long-wavelength lasers. Multilayer In-tin oxide (ITO)/InP structures are employed in solar cells [25]. A new direction of research is the development of perfect MIS structures through preliminary passivation of the InP surface by plasma oxidation. An insulating layer is prepared by deposition (on the passivated surface) of a thin metallic film (Al, Bi, Sb) with subsequent plasma oxidation [26–28]. SiO_2/InP structures are fabricated through the chemical deposition of SiH_4 molecules on a passivated surface followed by plasma oxidation [24]. In all these cases, the interface turns out to be multiphase.

3. OBJECTS OF STUDY

The study was carried out on samples similar to those obtained in [6], where a record-low density of states of the NatO–InP/InP interface ($N_{ss} \sim 4 \times 10^{10}$ eV^{-1} cm^2) and hysteresis of the C–V characteristics ($\Delta U \sim 0.2$ eV) were demonstrated. The XPS method was used in this study for controlling the quality of the NatO–InP chemical composition by monitoring the position of the center of gravity of the experimental line and the shifts of this center caused by variations in the technological parameters. The native oxide layer was formed on the InP surface by plasma oxidation. Its thickness, as derived by layer-by-layer ion milling, was 3–5 nm, which was found to agree with ellipsometric measurements. Earlier studies and the present study were performed on an LHS-11 (Leybold) electron spectrometer. The samples were subjected to AlK_α x rays ($h\nu$ = 1486.6 eV). The spectra of the photoelectrons emitted from the inner (core) shells of indium and phosphorus, In3$d_{5/2}$ and P2p, were measured. Figures 1 and 2 present typical spectra with the quasi-continuous background subtracted. The NatO–InP spectra exhibit a common bell-shaped photoelectron line, which has to be decomposed into the primary constituents corresponding to different chemical phases. This problem is aggravated by the presence of several oxide phases with very similar binding energies of core electrons forming the single bell-shaped photoelectron line. InP is known to produce the following thermodynamically stable oxides: $In(PO_3)_3$ (1), $InPO_4$ (2), $InPO_3$ (3), In_2O_3 (4), and P_2O_5 (7). Tables 1 and 2 list for these compounds the electron binding energies E_b for the phosphorus 2p and indium 3$d_{5/2}$ shells, respectively, as well as data for the starting material InP (5), metallic indium In (6), and elemental phosphorus P (8). We solve below the problem of unfolding an experimental line into its primary constituents using the common method and proposed methods. Comparison of these solutions offers deeper insight into the potential of the latter method.

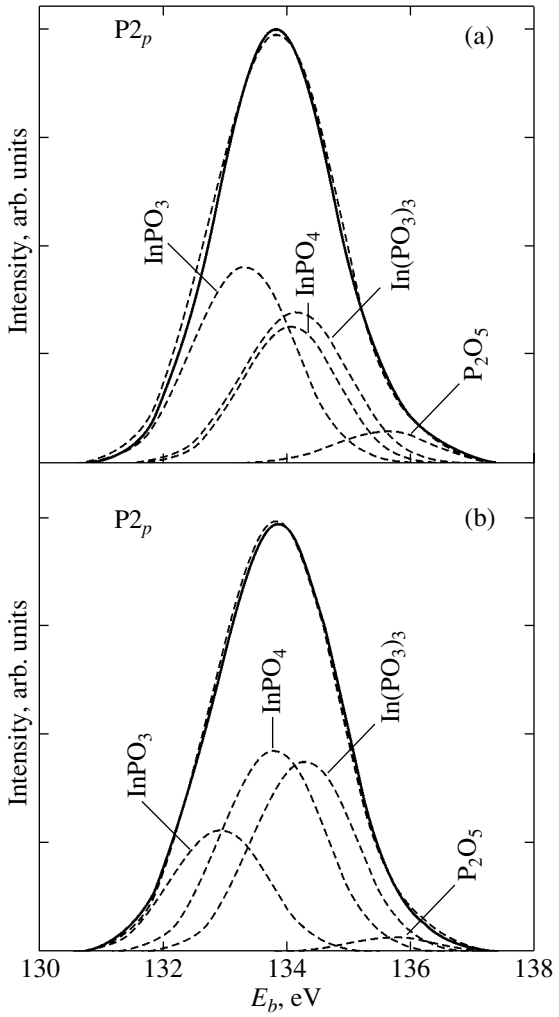

Fig. 1. Phosphorus P2*p* photoelectron spectra with the continuum background removed. Solid curve is an experimental spectrum. Dashed curves represent primary constituents corresponding to different chemical phases and also show the total model spectrum. Panels (a) and (b) relate to spectral decomposition performed by the common method and proposed methods, respectively.

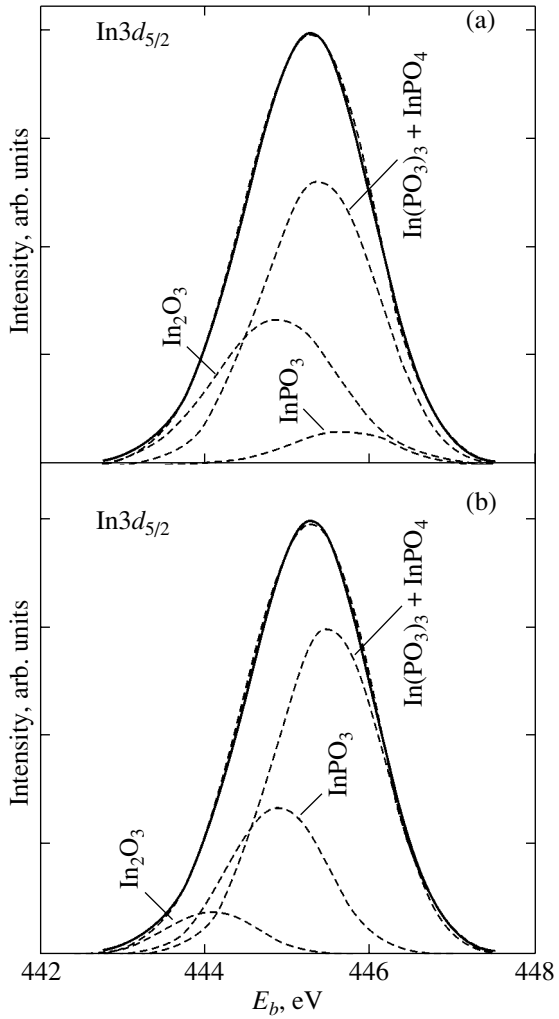

Fig. 2. Indium In3$d_{5/2}$ photoelectron spectra with the continuum background removed. Solid curve is an experimental spectrum. Dashed curves represent primary constituents corresponding to different chemical phases and also show the total model spectrum. Panels (a) and (b) relate to spectral decomposition performed by the common method and proposed methods, respectively.

4. DETERMINATION OF THE CHEMICAL COMPOSITION OF NATO–INP BY TRADITIONAL XPS

We assume that the number of possible chemical phases in the problem is known. The shape of the indium and phosphorus lines was derived from the photoelectron lines of unoxidized InP. For the binding energies of indium and phosphorus in the above compounds, we took values obtained by averaging the literature data (Tables 1, 2). Note that the values obtained in this way have errors as large as $\delta E_b \sim \pm 0.7$ eV, although the errors indicated in the corresponding publications generally do not exceed ±0.1 eV. The content of the chemical phases was determined from the amplitudes of the primary constituents, which were derived by minimizing the difference between the areas bounded by the fitting envelope and by the experimental curve. Figures 1a and 2a present the results of such a decomposition carried out in accordance with the prototype. The version thus obtained cannot, however, be considered acceptable, because the contents of the like phases derived independently from the indium and phosphorus lines differ strongly. Indeed, the sum of phases "1 + 2" (P) as found from the phosphorus line yields 40%, while the sum "1 + 2" (In) obtained from the indium line is 74%. The values of the fraction of phase 3 ($InPO_3$) determined independently from the indium and phosphorus lines differ by nearly an order of magnitude (41 and 5%). Variations in the width of the primary lines do not reduce these differences. It may thus be concluded that insufficient accuracy in determining the binding energy, errors in measurements of the spectra

and of the shape of the instrument function, and calculation accuracy, as well as errors involved in correcting for static charging of a dielectric sample under irradiation, do not hinder reliable determination of the chemical composition of a complex system.

5. DETERMINATION OF THE CHEMICAL COMPOSITION AND CORE-ELECTRON BINDING ENERGIES OF NatO–InP BY THE NEW XPS METHOD

5.1. Determination of Chemical Composition

Decomposition of a photoelectron spectrum into primary constituents in the prototype method has a unique solution. However, as shown above, this solution may be unacceptable because of the use of inaccurate or completely incorrect values of the core-electron binding energies E_b in chemical phases. The idea underlying the proposed approach consists actually in carrying out a self-consistent analysis of photoelectron lines of two or more elements present in the material under study [4]. It turns out that no self-consistent solution can be found without introducing additional fitting parameters. We accepted for such free parameters the binding energies E_b, because the reliability and accuracy of their determination from experiments with reference samples is entirely inadequate in many cases. The requirement that the contents of different chemical phases derived from decomposing spectra of two or more elements be identical makes the solution of the problem unique. An important implication of this approach is the possibility of dispensing with reference samples and determining, in one experiment, not only the chemical composition of a material but also the core-electron binding energies of the elements entering these phases. As will be shown subsequently, the accuracy and reliability of determination of these energies are substantially higher than those of the relevant data cited in the literature.

To illustrate the potential of the proposed approach, let us analyze the chemical composition of the phase of the above indium phosphide plasma oxide. The decomposition basis necessary for analysis is well known and consists of the five thermodynamically stable indium phosphide oxides mentioned above and listed in Tables 1 and 2. The binding energies E_b of In3$d_{5/2}$ and P2p core electrons in these compounds are known, although with a large error ($\delta E_b \sim \pm 0.3$–0.7) (Tables 1, 2). In contrast to the prototype, however, these data are not needed in our modification of the method. Only information on the decreasing order of these energies in the above compounds is used: $E_7^{\mathrm{P}} > E_1^{\mathrm{P}} > E_2^{\mathrm{P}} > E_3^{\mathrm{P}}$ ($\geqslant E_8^{\mathrm{P}} > E_5^{\mathrm{P}}$) and $E_1^{\mathrm{In}} > E_2^{\mathrm{In}} > E_3^{\mathrm{In}} > E_4^{\mathrm{In}} > E_5^{\mathrm{In}}$. Furthermore, this sequence for the above oxides was obtained independently earlier [6] from thermodynamic estimates. As a zero approximation for the above binding energies in our example, we chose the average energies from Tables 1 and 2. However, the final result presented below can be obtained for any choice of these energies from an interval of the experimental spectra, provided the above inequalities are preserved. The experimental spectral lines were unfolded using a Gaussian approximation of the spectrometer instrument function, which was determined in experiments with unoxidized indium phosphide. Variation of the primary constituent lines in width did not change the results of the decomposition.

Table 1. Phosphorus P2p core electron binding energies in various chemical compounds

7	1	2	3	8	5	References
P_2O_5	$In(PO_3)_3$	$InPO_4$	$InPO_3$	P	InP	
135.5	133.7	134.1	–	130.2	128.8	[7]
–	134.6	134.2	–	–	128.8	[8]
135.4	–	134.2	–	–	129.2	[9]
–	–	134.3	–	–	129.2	[10]
–	–	–	–	–	128.6	[11]
135.8	–	133.8	133.3	–	128.8	[12]
136.0	–	134.0	133.5	–	129.0	[13]
–	–	136.0	133.5	–	129.0	[14]
–	–	–	–	–	–	[15]
135.8	–	133.1	–	–	–	[16]
135.7 ± 0.3	134.2 ± 2.0	134.1 ± 0.7	133.4 ± 0.2	130.2	128.9 ± 0.2	Mean
135.8 ± 0.1	134.3 ± 0.1	133.9 ± 0.1	132.9 ± 0.1	–	128.8 ± 0.1	This work

Table 2. Indium In3$d_{5/2}$ core electron binding energies in various chemical compounds

1	2	3	4	5	6	References
$In(PO_3)_3$	$InPO_4$	$InPO_3$	In_2O_3	InP	In	
445.4	445.7	–	444.7	444.4	444.0	[7]
445.7	445.7	–	444.7	443.9	–	[8]
–	–	–	–	–	–	[9]
–	445.6	–	444.8	444.4	444.0	[10]
–	–	–	444.4	444.1	443.6	[11]
–	446.4	446.1	445.4	444.6	–	[12]
–	446.0	445.7	445.0	444.2	–	[13]
–	446.0	445.7	445.0	444.2	–	[14]
–	–	–	444.7	–	–	[15]
–	–	–	445.4	444.6	–	[16]
445.6 ± 0.7	445.9 ± 0.5	445.8 ± 0.5	444.9 ± 0.3	444.3 ± 0.2	443.9 ± 0.4	Mean
445.5 ± 0.1	445.5 ± 0.1	444.9 ± 0.1	444.2 ± 0.1	444.0 ± 0.1	443.7 ± 0.1	This work

The results of the final decomposition of indium and phosphorus spectra are presented in Figs. 1b and 2b, respectively. Because of phases 1 and 2 being similar in binding energies, their sum envelope is shown in the indium spectrum. The line of unoxidized InP (5) also falls onto the low-energy tail of this spectrum. Its contribution is small, however, as follows from the phosphorus spectrum. The small contributions deriving from unoxidized InP (5) and elemental phosphorus P (8) manifest themselves in the phosphorus spectrum as a single weak line separated from the oxide spectrum by about 5 eV. The convergence of the iteration procedure turned out to be very fast. Only five iteration cycles were needed to complete the decomposition. The fractions of chemical phases 1, 2, 3, 4, and 7 turned out to be 16, 49, 29, 4, and 2%, respectively. In the last decomposition, the chemical phase fractions derived from the indium and phosphorus spectra coincide to within 1–3%. Within these limits, the relative error in determining the fractions of main phases does not exceed 5–10%.

Summing up the above steps, we propose the following algorithm for the decomposition of a spectrum in lines, for instance, of two elements.

(1) Determination of the largest possible number of chemical phases, setting the order of the binding energies E_b of each element chosen for the analysis, and zero-approximation choice of any values of E_b within the experimental line.

(2) Approximation of the experimental spectra by a set of primary lines centered on the $E_{b,i}^{1,2}$ energies, and determination of the relative chemical phase fractions $C_{b,i}^1$, $C_{b,i}^2$, … for each of the elements under analysis (b is the number of the chemical phase; 1 and 2 are the numbers of the elements under study or of the spectral lines; i is the iteration cycle index). Here, the relative fraction is understood to be the ratio of the corresponding primary line area (corrected for the stoichiometric coefficient of the phase) to the sum of the areas of the primary lines of the phases common to each of the elements under analysis. The composition ($C_{b,i}^1$, $C_{b,i}^2$, …) is determined by varying the intensity of the primary lines (and the width, if the width of the instrument function is less than the natural line width) and minimizing the difference between the experimental and calculated spectra.

(3) Determination of the difference $\Delta_{b,i}^{2-1} = C_{b,i}^2 - C_{b,i}^1$ between the relative chemical phase fractions obtained for each element.

(4) The iteration procedure comes to an end if $\Delta_{b,i}^{2-1} < \delta$ (the preset error of determination of the chemical composition). Determining the chemical composition in molecular percentage by renormalizing the relative chemical phase fractions to the total area bounded by the primary lines of all chemical phases present in the sample.

(5) If $\Delta_{b,i}^{2-1} > \delta$, then the step $\Delta E_{b,i}^{1,2}$ is chosen to minimize this difference and a new iteration cycle is performed with a new set of energies $E_{b,i+1}^{1,2}$; i.e., we return to the second point of the proposed algorithm.

This algorithm was also used to advantage in an analysis of copper oxide films grown by magnetron sputtering with the use of a source of atomic oxygen [5].

5.2. Core-Electron Binding Energies E_b in Native InP Oxides

The above unfolding procedure yielded considerably more accurate and reliable binding energies. As seen from Tables 1 and 2, the data obtained in this study are generally close to the data derived by averaging over many sources, although in some cases the difference may be as large as 0.6–0.9 eV. Significantly, the systematic error of determination of the binding energy was reduced by a few times. The total error for the main phases did not exceed $\delta E_b \sim \pm 0.1$ eV. Shifting the center of the primary line produced in the final decomposition by an amount larger than 0.1 eV does not allow us to reach the preset error of determination. The conclusion that the reliability of determining the binding energy is improved in the above example is based on the fact that, if this quantity had been found with insufficient accuracy, the energy E_b could be identified with a wrong compound. For instance, the In3$d_{5/2}$ binding energy found in [12] for $InPO_3$ (446.1 eV) exceeds by 0.2 eV the energy for the $InPO_4$ oxide averaged over many sources instead of being less than this value (Tables 1, 2). The P2p binding energy determined in [14] for $InPO_4$ (136.0 eV) exceeds by 0.2 eV the averaged value for P_2O_5, thus also changing the sequence of the above phases. By contrast, the P2p binding energy for $InPO_4$ (136.0 eV) quoted in [16] is not 0.7–1.0 eV higher but rather 0.3 eV smaller than the averaged value for $InPO_3$. Hence, the technological processes based on these erroneous figures would be aimed at producing incorrect compounds.

5.3. The Surface To Be Oxidized Should Be Enriched in Phosphorus

The above illustration shows that the total fraction of the most stable and dielectrically strong $InPO_4$ and $In(PO_3)_3$ oxides in samples prepared by plasma oxidation may be as high as 65%, with the fraction of the undesirable oxide In_2O_3 not exceeding 4%. From the chemical formulas of these oxides, it follows that, in order to reach these figures, the surface to be oxidized has to be enriched in phosphorus. The conditions produced in the plasma oxidation technology employed here are apparently favorable for outdiffusion of this element from the bulk of the material. Preliminary dep-

osition of a certain amount of phosphorus onto the surface to be oxidized can conceivably change the chemical composition in the desired direction and thus improve the quality of the oxide and of the interface.

6. CONCLUSIONS

Thus, a new method has been proposed for analyzing the chemical phase composition of a substance and determining the core-electron binding energies, which is a modification of the XPS technique. In contrast to the prototype, this method is standardless. The method improves the reliability and accuracy of quantitative determination of the chemical composition of a substance and of the core-electron binding energies of atoms in the chemical phases under study. Indeed, in the above example of determining the NatO–InP chemical phase composition, the relative error of determination of the main phase fractions did not exceed 5–10%. The systematic error of determining the binding-energy was reduced by a few times. The total error for the main phases did not exceed 0.1 eV.

ACKNOWLEDGMENTS

This study was supported by the Ministry of Industry, Science, and Technology of the Russian Federation (program "Physics of Solid-State Nanostructures") and the Presidium of the Russian Academy of Sciences (program "Low-Dimensional Quantum Structures").

REFERENCES

1. K. Siegbahn, C. Nordling, A. Fahlman, R. Nordberg, K. Hamrin, J. Hedman, G. Johansson, T. Bergmark, S.-E. Karlsson, I. Lindgren, and B. Lindberg, *Atomic, Molecular and Solid State Structure Studied by Means of Electron Spectroscopy* (Almqvist and Wiksells, Uppsala, 1967; Mir, Moscow, 1971).
2. *Practical Surface Analysis by Auger and X-ray Photoelectron Spectroscopy*, Ed. by D. Briggs and M. Seah (Wiley, New York, 1983; Mir, Moscow, 1987).
3. D. Woodruff and T. Delchar, *Modern Techniques of Space Science* (Cambridge Univ. Press, Cambridge, 1986; Mir, Moscow, 1989).
4. Yu. S. Gordeev, V. M. Mikushkin, and S. E. Sysoev, RF Patent No. 2,170,421, Byull. Izobret., No. 19 (2001).
5. É. M. Sher, V. M. Mikushkin, S. E. Sysoev, and B. T. Melekh, Zh. Tekh. Fiz. **70** (3), 78 (2000) [Tech. Phys. **45**, 365 (2000)].
6. E. D. Belyakova, A. V. Gabaraeva, A. T. Gorelenok, R. V. Karzhavin, V. M. Mikushkin, S. E. Sysoev, and N. M. Shmidt, Poverkhnost, No. 7, 88 (1992).
7. G. Hollinger, E. Bergignat, J. Joseph, and Y. Robach, J. Vac. Sci. Technol. A **3**, 2082 (1985).
8. Maria Faur, Mircea Faur, D. T. Jayne, M. Goradia, and C. Goradia, Surf. Interface Anal. **15**, 641 (1990).
9. H. Ishii, H. Hasegawa, A. Ishii, and H. Ohno, Appl. Surf. Sci. **41/42**, 390 (1989).
10. S. M. Thurgate and N. E. Erickson, J. Vac. Sci. Technol. A **8**, 3669 (1990).
11. C. W. Wilmsen and R. W. Kee, J. Vac. Sci. Technol. **15**, 1513 (1978).
12. I. K. Han, E. K. Kim, J. I. Lee, S. H. Kim, K. N. Kang, Y. Kim, H. Lim, and H. L. Park, J. Appl. Phys. **81**, 6986 (1997).
13. Y. S. Lee and W. A. Anderson, J. Appl. Phys. **65** (10), 4051 (1989).
14. N. Shibata and H. Ikoma, Jpn. J. Appl. Phys., Part 1 **31** (12A), 3976 (1992).
15. L. L. Kazmerski, P. J. Ireland, P. Sheldon, T. L. Chu, S. S. Chu, and C. L. Li, J. Vac. Sci. Technol. **17**, 1061 (1980).
16. A. Guivarc'h, H. L'Haridon, and G. Pelous, J. Appl. Phys. **55** (4), 1139 (1984).
17. Yun Sun, Zhi Liu, F. Machuca, P. Pianetta, and W. E. Spicer, J. Vac. Sci. Technol. A **21** (1), 219 (2003).
18. P. Legay, F. Caillet, J. Decobert, L. Leprince, G. Le Roux, and M. Quillec, J. Appl. Phys. **85** (4), 2428 (1999).
19. D. Pulver, C. W. Wilmsen, D. Niles, and R. Kee, J. Vac. Sci. Technol. B **19** (1), 207 (2001).
20. J. van de Ven, J. J. M. Binsma, and N. M. A. de Wild, J. Appl. Phys. **67** (12), 7568 (1990).
21. P. N. K. Deenapanray, A. Martin, P. Lever, and C. Jagadish, Electrochem. Solid-State Lett. **5** (6), G41 (2002).
22. L. S. Berman, A. D. Gabaraeva, A. V. Kamanin, I. Karimov, L. E. Klyachkin, L. V. Sharonova, and N. M. Shmidt, Pis'ma Zh. Tekh. Fiz. **22** (2), 65 (1996) [Tech. Phys. Lett. **22**, 76 (1996)].
23. A. T. Gorelenok, N. D. Ilyinskaya, I. A. Mokina, and N. M. Shmidt, in *Semiconductor Technology: Processing and Novel Fabrication Techniques*, Ed. by M. E. Levinstein and M. S. Shur (Wiley, New York, 1997).
24. M. P. Besland, S. Jourba, M. Lambrinos, P. Louis, P. Viktorovich, and G. Hollinger, J. Appl. Phys. **80** (5), 3100 (1996).
25. J. Henry and J. Livingstone, in *Design, Fabrication, and Characterization of Photonic Devices II*, Ed. by Marek Osinski, Soo-Jin Chua, and Akira Ishibashi (SPIE, Bellingham, 2001); Proc. SPIE **4594**, 447 (2001).
26. R. Touhami, S. Ravelet, M. C. E. Yagoub, and H. Baudrand, J. Appl. Phys. **94** (10), 6574 (2003).
27. Sh. Morikita and H. Ikoma, J. Vac. Sci. Technol. A **21** (1), 226 (2003).
28. T. Motegy, J. Tomita, and H. Ikoma, Jpn. J. Appl. Phys. Lett. **38** (4B), L420 (1999).

Translated by G. Skrebtsov

Physics of the Solid State, Vol. 46, No. 10, 2004, pp. 1836–1841. Translated from Fizika Tverdogo Tela, Vol. 46, No. 10, 2004, pp. 1776–1780.

SEMICONDUCTORS AND DIELECTRICS

Investigation of the Electronic Structure and Chemical Bonding of Lead Hexacyanoferrate(III)

V. M. Zaĭnullina*, M. A. Korotin, and L. G. Maksimova***

** Institute of Solid-State Chemistry, Ural Division, Russian Academy of Sciences, Pervomaĭskaya ul. 91, Yekaterinburg, 620219 Russia*

*** Institute of Metal Physics, Ural Division, Russian Academy of Sciences, ul. S. Kovalevskoĭ 18, Yekaterinburg, 620219 Russia*

e-mail: Veronika@ihim.uran.ru, mkorotin@optics.imp.uran.ru

Received December 1, 2003; in final form, March 10, 2004

Abstract—The electronic structure of lead hexacyanoferrate(III) is calculated by the *ab initio* tight-binding linear muffin-tin orbital (TB-LMTO) method in the LSDA + U approximation. The influence of vacancies in the lead sublattice on the electronic spectrum, chemical bonding, and magnetic properties of the $Pb_{1.5}Fe(CN)_6$ phase is investigated. Analysis of the electronic spectrum shows that this compound is characterized by semiconductor conductivity. It is demonstrated that the semiconductor gap is associated with the charge ordering of iron(III) ions. © *2004 MAIK "Nauka/Interperiodica".*

1. INTRODUCTION

Recently, Polyakov *et al.* [1] synthesized anhydrous lead and tin hexacyanoferrates(II) and hexacyanoferrates(III). X-ray and neutron diffraction investigations revealed that the $Pb_2Fe(CN)_6$, $Pb_{1.5}Fe(CN)_6$, and $Sn_2Fe(CN)_6$ phases crystallize in a trigonal crystal system [2]. These compounds belong to the group of cyanometallate complexes of the $A_k^{(II)}[Fe^{(II, III)}(CN)_6]_m^{n-}$ type (where *A* is a transition metal cation). The majority of these compounds possess high Curie temperatures and good ion-exchange properties (the ability of transition metal cations involved in the first coordination sphere of the complexes to exchange with heavy univalent alkali metal ions in solutions) [3–6]. Owing to their physicochemical properties, the *p* and *d* element hexacyanoferrates can be used as inorganic sorbents and precursors for designing three-dimensional molecular magnets with controlled magnetic moments [3–6].

It is known that the magnetic ordering in hexacyanoferrates is associated with the indirect exchange interactions through CN groups [3, 4], whereas the Fe–Fe direct interactions are absent, because the distances between the nearest neighbor iron ions are usually larger than 6 Å. The magnetic interactions between $Fe(CN)_6$ octahedra occur through an *A* magnetic ion according to the scheme …–$(NC)_5$–Fe^{III}–CN–*A*–NC–Fe^{III}–$(CN)_5$–…, where *A* = Fe, Co, Ni, Cr, and Mn. In the $Pb_{1.5}Fe(CN)_6$ compound, $Fe(CN)_6$ octahedra are joined through Pb^{2+} ions. At present, the origin of magnetic interactions in lead hexacyanoferrate is not clearly understood. Quantum-chemical investigations of the electronic spectra and chemical bonding in cyanometallate complexes are predominantly reduced to cluster calculations of crystal lattice fragments of the $(CN)_5$–*A*–NC–*B*–$(CN)_5$ type [7, 8]. The exception is provided by a few recent works [9–11]. Ryzhkov *et al.* [9] calculated the electronic structure of the $Pb_2Fe(CN)_6$ compound and the effective charges at atoms (three-dimensional integrals of the charge density over spatial domains between minima of the electron density) by the discrete variation method within an extended-cluster model. The effective charge at iron atoms varied from 2.35 to 2.75 and appeared to be greater than that corresponding to their formal oxidation state in the $Pb_2Fe(CN)_6$ compound. Zhukov *et al.* [10] and Zaĭnullina *et al.* [11] analyzed the electronic spectra and chemical bonding in the $Pb_2Fe(CN)_6$, $Pb_{1.5}Fe(CN)_6$, and $Sn_2Fe(CN)_6$ phases in the framework of the *ab initio* tight-binding linear muffin-tin orbital (TB-LMTO) approach and Hückel band calculations.

In this work, we investigated the magnetic properties of the $Pb_{1.5}Fe(CN)_6$ compounds. For this purpose, the electronic structure of $Pb_{1.5}Fe(CN)_6$ was calculated by the *ab initio* TB-LMTO method in the LSDA + U approximation [12].

2. CRYSTAL STRUCTURE

According to x-ray and neutron powder diffraction data obtained with the Rietveld method, the $Pb_{1.5}Fe(CN)_6$ anhydrous compound crystallizes in a trigonal crystal system (space group $P\bar{3}$, $Z = 1$) with the lattice parameters $a = 7.1879(3)$ Å and $c = 5.5092(4)$ Å [11]. The $Pb_{1.5}Fe(CN)_6$ compound is isostructural to the $Pb_2Fe(CN)_6$ compound (Table 1). The structure of the $Pb_{1.5}Fe(CN)_6$ compound consists of layers formed by $[Fe(CN)_6]^{n-}$ complexes, where $n = 3$ and

4 (Fig. 1). Iron ions Fe^{2+} and Fe^{3+} are located inside these complexes and coordinate six $(CN)^-$ groups. Lead ions are positioned within distorted octahedra formed by six nitrogen ions belonging to the six nearest $Fe(CN)_6$ complexes (three complexes from one layer and three complexes from another layer). There are three long and three short Pb–N interatomic distances. The $Pb_2Fe(CN)_6$ and $Pb_{1.5}Fe(CN)_6$ compounds have a layered structure: triads of the nearest $[Fe(CN)_6]^{n-}$ complexes are joined together into layers by bridging lead atoms. The same bridging lead atoms (the coordination number is 3 + 3) link the nearest triad of the complexes from the adjacent layer. The interaction between complexes occurs through nitrogen–lead–nitrogen bonds.

In the crystal lattice of the $Pb_{1.5}Fe(CN)_6$ compound, unlike the crystal lattice of the $Pb_2Fe(CN)_6$ compound, approximately a quarter of the lead positions turn out to be vacant. Vacancies in the lead sublattice are distributed in a random manner.

Table 1. Structural parameters of the $Pb_2Fe(CN)_6$ and $Pb_{1.5}Fe(CN)_6$ phases

Atom (position)	*x*/*a*	*y*/*b*	*z*/*c*	*N*
$Pb_2Fe(CN)_6$				
Pb(2*d*)	1/3	2/3	0.6005(5)	1.00
Fe(1*a*)	0	0	0	1.00
C(6*g*)	0.0654(6)	0.2502	0.1956(8)	1.00
N(6*g*)	0.3014(5)	0.9053	0.3070(7)	1.00
$Pb_{1.5}Fe(CN)_6$				
Pb(2*d*)	1/3	2/3	0.5959(6)	0.91
Fe(1*a*)	0	0	0	1.00
C(6*g*)	0.0595(7)	0.2455(7)	0.1979(9)	1.00
N(6*g*)	0.3016(6)	0.9085(5)	0.3093(8)	1.00

Note: *N* is the occupancy of the atomic position.

3. CALCULATION TECHNIQUE

The electronic structure of lead hexacyanoferrate(III) was calculated in terms of the LSDA + U local spin density functional [12], which includes one-site Coulomb correlations.

The calculations were performed with a cell of composition $Pb_3[Fe(CN)_6]_2E_{39}$, where E stands for empty spheres. Since the methods under consideration were developed and used for close-packed structures, additional empty spheres were introduced into the atomic basis set of hexacyanoferrate with a rather loose structure. The empty spheres were predominantly located between layers composed of iron–carbon–nitrogen octahedra. The computational cell for the $Pb_{1.5}Fe(CN)_6$ phase was constructed in the following way. First, the composition of the computational cell was chosen such that it would be most similar to the composition of the phase under investigation. Second, the cell with the minimum atomic basis set was used for this composition. The chosen cell of the composition $Pb_3[Fe(CN)_6]_2E_{39}$ was obtained through double translation of the trigonal unit cell along the *c* axis and removal of one out of four lead atoms. The symmetry of this cell was lower than that of the unit cell of the $Pb_2Fe(CN)_6$ phase. The model structure of the $Pb_{1.5}Fe(CN)_6$ phase contained two types of nonequivalent iron atoms (Fe1, Fe2), three types of nonequivalent lead atoms, and six types of carbon and nitrogen atoms. The Fe2 atom was positioned closer to the lead vacancy. Our model of the cell was based on the assumption that defects (lead vacancies) are located at regular intervals.

The basis set of valence orbitals of the $Pb_{1.5}Fe(CN)_6$ phase included the valence *ns* and *np* orbitals of Pb, C, N, and E atoms and the 4*s*, 4*p*, and 3*d* orbitals of Fe atoms. The $(n + 1)d$ orbitals of C and N atoms and the *nd* states of Pb atoms were taken into account only within the down-folding approach [13], which is based on the Löwdin perturbation theory [14]. The calculations were performed using 32 *k* points in the Brillouin zone (12 *k* points per irreducible part of the Brillouin zone). For the $Pb_{1.5}Fe(CN)_6$ phase, the optimum radius ratios r_{Pb}/r_C and r_{Fe}/r_C were equal to 3 and 1.92, respectively. It was assumed that, in the $Pb_{1.5}Fe(CN)_6$ structure, the radius of the empty sphere occupying a lead site is equal to the atomic radius of lead.

It turned out that the results of nonmagnetic calculations for the $Pb_{1.5}Fe(CN)_6$ phase are inconsistent with experimental data. The absence of the band gap at the Fermi level in the electronic spectrum of the $Pb_{1.5}Fe(CN)_6$ crystal is associated with the fact that strong correlation effects characteristic of iron compounds were ignored in the LSDA calculations. For this reason, the *ab initio* calculations for the $Pb_{1.5}Fe(CN)_6$ phase were performed in the LSDA + U approximation, which provides a way of analyzing systems with strong Coulomb correlations. The parameters used in the calculations were as follows: $U = 8.0$ eV and $J = 0.88$ eV.

The schemes of filling 3*d* orbitals of iron ions in the $Pb_{1.5}Fe(CN)_6$ phase were examined by calculating the

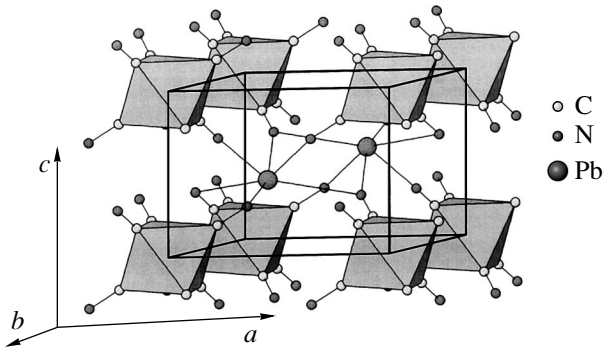

Fig. 1. Crystal structure of the $Pb_2Fe(CN)_6$ phase.

Table 2. Atomic parameters used in the extended Hückel calculations: the ionization potentials of valence orbitals H_{ii}, the exponents ξ_i, and the weight coefficients C_i of exponents in the expressions for atomic orbitals of the Slater type [17]

Atom	Orbital	H_{ii}, eV	$\xi_1(C_1)$ $\xi_2(C_2)$
Pb	6*s*	15.7	2.35 (1.00)
	6*p*	8.0	2.06 (1.00)
Fe	4*s*	9.10	1.90 (1.00)
	4*p*	5.32	1.90 (1.00)
	3*d*	12.60	5.35 (0.5505)
			2.0 (0.6260)
C	2*s*	21.4	1.625 (1.00)
	2*p*	11.4	1.625 (1.00)
N	2*s*	26.0	1.95 (1.00)
	2*p*	13.4	1.95 (1.00)

occupation matrices for Fe^{3+} ions in a local coordinate system. The local coordinate system is a Cartesian coordinate system that involves an iron atom at the origin and is obtained by transforming a trigonal coordinate system into a cubic coordinate system [15]. As a result, the *E*2, *E*1, and *A*1 3*d* orbitals of iron atoms (characterizing the trigonal crystal system) are transformed into the e_g and t_{2g} orbitals.

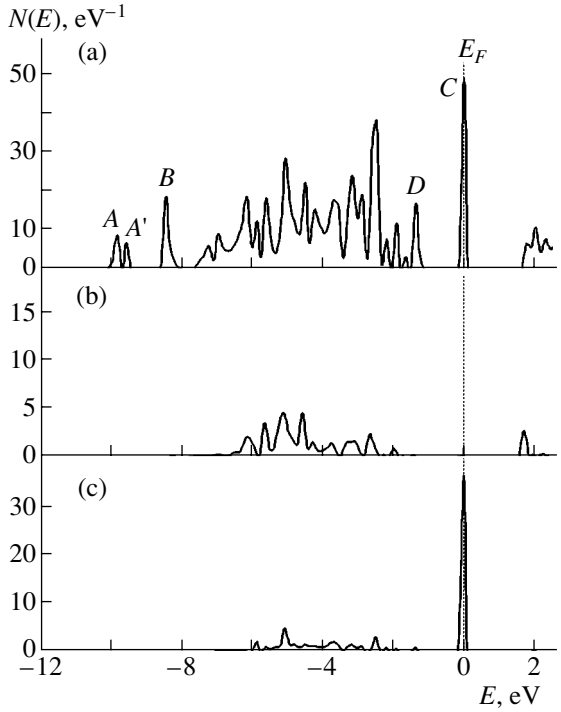

Fig. 2. Densities of states for the $Pb_{1.5}Fe(CN)_6$ semimetal compound: (a) the total density of states and (b) Fe1 3*d* and (c) Fe2 3*d* partial densities of states. LSDA + U calculations.

The nature and strength of the chemical interactions in the $Pb_{1.5}Fe(CN)_6$ compound were analyzed in the framework of semiempirical extended Hückel calculations [16]. The standard parameters used in the extended Hückel calculations are tabulated in [17] and presented in Table 2.

4. RESULTS AND DISCUSSION

The electronic structures calculated in the LSDA approximation for the $Pb_2Fe(CN)_6$ and $Pb_{1.5}Fe(CN)_6$ phases were discussed in our earlier works [10, 11]. According to the calculations, the electronic band structure of these phases is characterized by a large number of sharp narrow peaks. This is typical of molecular crystals. In the electronic spectrum of the compounds, it is possible to distinguish four bands. The band observed in the low-energy range corresponds to the Pb 6*s* and Fe 4*s* states. This band is split into two bands for the $Pb_{1.5}Fe(CN)_6$ phase. The broad valence band is formed by the hybrid C 2*p* and N 2*p* states with a considerable contribution from the Fe 3*d* and Pb 6*s* states. In the vicinity of the Fermi level, the Fe 3*d* states are substantially split into two narrow peaks corresponding to the t_{2g} and e_g types of cubic symmetry.

As follows from the results of nonmagnetic calculations, the $Pb_{1.5}Fe(CN)_6$ phase has metallic conductivity. The Fermi level corresponds to the maximum of the narrow peak, which is predominantly attributed to the Fe 3*d* states.

In order to take into account the correlation effects, which are most likely rather strong for the $Pb_{1.5}Fe(CN)_6$ phase, the calculations were carried out in the LSDA + U approximation. These calculations resulted in two stable solutions (with close values of the total energy) for ferromagnetic ordering of iron ions. The first and second solutions correspond to a semiconductor with a band gap of 1.18 eV and a semimetal, respectively. For both solutions, the magnetic moment is equal to 2 μ_B per $Pb_3[Fe(CN)_6]_2E_{39}$ computational cell. The total and partial densities of states for the $Pb_{1.5}Fe(CN)_6$ phase with metallic and semiconductor conductivities are depicted in Figs. 2 and 3. The total density of states for the $Pb_{1.5}Fe(CN)_6$ phase with metallic conductivity (Fig. 2) is intermediate in shape and band location between the electronic spectra of the nonmagnetic phases $Pb_2Fe(CN)_6$ and $Pb_{1.5}Fe(CN)_6$. The calculated magnetic moments of $Fe1^{3+}$ and $Fe2^{3+}$ ions are identical and equal to 1 μ_B. The analysis of the occupation matrices for Fe^{3+} ions in the local coordinate system (see Section 3) enables us to propose the scheme of filling of the 3*d* orbitals of these ions (Fig. 4a). Both iron ions are in a low-spin state (have one unpaired electron in the 3*d* orbitals).

The electronic spectrum determined within the LSDA + U approximation for the $Pb_{1.5}Fe(CN)_6$ phase with semiconductor conductivity (Fig. 3) differs substantially from the electronic spectrum obtained on the

basis of nonmagnetic calculations [11]. Three peaks (*C*', *D*', *C*") associated with the Fe2 3*d* states appear at energies of –7.4, –6.7, and 1.2 eV. Three peaks corresponding to the Fe1 3*d* states are observed in the energy range from –1.2 to 0 eV. A considerable contribution to the density of states in the range of the peaks *D* and *D*' is made by the valence *ns* and *np* states of carbon, nitrogen, and lead ions. The bands of the Pb 6*s* states (peaks *A*, *A*') and Fe 4*s* states (peak *B*) are shifted toward the low-energy range in the electronic spectrum of the $Pb_{1.5}Fe(CN)_6$ phase as compared to their positions in the spectrum of the $Pb_2Fe(CN)_6$ phase. The calculated magnetic moments of iron ions in the $Pb_{1.5}Fe(CN)_6$ semiconductor are equal to 0 and 1.97 μ_B for the Fe1 and Fe2 ions, respectively. The analysis of the occupation matrices for the $Fe1^{3+}$ and $Fe2^{3+}$ ions in the local coordinate system made it possible to propose different schemes of filling of the 3*d* orbitals of iron ions. The Fe1 iron ion is nonmagnetic; i.e., it is in the low-spin state. The Fe2 iron ion has two unpaired electrons in the 3*d* orbital (intermediate state). As a rule, trivalent iron ions in the low-spin state have a $t_{2g}^{\uparrow 3}t_{2g}^{\downarrow 2}$ configuration (Fig. 4a). The Fe^{3+} ions with magnetic moments equal to 0 and 1.97 μ_B in the $Pb_{1.5}Fe(CN)_6$ semiconductor can be represented using either of two possible schemes. In the first scheme, the presence of trivalent iron ions with these magnetic moments is due to a strong hybridization of the Fe 3*d* orbitals and the C 2*p* orbitals (Fig. 4b). According to the second scheme, the aforementioned magnetic moments of the iron ions are associated with the charge ordering of Fe^{2+} and Fe^{4+} ions (Fig. 4c).

In the former case, a strong Fe 3*d*–C 2*p* hybridization results in electron transfer from one carbon ion to the t_{2g} level of the $Fe1^{3+}$ ion in the low-spin state and from another carbon ion to the e_g orbitals of the $Fe2^{3+}$ ion in the intermediate state (Fig. 4b). This scheme provides a satisfactory explanation of the electron distribution only for the semiconductor, even though it remains unclear how the t_{2g} orbitals of iron ions can participate in the hybridization with the 2*p* orbitals of carbon ions. For the semimetal compound, the strong hybridization scheme cannot explain the unit magnetic moment of iron(III) ions.

A more conclusive explanation for the difference between the calculated local magnetic moments of the Fe1 and Fe2 iron ions in the $Pb_{1.5}Fe(CN)_6$ semiconductor is based on the assumption that there is a charge ordering of Fe^{2+} and Fe^{4+} ions (Fig. 4c). This assumption is confirmed by three arguments. First, in the framework of this scheme, an approximately identical Fe 3*d*–C 2*p* hybridization is observed for both solutions (semiconductor and semimetal). Second, the charge ordering of iron(III) ions in the $Pb_{1.5}Fe(CN)_6$ phase is supported by an energy gain when the high-energy e_g states remain unoccupied. Finally, third, the validity of the above assumption is confirmed by the different charges in the 3*d* orbitals inside spheres of the Fe1 and Fe2 ions: their difference is equal to 0.5*e*. We give preference to the second scheme for explaining the charge polarization of iron ions, according to which the charge ordering of iron(III) ions (Fe^{2+}, Fe^{4+}) is responsible for the experimentally revealed semiconductor properties of the $Pb_{1.5}Fe(CN)_6$ phase [18].

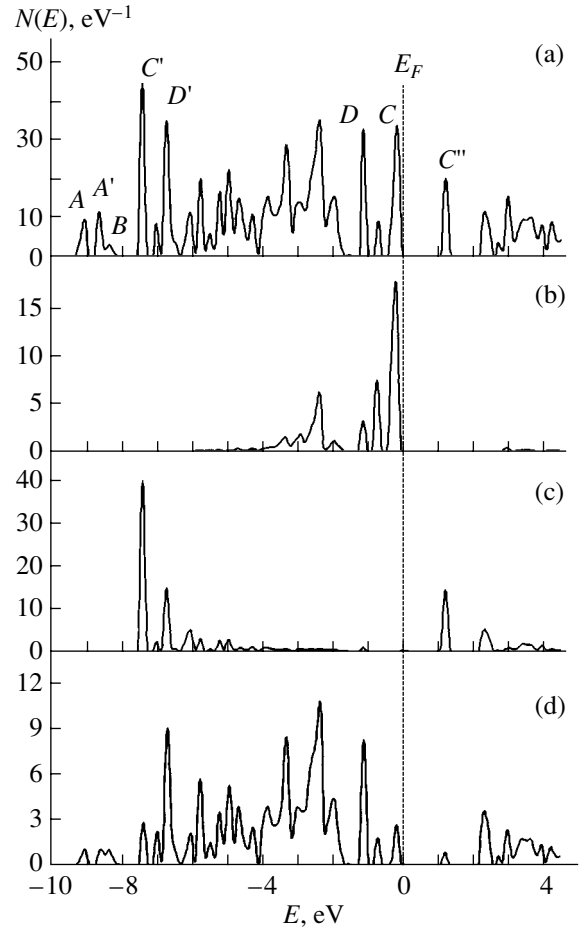

Fig. 3. Densities of states for the $Pb_{1.5}Fe(CN)_6$ semiconductor: (a) the total density of states and (b) Fe1 3*d*, (c) Fe2 3*d*, and (d) C 2*p* partial densities of states.

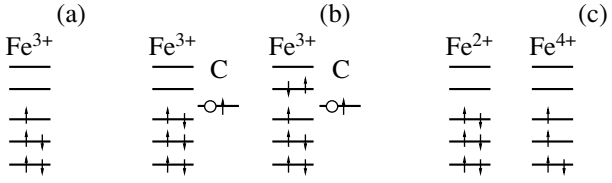

Fig. 4. Schemes illustrating the charge polarization of iron ions in (a) the $Pb_{1.5}Fe(CN)_6$ semimetal compound and the $Pb_{1.5}Fe(CN)_6$ semiconductor for (b) strong Fe3*d*–C2*p* hybridization and (c) charge ordering of iron ions.

In addition to the calculations of the electronic structure and magnetic characteristics of the $Pb_{1.5}Fe(CN)_6$ phase, we analyzed the chemical interactions in the framework of the extended Hückel method.

Table 3. Bond lengths L and overlap populations Q of crystal orbitals in the $Pb_2Fe(CN)_6$ and $Pb_{1.5}Fe(CN)_6$ phases

Crystal		Pb–N1	Pb–N2	Fe–C	C–N
$Pb_2Fe(CN)_6$	L, Å	2.429	2.901	1.926	1.131
	Q, e	0.258	0.018	0.571	1.699
$Pb_{1.5}Fe(CN)_6$	L, Å	2.442	2.911	1.932	1.145
	Q, e	0.264	0.042	0.569	1.667

The pair interactions were estimated using the Mulliken overlap population Q of the bond. This quantity characterizes the covalent component of chemical bonding in solids. For a crystal with due regard for translational symmetry of the wave function φ_i, the overlap population of the crystal orbitals of atoms located at the points **l** and **m** can be written in the following form:

$$Q_{lm} = 2\sum_k \sum_{i\in l} \sum_{j\in m} \exp(i\mathbf{k}(\mathbf{m}-\mathbf{l}))c_k^{i*}c_k^j \times \int \varphi_i^*(\mathbf{r}-\mathbf{l})\varphi_j(\mathbf{r}-\mathbf{m})d^3\mathbf{r},$$

where k stands for the numbering of occupied crystal orbitals.

The overlap populations of the crystal orbitals, which were calculated from the above relationship, are listed in Table 3. For comparison, the corresponding values for the $Pb_2Fe(CN)_6$ phase are also given in this table. It is evident that the dominant role in the chemical bonding in the hexacyanoferrate structure is played by the Fe–C and C–N strong covalent interactions in layers composed of $Fe(CN)_6$ octahedra. The overlap population of the crystal orbitals for the C–N bonds is nearly three times higher than that for the Fe–C bonds. The long Pb–N2 bonds make an insignificant contribution. The changeover from the $Pb_2Fe(CN)_6$ phase to the $Pb_{1.5}Fe(CN)_6$ phase is accompanied by a strengthening of the Pb–N bonds, an insignificant decrease in the strength of the Fe–C bonds, and a weakening of the C–N interactions. The overlap populations of the crystal orbitals for the Fe–C and C–N bonds correlate well with their lengths (Table 3). The situation is different for the Pb–N interactions. An increase in the length of the Pb–N bond in the $Pb_{1.5}Fe(CN)_6$ phase is attended by an increase in the strength of this bond. The tendency observed in changes in the bond strength of the lead hexacyanoferrate(III) indicates that the electron density can easily be redistributed in the system of bonds …–Fe–C≡N–Pb–…. An enhancement of the Pb–N interactions is caused by the transfer of electron density from nitrogen atoms in the vicinity of vacancies to lead atoms. The shift of the electron density from iron ions to lead vacancies through a chain of C–N bonds leads to a decrease in the strength of the Fe–C bonds and an increase in the strength of the Pb–N bonds adjacent to the vacancy. This effect is confirmed by the magnetic calculations of the electronic spectrum. The Pb 6*s* states in the electronic spectrum of the $Pb_{1.5}Fe(CN)_6$ phase are shifted toward the low-energy range (Fig. 3a) as compared to those in the spectrum of the $Pb_2Fe(CN)_6$ phase.

5. CONCLUSIONS

Thus, the electronic structure of the recently synthesized lead hexacyanoferrate(III) was calculated by the TB-LMTO method in the LSDA + U approximation. It was found that the $Pb_{1.5}Fe(CN)_6$ phase possesses a semiconductor conductivity, which is in agreement with experimental data. The distinguishing feature in the electronic structure of compounds belonging to this class is that the Fe 3*d* states are strongly split into two narrow peaks (corresponding to the t_{2g} and e_g types of cubic symmetry) in the vicinity of the Fermi level. The semiconductor conductivity in the $Pb_{1.5}Fe(CN)_6$ phase can be associated with the charge ordering of Fe^{2+} and Fe^{4+} iron ions. It was revealed that strong covalent interactions occur in iron–carbon–nitrogen octahedra. The Pb–N interactions have a mixed ionic–covalent character.

ACKNOWLEDGMENTS

This work was supported by the Russian Foundation for Basic Research, project nos. 02-03-32806 and 01-02-17063. V.M. Zaĭnullina acknowledges the support of the Russian Science Foundation.

REFERENCES

1. E. V. Polyakov, T. A. Denisova, L. G. Maksimova, N. A. Zhuravlev, and L. Yu. Buldakova, Zh. Neorg. Khim. **45** (2), 334 (2000).
2. V. G. Zubkov, A. P. Tyutyunnik, I. F. Berger, L. G. Maksimova, T. A. Denisova, E. V. Polyakov, and I. G. Kuplun, Solid State Sci. **3** (3), 361 (2001).
3. I. V. Tanaeva, *Chemistry of Ferrocyanides* (Nauka, Moscow, 1971) [in Russian].
4. V. V. Pavlishchuk, Teor. Éksp. Khim. **33** (6), 341 (1997).
5. Massaaki Ohba, Nobuo Fukita, and Hisashi Okawa, J. Chem. Soc., Dalton Trans., No. 10, 1733 (1997).
6. I. A. Koval', K. B. Yatsimirskiĭ, S. Trofimenko, and V. V. Pavlishchuk, Teor. Éksp. Khim. **34** (6), 351 (1998).
7. M. Verdaguer, A. Bleuzen, V. Marvaud, J. Vaisserman, M. Seuleiman, C. Desplanches, A. Sculler, C. Train, R. Garde, G. Gelly, C. Lomenech, I. Rosenman, P. Veillet, C. Cartier, and F. Villain, Coord. Chem. Rev. **190–192**, 1023 (1999).
8. T. Mallah, S. Thiebaut, M. Verdaguer, and P. Veillet, Science **262**, 1554 (1993).
9. M. V. Ryzhkov, T. A. Denisova, V. G. Zubkov, and L. G. Maksimova, Zh. Strukt. Khim. **41** (6), 1123 (2000).

10. V. P. Zhukov, V. M. Zainullina, V. G. Zubkov, T. A. Denisova, and A. P. Tyutyunnik, Solid State Sci. **3** (5), 539 (2001).

11. V. M. Zaĭnullina, V. P. Zhukov, V. G. Zubkov, A. P. Tyutyunnik, L. G. Maksimova, and T. A. Denisova, Zh. Strukt. Khim. (in press).

12. A. I. Liechtenstein, V. I. Anisimov, and J. Zaanen, Phys. Rev. B **52** (8), R5467 (1995).

13. W. R. L. Lambrecht and O. K. Andersen, Phys. Rev. B **34** (4), 2439 (1986); O. K. Andersen and O. Jepsen, Phys. Rev. Lett. **53** (27), 2571 (1984).

14. P.-O. Löwdin, J. Chem. Phys. **19** (11), 1396 (1951).

15. K. Terakura, T. Oguchi, A. R. Williams, and J. Kübler, Phys. Rev. B **30** (8), 4734 (1984).

16. M.-H. Whangbo and R. Hoffman, J. Am. Chem. Soc. **100**, 6093 (1978).

17. S. Alvarez, *Tables of Parameters for Extended Huckel Calculations* (Univ. de Barcelona, Barcelona, 1989).

18. V. M. Zaĭnullina, V. G. Zubkov, A. P. Tyutyunnik, D. G. Kellerman, S. N. Shkerin, L. G. Maksimova, and T. A. Denisova, in *Proceedings of XXI International Chugaev Conference on Coordination Chemistry* (Kiev, 2003).

Translated by O. Borovik-Romanova

Physics of the Solid State, Vol. 46, No. 10, 2004, pp. 1842–1844. Translated from Fizika Tverdogo Tela, Vol. 46, No. 10, 2004, pp. 1781–1783.

SEMICONDUCTORS AND DIELECTRICS

Phosphorescence of CaF_2–Dy Crystals

V. V. Pologrudov and I. V. Grigorov

Irkutsk State University, ul. Lermontova 126, Irkutsk, 664003 Russia

e-mail: iohann@mail.ru

Received August 25, 2003; in final form, February 19, 2004

Abstract—The decay kinetics of phosphorescence excited by x-rays in a CaF_2–Dy crystal is investigated. It is found that localized charge carriers recombine through tunneling. The conclusion is drawn that, in the initial stages of x-ray irradiation, the accumulation of charge carriers occurs in pairs. This process is caused by the formation of excimer-like molecular states during excitation of the crystal. © *2004 MAIK "Nauka/Interperiodica".*

1. INTRODUCTION

Ionizing radiation generates free (band) charge carriers in a crystal and causes localization of opposite charges in hole and electron traps. It is generally believed that, since the electron and hole traps are point microdefects, they have no effect on each other and, hence, the localization of carriers of like charges occurs irrespective of whether the carriers of opposite charges are in a free or localized state. The concept of opposite charge carriers that do not interact either at the instant of localization or during further phosphorescence underlies the theory of phosphorescence [1] and many studies devoted to relaxation processes in excited phosphors.

Experimental observation of pair accumulation of charge carriers in wide-band-gap (ionic) crystals [2, 3] lent impetus to theoretical treatment of statistic (random) [4] and correlated [5, 6] or genetic [4] pairs. In those (and other) works, the question as to how one charge carrier affects another carrier of opposite charge was not considered. However, the possibility of localizing a charge carrier residing in a field of an oppositely charged carrier is of fundamental importance in elucidating the mechanism of carrier interaction.

The pair accumulation of charge carriers clearly manifests itself in tunneling luminescence. According to the tradition approach, which is based on the gas-kinetics theory of carrier interaction, the electronic processes associated with a point defect occur within a lattice site. Since tunneling suggests that the wave functions of the electronic states of spatially separated defects overlap, the gas-kinetics approximation is obviously invalid in this case. The possibility of a charged recombination center affecting the energy parameters of a trap is allowed for by the diffusion theory of phosphorescence [7] (a version of the classical approach to the description of motion of an electron prior to localization or recombination). However, according to this theory, the probability of carrier capturing in a trap residing in a field of a localized hole is negligible. In our previous papers [8–10], particular attention was drawn to the fact that the range of unrelaxed electronic states of point defects is large enough for spatially separated defects to interact with each other due to the overlap of the wave functions of their electronic states. From this point of view, in the present work, we studied the decay kinetics of phosphorescence of CaF_2 crystals activated with dysprosium.

2. EXPERIMENTAL TECHNIQUE

In our experiments, the phosphorescence with wavelength λ = 585 nm, which corresponds to the $4f \longrightarrow 4f$ intraconfigurational transitions of trivalent dysprosium, was measured after exposure of the crystal to x-ray irradiation (10 mA, 40 kV, BSV2-Cu tube, URS-55 x-ray apparatus) in the time range from several seconds to tens of minutes. The measurements were carried out at room temperature and liquid-nitrogen temperature. The phosphorescence was recorded using a monochromator, an FÉU-79 photomultiplier, and a recording potentiometer with a periodic time of 1 s. The activator content in crystals varied from 0.4 to 1.3 mol %.

3. RESULTS AND DISCUSSION

Figure 1 shows the phosphorescence decay for two crystals at different activator contents after 30-s exposure to x-ray irradiation. The decay curves are described by the Becquerel law; i.e., they are approximated well by hyperbolas of the form

$$J = (a + bt)^{-\alpha}, \quad (1)$$

where a, b, and α are constants.

It can be seen from Fig. 1 that the exponent α for the crystal at a higher activator content ($\alpha \approx 0.7$) is larger than that for the crystal at a lower activator content ($\alpha \approx 0.6$). As the time of exposure to x-ray irradiation increases (Fig. 1), the decay curve in log–log coordinates becomes gently flattened; i.e., at a long time of exposure to x-ray irradiation, the exponent of the hyperbola decreases to $\alpha \approx 0.5$ for crystals with differ-

1063-7834/04/4610-1842$26.00 © 2004 MAIK "Nauka/Interperiodica"

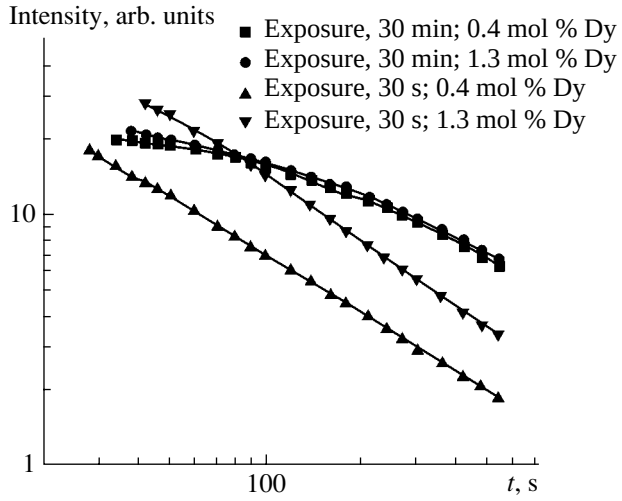

Fig. 1. Phosphorescence decay in CaF_2 : Dy crystals at room temperature.

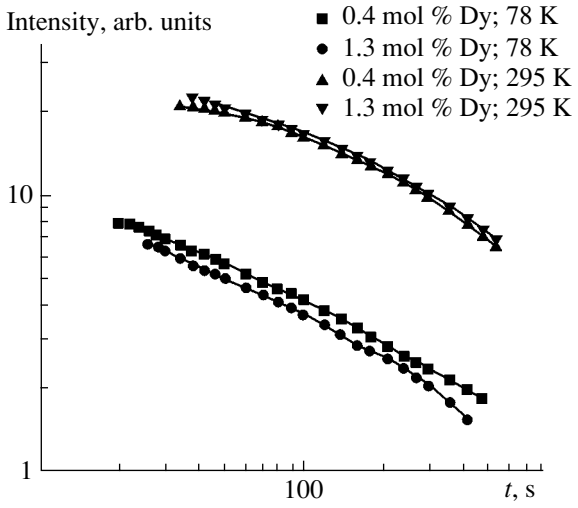

Fig. 2. Phosphorescence decay in CaF_2 : Dy crystals at temperatures of 78 and 295 K after 30-min exposure to x-ray irradiation.

ent contents. In the case when the crystals irradiated at room temperature are cooled to liquid-nitrogen temperature, the phosphorescence persists but its intensity slightly decreases, which has virtually no effect on the decay curve (Fig. 2).

Both the temperature behavior of phosphorescence and the decay curves approximated by hyperbolas with exponents less then unity indicate that localized charge carriers recombine through tunneling without the participation of band states. In this case, the decay kinetics of phosphorescence can be represented by the expression

$$J = \int_0^\infty f(r) w_T e^{-w_T t} dr, \qquad (2)$$

where $f(r)$ is the function describing the distribution of localized electrons over the distance r with respect to the occupied hole centers. This function depends on the overlap integral of the orbitals S of the electron and hole centers and on the probability of finding a nearest neighbor w: $f(r) \sim Sw$, where w_T is the probability of the tunneling transition and t is the time. The probability of finding a nearest neighbor w is the function of the concentration of localized charge carriers. Under the assumption that both the hole and electron traps are generated by an impurity, the probability w can be written in the form [11]

$$w = 4\pi r^2 c \exp(-4\pi r^3 c/3),$$

where c is the concentration of defects. It is known that, in CaF_2–Dy crystals, the Dy^{3+} ions transform into Dy^{2+} ions under x-ray irradiation and serve as electron-trapping centers [12]. Experimental investigations have revealed activator holes of two types: (i) holes of the first type are localized in the vicinity of a rare-earth ion [13], and (ii) holes of the second type are localized immediately at a rare-earth ion, thus changing its charge state (in our case, to Dy^{4+}) [14, 15]. In our consideration, the structure of hole centers is of little significance, because, in both cases, the electron–hole recombination is accompanied by emission of the rare-earth ion. The curves described by expression (2) are approximated well by hyperbolas of form (1) [9]. It should be noted that, in this case, the higher the concentration of defects, the larger the slope of the curves.

The experimentally observed increase in the exponent of the approximating hyperbola with an increase in the activator content is consistent with expression (2). Prolonged excitation of the crystal under ionizing radiation modifies the distribution function $f(r)$ due to recombination phosphorescence. In essence, the recombination phosphorescence involves the annihilation of previously generated pairs; i.e., the phosphorescence is favorable for the generation of pairs with a large spacing between localized charge carriers in interacting pairs. This leads to a decrease in the exponent α of the hyperbola, which is observed in the experiments. This effect should be more pronounced for crystals with a higher impurity content, which is also the case.

4. CONCLUSIONS

The experimental results obtained in this study allowed us to conclude that, in the initial stages of x-ray irradiation of the crystal, the accumulation of charge carriers occurs in pairs. This is explained by the formation of short-lived excimer-like molecular states during excitation of the crystal [16].

ACKNOWLEDGMENTS

This work was performed within the framework of the program "Universities of Russia," project UR.01.01.045.

REFERENCES

1. Ch. B. Lushchik, Tr. Inst. Fiz. Astron. Akad. Nauk Est., No. 3, 230 (1995).
2. G. Chiarott and N. Inchauspe, Phys. Rev. **109** (2), 345 (1958).
3. R. G. Kaufman and W. B. Hadley, J. Chem. Phys. **47** (1), 264 (1967).
4. É. D. Aluker, D. Yu. Lusis, and S. A. Chernov, *Electronic Excitations and Radioluminescence in Alkali Halide Metals* (Zinatne, Riga, 1979) [in Russian].
5. H. von Seggern, Cryst. Lattice Defects Amorphous Mater. **18** (1–3), 399 (1989).
6. H. von Seggern, Braz. J. Phys. **29** (2), 254 (1999).
7. V. V. Antonov-Romanovskiĭ, *Photoluminescence Kinetics of Crystals* (Nauka, Moscow, 1966) [in Russian].
8. V. V. Pologrudov and E. N. Karnaukhov, Fiz. Tverd. Tela (Leningrad) **27** (5), 1380 (1985) [Sov. Phys. Solid State **27**, 833 (1985)].
9. V. V. Pologrudov and E. N. Karnaukhov, Fiz. Tverd. Tela (Leningrad) **31** (2), 179 (1989) [Sov. Phys. Solid State **31**, 275 (1989)].
10. V. V. Pologrudov, FMR **1/2**, 51 (2002).
11. S. Chandrasekhar, *Stochastic Problems in Physics and Astronomy* (AIP, New York, 1943; Inostrannaya Literatura, Moscow, 1947).
12. J. L. Merz and P. S. Pershan, Phys. Rev. **162** (1), 217 (1967).
13. Yu. S. Gromovoĭ, V. G. Grachev, and V. V. Teslenko, Fiz. Tverd. Tela (Leningrad) **16** (1), 122 (1974) [Sov. Phys. Solid State **16**, 71 (1974)].
14. S. Kh. Batygov, *Spectroscopy of Crystals* (Moscow, 1970), p. 167 [in Russian].
15. S. Kh. Batygov, Tr. Fiz. Inst. im. P.N. Lebedeva, Akad. Nauk SSSR **60** (1), 131 (1972).
16. V. V. Pologrudov and E. N. Karnaukhov, Fiz. Tverd. Tela (Leningrad) **32** (6), 1727 (1990) [Sov. Phys. Solid State **32**, 1005 (1990)].

Translated by N. Korovin

Physics of the Solid State, Vol. 46, No. 10, 2004, pp. 1845–1850. Translated from Fizika Tverdogo Tela, Vol. 46, No. 10, 2004, pp. 1784–1789.

SEMICONDUCTORS AND DIELECTRICS

Nuclear Spin Resonance Study of the Ion Mobility in a $KHSeO_4$ Crystal

Yu. N. Ivanov*, A. A. Sukhovskiĭ*, I. P. Aleksandrova*, J. Totz, and D. Michel****

** Kirensky Institute of Physics, Siberian Division, Russian Academy of Sciences, Akademgorodok, Krasnoyarsk, 660036 Russia*

e-mail: yuni@iph.krasn.ru

*** Leipzig University, Leipzig, D-04103 Germany*

Received February 24, 2004

Abstract—The ion mobility in a crystal of partially deuterated potassium hydroselenate (KHSe) was studied using nuclear spin resonance (NSR) of ^{1}H, ^{2}H, ^{77}Se, and ^{39}K in a wide temperature range. The temperature dependences of the deuterium NSR spectra above 360 K exhibit changes in the line shape characteristic of chemical exchange processes. These exchange processes were studied in detail using two-dimensional ^{2}H NSR spectroscopy. It was ascertained that the exchange between deuterons of hydrogen bonds take place in the entire temperature range under study. However, the measured conductivity was approximately one-hundredfold lower than that estimated from the exchange frequencies. It was assumed that the low conductivity in the temperature range under study is caused by closed dimers of SeO_4 groups in the KHSe structure. © *2004 MAIK "Nauka/Interperiodica".*

1. INTRODUCTION

Study of the ion (chemical) exchange processes in crystals with ionic conductivity is a topical problem of solid-state physics due to the wide practical application of such compounds in modern engineering. Recently [1–3], we studied the microscopic mechanism of proton transport in the ammonium hydroselenate (AHSe) crystal. In the structure of this crystal, tetrahedral SeO_4 groups are joined by linear hydrogen bonds into quasi-one-dimensional chains aligned along the **b** axis. Such crystals can be good model objects to test various assumptions on microscopic mechanisms of ionic conductivity. In [1–3], it was shown that the ionic conductivity in AHSe and its isotropic nature are caused by proton exchanges between hydrogen bond chains. It might be expected that proton exchange similar to that in the AHSe paraelectric phase also takes place in other crystals with hydrogen bond chains. From this viewpoint, it is of interest to study ion transport in the potassium hydroselenate (KHSe) crystal, whose structure is characterized by hydrogen bond chains that alternate with layers of closed "dimers" of SeO_4 groups [4].

As in the case of the AHSe crystal, KHSe was partially deuterated (~80% of protons are substituted by deuterium nuclei), which allowed us to apply NSR of quadrupole nuclei to study proton (deuteron) transport processes. In addition to conventional NSR Fourier spectroscopy, we used two-dimensional (2D) NSR spectroscopy, which provided a unique opportunity to study elementary processes in the chemical exchange of deuterons. Since, apart from protons, other lattice ions can contribute to the conductivity, NSR spectra of ^{39}K and ^{77}Se were studied in a wide temperature range. The NSR spectroscopy data were compared to dielectric measurements at a frequency of 1 kHz.

2. EXPERIMENTAL

Partially deuterated (80%) $KHSeO_4$ crystals were grown from an aqueous solution containing excess H_2SeO_4 and an appropriate amount of heavy water. The same samples were used in NSR and dielectric measurements. ^{2}H NSR measurements were carried out using a BRUKER MSL 300 spectrometer with a Larmor frequency of 46.073 MHz. The duration of a 90° pulse was ~4 μs. To eliminate the "dead time" effect of the NSR spectrometer receiver, a spin-echo sequence with a time of 25 μs between pulses was used. Moreover, proton decoupling was employed to suppress broadening of ^{2}H NSR lines because of the dipole–dipole interaction with remaining protons. Two-dimensional NSR studies were carried out using a spin-echo sequence $(\pi/2)_x - t_1 - (\pi/2)_{-x} - \tau_m - (\pi/2)_x - \tau - (\pi/2)_y - \tau - t_2$, where t_1, t_2, τ, and τ_m are the evolution time, measurement time, time between pulses, and mixing time, respectively. NSR spectra of ^{39}K and ^{77}Se were measured using an AVANCE 300 spectrometer at Larmor frequencies of 13.9 and 57.301 MHz, respectively. To increase the signal intensity from rare ^{77}Se nuclei, the cross-polarization method [5] was used. ^{1}H NSR measurements were performed using a laboratory-made pulsed NSR spectrometer with a proton Larmor frequency of 27.0 MHz.

1063-7834/04/4610-1845$26.00 © 2004 MAIK "Nauka/Interperiodica"

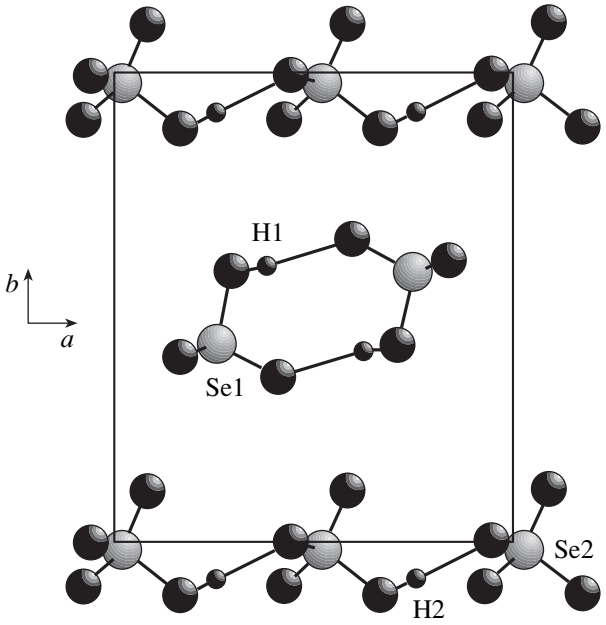

Fig. 1. Fragment of the $KHSeO_4$ structure (hydrogen bond chains and one chain of dimers).

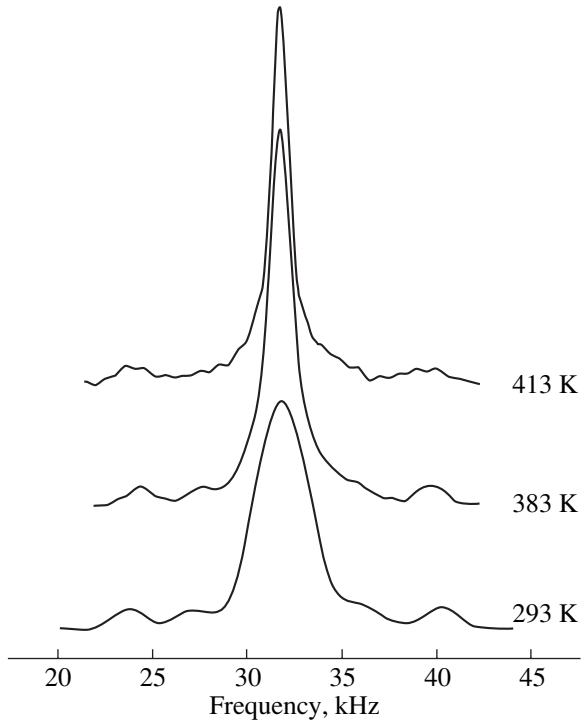

Fig. 2. Temperature dependence of proton spectra in KHSe.

The dielectric susceptibility was measured at a frequency of 1 kHz using the bridge method in the temperature range 350–450 K. Samples ~0.8-mm thick were cut from a KHSe single crystal. Thin gold films were employed as electrodes in dielectric measurements.

3. RESULTS AND DISCUSSION

The KHSe crystal is characterized by orthorhombic symmetry; its space group is P_{bca}, a = 8.690 Å, b = 10.053 Å, and c = 19.47 Å (Z = 16) [4]. The main difference between the KHSe structure and the previously studied AHSe structure [6] is that only half the SeO_4 groups in KHSe are hydrogen-bonded into infinite chains similar to those in the AHSe structure and aligned along the **a** axis. The remaining SeO_4 groups are hydrogen-bonded in pairs into relatively separate dimers (Fig. 1). Each dimer is characterized by a symmetry center, and the dimer plane is almost parallel to the (001) crystallographic plane. The positions of hydrogen bond protons were not determined in [4]; however, they can be approximately determined from structural data on the potassium hydrosulfate $KHSO_4$ crystal [7, 8] by taking into account that these crystals are isomorphous. However, this assumption is not quite correct, since it is indicated in [4] (based on data on the relevant O…O distances) that hydrogen bonds in the KHSe crystal are significantly stronger than those in $KHSO_4$.

As mentioned above, ~80% of protons in the KHSe crystal are substituted by deuterium nuclei; i.e., protons are "rare" nuclei. This circumstance allows precise localization of protons in KHSe using ^{1}H NSR. Figure 2 shows typical ^{1}H NSR spectra in KHSe measured at various temperatures and for a crystal orientation such that the **c** axis is perpendicular to the external magnetic field $\mathbf{B}_0$ and the angle between the **a** axis and the field $\mathbf{B}_0$ is 45°. We can see from Fig. 2 that two Pake doublets belonging to two magnetically nonequivalent pairs of dimer protons are well resolved due to a significant decrease in the intermolecular dipole–dipole interaction between protons. The central spectral line belongs to protons of hydrogen bond chains and dimers in which only one proton is substituted by deuterium. It is worth mentioning that the degree of sample deuteration can be determined independently from the relative intensity of spectral components. The intensity of each component of the Pake doublets is 4.7 ± 0.3% of the total intensity of the proton spectrum. Simple calculations show that this value corresponds to substitution of 81.2% of protons by deuterium. The orientation dependences of doublet splitting were used to determine the distances between dimer protons and the proton–proton vector orientation in the crystal (r = 2.450 Å; direction cosines, 0.590, –0.810, –0.091). Since the determined parameters differ substantially from the values obtained for the $KHSO_4$ structure (r = 2.7197 Å; direction cosines, 0.7485, –0.6630, –0.0139) [7], the orientation dependences of the second moments of the proton spectrum with respect to the three crystallographic axes were measured to correct the coordinates of all protons in KHSe. Figure 3a shows the experimental (symbols) and calculated (solid lines) angular dependences of the second moments of the ^{1}H NSR spectra. The second moments were calculated using the proton coordinates

determined for the $KHSO_4$ structure and taking into account all magnetic isotopes of the sample in a sphere 40 Å in radius. We can see from Fig. 3b that the experimental and calculated angular dependences of the second moments of the proton spectra largely disagree. We developed a computer program allowing determination of the proton positions in the structure by varying the proton coordinates, which provides the best fit to the experimental curves. The determined proton coordinates are listed in Table 1. The angular dependences of the second moments of the proton spectra calculated using the data from Table 1 are shown in Fig. 3b, together with the experimental data. The corrected proton coordinates are also in good agreement with the results of the Pake analysis of the proton spectra.

The temperature dependences of proton spectra of KHSe were studied in the temperature range 283–403 K. Figure 2 shows ^{1}H spectra of KHSe at temperatures of 283, 383, and 413 K. We can see from Fig. 2 that the splittings between the components of Pake doublets remain unchanged in the entire temperature range under consideration, while the width of the spectral components gradually decreases with increasing temperature. These data indicate that the protons belonging to hydrogen bond chains are mobile and that there is not an appreciable exchange of dimer protons. Of course, it is impossible to determine the proton motion characteristics from these spectra. We can make only estimates (see [9, Section 10]) of the correlation time τ_c of proton exchange in hydrogen bond chains by using the change in the spectral component width. The estimations yield $\tau_c \sim 5 \times 10^{-4}$ s at $T = 383$ K.

To study the microscopic characteristics of KHSe, we recorded ^{2}H NSR spectra of partially deuterated KHSe. Deuterium nuclei have an electric quadrupole moment, which allows determination of the electric field gradient (EFG) tensor at the position of the nucleus under study. In the case of a strong external magnetic field $\mathbf{B}_0$, when the Zeeman interaction energy significantly exceeds the interaction energy between the nucleus quadrupole moment and the intracrystalline field. The latter interaction results in perturbation of the equidistant Zeeman levels and in splitting of the NSR line into $2I$ components (I is the nucleus spin) arranged symmetrically with respect to the frequency ν_0 of the Larmor precession in the field $\mathbf{B}_0$ [10]. Hence, the deuteron NSR spectrum ($I_D = 1$) consists of doublets, whose number for a single-crystal sample is dictated in general by the number of magnetically nonequivalent deuterium nuclei. The quadrupole splitting $\nu_2 - \nu_1$ is given by [10]

$$\nu_2 - \nu_1 = \frac{6eQ}{4h} V_{zz}^{\mathrm{LAB}} = \Phi_{zz}, \qquad (1)$$

where Q is the quadrupole moment of the nucleus, e is the electron charge, h is Planck's constant, and V_{zz} is the z component of the EFG at the nucleus site (field $\mathbf{B}_0$ is directed along the z axis). The orientation dependences

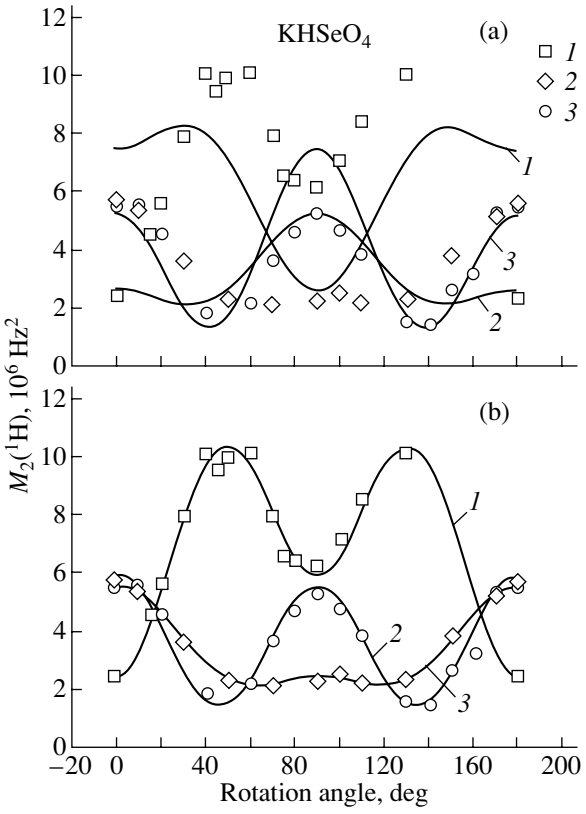

Fig. 3. Calculated (solid curves) and experimental (symbols) angular dependences of the second moments of proton spectra in KHSe for rotation about the **a**, **b**, **c** axes (curves *3*, *2*, *1*, respectively). The proton coordinates (a) are taken from [7] and (b) determined by fitting.

of quadrupole splittings can be used to determine (using the well-known Volkoff method [11]) all components V_{ij} of the EFG tensor for each structurally nonequivalent position of deuterium in the crystal in the laboratory coordinate system. The EFG tensor (instead of V_{ij}, for simplicity, we use their values Φ_{ij} in frequency units) is a symmetric second-rank tensor with zero trace and reflects the point symmetry of the position of the nucleus under study.

It is known that the direction of the principal axis of the EFG tensor Φ_{33} for hydrogen bonds approximately coincides with the O…O bond direction [12], which makes it possible to attribute each EFG tensor to a certain hydrogen bond in the crystal. Thus, the ^{2}H magnetic resonance in partially deuterated KHSe extends

Table 1. Corrected proton coordinates (in units of the unit cell parameters) in the KHSe crystal determined from the angular dependences of the second moments

	x	*y*	*z*
H1	0.4179	0.6025	0.0061
H2	0.2278	0.0907	0.2862

Table 2. Parameters of EFG tensors at $T = 295$ K for protons of hydrogen bond chains H2 and of dimers H1 of the KHSe crystal

H2				H1			
Principal values of EFG tensors Φ_{ii}, kHz	Direction cosines with respect to the crystallographic axes			Principal values of EFG tensors Φ_{ii}, kHz	Direction cosines with respect to the crystallographic axes		
	a	**b**	**c**		**a**	**b**	**c**
$\Phi_{11} = -125.0$	0.164	−0.342	0.926	$\Phi_{11} = -142.6$	−0.016	0.046	0.999
$\Phi_{22} = -95.4$	−0.459	0.805	0.377	$\Phi_{22} = -103.6$	−0.186	0.981	−0.48
$\Phi_{33} = 219.4$	−0.874	−0.485	−0.027	$\Phi_{33} = 244.7$	−0.982	−0.187	0.0

the capabilities of the NSR method significantly and makes it possible to separately study the dynamic characteristics of protons belonging to hydrogen bonds of chains and dimers.

Two different EFG tensors were determined from the angular dependences of the ^{2}H NSR spectra at 300 K (Table 2). The principal axes (Φ_{33}) of these two tensors almost coincide in direction with the hydrogen bonds of O…O chains and dimers, respectively. Thus, it is possible to unambiguously relate each of these EFG tensors to the corresponding proton position in the KHSe crystal structure.

The typical temperature dependence (in the range from 295 to 400 K) of ^{2}H NSR spectra in KHSe is shown in Fig. 4. These spectra were measured for the crystal orientation where the **b** axis is perpendicular to the external magnetic field $\mathbf{B}_0$ and the angle between the **a** axis and the field $\mathbf{B}_0$ is 40°. In this case, two quartets of lines are observed. The two central doublets (Fig. 4) correspond to deuterons of hydrogen bond chains, and the two doublets with splitting ~60 kHz belong to dimer deuterons. It follows from Fig. 4 that there are no significant changes in the spectrum of dimer deuterons in the entire temperature range under study. In the spectra of hydrogen bond deuterons, appreciable changes take place at temperatures above 350 K. The lines of the inner quartet initially broaden with temperature and form a doublet above 375 K. Its components narrow as the sample is further heated. These data unambiguously indicate that there is a chemical exchange of deuterons in the system of hydrogen bonds of the crystal. The chemical exchange rate can be estimated from the temperature dependence of the spectra by using the NSR line shape and the well-known Anderson theory [13]. The chemical exchange rates obtained in this way are 1.4×10^3, 2.8×10^3, and 4.5×10^3 s^{-1} at 365, 375, and 380 K, respectively.

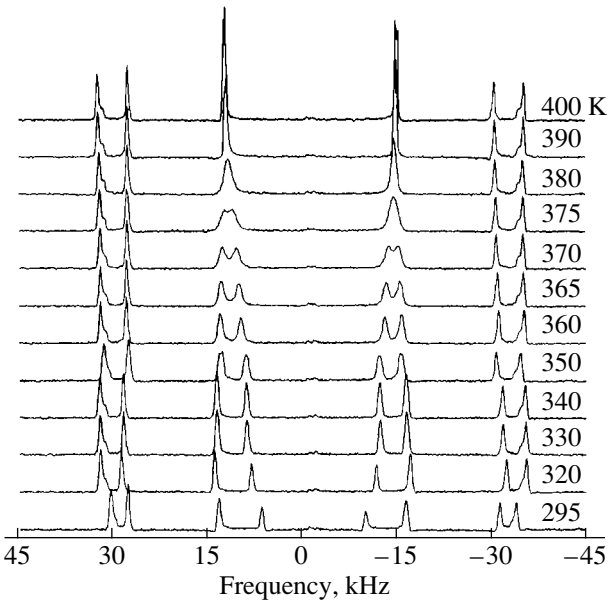

Fig. 4. Temperature dependence of quadrupole splittings in KHSe.

To obtain more detailed information on the microscopic mechanism of deuteron mobility, the exchange rate, and the activation energy for this process, the 2D ^{2}H NSR spectroscopy technique was used. A mathematical description of the chemical exchange processes and exchange rate calculations from 2D NSR spectra can be found in many well-known papers [14, 15] and are briefly described in our previous papers [1–3]. The chemical exchange is described by the basic equation [9]

$$\frac{\partial n_i}{\partial t} = \sum_j^n p_{ij} n_j, \tag{2}$$

where p_{ij} is the probability of the transition between positions i and j and n_j is the population of the corresponding state.

In matrix notation, Eq. (2) can be written as $\dot{\mathbf{n}} = \hat{p}\mathbf{n}$, and its solution is

$$\mathbf{n}(t) = \exp(\hat{p} \cdot t)\mathbf{n}_0 = \hat{A}(t)\mathbf{n}_0, \tag{3}$$

where the components of the vector $\mathbf{n}_0 = \{n_{01}, \ldots, n_{0i}\} - n_{0i}$ are equal to the number of deuterons at position i at the instant of time $t = 0$ and the components of the vector $\mathbf{n}(t) = \{n_1, \ldots, n_i\} - n_i$ are equal to the number of deuterons at the same position at the instant $t = \tau_m$. The components $A_{ij}(t)$ of the exchange matrix $\hat{A}(t)$ in Eq. (3),

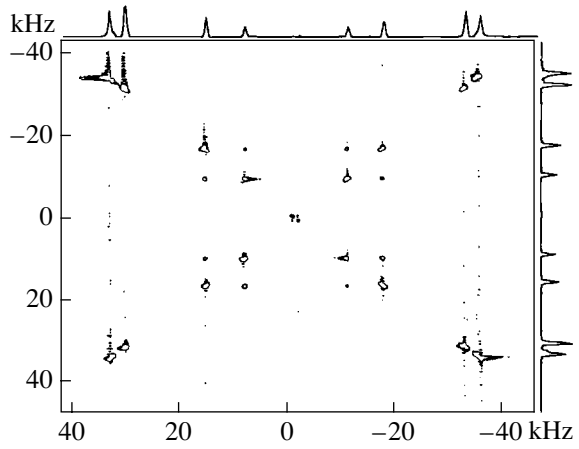

Fig. 5. 2D ^{2}H NSR exchange spectrum of KHSe at a temperature of 300 K and a mixing time of 100 ms.

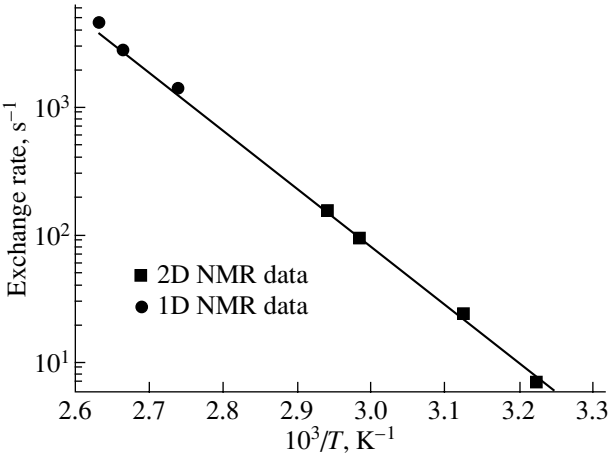

Fig. 6. Temperature dependence of the deuteron exchange rate in KHSe according to one- and two-dimensional NSR spectroscopy data.

which completely define the dynamics of the deuteron (proton) exchange in the crystal, can be determined from the intensities of the corresponding off-diagonal peaks of 2D NSR spectra of deuterium [14, 15]. 2D NSR experiments in KHSe were carried out in the temperature range from 300 to 340 K and in the same orientation as in the case of the one-dimensional (1D) spectra in Fig. 4. This temperature range was chosen since the mixing time τ_m in 2D experiments should satisfy the condition $T_2 < \tau_m < T_1$; moreover, the intensity of off-diagonal peaks at this mixing time should be sufficient to accurately determine the exchange rate. These conditions can be satisfied only in the indicated temperature range. The typical 2D ^{2}H NSR nuclear spectrum of KHSe (at 300 K and a mixing time of 100 ms) is shown in Fig. 5. The off-diagonal peaks (see, e.g., [14, 15]) in Fig. 5 suggest that the deuteron exchange takes place between magnetically nonequivalent positions of deuterons belonging to nearby chains of hydrogen bonds. In this case, as in AHSe, a simple two-position exchange is observed. To determine the rate of this process, a single measurement with a correctly selected mixing time at a given temperature is sufficient [1].

Figure 6 shows the temperature dependence of the exchange rate constructed using the data from 1D and 2D NSR spectroscopy. The solid line is a fit of this dependence to the Arrhenius equation with an activation energy E_a:

$$p(T) = p_0 \exp(E_a/RT). \quad (4)$$

It should be noted that the 2D-spectroscopy data and the estimates based on 1D spectra agree well and yield a value of ~85 kJ/mol for the activation energy of the exchange process and the preexponential factor $p_0 = 2.7 \times 10^{15}$ s^{-1}. It follows from Fig. 6 that the temperature dependences of the line shape observed in the 1D spectra of deuterium at higher temperatures are dictated by the same deuteron exchange type as the cross peaks in 2D spectra.

As noted above, in contrast to the AHSe crystal, layers of hydrogen bond chains in KHSe are separated by dimer layers, and the exchange process can result in exchange only within a single layer. Hence, strong anisotropy in the ionic conductivity can be expected in KHSe. However, no appreciable anisotropy was detected in this crystal in preliminary measurements. Since, apart from protons, other ions can, in principle,

Table 3. Parameters of the magnetic shielding tensors at $T = 295$ K for two structurally nonequivalent selenium nuclei of the KHSe crystal

Se1				Se2			
Principal values of MS tensors Φ_{ii}, Hz	Direction cosines with respect to the crystallographic axes			Principal values of MS tensors Φ_{ii}, Hz	Direction cosines with respect to the crystallographic axes		
	a	**b**	**c**		**a**	**b**	**c**
$\Phi_{11} = -12531$	0.0	0.0	–1	$\Phi_{11} = -10171$	–0.466	0.837	–0.285
$\Phi_{22} = -842$	0.981	–0.193	0.0	$\Phi_{22} = -3138$	–0.200	0.214	0.956
$\Phi_{33} = 12045$	0.193	0.981	0.0	$\Phi_{33} = 12795$	0.862	0.503	0.068

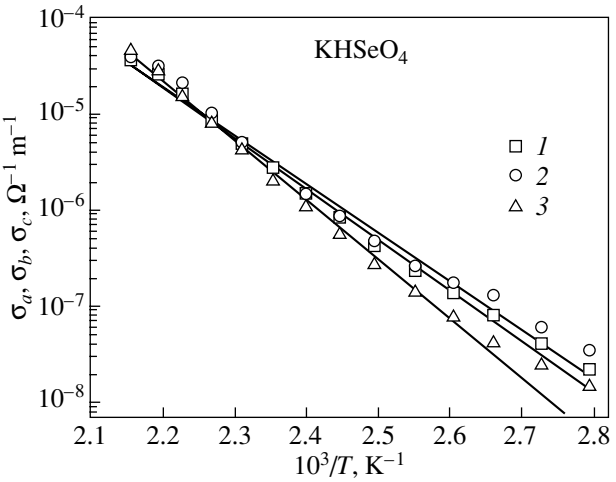

Fig. 7. Temperature dependence of the KHSe crystal conductivity along the **a**, **b**, **c** crystallographic axes.

contribute to the KHSe conductivity, we studied the temperature dependences of ^{77}Se and ^{39}K NSR spectra.

The parameters of the two tensors of magnetic shielding (MS) at selenium nucleus sites that belong to SeO_4 groups hydrogen-bonded into chains and dimers, respectively, were determined from the orientation dependence of ^{77}Se NSR spectra at a temperature of 295 K (Table 3). The MS tensor parameters are typical of hydrogen-bonded SeO_4 groups. The parameters of both MS tensors remain unchanged in the entire temperature range under consideration (295–420 K). Changes were likewise not detected in ^{39}K NSR spectra in this range. Thus, both selenium and potassium nuclei cannot contribute appreciably to the KHSe ionic conductivity (at least up to 420 K).

Dielectric measurements were carried out at a fixed frequency of 1 kHz for three cuts in the KHSe crystal perpendicular to the **a**, **b**, **c** crystallographic axes. The bridge method with a measuring field of ~1 V/mm was used. The measurement results are shown in Fig. 7. Significant anisotropy is not observed in the ionic conductivity, which contradicts the above considerations. Moreover, the measured conductivity is approximately two orders of magnitude lower than that estimated by us from the exchange frequencies obtained in the 2D experiments. It is also worth noting that the activation energy determined from the temperature dependence of the conductivity (~110 kJ/mol) differs significantly from that for the exchange process observed in NSR experiments using the deuterium 2D spectroscopy technique (85 kJ/mol).

As mentioned above, this situation differs from that observed in the AHSe crystal, where the proton exchange between chains (approximately with the same activation energy and exchange rates) completely defines the ionic conductivity. This seems to be caused by dimers existing in the KHSe structure, which are not involved in the proton exchange in the temperature range under study.

We are currently carrying out additional studies to refine data on the proton transport mechanism in the KHSe crystal.

ACKNOWLEDGMENTS

The study was supported by the federal program of support for leading scientific schools, project no. NSh-939.2003.2.

REFERENCES

1. Yu. N. Ivanov, J. Totz, D. Michel, G. Klotzsche, A. A. Sukhovsky, and I. P. Aleksandrova, J. Phys.: Condens. Matter **11** (18), 3151 (1999).
2. J. Totz, D. Michel, Yu. N. Ivanov, I. P. Aleksandrova, J. Petersson, and A. Klöpperpieper, Appl. Magn. Reson. **17** (2–3), 243 (1999).
3. Yu. N. Ivanov, A. A. Sukhovskiĭ, I. P. Aleksandrova, J. Totz, and D. Michel, Fiz. Tverd. Tela (St. Petersburg) **44** (6), 1032 (2002) [Phys. Solid State **44**, 1077 (2002)].
4. J. Baran and T. Lis, Acta Crystallogr. C **42** (3), 270 (1986).
5. A. Pines, M. G. Gibby, and J. S. Waugh, J. Chem. Phys. **59** (2), 569 (1973).
6. K. S. Aleksandrov, A. I. Kruglik, S. V. Misyul', and M. A. Simonov, Kristallografiya **25** (5), 1142 (1980) [Sov. Phys. Crystallogr. **25**, 654 (1980)].
7. F. A. Cotton, B. A. Frenz, and D. L. Hunter, Acta Crystallogr. B **31** (1), 302 (1975).
8. F. Payan and R. Haser, Acta Crystallogr. B **32** (6), 1875 (1976).
9. A. Abragam, *The Principles of Nuclear Magnetism* (Clarendon, Oxford, 1961; Inostrannaya Literatura, Moscow, 1963).
10. R. V. Pound, Phys. Rev. **79** (4), 685 (1950).
11. G. V. Volkoff, H. E. Petch, and D. W. Smellie, Phys. Rev. **84** (3), 602 (1951).
12. J. Soda and T. Chiba, J. Phys. Soc. Jpn. **26** (2), 249 (1969).
13. P. W. Anderson, J. Phys. Soc. Jpn. **9** (3), 316 (1954).
14. C. Schmidt, B. Blümich, and H. W. Spiess, J. Magn. Reson. **79** (2), 269 (1988).
15. S. Kaufmann, S. Wefing, D. Schaefer, and H. W. Spiess, J. Chem. Phys. **93** (1), 197 (1990).

Translated by A. Kazantsev

Physics of the Solid State, Vol. 46, No. 10, 2004, pp. 1851–1853. Translated from Fizika Tverdogo Tela, Vol. 46, No. 10, 2004, pp. 1790–1792.

DEFECTS, DISLOCATIONS, AND PHYSICS OF STRENGTH

Reversible Changes in the Microhardness of Silicon Crystals under Electron Irradiation with Low Doses

Yu. I. Golovin, A. A. Dmitrievskiĭ, I. A. Pushnin, and N. Yu. Suchkova

Tambov State University, Internatsional'naya ul. 33, Tambov, 392622 Russia

e-mail: dmitr2002@tsu.tmb.ru

Received February 10, 2004

Abstract—Reversible softening of silicon single crystals under β irradiation with low doses ($D < 1$ cGy) is revealed. The peaks observed in the dependence of the microhardness of silicon on the fluence are explained by the multistage competing processes of transformations of radiation-induced defects. © *2004 MAIK "Nauka/Interperiodica".*

1. INTRODUCTION

Although the influence of radiation defects on the physical properties of semiconductor crystals has been studied intensively [1–3], some problems remain unsolved. One of these problems is associated with the nontrivial effect of low doses of ionizing radiation ($D <$ 1 cGy) on the plastic properties of solids. It is known that, in a number of cases, irradiation with low doses brings about softening of crystals (instead of conventional hardening under irradiation with moderate doses) [4–6], an increase in the maxima of the internal friction in polymers [7], and reversible suppression of the magnetoplastic effect in single crystals of fullerite C_{60} [8]. Golan *et al.* [9] revealed that, under neutron irradiation with a small fluence, the microhardness of silicon changes in an intricate manner. However, the phenomenology and mechanism of the influence of low-dose radiation on the physical and mechanical properties of crystals are still poorly understood.

The goal of this work was to reveal and investigate the changes in the plastic properties of silicon crystals under β irradiation with a fluence $F < 10^{12}$ cm^{-2}.

2. SAMPLE PREPARATION AND EXPERIMENTAL TECHNIQUE

Experiments were performed with dislocation-free single-crystal silicon samples of two types: Si-1 crystals grown by the Czochralski method (10 Ω cm) and Si-2 crystals prepared using the crucibleless method (600 Ω cm). The crystals had the form of plates $1 \times 5 \times 7$ mm in size. The samples were irradiated with the use of two radioactive sources ^{90}Sr + ^{90}Y with activities $A_1 = 14.5$ and $A_2 = 1.34$ MBq, respectively. In both cases, the mean energy of electrons was 0.56 MeV and the fluence did not exceed 1.1×10^{12} cm^{-2}.

The Vickers microhardness H of the (111) surfaces was measured on a PMT-3 microhardness tester. For these measurements, the samples were periodically withdrawn from the irradiation chamber. Later on, the time spent on measuring the microhardness was taken into account (i.e., it was subtracted from the total time of the experiment) when constructing the dose dependence of the microhardness. The load on the indenter was 1 N, and the loading time was 10 s. Each point in the dependences was obtained by averaging 20 individual measurements of the microhardness H. Irradiation and all other manipulations with samples were carried out in air at room temperature.

3. RESULTS AND DISCUSSION

It is found that β irradiation of silicon crystals with low doses leads to a nonmonotonic variation in the microhardness H (Fig. 1). For a radioactive source with activity A_1, the dependence $H(F)$ exhibits two peaks of softening in the ranges of fluences F from 10^{10} to 7×10^{10} cm^{-2} and from 1.8×10^{11} to 4×10^{11} cm^{-2}. The polymodal dependence $H(F)$ is characteristic of both types of studied samples (Fig. 1, curves *1*, *2*). Check experiments demonstrated that the microhardness of the Si-1 samples not irradiated by β particles remains unchanged (within the limits of experimental error) over the period of time required to measure the dose dependence of the microhardness (Fig. 1, curve *3*).

According to [10, 11], the microhardness of silicon single crystals at room temperature is determined primarily by the mobility of nonequilibrium point defects and, possibly, the phase transitions occurring under indentation. The dislocations do not contribute significantly to the microhardness H by virtue of their small amount and low mobility. As was shown in [3, 12], the exposure of crystals to β radiation brings about the generation of Frenkel pairs, i.e., vacancies (V) and interstitial silicon atoms Si_i. By convention, the Frenkel pairs are called primary radiation defects. They are quasi-uniformly generated in depth along the trajectory of fast electrons due to cascades of collisions of the elec-

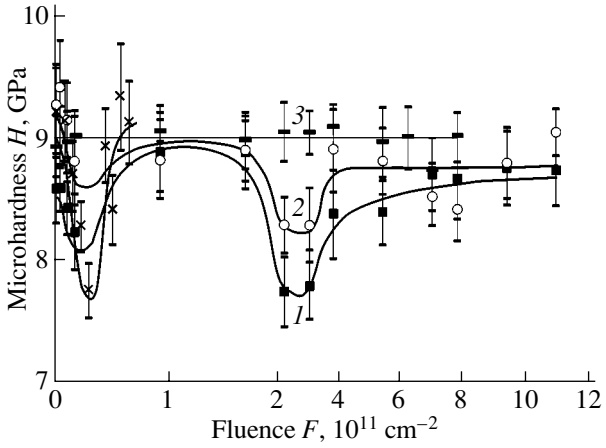

Fig. 1. Dependences of the microhardness H on the fluence F for (*1*) the Si-1 crystals grown by the Czochralski method and irradiated from a source with activity A_1 = 14.5 MBq, (*2*) the Si-2 crystals grown by the crucibleless method and irradiated from a source with activity A_1 = 14.5 MBq, and (*4*) the Si-1 crystals irradiated from a source with activity A_2 = 1.34 MBq. Curve *3* shows the dependence of the microhardness H for the Si-1 crystals not exposed to irradiation on the time normalized to the fluence of irradiated samples.

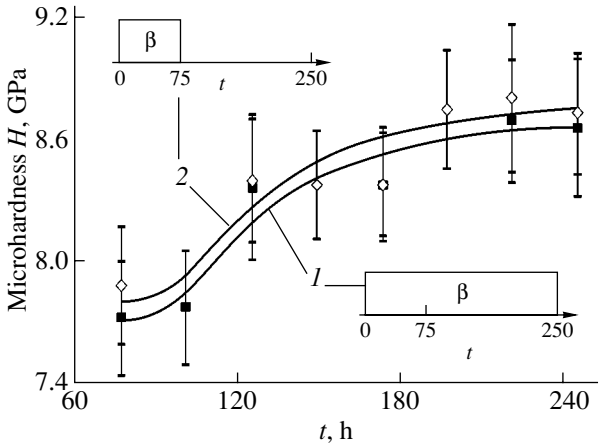

Fig. 2. Kinetics of recovery of the initial microhardness H of the Si-1 crystals irradiated to $F = 2.5 \times 10^{11}$ cm^{-2}: (*1*) under β irradiation and (*2*) in the absence of β irradiation.

trons with lattice atoms [3]. After 10-h irradiation with activity A_1 (the maximum corresponding to the first softening), the concentration of Frenkel pairs n_F can reach ~10^{17} cm^{-3}. This value was calculated under the assumption that the mean depth of penetration h of β electrons is approximately equal to 15 μm and the energy E_F required to generate a single Frenkel pair is 59 eV [1]. Therefore, the upper bound of n_F is comparable to the concentration of intrinsic defects of the sample. In the case when the mass transfer upon indentation of the sample predominantly occurs through mobile point defects, the radiation-stimulated increase in the concentration of Frenkel pairs can be responsible for the decrease in the microhardness of silicon crystals [the first peak in the dose dependence of the microhardness $H(F)$].

The Frenkel pairs generated under irradiation are metastable, and, at room temperature, part of them disappear as a result of mutual annihilation. During migration, the separated components of the pairs interact with impurity atoms of the crystal, thus generating more complex stable secondary radiation defects [12]. Therefore, irradiation of silicon crystals initiates at least two competing processes: (i) the generation of nonequilibrium primary radiation defects and (ii) the generation of the more stable secondary radiation defects. The kinetics of the latter process depends on the concentration of Frenkel pairs n_F. Hence, it seems likely that the stage of the occurrence of the competing processes that is responsible for the kink in the dose dependence of the microhardness $H(F)$ should come into play after a certain amount of primary radiation defects is generated. Consequently, the kink location in the curve $H(F)$ should depend on the intensity of irradiation. This is confirmed by the results of measuring the dose dependence of the microhardness $H(F)$ for the Si-1 samples irradiated from sources with activities A_1 and A_2 (Fig. 1, curves *1*, *4*). For different activities of the radioactive sources, the first peak of softening is observed at identical fluences but for different exposures of the samples to irradiation.

It is well known [11] that the most active impurities involved in the formation of radiation-induced defect complexes are oxygen and carbon. The concentrations of oxygen atoms in the Si-1 and Si-2 samples differ by several orders of magnitude. However, in our experiments, the microhardnesses of the Si-1 and Si-2 crystals under β irradiation changed synchronously (Fig. 1, curves *1*, *2*). Consequently, it can be assumed that, in our case, the majority impurity is carbon, whose concentration in samples of both types amounts to ~10^{16}–10^{17} cm^{-3}. Apparently, it is the carbon concentration that limits the sink of vacations with the formation of *V*–C complexes. In our opinion, this circumstance and possible further transformations of secondary radiation defects account for the second peak in the dose dependence of the microhardness $H(F)$ (Fig. 1).

In the case when the exposure of the sample to fast electrons is interrupted at the stage of the second softening ($F = 2.5 \times 10^{11}$ cm^{-2}), the microhardness regains its initial value (Fig. 2). The duration of spontaneous recovery of the microhardness H (in the absence of irradiation) almost coincides with the duration of β-stimulated recovery (the sample is continuously irradiated by electrons). Therefore, it can be assumed that the observed recovery of the microhardness H at this stage of transformations of radiation defects is caused by the processes initiated by smaller doses of irradiation rather than by further irradiation of silicon.

4. CONCLUSIONS

Thus, we revealed a nonmonotonic variation in the microhardness of silicon single crystals under β irradiation with low doses. The nonmonotonic character of the dose dependence of the microhardness $H(F)$ can be explained by the multistage competing processes of transformations of radiation-induced defects.

ACKNOWLEDGMENTS

This work was supported by the Russian Foundation for Basic Research (project no. 02-02-17571) and the program "Universities of Russia" (project no. UR.01.01.013).

REFERENCES

1. V. S. Vavilov, *Effects of Radiation on Semiconductors* (Fizmatgiz, Moscow, 1963; Consultants Bureau, New York, 1965).
2. V. V. Kozlovskiĭ, V. A. Kozlov, and V. N. Lomasov, Fiz. Tekh. Poluprovodn. (St. Petersburg) **34** (2), 129 (2000) [Semiconductors **34**, 123 (2000)].
3. V. A. Kozlov and V. V. Kozlovskiĭ, Fiz. Tekh. Poluprovodn. (St. Petersburg) **35** (7), 769 (2001) [Semiconductors **35**, 735 (2001)].
4. V. A. Makara and N. N. Novikov, Fiz. Khim. Obrab. Mater., No. 6, 137 (1973).
5. S. Fujita, K. Maeda, and S. Hyodo, Phys. Status Solidi A **109**, 383 (1988).
6. Yu. I. Golovin, A. A. Dmitrievskiĭ, R. K. Nikolaev, and I. A. Pushnin, Dokl. Akad. Nauk **385** (1), 1 (2002) [Dokl. Phys. **47**, 485 (2002)].
7. A. G. Lipson, D. M. Sakov, V. I. Savenko, and E. I. Saunin, Pis'ma Zh. Éksp. Teor. Fiz. **70** (2), 118 (1999) [JETP Lett. **70**, 123 (1999)].
8. Yu. I. Golovin, A. A. Dmitrievskiĭ, R. K. Nikolaev, and I. A. Pushnin, Fiz. Tverd. Tela (St. Petersburg) **45** (1), 187 (2003) [Phys. Solid State **45**, 197 (2003)].
9. G. Golan, E. Rabinovich, A. Inberg, A. Axelevitch, M. Oksman, Y. Rosenwaks, A. Kozlovsky, P. G. Rancoita, M. Rattaggi, A. Seidman, and N. Croitoru, Microelectron. Reliab. **39**, 1497 (1999).
10. B. Ya. Farber, V. I. Orlov, V. I. Nikitenko, and A. H. Heuer, Philos. Mag. A **78**, 671 (1998).
11. Yu. I. Golovin, A. I. Tyurin, and B. Ya. Farber, Philos. Mag. A **82** (10), 1857 (2002).
12. E. M. Verbitskaya, V. K. Eremin, A. M. Ivanov, Z. Li, and B. Schmidt, Fiz. Tekh. Poluprovodn. (St. Petersburg) **31** (2), 235 (1997) [Semiconductors **31**, 127 (1997)].

Translated by O. Moskalev

Physics of the Solid State, Vol. 46, No. 10, 2004, pp. 1854–1858. Translated from Fizika Tverdogo Tela, Vol. 46, No. 10, 2004, pp. 1793–1796.

DEFECTS, DISLOCATIONS, AND PHYSICS OF STRENGTH

Statistics of Microcracks in Heterogeneous Materials (Granites)

V. I. Vettegren*, V. S. Kuksenko*, N. G. Tomilin*, and M. A. Kryuchkov**

** Ioffe Physicotechnical Institute, Russian Academy of Sciences, Politekhnicheskaya ul. 26, St. Petersburg, 194021 Russia*

e-mail: Victor.Vettegren@mail.ioffe.ru

*** St. Petersburg State Electrotechnical University, ul. Professora Popova 5, St. Petersburg, 197376 Russia*

Received February 19, 2004

Abstract—The amplitude distributions of acoustic emission signals from granites under compressive stresses are expanded into a power series of gamma functions. It is established that the mean amplitude of each term in the expansion falls in the range of acoustic emission signals corresponding to the hierarchical levels of the crack formation in loaded granites. On this basis, a model of crack formation is proposed according to which the size distribution of microcracks in granites under load rapidly attains a thermodynamically optimum form for each hierarchical level of crack formation. The results of calculating the mean sizes and evolution of microcracks at each hierarchical level are in good agreement with the experimental data. © *2004 MAIK "Nauka/Interperiodica".*

1. INTRODUCTION

Earlier investigations [1–3] into the fracture of strained solids have demonstrated that a fracture nucleus arises when the microcrack concentration X_C in the bulk of the material reaches a value at which the mean distance $\langle L\rangle$ between the microcracks exceeds their mean size $\langle y\rangle$ by a factor of $e \approx 2.7$; that is,

$$\frac{\langle L\rangle}{\langle y\rangle} = \frac{1}{\sqrt[3]{X_C}} \approx 2.7. \qquad (1)$$

On this basis, Zhurkov *et al.* [2] proposed a two-stage model of fracture. It was assumed that stresses applied to a solid bring about the formation and accumulation of microcracks of approximately identical size. When the concentration of microcracks reaches a threshold value X_C, there arise regions where microcracks rapidly grow, which leads to fracture of the sample.

However, as follows from analyzing the dynamics of the probability density of acoustic emission signals from loaded granites [4–6], the fracture kinetics has a more complex character: all the signals can be separated into four hierarchical levels at which the mean signal amplitude $\langle A\rangle$ changes by a multiple of three and the number of signals at the neighboring levels varies in antiphase.

It is known that the amplitude of acoustic emission signals is approximately proportional to the size of microcracks. This gave grounds to formulate a hierarchical model describing the fracture of natural rocks [4–6]. According the hierarchical model, the first stage of fracture involves the accumulation of noninteracting microcracks of the first level. When the concentration of these microcracks in the bulk of the material reaches a critical value X_C satisfying relationship (1), the microcracks begin to grow. This leads to the formation of microcracks of the second level. In turn, microcracks of the second level accumulate until their concentration again reaches a critical value X_C. As a result, there arise microcracks of the third level and the process occurs over and over.

2. MODEL

Since the number of acoustic emission signals from granites under load [4–6] amounts to several tens of thousands, the amplitude distributions of these signals should obey the laws of statistical physics. Hence, the amplitude A_{i+1} of acoustic emission signals arising upon the formation of microcracks at the $(i + 1)$st level will be measured in terms of the amplitude of acoustic emission signals upon the formation of microcracks at the ith level: $A_{i+1} = CA_i$. If the system of microcracks is quasi-closed, the amplitude distribution of acoustic emission signals $n_i(A_i)$ at the ith hierarchical level can be represented by the expression [7]

$$n_i(A_i) = n_{0,i}\left(\frac{A_i}{\langle A_{i-1}\rangle}\right)^2 \exp\left(-\frac{A_i}{\langle A_{i-1}\rangle}\right), \qquad (2)$$

where $\langle A_{i-1}\rangle$ is the mean amplitude of acoustic emission signals upon the formation of microcracks at the $(i - 1)$st level and $n_{0,i}$ is the normalizing constant.

Microcracks form an ensemble with a continuously varying configuration. These variations in the ensemble configuration can be described as fluctuations of a multicomponent liquid that are stabilized by the entropy of mixing. Under equilibrium conditions, the entropy of mixing should be maximum. For this reason, the preexponential factor in expression (2) for the distribution of defects contains the factor $(A_i/\langle A_{i-1}\rangle)^2$ [8].

The amplitude distribution of acoustic emission signals upon the formation of microcracks at m levels has the form

$$N(A) \approx \sum_{i=1}^{m} n_{0,i}\left(\frac{A_i}{\langle A_{i-1}\rangle}\right)\exp\left(-\frac{A_i}{\langle A_{i-1}\rangle}\right). \quad (3)$$

The mean amplitude of acoustic emission signals upon the formation of microcracks at the $(i+1)$st hierarchical level is determined from the relationship

$$\langle A_{i+1}\rangle = \frac{\int_0^\infty \left(\frac{A_{i+1}}{\langle A_i\rangle}\right)^3 \exp\left(-\frac{A_{i+1}}{\langle A_i\rangle}\right) dA_{i+1}}{\int_0^\infty \left(\frac{A_{i+1}}{A_i}\right)^2 \exp\left(-\frac{A_{i+1}}{\langle A_i\rangle}\right) dA_{i+1}} = 3\langle A_i\rangle \quad (4)$$

and, as can be seen, exceeds the mean amplitude of acoustic emission signals for microcracks of the ith level by a factor of 3. This result is in excellent agreement with the approximate empirical value obtained in [4–6] for the ratio between the mean amplitudes of acoustic emission signals arising upon the formation of microcracks at the neighboring levels.

3. EXPERIMENTAL TECHNIQUE

The experimental technique used in our measurements was described in detail in [4]. Hence, we will dwell only briefly on the main features. The experiments were performed with cylindrical samples of two fine-grained granites (Westerly nos. 39 and 42) and one coarse-grained granite (Harcourt no. 43). Here, numbers 39, 42, and 43 are the experiment numbers in [4]. The samples were subjected to constant hydrostatic pressure and uniaxial compression. The acoustic emission signals were detected with a temporal resolution of 10^{-4} s. The data were obtained in the form of a chronological sequence of acoustic emission signals whose amplitude was reduced to a reference sphere 10 mm in radius. The measurements were terminated at the instant a load began to decrease drastically, which indicated the loss of bearing capacity of the sample.

4. AMPLITUDE DISTRIBUTIONS OF ACOUSTIC EMISSION SIGNALS

Figure 1 shows the amplitude distributions of acoustic emission signals from Westerly granite no. 39 and Harcourt granite no. 43. The amplitude distribution of acoustic emission signals from Westerly granite no. 42 has a similar shape. In order to describe these distributions with the use of relationship (3), we varied the number of distributions m, the mean amplitude $\langle A_1\rangle$, and the normalizing constant $n_{0,i}$ until the calculated distributions fitted the experimental data fairly well.

It turned out that the amplitude distributions of all acoustic emission signals for all the granite samples studied are adequately described by the sum of three or four terms of the series expansion in gamma functions (Fig. 1).

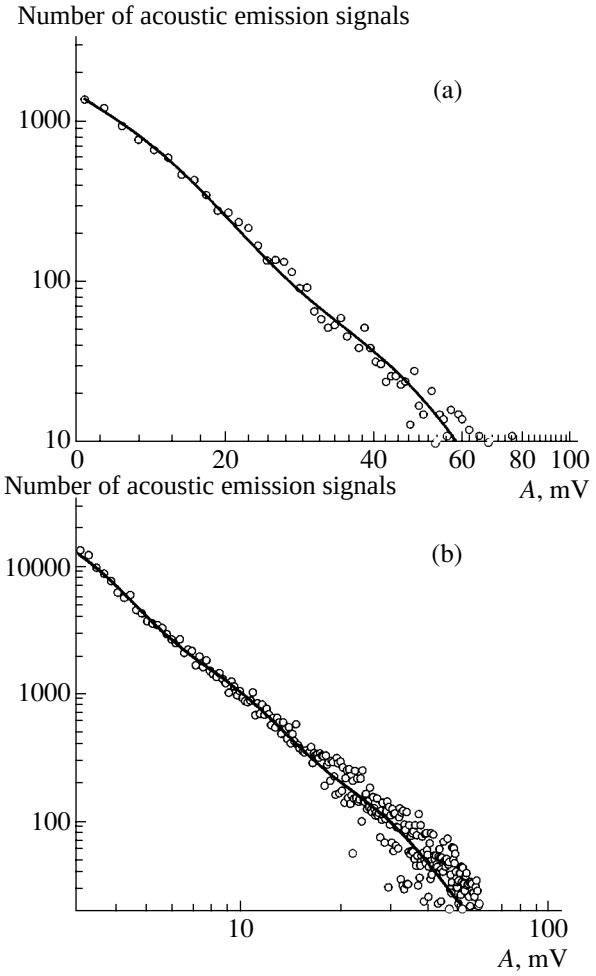

Fig. 1. Approximation of the amplitude distributions of acoustic emission signals according to relationship (3) for (a) Westerly granite no. 39 and (b) Harcourt granite no. 43.

Table 1 presents the mean amplitudes $\langle A_i\rangle$ determined in this work and amplitude ranges ΔA_i for acoustic emission signals according to the data obtained in [3–6] for three hierarchical levels of the crack formation in granites. It can be seen from Table 1 that the mean amplitude $\langle A_i\rangle$ falls in the range ΔA_i. This result suggests that each term in sum (3) characterizes the distribution of microcracks over the corresponding hierarchical level of the crack formation.

As was noted above, the inference regarding the existence of the hierarchical levels of the crack formation in granites was made from analyzing the dynamics of the probability density of acoustic emission signals and revealing the amplitude ranges ΔA_i in which the probability density varies in antiphase. Consequently, it could be expected that the number of acoustic emission signals with a mean amplitude differing by a factor of 3 should also vary in antiphase. In order to verify this

Table 1. Mean amplitudes $\langle A_i \rangle$ determined in this work and amplitude ranges ΔA_i for acoustic emission signals according to the data obtained in [3–6] for three hierarchical levels of the crack formation in granites

Level	No. 39		No. 42		No. 43	
	$\langle A_i \rangle$	ΔA_i	$\langle A_i \rangle$	ΔA_i	$\langle A_i \rangle$	ΔA_i
	mV					
1	9	2.7–9	3.3	1.6–5	6.3	2.7–6
2	27	9–30	10	5–20	20	6–40
3	71	30–90	30	20–65	61	40–90

assumption, we performed sampling from the entire set of acoustic emission signals at 10^3-s intervals. For each sample, the amplitude distribution of acoustic emission signals was calculated and then approximated by relationship (3). The data obtained were used to construct the time dependences of the number of amplitudes with the mean value $\langle A_i \rangle$. The results of calculations are presented in Figs. 2 and 3.

It can be seen from Figs. 2 and 3 that the number of microcracks with a mean signal amplitude differing by a factor of 3 actually varies in antiphase. (Note that, for Harcourt granite no. 43, the time dependence of the number of microcracks deviates from this behavior in the vicinity of 35×10^3 s most likely due to the formation of an intermediate fracture nucleus [4–6].) These findings also confirm the statement that the gamma functions adequately describe the distribution of microcracks over the hierarchical levels of the crack formation.

Under equilibrium conditions, the preexponential factor $n_{0,i}$ in expression (2) takes the form [9]

$$n_{0,i} = \frac{(1-p_i)^3}{2}, \quad (5)$$

where $p_i \equiv \exp(-\langle A \rangle^{-1})$.

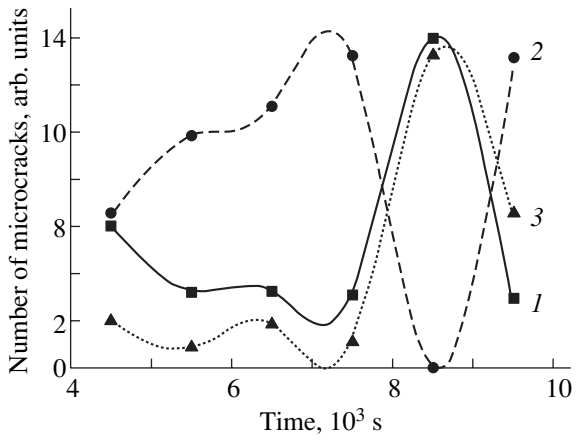

Fig. 2. Time dependences of the number of microcracks at the (*1*) first, (*2*) second, and (*3*) third hierarchical levels of the crack formation in Westerly granite no. 39.

Since $\langle A_2 \rangle / \langle A_1 \rangle = 3$, the ratio between the preexponential factors $\eta_1 \equiv n_{0,1}/n_{0,2}$ and $\eta_2 \equiv n_{0,2}/n_{0,3}$ under equilibrium conditions should be equal to 27. However, the values of η_1 and η_2 in Table 2 indicate the absence of a valuation equilibrium. This is also supported by the antiphase variations in the concentration of microcracks revealed in [4–6]. Nonetheless, the amplitude distribution of acoustic emission signals had time to attain an equilibrium form at each hierarchical level within the time interval (10^3 s) which we chose for calculating the distributions.

5. RESULTS AND DISCUSSION

Recent investigations have demonstrated that size distributions of various objects (nanodefects [9–11], corrosion spots [12] and misoriented dislocation walls [13, 14] on metal surfaces, structural blocks of different types in polymers [15, 16], aggregates of carbon black in rubber, bacteria, fungi and segments of protein molecules [10], etc.) can be described as a gamma function

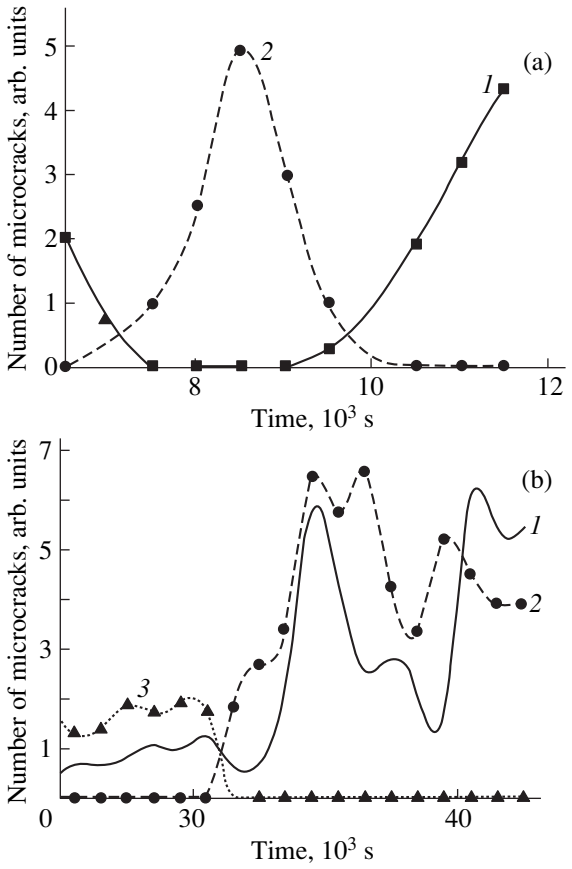

Fig. 3. Time dependences of the number of microcracks in (a) Westerly granite no. 42 at the (*1*) second and (*2*) third hierarchical levels of the crack formation and (b) Harcourt granite no. 43 at the (*1*) first, (*2*) second, and (*3*) third hierarchical levels.

or expanded into a power series of several gamma functions. Therefore, the description of the size distribution of microcracks in granites in the form of a sum of equilibrium gamma functions is not an exception. This can be explained by the fact that all the aforementioned objects have managed to be formed completely in a time that is considerably shorter than the observing time. It is known [7] that the gamma distribution has a thermodynamically optimum form; i.e., in this case, the configurational entropy of the system is maximum and the distribution of acoustic emission signals at each hierarchical level corresponds to the second law of thermodynamics.

As was already mentioned, the mean sizes of microcracks differ by a factor of 3. In [9–11], it was found that the mean sizes of nanodefects on the metal surface also differ by a factor of 3. This ratio of mean sizes proved to be valid for structural blocks of different types in polymers [15, 16] and corrosion spots on the metal surface [12]. Furthermore, the mean sizes of structural formations in rocks, products of their grinding, and geoblocks differ by a factor of 2 to 7 [17, 18]. Therefore, the ratio of mean sizes of defects and structural formations is close to 3 for different solids over a wide range of sizes (from 10^{-6} to 10^{6} m). It was noted above that this ratio of mean sizes holds under the following two conditions: (i) objects of the subsequent hierarchical level are formed from objects of the preceding level, and (ii) the number of these objects at each hierarchical level has managed to reach a statistically significant value during the time of observation. It seems likely that, in each of the aforementioned cases, both these conditions are satisfied.

It was shown earlier in [9–11] that, apart from the concentration of microcracks, the concentration of nanodefects with sizes ranging from 10 to 500 nm also varies in antiphase at the surface of loaded metals. Therefore, the number of defects at the neighboring hierarchical levels changes in antiphase not only in granites but also in metals and the range of linear sizes of such defects amounts to approximately five orders of magnitude. This change in the number of defects in antiphase is associated with the fact that nanodefects and microcracks of the subsequent hierarchical level are formed only from nanodefects and microcracks of the preceding level. The formation and accumulation of nanodefects and microcracks occur most rapidly at the first hierarchical level. These processes set the stage for the formation and accumulation of nanodefects and microcracks at the second hierarchical level. Since some of the nanodefects and microcracks of the first hierarchical level are involved in the population of the second hierarchical level, the number of nanodefects and microcracks at the neighboring hierarchical levels changes in antiphase.

Table 2. Ratios η_1 and η_2 for microcracks of the neighboring hierarchical levels at the instant of granite fracture

	No. 39	No. 42	No. 43
η_1	95	70	90
η_2	180	135	250

6. CONCLUSIONS

Therefore, under nonequilibrium conditions, the size distribution of microcracks in the bulk of loaded granites attains a thermodynamically optimum form at the hierarchical levels of the crack formation, even though the number of microcracks at these levels differs significantly from the equilibrium value. The mean sizes of microcracks at the neighboring hierarchical levels of the crack formation differs by a factor of 3. The number of microcracks at the neighboring hierarchical levels changes in antiphase.

ACKNOWLEDGMENTS

This work was supported by the Russian Foundation for Basic Research (project nos. 03-05-64831, 02-05-39017, and 02-05-08003) and the international Scientific and Technical Center (project no. 1745).

REFERENCES

1. V. S. Kuksenko, V. S. Ryskin, V. I. Betechtin, and A. I. Slutsker, Int. J. Fract. Mech. **11** (5), 829 (1975).
2. S. N. Zhurkov, V. S. Kuksenko, V. N. Savel'ev, and U. Sultonov, Izv. Akad. Nauk SSSR, Fiz. Zemli, No. 6, 11 (1977).
3. V. A. Petrov, A. Ya. Bashkarev, and V. I. Vettegren, *Physical Principles for Prediction of the Fracture in Structural Materials* (Politekhnika, St. Petersburg, 1993) [in Russian].
4. V. Kuksenko, N. Tomilin, E. Damaskinskaja, and D. Lockner, Pure Appl. Geophys. **146** (1), 253 (1996).
5. N. G. Tomilin, E. E. Damaskinskaya, and V. S. Kuksenko, Fiz. Tverd. Tela (St. Petersburg) **36** (10), 3101 (1994) [Phys. Solid State **36**, 1649 (1994)].
6. N. G. Tomilin and V. S. Kuksenko, in *The Earth Science: Physics and Mechanics of Materials* (Vuzovskaya Kniga, Moscow, 2002), p. 117 [in Russian].
7. B. L. Lavenda, *Statistical Physics: A Probabilistic Approach* (Wiley, New York, 1997).
8. H.-G. Kilian, R. Metzler, and B. J. Zink, Chem. Phys. **107** (12), 8997 (1997).
9. H.-G. Kilian, V. I. Vettegren, and V. N. Svetlov, Fiz. Tverd. Tela (St. Petersburg) **42** (11), 2024 (2000) [Phys. Solid State **42**, 2083 (2000)]; Fiz. Tverd. Tela (St. Petersburg) **43** (11), 2107 (2001) [Phys. Solid State **43**, 2199 (2001)].
10. H.-G. Kilian, M. Koepf, and V. I. Vettegren, Prog. Colloid Polym. Sci. **117** (2), 172 (2001).

11. A. Ya. Bashkarev, V. I. Vettegren, and V. N. Svetlov, Fiz. Tverd. Tela (St. Petersburg) **44** (7), 1260 (2002) [Phys. Solid State **44**, 1316 (2002)].

12. V. I. Vettegren, A. Ya. Bashkarev, and G. I. Morozov, Pis'ma Zh. Tekh. Fiz. **28** (13), 1 (2002) [Tech. Phys. Lett. **28**, 533 (2002)].

13. M. Miodownik, A. W. Godfray, E. A. Holm, and D. A. Hughes, Acta Mater. **47** (9), 2661 (1999).

14. D. A. Hughes, Q. Liu, D. S. Hhrzan, and N. Hansen, Acta Mater. **45** (1), 105 (1997).

15. S. V. Bronnikov, T. E. Sukhanova, and L. A. Laĭus, Vysokomol. Soedin., Ser. A **44** (6), 940 (2002).

16. V. Bronnikov and T. E. Sukhanova, Image Anal. Steriology **20** (1), 105 (2001).

17. M. A. Sadovskiĭ, Dokl. Akad. Nauk SSSR **247** (4), 329 (1979) [Sov. Phys. Dokl. **24**, 586 (1979)].

18. M. A. Sadovskiĭ, *Discrete Properties of the Geophysical Medium* (Nauka, Moscow, 1989) [in Russian].

Translated by O. Borovik-Romanova

Physics of the Solid State, Vol. 46, No. 10, 2004, pp. 1859–1862. Translated from Fizika Tverdogo Tela, Vol. 46, No. 10, 2004, pp. 1797–1800.

DEFECTS, DISLOCATIONS, AND PHYSICS OF STRENGTH

The Influence of Heat Treatment on the Ultrasonic Velocity and Elastic Moduli of a Zr–Cu–Ni–Al–Ti Bulk Metallic Glass

G. E. Abrosimova*, N. P. Kobelev*, E. L. Kolyvanov*, and V. A. Khonik**

** Institute of Solid-State Physics, Russian Academy of Sciences, Chernogolovka, Moscow oblast, 142432 Russia*
e-mail: kobelev@issp.ac.ru
*** Voronezh State Pedagogical University, ul. Lenina 86, Voronezh, 394043 Russia*
Received October 30, 2003; in final form, February 26, 2004

Abstract—The influence of heat treatment at temperatures up to 550°C on the elastic properties of the $Zr_{52.5}Cu_{17.9}Ni_{14.6}Al_{10}Ti_5$ bulk amorphous alloy is investigated using acoustical measurements. The results obtained are compared with calorimetric and x-ray diffraction data. © *2004 MAIK "Nauka/Interperiodica".*

1. INTRODUCTION

It is known that metallic glasses exhibit a number of unique physical properties. Considerable recent progress achieved in the technology for producing bulk metallic glasses (alloys with a low critical cooling rate that makes it possible to prepare amorphous ingots weighing up to 1 kg or even more [1, 2]) has offered strong possibilities for their use as structural materials. In this respect, investigating the processes of elastic and inelastic mechanical relaxation in metallic glasses within different temperature ranges is of particular importance. Acoustical measurements provide a large amount of information on mechanical relaxation in solids. In recent years, there have appeared a number of works concerned with the study of the elastic characteristics of bulk metallic glasses at different stages of heat treatment [3–13]. It has been established that, for all the materials studied, the elastic moduli increase after crystallization. However, the results obtained by different researchers for temperatures below the crystallization point differ significantly. For example, in [3, 4, 6, 8–13], it was found that the elastic moduli increase upon annealing at temperatures below the crystallization temperature. On the other hand, virtually no variations in the elastic characteristics before crystallization were revealed in [5, 7]. Furthermore, it was noted in [4, 6, 8, 11] that the aforementioned variations in the elastic moduli occur either in the vicinity of the glass transition temperature or above it. However, in [3, 9, 12, 13], an increase in the elastic moduli was observed at temperatures below the glass transition point. It should be noted that, in [3–13], the elastic moduli were measured using bulk metallic glasses of different compositions, under different heat treatment conditions, and in different frequency ranges. Therefore, it remains unclear whether the observed discrepancies between the results obtained by different authors are associated with the differences in the alloy compositions, preparation techniques, temperature–time conditions, or other factors. In this respect, analysis of the influence of the heat treatment temperature on the elastic properties of bulk metallic glasses is an important problem. The purpose of the present work was to investigate how heat treatment at temperatures below and above the crystallization point affects the elastic properties of the $Zr_{52.5}Cu_{17.9}Ni_{14.6}Al_{10}Ti_5$ bulk metallic glass.

2. SAMPLE PREPARATION AND EXPERIMENTAL TECHNIQUE

A master alloy was prepared by induction levitation melting under vacuum. A metallic glass was produced by quenching the melt into an evacuated copper mold at room temperature. The mean quenching rate of melts was directly measured using a thermocouple placed in a quenching cavity and a digital transducer operating at a frequency of 32 KHz. The quenching rate in the vicinity of the glass transition temperature was estimated at 70 K/s $\le \dot{T} \le$ 350 K/s. The procedure for preparing glasses was described in detail in [10, 14]. The ingots thus prepared were $3 \times 6 \times 70$ mm in size. For measurements, samples (~$3 \times 5 \times 6$ mm in size) were produced by electric-arc cutting with subsequent mechanical grinding. The elastic moduli were estimated using the acoustical method. The velocities of longitudinal and shear ultrasonic waves were measured at room temperature by the pulse echo technique at a frequency of 5 MHz in the transmission geometry [15]. The accuracy in measuring the velocities was approximately equal to 0.25% for shear waves and 0.5% for longitudinal waves. The samples were heat treated in vacuum at a residual pressure of ~10^{-2} Pa under heating at a constant rate (~20 K/min) to a specified temperature with subsequent rapid cooling (at a rate higher than 200 K/min) to room temperature. In order to estimate the change in the density of the material due to heat treatment, the linear sizes of the samples were measured accurate to within 0.1% before and after annealing. All the measurements

1063-7834/04/4610-1859$26.00 © 2004 MAIK "Nauka/Interperiodica"

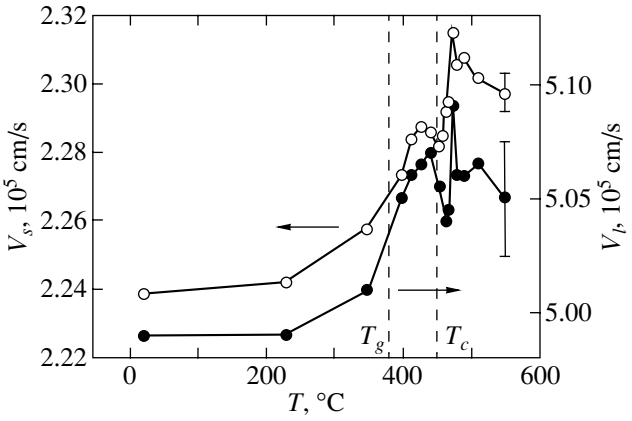

Fig. 1. Dependences of the velocities of shear (V_s) and longitudinal (V_l) ultrasonic waves (frequency, 5 MHz) at room temperature on the annealing temperature for the $Zr_{52.5}Cu_{17.9}Ni_{14.6}Al_{10}Ti_5$ alloy. The errors are given for each dependence.

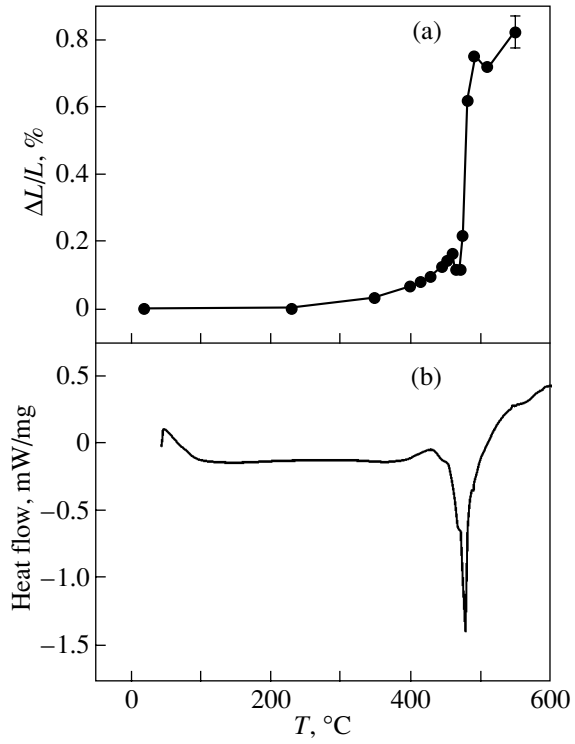

Fig. 2. (a) Dependence of the relative decrease in the linear size of Zr–Cu–Ni–Al–Ti alloy samples on the annealing temperature and (b) DSC thermogram of the Zr–Cu–Ni–Al–Ti bulk amorphous alloy at a heating rate of 22 K/min.

were performed with samples prepared from the same ingot. The structure of the samples was investigated using x-ray diffraction analysis on a SIEMENS D-500 diffractometer (CuK_α radiation). Differential scanning calorimetric (DSC) data were obtained on a Perkin-Elmer DSC-7 instrument.

3. RESULTS AND DISCUSSION

The ultrasonic velocities in the as-quenched samples at room temperature coincide to within the experimental error of the velocity measurement. The dependences of the velocities of shear and longitudinal ultrasonic waves at room temperature on the annealing temperature are shown in Fig. 1. As is seen from this figure, the dependence of the transverse velocity of sound on the annealing temperature is characterized by several temperature ranges. The heat treatment has virtually no effect on the elastic characteristics of the glass at temperatures up to approximately 200°C and leads to an increase in the ultrasonic velocity at higher temperatures (by approximately 2% at temperatures of 420–430°C). The ultrasonic velocity remains constant within the limits of experimental error in the temperature range 420–460°C and drastically increases (by approximately 1%) in the range 460–470°C. With a further increase in the annealing temperature, there appears a tendency toward decrease in the ultrasonic velocity. The dependence of the velocity of longitudinal waves on the annealing temperature exhibits qualitatively a similar behavior (Fig. 1); however, the observed changes are less pronounced and predominantly appear to be within the limits of experimental error.

Judging from the data on the relative change in the linear size of the samples (Fig. 2a), the alloy density changes only slightly (the maximum increase is no more than ~0.3%) upon annealing up to a temperature of ~470°C and then almost jumpwise increases by approximately 2%.

Figure 2b shows the DSC thermogram measured for a similar alloy at a heating rate (22 K/min) approximately equal to that used in heat treatment of the samples. At lower heating rates, the thermograms exhibit two well-resolved peaks corresponding to crystallization. However, it can be seen from Fig. 2b that, at a heating rate of 22 K/min, the first and second crystallization peaks almost coincide with each other. The onset of crystallization (T_c) is observed at approximately 450°C, the temperature of the exothermal effect at the maximum is equal to 475°C, and the crystallization is completed for the most part at 550°C. The onset of devitrification (T_g) is observed at approximately 380°C, and the temperature of the endothermal effect at the maximum is equal to 425°C.

The dependences of the shear modulus and the longitudinal elastic modulus on the annealing temperature (constructed with due regard for the change in the density) are depicted in Fig. 3. As can be seen from Fig. 3, these dependences have two characteristic portions: the moduli increase gradually in the temperature range 200–420°C (by approximately 4.5% for the shear modulus and 3% for the longitudinal modulus) and sharply in the range 470–480°C (by approximately 3.5 and 2% for the shear and longitudinal moduli, respectively). Therefore, the first portion of the increase in the elastic moduli begins at temperatures considerably below the

glass transition point and is completed approximately at the maximum of the endothermal effect. This increase in the elastic moduli is accompanied by an insignificant change in the density of the metallic glass. The second portion of the increase in the elastic characteristics of the alloy corresponds to the maximum of the exothermal effect, i.e., the crystallization of the alloy.

The observed changes in the properties of the glass under investigation correlate with the structural transformations. As was noted above, the as-quenched samples have an amorphous structure and their x-ray diffraction patterns contain only diffuse maxima. Figure 4 shows a typical x-ray diffraction pattern (curve *1*). No noticeable structural transformations occur upon annealing at temperatures below 450°C. At higher temperatures, the sample begins to crystallize. Curves *2–4* in Fig. 4 illustrate the crystallization with a change in the annealing temperature from 470 to 550°C. The crystallized sample contains three crystalline phases, namely, the hexagonal phase with lattice parameters a = 8.007 Å and c = 3.27 Å (structural type Zr_6CoAl_2, space group P–62m), the hexagonal phase Zr(Ti)CuNi with lattice parameters a = 5.259 Å and c = 8.619 Å (structural type $MgZn_2$, space group $P6_3/mmc$), and the tetragonal phase Zr_2Ni with lattice parameters a = 6.586 Å and c = 5.281 Å (space group $I4/mcm$). Figure 5 shows a fragment of the experimental x-ray diffraction pattern (curve *4* in Fig. 4), the calculated x-ray diffraction pattern (the sum of the contributions from the three aforementioned phases), and the reflections contributing to the total diffraction curve. The hexagonal phase of the Zr_6CoAl_2 structural type was previously observed upon crystallization of the amorphous phase and after mechanical activation [16, 17]. Note that the lattice parameters of this phase vary insignificantly depending on the chemical composition of the alloy. The hexagonal phase of the Zr(Ti)CuNi structural type was also observed upon crystallization of zirconium-based amorphous alloys [18]. The Zr_2Ni phase is the equilibrium phase in the Zr–Ni system (JCPDS card no. 18-0466). The lattice parameters of the Zr(Ti)CuNi phase slightly differ from those available in the literature. This can be explained by the difference in the ratio between the chemical elements in the studied sample. It should be noted that, in the Zr_6CoAl_2-type phase, the positions of cobalt atoms are occupied by other metal atoms (nickel, copper), whereas zirconium atoms can be partially replaced by titanium atoms; therefore, the lattice parameters are also different.

According to the calorimetric data, the crystallization of the alloy involves two stages. However, judging only from the x-ray diffraction data, we cannot reveal the phase that crystallizes at the first stage. In particular, the first Bragg reflection arising in the x-ray diffraction pattern (the line at an angle $2\theta \sim 39°$) can be identified either as the (300) line attributed to the Zr_6CoAl_2-type phase or as the (112) line of the Zr_2Ni phase. Either of these reflections is one of the most intense reflection in

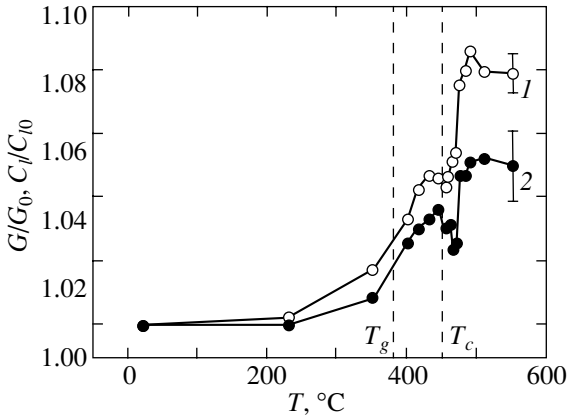

Fig. 3. Dependences of the relative change in (*1*) the shear modulus G and (*2*) the longitudinal elastic modulus C_l on the annealing temperature for the Zr–Cu–Ni–Al–Ti alloy.

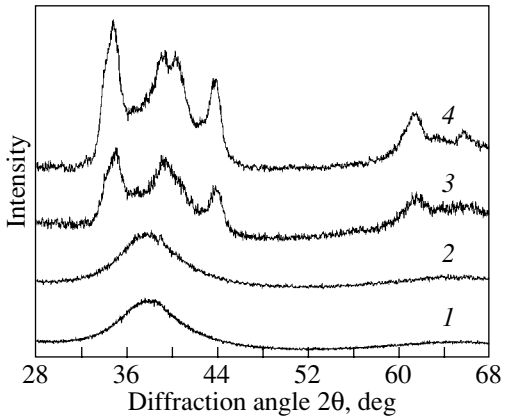

Fig. 4. X-ray diffraction patterns of Zr–Cu–Ni–Al–Ti alloy samples at different stages of heat treatment: (*1*) the as-quenched sample and the samples after annealing at temperatures of (*2*) 470, (*3*) 490, and (*4*) 550°C.

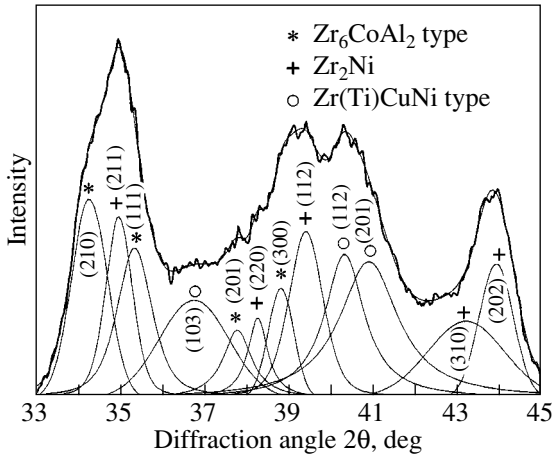

Fig. 5. Experimental (thick line) and calculated (thin lines) diffraction patterns of the Zr–Cu–Ni–Al–Ti alloy after annealing at 550°C.

the diffraction pattern of the corresponding structure. Consequently, these structures cannot be differentiated at the early stage of the crystallization. An increase in the temperature leads to the crystallization of all three phases. As a result, diffraction patterns *3* and *4* contain reflections of all these phases. The analysis of the x-ray diffraction patterns demonstrated that the volume fractions of the phases after heating to 550°C can be considered to be identical within the limits of experimental error.

4. CONCLUSIONS

Thus, the results obtained are in qualitative agreement with the data available in the literature on the influence of heat treatment on the elastic properties of bulk metallic glasses. The dependences of the elastic properties on the annealing temperature for the Zr–Cu–Ni–Al–Ti alloy under investigation involve two characteristic portions. In the first portion, the elastic moduli increase in the range corresponding to the amorphous state. The observed changes in the shear modulus are similar to those revealed earlier in [13] for the same alloy at frequencies in the hertz range and can be explained in the framework of the model proposed in [13]. According to this model, the change in the elastic characteristics of the metallic glass in the aforementioned temperature range is associated with the irreversible relaxation of nonequilibrium energy states of centers of the elastic-dipole type. In the second portion of the dependences of the elastic properties on the annealing temperature, the increase in the elastic moduli is governed by the crystallization of the alloy. This behavior is typical of all metallic glasses. However, it should be noted that the change observed in the shear modulus upon crystallization turned out to be relatively small (approximately 3.5%). As a result, the difference between the shear moduli for the quenched and crystallized alloys is approximately equal to 8%. This difference is substantially smaller than that available in the literature for other bulk glasses, including glasses of similar composition [7, 8, 10–12]. At present, it is difficult to answer the question as to whether this difference is a specific feature of the studied glass or is associated with the conditions used for its preparation and heat treatment. It seems likely that, in the future, it will be expedient to investigate how the heat treatment conditions affect the behavior of the elastic properties and the evolution of the structure of bulk metallic glasses.

ACKNOWLEDGMENTS

This work was supported by the US Civilian Research and Development Foundation for the Independent States of the Former Soviet Union (grant no. RP1-2320-VO-02) and the Ministry of Science and Technology of the Russian Federation (project no. NSh-2169.2003.2).

REFERENCES

1. A. Inoue, Acta Mater. **48**, 279 (2000).
2. W. L. Johnson, MRS Bull. **24**, 42 (1999).
3. A. S. Bains, C. A. Gordon, A. V. Granato, and R. B. Schwarz, J. Alloys Compd. **310**, 20 (2000).
4. L. M. Wang, W. H. Wang, R. J. Wang, Z. J. Zhan, D. Y. Dai, L. L. Sun, and W. K. Wang, Appl. Phys. Lett. **77**, 1147 (2000).
5. N. Nishiyama, A. Inoue, and J. Z. Jiang, Appl. Phys. Lett. **78**, 1985 (2001).
6. W. H. Wang, L. L. Li, M. X. Pan, and R. J. Wang, Phys. Rev. B **63**, 052204 (2001).
7. V. Kervin, M.-L. Vaillant, T. Rouxel, M. Huger, T. Gloriant, and Y. Kawamira, Intermetallics **10**, 1289 (2002).
8. W. H. Wang, Ann. Chim. Sci. Mater. **27** (5), 99 (2002).
9. Y. Hiki, T. Yagi, T. Aida, and S. Takeuchi, J. Alloys Compd. **355**, 42 (2003).
10. O. P. Bobrov, V. A. Khonik, S. N. Laptev, and M. Yu. Yazvitsky, Scr. Mater. **49**, 255 (2003).
11. T. Ichitsubo, S. Kai, H. Ogi, M. Hirao, and K. Tanaka, Scr. Mater. **49**, 267 (2003).
12. Y. Zhang, D. Q. Zhao, R. J. Wang, and W. H. Wang, Acta Mater. **51**, 1971 (2003).
13. N. P. Kobelev, E. L. Kolyvanov, and V. A. Khonik, Fiz. Tverd. Tela (St. Petersburg) **45** (12), 2124 (2003) [Phys. Solid State **45**, 2225 (2003)].
14. A. E. Berlev, O. P. Bobrov, K. Csach, V. L. Kaverin, V. A. Khonik, K. Kitagawa, J. Miškuf, and A. Yurikova, J. Appl. Phys. **92** (10), 5898 (2002).
15. N. P. Kobelev, R. K. Nikolaev, Ya. M. Soĭfer, and S. S. Khasanov, Fiz. Tverd. Tela (St. Petersburg) **40** (1), 173 (1998) [Phys. Solid State **40**, 154 (1998)].
16. W. Chen, Y. Wang, J. Qiang, and C. Dong, Acta Mater. **51**, 1899 (2003).
17. J. Saida, M. S. El-Eskandarany, and A. Inoe, Scr. Mater. **48**, 1397 (2003).
18. A. Spiriano, Philos. Mag. B **76**, 529 (1997).

Translated by O. Borovik-Romanova

Physics of the Solid State, Vol. 46, No. 10, 2004, pp. 1863–1867. Translated from Fizika Tverdogo Tela, Vol. 46, No. 10, 2004, pp. 1801–1805.

DEFECTS, DISLOCATIONS, AND PHYSICS OF STRENGTH

Stress Relaxation and Viscosity of a Bulk $Pd_{40}Cu_{30}Ni_{10}P_{20}$ Metallic Glass under Isochronous Heating Conditions

O. P. Bobrov*, S. N. Laptev*, H. Neuhäuser, V. A. Khonik*, and K. Csach*****

**Voronezh State Pedagogical University, ul. Lenina 86, Voronezh, 394043 Russia*

e-mail: khonik@vspu.ac.ru

***Braunschweig Technical University, Braunschweig, D-38106 Germany*

****Institute of Experimental Physics, Košice, 04353 Slovakia*

Received February 26, 2004

Abstract—Isochronous relaxation of tensile stresses is measured in a bulk $Pd_{40}Cu_{30}Ni_{10}P_{20}$ metallic glass in the initial state and after certain thermal treatments. The results of measurements are used to find the energy spectrum of irreversible structural relaxation, from which the temperature dependence of shear viscosity is then calculated. This dependence is also found independently from measurements of creep in the same glass. The calculated viscosity is shown to agree well with the experimental data. © *2004 MAIK "Nauka/Interperiodica".*

1. INTRODUCTION

Increased attention has recently been given to so-called bulk metallic glasses (MGs), which have a low (10^2–10^{-1} K/s and lower) critical quenching rate and can be prepared in the form of rods (plates) up to several centimeters in diameter (thickness) [1, 2]. These glasses are attracting interest for both fundamental studies and practical application. In contrast to ribbons, bulk MGs are relatively stable against crystallization above the glass transition point T_g. For this reason, their mechanical properties and other properties in this temperature range have been the subject of many studies. On the other hand, very little is known about homogeneous plastic deformation of bulk MGs below the glass transition temperature. This is especially true in regard to experimental data on creep and stress relaxation, which are of practical importance and, furthermore, allow one to establish regularities in the kinetics of homogeneous plastic flow in bulk MGs and theoretically calculate the shear viscosity, an important characteristic of the atomic mobility. To our knowledge, there are only a few publications devoted to this subject [3–8].

The quenching rates at which bulk MGs are usually prepared are three to four orders of magnitude lower than those achieved in preparing typical MG ribbons. Therefore, according to the commonly accepted model (see, e.g., [9]), the frozen-in excess free volume in bulk MGs should be noticeably less than that in MG ribbons. In this case, one might expect the atomic mobility in bulk MGs to be significantly lower, because, according to the free-volume models frequently used to interpret experimental data, the viscosity decreases *exponentially* with decreasing excess free volume [10]. However, the study of creep performed in [4] revealed that the kinetics of plastic deformation of bulk Zr-based MGs is similar to that of ribbon samples of the same chemical composition. Therefore, the question arises as to whether this conclusion is universal (i.e., independent of chemical composition). Moreover, this finding casts some doubt on the assertion that the excess free volume dictates the kinetics of atomic mobility and determines the concentration of relaxation centers responsible for homogeneous plastic deformation.

The objectives of this study were (i) to measure stress relaxation in a bulk Pd-based MG under isochronous heating; (ii) to interpret the deformation kinetics in terms of a model of directional structural relaxation (DSR), which has been developed in recent years and is an alternative to the free-volume models (see [3–8, 11] and references therein); and (iii) to verify the adequacy of this interpretation by comparing our results with independent experimental data on creep obtained on bulk and ribbon samples of the same MG.

2. EXPERIMENTAL

An initial alloy of composition $Pd_{40}Cu_{30}Ni_{10}P_{20}$ (at. %) was prepared by directly alloying constituents with a purity higher than 99.95%, using the double-zone technique, in a thick-wall quartz ampoule under a controlled phosphorus pressure. A melt of this composition was quenched into a copper mold under vacuum at a pressure of $\approx 7 \times 10^{-3}$ Pa. The quenching rate R was measured directly with a thermocouple placed in the center of the quenching cavity, whose signal was digitized at a frequency of 32 kHz. The glass formation was found to occur in the range $70 < R < 350$ K/s. Details of the quenching technique can be found in [4]. Quenched ingots were $2 \times 5 \times 60$ mm in size and were carefully monitored for trace crystalline phases using x-ray diffraction. A similar initial amorphous alloy was also pre-

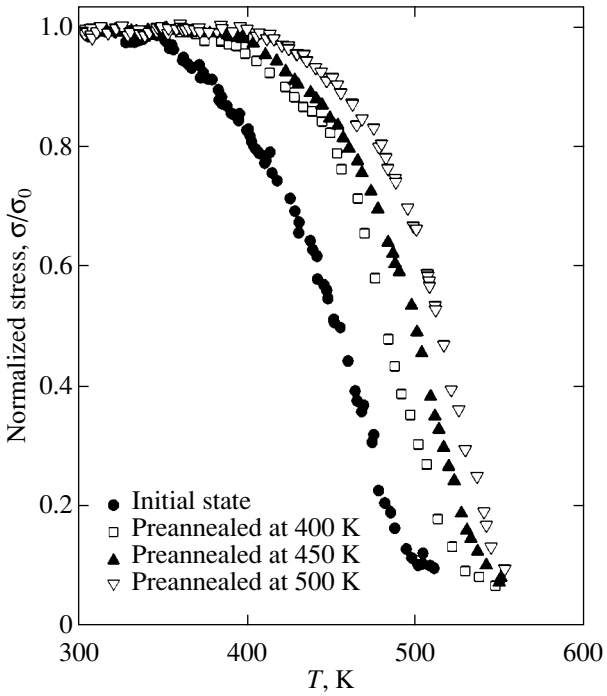

Fig. 1. Relaxation kinetics of normalized tensile stress in a bulk $Pd_{40}Cu_{30}Ni_{10}P_{20}$ metallic glass under linear heating in the initial state and after annealings over 15 min at the temperatures indicated. Heating rate, 5 K/min.

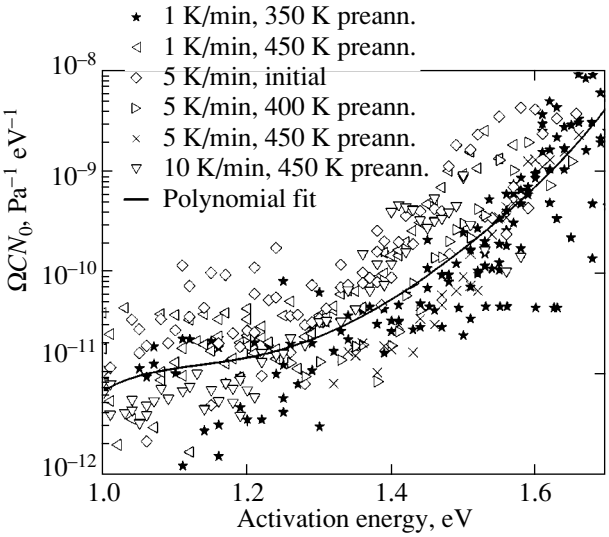

Fig. 2. Activation energy spectrum of irreversible structural relaxation of a bulk $Pd_{40}Cu_{30}Ni_{10}P_{20}$ metallic glass as calculated from isochronous stress relaxation curves for the preliminary thermal treatments and heating rates indicated. The solid curve is a fit of a fifth-degree polynomial to the data.

pared in the form of ribbons 27–34 μm thick and 0.6–0.8 mm wide by using conventional single-roller spinning in vacuum. The rate of melt quenching in this method for fabricating MGs is typically 10^6 K/s.

Tensile-stress relaxation was measured under isochronous heating conditions using a string-type testing machine. Each measurement was taken twice under given experimental conditions, which made it possible to eliminate data distortions caused by parasitic thermal expansion of the testing machine by using a specially developed technique for data processing. Details of the experiment and a detailed analysis of the results obtained can be found in [17]. Creep measurements were made with a Setaram TMA 92 quartz thermomechanical analyzer. In order to eliminate the parasitic thermal expansion of the analyzer, as in the preceding case, each measurement was made twice under the given conditions. Details of such measurements and of the data treatment technique can be found in [3]. DSC thermograms were taken with a Perkin-Elmer DSC-7 differential scanning calorimeter.

3. EXPERIMENTAL RESULTS AND DISCUSSION

Figure 1 shows temperature dependences of the normalized stress $\sigma(T)/\sigma_0$ (where σ_0 is the initial value of the relaxing stress, which was typically equal to ≈210 MPa) for the bulk MG under study measured at a heating rate of 5 K/min in the initial state and after preliminary annealings over 15 min at the temperatures indicated. Relaxation in samples in the initial state begins in the region of $T \approx 350$ K, and the stress drops down to 10% of the initial value near $T = 500$ K. (Experimental points corresponding to stresses lower than $\sigma \approx$ 15–20 MPa are not shown in Fig. 1, because the formula for the string technique [7] overestimates the stress.) Preliminary thermal treatments at 400, 450, and 500 K cause the relaxation curves to shift to higher temperatures (Fig. 1). However, in all cases, the stress $\sigma \approx 0.1\sigma_0$ is reached below the glass-transition temperature T_g, which is ≈553–555 K, according to DSC data obtained at a heating rate of 5 K/min (see inset to Fig. 3). Increasing the initial stress up to 450 MPa causes the relaxation curves to shift only slightly (by 3–6 K) to lower temperatures, which indicates that the activation volume for relaxation is small. Increasing (decreasing) the heating rate up to 10 K/min (down to 1 K/min) causes an approximately parallel shift of these curves to higher (lower) temperatures by 10–15 K. It should be noted that, on the whole, the experimental data obtained in this study are close to those obtained earlier for a bulk $Zr_{52.5}Ti_5Cu_{17.9}Ni_{14.6}Al_{10}$ [7], with the only difference that stress relaxation in this glass begins at higher temperatures. To our knowledge, there are no other data on isochronous stress relaxation in bulk MGs in the available literature. We also note that the results mentioned above are, on the whole, similar to torque relaxation curves for MG ribbons (see [12, 13] and references in [7]).

In a stress relaxation test, the total strain ε_{tot} is the sum of the elastic strain $\sigma/2G$ (G is the shear modulus) and plastic strain ε_{pl}:

$$\varepsilon_{tot} = \frac{\sigma(t)}{2G} + \varepsilon_{pl}(t). \quad (1)$$

The homogeneous plastic strain in an MG below T_g is due to irreversible structural relaxation oriented by the external stress and can be adequately described in terms of the DSR model mentioned above (see [2–8, 12, 13] and the review in [11]). In this model, the strain ε_{pl} is generally written as [11, 12]

$$\varepsilon_{pl} = \sigma\Omega C \int_{E_{min}}^{E_{max}} N_0(E)\Theta(E, T)dE. \quad (2)$$

Here, Ω is the volume involved in an elementary relaxation act; C is a parameter taking into account the orienting effect of the external stress on the elementary act; $N_0(E)$ is the energy spectrum of irreversible structural relaxation, which is defined as the number of relaxation centers per unit volume per unit activation energy (E) range; E_{min} and E_{max} are the lower and upper limits of the energy spectrum, respectively; and Θ is a characteristic annealing function, which is defined in the case of isochronous stress relaxation as [12]

$$\Theta(E, T) = \exp\left[\nu\tau\exp\left(-\frac{E}{kT_a}\right)\right]$$
$$\times\left[1 - \frac{1}{2}\exp\left(-\nu\int_{T_R}^{T}\exp\left(-\frac{E - \sigma(T)V}{kT}\right)\frac{dT}{\dot{T}}\right)\right. \quad (3)$$
$$\left. - \frac{1}{2}\exp\left(-\nu\int_{T_R}^{T}\exp\left(-\frac{E + \sigma(T)V}{kT}\right)\frac{dT}{\dot{T}}\right)\right],$$

where ν is the frequency of attempts to overcome the activation barrier, τ is the duration of the preliminary annealing at temperature T_a, k is the Boltzmann constant, V is the relaxation activation volume, $\dot{T}$ is the heating rate, T_R is the initial (room) temperature of relaxation, and $\sigma(T)$ is the current value of the relaxing stress. After substituting Eqs. (2) and (3), Eq. (1) takes the form of a Fredholm integral equation of the second kind. If the function $\sigma(T)$ is determined from experiment, this equation can be solved numerically. As a result, we find the function $\Omega CN_0(E)$, which is (to within the multiplying constant ΩC) the activation energy spectrum (AES) of the irreversible structural relaxation.

In this way, we calculated the function $\Omega CN_0(E)$ for the MG under study. Details of the calculation algorithm can be found in [12]. Numerical calculations were performed for $\nu = 10^{13}$ s^{-1} and $T_R = 300$ K. The parameters τ, T_a, and $\dot{T}$ were taken equal to their experimental values. The activation volume was an adjustable parameter. By solving the inverse problem (determining the kinetics of stress relaxation from the given function $\Omega CN_0(E)$), it was found that the value $V = 0.02$ nm^3 is optimal, as in the case of MG ribbons [12]. If we assume that, for a closely packed glass structure, the average volume per atom is $V_{at} = a^3/4$ (a is the average interatomic spacing) and $a = 0.275$ nm for pure Pd [14], then the value of V indicated above is approximately $4V_{at}$. In this case, the activation work is $\sigma V \approx 0.02$ eV. This value is much less than the activation energy for irreversible structural relaxation $E \approx 1.0$–1.7 eV (Fig. 2), which indicates that the external stress influences the relaxation kinetics only weakly, as in the case of other MGs (see, e.g., [7]).

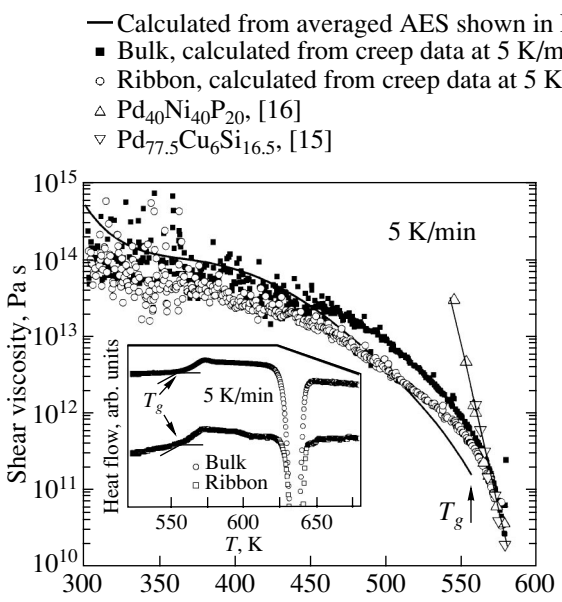

Fig. 3. Temperature dependences of the viscosity of a $Pd_{40}Cu_{30}Ni_{10}P_{20}$ metallic glass as calculated from Eq. (4) for a heating rate of 5 K/min (using the energy spectrum of irreversible structural relaxation shown in Fig. 2), as well as determined from the creep kinetics of bulk and ribbon samples for the same heating rate. Literature data on the quasi-equilibrium viscosity of Pd-based MGs are also shown and fitted by a straight line. The inset shows DSC thermograms for bulk and ribbon samples of $Pd_{40}Cu_{30}Ni_{10}P_{20}$ taken at a heating rate of 5 K/min. Arrows indicate the glass transition temperature T_g.

Figure 2 shows the quantity $\Omega CN_0(E)$ calculated from various stress relaxation curves. This quantity is seen to increase rapidly with activation energy and be close in magnitude to its values in other ribbon and bulk MGs [3, 5, 8, 12]. The points are rather widely scattered, which is primarily due to the scatter of points in the original stress relaxation curves (Fig. 1). The solid curve in Fig. 2 is a fit of a fifth-degree polynomial to the calculation data.

It is of fundamental importance to establish whether the energy spectrum of irreversible structural relaxation

[i.e., the function $\Omega CN_0(E)$] obtained by us is indeed a universal material parameter characterizing the kinetics of structural relaxation and accumulation of macroscopic plastic deformation in a specific MG under various experimental conditions. It was indicated in [3, 5, 8] that activation energy spectra determined independently, within the DSR model, from isochronous and isothermal creep data for the same MG agree well with each other. Below, we describe another method for verifying the activation energy spectrum. In this method, the shear viscosity is calculated using this spectrum and compared with the viscosity determined directly from independent experimental creep data. In the latter case, the shear viscosity is calculated from the formula $\eta = \sigma/3\dot{\varepsilon}$, where $\dot{\varepsilon}$ is the longitudinal-strain rate, which is determined by differentiating creep curves.

Within the DSR model, the temperature dependence of the shear viscosity is given by [3, 11]

$$\eta(T) = [3AN_0(E(T))\Omega C\dot{T}]^{-1}, \qquad (4)$$

where the activation energy is a linear function of temperature, $E = AT$ (this linear dependence was also used to convert the temperature into activation energy in the aforementioned method for determining the activation energy spectrum from stress relaxation data [12]), with the constant $A \approx 3.1 \times 10^{-3}$ eV/K. Figure 3 shows the shear viscosity calculated from Eq. (4) for the heating rate $\dot{T} = 5$ K/min using the averaged values of $\Omega CN_0(E)$, represented in Fig. 2 by the solid curve. It can be seen from Fig. 3 that the calculations agree well with the viscosity determined from experimental creep data for bulk samples. Indeed, at temperatures $T \le 460$ K, the calculated and experimental data almost coincide. At higher temperatures, the calculated viscosity is somewhat lower than the experimental values, but the discrepancy is not significant when it is taken into account that the data on ΩCN_0 (Fig. 2) are widely scattered. Thus, the activation energy spectrum is calculated correctly and the DSR model adequately describes the kinetics of structural relaxation and accumulation of plastic deformation.

Figure 3 also shows the data on the quasi-equilibrium viscosity of glasses of analogous composition taken from [15, 16] (fitted by a straight line). At temperatures $T \ge 560$ K, these data almost coincide with the values of viscosity determined from our measurements of creep in bulk and ribbon MG samples. At lower temperatures, our data give lower values of viscosity and the difference increases rapidly with decreasing temperature. Measurements of creep at various heating rates showed that the temperature range $T \approx 550$–560 K corresponds to a transient state. Indeed, below this range, the viscosity depends fairly strongly on the heating rate, whereas at higher temperatures it becomes independent of temperature (these findings will be published in a later paper). The dependence of the viscosity on the heating rate (at $T < 550$ K) indicates that the strain rate in this temperature range is determined by irreversible structural relaxation, while the absence of this dependence (at $T > 560$ K) suggests that the material reached a quasi-equilibrium structural state [3, 4]. Therefore, the temperature $T = T_g \approx 555$ K is the glass transition point. This conclusion is also supported by the fact that the $\eta(T)$ curve exhibits a noticeable break near 555 K. DSC measurements gave the same value for T_g (see inset to Fig. 3). Note that this value of T_g corresponds to a viscosity of approximately 10^{12} Pa s. This value of η is generally agreed to correspond to glass formation [17].

We emphasize that the temperature dependences of the viscosity obtained in creep tests on bulk and ribbon samples are very similar (Fig. 3). At $T \le 450$ K, these dependences almost coincide, even though the corresponding quenching rates differ by approximately four orders of magnitude. At higher temperatures, the viscosity of ribbon samples is somewhat lower than that of bulk samples. Therefore, in ribbon samples, the volume density of relaxation centers is higher in the high-energy part of the activation energy spectrum and is the same in the low-energy part. The same conclusion was also drawn earlier in [4] for a bulk Zr-based glass. We note, however, that in certain cases the creep test data suggest that the temperature dependences of the viscosity of bulk and ribbon samples are almost identical throughout the entire temperature range studied.

The DSC thermograms for bulk and ribbon samples are also similar; namely, the glass transition temperatures are equal to within 1–2 K (inset to Fig. 3) and the corresponding endothermic and exothermic effects are also very similar in these samples. It should be noted that in the literature there are data according to which the density of Pd-based glasses decreases noticeably with increasing quenching rate. For example, it was reported in [18] that the density of $Pd_{77.5}Cu_6Si_{16.5}$ glass ribbons is 0.2% lower than that of bulk samples (cylinders 2 mm in diameter). In [19], it was established that, in a $Pd_{40}Ni_{10}Cu_{30}P_{20}$ metallic glass, an increase in the quenching rate from 1.6 to 500 K/s also causes the density to decrease by 0.2%. This decrease is only three times less than the increase in the density of bulk $Pd_{39}Ni_{10}Cu_{30}P_{21}$ on crystallization [20] and is comparable to the change in the density of MGs on structural relaxation. However, it is known that the change in the viscosity of MGs caused by structural relaxation can be as large as five orders of magnitude [21]. Therefore, if the change in viscosity is associated with a change in the excess free volume (i.e., in density), then a change in the quenching rate would cause a noticeable difference in viscosity between bulk and ribbon MG samples, which is not, in fact, the case. This fact calls into question the free-volume model [10], according to which the relaxation centers responsible for homogeneous plastic flow in MGs are associated with local regions with an increased excess free volume. In our opinion, the relaxation centers responsible for homogeneous plastic flow in MGs can be described in terms of the

interstitial model of the condensed state of matter [22, 23], in which relaxation centers can be identified with defects analogous to interstitial dumbbells in crystals. These defects are highly sensitive to external shear stresses but are not associated with fluctuations in the excess free volume.

4. CONCLUSIONS

It has been found that stress relaxation in a bulk $Pd_{40}Cu_{30}Ni_{10}P_{20}$ glass under isochronous heating conditions begins near T = 350 K. Preliminary thermal treatment shifts the onset of relaxation to higher temperatures. In any case, complete stress relaxation is reached below the glass transition point. Using the directional structural relaxation model, the energy spectrum of irreversible structural relaxation has been found from stress relaxation data and the temperature dependence of the shear viscosity has been calculated using this spectrum. It was shown that this temperature dependence is close to that determined from independent creep test data for bulk and ribbon samples of the same MG. The fact that the viscosity values for bulk and ribbon samples are similar (even though the quenching rates for them differ by four orders of magnitude) casts doubt on the assumption that the relaxation centers responsible for homogeneous plastic flow are associated with the excess free volume.

ACKNOWLEDGMENTS

This study was supported by the U.S. Civilian Research and Development Foundation (CRDF), grant RP1-2320-VO-02.

REFERENCES

1. W. L. Johnson, MRS Bull. **24** (10), 42 (1999).
2. A. Inoue, Mater. Sci. Found. **4**, 116 (1999).
3. A. E. Berlev, O. P. Bobrov, K. Csach, V. L. Kaverin, V. A. Khonik, K. Kitagawa, J. Miškuf, and A. Yurikova, J. Appl. Phys. **92** (10), 5898 (2002).
4. A. E. Berlev, O. P. Bobrov, V. A. Khonik, K. Csach, A. Juríková, J. Miškuf, H. Neuhäuser, and M. Yu. Yazvitsky, Phys. Rev. B **68** (13), 132203 (2003).
5. M. Ohta, A. E. Berlev, V. A. Khonik, and K. Kitagawa, Philos. Mag. **83** (30), 3463 (2003).
6. O. P. Bobrov, S. N. Laptev, and V. A. Khonik, Vestn. Tambov. Univ. **8** (4), 525 (2003).
7. O. P. Bobrov, V. A. Khonik, and S. N. Laptev, Scr. Mater. **50** (3), 337 (2004).
8. O. P. Bobrov, S. N. Laptev, and V. A. Khonik, Fiz. Tverd. Tela (St. Petersburg) **46** (3), 457 (2004) [Phys. Solid State **46**, 470 (2004)].
9. S. R. Elliott, *Physics of Amorphous Materials*, 2nd ed. (Longman, Harlow, 1990).
10. F. Spaepen, Acta Metall. **25** (4), 407 (1977).
11. V. A. Khonik, J. Non-Cryst. Solids **296** (3), 147 (2001).
12. O. P. Bobrov, V. A. Khonik, and V. S. Zhelezny, J. Non-Cryst. Solids **223** (3), 241 (1998).
13. O. P. Bobrov, A. T. Kosilov, and V. A. Khonik, Fiz. Tverd. Tela (St. Petersburg) **38** (4), 1086 (1996) [Phys. Solid State **38**, 601 (1996)].
14. C. J. Smithells, *Metals Reference Book*, 5th ed. (Butterworths, London, 1976; Metallurgiya, Moscow, 1980).
15. R. Bush, A. Masuhr, E. Bakke, and W. L. Johnson, Mater. Res. Soc. Symp. Proc. **455**, 369 (1997).
16. G. Wilde, G. P. Görler, R. Willnecker, and H. J. Fecht, Appl. Phys. **87** (3), 1141 (2000).
17. P. G. Debenedetti and F. H. Stillinger, Nature **410** (8), 259 (2001).
18. H. S. Chen, J. Appl. Phys. **46**, 3289 (1978).
19. X. Hu, S. C. Ng, Y. P. Feng, and Y. Li, Phys. Rev. B **64**, 172 201 (2001).
20. L. M. Wang, W. H. Wang, R. J. Wang, Z. J. Zhan, D. Y. Dai, L. L. Sun, and W. K. Wang, Appl. Phys. Lett. **77** (8), 1147 (2000).
21. A. I. Taub and F. Spaepen, Scr. Metall. **13**, 195 (1979).
22. A. V. Granato, Phys. Rev. Lett. **68** (7), 974 (1992).
23. A. V. Granato, J. Non-Cryst. Solids **307–310**, 376 (2002).

Translated by Yu. Epifanov

Physics of the Solid State, Vol. 46, No. 10, 2004, pp. 1868–1872. Translated from Fizika Tverdogo Tela, Vol. 46, No. 10, 2004, pp. 1806–1810.

DEFECTS, DISLOCATIONS, AND PHYSICS OF STRENGTH

Wavelet Transform as a Method for Studying the Fractal Properties of the Surface of Amorphous Metals under Mechanical Load

V. L. Hilarov*, V. E. Korsukov*, P. N. Butenko, and V. N. Svetlov***

** Ioffe Physicotechnical Institute, Russian Academy of Sciences, Politekhnicheskaya ul. 26, St. Petersburg, 194021 Russia*
e-mail: Vladimir.Hilarov@mail.ioffe.ru

*** St. Petersburg State Technical University, Politekhnicheskaya ul. 29, St. Petersburg, 195251 Russia*

Received March 9, 2004

Abstract—The effect of mechanical tension on the multifractal characteristics of the lateral surface of a $Fe_{77}Ni_1Si_9B_{13}$ amorphous alloy is studied by scanning tunneling microscopy (STM). It is established that, at small loads, the surface is smoothed out much as a crumpled sheet of paper is smoothed out under tension. With an increase in the load, there appears a tendency to the formation of a fractal structure on the surface. © *2004 MAIK "Nauka/Interperiodica".*

Scanning tunneling microscopy (STM) has been widely used to study the structure of solid surfaces on the microscale and nanoscale levels. The experimental data are represented in the form of a surface profile, i.e., the dependence of the height $z(x, y)$ on the coordinates (x, y) of different points on the surface. As a rule, the function $z(x, y)$ is extremely irregular. Therefore, it is appropriate to use statistical methods for investigating the geometric properties of the surface.

In recent years, the particular interest has been expressed by researchers in statistical and, especially, fractal properties of surfaces, i.e., self-similar behavior of the surface profile on various scales [1]. Many surfaces of different physical nature have been studied and treated as fractal surfaces, at least, in a limited range of scales.

The fractal properties of metal and semiconductor surfaces have been extensively studied under the action of external factors (for example, mechanical tension [2–8]). It has been found that the mechanical field strongly affects the surface geometry and, in particular, the fractal properties of the surface.

A setup for tensile testing (including a sample, a testing machine for uniaxial tension, a scanning tunneling microscope, a personal computer, and an interface for connecting it to the microscope) was described in [2]. The procedure for preparing samples of the $Fe_{77}Ni_1Si_9B_{13}$ amorphous alloy studied in the present work was described in [7]. The topograms illustrating the change in the geometry of the surface of the amorphous iron alloy subjected to different uniaxial tensions are given in Fig. 1.

The fractal dimension was calculated by several methods. Method *a* is based on the "box counting" or "covering" algorithm for two points on the surface. The dependence of the fractal dimension on the load exhibits a nonmonotonic behavior: the fractal dimension first decreases sharply and then increases drastically. Moreover, it should be noted that an increase in the fractal dimension at neighboring points was not necessarily observed with an increase in the load. We believe that this method for determining the fractal dimension does not completely reproduce the observed surface relief. The topograms obtained with the use of a scanning tunneling microscope usually contained 200 points along the vertical cross section (scan) and had a maximum of 200 scans (a total of 40 000 points). When the surface of size L is covered with cells of size l, their number increases as $n = 2^{3i}$ depending on the size ratio $i = L/l$. Hence, at $i = 5$, we have $n = 32\,768$; i.e., when the scale decreases by a factor of 5, the number of cells necessary for covering becomes comparable to the number of experimental points. Consequently, for a smaller scale, there are no points to cover cells (the database must contain a considerably larger number of experimental points). Therefore, the fractal dimension obtained according to the covering algorithm appears to be of the order of two on large scales. A similar situation occurs with the amplitude normalization algorithm (method *b*). At the same time, spectral analysis allows one to determine the fractal dimension on small scales.

The spectral fractal dimension calculated from the correlator power density spectrum (method *c*) $C(\Delta x) = \langle z(x + \Delta x)z(x)\rangle$, i.e., the quantity

$$S(\omega) = \int_{-\infty}^{\infty} C(\Delta x)\exp(i\omega\Delta x)d\Delta x, \qquad (1)$$

is unreliably determined, because the quantity $S(\omega)$ is characterized by a large spread of points.

1063-7834/04/4610-1868$26.00 © 2004 MAIK "Nauka/Interperiodica"

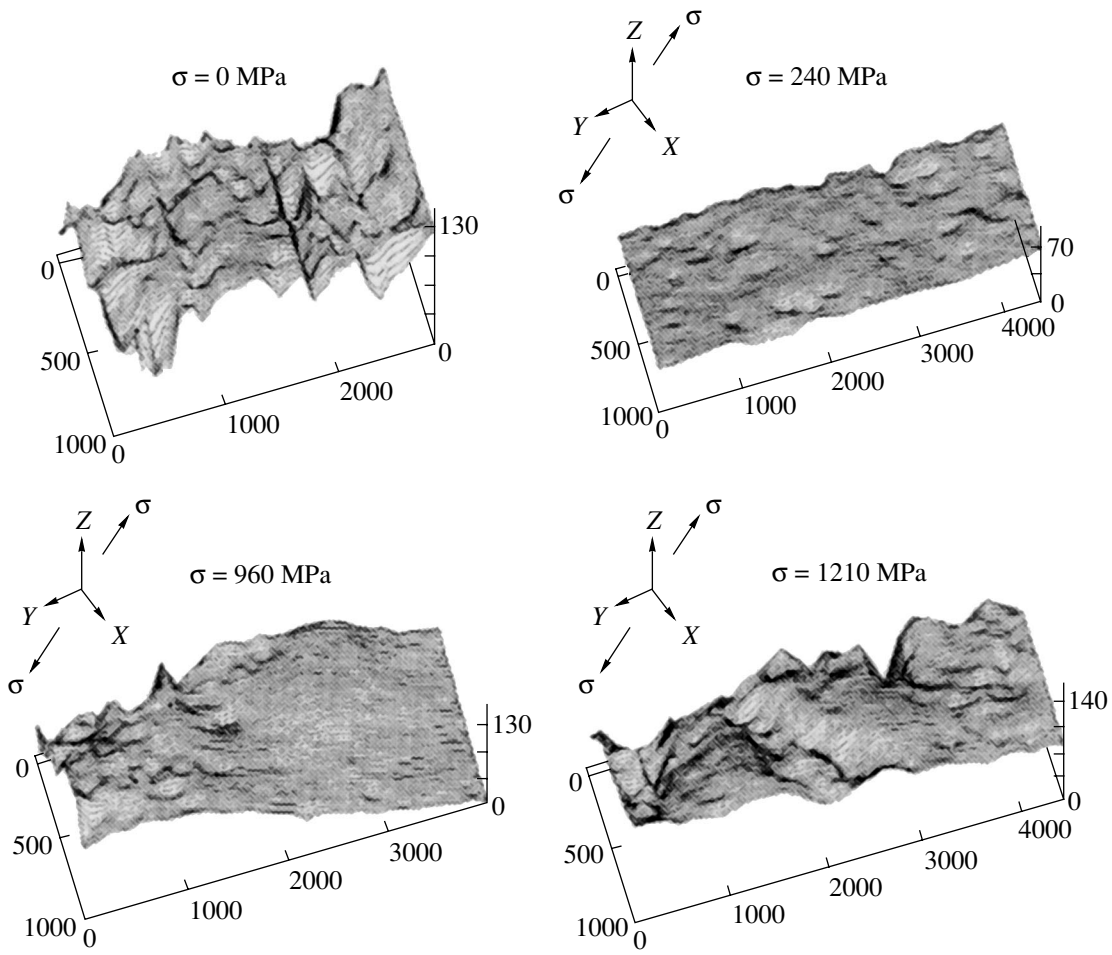

Fig. 1. STM topograms illustrating the change in the geometry of the surface of an amorphous alloy subjected to increasing uniaxial tension.

Among the aforementioned methods, only the first approach is appropriate for a three-dimensional situation. The other two techniques involve the analysis of two-dimensional curves, namely, vertical cross sections of the surface profiles along the chosen directions. The fractal dimensions calculated for surfaces according to methods *a* and *b* are close to each other and differ from 2.0 by no more than 10%. This corresponds to the dimension of a flat surface and differs significantly from the fractal dimension obtained by method *c* (of the order of 2.5). Such a difference is associated with the fact that the surfaces are self-affine objects rather than fractal objects. Fractal objects are structures that are transformed into statistically equivalent structures by a similarity transformation,

$$z(\lambda x) = \lambda z(x), \tag{2}$$

i.e., by the scaling of the x coordinate along one direction and the same scaling of the z coordinate along another direction. Flat surfaces with a roughness do not possess this property, because the directions along and across the surface are not equivalent. These surfaces remain statistically equivalent after an affine transformation of the form

$$z(\lambda x) = \lambda^H z(x), \tag{3}$$

where the Hurst coefficient satisfies the inequality $0 \le H \le 1$.

Self-affine surfaces do not have a specific fractal dimension. On large scales, their covering dimension is approximately equal to 2. This corresponds to the dimension of a flat surface. At the same time, the fractal dimension on small scales is determined by the Hurst coefficient H ($d = 2 - H$ or $1/H$ depending on the definition).

The approach based on the wavelet transform makes it possible to construct characteristics similar to quantity (1) for calculating the fractal dimension [9] and is free of many disadvantages inherent in methods *a*, *b*, and *c*. Note that the basis functions used for the Fourier transform have the form $\exp(ix) = \cos x + i\sin x$, consist of a set of sine waves with different frequencies, and are delocalized in space. By contrast, the basis functions in the wavelet transform are given by strongly localized

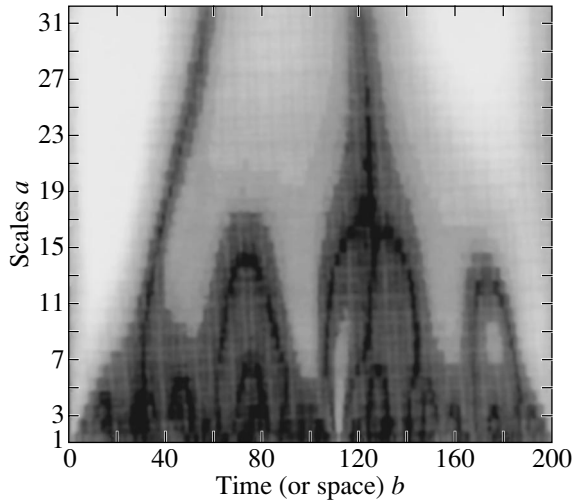

Fig. 2. Wavelet transform of the surface relief.

soliton-like functions. In particular, this can be a sombrero function derived from the second derivative of the Gaussian function,

$$\psi(x) = \frac{\partial^2}{\partial x^2}\exp\left(-\frac{x^2}{2}\right). \quad (4)$$

The basis set of the wavelet transform is constructed through continuous scaling transformations and translations $\psi(x)$, which can be written in the form

$$\psi_{a,b}(x) = \psi\left(\frac{x-b}{a}\right).$$

Here, a is the scaling coefficient and b is the translation parameter. Then, the wavelet transform can be defined as the integral transformation

$$W(a,b) = \frac{1}{\sqrt{a}}\int_{-\infty}^{\infty} z(x)\psi\left(\frac{x-b}{a}\right)dx. \quad (5)$$

By applying the wavelet transform, we obtain a function of two variables (a, b) that carries information regarding the spatial distribution of inhomogeneities of different scales (defect sizes). Figure 2 presents an example of the wavelet transform of the initial surface shown in Fig. 1.

The statistical regularities in a defect structure of the surface can be judged even from the form of the wavelet transform coefficients. Specific manifestations of different defects in the spectra of the wavelet transform coefficients have been obtained for model systems and described in numerous reviews (see, for example, [10, 11]). Without going into detail, we note that a dendritic structure typical of self-similar fractal systems can be seen in Fig. 2.

Above, it was silently assumed that the surface has a fractal structure with a single fractal dimension. This assumption is equivalent to the fact that the surface roughness does not depend on the point chosen on this surface. Apparently, this simplified assumption is unlikely to hold in reality, because it is more probable that there are spatial fluctuations in roughness. It is known [1] that, in this situation, the system cannot be characterized by a single regularity parameter (fractal dimension). Therefore, it is necessary to introduce a local characteristic that varies from point to point, namely, the Hölder index $h(x)$. These systems are referred to as self-affine multifractals. The wavelet analysis enables one to describe these systems adequately. If the function describing the system possesses a singularity with the Hölder index $h(x_0)$ at the point x_0, the wavelet transform of this function on small scales has a scaling in the form

$$W(x_0, b) \sim b^{h(x_0)}. \quad (6)$$

Such a scaling occurs in the case when the analyzing wavelet is appropriately chosen; i.e., the number of its zero moments,

$$\int_{-\infty}^{\infty} x^m \psi(x)dx = 0, \quad \forall m: 0 \le m < n_\psi,$$

obeys the inequality $n_\psi > h(x_0)$.

The wavelet analysis provides a way of determining quantitative characteristics of multifractal systems, such as the multifractal dimension spectrum $D(q)$, the multifractal spectrum $f(h)$, and other related quantities. For this purpose, it is expedient to use the formalism of fractal thermodynamics (see [12] and references therein). This formalism is based on the principle of the wavelet transform modulus maximum, which, in turn, rests on the construction of the partition function of the wavelet coefficients:

$$Z(q,a) = \sum_{b_i(a)} |W(a,b)|^q \propto a^{\tau(q)}. \quad (7)$$

The sum in formula (7) is taken over points in the space at which the wavelet transform modulus is maximum (over the local modulus maxima). In [9], it was shown that the framework composed of the lines corresponding to the modulus maximum contains all information on the distribution of singularities of the initial surface.

As was noted in [12–14], there is a close similarity between the multifractal formalism and thermodynamics. In particular, the quantity $\tau(q)$ plays the role of a free energy and the quantity q serves as a reciprocal of the temperature. The role of the energy is played by the Hölder index h, and the singularity spectrum $f(h)$ fulfills the function of the entropy.

The multifractal properties of the surface profiles obtained by scanning tunneling microscopy were calculated along the scans of the topograms with subsequent averaging over the scans. The dependence $\tau(q)$

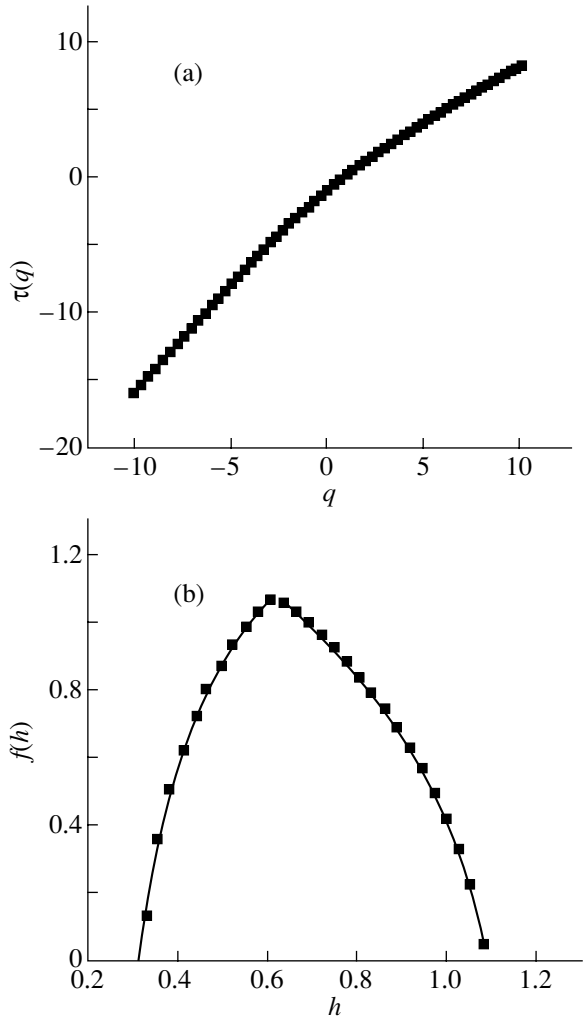

Fig. 3. (a) Dependence of the mass exponent $\tau(q)$ on q and (b) the multifractal spectrum $f(h)$.

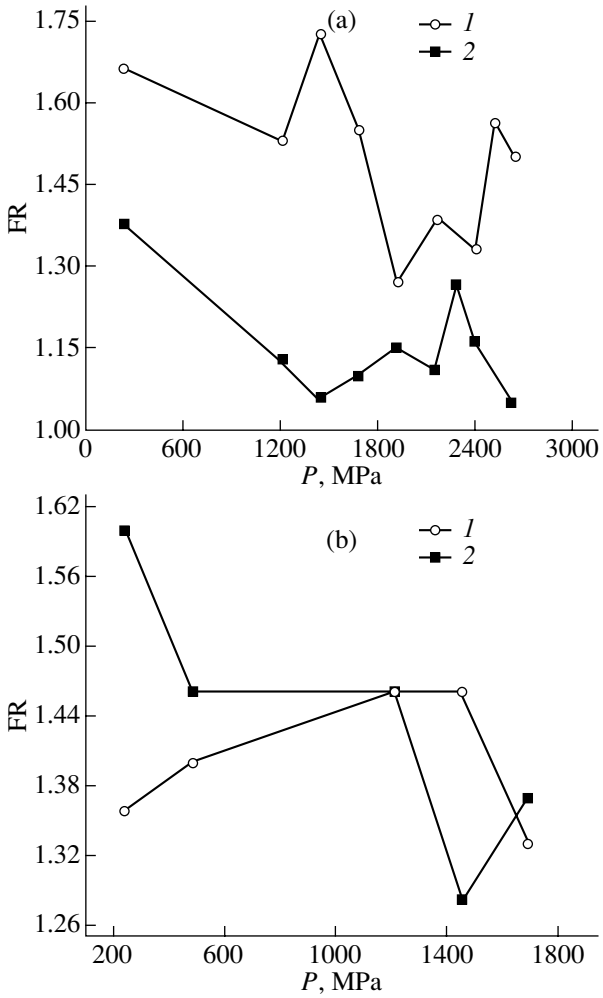

Fig. 4. Dependences of the fractal dimension on the load P for (a, b) two experimental runs at (*1*, *2*) different points on the surface.

can be calculated from relationship (7) with the use of the $\log Z(q, a) - \log a$ linear approximation. Then, the derived dependence $\tau(q)$ serves for determining the spectrum $f(h)$. These calculations were performed with the Wavelab 8.02 program package developed at Stanford University. As an example, the calculated dependences $\tau(q)$ and $f(h)$ are shown in Fig. 3.

The dependence $\tau(q)$ for the surface under investigation exhibits a nonlinear behavior, and the spectrum $f(h)$ is broadened as compared to the spectrum of a Brownian curve. The intensity of the spectrum at the maximum is determined to be $f(h) \approx 1$. This indicates that the straight line again serves as a measure of the dimension, and the surface is represented by a self-affine multifractal.

It can be expected that the application of mechanical stresses to the samples should lead to changes in the multifractal spectra. These changes are described by the following numerical characteristics: the fractal dimension (FR) $D_S = 1 - \tau(1)$, the half-width of the multifractal spectrum $\Delta = h_0 - h_{\min}$, and the scaling exponent of the spectral density $\beta = 2 + \tau_2$.

The dependences of the fractal dimension on the load for two experimental runs at different points on the surface are plotted in Fig. 4.

Despite a large spread of data due to both experimental limitations (drift of the scanning tunneling microscope tip from the region of observation, measurements in air) and computational factors (200 points per scan cannot provide good statistics), we revealed a number of regularities in the behavior of the fractal dimension under load. The fractal dimension of the surface decreases at the initial stage of mechanical loading. A further increase in the mechanical load leads to an increase in the fractal dimension (see Fig. 4a, because the data presented in Fig. 4b were obtained at insufficiently large mechanical stresses).

The dependences of the half-width and the location of the multifractal spectrum at the maximum on the

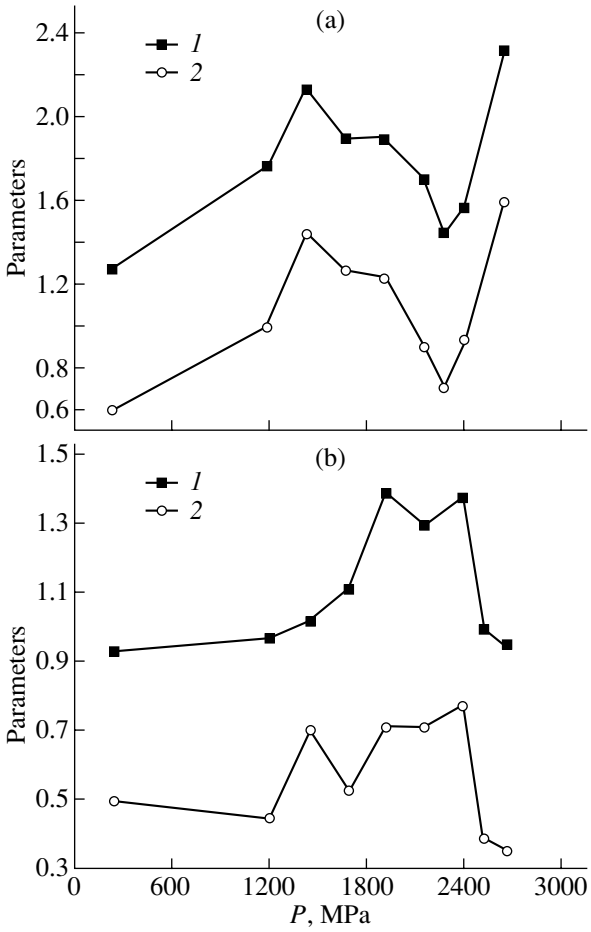

Fig. 5. Dependences of (*1*) the location and (*2*) the half-width of the multifractal spectrum at the maximum on the load for one experimental run at two different points (a) 1 and (b) 2 on the surface.

load are depicted in Fig. 5 for one experimental run at two different points on the surface.

It can be seen from Fig. 5 that, at the initial stage of mechanical loading, the total spectrum of singularities shifts toward larger Hölder indices. This is accompanied by an increase in the width of the spectrum. Therefore, we can infer that the surface experiences smoothing out (the surface flatness is improved) at the initial stage. However, this smoothing out is not uniform over the surface, because the degree of roughness determined by the width of the spectrum also increases.

As a rule, a further increase in the mechanical load results in the opposite behavior of the singularity spectrum: the spectrum width decreases and the spectrum itself shifts toward smaller Hölder indices. This suggests that, at this stage of mechanical loading, the system tends to form a new single-fractal structure.

We believe that the surface is smoothed out under small mechanical stresses, because the initial surface of the amorphous alloy was formed under nonequilibrium conditions (by spinning from a melt). Therefore, the initial surface has a considerable roughness. The response of this surface to tensile mechanical stresses is similar to smoothing out a crumpled sheet of paper under tension. A tendency to the formation of a new fractal structure at higher stresses reflects the early stage of surface fracture. The final stage of fracture frequently proceeds through a self-organized criticality state characterized by the formation of self-similar fractal structures.

REFERENCES

1. J. Feder, *Fractals* (Plenum, New York, 1988; Mir, Moscow, 1991).
2. S. N. Zhurkov, V. E. Korsukov, A. S. Luk'yanenko, B A. Obidov, V. N. Svetlov, and A. P. Smirnov, Pis'ma Zh. Éksp. Teor. Fiz. **51** (6), 324 (1990) [JETP Lett. **51**, 370 (1990)].
3. V. E. Korsukov, A. S. Luk'yanenko, B. A. Obidov, and V. N. Svetlov, Pis'ma Zh. Éksp. Teor. Fiz. **55** (10), 595 (1992) [JETP Lett. **55**, 621 (1992)].
4. V. E. Korsukov, A. S. Luk'yanenko, B. A. Obidov, V. N. Svetlov, and E. V. Stepin, Pis'ma Zh. Éksp. Teor. Fiz. **57** (6), 343 (1993) [JETP Lett. **57**, 358 (1993)].
5. V. Korsukov, A. Lukyanenko, and B. Obidov, Surf. Rev. Lett. **5** (1), 37 (1998).
6. N. N. Gorobeĭ, S. A. Knyazev, V. E. Korsukov, A. S. Luk'yanenko, B. A. Obidov, and V. E. Khartsiev, Pis'ma Zh. Tekh. Fiz. **28** (1), 54 (2002) [Tech. Phys. Lett. **28**, 23 (2002)].
7. V. I. Betekhtin, P. N. Butenko, V. L. Hilarov, V. E. Korsukov, A. S. Luk'yanenko, B. A. Obidov, and V. E. Khartsiev, Pis'ma Zh. Tekh. Fiz. **28** (1), 60 (2002) [Tech. Phys. Lett. **28**, 26 (2002)].
8. V. I. Betekhtin, N. N. Gorobeĭ, S. A. Knyazev, V. E. Korsukov, A. S. Luk'yanenko, B. A. Obidov, and A. N. Tomilin, Pis'ma Zh. Tekh. Fiz. **28** (7), 63 (2002) [Tech. Phys. Lett. **28**, 893 (2002)].
9. S. Mallat and W. L. Hwang, IEEE Trans. Inf. Theory **38**, 617 (1992).
10. V. V. Zverev, A. G. Zalazinski, V. I. Novozhonov, and A. P. Polyakov, J. Appl. Mech. Tech. Phys. **42**, 363 (2001).
11. N. M. Astaf'eva, Usp. Fiz. Nauk **166**, 1145 (1996) [Phys. Usp. **39**, 1085 (1996)].
12. A. Arneodo, E. Bacry, and J. F. Muzy, Physica A (Amsterdam) **213**, 232 (1995).
13. P. Collet, J. Lebowitz, and A. Porsio, J. Stat. Phys. **47**, 609 (1987).
14. M. J. Fiegenbaum, J. Stat. Phys. **46**, 919 (1987).

Translated by O. Moskalev

Physics of the Solid State, Vol. 46, No. 10, 2004, pp. 1873–1877. Translated from Fizika Tverdogo Tela, Vol. 46, No. 10, 2004, pp. 1811–1815.

DEFECTS, DISLOCATIONS, AND PHYSICS OF STRENGTH

Elasticity and Inelasticity of Biomorphic Silicon Carbide Ceramics

B. K. Kardashev*, Yu. A. Burenkov*, B. I. Smirnov*, A. R. de Arellano-Lopez, J. Martinez-Fernandez**, and F. M. Varela-Feria****

** Ioffe Physicotechnical Institute, Russian Academy of Sciences, Politekhnicheskaya ul. 26, St. Petersburg, 194021 Russia*
e-mail: smir.bi@mail.ioffe.ru
*** Universidad de Sevilla, Sevilla, 41080 Spain*
Received March 11, 2004

Abstract—The effect of the vibration strain amplitude on the Young modulus and ultrasonic absorption (internal friction) in biomorphic SiC ceramics is investigated in the temperature range 116–296 K. The biomorphic SiC ceramics is prepared through pyrolysis of eucalyptus with subsequent infiltration of silicon. It is demonstrated that the vibration loading of samples in air and under vacuum is accompanied by a number of unexpected effects. The behavior of the studied ceramics is governed by at least two mechanisms, which, to a large extent, are responsible for the elastic and inelastic properties of the material. One mechanism is associated with the adsorption–desorption of environmental molecules (hypothetically, owing to the presence of pores and residual carbon), and the other mechanism involves microplastic deformation due to the motion of dislocations or other (similar) structural units. © *2004 MAIK "Nauka/Interperiodica".*

1. INTRODUCTION

Over the last decade, there has been considerable research interest in the study of the physicomechanical properties of biomorphic silicon carbide ceramics (which are often referred to as ecoceramics, i.e., environment conscious ceramics) [1–11]. This interest stems from the fact that the above ceramic materials possess a high strength, good oxidation and corrosion resistance, high thermal conductivity, and resistance to thermal shocks.

Moreover, the advantage of ecoceramic materials is that the method for preparing them is based on the use of a prior-chosen type of wood. The method involves pyrolysis (carbonization) of the product (sample) precursor with subsequent silicon infiltration in order to produce silicon carbide retaining a wood structure. Compared to other methods used for preparing SiC ceramic materials, the above technique has a number of advantages, such as the possibility of specifying the sample shape in advance, the high rate and low temperature of production, and the low density of materials. It has been established experimentally that biomorphic SiC ceramic materials possess good mechanical properties at high temperatures [4–11].

In our previous work [9], we examined the influence of high temperatures (up to 1000°C) on the Young modulus of biomorphic SiC ceramics prepared from eucalyptus and oak. In this work, we concentrated our attention on investigating the acoustical properties (Young modulus, decrement of elastic vibrations) of eucalyptus-based SiC ecoceramics over a wide range of vibration strain amplitudes at temperatures T = 116–296 K.

2. SAMPLE PREPARATION AND EXPERIMENTAL TECHNIQUE

Biomorphic SiC ceramic samples were prepared by vacuum infiltration of molten silicon into a porous carbonized wood (white eucalyptus) after pyrolysis in an argon atmosphere at 1000°C [5]. The final SiC product had a cellular structure extended along the direction of tree growth and contained residual carbon and pores partially filled with silicon [11].

For acoustical measurements, the samples were produced in the form of rectangular rods (~16 mm^2) ~50 mm long, which were oriented along the direction of tree growth.

Acoustical investigations were performed using the composite oscillator method. The experimental technique was described in detail in [12]. Longitudinal vibrations at a frequency f of approximately 100 kHz were excited in the sample with a quartz transducer. The Young moduli $E \sim f^2$ and the logarithmic decrements δ were measured in experiments. The sample density ρ = 2.37 g/cm^3, which was necessary for calculating the elastic moduli, was determined by hydrostatic weighing at room temperature. The vibration strain amplitude ε in our experiments was varied from $\sim 10^{-7}$ to 3.0×10^{-4}.

The measurement procedure was as follows. Initially, the amplitude dependences $E(\varepsilon)$ and $\delta(\varepsilon)$ were measured for the as-prepared sample stored for a long time in air at atmospheric pressure and room temperature. Then, the acoustical system (the quartz transducer with the cemented sample) was placed in vacuum with a residual pressure of approximately 10^{-3} mm Hg. The

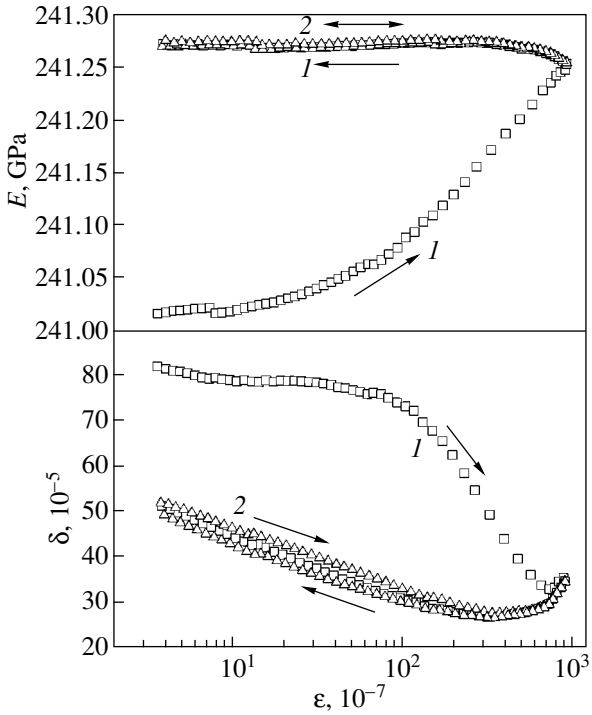

Fig. 1. Amplitude dependences of the Young modulus E and the decrement δ for the as-prepared biomorphic SiC ceramic sample. The dependences were sequentially measured two times at approximately 1-min intervals in air at atmospheric pressure and T = 296 K: (*1*) first run and (*2*) second run. Arrows indicate the direction of change in the vibration strain amplitude ε.

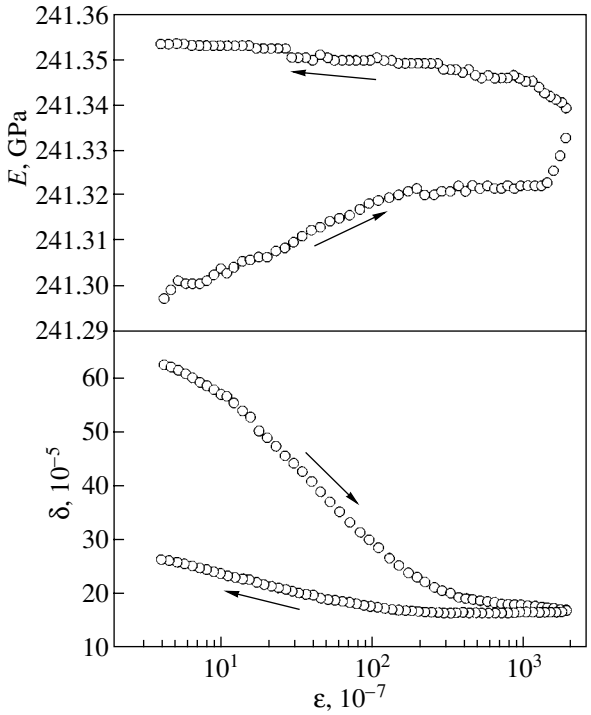

Fig. 2. Amplitude dependences of the Young modulus E and the decrement δ for the biomorphic SiC ceramic sample stored in air at atmospheric pressure. The data were obtained at T = 294 K within four weeks of the first measurements of the amplitude dependences shown in Fig. 1. Arrows indicate the direction of change in the vibration strain amplitude ε.

subsequent measurements of the temperature and amplitude dependences of the Young modulus E and the decrement δ in the temperature range 116–296 K were carried out under vacuum.

3. RESULTS AND DISCUSSION

Figure 1 shows the dependences $E(\varepsilon)$ and $\delta(\varepsilon)$ for a biomorphic SiC ceramic sample that was subjected to large-amplitude strains for the first time after preparation. It can be seen from Fig. 1 that an increase in the vibration strain amplitude leads to a considerable increase in the measured (effective) elastic modulus and a decrease in the decrement (except for the several last points at large amplitudes ε, at which the decrement somewhat increases). The changes in the modulus and decrement are irreversible to a large extent. Actually, with a subsequent decrease in the vibration strain amplitude, the elastic modulus E at small amplitudes ε appears to be larger than the initial modulus and, by contrast, the decrement δ decreases by a factor of approximately 1.5. Upon a repeated increase in the strain amplitude ε, the dependences $E(\varepsilon)$ and $\delta(\varepsilon)$ virtually coincide with those obtained upon a decrease in the strain amplitude and qualitatively differ from the initial dependences. Indeed, at large amplitudes, the modulus decreases and the decrement increases with an increase in ε (this behavior, as a rule, is observed for various crystalline [12] and other materials, including fibrous monoliths [13]). Note that, in the repeated measurements, the decrement at small and moderate amplitudes also decreases with an increase in the amplitude ε, even though the irreversibility in this case becomes insignificant.

During storage of the sample in air at atmospheric pressure, the dependences $E(\varepsilon)$ and $\delta(\varepsilon)$ tend to regain their original form. However, complete recovery requires a very long time. This can be judged from a comparison of the data presented in Figs. 1 and 2 (the data in Fig. 2 were obtained within 28 days of the first measurements).

Then, similar experiments were performed for the same sample with the acoustical system placed in a vacuum chamber. When analyzing the experimental data obtained at room temperature (compare Fig. 3 with Figs. 1, 2), it is worth noting that the magnitude of the elastic modulus E increases and the decrement δ substantially decreases under vacuum. However, qualitatively, the dependences $E(\varepsilon)$ and $\delta(\varepsilon)$ measured under vacuum remain almost unchanged: an insignificant hysteresis is usually observed in the first run, the dependences $\delta(\varepsilon)$ exhibit a minimum at moderate amplitudes,

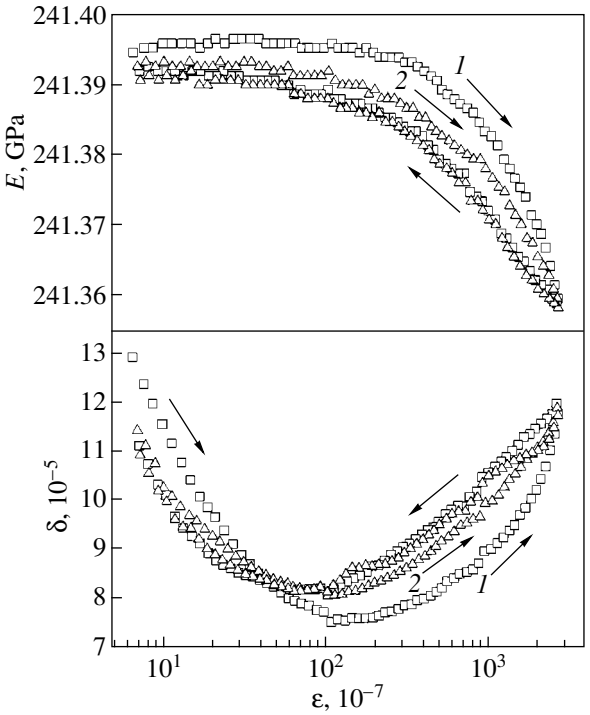

Fig. 3. Amplitude dependences of the Young modulus E and the decrement δ for the biomorphic SiC ceramic sample preliminarily subjected to large-amplitude strains at low temperatures. The dependences were sequentially measured two times at approximately 1-min intervals under vacuum at $T = 296$ K: (*1*) first run and (*2*) second run. Arrows indicate the direction of change in the vibration strain amplitude ε.

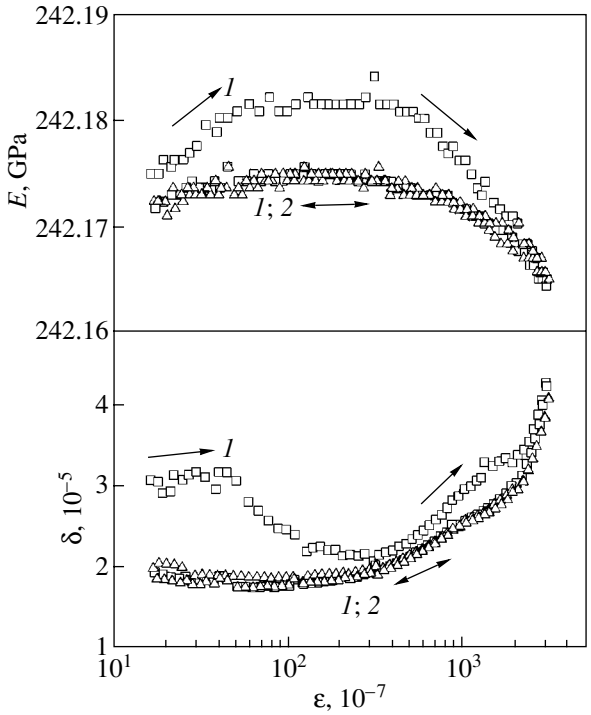

Fig. 4. Amplitude dependences of the Young modulus E and the decrement δ for the biomorphic SiC ceramic sample preliminarily subjected to large-amplitude strains at room temperature. The dependences were sequentially measured two times at approximately 1-min intervals under vacuum at $T = 116$ K: (*1*) first run and (*2*) second run. Arrows indicate the direction of change in the vibration strain amplitude ε.

and the Young modulus E passes through a very weak flattened maximum (most pronounced in the first run upon an increase in the amplitude ε) and gradually decreases with an increase in the strain amplitude.

A similar behavior of the dependences $E(\varepsilon)$ and $\delta(\varepsilon)$ [though more complex for the dependence $\delta(\varepsilon)$ in the first run] is observed at a temperature of 116 K (Fig. 4). In this case, the maximum in the curve $E(\varepsilon)$ obtained in the first run is more pronounced than that at room temperature (compare with Fig. 3). Furthermore, this maximum is also observed upon repeated measurements. On the other hand, the minimum in the dependence $\delta(\varepsilon)$ becomes very weak upon repeated measurements.

The temperature dependences of the Young modulus and the decrement in the temperature range 116–296 K under vacuum are plotted in Fig. 5. As can be seen from this figure, the elastic modulus gradually increases with a decrease in the temperature and the dependences measured upon cooling and heating of the sample coincide with a good accuracy. At the same time, the dependence of the decrement exhibits a weak broad maximum in the temperature range 230–280 K. Moreover, the curves $\delta(T)$ obtained upon cooling and heating do not coincide with each other. This is primarily associated with the effect of large-amplitude strains: it can be seen from the amplitude dependences measured at 116 K (Fig. 4) that the above effect leads to a decrease in the decrement by a factor of approximately 1.5.

The irreversible changes in the elastic modulus and the decrement of the initial sample placed in vacuum and after measuring the amplitude dependences can be explained by the desorption of air molecules (necessarily contained in the porous biomorphic SiC ceramic material). This desorption is substantially enhanced under large-amplitude strains. On the other hand, partial recovery of the original dependences $E(\varepsilon)$ and $\delta(\varepsilon)$ due to the storage of the sample in air for four weeks is associated with the adsorption of air molecules.

Undeniably, the presence of pores and residual carbon in the ceramic sample favors the adsorption of air molecules by the material. We can assume that, under particular external conditions, gas and water molecules can be desorbed from the sample. Actually, it was found that, immediately after placing the sample in the vacuum chamber when desorption becomes more intensive, the measured elastic modulus begins to increase and the decrement decreases continuously. A similar effect is observed under large-amplitude strains (Figs. 1, 2) in the course of the first run, but it is even more pronounced. The influence of adsorbed molecules (if not so strong)

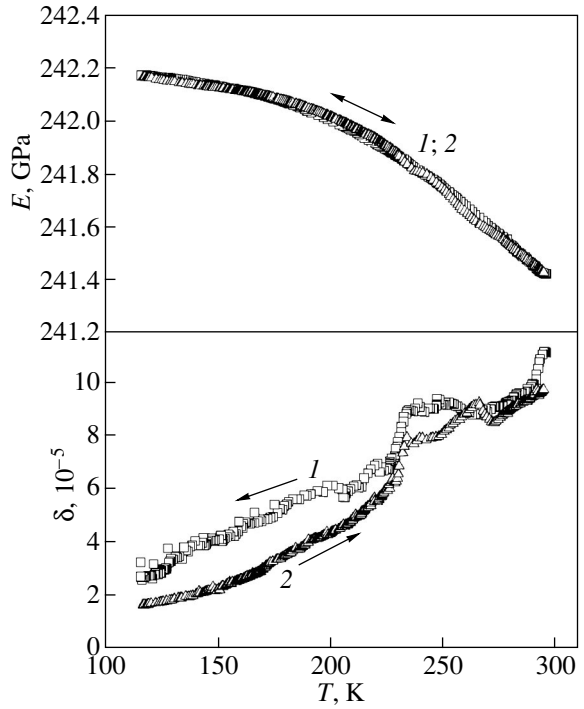

Fig. 5. Temperature dependences of the Young modulus E and the decrement δ upon (*1*) cooling and (*2*) heating of the biomorphic SiC ceramic sample preliminarily subjected to large-amplitude strains at room temperature. The dependences were measured under vacuum at $\varepsilon = 1.0 \times 10^{-6}$. Arrows indicate the direction of change in the temperature.

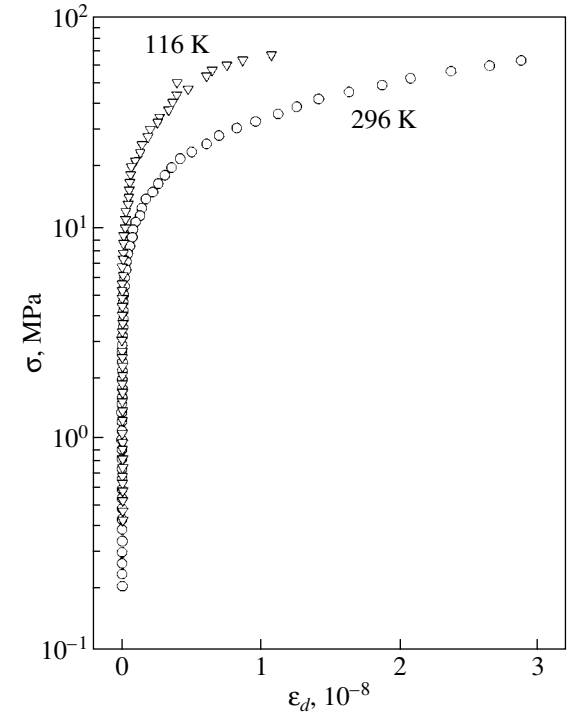

Fig. 6. Stress–microplastic strain curves constructed from the acoustical data for the biomorphic SiC ceramic sample at temperatures of 116 and 296 K.

also manifests itself in the repeated measurements (Figs. 1, 3) and at lower temperatures (Fig. 4). Most likely, the complex behavior of the dependence $\delta(\varepsilon)$ observed in the first run in Fig. 4 can be attributed to the presence of different gas molecules (entering into the air composition) in the sample.

The adsorption–desorption effect can be partially reversible. This can be judged from the reversible decrease in the decrement and the reversible increase in the Young modulus with an increase in the strain amplitude (at moderate amplitudes ε). The reversible effect for the decrement most clearly manifests itself in the dependences shown in Figs. 1 and 3 (curves *2*). The reversible increase in the elastic modulus with an increase in the strain amplitude is most pronounced at low temperatures (the initial portion in curve *2* in Fig. 4).

Moreover, adsorbed molecules affect the temperature dependences of the decrement (Fig. 5). The absorption maximum, which is observed in the temperature range of water solidification and whose shape is substantially changed under large-amplitude strains at 116 K, indicate that there is a mechanism of ultrasonic absorption due to the adsorption of molecules foreign to the given material (silicon carbide).

On the other hand, the response of the ceramic material to the external force field appears to be associated not only with the molecules of adsorbed gases and water. As was noted above, the decrease in the elastic modulus and the increase in the decrement with an increase in the strain amplitude in the range of large amplitudes (Figs. 1–4) are characteristic of many materials with a high plasticity [12]. This behavior of the parameters E and δ for the ceramic material under investigation suggests that the material contains structural units similar to mobile dislocations, which are responsible for the considerable microplastic strain in response to ultrasound in crystals. The microplastic properties of the SiC ecoceramic material at two temperatures are compared in Fig. 6. The procedure for constructing the stress σ–microplastic strain ε_d curves from the dependences $E(\varepsilon)$ was described in [14, 15]. In the present work, these curves for the SiC ecoceramic material were constructed using curves *2* shown in Figs. 3 and 4. It can be seen from Fig. 6 that a decrease in the temperature results in an increase in the elastic limit (by approximately two times). This is typical of many metals and also covalent and ionic crystals.

4. CONCLUSIONS

Thus, the above investigation demonstrated that the behavior of the biomorphic SiC ceramic material is governed by at least two mechanisms, which affect the elastic and inelastic properties of the material. The first mechanism involves the adsorption–desorption of environmental molecules (hypothetically, owing to the presence of pores and residual carbon). The second mechanism is associated with the microplastic defor-

mation due to the fact that the ceramic material contains dislocations or other (similar) structural units, which are able to execute vibrational motions in response to ultrasound and to contribute to both the ultrasonic absorption and the nonlinear inelastic deformation.

ACKNOWLEDGMENTS

This work was supported by the Russian Foundation for Basic Research (project no. 04-03-33183) and Ministerio de Ciencia y Technologia of Spain (project MAT 2003-05202-C02-01).

REFERENCES

1. T. Ota, M. Takahashi, M. Ozawa, and H. Suzuki, J. Am. Ceram. Soc. **78** (12), 3409 (1995).
2. D. Kovar, B. H. King, R. W. Trice, and J. W. Halloran, J. Am. Ceram. Soc. **80** (10), 2471 (1997).
3. R. Naslain, Adv. Compos. Mater. **8** (1), 3 (1999).
4. H. Sieber, C. Hoffmann, A. Kaindl, and P. Greil, Adv. Eng. Mater. **2** (3), 105 (2000).
5. M. Singh, Ceram. Eng. Sci. Proc. **21** (4), 39 (2000).
6. J. Martinez-Fernandez, F. Varela-Feria, and M. Singh, Scr. Mater. **43**, 813 (2000).
7. J. Martinez-Fernandez, F. Varela-Feria, S. Lopez Pombero, A. R. de Arellano-Lopez, and M. Singh, Ceram. Eng. Sci. Proc. **22** (3), 135 (2001).
8. F. M. Varela-Feria, J. Martinez-Fernandez, A. R. de Arellano-Lopez, and M. Singh, J. Eur. Ceram. Soc. **22**, 2719 (2002).
9. B. I. Smirnov, Yu. A. Burenkov, B. K. Kardashev, F. M. Varela-Feria, J. Martinez-Fernandez, and A. R. de Arellano-Lopez, Fiz. Tverd. Tela (St. Petersburg) **45** (3), 456 (2003) [Phys. Solid State **45**, 482 (2003)].
10. J. Martinez-Fernandez, A. Munoz, A. R. de Arellano-Lopez, F. M. Varela-Feria, A. Dominigues-Rodrigues, and M. Singh, Acta Mater. **51**, 3259 (2003).
11. A. R. de Arellano-Lopez, J. Martinez-Fernandez, P. Gonzalez, C. Dominiguez, V. Fernandez-Quero, and M. Singh, Int. J. Appl. Ceram. Technol. **1**, 95 (2004).
12. S. P. Nikanorov and B. K. Kardashev, *Elasticity and Dislocation Inelasticity of Crystals* (Nauka, Moscow, 1985) [in Russian].
13. B. K. Kardashev, B. I. Smirnov, D. Singh, R. C. Goretta, and A. R. de Arellano-Lopez, Fiz. Tverd. Tela (St. Petersburg) **45** (3), 451 (2003) [Phys. Solid State **45**, 477 (2003)].
14. V. M. Chernov, B. K. Kardashev, L. M. Krjukova, L. I. Mamaev, O. A. Plaksin, A. E. Rusanov, M. I. Solomin, V. A. Stepanov, S. N. Votinov, and L. P. Zavialsky, J. Nucl. Mater. **257**, 263 (1998).
15. B. I. Smirnov, Yu. A. Burenkov, B. K. Kardashev, D. Singh, K. C. Goretta, and A. R. de Arellano-Lopez, Fiz. Tverd. Tela (St. Petersburg) **43** (11), 2010 (2001) [Phys. Solid State **43**, 2094 (2001)].

Translated by O. Borovik-Romanova

Physics of the Solid State, Vol. 46, No. 10, 2004, pp. 1878–1883. Translated from Fizika Tverdogo Tela, Vol. 46, No. 10, 2004, pp. 1816–1820.

MAGNETISM AND FERROELECTRICITY

Inhomogeneous Magnetic States in the $Nd(Mn_{1-x}Cr_x)O_3$ System

I. O. Troyanchuk*, M. V. Bushinsky*, N. V. Pushkarev, and N. Yu. Bespalaya*****

**Institute of Solid-State and Semiconductor Physics, National Academy of Sciences of Belarus, ul. P. Brovki 17, Minsk, 220072 Belarus*

e-mail: bushinsky@ifttp.bas-net.by

***International State Ecological University, ul. Dolgobrodskaya 23, Minsk, 220009 Belarus*

****Belavtotraktorostroenie Republican R & D Enterprise, ul. Akademicheskaya 12, Minsk, 220072 Belarus*

Received January 29, 2004

Abstract—The crystal structure and magnetic properties of the $Nd(Mn_{1-x}Cr_x)O_3$ system ($x \le 0.85$) have been studied. Substitution of chromium for manganese was shown to induce a transition from the antiferromagnetic to ferromagnetic state ($x \approx 0.2$) and a decrease in the critical temperature followed, conversely, by an increase in the Néel temperature and decay of spontaneous magnetization. At low temperatures, the magnetization was found to behave anomalously as a result of magnetic interaction between the ferromagnetic and antiferromagnetic phases. The formation of the ferromagnetic phase is attributed to destruction of cooperative static orbital ordering, while the coexistence of different magnetic phases is most probably due to internal chemical inhomogeneity of the solid solutions. © *2004 MAIK "Nauka/Interperiodica".*

1. INTRODUCTION

$La_{1-x}Sr_xMnO_3$-type manganites serve as model objects in studying the relation between magnetic interactions, electron transport properties, and orbital and charge ordering. To date, the best studied of this type of manganites are $LaMnO_3$- and $PrMnO_3$-based systems in which the lanthanide ions are replaced by strontium and calcium. Such substitution drives the antiferromagnetic state to the ferromagnetic state, with the metal–insulator transition occurring in some compositions near the Curie point. In strongly doped compositions, charge ordering brings about carrier localization, with the ensuing antiferromagnetic interaction becoming again stabilized. There is, however, another scenario by which the manganite properties can undergo a radical transformation, namely, substitution of the manganese ions by other ions of a suitable size. For instance, substitution of chromium for manganese in the $La(Mn_{1-x}Cr_x)O_3$ system also gives rise to the appearance of a strongly pronounced ferromagnetic component, but it does not bring about the onset of metallic properties [1]. The system remains in the insulating state, although below T_C a noticeable magnetoresistive effect was observed [2, 3]. The change in the properties of charge-ordered manganites is the strongest under chromium doping. Small additions of chromium ions (2–4%) to $Pr_{0.5}Ca_{0.5}MnO_3$ culminate in complete destruction of the antiferromagnetic charge-ordered state and lead to the formation of the ferromagnetic metallic phase [4]. Note that the magnetic and electron transport properties of manganites also change dramatically under replacement by other 3*d* ions or diamagnetic ions of the type of Al^{3+}, Ga^{3+}, and Mg^{2+}, but the effect is the strongest in the case of chromium ions. Spectroscopic studies showed the chromium ions to reside in the trivalent state and interact antiferromagnetically with the manganese subsystem [5]. This behavior is not characteristic of double exchange–type interactions, which should be positive. High chromium concentrations ($x \sim 0.5$) in the $Nd_{0.6}Ca_{0.4}(Mn_{1-x}Cr_x)O_3$ system apparently result in ordering of the manganese and chromium ions, which strongly increases the Néel temperature T_N and affects the magnetic properties [6]. The origin of the strong effect of chromium ions on the magnetic properties of the manganites remains unclear; therefore, we undertook a study of the $Nd(Mn_{1-x}Cr_x)O_3$ system. Substitution of chromium for the manganese ions in this system formally does not change the trivalent state of the manganese. Neodymium ions have a considerably smaller radius than the ions of lanthanum, which gives rise to stronger distortions of the crystal structure and more pronounced carrier localization as compared to $LaMnO_3$-based systems.

2. EXPERIMENT

Samples of the $Nd(Mn_{1-x}Cr_x)O_3$ system were prepared by solid-phase reactions in air. Simple oxides Nd_2O_3, Mn_2O_3, and Cr_2O_3 were mixed in stoichiometric proportion, pelletized, and calcined at 1050°C. After this, the pellets were ground again and pressed. The final synthesis was performed at T = 1450°C in air for 6 h, followed by cooling to room temperature at a rate of 150°C per hour. X-ray phase analysis carried out on a DRON-3R diffractometer with CuK_α radiation did not reveal any foreign phases. Thermogravimetric analysis was performed by decomposing the samples into simple oxides Nd_2O_3, MnO, and Cr_2O_3. Magnetic measurements were run on a QI-3001 commercial vibrating-

Unit cell parameters of $Nd(Mn_{1-x}Cr_x)O_3$ compositions

x	0	0.08	0.11	0.2	0.3	0.4	0.5	0.6	0.7	0.85
a, Å	5.402	5.401	5.404	5.416	5.419	5.418	5.416	5.412	5.412	5.423
b, Å	5.790	5.671	5.682	5.653	5.608	5.552	5.529	5.508	5.496	5.503
c, Å	7.551	7.591	7.598	7.634	7.654	7.678	7.684	7.675	7.680	7.687

sample magnetometer in the temperature range 4.2–300 K. Electrical conductivity measurements were carried out by the conventional four-probe method. Indium contacts were applied ultrasonically. The unit cell parameters were Rietveld-refined using the FullProf program.

The elastic properties were studied by the resonance method in the sonic frequency range on 50-mm-long cylindrical samples 6 mm in diameter.

3. RESULTS AND DISCUSSION

Thermogravimetric analysis showed samples with a high manganese ion concentration ($x < 0.5$) to be nonstoichiometric. Their composition can be roughly represented by the chemical formula $Nd(Mn_{1-x}Cr_x)O_{3.02}$–$Nd(Mn_{1-x}Cr_x)O_{3.04}$, with the excess oxygen content decreasing as the content of chromium increases. It is known that off-stoichiometry in oxygen in the nonstoichiometric $LaMnO_{3+\lambda}$ is accounted for by the formation of lanthanum and manganese vacancies, with part of the manganese ions becoming quadrivalent [7]. The same mechanism is apparently realized in the $Nd(Mn_{1-x}Cr_x)O_{3+\lambda}$ system.

X-ray structural analysis showed all samples to have an orthorhombically distorted perovskite structure, with $NdMnO_3$ and similar compounds being characterized by the so-called O' orthorhombic structure ($c/\sqrt{2} < a \le b$), whereas chromium-enriched samples are O orthorhombic ($a < c/\sqrt{2} < b$).

The unit cell parameters of some relevant compounds are listed in the table.

It is common knowledge that O' orthorhombic cell distortions may be caused by cooperative orbital ordering [1]. Indeed, $NdMnO_3$ is an orbitally ordered antiferromagnet [8]. Orbital disordering in this compound is a first-order phase transition occurring in the temperature interval 1050–1100 K [9]. The trivalent chromium ions are not of the Jahn–Teller type; hence, their replacement by these ions should give rise to a gradual decrease in the temperature at which the orbital ordering occurs and, eventually, to its disappearance, because $NdCrO_3$ does not exhibit any indications of orbital ordering. One of the methods most sensitive to phase transformations is based on measurements of the elastic properties. This stimulated our study of the elastic properties of the $Nd(Mn_{0.92}Cr_{0.08})O_{3.04}$ sample in the range 300–750 K. The results of the study are shown in Fig. 1. The resonance frequency squared (which is proportional to the Young modulus) does not reveal strongly pronounced anomalies associated with cooperative phase transformations. However, the presence of a minimum strongly broadened in temperature is characteristic of structurally unstable and inhomogeneous compositions. It is well known that the Young modulus usually decreases with increasing temperature.

Electrical conductivity measurements revealed that all the compounds are semiconducting and do not exhibit strongly pronounced resistivity anomalies in the temperature interval 77–300 K.

Figure 2 depicts FC magnetization measurements (in the heating mode following field cooling) in weak fields. We readily see that the $NdMn_{1-x}Cr_xO_3$ compositions can be conventionally divided into three different concentration intervals.

In the first concentration interval ($0 \le x \le 0.11$), the Néel temperature decreases with increasing chromium concentration up to 60 K. The Néel point T_N of $NdMnO_3$ is known to be 87 K [10]. After this, the transition temperature starts to grow gradually, to reach 112 K in the $x = 0.5$ composition. As the chromium content continues to increase, the FC magnetization curves switch to a qualitatively different behavior. The falloff of magnetization with increasing temperature becomes smoother, although the break near the Néel point remains clearly pronounced. The anomalous behavior is most strongly manifest in the composition with $x = 0.85$. In this composition, the magnetization becomes negative with decreasing temperature, whereas near

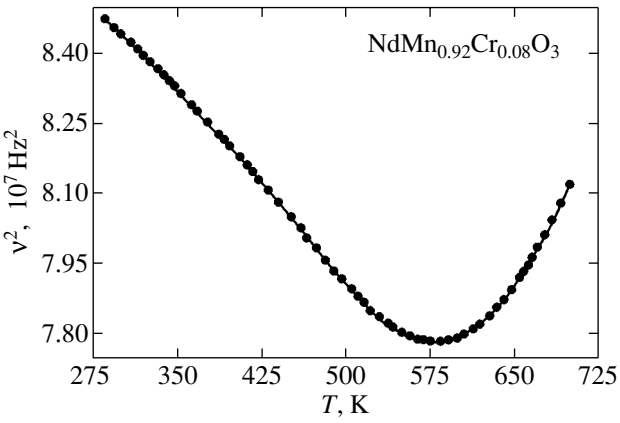

Fig. 1. Square of the resonance frequency plotted vs. temperature.

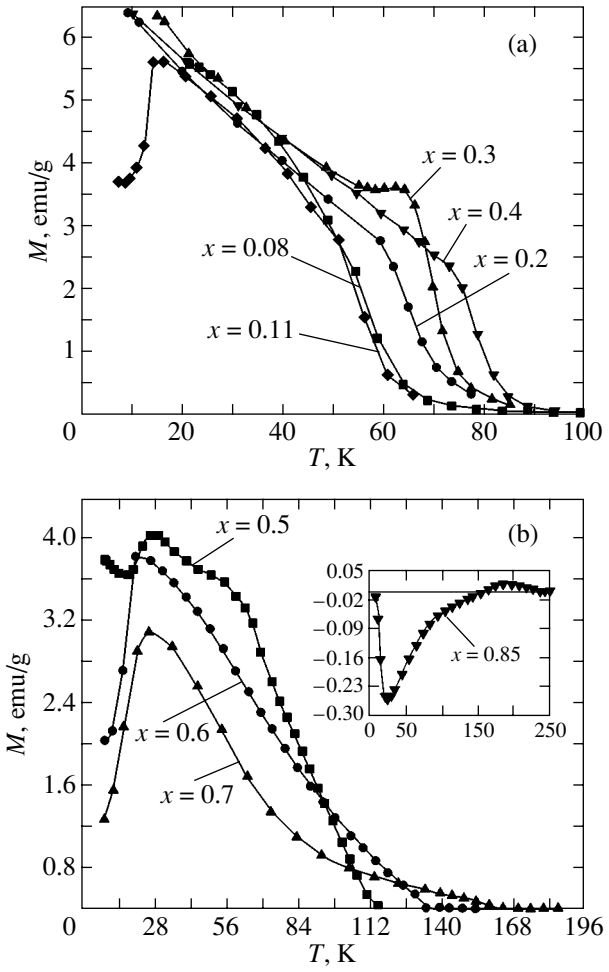

Fig. 2. FC magnetization of samples with (a) $0.08 \le x \le 0.4$ and (b) $0.5 \le x \le 0.85$.

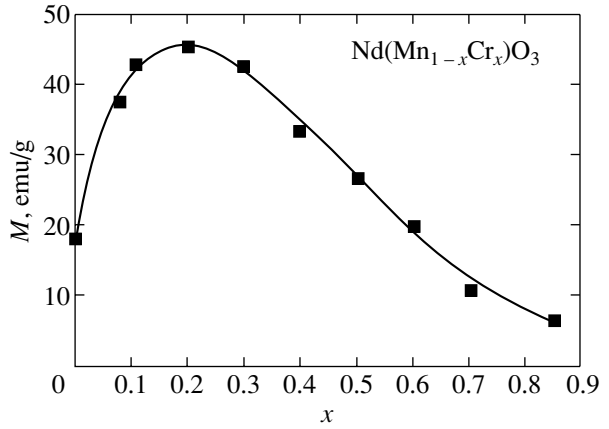

Fig. 3. Dependence of magnetization in a field $H = 14$ kOe on chromium ion concentration.

liquid-helium temperatures a sharp increase in the FC magnetization was seen to occur (Fig. 2). At low temperatures, the ZFC magnetization (measured in the heating mode following zero-field cooling) is far lower than the FC magnetization, but as the temperature is increased, the difference decreases, until the two types of magnetization measurement become practically equal in magnitude in the vicinity of the Néel point. A large difference between the FC and ZFC magnetizations was observed in strongly anisotropic cobaltites with a perovskite structure [11]. We believe that, by analogy with the cobaltites, the $Nd(Mn_{1-x}Cr_x)O_3$ system is magnetically stiff. This conclusion is supported by $\sigma(H)$ measurements performed at low temperatures. The magnetization does not saturate up to 16 kOe, the maximum field attainable with the setup employed. The coercive force of samples with high manganese contents reaches 5–7 kOe at liquid-helium temperature. As the manganese content increases, the magnetic anisotropy decreases but remains fairly large even in the $x = 0.85$ sample (Fig. 3). In this composition, even at a high temperature, an external magnetic field of 100 Oe is not high enough to reorient the magnetic moment directed against the field. Figure 3 plots the magnetization measured as a function of chromium concentration in a field of 14 kOe. Near the compositions $x = 0.2$ and 0.3, the magnetization reaches a maximum of about $2\mu_B$ per formula unit. Unfortunately, the relatively weak magnetic fields used in this study did not permit us to determine the spontaneous magnetic moment, which should definitely be larger than two Bohr magnetons per formula unit in the interval $0.1 \le x \le 0.3$.

At low temperatures, the $x = 0.08$ and 0.11 compositions exhibited strong anomalies in the ZFC and FC magnetization curves, a feature characteristic of a phase transformation (Fig. 4). At this phase transition, the FC magnetization drops sharply with decreasing temperature, whereas the ZFC magnetization passes through a maximum. This transition was studied in considerable detail in [12] and interpreted within a model according to which the system is made up of coexisting exchange-coupled antiferromagnetic and ferromagnetic phases. In the antiferromagnetic (or, more precisely, weakly ferromagnetic) phase, the manganese ion magnetic moments are oriented antiparallel to the weak ferromagnetism vector, whereas in the ferromagnetic phase they have parallel orientation. At low temperatures, the magnetic moments of neodymium ions in the antiferromagnetic phase undergo reorientation because of interaction with the ferromagnetic phase. Magnetic anisotropy precludes the sample moment from aligning with a weak external magnetic field.

We believe that this two-phase model can adequately interpret the magnetic properties of the system in the chromium doping region up to $x = 0.11$. Chromium doping gives rise to the formation of ferromagnetic clusters, thus lowering the Néel point. The $x = 0.08$ and 0.11 compositions consist apparently of interpenetrating antiferromagnetic and ferromagnetic phases. At concentrations of about $0.2 \le x \le 0.3$, the ferromagnetic component largely dominates over the antiferromagnetic phase (which is apparently made up of small clusters) and the FC magnetization does not

exhibit any anomalous behavior at low temperatures. A similar behavior of the magnetization was observed in the $Nd_{1-x}Ca_xMnO_3$ system doped by quadrivalent manganese ions [12].

A question may arise as to what is responsible for the formation of the ferromagnetic phase. Substitution of chromium for the manganese ions does not change the charge state of the 3*d* ions, the electrical conductivity does not grow, and therefore double exchange cannot account for the formation of the ferromagnetic phase. The origin of the ferromagnetic phase is most probably associated with destruction of the static cooperative d_{z^2} ordering characteristic of the $AMnO_3$ manganites. This type of orbital ordering results in an *A*-type antiferromagnetic structure. According to Goodenough [1], an orbitally disordered phase should be characterized by ferromagnetic coupling between the Mn^{3+} ions. Indeed, Cr^{3+} ions are not of Jahn–Teller type, so substitution of Cr^{3+} for the Mn^{3+} ions should bring about the removal of orbital ordering. The anomaly seen in the temperature dependence of the Young modulus (Fig. 1) originates apparently from the system residing in an inhomogeneous structural state, with the fraction of the orbitally ordered phase being small. As the temperature is increased, microregions of the orbitally ordered phase become gradually disordered.

We believe therefore that, in the concentration region $x \leq 0.3$, the system is in a magnetically and structurally mixed state. The antiferromagnetic and ferromagnetic phases differ in terms of orbital dynamics and the extent of local distortions. The orbital dynamics in the ferromagnetic phase is much faster, and the distortions of the MnO_6 octahedra are smaller. Note that the antiferromagnet–ferromagnet transition was observed earlier in systems with manganese ions substituted for by Ga [1], Sc, and Nb [13]. In all these cases, the transition was accompanied by total or partial removal of cooperative static Jahn–Teller distortions.

As the chromium concentration rises to $x = 0.3$, the Néel temperature increases, whereas the spontaneous magnetization falls off. In our opinion, this falloff is caused by two factors. One of them is that the magnetic moments of trivalent chromium ions are oriented, according to [5], antiparallel to those of the manganese ions in the ferromagnetic phase, thus reducing the net magnetic moment of this phase. The second factor is apparently associated with the formation of clusters in which the chromium content is close to or dominates over that of the manganese. It is well known that $NdCrO_3$ is a weak ferromagnet with a Néel temperature of about 240 K [14], which far exceeds T_N of $NdMnO_3$. In the phase with a chromium-to-manganese content ratio that is close to unity, the manganese and chromium ions apparently become arranged in short-range order. This ordering is, however, only partial because of the Cr^{3+} and Mn^{3+} ions having similar radii and the same oxidation states. Apparently, in the $La(Mn_{1-x}Me_x)O_3$ systems (*Me* = Ga, Cr, Co, Fe), the *Me* and manganese ions are

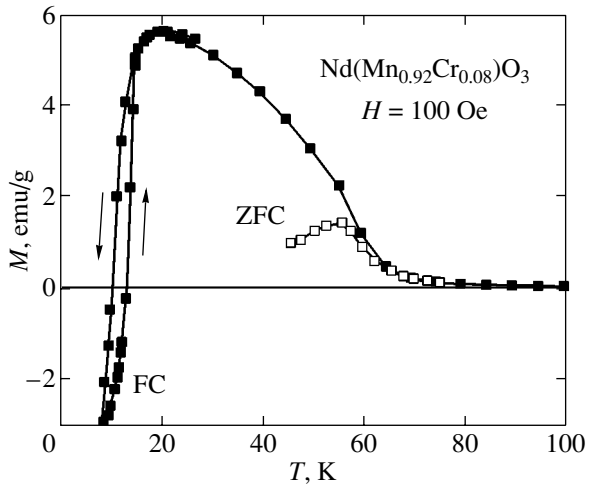

Fig. 4. ZFC and FC magnetizations of a $Nd(Mn_{0.92}Cr_{0.08})O_3$ sample. Arrows indicate the direction of temperature variation.

also prone to ordering [1]. The magnetic moments of manganese ions in a partially ordered phase are directed opposite to those of the chromium ions. At low temperatures, the compositions with $0.3 \leq x \leq 0.7$ exhibited a sharp decrease in magnetization. This phenomenon is most likely due to neodymium ion reorientation as a result of the coexistence of exchange-coupled phases differing in the sign of the *f–d* exchange interaction; more specifically, the *f–d* exchange is positive in the ferromagnetic phase disordered in the chromium and manganese ion positions, whereas the *f–d* exchange is negative in the partially ordered phase. The mechanism of this phenomenon rests on the same factors as in weakly doped compositions $Nd_{1-x}Ca_xMnO_3$ [12] and $Nd(Mn_{0.9}Me_{0.1})O_3$ (*Me* = Fe, Mg, Al, Cr) [15].

The behavior of the magnetization of the $Nd(Mn_{0.15}Cr_{0.85})O_3$ composition is radically different (Fig. 2), which is indicative of a change in the ground magnetic state. We believe that this sample consists predominantly of the phase in which the manganese and chromium ions are distributed at random and of a small amount of a phase with partially ordered manganese and chromium ions. The different decrease in magnetization observed to occur with decreasing temperature ($T \sim 150$ K) can be explained in terms of the model of two sublattices, on one of which ordering occurs within a broad temperature interval because of the magnetic interactions being weak. Such a "weak" sublattice could be that of neodymium ions. In ferro- and ferrimagnetic phases, the contribution of the neodymium sublattice to magnetization at high temperatures is not very strong because of the high magnetic moment of the manganese sublattice; however, in the weak ferromagnet $NdMnO_3$, this contribution becomes noticeable even in the immediate vicinity of the Néel point [15]. $NdCrO_3$ is likewise a weak ferromagnet, and $Nd(Mn_{1-x}Cr_x)O_3$ solid solutions with a low manganese

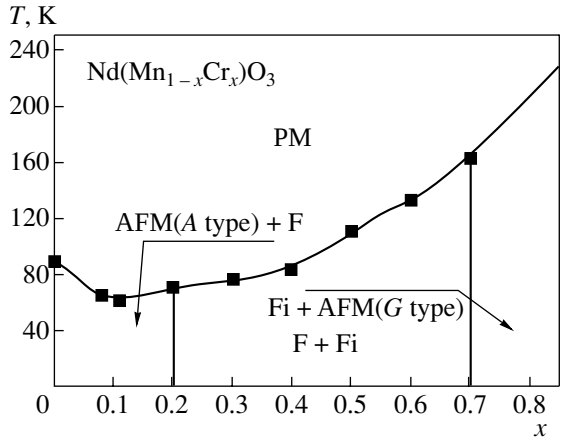

Fig. 5. Magnetic phase diagram of the $Nd(Mn_{1-x}Cr_x)O_3$ system. Notation: PM stands for the paramagnetic phase, AFM is antiferromagnetic, F is ferromagnetic, and Fi is ferrimagnetic.

content, $x = 0.85$, apparently also preserve the *G*-type antiferromagnetic structure characteristic of $NdCrO_3$. At low temperatures, the magnetic moment of $Nd(Mn_{0.15}Cr_{0.85})O_3$ becomes capable of aligning with an external magnetic field. This phenomenon can be understood in terms of the homogeneous model. As the temperature is lowered, the magnetic anisotropy and the magnetic moment of the neodymium sublattice increase. However, the magnetic moment of neodymium increases faster than the anisotropy does and a weak magnetic field of 100 Oe is sufficient to reorient the magnetic moment of the sample.

Figure 5 shows a hypothetical magnetic phase diagram of the $Nd(Mn_{1-x}Cr_x)O_3$ system, in which four types of magnetic states are realized (*A*-type antiferromagnetic structure characteristic of orbitally ordered $NdMnO_3$, orbitally disordered ferromagnetic phase, phase with partial manganese and chromium ordering, and *G*-type antiferromagnetic phase typical of $NdCrO_3$). The concentration-driven magnetic phase transformations in manganites are treated within different models, namely, electronic phase separation [16], structural inhomogeneity [17], and magnetic moment noncollinearity [18]. It was shown in [19], however, that the manganites are chemically inhomogeneous objects and consist of nanoclusters differing in chemical composition and in structural distortion. Because the manganese and chromium ions in the $Nd(Mn_{1-x}Cr_x)O_3$ system have the same valence, we believe that chemical inhomogeneity initiates structural and magnetic inhomogeneity. The transition from one type of magnetic phase to another occurs through the realization of a magnetically mixed state because of the solid solutions being inherently inhomogeneous.

4. CONCLUSIONS

A study has been carried out of the crystal structure and elastic and magnetic properties of $Nd(Mn_{1-x}Cr_x)O_3$ perovskite solid solutions. The crystal structure study showed these compounds to be structurally single-phase with an orthorhombically distorted unit cell. Lightly doped compositions are in a completely or partially orbitally ordered state. Lifting of orbital ordering drives a transition from the antiferromagnetic to inhomogeneously ferromagnetic state. The low-temperature anomalies in the magnetic properties were accounted for as being due to magnetic interaction between the exchange-coupled antiferromagnetic and ferromagnetic phases. It is assumed that a phase with short-range order in the manganese and chromium ion arrangement appears in the concentration interval $0.3 \le x \le 0.7$. Microdomains of this phase coexist with those of the ferromagnetic phase. The magnetic moments of chromium ions are oriented antiparallel to those of the manganese ions. The $x = 0.85$ composition undergoes antiferromagnetic ordering similar to the *G*-type antiferromagnetic structure of $NdCrO_3$. The concentration-driven phase transformations occur through the realization of a mixed magnetic state because of the solid solutions being inherently inhomogeneous.

ACKNOWLEDGMENTS

This study was supported by the Belarus Foundation for Basic Research (project no. F03-191) and the state foundation program “Nanomaterials and Nanotechnologies.”

REFERENCES

1. J. B. Goodenough, A. Wold, R. J. Arnott, and N. Menyuk, Phys. Rev. **124**, 373 (1961).
2. Y. Sun, W. Tong, X. Xu, and Y. Zhang, Phys. Rev. B **63**, 174438 (2001).
3. R. Gundakaram, A. Arulraj, P. V. Vanitha, C. N. R. Rao, N. Gayathri, A. K. Raychaudhuri, and A. K. Cheetham, J. Solid State Chem. **127**, 354 (1996).
4. L. Pi, S. Hébert, C. Yaicle, C. Martin, A. Maignan, and B. Raveau, J. Phys.: Condens. Matter **15**, 2701 (2003).
5. O. Toulemonde, F. Studera, A. Barnabé, A. Maignan, C. Martin, and B. Raveau, Eur. Phys. J. B **4**, 159 (1998).
6. I. O. Troyanchuk, M. V. Bushinskiĭ, V. V. Eremenko, V. A. Sirenko, and G. Shimchak, Fiz. Nizk. Temp. **28**, 61 (2002) [Low Temp. Phys. **28**, 45 (2002)].
7. J. A. M. van Roosmalen and E. H. P. Cordfunke, J. Solid State Chem. **110**, 109 (1994).
8. A. Muñoz, J. A. Alonso, M. J. Martínez-Lope, J. L. García-Muñoz, and M. T. Fernández-Díaz, J. Phys.: Condens. Matter **12**, 1361 (2000).
9. N. V. Kasper and I. O. Troyanchuk, J. Phys. Chem. Solids **56**, 1601 (1996).
10. I. O. Troyanchuk, D. D. Khalyavin, S. V. Trukhanov, and H. Szymczak, J. Phys.: Condens. Matter **11**, 8707 (1999).

11. R. Ganguly, A. Maignan, C. Martin, M. Hervieu, and B. Raveau, J. Phys.: Condens. Matter **14**, 8595 (2002).
12. I. O. Troyanchuk, V. A. Khomchenko, H. Szymczak, and M. Baran, JETP **97** (6), 1231 (2003).
13. I. O. Troyanchuk, M. V. Bushinsky, H. Szymczak, K. Bärner, and A. Maignan, Eur. Phys. J. B **28**, 75 (2002).
14. J. B. Goodenough and J. M. Longo, in *Landolt-Boernstein. Numerical Data and Functional Relationships in Science and Technology. New Series*, Ed. by K. H. Hellwege (Springer, New York, 1971), Group 3, Vol. 4, p. 228.
15. I. O. Troyanchuk, J. Magn. Magn. Mater. **231**, 53 (2001).
16. É. L. Nagaev, Usp. Fiz. Nauk **166**, 833 (1996) [Phys. Usp. **39**, 781 (1996)].
17. S. Autret, A. Maignan, C. Martin, M. Hervieu, V. Hardy, S. Hébert, and B. Raveau, Appl. Phys. Lett. **82**, 4746 (2003).
18. P. G. de Gennes, Phys. Rev. **118**, 141 (1960).
19. T. Shibata, B. Bunker, J. F. Mitchell, and P. Schiffer, Phys. Rev. Lett. **88**, 207205 (2002).

Translated by G. Skrebtsov

Physics of the Solid State, Vol. 46, No. 10, 2004, pp. 1884–1890. Translated from Fizika Tverdogo Tela, Vol. 46, No. 10, 2004, pp. 1821–1827.

MAGNETISM AND FERROELECTRICITY

Phase Separation Induced by Oxygen Isotope Substitution in Manganites of the $Sm_{1-x}Sr_xMnO_3$ System

N. A. Babushkina*, E. A. Chistotina*, O. Yu. Gorbenko, A. R. Kaul**, K. I. Kugel***, A. I. Kurbakov****, V. A. Trunov****, and J. André*******

**Russian Research Centre Kurchatov Institute, pl. Kurchatova 1, Moscow, 123182 Russia*

***Moscow State University, Vorob'evy gory, Moscow, 119899 Russia*

****Institute of Theoretical and Applied Electrodynamics, Russian Academy of Sciences, Izhorskaya ul. 13/19, Moscow, 127412 Russia*

*****Konstantinov St. Petersburg Nuclear Physics Institute, Russian Academy of Sciences, Gatchina, Leningrad oblast, 188350 Russia*

e-mail: KURBAKOV@pnpi.spb.ru

******Laboratoire Leon Brillouin, Saclay, Gif-sur-Ivette, 91191 France*

Received February 3, 2004

Abstract—The effect of $^{16}O \longrightarrow {}^{18}O$ isotope substitution on the electrical and magnetic properties of the manganite system $Sm_{1-x}Sr_xMnO_3$ has been studied. It is shown that oxygen isotope substitution brings about a substantial change in the phase diagram in the intermediate region $0.4 < x < 0.6$ between the ferromagnetic metal and antiferromagnetic insulator regions and induces phase separation and transformation of the ground metallic into insulating state for $x = 0.475$ and 0.5. The specific features of the metal–insulator transitions in the Sm–Sr system and the nature of the low-temperature phase are discussed. © *2004 MAIK "Nauka/Interperiodica".*

1. INTRODUCTION

Recent theoretical and experimental studies [1, 2] have revealed that the tendency toward phase separation and the formation of inhomogeneous states, which usually include ferromagnetic (FM) and antiferromagnetic (AFM) regions, should be taken into account in describing the properties of manganites within a broad range of temperatures and magnetic fields. We used the $^{16}O \longrightarrow {}^{18}O$ isotope substitution as a unique tool to probe the various features of phase separation in manganites and as a specific method to transform the ground state.

It was shown in [3, 4] that the isotope effect becomes particularly strongly manifest in the vicinity of magnetic phase transformations. It was also found in [4, 5] that the $^{16}O \longrightarrow {}^{18}O$ isotope substitution in manganites of the $(La_{1-y}Pr_y)_{0.7}Ca_{0.3}MnO_3$ system with a critical value $y = 0.75$ drives the metal–insulator transition (the giant isotope effect). The variation of electrical properties correlates closely with that of the magnetic characteristics revealed in neutron diffraction measurements [6].

Naturally, it appeared of interest to study the effect of oxygen isotope substitution near another critical point in the phase diagram of manganites, $x = 0.5$, where the region of hole doping crosses over to that of electron doping, with a charge-ordered state setting in for many manganites. We studied the $Sm_{1-x}Sr_xMnO_3$ system, which is characterized by a fairly complex phase diagram [7] that is particularly intricate at Sm–Sr substitution concentrations of $0.4 < x < 0.6$; these compositions are intermediate between those of a ferromagnetic metal and an antiferromagnetic insulator. A significant feature of the $Sm_{1-x}Sr_xMnO_3$ system is the large disorder factor σ^2 of the cations occupying the A positions in the ABO_3 perovskite structure ($\sigma^2 = \overline{r_A^2} - \bar{r}_A^2$); this disorder apparently fosters suppression of the ferromagnetism (the values of the Curie temperature T_C are fairly low) and, possibly, affects the charge-ordering state [8]. X-ray, neutron, and electron diffraction measurements suggest that charge ordering in the $Sm_{1-x}Sr_xMnO_3$ system is of a local character and has no long-range order. This conclusion is supported by NMR [9] and Raman spectroscopy [10] data. A study of the magnetic structure [11, 12] of the $^{154}Sm_{0.6}Sr_{0.4}MnO_3$ system by powder neutron diffraction, combined with measurements of the second harmonic of magnetization and small-angle polarized-neutron scattering, showed that the magnetic contribution to diffraction for $T < 180$ K can be interpreted as implying coexistence of the FM and AFM phases. Of particular interest are compositions with x between 0.4 and 0.5. It was found in [13] that the composition with $x = 0.45$ differs substantially in terms of the character of magnetic ordering from that with $x = 0.4$. Neutron diffraction measurements performed on $^{152}Sm_{0.55}Sr_{0.45}MnO_3$ suggest the onset of only ferro-

magnetic ordering in the temperature interval $T <$ 130 K. Moreover, cooperative Jahn–Teller distortions are markedly suppressed near the phase transition [14]. It was pointed out in [15] that the magnetoresistance in $Sm_{1-x}Sr_xMnO_3$ reaches a maximum at $x = 0.45$. This composition also exhibits a number of other remarkable features not seen at $x = 0.4$ and 0.5. A jump in the electrical resistivity [16], a sharp change in the volume expansion and volume magnetostriction coefficients near the Curie temperature [17], and some features in the temperature dependence of the heat capacity were observed [18]. The decrease in Jahn–Teller structural distortions, the abrupt change in volume expansion, and the heat capacity features indicate a substantial redistribution in the phonon spectrum near T_C. The isotope effect observed under oxygen substitution suggests that a large part is played by the phonon degrees of freedom in the variation of the magnetic characteristics of $Sm_{1-x}Sr_xMnO_3$ in the vicinity of the metal–insulator phase transition.

The high sensitivity of all physical characteristics to small deviations in composition and the still inadequate information on the properties of the $Sm_{1-x}Sr_xMnO_3$ manganites in the intermediate region of the phase diagram encouraged investigation of neighboring compositions ($x = 0.425$, 0.450, 0.475, 0.500, 0.525), which is reported in the present communication. We followed the evolution of the $Sm_{1-x}Sr_xMnO_3$ phase diagram in the above composition range under oxygen isotope substitution.

2. EXPERIMENTAL RESULTS

2.1. Samples and Measurement Techniques

The technology for preparing samples of $Sm_{1-x}Sr_xMnO_3$ is described in [17]. The process used to enrich samples with the ^{18}O isotope is similar to that described in [4, 5]. We measured the dc electrical resistivity by a standard four-probe method in the temperature interval from 4.2 to 280 K in dc magnetic fields ranging from 0 to 4 T. Samples were 7-mm-long, 1×1-mm parallelepipeds. The current and the magnetic field were directed along the long side of the sample. Measurements of the magnetic susceptibility $\chi_{ac}(T)$ were carried out in an ac magnetic field at a frequency of 667 Hz and with an amplitude of about 0.4 Oe.

Neutron experiments were performed at Laboratoire Leon Brillouin (Saclay, France) on a G4.1 high-intensity diffractometer ($\lambda = 2.4266$ Å, $12° \le 2\theta \le 92°$) and were aimed at determining the temperature evolution of the crystal and magnetic structures. Using the ^{152}Sm isotope made it possible to substantially reduce neutron absorption by samarium and to increase the diffraction contrast because of the negative amplitude of coherent scattering by ^{152}Sm ($b = -0.5 \times 10^{-12}$ cm). The samples to be studied were placed in a cylindrical vanadium container 2 mm in diameter. The container with the sample was fixed in a cryostat designed for neutron measurements. The samples were cooled to 1.4 K, and diffraction patterns were taken in the heating mode at $T = 1.4$, 15, 30, 45, 60, 100, 150, 200, and 300 K for the $^{152}Sm_{0.55}Sr_{0.45}Mn^{16}O_3$ sample; at $T = 1.4$, 15, 30, 45, 60, 75, 90, 120, and 300 K for the $^{152}Sm_{0.55}Sr_{0.45}Mn^{18}O_3$ sample; at $T = 1.4$, 45, 70, 80, 90, 105, and 120 K for the $^{152}Sm_{0.5}Sr_{0.5}Mn^{16}O_3$ sample; and at $T = 1.4$, 45, 70, 80, 90, 105, 150, and 185 K for the $^{152}Sm_{0.5}Sr_{0.5}Mn^{18}O_3$ sample. These measurement modes were chosen because of the specific features in the temperature behavior of the $\chi_{ac}(T)$ curves.

2.2. Isotope Substitution Effect in the $Sm_{1-x}Sr_xMnO_3$ System

We are going to discuss now the data obtained on the effect of the $^{16}O \longrightarrow {}^{18}O$ isotope substitution on the properties of the $Sm_{1-x}Sr_xMnO_3$ system with different Sr contents ($x = 0.425$, 0.450, 0.475, 0.500, 0.525) in the transition region between the ferromagnetic metal (FMM) and antiferromagnetic insulator (AFMI). In this system, we observed the metal–insulator transition induced by the $^{16}O \longrightarrow {}^{18}O$ substitution near the boundary between the transition region and the AFMI region (a similar transition was earlier detected at the FMM–AFMI boundary in $(LaPr)CaMnO_3$ [4, 5]).

Figure 1 plots the temperature dependences of electrical resistivity for all samples annealed in ^{16}O and ^{18}O that were measured. It was found that the samples annealed in ^{16}O transferred to the metallic state with a decrease in temperature for all concentrations, with the exception of $x = 0.525$. The samples annealed in ^{18}O remained metallic for two compositions only ($x =$ 0.425, 0.450); the others become insulators. Hence, the samples with $x = 0.475$ and 0.500 undergo a crossover from the metallic to insulating state at low temperatures when subjected to oxygen isotope substitution (see inset to Fig. 1a). A relatively weak external magnetic field ($H = 1$ T) transfers the samples with ^{18}O back to the metallic state (see inset to Fig. 1b).

As is evident from these data, the $^{16}O \longrightarrow {}^{18}O$ isotope substitution shifted the T_{MI} temperature corresponding to the maximum of electrical resistivity at the crossover to the metallic state to low temperatures, with an attendant considerable increase in temperature hysteresis. The electrical resistivity at the T_{MI} point increased by approximately 30 times as compared to the $Sm_{0.55}Sr_{0.45}Mn^{16}O_3$ sample.

As the external magnetic field is increased, the maximum in ρ at T_{MI} decreases and shifts toward higher temperatures and the temperature hysteresis becomes smaller. The values of T_{MI} for samples with ^{18}O depend on the magnetic field more strongly than those of samples with ^{16}O. As the magnetic field is increased, the quantity $\Delta T_{MI} = T_{MI}(^{16}O) - T_{MI}(^{18}O)$ decreases. The

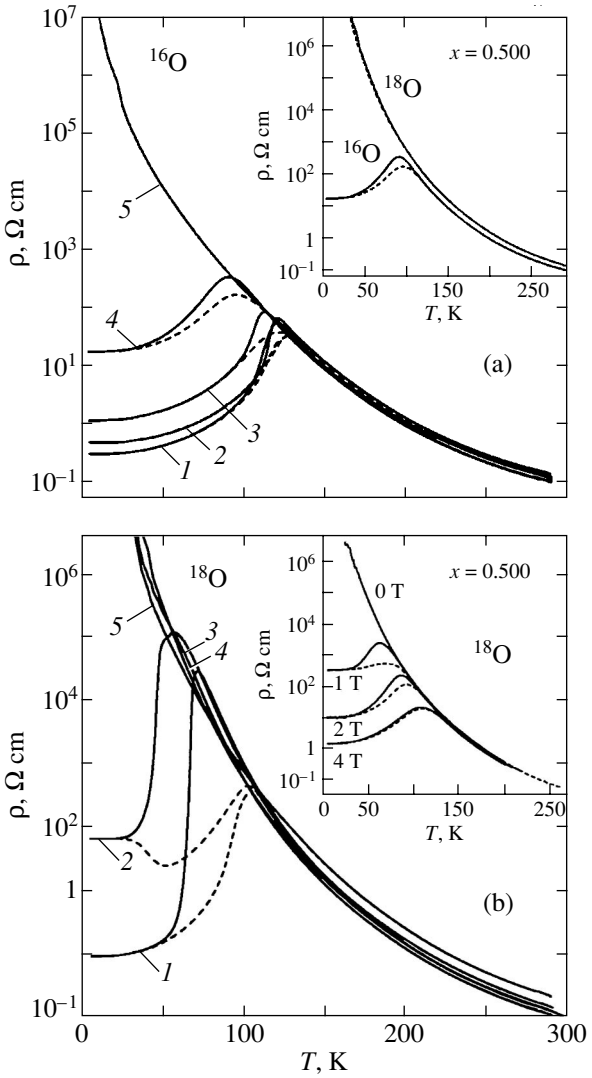

Fig. 1. Temperature dependences of the electrical resistivity of $Sm_{1-x}Sr_xMnO_3$ samples with (*1*) x = 0.425, (*2*) 0.450, (*3*) 0.475, (*4*) 0.500, and (*5*) 0.525 annealed in (a) ^{16}O and (b) ^{18}O. Insets: (a) metal–insulator transition at x = 0.500 induced by the ^{16}O ⟶ ^{18}O substitution and (b) variation of ρ(T) with increasing magnetic field for the ^{18}O sample (x = 0.500). The solid and dashed lines refer to the cooling and heating modes, respectively.

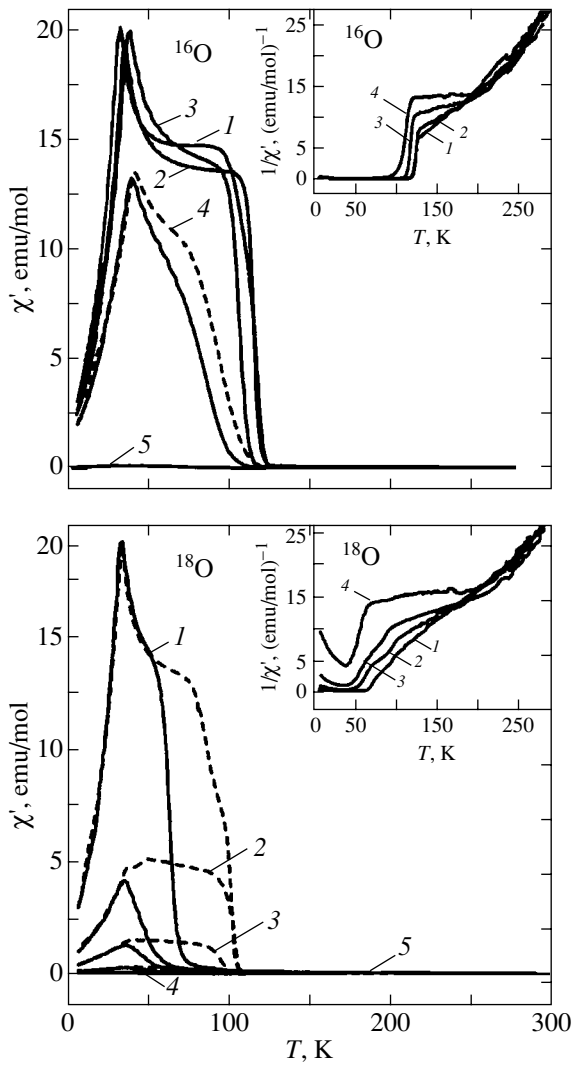

Fig. 2. Temperature dependences of the magnetic susceptibility of $Sm_{1-x}Sr_xMnO_3$ samples with (*1*) x = 0.425, (*2*) 0.450, (*3*) 0.475, (*4*) 0.500, and (*5*) 0.525 annealed in (a) ^{16}O and (b) ^{18}O. Insets show the temperature dependence of inverse susceptibility. The solid and dashed lines refer to the cooling and heating modes, respectively.

magnetoresistance MR = Δρ/ρ(H) near T_{MI}, which is governed by suppression of ρ by the magnetic field, depends on the isotopic enrichment. In samples with ^{16}O, we have MR ≈ 40, and in samples with ^{18}O, the maximum value of MR is shifted to lower temperatures and reaches a colossal value of ≈10^3.

An analysis of ρ(T) reveals thermally activated behavior above T_C. In the paramagnetic region, the resistivity can be described in terms of the model of small polarons in the adiabatic regime [19]:

$$\rho(T) = AT\exp(W_P/kT),$$

where W_P is the small-polaron energy. The values of W_P and of the prefactor A were determined using the relation connecting ρ/T with 1/T. It was found that, as the oxygen atomic mass increases to that of ^{18}O, W_P grows and A decreases, which correlates qualitatively with studies [20, 21] on the isotope effects in other manganites. It follows that the introduction of a heavier oxygen isotope brings about a polaron-induced narrowing of the conduction band.

Figures 2a and 2b present the temperature dependences of magnetic susceptibility of samples annealed in ^{16}O and ^{18}O, respectively. These dependences, plotted for samples with ^{16}O and x = 0.425, 0.450, and 0.475, are similar in terms of both the value of χ and T_C.

Obviously enough, all these samples exhibit homogeneous FM ordering at low temperatures.

The crossover to the FM state in samples with ^{16}O is sharper and occurs at a higher temperature, which correlates well with the electrical resistivity data. The Curie temperature shift ΔT_C is the same for ^{16}O and ^{18}O ($\approx$40 K), as is the shift ΔT_{MI} derived from the $\rho(T)$ relation. In samples with ^{18}O and compositions $x \geq 0.450$, the values of χ are substantially smaller than those for samples with ^{16}O and T_C also decreases. The susceptibility of samples with ^{18}O exhibits a noticeably increased temperature hysteresis as compared to that for the composition with ^{16}O (i.e., the behavior of the susceptibility is identical to that of $\rho(T)$ for samples with ^{18}O).

For all samples, the function $\chi_{ac}(T)$ exhibits a sharp maximum at $T \approx 40$ K. The decrease in susceptibility after 40 K originates from the increasing stiffness of the ferromagnetic domain structure [22]. Note also that all measurements were conducted on several samples. The pattern of the magnetic susceptibility behavior and the characteristic temperatures were the same for the samples with ^{18}O.

For $x = 0.500$, the value of χ decreases sharply and T_C shifts toward lower temperatures, thus indicating a decrease in the FM phase volume. In the $x = 0.525$ composition, the susceptibility becomes very small and FM ordering disappears completely. Thus, the measurements of the magnetic susceptibility in samples with ^{18}O showed that, as the Sr concentration increases, the volume of the FM phase decreases strongly and becomes insufficient for cluster-based percolation and the samples transfer to the insulating state [at $x = 0.475$ and 0.500, according to the $\rho(T)$ data]. Thus, the $^{16}O \longrightarrow {}^{18}O$ isotope substitution in the $Sm_{1-x}Sr_xMnO_3$ system substantially changes the phase diagram near the boundaries of the FM metallic phase, in the intermediate region ($0.4 < x < 0.6$), and in the AFM insulating state.

2.3. Discussion of Neutron Diffraction Data

Neutron diffraction studies performed on samples of $^{152}Sm_{0.5}Sr_{0.5}Mn^{16}O_3$, $^{152}Sm_{0.5}Sr_{0.5}Mn^{18}O_3$ (Fig. 3), $^{152}Sm_{0.55}Sr_{0.45}Mn^{16}O_3$, and $^{152}Sm_{0.55}Sr_{0.45}Mn^{18}O_3$ (Fig. 4) revealed good agreement with the above measurements of the temperature dependences of electrical resistivity and magnetic susceptibility. Moreover, these studies unambiguously identified the types of magnetic ordering and their evolution with temperature. (Neutron diffractograms were refined by the Rietveld procedure using the FULLPROF code.) As seen, for instance, from the neutron diffraction patterns shown in Fig. 3, the ground magnetic state for the $^{152}Sm_{0.5}Sr_{0.5}Mn^{16}O_3$ sample is a mixture of the FM and *A*-type AFM phases, with the FM phase being dominant. The FM moment

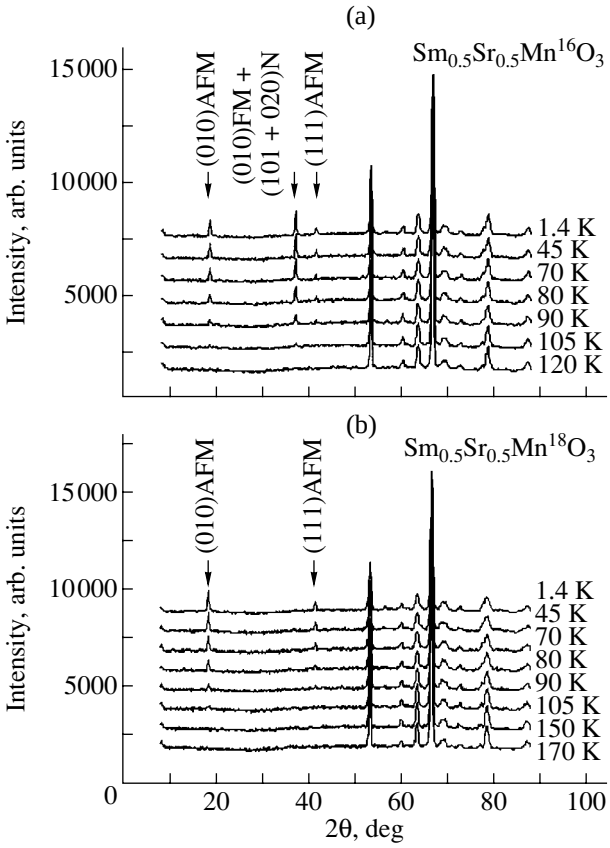

Fig. 3. Experimental powder neutron diffractograms measured on samples of (a) $^{152}Sm_{0.5}Sr_{0.5}Mn^{16}O_3$ and (b) $^{152}Sm_{0.5}Sr_{0.5}Mn^{18}O_3$ at different temperatures in heating runs. Arrows identify the strongest magnetic reflections.

calculated from a Rietveld-refined neutron diffractogram measured at 1.4 K was found to be $m_F = 2.13(7)$ μ_B/Mn, whereas the AFM moment was $m_{AF} = 1.04(4)$ μ_B/Mn. The ground state for the $^{152}Sm_{0.5}Sr_{0.5}Mn^{18}O_3$ sample is purely of the antiferromagnetic *A* type, with the AFM moment $m_{AF} = 1.84(5)$ μ_B/Mn at $T = 1.4$ K. The samples also differ in terms of the temperature of magnetic ordering. Significantly, the magnetic moments obtained are small. Their magnitudes, as well as the pattern of their temperature behavior (the absence of a plateau at low temperatures), indicate that complete magnetic ordering is not attained even at $T = 1.4$ K.

The neutron powder diffraction patterns obtained on the $^{152}Sm_{0.55}Sr_{0.45}Mn^{16}O_3$ and $^{152}Sm_{0.55}Sr_{0.45}Mn^{18}O_3$ samples directly confirm the formation of an inhomogeneous state and the onset of both FM and AFM ordering in samples with ^{18}O. As follows from the diffraction patterns presented in Fig. 4a, the samples with ^{16}O undergo only an FM transition at $T \approx 120$ K, which is in full agreement with the data from [13, 14, 23] obtained on samples with a natural abundance of oxygen.

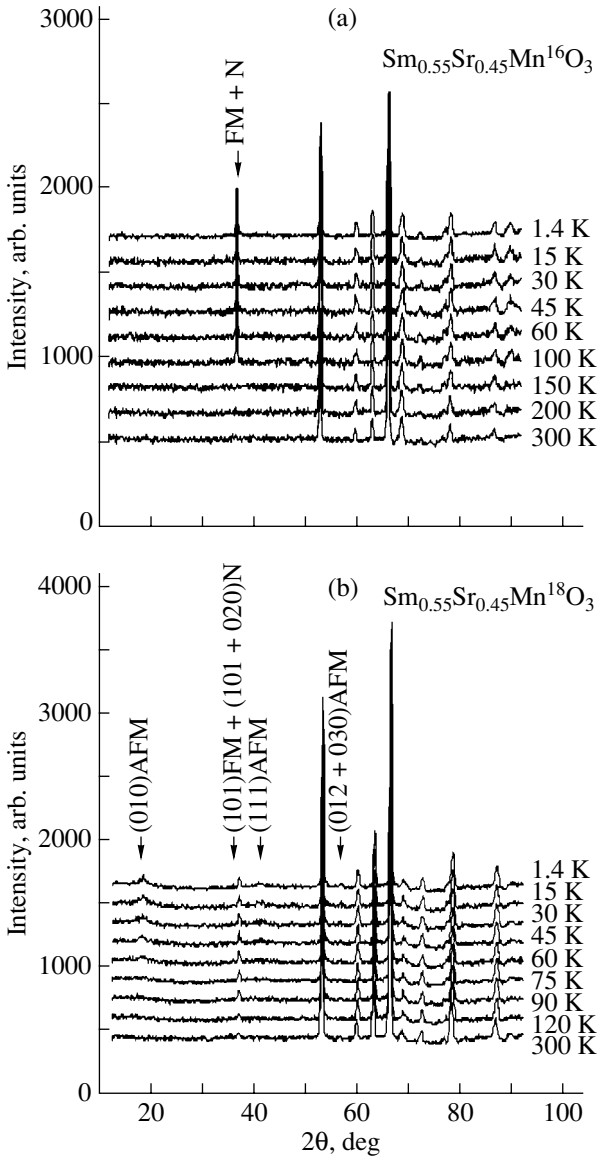

Fig. 4. Experimental powder neutron diffractograms measured on samples of (a) $^{152}Sm_{0.55}Sr_{0.45}Mn^{16}O_3$ and (b) $^{152}Sm_{0.55}Sr_{0.45}Mn^{18}O_3$ at different temperatures in heating runs. Arrows identify the strongest magnetic reflections.

In the sample with ^{18}O, AFM-ordered *A*-type regions form above the Curie point. These regions grow in volume with decreasing temperature. At $T \approx 100$ K, FM regions start to nucleate. The data obtained on the magnetic susceptibility and electrical resistivity can be interpreted in the following way. Initially, FM regions appear only where AFM regions have not yet formed. This seems only natural, because destruction of the AFM order would require additional energy expenditure. The electrical resistivity continues to grow under cooling, because the increase in the volume of AFM regions is a dominant effect. While the FM regions also grow in volume, percolation over the FM regions sets in only at 70 K. After this, the electrical resistivity naturally decreases. As the temperature is lowered still more, neutron diffraction reveals the formation of an AFM state with long-range order. Neutron diffraction spectra exhibit narrow maxima on broad pedestals in the positions corresponding to *A*-type magnetic ordering; the widths of these maxima are determined by the diffractometer resolution. As a result, both types of magnetic ordering coexist at very low temperatures.

Thus, in contrast to the sample with ^{16}O, the sample with ^{18}O does not transfer to the homogeneous FM state; furthermore, this state does not become prevalent over the sample volume. The FM moment m_F = 0.80(9) μ_B/Mn at the lowest temperature reached (1.4 K) and the low-temperature value of the magnetic susceptibility are smaller than those for the sample with ^{16}O. The reversible evolution of the AFM regions under heating may be kinetically hindered; therefore, there is only one jump in the temperature dependence of the susceptibility near 100 K. The maximum in resistivity also shifts to this temperature (the resistivity under heating is smaller because of the larger volume of the FM phase). It should be pointed out that the *A*-type AFM ordering is incompatible with CE-type charge ordering. Thus, the isotope effect observed in $Sm_{0.55}Sr_{0.45}MnO_3$ is in no way related to a manifestation of charge ordering, which is characteristic of the $(La_{1-y}Pr_y)_{0.7}Ca_{0.3}MnO_3$ system.

As for the crystal structure, the results obtained for all the above compounds of the $Sm_{1-x}Sr_xMnO_3$ system are identical to those for the $Sm_{0.55}Sr_{0.45}MnO_3$ composition [14]. The crystal structure of the samples with ^{16}O and ^{18}O is described well by the *Pnma* orthorhombic space group. No structural transitions were revealed in the temperature interval studied, from 300 down to 1.4 K. The lattice constants show that the structure of these samples is characterized by the relations $c > a > b/\sqrt{2}$ at all temperatures.

Thus, our experimental studies revealed changes in the magnetic phase diagram caused by the $^{16}O \longrightarrow {}^{18}O$ isotope substitution in the $Sm_{1-x}Sr_xMnO_3$ system.

2.4. Phase Diagram of the $Sm_{1-x}Sr_xMnO_3$ System

The $Sm_{1-x}Sr_xMnO_3$ compositions in which the oxygen isotope substitution was carried out exhibit a change in the phase diagram shown in Fig. 5. This change is supported by the totality of our measurements and by a comparison with powder neutron diffraction data available for the compositions $^{154}Sm_{0.6}Sr_{0.4}MnO_3$ [11, 12] and $^{152}Sm_{0.5}Sr_{0.5}MnO_3$ [24]. The magnetic ground state of these two compositions is determined by a mixture of the FM with the *A*-type AFM state. While the FM-phase content in them is practically the same ($m_F \approx 2.6$ μ_B/Mn), the content of the AFM com-

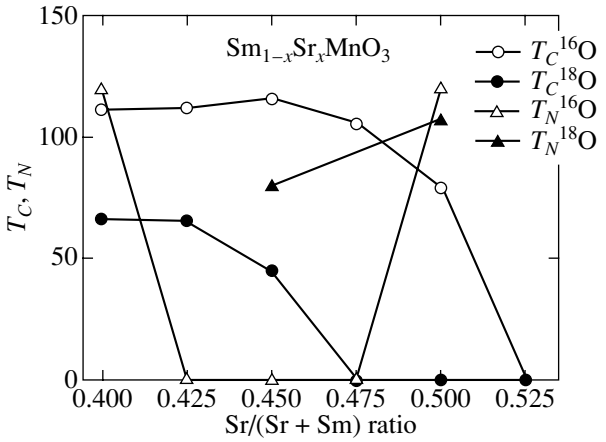

Fig. 5. Phase diagram of the $Sm_{1-x}Sr_xMnO_3$ system with different oxygen isotope compositions.

ponent in the 0.5–0.5 composition is considerably larger (m_{AF} = 3.4μ_B/Mn) than that in the 0.6–0.4 compound (m_{AF} = 0.5μ_B/Mn).

On the whole, the character of change in the phase diagram induced by oxygen isotope substitution $^{16}O \longrightarrow {}^{18}O$ can be traced to a suppression of stability of the FM metallic state: (1) the Curie temperature decreases noticeably for all compositions, (2) the narrow domain of existence of the homogeneous FM state vanishes, and (3) AFM ordering is now observed to set in throughout the compositional range studied. The isotope effect in the compositional range covered manifests itself strongly near $x = 0.5$ and substantially more weakly near $x = 0.4$.

This character of the isotope effect suggests that it is related to orbital ordering of Jahn–Teller centers in the $Sm_{1-x}Sr_xMnO_3$ structure. This is also argued for by the structural characteristics associated with orbital ordering. Indeed, the $Sm_{0.5}Sr_{0.5}Mn^{16}O_3$ compound, exactly like $Sm_{0.55}Sr_{0.45}Mn^{18}O_3$ and $Sm_{0.5}Sr_{0.5}Mn^{18}O_3$, has a crystal structure with the unit cell parameters $c > a > b/\sqrt{2}$, whereas the $Sm_{0.6}Sr_{0.4}MnO_3$ compound has an *O*-type structure ($c = a > b/\sqrt{2}$) at high temperatures and an *O*'-type structure ($a > c > b/\sqrt{2}$) in the low temperature range. The electron–phonon coupling is apparently more efficient in the former than in the latter case, as a result of which the isotope effect is stronger.

It should be stressed once more that *A*-type AFM ordering is incompatible with the *CE*-type charge ordering. In this respect, the $Sm_{1-x}Sr_xMnO_3$ system differs substantially from the $(La_{1-y}Pr_y)_{0.7}Ca_{0.3}MnO_3$ system studied earlier, which likewise reveals a metal–insulator transition driven by the oxygen isotope exchange. Thus, the manifestation of the isotope effect in manganites is not related to any specific features of the manganite ground state; at the same time, this effect is apparently highly sensitive to details of orbital ordering (the cooperative Jahn–Teller effect).

3. CONCLUSIONS

The $^{16}O \longrightarrow {}^{18}O$ isotope substitution gives rise to pronounced changes in the phase diagram of the $Sm_{1-x}Sr_xMnO_3$ manganites in the concentration interval $0.4 < x < 0.6$. Furthermore, this substitution induces separation of $Sm_{1-x}Sr_xMnO_3$ compounds into FM and *A*-type AFM phases for $x \geq 0.45$. For concentrations $x \geq 0.475$, the low-temperature metallic state transforms into the insulating phase under oxygen isotope substitution; this transition is reversible under application of an external magnetic field. All the above experimental findings concerning the isotope effects suggest that the corresponding processes should involve both spin and dynamic degrees of freedom. These considerations should be taken into account when analyzing such processes.

ACKNOWLEDGMENTS

The authors express sincere gratitude to A.N. Taldenkov and A.V. Inyushkin for helpful cooperation and discussions.

This study was supported by the Russian Foundation for Basic Research (project nos. 01-02-16240, 02-02-16078, 02-03-33258, 00-15-96570), CRDF (project no. RP2-2355-MO02), INTAS (project no. 01-2008), NWO (project no. 047-008-017), and the State Research Program (project no. 40.012.1.1.1149).

REFERENCES

1. E. Dagotto, T. Hotta, and A. Moreo, Phys. Rep. **344**, 1 (2001).
2. M. Yu. Kagan and K. I. Kugel, Usp. Fiz. Nauk **171**, 577 (2001) [Phys. Usp. **44**, 553 (2001)].
3. Guo-meng Zhao, H. Keller, J. Hoffer, A. Shengelaya, and K. A. Muller, Solid State Commun. **104**, 57 (1997).
4. N. A. Babushkina, L. M. Belova, O. Yu. Gorbenko, A. R. Kaul, A. A. Bosak, V. I. Ozhogin, and K. I. Kugel, Nature **391**, 159 (1998).
5. N. A. Babushkina, L. M. Belova, V. I. Ozhogin, O. Yu. Gorbenko, A. R. Kaul, A. A. Bosak, D. I. Khomskii, and K. I. Kugel, J. Appl. Phys. **83**, 7369 (1998).
6. A. M. Balagurov, V. Yu. Pomjakushin, D. V. Sheptyakov, V. L. Aksenov, N. A. Babushkina, L. M. Belova, A. N. Taldenkov, A. V. Inyushkin, P. Fischer, M. Gutmann, L. Keller, O. Yu. Gorbenko, and A. R. Kaul, Phys. Rev. B **60**, 383 (1999).
7. C. Martin, A. Maignan, M. Hervieu, and B. Raveau, Phys. Rev. B **60**, 12 191 (1999).
8. B. Raveau, A. Maignan, C. Martin, and M. Hervieu, Chem. Mater. **10**, 2641 (1998).
9. A. I. Shames, A. Yakubovsky, V. Amelichev, O. Gorbenko, and A. Kaul, Solid State Commun. **121**, 103 (2002).

10. E. Saitoh, Y. Tomioka, T. Kimura, and Y. Tokura, J. Magn. Magn. Mater. **239**, 170 (2002).
11. I. D. Luzyanin, V. A. Ryzhov, D. Yu. Chernyshov, A. I. Kurbakov, V. A. Trounov, A. V. Lazuta, V. P. Khavronin, I. I. Larionov, and S. M. Dunaevsky, Phys. Rev. B **64**, 094 432 (2001).
12. V. V. Runov, D. Yu. Chernyshov, A. I. Kurbakov, M. K. Runova, V. A. Trunov, and A. I. Okorokov, Zh. Éksp. Teor. Fiz. **118**, 1174 (2000) [JETP **91**, 1017 (2000)].
13. J. M. De Teresa, M. R. Ibarra, P. Algarabel, L. Morellon, B. Garcia-Landa, C. Marquina, C. Ritter, A. Maignan, C. Martin, B. Raveau, A. Kurbakov, and V. Trounov, Phys. Rev. B **65**, 100403 (2002).
14. A. V. Lazuta, V. A. Ryzhov, A. I. Kurbakov, V. A. Trounov, I. I. Larionov, O. Gorbenko, and A. Kaul, J. Magn. Magn. Mater. **258–259**, 315 (2003).
15. F. Damay, N. Nguen, A. Maignan, M. Hervieu, and B. Raveau, Solid State Commun. **98**, 997 (1996).
16. Y. Tomioka, H. Kuwahara, A. Asamitsu, M. Kasai, and Y. Tokura, Appl. Phys. Lett. **70**, 3609 (1997).
17. A. Abramovich, L. Koroleva, A. Michurin, O. Gorbenko, and A. Kaul, Physica B (Amsterdam) **293**, 38 (2000).
18. A. M. Aliev, Sh. B. Abdulvagidov, A. B. Batdalov, I. K. Kamilov, O. Yu. Gorbenko, and V. A. Amelichev, Pis'ma Zh. Éksp. Teor. Fiz. **72**, 668 (2000) [JETP Lett. **72**, 464 (2000)].
19. D. Emin and T. Holstein, Ann. Phys. (N.Y.) **53**, 439 (1969).
20. J. P. Franck, I. Isaak, W. Chen, J. Chrzanowski, and J. C. Irwin, Phys. Rev. B **58**, 5189 (1998).
21. Guo-meng Zhao, Y. S. Wang, D. J. Kang, W. Prellier, M. Rajeswari, H. Keller, T. Venkatesan, C. W. Chu, and R. L. Greene, Phys. Rev. B **62**, R11 949 (2000).
22. R. P. Borges, F. Ott, R. M. Thomas, V. Skumryev, J. M. D. Coey, J. I. Arnaudas, and L. Ranno, Phys. Rev. B **60** (18), 12847 (1999).
23. A. M. Aliev, Sh. B. Abdulvagidov, A. B. Batdalov, I. K. Kamilov, O. Yu. Gorbenko, V. A. Amelichev, A. R. Kaul, A. I. Kurbakov, and V. A. Trunov, Fiz. Tverd. Tela (St. Petersburg) **45**, 124 (2003) [Phys. Solid State **45**, 130 (2003)].
24. A. I. Kurbakov, A. V. Lazuta, V. A. Ryzhov, V. A. Trounov, I. I. Larionov, C. Martin, M. Hervieu, and B. Raveau (in press).

Translated by G. Skrebtsov

Physics of the Solid State, Vol. 46, No. 10, 2004, pp. 1891–1894. Translated from Fizika Tverdogo Tela, Vol. 46, No. 10, 2004, pp. 1828–1930.

MAGNETISM AND FERROELECTRICITY

Nonlinear Magnetic Resonance in the $(CH_3NH_3)_2CuBr_4$ Crystal

G. S. Patrin[1, 2], N. V. Volkov[1], and I. V. Prokhorova[2]

[1] *Kirensky Institute of Physics, Siberian Division, Russian Academy of Sciences, Akademgorodok, Krasnoyarsk, 660036 Russia*

[2] *Krasnoyarsk State University, pr. Svobodnyĭ 79, Krasnoyarsk, 660041 Russia*

e-mail: patrin@iph.krasn.ru

Received February 10, 2004

Abstract—The nonlinear microwave absorption in the $(CH_3NH_3)_2CuBr_4$ antiferromagnetic crystal is investigated experimentally. The temperature and angular dependences of the parameters of nonlinear resonance and the dependences of these parameters on the microwave pump power are analyzed. It is found that the nonlinear properties deteriorate with decreasing temperature and the linear and nonlinear contributions are competitive in character. © *2004 MAIK "Nauka/Interperiodica".*

1. INTRODUCTION

The compound $(CH_3NH_3)_2CuBr_4$ belongs to the family of layered perovskite-like crystals [1], in which the methyl ammonium group serves as a bridge between the planes containing copper magnetic ions (electron configuration d^9, $S = 1/2$). According to the magnetic static [2] and nuclear magnetic resonance [3] data, this crystal is an antiferromagnet with the antiferromagnetic vector directed along the *c* axis of the crystal, the ordering temperature $T_N \approx 15.8$ K, and a four-sublattice magnetic structure of the cross type. More recent investigations into the magnetic static properties demonstrated [4, 5] that this crystal is not a simple quasi-two-dimensional magnet and cannot be described in the framework of the standard Heisenberg model. In particular, the temperature dependence of the magnetization does not exhibit a maximum characteristic of low-dimensional systems, the temperature of the transition to the ordered state substantially depends on the magnetic field, and traces of magnetic correlations at such a low temperature of magnetic ordering are observed up to temperatures of the order of one hundred of degrees. As follows from the experimental data treated in terms of the standard molecular-theory approach [6], the paramagnetic Curie temperatures are different for parallel and perpendicular orientations: $\Theta_c^{\parallel} = -80$ K and $\Theta_n^{\perp} = -190$ K (here, the signs "||" and "⊥" stand for **H** || **c** and **H** ⊥ **c**, respectively).

In this respect, the question arises as to the nature of magnetic interactions and the mechanisms responsible for the formation of the magnetic structure.

Earlier [7, 8], we investigated the nonlinear microwave absorption, which is similar to the nonlinear resonance of a classical anharmonic oscillator in the $(CH_3NH_3)_2CuCl_4$ ferromagnetic crystal. For this crystal, we analyzed the nonlinear behavior of the microwave absorption in the oscillator approximation and the effect of light-induced change in the magnetic state in the bistable mode at nonlinear magnetic resonance, which allowed us to determine the line of unstable dynamic equilibrium experimentally.

This paper reports on the results of experimental investigations into the nonlinear dynamic properties of the $(CH_3NH_3)_2CuBr_4$ antiferromagnetic crystal.

2. SAMPLES AND EXPERIMENTAL TECHNIQUE

Samples were prepared in the form of 2 × 2-mm plates with thickness $t \sim 0.2$–0.3 mm. The **c** axis of the crystal was oriented perpendicularly to the plane of the plate. The experiment was performed with a rectangular cavity (mode TE_{102}, quality factor $Q \approx 1000$) operating at the microwave frequency $f = 10.3$ GHz. The power of the microwave oscillator was $P \leq 200$ mW.

3. RESULTS AND DISCUSSION

The geometry of the experiment and a fragment of the crystal structure in the laboratory system of coordinates are presented in Fig. 1. It is found that, upon cooling in the linear regime, as the temperature approaches T_N (the paramagnetic region), the resonance field tends to zero independently of the direction of the magnetic field with respect to the crystallographic axes of the crystal. When the temperature of the antiferromagnetic transition is passed, zero magnetic fields change and there appears a magnetic resonance line. With a further decrease in the temperature, this lines substantially shifts toward the range of strong magnetic fields but does not come to the plateau up to a temperature $T = 4.2$ K. This behavior of the resonance absorption in the

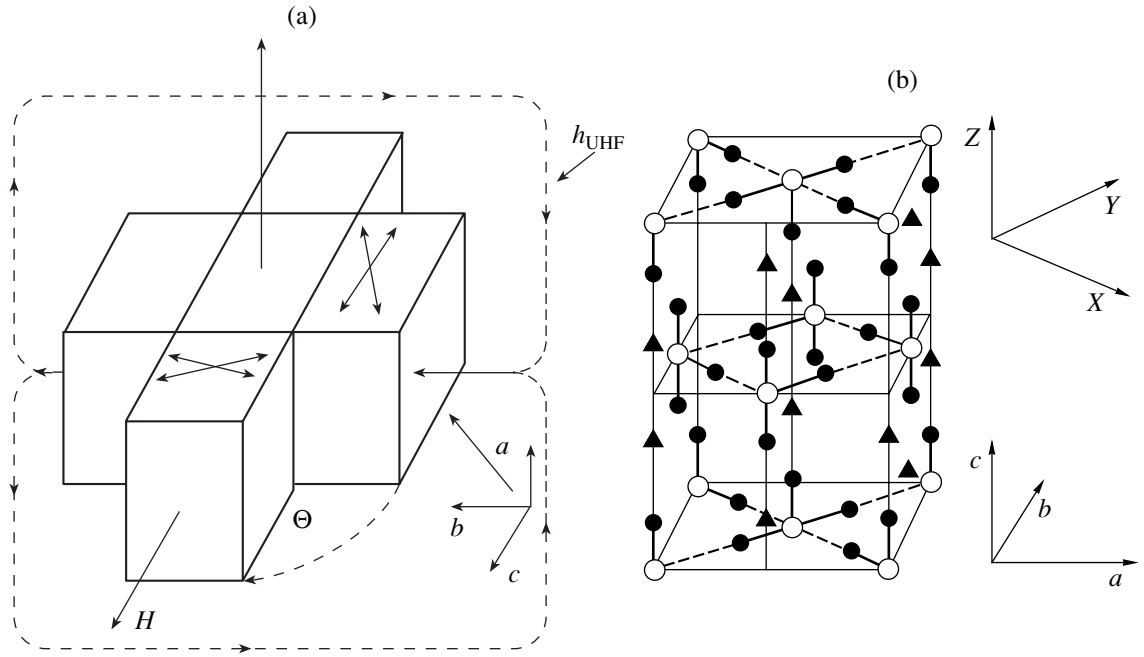

Fig. 1. (a) Directions of the magnetic constant (H) and microwave (h_{UHF}) fields with respect to the crystallographic axes. (b) A fragment of the crystal structure in the laboratory system of coordinates. Open circles represent copper ions, closed circles indicate bromine ions, and triangles correspond to methyl ammonium groups.

ordered region suggests that the spectrum of magnetic excitations can have a gap character.

At a higher microwave power, the $(CH_3NH_3)_2CuBr_4$ crystal is characterized by a nonlinear magnetic resonance in the magnetically ordered region. This resonance is similar to the resonance of an anharmonic oscillator [9], whose behavior can be described by the equation of motion

$$(d^2x/dt^2) + 2\lambda(dx/dt) + \omega_0^2 x + \beta x^3 = P\cos(\Omega t). \quad (1)$$

All the designations used in this equation of motion are traditional. It is known that, as a first approximation, the solution to this equation for stationary amplitude has the form

$$\varepsilon = \mu A^2 \pm \{[P/(2\Omega A)]^2 - \lambda^2\}^{1/2}, \quad (2)$$

where $\varepsilon = \Omega - \omega_0$ is the difference between the frequency of the external driving force and the frequency of the linear resonance and $\mu = 3\beta/8\Omega$ is the coefficient of nonlinearity. In our experiment, the line of microwave absorption in the nonlinear regime has the shape shown in the inset to Fig. 2. This line shape is typical of systems with $\beta < 0$. In the experiment, we measured the magnetic field H_1 (the first cutoff field) and the hysteresis width ΔH_h. It is known that, at cutoff points, the derivative is infinite, i.e., $dA/d\varepsilon = \infty$, which leads to the following expression for detunings [9]:

$$\varepsilon_{1,2} = 2\mu A^2 \pm \{\mu^2 A^4 - \lambda^2\}^{1/2}. \quad (3)$$

Then, from the consistency between Eqs. (2) and (3), we can determine the hysteresis width

$$\Delta\varepsilon = \varepsilon_2 - \varepsilon_1 = 2\{\mu^{2/3}(P/2\Omega)^{4/3} - \lambda^2\}^{1/2}. \quad (4)$$

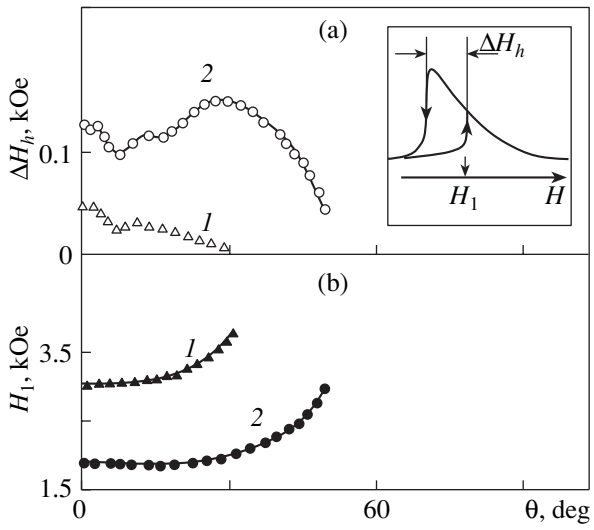

Fig. 2. Angular dependences of the parameters of the nonlinear magnetic resonance: (a) the hysteresis width ΔH_h and (b) the cutoff field H_1. T = (*1*) 5.5 and (*2*) 8 K. The inset shows the shape of the microwave absorption line.

In our case, we have $H_1 = (\Omega + \varepsilon_1)/\gamma$ and $\Delta H_h = \Delta\varepsilon/\gamma$, where γ is the gyromagnetic ratio. The nonlinear properties most clearly manifest themselves in the behavior of the hysteresis width. In actual fact, as follows from relationship (4), the hysteresis width is proportional to the coefficient of nonlinearity μ and is not masked by virtually any means. The quantity λ can always be measured in the linear regime. At the same time, the shift of the line as a whole (and, consequently, ε_1) depends not only on the coefficient of nonlinearity μ but also on the crystalline magnetic anisotropy and the exchange anisotropy. Figure 2 shows the angular dependences of the parameters H_1 and ΔH_h measured at different temperatures (see caption to Fig. 2). In this case, the angle θ is reckoned from the **c** axis of the crystal. It can be seen from Fig. 2 that, as the temperature increases, the θ range of existence of the nonlinear resonance increases and the nonlinear properties become more pronounced. This is clearly seen from the temperature dependences of the nonlinear resonance parameters obtained at the paramagnetic Curie temperature $\theta = 0$ (Fig. 3). In the temperature range from $T = 4.2$ K to T_N, the hysteresis width ΔH_h changes by more than one order of magnitude. A strong nonlinear resonance of the same shape as in the inset to Fig. 2 is observed in the vicinity of the temperature of the transition to the magnetically ordered state T_N in the range $\Delta T \approx 2$ K.

The behavior of the nonlinear absorption as a function of the microwave pump power is illustrated in Fig. 4. It can be seen that the hysteresis width ΔH_h with a change in the power of microwave radiation (which is the equivalent of the quantity P in the oscillator model) is qualitatively described by relationship (4). The only difference is observed in the vicinity of $\alpha \sim 1$. The measured field H_1 is linearly dependent on the microwave power.

In contrast with the case of the well-known resonance in the $(CH_3NH_3)_2CuCl_4$ ferromagnetic crystal [7], when the nonlinear magnetic resonance is most pronounced in the geometry $\mathbf{H} \perp \mathbf{c}$, the nonlinear magnetic resonance in the $(CH_3NH_3)_2CuBr_4$ antiferromagnetic crystal most clearly manifests itself in the geometry $\mathbf{H} \parallel \mathbf{c}$. In the latter case, it is also unusual that the line shape of nonlinear microwave absorption is inverted. This means that, for the bromide crystal, the direction of the nonlinear component of the elastic force coincides with the direction of the high-frequency component of the magnetic field (external force). This is quite possible (Fig. 1) when the molecular field induced by the nonlinear contribution lies in the (**a**–**b**) plane. In the case when the magnetic field **H** is directed along the **c** axis, the magnetic sublattices are equivalent in pairs, which manifests itself as the degeneracy of the resonance frequencies in the linear regime. As regards the nonlinear magnetic resonance, at first glance, there are no special prerequisites for its origin. The copper ion has a spin $S = 1/2$. This implies that the intralayer spin exchange interaction has a Heisenberg form and that the crystalline magnetic anisotropy should be relatively weak, which is observed in the experiment. Furthermore, magnetic ions in different layers are widely separated (by a distance of the order of at least two methyl ammonium groups), and, therefore, the exchange between the layers should be insignificant. The foregoing suggests that there should exist a strong interaction between magnetic ions in different layers. Apparently, this interaction is the Jahn–Teller interaction between degenerate orbital states through which the spins of ions also interact. The nonlinear spin dynamics can be enhanced by the nonlinear interaction of resonant modes in the region of resonance overlapping.

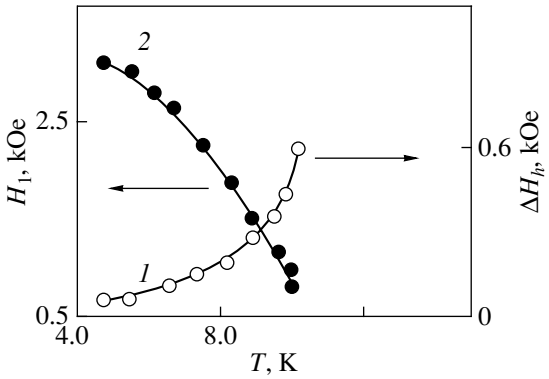

Fig. 3. Temperature dependences of the parameters of the nonlinear resonance: (*1*) hysteresis width and (*2*) cutoff field. $\theta = 0$.

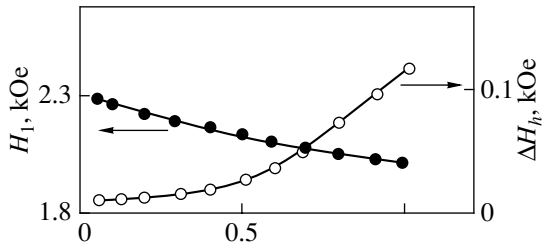

Fig. 4. Dependences of H_1 and ΔH_h on the reduced power of microwave radiation ($\alpha = P_{UHF}/(P_{UHF})_{max}$). $\Theta = 0$, $T = 8$ K.

A more correct answer to the question regarding the specific features of the magnetic structure and the nature of the spin dynamics can be provided by theoretical analysis with due regard for all interactions.

ACKNOWLEDGMENTS

This work was supported by the federal program "Universities of Russia—Basic Research," project no. UR.01.01.044.

REFERENCES

1. K. S. Aleksandrov and V. B. Beznosikov, *Perovskite-Like Crystals* (Nauka, Novosibirsk, 1977) [in Russian].
2. Y. Kimishima, J. Phys. Soc. Jpn. **49**, 62 (1980).
3. Y. Suzuki, K. Tsuru, Y. Kimishima, and H. Kubo, J. Phys. Soc. Jpn. **50**, 1479 (1981).
4. N. V. Fedoseeva, N. V. Volkov, and G. S. Patrin, Fiz. Tverd. Tela (St. Petersburg) **45**, 472 (2003) [Phys. Solid State **45**, 499 (2003)].
5. G. S. Patrin, N. V. Volkov, and I. V. Prokhorova, J. Magn. Magn. Mater. **258–259**, 131 (2003).
6. E. A. Turov, A. V. Kolchanov, V. V. Men'shinin, I. F. Mirzoev, and V. V. Nikolaev, *Symmetry and Physical Properties of Antiferromagnets* (Fizmatlit, Moscow, 2001) [in Russian].
7. G. S. Patrin and N. V. Volkov, J. Magn. Magn. Mater. **151**, 189 (1995).
8. G. S. Patrin and N. V. Volkov, Pis'ma Zh. Éksp. Teor. Fiz. **64**, 841 (1996) [JETP Lett. **64**, 898 (1996)].
9. M. I. Rabinovich and D. I. Trubetskov, *Introduction to the Theory of Oscillations and Waves* (Nauka, Moscow, 1984) [in Russian].

Translated by O. Moskalev

Physics of the Solid State, Vol. 46, No. 10, 2004, pp. 1895–1905. Translated from Fizika Tverdogo Tela, Vol. 46, No. 10, 2004, pp. 1831–1840.

MAGNETISM AND FERROELECTRICITY

Changes in the Electronic, Optical, and Magnetic Properties of LaSrMnO Films upon Transition from the Rhombohedral Phase to the Orthorhombic Phase

V. D. Okunev*, Z. A. Samoĭlenko*, T. A. D'yachenko*, R. Szymczak, S. J. Lewandowski**, H. Szymczak**, M. Baran**, and P. Gierlowski****

** Donetsk Physicotechnical Institute, National Academy of Sciences of Ukraine, Donetsk, 83114 Ukraine*

*** Instytut Fizyki PAN, 02-668 Warsaw, Poland*

e-mail: okunev@mail.fti.ac.donetsk.ua

Received September 26, 2003; in final form, February 24, 2004

Abstract—The properties of LaSrMnO films are investigated in the temperature range of the transition from the rhombohedral phase to the orthorhombic phase (600–650°C). It is shown that, with a variation in the growth temperature T_s, the change in the film properties is governed by the interaction of Mn–O metallic (ferromagnetic) clusters in the dielectric (antiferromagnetic) matrix. At $T_s \le 600$°C, the low density of e_g states and the dielectric gap (E_g = 0.3–0.5 eV) are responsible for the following features: (i) the optical transparency in the range $\hbar\omega$ = 0.5–2 eV, (ii) the difference between the FC and ZFC magnetizations $M(T)$, (iii) the high resistance, and (iv) the appearance of the portions $R(T) \approx$ const in the dependence $R(T)$ due to the transformation of clusters into a system of tunnel-coupled quantum dots. At $T_s \ge 650$°C, the local increase in the atomic and electronic densities leads to a decrease in the optical transmission and the resistance by three to nine orders of magnitude, the appearance of a maximum and a minimum in the dependences $R(T)$ of the LaSrMnO films, and an increase in the magnetization M(10 K) by one order of magnitude. The inference is drawn that magnetic ordering of the system of tunnel-coupled clusters encourages an increase in the cluster size and in the content of the metallic (ferromagnetic) phase. © *2004 MAIK "Nauka/Interperiodica".*

1. INTRODUCTION

Considerable recent interest expressed by researchers in lanthanum manganese oxides LaSrMnO with a giant magnetoresistance effect stems from the fact that these compounds exhibit a great variety of interesting properties and hold much promise for practical application. Lanthanum manganese oxides can have different perovskite (from cubic to orthorhombic) structures depending on the technique used in their preparation and stresses arising in the system [1–5]. The structural diversity entails a wide variety of properties. For example, the transition from a rhombohedral phase to an orthorhombic phase leads not only to qualitative changes in the optical spectra and temperature dependences $R(T)$ but also to a decrease in the resistance by seven to ten orders of magnitude [6]. The most interesting objects of investigation appear to be samples with a transition structure. These samples can be prepared by growing films at temperatures T_s from 600 to 670°C (where T_s is the synthesis temperature) [6]. The elastic stresses arising at the film–substrate interface can both suppress and induce the phase transition. The films grown on $SrLaGaO_4$ substrates are characterized by the lowest temperature of the phase transition. The influence of the orientation of substrates and related stresses on the properties of manganite thin films was thoroughly analyzed by Boĭkov *et al.* [7]. In the present work, we investigated how the change in the type of atomic ordering (upon transition from the rhombohedral structure to the orthorhombic structure) affects the physical properties of manganite films.

2. FILM PREPARATION AND EXPERIMENTAL TECHNIQUE

Films were prepared through pulsed laser sputtering of a $La_{0.6}Sr_{0.2}Mn_{1.2}O_3$ target with the use of a KrF excimer laser ($\tau \approx 25$ ns, energy density Φ = 3.0 J/cm^2 at a target, oxygen pressure in a working chamber P_0 = 300 mTorr). The nonstoichiometric composition with excess manganese was taken in order to stimulate the cluster formation in the structure of samples [6]. The films were deposited on $SrLaGaO_4$ substrates at T_s = 450–730°C.

Pulsed laser deposition is a unique technique that provides a means for growing high-quality films of complex composition in which the target stoichiometry of chemical elements is retained [8–12]. Coincidence of the film and target compositions was confirmed by the following experimental results. (1) At high growth temperatures (T_s > 670°C), the films contain the only phase corresponding to the target, namely, the orthorhombic phase (*Pnma*) with the reference parameters of

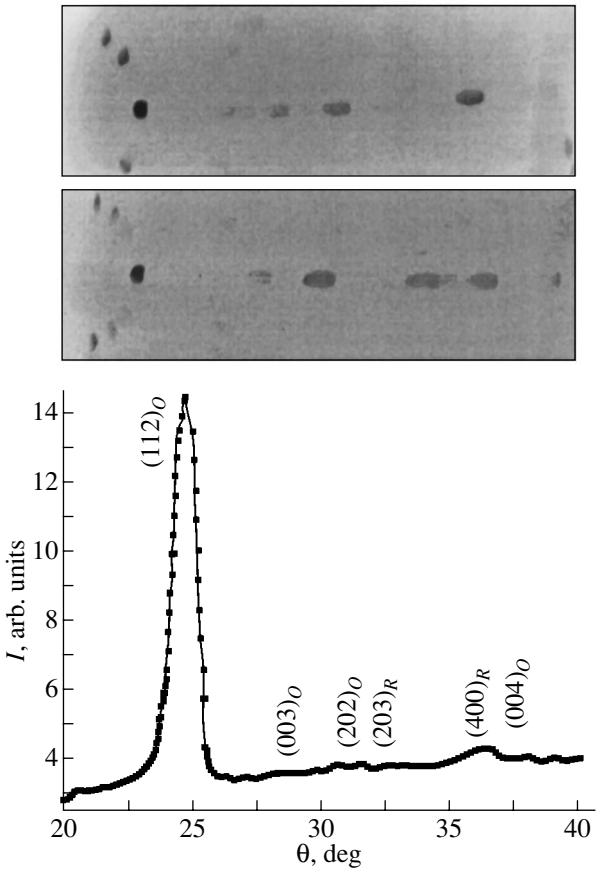

Fig. 1. A general view of the diffraction pattern of $La_{0.6}Sr_{0.2}Mn_{1.2}O_3$ films (Laue reflections and microphotometric curve obtained along the axial line of the powder diffraction pattern).

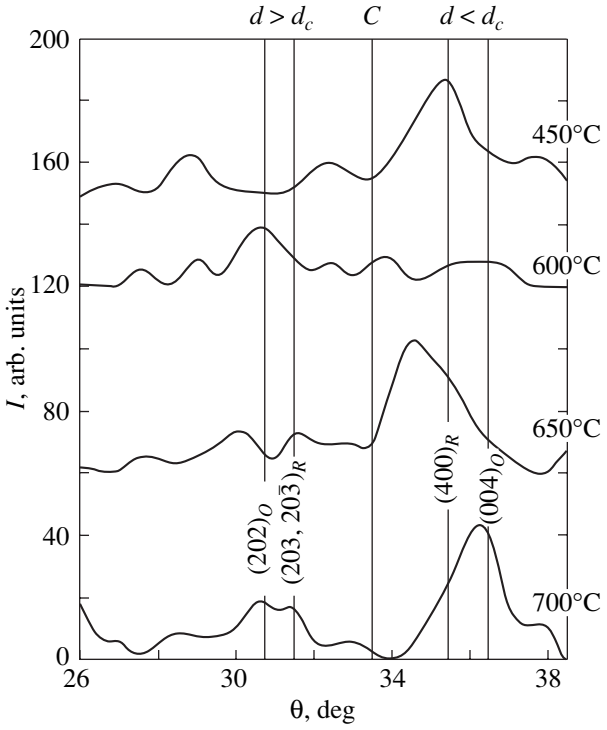

Fig. 2. Fragments of the diffraction patterns in the range of scattering from Mn–O clusters in $La_{0.6}Sr_{0.2}Mn_{1.2}O_3$ films grown at temperatures T_s = 450, 600, 650, and 700°C.

the crystal lattice [6]. (2) The Curie temperature T_C = 310 K determined from the magnetization measurements of the films grown at T_s = 700°C is close to the Curie temperature T_C = 311 K for the target.

The film structure was studied by the photomethod with the use of long-wavelength CrK_α radiation. This method simplifies the recording of diffuse x-ray scattering in clustered solid solutions, as is the case for our objects of investigation. The electrical measurements in the temperature range 4.2–300 K were performed using the standard methods. The optical transmission spectra of the films were recorded at room temperature in the range $\hbar\omega$ = 0.5–3.5 eV on a modified SP 700 C spectrophotometer. The magnetic measurements were carried out on a SQUID magnetometer in the temperature range 4.2–300 K.

3. RESULTS

3.1. Film Structure

The structure of the LaSrMnO films was modified by varying the growth temperature in the range 450 < T_s < 730°C. Previous diffraction investigations of $La_{0.6}Sr_{0.2}Mn_{1.2}O_3$ films grown in the same temperature range revealed that an increase in the synthesis temperature T_s leads to structural transformations in the samples according to the scheme

$$R\ (\bar{3}c) \xrightarrow[T_s < 650°C]{} R\ (\bar{3}c) + O\ (Pnma)$$

$$\xrightarrow[T_s > 670°C]{} O\ (Pnma)$$

with the transition from the single-phase rhombohedral modification R $(\bar{3}c)$ to the two-phase modification in the range T_s = 650–670°C and then to the single-phase orthorhombic modification O (*Pnma*) [6]. It can be seen from the diffraction pattern (Fig. 1) that, in the heterogeneous phase of the crystal films, clusters with a mesoscopic-range order and mesoscopic sizes are coherently embedded in the matrix structure with a long-range order.

The clusters formed by the family of Mn–O planes play the most important role, because they provide the conducting and magnetic properties of LaSrMnO films. These clusters are characterized by the (203, 20$\bar{3}$)$_R$ and (400)$_R$ reflections in the rhombohedral phase and the (202)$_O$ and (004)$_O$ reflections in the orthorhombic phase (Fig. 2). The sizes of Mn–O clusters were calculated with due regard for the width of the above diffuse

maxima on the basis of the Kitaĭgorodskiĭ technique developed in our previous work [13]. The calculated sizes fall in a narrow range in the vicinity of 100 Å. A comparison of the diffuse maxima for different samples (Fig. 2) shows that the fundamental structural transformations are associated with the change in the ratio between the extended and contracted planes in the clusters. This ratio indicates the presence of internal stresses in mesoscopic regions (clusters) and manifests itself in the asymmetry of the corresponding diffuse maxima. Let us analyze the changes in the diffuse scattering intensities for the discrete diffraction angles θ (Fig. 2). These angles are chosen according to their correspondence with the interplanar distances $d = n\lambda/2\sin\theta$ (the Bragg–Wulff equation), which are equal to the Mn–O bond lengths for the rhombohedral and orthorhombic phases in manganites [14].

It is worth noting that the chosen angles θ are symmetrically located with respect to central line *C*, which divides the studied range of diffraction angles into two structurally symmetric (with respect to reflections indicated by the four vertical lines in Fig. 2) ranges: with larger interionic (interplanar) distances $d > d_c$ (to the left of line *C*) and smaller interionic (interplanar) distances $d < d_c$ (to the right of line *C*). By determining the intensities at the aforementioned points to the left and the right of line *C* in diffraction patterns of the studied films, we analyzed how the growth temperature affects the total intensities of the $(202)_O$ and $(203,\ 20\bar{3})_R$ reflections (Fig. 3a, curve $d_<$) and the $(400)_R$ and $(004)_O$ reflections (Fig. 3a, curve $d_<$). It can be seen from Fig. 3a that, in the films grown at temperatures close to $T_s = 600$°C, "extended states" are dominant in the structure ("loosening region"), because the intensity $I(d_>)$ exceeds the intensity $I(d_<)$. On the other hand, in the samples grown at $T_s < 600$°C or $T_s > 600$°C, "contracted states" of structural elements are dominant. This is associated with the enhancement of the Mn–O interactions in the samples grown at these temperatures as compared to those deposited at $T_s = 600$°C.

By summing up the intensities at all four above points in the diffraction patterns in Fig. 2, we can compare the density of structural states associated with the Mn–O clusters, including clusters that contain comparable amounts of Mn^{3+} and Mn^{4+} ions responsible for the metallic conductivity and ferromagnetism. As can be seen from Fig. 3b, the intensity in the range 450°C < T_s < 600°C is considerably lower than that in the range 600°C < T_s < 700°C. This suggests that the density of the aforementioned structural states in the rhombohedral phase is lower than the density of these states in the orthorhombic phase. The results obtained are in agreement with the data on the electronic and optical properties of the films.

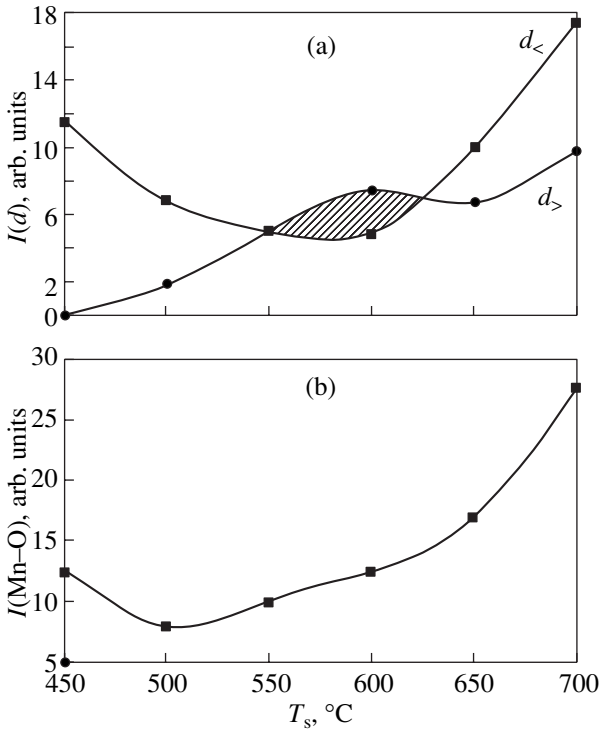

Fig. 3. Intensity of coherent x-ray scattering from the grown films as a function of the temperature T_s (a) for extended ($d_>$) and contracted ($d_<$) planes of Mn–O clusters and (b) at discrete angles in the diffraction patters of Mn–O clusters.

3.2. Optical Transmission Spectra

The changes in the electronic structure of the LaSrMnO films in the phase transition range can be judged from the optical transmission spectra (Fig. 4). The films grown at $T_s < 600$°C (rhombohedral phase) are characterized by a high optical transparency in the long-wavelength spectral range ($\hbar\omega < 2$ eV). In this range, the spectra contain two maxima *A* and *C* with close intensities. The minimum *B* (at $\hbar\omega \approx 1.1$ eV) separating the maxima indicates a maximum in the density of electronic states participating in the optical transitions. The presence of metallic clusters manifests itself in spectral portions *OA* associated with the absorption by free charge carriers at $\hbar\omega < 0.8$ eV. These portions are characterized by a decrease in the transmission *t* with a decrease in $\hbar\omega$. Portions *OA* can be observed because the maximum quantum energy possible upon intraband optical transition and the corresponding Fermi energy in clusters with the metallic conductivity are smaller than the optical band gap. This explains the high optical transparency of the films in the long-wavelength spectral range.

The absorption edge is smeared, and a gap with a width of ≈2.5 eV can be revealed in Fig. 4b from a drastic decrease in the transmission $t(\hbar\omega)$. The shift of the threshold energies toward the long-wavelength range to 1.2 eV (maximum *C* in curves *1, 2* in Fig. 4a) is due to the presence of the clusters with metallic conductivity

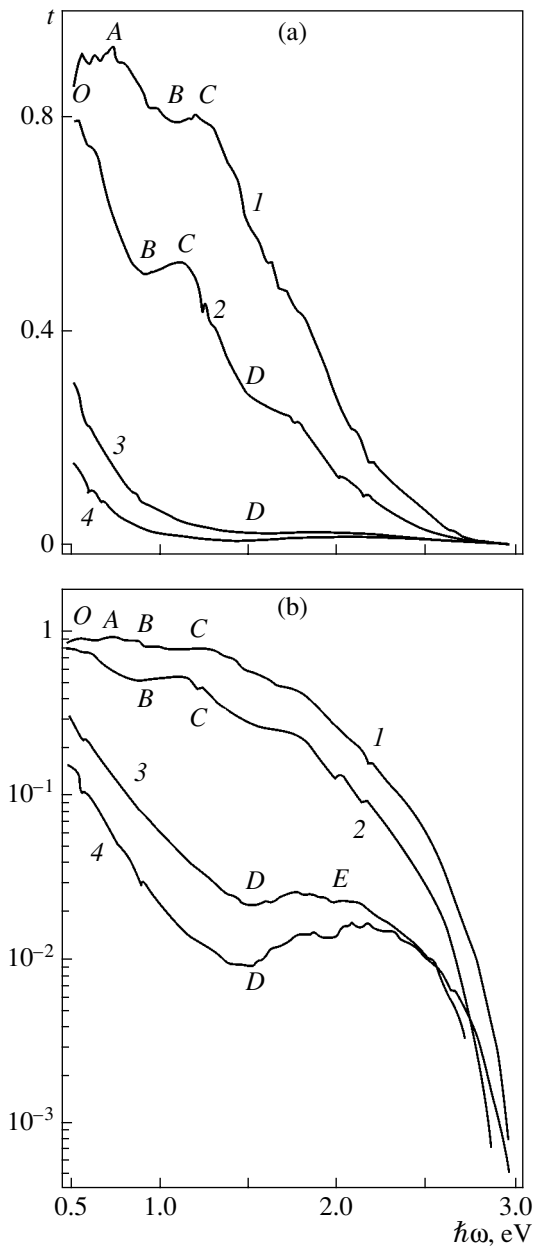

Fig. 4. Optical transmission spectra of the LaSrMnO films grown at T_s = (*1*) 450, (*2*) 600, (*3*) 650, and (*4*) 700°C.

in the $R\bar{3}c$ dielectric phase and the influence of electron tunneling on the interband optical transitions [15]. Owing to internal electric fields, the threshold energy of interband transitions decreases substantially. In this case, the short-wavelength range of the spectrum can be approximated by a linear dependence of the transmission on the photon energy:

$$t = f(r)[C - B\hbar\omega], \quad (1)$$

where $B = \alpha(\omega_t)d/\delta_0$, $C = \alpha(\omega_t)d[1 + \hbar\omega_t/\delta_0]$, ω_t is the threshold frequency, d is the film thickness, and δ_0 is the characteristic energy. This dependence agrees with the behavior of curve *1* (at $\hbar\omega$ = 1.2–2.2 eV).

The content C_m of the metallic phase (portion *OA*) can be conveniently determined using the function [15, 16]

$$\frac{1}{t}\frac{dt}{d(\hbar\omega)} \sim C_m p, \quad (2)$$

where p is the hole concentration. According to the data obtained in our previous work [17], we have C_m = 0.02–0.05 at T_s < 600°C. The spectrum of the film deposited at T_s = 600°C is similar in shape and transmission t to the spectrum of the sample grown at T_s = 450°C (Figs. 4a, 4b). The transmission spectrum contains the long-wavelength minimum (at $\hbar\omega$ = 0.9 eV) characteristic of the samples grown at low temperatures T_s. However, the portion associated with the absorption by free charge carriers is absent.

The samples synthesized at T_s > 600 are less optically transparent. The transmission spectra of the samples thus synthesized were studied by Kaplan *et al.* [18] and Okimoto *et al.* [19]. These spectra have a simpler structure: they contain one minimum *D* at $\hbar\omega \sim 1.5$ eV and one maximum *E* in the range 1.7–2.2 eV (Fig. 4b). It should be noted that the minimum at 1.5 eV typical of the samples with an orthorhombic structure manifests itself in the spectrum of the film grown at T_s = 450°C and is clearly observed in the spectrum of the film deposited at T_s = 600°C (Fig. 4a). As the synthesis temperature increases from 600 to 650°C, the transmission decreases sharply and the spectra at 650 and 700°C differ only slightly. This can be judged from the comparative absorption spectra (α at T_s = 700°C)/(α at T = 450, 600, 650°C). The ratio of the quantities α for the samples deposited at T_s = 700 and 650°C decreases exponentially with an increase in the photon energy (Fig. 5, curve *3*). The increase in the density of states (by no more than a factor of 1.5) with a decrease in $\hbar\omega$ suggests an increase in the concentration of free charge carriers. Actually, the optical absorption coefficient α is proportional to the optical conductivity $\sigma(\omega)$, which agrees well with the behavior of the dc conductivity:

$$\alpha = 4\pi\sigma(\omega)/n_0 c, \quad (3)$$

where n_0 is the refractive index and c is the speed of light. In the long-wavelength range, the intraband optical transitions dominate and a decrease in $\hbar\omega$ leads to an increase in the contribution of free charge carriers to the optical absorption coefficient α [20]. Therefore, we can draw the inference that curve *3* indicates an increase in the content of the metallic phase with an increase in the synthesis temperature T_s from 650 to 700°C. This is confirmed by a decrease in the resistivity (from 3.2×10^{-1} to 3.65×10^{-2} Ω cm at T = 290 K, from 5×10^{-2} to 3.6×10^{-3} Ω cm at T = 4.2 K). The absorption by free charge carriers is observed in the spectra of the films in the orthorhombic phase (T_s > 600°C) at $\hbar\omega$ <

0.2 eV [20] and, hence, does not manifest itself in the spectra shown in Fig. 4. In the two other cases (Fig. 5, curves *1*, *2*), the relative spectra are substantially more complex. These spectra reflect the main features of the transmission spectra in Fig. 4a and confirm the similarity of the electronic structures of the samples grown at T_s = 450 and 600°C.

At $\hbar\omega > 2.2$ eV, the transmission rapidly decreases with an increase in $\hbar\omega$. It can be seen from the curves in Fig. 4b that, despite qualitative and quantitative differences between the optical spectra of the films with orthorhombic and rhombohedral structures, their spectra are very similar to each other in the short-wavelength range. We can assume that, in this range, the optical transitions occur through the same mechanisms. The results obtained allow us to determine the band gaps in the density of states. Our samples belong to systems with a disordered structure for which the dependence $\alpha(\hbar\omega)$ is described by the relationship [21]

$$\alpha(\hbar\omega) \sim (\hbar\omega - E_{g\,\mathrm{opt}})^2/\hbar\omega, \qquad (4)$$

where $E_{g\,\mathrm{opt}}$ is the optical band gap. For the films grown at T_s = 650 and 700°C, the approximation of the dependences $(\alpha\hbar\omega)^{1/2}$ in the long-wavelength range to zero leads to $E_{g1} \sim 0$ eV (Fig. 6). This important result is typical of strongly correlated systems with metallic conductivity and experimentally corroborates the presence of a quasi-metallic band of free charge carriers (centered at $\hbar\omega = 0$ eV in the absorption spectra) in doped metal oxides [22].

At high energies, the range in which the dependence of the absorption coefficient α on $\hbar\omega$ is linearized in the $\hbar\omega$–$(\alpha\hbar\omega)^{1/2}$ coordinates is limited by the band gap E_{g3} = 1.5 eV (Fig. 6). This band gap is characteristic of manganites with an orthorhombic structure [18–20, 22] and can be determined from the minima in spectra *3* and *4* in Fig. 4b. For the rhombohedral phase, this gap weakly manifests itself in the spectra (Fig. 4, curves *1*, *2*).

A similar approximation of spectra *1* and *2* of the films in the rhombohedral phase (grown at T_s = 450, 600°C) results in a nonzero value of the band gap E_{g2} = 0.25 eV (Fig. 6).

In the short-wavelength range, the energy gap with E_{g4} = 2.35 eV ± 0.1 eV is found for all the samples (Figs. 4, 6).

The energy splitting Δ_{cf} between the e_g and t_{2g} states in the octahedral crystal field of manganites depends on the charge state of Mn ions and, correspondingly, on the Mn–O distance (the splitting Δ_{cf} decreases with an increase in the Mn–O interionic distance) [4]. For Mn^{4+} and Mn^{3+} ions, the splittingsΔ_{cf} are equal to 2.4 and 1.5 eV. This is in agreement with the results obtained in studies of the optical spectra.

As follows from the data presented in Figs. 4–6, the density of electronic states in the samples with an orthorhombic structure is considerably higher than that

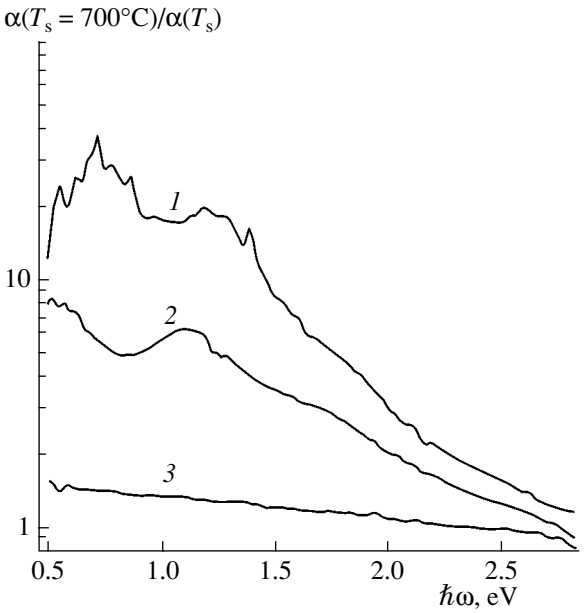

Fig. 5. Comparative optical transmission spectra of the film samples: (*1*) α(700)/α(450), (*2*) α(700)/α(600), and (*3*) α(700)/α(650).

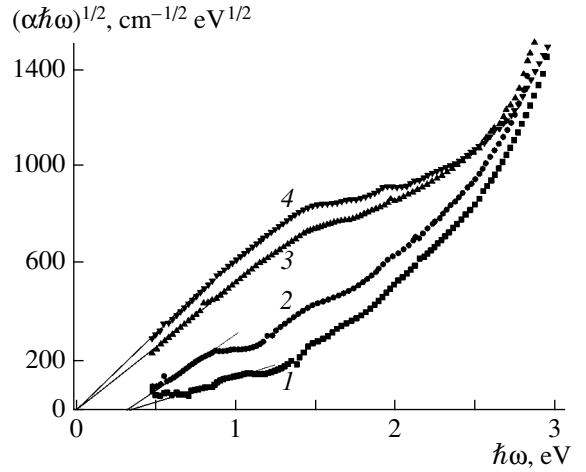

Fig. 6. Absorption spectra of the films grown at T_s = (*1*) 450, (*2*) 600, (*3*) 650, and (*4*) 700°C in the $\hbar\omega$–$(\alpha\hbar\omega)^{1/2}$ coordinates.

in the samples with a rhombohedral structure. This can be associated with the larger volume of the unit cell in the latter structure: $V_R/V_O \approx 2$. In the long- and medium-wavelength spectral ranges, including $\hbar\omega \sim 1.5$ eV, the contribution of Mn^{3+} ions to the density of states is large and the densities of states in the above structures can differ by more than one order of magnitude (Fig. 5).

The energy gaps with E_{g1} and E_{g2} in the density of e_g states responsible for the *p*-type conductivity of manganites are formed as a result of the removal of orbital degeneracy due to distortions inherent in the Jahn–

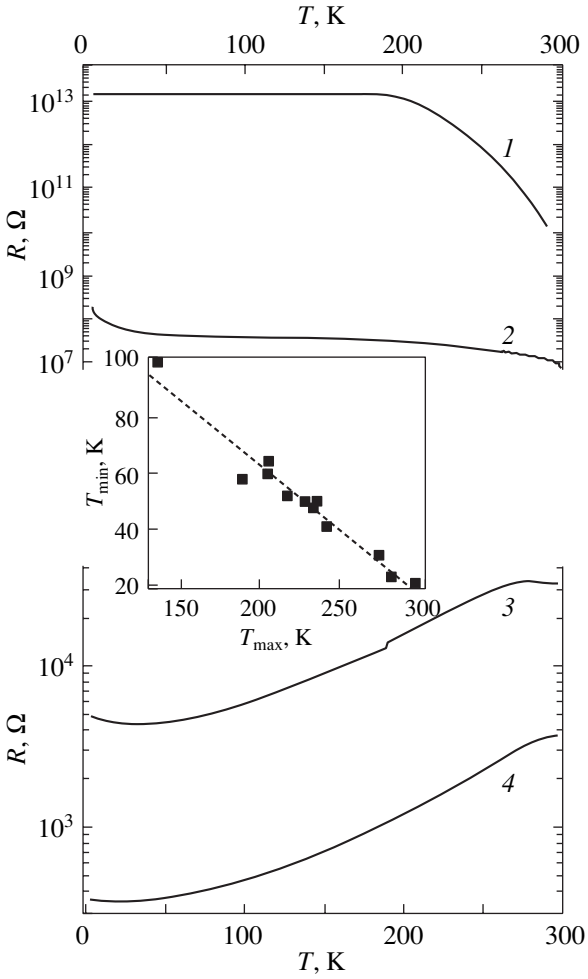

Fig. 7. Temperature dependences of the electrical resistance of the films grown at T_s = (*1*) 450, (*2*) 600, (*3*) 650, and (*4*) 700°C.

Teller effect. For the orthorhombic structure, these distortions are small (as compared to those in a cubic structure), the splittings between the x^2–y^2 and z^2 states are virtually absent, and we have $E_{g1} = 0$ eV. This is in agreement with the inference made by Naĭsh [3], according to which the orbital splitting between the x^2–y^2 and z^2 states for orthorhombic magnets is either small or altogether absent.

The situation is different for the samples with a rhombohedral structure characterized by large distortions. As can be seen from Fig. 6, the band gap E_{g2} is approximately equal to 0.25 eV. The location of the minima in the transmission spectra (at 0.9–1.1 eV in Fig. 4) most likely characterizes the difference between the maxima in the density of the x^2–y^2 and z^2 states.

3.3. Electrical Conductivity

The differences in the atomic and electronic subsystems of the LaSrMnO films lead to the change in the behavior of the temperature dependence of the electrical resistance $R(T)$. For the samples grown at $T_s \le 600$°C, the temperature dependences of the resistance exhibit portions with $R(T) \approx$ const at temperatures below T_{crit} = 160–230 K (Fig. 7 curves *1*, *2*).

The portions $R(T) \approx$ const were previously observed for dielectric manganites of compositions $La_{0.82}Ca_{0.18}MnO^{3+\delta}$ [23], $Nd_{0.7}Ba_{0.3}MnO_3$, $Nd_{0.7}Sr_{0.3}MnO_3$ [4, 24], $Pr_{0.65}Ca_{0.35}MnO_3$ [25], $La_{0.7}Ba_{0.3}MnO_3$ [26], $La_{2/3}Ba_{1/3}(Mn_{0.9}Co_{0.1})O_3$ [27], and $La_{0.6}Sr_{0.2}Mn_{1.2}O_3$ [17, 28]. In [4, 24] it was shown that films with high resistivities ρ and portions $\rho(T)$ = const contain nanometer-sized inclusions. A similar effect also manifests itself in amorphous and crystalline YBaCuO films that involve small-sized clusters with metallic conductivity in a dielectric medium [13, 16, 17, 28].

The nature of the observed phenomenon is explained by the electron tunneling between metallic clusters, which, at low temperatures, transform into quantum dots with a discrete energy spectrum. It is believed that the most probable mechanism is the elastic tunneling between quantum dots under the conditions of the Kondo effect, which provides the formation of a window in the Coulomb blockage [29–31].

The growth temperature T_s = 600°C is the temperature at which the grown film is characterized by the portion $R(T)$ = const due to the influence of the system of tunnel-coupled quantum dots on the electrical properties of the samples. On the other hand, this portion $R(T)$ exhibits a weak maximum (T_{max} = 135 K) and a minimum (T_{min} = 100 K) at which the resistances differ by ~0.35%. This is associated with the effect of magnetic ordering on the electrical conductivity of the system of quantum dots. Upon cooling below the temperature T_{min}, the resistance again increases, as is the case with low-resistance samples having an orthorhombic structure.

For the films prepared at $T_s \ge 650$°C, the dependence $R(T)$ exhibits a maximum R_{max} in the vicinity of the Curie temperature (Fig. 7, curves *3*, *4*) [1–7]. At this point, the semiconductor behavior of the dependence $R(T)$ with $(dR/dT) < 0$ gives way to a metallic behavior with $(dR/dT) > 0$. Unlike the film deposited at T_s = 600°C with $(R_{max} - R_{min})/R_{max}$ = 0.35%, the film synthesized at T_s = 650°C has a resistance R_{max} that is larger than the resistance R_{min} by a factor of 7.5.

For the films grown at T_s = 650 and 700°C, the electrical conductivities equal to 3 and 27 Ω^{-1} cm^{-1} at T_{max} are one or two orders of magnitude lower than the minimum metallic conductivity [21, 32]

$$\sigma_{min} = (\pi e^2)/4z\hbar a(B/V_0)^2_{crit}, \qquad (5)$$

where z is the coordination number, V_0 is the amplitude of the random potential, and B is the band width. The minimum conductivity σ_{min} for LaSrMnO is no lower

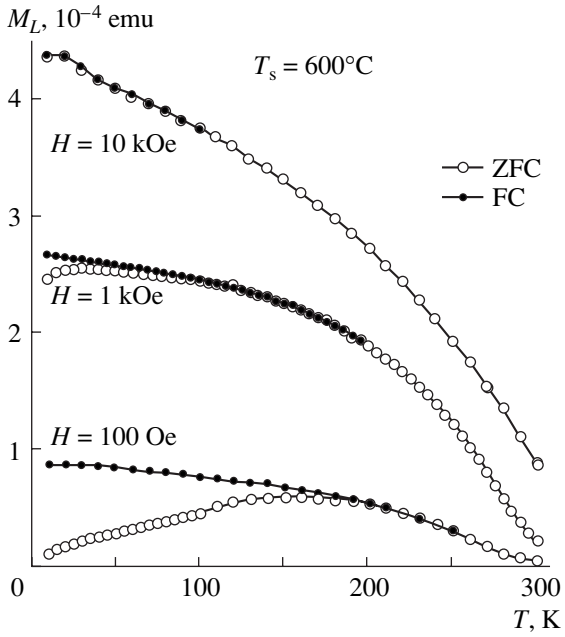

Fig. 8. Temperature dependences of the magnetization of the film grown at T_s = 600°C.

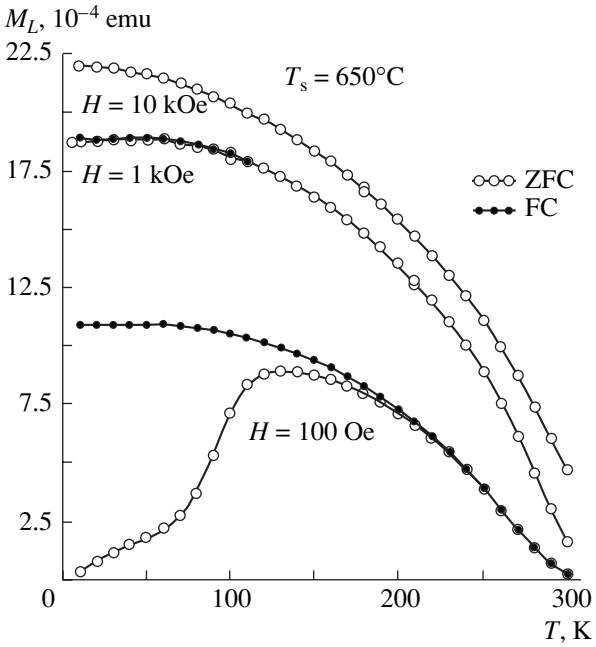

Fig. 9. Temperature dependences of the magnetization of the film grown at T_s = 650°C.

than 100 Ω^{-1} cm^{-1} [6, 33]. Therefore, the transition from a dielectric phase to a metallic phase for the samples under investigation in the vicinity of the temperature T_{max} does not occur and the similarity between the dependence $R(T)$ and the behavior of the resistance for metals is explained by the magnetic ordering, which leads to a decrease in the activation energy in the dielectric state of the films [34].

3.4. Magnetic Properties

Despite the considerable differences in the structure and the electrical and optical properties of the films grown at T_s = 600 and 650°C, there are many similarities in their magnetic properties (Figs. 8, 9). When measuring the magnetization $M(T)$ after cooling of the sample in a magnetic field (FC measurements), the magnetization M increases with a decrease in the temperature. However, the portion $M(T)$ = const (at $T < 60$ K) for the film deposited at T_s = 650°C is observed only in magnetic fields of 100 Oe and 1 kOe. At H = 10 kOe, the magnetization continuously increases with a decrease in the temperature. For the film grown at T_s = 600°C, the portion $M(T)$ = const is observed in a narrow range at $T < 40$ K only in weak fields (H = 100 Oe).

In weak fields, the dependences of the FC magnetization $M(T)$ differ significantly from the dependences $M(T)$ obtained after cooling the samples in a zero magnetic field (ZFC measurements). The ZFC dependences in weak fields have a bell-shaped form characteristic of cluster spin glasses or hard magnetic materials [35, 36]. With an increase in the field strength, the difference between the FC and ZFC dependences becomes weaker and disappears altogether for both samples in the field H = 10 kOe. On the other hand, this difference in the field H = 1 kOe is absent for the film grown at T_s = 650°C and remains significant for the film deposited at T_s = 600°C (Figs. 8, 9).

A comparison of the behavior of the films prepared at temperatures T_s = 600 and 650°C revealed a significant difference between the magnetizations: the FC magnetization (at T = 5 K) of the film grown at T_s = 650°C is higher than the magnetization of the film synthesized at T_s = 600°C by a factor of 5 in the field H = 10 kOe and by a factor of 14 in the field H = 100 Oe.

4. DISCUSSION

The relation of the electrical, optical, and magnetic properties of the films to their structure is of great interest. As follows from the x-ray diffraction data, the contents $C_{Mn–O}$ of Mn–O clusters in the films grown at T_s = 600 and 650°C differ insignificantly and are equal to 10.7 and 11.1%, respectively. According to the optical measurements, the contents C_m of the metallic phase in the same samples are equal to 0.5 and 8.5%, respectively. As is known [4], the Mn–O distance decreases with an increase in the charge state of Mn ions and is minimum for the Mn^{4+}–O bond. The observed changeover to the predominance of contracted planes in Mn–O clusters with an increase in the synthesis temperature T_s (Figs. 1, 2) reflects an increase in the content of Mn^{4+} ions. At the same time, the close values of $C_{Mn–O}$ and C_m for the film synthesized at T_s = 650°C and the

substantial difference between these quantities for the film prepared at T_s = 600°C demonstrate that not all Mn–O clusters but clusters characterized by contracted planes (Figs. 2–4, range $d < d_c$) predominantly contribute to the metallic conductivity. The metallic clusters containing highly ionized Mn ions (Mn^{3+}, Mn^{4+}) bonded to oxygen play an important role in the electrical conduction of the samples (an increase in C_m with a change in the growth temperature T_s from 600 to 650°C results in a decrease in the resistivity at liquid-nitrogen temperatures by four orders of magnitude) and substantially affect the optical and magnetic properties of the films.

For the film grown at T_s = 650°C, the dependence $R(T)$ in the range 30.7 K < T < 280 K exhibits a metallic behavior with $\sigma = 3\ \Omega^{-1}\ cm^{-1}$ in the range of the maximum. This value of the conductivity is one or two orders of magnitude lower than the minimum conductivity $\sigma_{min} = 10^3$–$10^2\ \Omega^{-1}\ cm^{-1}$. Below the Curie temperature, the dependence $R(T)$ with the derivative $(dR/dT) > 0$ is governed by the influence of magnetic ordering on the electrical conductivity of the sample. This film is characterized by the gapless state (E_{g1} = 0 eV) and strong absorption over a wide spectral range due to the high density of states.

In the case when the film is deposited at T_s = 600°C with $\rho = 10^2\ \Omega$ cm (T = 300 K), the dependence $R(T)$ exhibits a different behavior: $R(T) \approx$ const with an accuracy of several percent in the range 60–170 K. This is explained by the participation of the system of tunnel-coupled quantum dots in the conduction and is typical of rhombohedral samples [6]. The structure of the film prepared at T_s = 600°C is intermediate between structures of two types. Orthorhombic clusters with metallic conductivity in the film are responsible for its specific features characteristic of low-resistance objects, namely, the occurrence of a weak maximum and a weak minimum in the dependence $R(T)$ and an increase in the resistance at $T < T_{min}$ (Fig. 7). The electronic and magnetic subsystems strongly interact in the temperature range from T_{max} to T_{min}. The temperatures T_{min} and T_{max} are related by the empirical expression

$$T_{min} = \alpha T_{max} + \gamma, \tag{6}$$

where α = –0.46 and γ = 154.32 (see inset to Fig. 7). The left end point (at T_{min} = 100 K, T_{max} = 135 K) in this straight line corresponds to the film synthesized at T_s = 600°C. The right end point corresponds to the film grown at T_s = 650°C.

No portions $R(T) \approx$ const are observed for the films in the orthorhombic phase. The spacing between the quantum-confinement levels depends on the cluster size D and the hole concentration p [(the density of states at the Fermi level $N(E_F)$] and can be represented by the relationship

$$\Delta \approx \frac{1}{D^3 N(E_F)} \approx \frac{1}{D^3 p/N(E_F)}. \tag{7}$$

According to the x-ray diffraction data, we have D = 140 and 130 Å for the films grown at T_s = 600 and 650°C, respectively. If the critical temperature T_{crit} of the crossover from the activation behavior of the temperature dependence of the resistance R to a behavior corresponding to $R(T) \approx$ const is determined by the condition

$$\Delta \approx kT_{crit}, \tag{8}$$

this temperature due to the high density of states in clusters with the orthorhombic structure appears to be too low for the portion $R(T)$ = const to be observed. A high critical temperature for the rhombohedral films (T_{crit} = 170 K at T_s = 600°C) suggests that the hole concentration in metallic rhombohedral clusters is lower than the hole concentration in clusters in films with an orthorhombic structure. Indeed, the optical absorption coefficients α proportional to the density of states $N(E)$ for the films prepared at T_s = 600 and 650°C differ significantly (by a factor of four or five at $\hbar\omega$ < 1.2 eV) only in the range in which intraband optical transitions associated with the absorption by free charge carriers are possible. For comparison, at $\hbar\omega$ > 2.0 eV, we have $\alpha(650)/\alpha(600) < 1.5$.

The density of states associated with the Mn^{3+}–O and Mn^{4+}–O interionic interactions affects the magnetic properties of the samples and the effect of the magnetic subsystem on the electrical properties. For the film grown at T_s = 650°C, the resistance upon cooling from 280 (T_{max}) to 30.7 K (T_{min}) decreases by one order of magnitude and the normalized derivative $(dR/dT)/R$ can be as large as 1.29% per degree at T = 209.2 K. However, the metallic state is not observed even at T_{min} ($\rho = 4.4 \times 10^{-2}\ \Omega$ cm) and the resistance again increases at temperatures below T_{min}. The temperature T_{min} can be attributed to the temperature of charge ordering [37–39]. By bringing the dependences $R(T)$ and $M(T)$ into coincidence, we find that the maximum in the dependence $R(T)$ corresponds to the slope in the dependence $M(T)$. Consequently, we can draw the inference that there are threshold states of the magnetic subsystem at which the electronic properties of the samples begin to change. The behaviors of dependences $R(T)$ and $M(T)$ correspond to each other. For example, the FC magnetization $M(T)$ and the resistance $R(T)$ vary only slightly at T < 80 K (Figs. 7, 9). Below the "freezing" temperature $T_f \approx$ 130 K at H = 100 Oe (ZFC measurements), the derivative dR/dT decreases considerably.

In the case of the film deposited at T_s = 600°C, cooling from T = 300 K leads to an increase in the resistance and the magnetization. At T < 180 K, the dependences of the FC magnetization $M(T)$ in weak fields (H =

100 Oe) and the resistance $R(T)$ flatten out and the ZFC magnetization $M(T)$ decreases. The magnetic ordering also affects the dependence $R(T)$. However, this effect on the electrical conductivity of the system formed by tunnel-coupled quantum dots is rather weak (the resistances at the maximum and the minimum differ by 0.35%). If the effect of the magnetic ordering on the electrical conductivity is evaluated according to the derivative dR/dT at $T < T_{max}$, this effect for the film prepared at $T_s = 650°C$ turns out to be three orders of magnitude weaker than that for the film synthesized at $T_s = 650°C$. It should be noted that the behavior of the LaSrMnO films (with ferromagnetic clusters), whose dependences contain portions $\rho(T) \approx$ const with nonmonotonic variations in $\rho(T)$, differs significantly from the behavior of YBaCuO films for which nonmonotonic variations in the portions $\rho(T) \approx$ const are absent [17].

The magnetization of the film deposited at $T_s = 600°C$ is one order of magnitude lower than that of the film grown at $T_s = 650°C$. Therefore, in order to provide the conditions at which the magnetic ordering affects the electrical properties, it is necessary to perform cooling to lower temperatures. This can be associated not only with the lower density of states but also with the weak effect of the magnetic ordering on the electrical conductivity of the system of tunnel-coupled quantum dots. Actually, the maximum in the dependence $R(T)$ at $T = 135$ K corresponds to the temperatures at which the FC magnetization $M(T)$ remains almost unchanged [$M(135\text{ K}) \approx 0.85M(10\text{ K})$ at $H = 100$ Oe, 1 kOe] and to the maximum in the dependence of the ZFC magnetization. For the film grown at $T_s = 650°C$ with $T_{max} = 277$ K, we have $M(277\text{ K}) = 0.05M(10\text{ K})$ and $M(277\text{ K}) = 0.14M(10\text{ K})$ in magnetic fields $H = 100$ Oe and 1 kOe, respectively.

According to the x-ray diffraction and optical absorption data, the content of the metallic phase in the films under investigation is determined to be $C_m < 20\%$. Since the percolation threshold for the metallic conductivity in the films is estimated at $C_m^{crit} \approx 0.5$ [40, 41], the tunneling is the main mechanism of electrical conduction. The magnetoresistance of the samples monotonically decreases with an increase in the temperature [6]. This is typical of spin-dependent tunneling [42, 43]. When electrons tunnel between metallic clusters through high-resistance interlayers, the resistivity can be written in the form

$$\rho = \rho_0 \exp(L/L_0), \tag{9}$$

where L is the mean distance between grains. In the case of a lattice composed of identical clusters, the intercluster distance is defined by the relationship

$$L = D/L_0[(\gamma C_m)^{-1/3} - 1], \tag{10}$$

where the factor γ is determined by the cluster shape. For flat clusters (the thickness is equal to one-third of the linear size D), we have $\gamma = 3$.

If the mechanism of magnetic ordering in samples with an inhomogeneous structure is associated with the tunneling coupling between ferromagnetic clusters, the coupling energy W decreases with an increase in the distance and can be represented in the following form:

$$W = W_0 \exp[-(L/L_1)]. \tag{11}$$

In the range of the maximum in the dependence $R(T)$, the thermal energy is at equilibrium with the energy W of tunneling coupling between clusters; that is,

$$kT_{max} = W. \tag{12}$$

The probability of electron tunneling between clusters can depend on the Coulomb blockage, which affects the electrical conductivity of granular systems [42], and decreases with an increase in the charge energy,

$$E_c = e^2/\varepsilon D, \tag{13}$$

where e is the elementary charge and ε is the permittivity. Since the cluster size varies only slightly, the magnetic properties are predominantly governed by the content C_m of the metallic phase and the density of states $N(E_F)$). An increase in the content C_m of the metallic phase (from 0.5 to 8.5%) with a change in the synthesis temperature T_s from 600 to 650°C and the corresponding decrease in the intercluster distance L lead to an increase in the coupling energy W by a factor of 14. This is accompanied by an increase in the magnetization. Moreover, an increase in the magnetization is favored by an increase in the density of states upon transition from the rhombohedral structure to the orthorhombic structure [6].

Let us consider the possible mechanism responsible for the decrease in the resistance of the films at $T < T_{max}$ in the case when the tunneling is the governing mechanism of interaction between clusters. As follows from the dependences depicted in Figs. 8 and 9, the size D of ferromagnetic clusters increases upon cooling of the samples. An increase in the size of ferromagnetic clusters in the antiferromagnetic matrix manifests itself in a decrease in the length of the portion $M =$ const with an increase in the field strength from 100 Oe to 10 kOe (Fig. 9) or in the absence of this portion in fields $H \geq 1$ kOe (Fig. 8). The temperature dependence of the cluster size can be obtained in an explicit form under the assumption that the cluster size D and the correlation length ξ in the percolation theory vary in a similar manner. As the content C_m of the metallic phase approaches the percolation threshold C_m^{crit}, the correlation length ξ increases according to the power law [40]

$$\xi(C_m) \sim \left|C_m - C_m^{crit}\right|^{-\nu},$$

where $\nu = 0.85$ is the critical exponent of the correlation length. By assuming that, upon cooling of the samples below the Curie temperature, the content C_m

of the metallic phase varies linearly with the temperature, that is,

$$C_m = C_m^{(0)} + B(T_{max} - T), \quad T \le T_{max}, \tag{14}$$

the dependence $D(T)$ can be represented in the form

$$D(T) \approx D^{(0)}\left|[C_m^{(0)} + B(T_{max} - T)] - C_m^{crit}\right|^{-\nu}. \tag{15}$$

Therefore, in the temperature range $\Delta T = T_{max} - T_{min}$, we have

$$\rho = \rho_0 \exp\left\{\frac{D^{(0)}}{L_0}\left|[C_m^{(0)} + B(T_{max} - T)] - C_m^{crit}\right|^{-\nu} \times \left[\gamma^{-\frac{1}{3}}[C_m^{(0)} + B(T_{max} - T)]^{-\frac{1}{3}} - 1\right]\right\}. \tag{16}$$

By introducing the designations $C_m^{(0)} + BT_{max} = X$ and $C_m^{(0)} + BT_{max} - C_m^{crit} = Y$ and taking into account that $BT/X < 1$, relationship (16) can be rewritten in the more instructive form

$$\rho = \rho_0 \exp\left\{\frac{D^{(0)}}{L_0}\frac{\left[(\gamma X)^{-1/3}\left(1 + \frac{1}{3}\frac{B}{X}T\right) - 1\right]}{|Y|^{\nu}\left|1 - \frac{B}{Y}T\right|^{\nu}}\right\}. \tag{17}$$

It can be seen from this expression that, for the model under consideration, the resistivity decreases with a decrease in the temperature. This behavior of the dependence $\rho(T)$ is in agreement with the experimental data.

5. CONCLUSIONS

Thus, the transition of LaSrMnO films from a rhombohedral structure to an orthorhombic structure was investigated in the critical range of growth temperatures (600–650°C). It was demonstrated that the fundamental difference between these films is associated with both the rhombohedral $\longrightarrow$ orthorhombic transformation of the dominant atomic order in the cluster structure and the changes in the content of the metallic phase and in the local density of atomic and electronic states. For films with a rhombohedral structure (prepared at the chosen temperatures, including $T_s = 600$°C), the distortions of the unit cell play an important role and the low density of states is caused by an increase in the interatomic distances with an increase in the unit cell volume.

It was shown that a decrease in the resistance of the LaSrMnO films with a decrease in the temperature is governed by the magnetic ordering of metallic clusters in the dielectric matrix and occurs at contents of the metallic (ferromagnetic) phase considerably below the percolation threshold. The formation of the magnetically ordered state is assisted by an enhancement of the interaction between tunnel-coupled clusters in the form of contracted planes involving Mn^{3+} and Mn^{4+} ions in comparable amounts.

The inference was made that the observed metallic behavior of the dependence $R(T)$ stems from the increase in the size and the concentration of metallic clusters due to an enhancement of the ferromagnetic interaction between them. When a continuous path for charge carriers over metallic regions is absent, the electrical conductivity of the films is limited by tunneling of charge carriers between the clusters.

At a low density of states, clusters with a decrease in the temperature can transform into a system of tunnel-coupled quantum dots. This manifests itself in the appearance of the portion $R(T) \approx$ const in the dependence $R(T)$.

ACKNOWLEDGMENTS

This work was supported in part by the Polish government, grant no. PBZ-KBN-013/T08/19.

REFERENCES

1. É. L. Nagaev, Usp. Fiz. Nauk **166** (8), 833 (1966) [Sov. Phys. Usp. **39**, 781 (1966)].
2. M. O. Dzero, L. P. Gor'kov, and V. Z. Kresin, Eur. Phys. J. B **14**, 459 (2000).
3. V. E. Naĭsh, Fiz. Met. Metalloved. **92** (5), 16 (2001).
4. J. M. D. Coey, M. Viret, and S. von Molnsr, Adv. Phys. **48** (2), 167 (1999).
5. M. B. Salamon and M. Jaime, Rev. Mod. Phys. **73**, 583 (2001).
6. Z. A. Samoĭlenko, V. D. Okunev, E. I. Pushenko, T. A. D'yachenko, A. Cherenkov, P. Gierlowski, S. J. Lewandowski, A. Abal'oshev, A. Klimov, and A. Szewczyk, Zh. Tekh. Fiz. **73** (2), 118 (2003) [Tech. Phys. **48**, 250 (2003)].
7. Yu. A. Boĭkov, T. Claeson, and A. Yu. Boĭkov, Fiz. Tverd. Tela (St. Petersburg) **45** (6), 1040 (2003) [Phys. Solid State **45**, 1090 (2003)].
8. Y. G. Zhao, R. C. Srivastava, P. Fournier, V. Smolyaninova, M. Rajeswari, T. Wu, Z. Y. Li, R. L. Greene, and T. Venkatesan, J. Magn. Magn. Mater. **220**, 161 (2000).
9. T. Venkatesan, X. D. Wu, R. Muenchausen, and A. Pique, MRS Bull. **17**, 54 (1992).
10. C. Ghica, M. Valeanu, L. C. Vistor, V. Teodorescu, C. Sandu, C. Ristoscu, I. N. Mihailescu, J. Werckmann, and J.-P. Deville, Int. J. Inorg. Mater. **3** (8), 1253 (2001).
11. S. Kanazawa, T. Ito, K. Yamada, T. Ohkubo, Y. Nomoto, T. Ishihara, and Y. Takita, Surf. Coat. Technol. **169–170**, 508 (2003).
12. R. K. Singh and J. Narayan, Phys. Rev. B **41** (13), 8843 (1990).
13. V. D. Okunev, Z. A. Samoilenko, V. M. Svistunov, A. Abal'oshev, E. Dynowska, P. Gierlowski, A. Klimov,

and S. J. Lewandowski, J. Appl. Phys. **85** (10), 7282 (1999).

14. Q. Huang, A. Santoro, J. W. Lynn, R. W. Erwin, J. A. Borchers, J. L. Peng, and R. L. Greene, Phys. Rev. B **55** (22), 14 987 (1997).
15. V. D. Okunev, Z. A. Samoilenko, A. Abal'oshev, A. Abal'osheva, P. Gierlowski, A. Klimov, S. J. Lewandowski, V. N. Varyukin, and S. Barbanera, Phys. Rev. B **62** (1), 696 (2000).
16. V. D. Okunev, Z. A. Samoĭlenko, V. A. Isaev, A. Klimov, and S. J. Lewandowski, Pis'ma Zh. Tekh. Fiz. **28** (2), 12 (2002) [Tech. Phys. Lett. **28**, 44 (2002)].
17. V. D. Okunev, N. N. Pafomov, V. A. Isaev, T. A. D'yachenko, A. Klimov, and S. J. Lewandowski, Fiz. Tverd. Tela (St. Petersburg) **44** (1), 150 (2002) [Phys. Solid State **44**, 157 (2002)].
18. S. G. Kaplan, M. Quijada, H. D. Drew, D. B. Tanner, G. C. Xiong, R. Ramesh, C. Kwon, and T. Venkatesan, Phys. Rev. Lett. **77** (10), 2081 (1996).
19. Y. Okimoto, T. Katsufuji, T. Ishikawa, T. Arima, and T Tokura, Phys. Rev. B **55** (7), 4206 (1997).
20. N. N. Loshkareva, Yu. P. Sukhorukov, E. V. Mostovshchikova, L. V. Nomerovannaya, A. A. Makhnev, S. V. Naumov, E. A. Gan'shina, I. K. Rodin, A. S. Moskvin, and A. M. Balbashov, Zh. Éksp. Teor. Fiz. **121** (2), 412 (2002) [JETP **94**, 350 (2002)].
21. N. F. Mott and E. A. Davis, *Electronic Processes in Non-Crystalline Materials*, 2nd ed. (Clarendon, Oxford, 1979; Mir, Moscow, 1982), Vol. 1.
22. A. S. Moskvin, E. V. Zenkov, Yu. D. Panov, N. N. Loshkareva, Yu. P. Sukhorukov, and E. V. Mostovshchikova, Fiz. Tverd. Tela (St. Petersburg) **44** (8), 1452 (2002) [Phys. Solid State **44**, 1519 (2002)].
23. M. F. Hundley and J. J. Neumeier, Phys. Rev. B **55** (17), 11 511 (1997).
24. M. D. Coey, M. Viret, L. Ranno, and K. Ounagjela, Phys. Rev. Lett. **75**, 3910 (1995).
25. V. G. Prokhorov, G. G. Kaminskiĭ, V. S. Flis, and Yang Pak Li, Fiz. Nizk. Temp. **25** (10), 1060 (1999) [Low Temp. Phys. **25**, 792 (1999)].
26. M. Ziese and C. Srinitiwarawong, Phys. Rev. B **58** (17), 11 519 (1998).
27. I. O. Troyanchuk, L. S. Lobanovskiĭ, D. D. Khalyavin, V. P. Yarunichev, N. V. Pushkarev, and G. Shimchak, Zh. Éksp. Teor. Fiz. **116** (2), 604 (1999) [JETP **89**, 321 (1999)].
28. V. D. Okunev, N. N. Pafomov, A. Abaleshev, H. Belska-Lewandowska, P. Gierlowski, A. Klimov, and S. Lewandowski, Pis'ma Zh. Tekh. Fiz. **26** (20), 20 (2000) [Tech. Phys. Lett. **26**, 903 (2000)].
29. L. I. Glazman and M. É. Raĭkh, Pis'ma Zh. Éksp. Teor. Fiz. **47**, 378 (1988) [JETP Lett. **47**, 452 (1988)].
30. T. K. Ng and P. A. Lee, Phys. Rev. Lett. **61**, 1768 (1988).
31. K. Kikoin and Y. Avishai, Phys. Rev. Lett. **86**, 2090 (2001).
32. N. F. Mott, *Metal–Insulator Transitions*, 2nd ed. (Taylor and Francis, London, 1990; Nauka, Moscow, 1979).
33. A. E. Kar'kin, D. A. Shulyatev, A. A. Arsenov, V. A. Cherepanov, and E. A. Filonova, Zh. Éksp. Teor. Fiz. **116** (2), 671 (1999) [JETP **89**, 358 (1999)].
34. N. G. Bebenin, R. I. Zaĭnullina, V. V. Mashkautsan, V. S. Gaviko, V. V. Ustinov, Ya. M. Mukovskiĭ, and D. A. Shulyatev, Zh. Éksp. Teor. Fiz. **117** (6), 1181 (2000) [JETP **90**, 1027 (2000)].
35. R. V. Demin, L. I. Koroleva, R. Shimchak, and G. Shimchak, Pisma Zh. Éksp. Teor. Fiz. **75** (7), 402 (2002) [JETP Lett. **75**, 331 (2002)].
36. I. O. Troyanchuk, O. S. Mantytskaya, A. N. Chobot, and G. Shimchak, Zh. Éksp. Teor. Fiz. **122** (2), 347 (2002) [JETP **95**, 300 (2002)].
37. S. F. Dubinin, V. E. Arkhipov, M. Ya. Mukovskiĭ, V. E. Naĭsh, V. D. Parkhomenko, and S. G. Teploukhov, Fiz. Met. Metalloved. **93** (3), 60 (2002).
38. É. A. Neĭfel'd, V. E. Arkhipov, N. A. Tumalevich, and Ya. M. Mukovskiĭ, Pis'ma Zh. Éksp. Teor. Fiz. **74** (11), 630 (2001) [JETP Lett. **74**, 556 (2001)].
39. U. Staub, G. I. Meijer, F. Fauth, R. Allenspach, J. G. Bednorz, J. Karpinski, S. M. Kazakov, L. Paolasini, and F. d'Acapito, Phys. Rev. Lett. **88** (12), 126402 (2002).
40. B. I. Shklovskiĭ and A. L. Éfros, *Electronic Properties of Doped Semiconductors* (Nauka, Moscow, 1979; Springer, New York, 1984).
41. A. B. Khanikaev, A. B. Granovskiĭ, and J.-P. Clerc, Fiz. Tverd. Tela (St. Petersburg) **44** (9), 1537 (2002) [Phys. Solid State **44**, 1611 (2002)].
42. J. S. Helman and B. Abeles, Phys. Rev. Lett. **37** (21), 1429 (1976).
43. S. Lee, H. Y. Hwang, B. I. Shraiman, W. D. Ratcliff, and S.-W. Cheong, Phys. Rev. Lett. **82** (22), 4508 (1999).

Translated by O. Borovik-Romanova

Physics of the Solid State, Vol. 46, No. 10, 2004, pp. 1906–1909. Translated from Fizika Tverdogo Tela, Vol. 46, No. 10, 2004, pp. 1841–1844.

MAGNETISM AND FERROELECTRICITY

Dielectric Properties of Thin $PbTiO_3$ Films

A. S. Sidorkin, A. M. Solodukha, L. P. Nesterenko, S. V. Ryabtsev, I. A. Bocharova, and G. L. Smirnov

Voronezh State University, Universitetskaya pl. 1, Voronezh, 394062 Russia

e-mail: sidorkin@dom.vsu.ru, sam@main.vsu.ru, phssd28@main.vsu.ru, bocharova@phys.vsu.ru, green_sm@list.ru

Received December 16, 2003

Abstract—The electrophysical properties and phase composition of thin lead titanate films prepared on various substrates by layer-by-layer magnetron sputtering of metals followed by annealing have been studied. The main parameters of the metal–ferroelectric film–metal multilayer structures, namely, the spontaneous polarization, coercive field, and permittivity, were studied for various substrate types and electrode materials. The conditions favorable for the formation of $PbTiO_3$ films that are similar in stoichiometry and phase composition were established. © *2004 MAIK "Nauka/Interperiodica".*

1. INTRODUCTION

Lead titanate–based thin-film ferroelectric structures have device potential in microelectronics in the area of memory elements, IR and ultrasonic sensors, and electric meters with a low threshold voltage. Also, $PbTiO_3$ films feature a high remanent polarization and good pyro- and piezoelectric properties. Recent publications report on the preparation of these films by using various techniques and on probing of their dielectric characteristics [1–4]. However, before progress in the development and use of $PbTiO_3$ films in devices becomes a reality, the problems associated with optimization of the parameters of thin-film structures will have to be solved.

This motivated the present investigation of the phase composition and dielectric properties of the above structures prepared under different conditions and with different materials used for the substrate and the electrodes. The substrate materials employed were polycrystalline titanium, single-crystal silicon, and polycor (Al_2O_3). Since the preparation and properties of lead titanate films on titanium and silicon substrates were already analyzed in detail in [5–7], we focus our attention primarily on samples prepared on polycor substrates.

2. PREPARATION OF THIN LEAD TITANATE FILMS

$PbTiO_3$ films on substrates of polycor (Al_2O_3) were prepared by depositing titanium and lead layer by layer. The metal layers were applied by plasma-enhanced magnetron sputtering in an argon environment. The sputtering was carried out without interruption in a chamber evacuated to a pressure $P = 0.33 \times 10^{-2}$ Pa. To obtain a polycrystalline film with a stoichiometric Ti/Pb ratio, the sputtering was performed with an excess of lead (~5 at. %) with respect to titanium to compensate for lead evaporation during the subsequent annealing.

To optimize the technology of film preparation, the annealing conditions of the layered structures thus formed were varied depending on the x-ray diffraction data and studies of the ferroelectric properties. The annealing was performed in a resistive furnace in oxygen and consisted of two stages. The first stage included annealing at 200°C for 10 min (lead oxidation reaction), and the second stage was performed at 600°C (likewise for 10 min) to complete the reaction between the titanium and lead oxides. After that, the sample was heated from room temperature to 650°C over 2 h.

Gradual heating of a sample from room temperature to 650°C over ~2 h was used as another method of annealing.

The structures subjected to the two-stage annealing exhibited thermally unstable dielectric properties; indeed, in three consecutive measurements of the temperature dependence of the sample capacitance, which were performed at temperatures ranging from room temperature to 600°C, the permittivity at the maximum decreased to become, in the third measurement, one-fifth of the value obtained in the first run. The dielectric hysteresis loops were close to elliptical in shape. This behavior finds explanation in the fact that the chemical reaction among the components (titanium, lead, oxygen), rather than coming to an end, became reactivated as the sample was heated during the dielectric measurements, which is corroborated by studies of the phase composition.

Continuous annealing with the temperature raised from room temperature to 650°C was found to be the optimum regime, because the lead titanate films grown in these conditions proved to have the best phase composition and thermally stable dielectric properties. The final film thickness after annealing was 1 μm.

1063-7834/04/4610-1906$26.00 © 2004 MAIK "Nauka/Interperiodica"

The film phase composition was checked by x-ray diffraction analysis. The samples obtained by two-stage annealing were a mixture of the $PbTiO_3$ stoichiometric perovskite phase, $PbTi_3O_7$ and $PbTi_3O_5$ nonstoichiometric phases, and unreacted metal oxides. The material obtained under continuous annealing revealed predominantly the stoichiometric phase. The diffraction pattern (Fig. 1) exhibits only distinct strong lines indicative of $PbTiO_3$.

Top and bottom electrodes were deposited on lead titanate films for measurement of their dielectric properties. Nickel, platinum, and gold metal films were used as electrodes to optimize the dielectric measurements. Ni and Pt were applied to a substrate by magnetron and cathode sputtering, respectively, and Au, by thermal deposition. The thickness of metal layers was varied from 100 to 500 nm. The metal layers applied to a dielectric substrate were tested for thermal stability by heating them to 750°C. When heated above 400°C, the nickel layer oxidized and lost metallic conduction. The gold layer persisted to a temperature of 600°C, above which a thin gold layer (300 nm) lost metallic conductivity as a result of interaction with the substrate. The platinum layer remained metallic up to 750°C for a thickness of 500 nm; thinner films degraded because of sublimation of the platinum oxide. As a result, in order to measure the dielectric properties of lead titanate films, we chose a platinum layer no less than 500 nm thick for the bottom electrode and gold for the top electrode, because thermal evaporation is more convenient for deposition of the top electrode. Note that platinum is the best choice for the bottom electrode material when studying the dielectric properties of ferroelectric films, which is supported by data from the literature [8, 9].

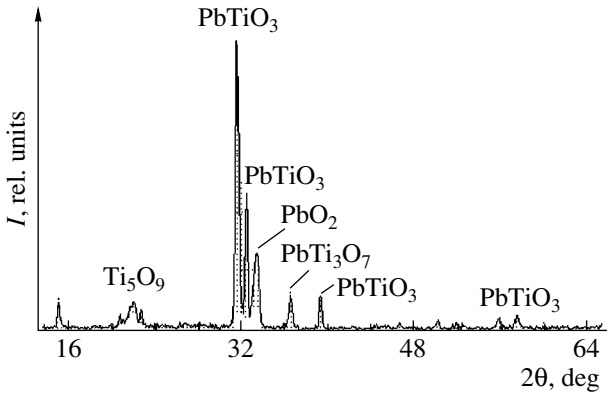

Fig. 1. Diffraction pattern of lead titanate $PbTiO_3$ films grown on a polycor substrate.

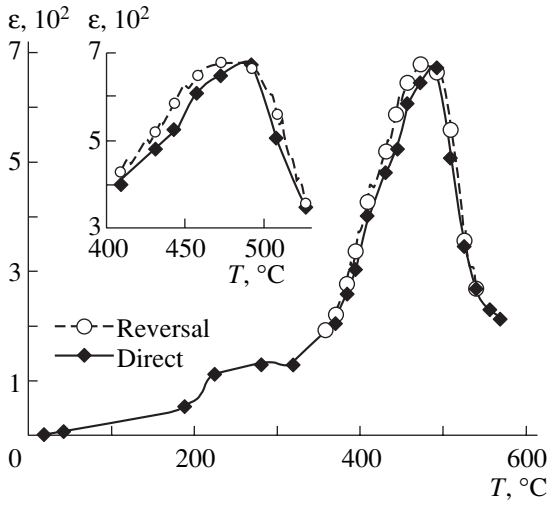

Fig. 2. Direct and reverse course of the temperature dependence of lead titanate film permittivity ε.

3. DIELECTRIC MEASUREMENTS

To determine the temperature behavior of the permittivity of lead titanate films on a polycor substrate, the sample capacitance was measured at a frequency of 1 kHz. The sample was placed in a resistive furnace, and the temperature was monitored with a chromel–alumel thermocouple. The heating rate was 2°C/min. Dielectric hysteresis loops were studied by means of an electronic attachment that made it possible to compensate for the conductivity contribution growing with temperature and to observe the loop caused by the nonlinear dielectric properties of the sample alone.

Figure 2 displays the temperature dependence of the permittivity, which is characteristic of ferroelectric materials and gives a curve with a maximum at a phase transition temperature of about 500°C. The permittivity exhibits a temperature hysteresis, which is typical of compounds undergoing a first-order phase transition and consists in a shift of the $\varepsilon(T)$ curve by about 10°C. There is also a small anomaly at a temperature of about 200°C; this anomaly should be assigned, according to the literature data, to the presence of electrons weakly bound to doubly charged centers, which become depleted when heated above 200°C, as observed with lead titanate single crystals [10]. The curve preserves its shape in repeated measurements.

The Curie–Weiss law was shown to be met; the $\varepsilon^{-1}(T)$ curve is displayed in Fig. 3. As follows from calculations, the "fourfold law" (~3.6–3.9) is satisfied for the material under study; i.e., the slopes of the ε^{-1} versus temperature straight lines measured above and below the Curie temperature differ by a factor of approximately 4. The Curie constant is $C \sim 4 \times 10^5$°C, which likewise supports the phase transition being first-order.

Figure 4 shows dielectric hysteresis loops at different temperatures. They have a shape characteristic of ferroelectric materials.

Figures 5 and 6 give the temperature dependences of the spontaneous polarization and coercive field for lead titanate films. Both quantities fall off with increasing

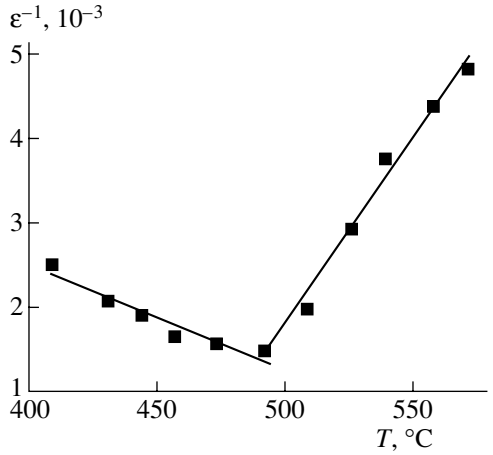

Fig. 3. Curie–Weiss law for $PbTiO_3$ films on a polycor substrate.

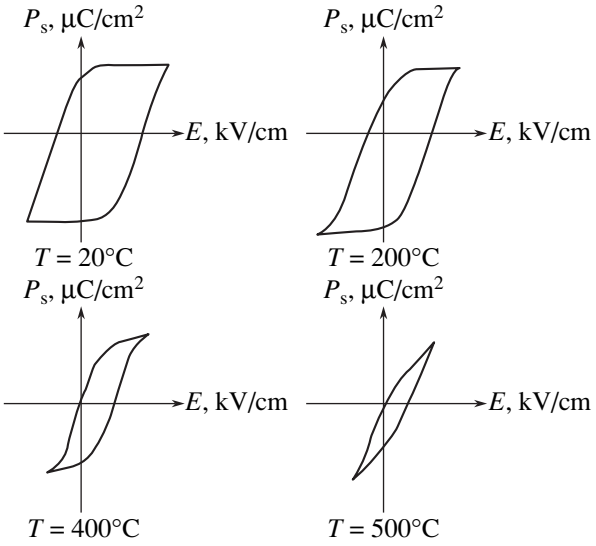

Fig. 4. Variation of dielectric hysteresis loops of $PbTiO_3$ films with increasing temperature.

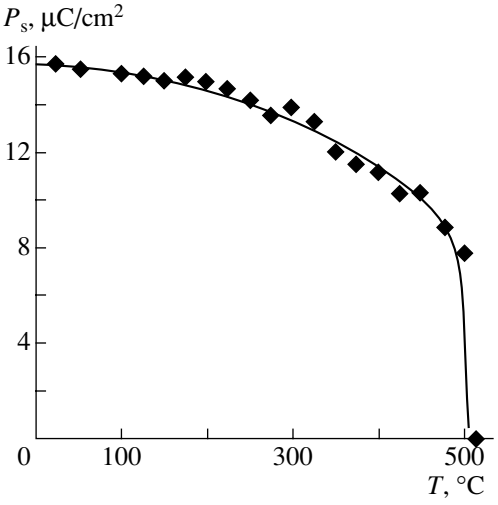

Fig. 5. Temperature dependence of the spontaneous polarization P_s of $PbTiO_3$ films.

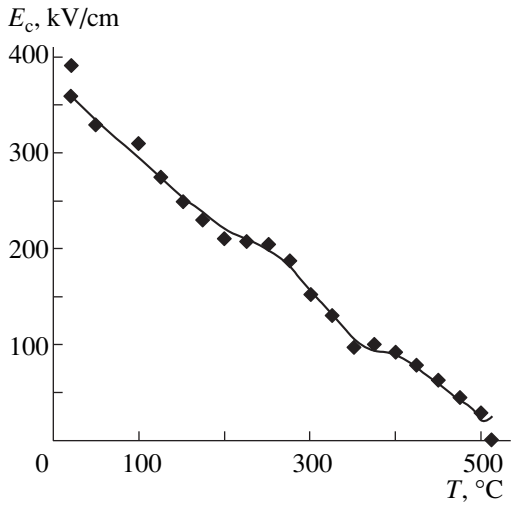

Fig. 6. Temperature dependence of the coercive field E_c of lead titanate films.

temperature to vanish at the Curie point, which bears out the ferroelectric nature of the material prepared. The shape of the $P_s(T)$ curve is characteristic of a ferroelectric undergoing a first-order phase transition.

The results from comparing films grown on different substrates are listed in the table. Note that the $\varepsilon(T)$, $P_s(T)$, $E_c(T)$, and $\varepsilon^{-1}(T)$ dependences for thin film structures grown on all the substrates studied follow a similar pattern characteristic of ferroelectric materials; namely, there is a phase transition point near 500°C and an anomaly at a temperature of about 200°C and the spontaneous polarization and coercive field vanish at the Curie point. The values of the Curie–Weiss constant are also similar and equal to $(3.6–3.9) \times 10^5$°C. However, the films grown on a polycor substrate feature a narrower maximum in $\varepsilon(T)$ at the phase transition point and the largest permittivity near the Curie temperature, as well as exhibiting the largest relative change in permittivity over the temperature range from room temperature to the phase transition point (see table). Structures formed on silicon have the broadest permittivity maximum. The dielectric hysteresis loops saturate only in films grown on a polycor substrate, while exhibiting the highest coercive fields in this case.

Parameters of lead titanate films on various substrates

Substrate material	ε		P_s, μC/cm^2 (T = 20°C)	E_c, kV/cm (T = 20°C)	References
	T = 20°C	$T = T_c$			
Si	40–60	550–600	10–25	100–300	[5–7]
Ti	30–50	200–250	18–20	80–100	[5–7]
Al_2O_3	10–30	650–700	14–16	200–400	This work

4. CONCLUSIONS

To sum up, lead titanate films grown on polycor substrates are a promising material for use in electronics and microelectronics. Their application in practice, however, would require additional studies of the stability of the properties of this material.

ACKNOWLEDGMENTS

This study was supported by CRDF (project no. VZ-010) and the Ministry of Education of the Russian Federation.

REFERENCES

1. M. Okuyama, J. Asano, T. Imai, Don-Hee, and J. Hamakawa, Jpn. J. Appl. Phys. **32**, 4107 (1993).
2. H. Maiwa, N. Ichinose, and K. Okazaki, Jpn. J. Appl. Phys. **31**, 3029 (1992).
3. T. Okamura, M. Adachi, T. Shiosaki, and A. Kawabata, Jpn. J. Appl. Phys. **30** (4), 727 (1991).
4. H. Funakubo, T. Hioki, M. Otsu, K. Shimozaki, and N. Mizutani, Jpn. J. Appl. Phys. **32**, 4175 (1993).
5. A. S. Sidorkin, L. P. Nesterenko, I. A. Bocharova, V. A. Sidorkin, and G. L. Smirnov, Ferroelectrics **286**, 335 (2003).
6. A. S. Sidorkin, A. S. Sigov, A. M. Khoviv, S. O. Yatsenko, and O. B. Yatsenko, Fiz. Tverd. Tela (St. Petersburg) **42** (4), 727 (2000) [Phys. Solid State **42**, 745 (2000)].
7. A. S. Sidorkin, A. S. Sigov, A. M. Khoviv, O. B. Yatsenko, and V. A. Logacheva, Fiz. Tverd. Tela (St. Petersburg) **44** (4), 745 (2002) [Phys. Solid State **44**, 774 (2002)].
8. I. L. Baginskiĭ and É. G. Kostsov, Mikroélektronika **26** (4), 278 (1997).
9. V. R. Palkar, S. C. Purandare, and R. Pinto, J. Phys. D: Appl. Phys. **32**, R1 (1999).
10. L. N. Korotkov, S. A. Gridnev, and A. A. Khodorov, Izv. Ross. Akad. Nauk, Ser. Fiz. **66** (6), 834 (2002).

Translated by G. Skrebtsov

Physics of the Solid State, Vol. 46, No. 10, 2004, pp. 1910–1913. Translated from Fizika Tverdogo Tela, Vol. 46, No. 10, 2004, pp. 1845–1848.

MAGNETISM AND FERROELECTRICITY

Photostimulated Conductivity in Relaxors

S. A. Migachev, M. F. Sadykov, and R. F. Mamin

Zavoĭskiĭ Physicotechnical Institute, Russian Academy of Sciences, Sibirskiĭ trakt 10/7, Kazan, Tatarstan, 420029 Russia

Received January 15, 2004

Abstract—Photoconductivity of lead magnesium niobate is studied, and the spectral dependence of the photoconductivity is measured in the vicinity of the permittivity maximum associated with a diffuse phase transition. Photostimulated currents due to the Dember effect are detected. Based on the data obtained, the structure of the density of states of defect energy levels is discussed. © *2004 MAIK "Nauka/Interperiodica".*

The ferroelectrics that undergo diffuse phase transitions (commonly called relaxors) remain the most intensively studied ferroelectrics [1–9]. Among these materials, lead magnesium niobate $PbMg_{1/3}Nb_{2/3}O_3$ (PMN) is the most known compound [1–5]. The continuing interest in these materials is due to their ferroelectric, piezoelectric, and optical properties and to their possible application in electronic engineering. In particular, optically transparent relaxors can accumulate information recorded by light. This effect is a result of the capture of photoexcited carriers by local centers.

Although relaxors have been studied for a long time, the physical mechanisms of the processes proceeding in them and the phenomena observed are still not completely understood. The main problem is adequate description of the relaxor behavior in the vicinity of the permittivity maximum. Furthermore, numerous experimental data [5] indicate that the low-temperature phase exhibits nonergodic behavior; i.e., the properties of this phase depend on the previous history of the sample. Recently, certain progress has been made in using a model in which the relaxor behavior is associated with the dynamics of polaron states forming via charge localization on defects [6–8]. Therefore, in order to understand the nature of relaxors, it is of importance to detect these states and investigate their properties. In this work, we measured the spectral dependence of photoconductivity and photostimulated current in lead magnesium niobate in order to study the properties of the defect subsystem in this compound.

Measurements were performed on a PMN sample $6.2 \times 4.5 \times 0.65$ mm in size. In order to measure the photocurrent, transparent electrodes 4.5×4.5 mm in size were deposited onto the optically finished (110)-oriented 6.2×4.5-mm faces of the sample. The optical transmission of the transparent electrodes was measured with an SF-46 spectrophotometer and was 0.5 or more for the incident light wavelength $\lambda \geq 300$ nm. The photocurrent was recorded with a dc U5-9 electrometric amplifier. The electrical conductivity was measured with an U5-9 amplifier and an E6-13A teraohmmeter. Illumination was provided by xenon discharge lamps or halogen incandescent lamps and an MDR-12 large-aperture monochromator with an entrance three quartz lens condenser. The light flux density transmitted through the monochromator was measured with an IMO-2 mean-power meter or a BKM-5a bolometer and was 0.5–7.5 mW/cm^2 in the range 350–1000 nm. The light wavelength was swept at a constant rate, which was typically in the range from 20 to 80 nm/min. The illumination spectral width could also be varied; most of the data were obtained for a spectral width of 9.6 nm. In the course of measurements, the temperature of the sample was maintained constant by blowing it with dry gaseous nitrogen and controlled by a copper–constantan thermocouple to within ±0.1 K.

The spectral dependences of the photostimulated current and dc conductivity were recorded at various temperatures. It was found that the dc conductivity of lead magnesium niobate at $T > 300$ K has an activation character and is due to thermal excitation of carriers from defect energy levels into the conduction band. The activation energy is of the order of $U_a = 0.65$ eV, which is the distance from the chemical potential level to the conduction band bottom. The spectral dependence of photoconductivity exhibits a well-defined maximum at a photon energy of 2.85 eV. Figure 1 shows the spectral dependences of the photostimulated current observed in our experiments at room temperature in the blue and UV spectral regions for the incident light wavelength swept in opposite directions. Curves *1* are obtained in a dc external electric field, and curves *2* are taken in the absence of an external field. The spectral dependences are obtained for opposite directions of wavelength sweep above $\lambda = 200$ nm. The characteristic peak with a maximum at 435 nm (2.85 eV) corresponds to a peak in the density of states of defect levels that is located below the conduction band bottom. A similar spectral dependence of photocurrent was observed in [4] in a (100)-oriented crystal; in our case, the photocurrent and light beam were directed along the [110] axis. It should

be noted that the photocurrent peak with a maximum at 435 nm is proportional to the external voltage applied between the electrodes and changes sign as the voltage is reversed. The magnitude and direction of the photocurrent caused by UV illumination (curves *2*) depend on both the wavelength sweep direction and the sweep rate. From photocurrent curves recorded at two sweep rates differing by five times, it can be seen that, as the sweep rate decreases, the photocurrent decreases significantly in magnitude in the vicinity of the maximum at 330 nm and remains unchanged in the vicinity of the maximum at 435 nm. The peak at 330 nm corresponds to the photocurrent associated with direct excitation of carriers from the valence into the conduction band (the band gap is 3.4 eV for PMN). In our case, this current is due to the longitudinal Dember effect (which arises in the spectral region of strong light absorption), because the sample is illuminated through transparent electrodes. The direction of this current depends on the sign of the wavelength sweep rate during recording of the photocurrent. The magnitude of the photocurrent depends on the wavelength sweep rate. In the case where the wavelength is increased, the photocurrent flows against the applied field. As the external voltage is removed, the photocurrent peak at 330 nm remains unchanged in both direction and magnitude. Therefore, the photocurrent due to the Dember effect is much higher than the conventional photoconduction current in this photoexcitation spectral region.

In [4], a sample was illuminated through a lateral face, i.e., perpendicular to the external field direction, and, therefore, the current mode discussed above could not arise in those experiments. It is most likely that the conventional photocurrent maximum (associated with excitation of carriers from the valence to the conduction band) was observed in [4] in this spectral region. In this case, the photocurrent must vanish after the applied voltage is removed.

The mechanism of the Dember effect is illustrated schematically in Fig. 2. This effect is due to the appearance of a spatial distribution of excited carriers $f(x)$ over a sample in the spectral region of strong absorption of light (in Fig. 2, this distribution is shown for two different wavelengths). In our case, the experimental situation is more complicated, because the photocurrent arises not due to the appearance of a distribution $f(x)$ over the sample but rather due to a variation in this distribution produced by changes to the light wavelength. The photoconductivity and spectroscopic data suggest that there is a fairly wide energy distribution of defect states near the bottom of the conduction band. Therefore, these states can be involved in a diffuse phase transition in relaxors [10].

Figure 3 illustrates the effect of prolonged illumination with the wavelength corresponding to the photoconductivity maximum in the visible region (435 nm) on the spectral dependence of photocurrent at a bias voltage of 100 V. In this case, a photoelectret state was

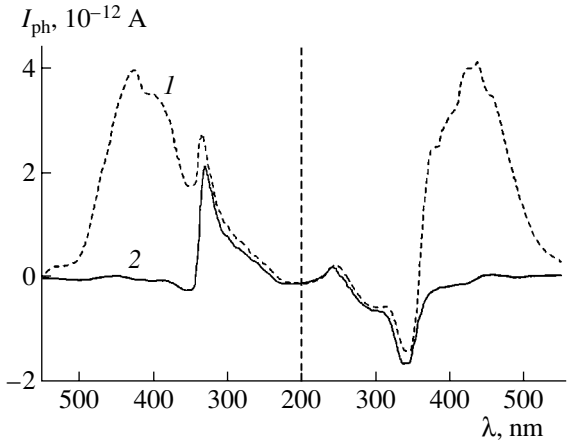

Fig. 1. Spectral dependence of photostimulated current in single-crystal lead magnesium niobate at room temperature for the external field E equal to (*1*) 140 and (*2*) 0 V/cm.

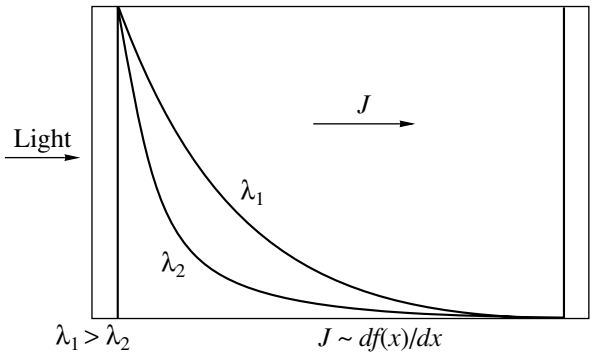

Fig. 2. Illustration of the Dember effect (schematic). The curves represent the distribution of excited carriers $f(x)$ over the sample for two different wavelengths.

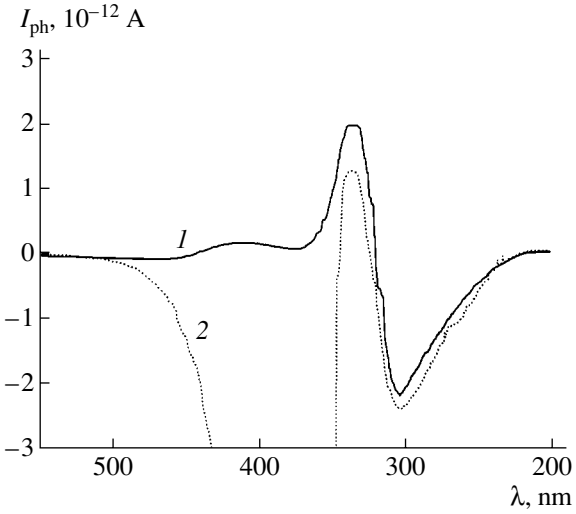

Fig. 3. Spectral dependences of photocurrent (*1*) before illumination in an external field and (*2*) after prolonged illumination at a wavelength of 435 nm in the presence of an externally applied voltage of 100 V. Both curves were recorded in the absence of an external voltage.

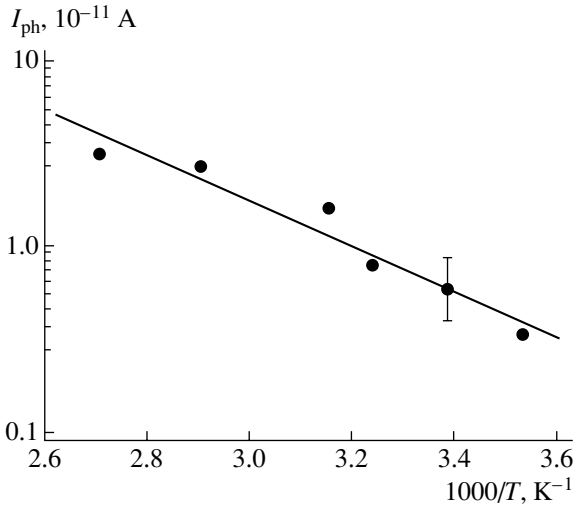

Fig. 4. Temperature dependence of photocurrent.

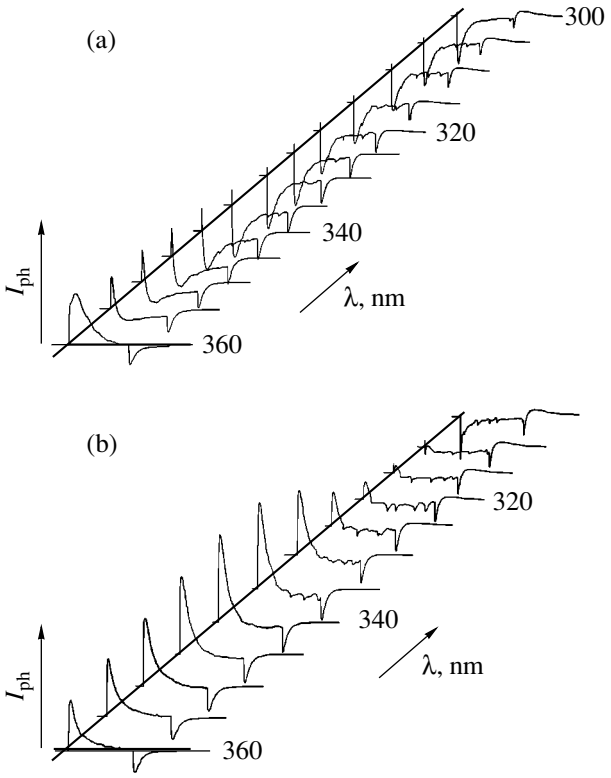

Fig. 5. Variation in the dynamics of photocurrent as illumination at different wavelengths is turned on and then off in the case where the wavelength is (a) decreased or (b) increased.

observed to occur [4]. The duration of illumination was chosen such that the effect reached saturation. The curves were recorded in the absence of an external field. Curve *1* was recorded before illumination, and curve *2*, after illumination under an external bias voltage of 100 V. Under these conditions, the maximum value of the photocurrent was as large as 12×10^{-12} A (in Fig. 3, this maximum corresponds to a minimum that is beyond the bottom boundary of the figure). Heating of the sample up to temperatures of 400–450 K followed by holding at these temperatures for 30 min and subsequent cooling to room temperature for one hour caused the extra photocurrent to disappear completely. Illumination of the crystal at a wavelength near 435 nm in the absence of a bias voltage also gradually decreased the induced photocurrent. The contribution to photocurrent due to the longitudinal Dember effect also arises in the case of illumination at 435 nm. This contribution causes an increase in photocurrent near λ = 435 nm (Fig. 3, curve *1*).

We also studied the temperature dependence of photocurrent. In Fig. 4, the maximum photocurrent (at λ = 435 nm) is plotted as a function of inverse temperature. The solid line is a fit to the Arrhenius law with an activation energy of U_1 = 0.23 eV. We note that under UV illumination the photocurrent is independent of temperature (to within experimental error) over the range 270–370 K. Figure 5 shows the variation in photostimulated current (measured in the absence of an external voltage) as illumination at different wavelengths was turned on and then off. The duration of illumination was always 600 s. The measurements were performed in the following order: the wavelength was first decreased from 360 to 300 nm in steps of 5 nm (Fig. 5a) and then increased from 300 to 360 nm in the same steps (Fig. 5b). Figure 6 shows analogous measurements of photocurrent under an externally applied voltage of 9 V. In this case, the duration of illumination was chosen such that the process reached a steady state. These studies of the dynamics of photostimulated current showed that both the magnitude and direction of photocurrent depend on the previous history of a sample, more specifically, on the conditions of illumination at different wavelengths, duration of illumination, and the presence or absence of an external electric field during illumination. The complexity of the kinetic processes that occur when illumination is turned on and then off indicates that there are two types of photoexcited carriers that differ in terms of their mobility. However, comprehensive studies on the properties of both types of carriers should be performed to make more detailed conclusions.

Based on the photoconductivity and spectroscopic data, we propose the following structure of the density of states for defect levels (Fig. 7). The defect levels lie U_1 = 0.23 eV below the conduction band bottom and form a fairly wide energy spectrum with a half-width of the order of 0.32 eV. This spectrum can provide a relaxation time distribution and temperature dependence that could explain the properties of relaxors [8, 10]. These defect states can be involved in diffuse phase transitions in relaxors and can be used to influence the properties of relaxors through illuminating them. It was shown in [9] that the carriers are localized in a temper-

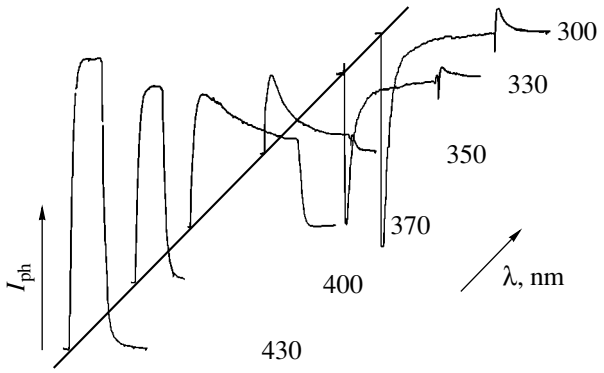

Fig. 6. Variation in the dynamics of photocurrent as illumination at different wavelengths is turned on and then off under a dc bias voltage of 9 V.

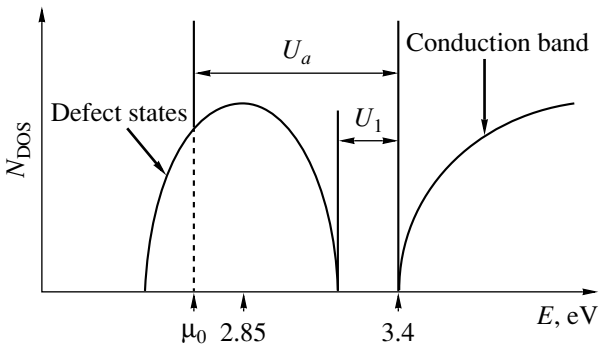

Fig. 7. Density of states for defect levels (schematic).

ature region near the phase transition point. The activation energy U_a = 0.65 eV is the energy separation between the bottom of the conduction band and the chemical potential in our sample. From the above discussion, it follows that the defect levels are less than half-filled (Fig. 7).

Thus, we have studied the spectral dependences of photoconductivity and photostimulated current in single-crystal lead magnesium niobate $PbMg_{1/3}Nb_{2/3}O_3$ in cases both where an externally applied voltage is present and absent. It has been shown that the photostimulated current that is independent of the magnitude and polarity of the external voltage is due to the Dember effect. The magnitude and direction of the photostimulated current depend on the previous sample illumination at various wavelengths. Based on the data obtained, the possible structure of the density of states for defect levels was proposed.

ACKNOWLEDGMENTS

This study was supported by the Russian Foundation for Basic Research, project no. 01-02-16350.

REFERENCES

1. G. A. Smolenskiĭ, V. A. Isupov, A. I. Agranovskaya, and S. N. Popov, Fiz. Tverd. Tela (Leningrad) **2** (10), 2906 (1960) [Sov. Phys. Solid State **2**, 2584 (1960)].
2. L. E. Cross, Ferroelectrics **76**, 241 (1987).
3. A. E. Glazounov and A. K. Tagantsev, Phys. Rev. Lett. **85**, 2192 (2000).
4. V. A. Trepakov, N. N. Kraĭinik, and A. V. Olifir, Fiz. Tverd. Tela (Leningrad) **18** (4), 1751 (1976) [Sov. Phys. Solid State **18**, 1019 (1976)].
5. E. V. Colla, E. Yu. Koroleva, N. M. Okuneva, and S. B. Vakhrushev, Phys. Rev. Lett. **74**, 1681 (1995).
6. R. F. Mamin, Pis'ma Zh. Éksp. Teor. Fiz. **58** (7), 534 (1993) [JETP Lett. **58**, 538 (1993)].
7. V. S. Vikhnin, R. Blinc, R. Pirc, S. E. Kapphan, I. L. Kislova, and P. A. Markovin, Ferroelectrics **268**, 257 (2002).
8. R. F. Mamin, Fiz. Tverd. Tela (St. Petersburg) **43** (7), 1262 (2001) [Phys. Solid State **43**, 1314 (2001)].
9. A. E. Krumin, U. I. Ilyin, and V. I. Dimza, Ferroelectrics **22**, 695 (1978).
10. R. F. Mamin, Izv. Ross. Akad. Nauk, Ser. Fiz. **67** (8), 1157 (2003).

Translated by Yu. Epifanov

Physics of the Solid State, Vol. 46, No. 10, 2004, pp. 1914–1916. Translated from Fizika Tverdogo Tela, Vol. 46, No. 10, 2004, pp. 1849–1851.

MAGNETISM AND FERROELECTRICITY

Specific Features of the Structure and Dielectric Relaxation of $PbWO_4$ in the Temperature Range $20 \le T \le 550$°C

A. P. Eremenko, N. B. Kofanova, L. E. Pustovaya, A. G. Rudskaya, B. S. Kul'buzhev, and M. F. Kupriyanov

Rostov State University, pr. Stachki 194, Rostov-on-Don, 344090 Russia

Received February 11, 2004

Abstract—An anomaly of the relaxor type is revealed in the permittivity of the $PbWO_4$ compound at a temperature of 370°C. This anomaly is associated with the local random displacements of lead and tungsten atoms in the nearest environment of oxygen atoms. *© 2004 MAIK "Nauka/Interperiodica".*

1. INTRODUCTION

The mineral stolzite $PbWO_4$ and its synthetic analogs prepared in the form of crystals are characterized by a high sensitivity of the luminescence properties to irradiation with high-energy particles and, hence, are very promising materials for relevant applications [1–4]. It is known that the $PbWO_4$ compound can crystallize either in a scheelite-type structure [5] or in a wolframite-type structure [6]. These structures differ significantly. In scheelite, tungsten cations are in the tetrahedral environment of oxygen anions (the coordination number is four). In wolframite, tungsten cations are in the octahedral environment (the coordination number is six). Richter *et al.* [7] obtained structural data for the monoclinic phase of $PbWO_4$ under high pressure. Since $PbWO_4$ crystals exhibit luminescence activity, increased research interest has been expressed in the defects and structural instability of these objects [8]. However, the temperature dependences of the dielectric properties of the $PbWO_4$ compound and the dielectric properties themselves are poorly understood.

Moreover, it is well known that lead- and tungsten-containing oxide compounds with a structure of the oxygen-octahedral type (for example, perovskites, potassium–tungsten bronzes, pyrochlores, etc.) possess a high dielectric activity. All these compounds are either ferroelectrics or antiferroelectrics (see, for example, [9]). As a rule, the nature of this activity is associated with the specific features revealed in the electronic states of lead and tungsten cations in oxide compounds and the interaction between these cations and oxygen anions of their nearest environment [10–12]. Furthermore, in a number of perovskite (including lead-containing) structures, strong effects of dielectric relaxation caused by defects in real crystals manifest themselves at different temperatures [13, 14].

The purpose of the present work was to reveal the specific features in the permittivity of the $PbWO_4$ compound over a wide temperature range and their correlation with variations in the structural parameters.

2. SAMPLE PREPARATION AND EXPERIMENTAL TECHNIQUE

Polycrystalline $PbWO_4$ was prepared according to the standard procedure of solid-phase synthesis from a stoichiometric mixture of PbO (analytical grade) and WO_3 (extra-pure grade) upon annealing at a temperature of 750°C for 6 h. The ceramic samples were produced by hot pressing at a temperature of 850°C and a pressure of 10^5 N/cm^2 for 1 h.

X-ray powder diffraction analysis of the synthesized $PbWO_4$ compound was performed on a DRON-3.0M diffractometer (CuK_α radiation, Ni filter) and revealed the presence of only one phase in the studied sample. The structural transformations of the ceramic $PbWO_4$ sample were investigated using x-ray diffractometry in a URD-2000 high-temperature chamber in the temperature range $20 \le T \le 550$°C during heating and cooling. The temperature at each point was stabilized accurate to within ±1 K. X-ray diffraction patterns in the 2θ range $20° \le 2\theta \le 65°$ (scan step, 0.08°; exposure time per frame, 1 s) were recorded at different temperatures on a "Roentgen-structure" measuring and computing complex based on a DRON-3.0M diffractometer and a computer with a Pentium processor.

The temperature–time conditions used in x-ray powder diffraction analysis are illustrated in Fig. 1. The x-ray powder diffraction patterns were processed using the full-profile analysis with the Powder Cell 2.3 program [15]. The unit cell parameters, positional parameters, and Debye–Waller factors of atoms were determined.

The temperature dependences of the permittivity of the $PbWO_4$ ceramic samples with applied silver electrodes were measured with the use of an E7-8 alternating-current bridge. The frequency of the measuring field was equal to 1 kHz.

1063-7834/04/4610-1914$26.00 © 2004 MAIK "Nauka/Interperiodica"

3. RESULTS AND DISCUSSION

The temperature dependences of the permittivity of the $PbWO_4$ compound measured during heating and cooling are shown in Fig. 2. It can be seen from this figure that, during heating, the permittivity ε abruptly increases at a temperature $T \approx 370$°C and reaches approximately 10^4. However, upon cooling, the permittivity ε is characterized by two diffuse maxima at temperatures of 320 and 400°C. It is found that, upon repeated heating of the sample (immediately after this sample was cooled), the temperature dependence of the permittivity $\varepsilon(T)$ is similar to the curve $\varepsilon(T)$ measured during cooling. The maximum in the temperature dependence of the permittivity $\varepsilon(T)$ measured during heating was restored within one day of keeping the sample at room temperature. At the same time, the temperature dependence of the permittivity $\varepsilon(T)$ measured at a frequency of 1 MHz does not exhibit any noticeable anomalies.

The full-profile analysis of the $PbWO_4$ compound was performed both at room temperature and in the entire temperature range covered. This made it possible to determine the temperature dependences of the unit cell parameters, positional parameters, and thermal parameters of atoms. As a result, we revealed the following structural features: (1) the symmetry of the structure of the $PbWO_4$ compound remains unchanged (tetragonal phase, $I4_1/a$); (2) during heating and cooling, the unit cell parameters vary monotonically (the thermal expansion coefficients of the unit cell parameters are as follows: $\alpha(a) = 1.1 \times 10^{-5}$ K^{-1} and $\alpha(c) = 2.7 \times 10^{-5}$ K^{-1}); and (3) the mean interatomic distances l(W–O) and l(Pb–O) in the temperature range 20–520°C change insignificantly [Δl(W–O)/$l_{room} = 4.5 \times 10^{-3}$, Δl(Pb–O)/$l_{room} = 7.6 \times 10^{-3}$].

Figures 3a and 3b show the temperature dependences of the isotropic Debye–Waller factors B for tungsten, lead, and oxygen atoms in the temperature range $20 \le T \le 450$°C. It should be noted that the isotropic Debye–Waller factors at room temperature have the following values: B(W) = 0.009 Å^2, B(Pb) = 0.003 Å^2, and B(O) = 0.02 Å^2.

Analysis of the curves depicted in Fig. 3 revealed the following features: (1) an increase in the temperature leads to a noticeable increase in the Debye–Waller factor for all atoms; (2) beginning from 200°C, the ratios between these parameters become unexpected, B(Pb) > B(W) > B(O); i.e., the ratios between the root-mean-square random displacements of the atoms from their positions in the structure are inverse with respect to the ratios between the atomic masses; (3) upon heating of the sample (Fig. 3a), the parameters B_j increase drastically at $T \approx 370$°C; and (4) upon cooling of the sample, the values of B(Pb) and B(W) at $T \approx 370$°C are not very high, whereas the parameter B(O) substantially decreases at temperatures below 250°C.

Thus, the temperature dependences of the Debye–Waller factors of atoms (unlike the other structural

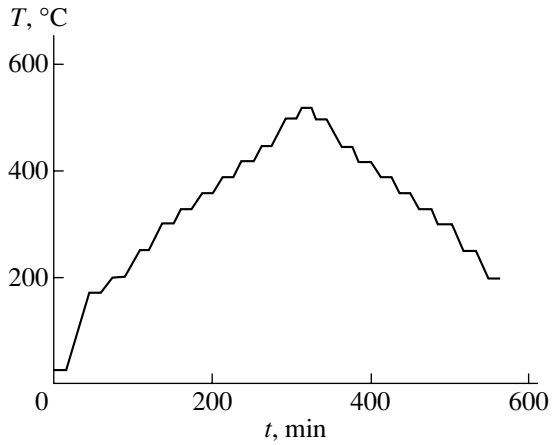

Fig. 1. Temperature–time conditions used in x-ray powder diffraction analysis of the $PbWO_4$ compound.

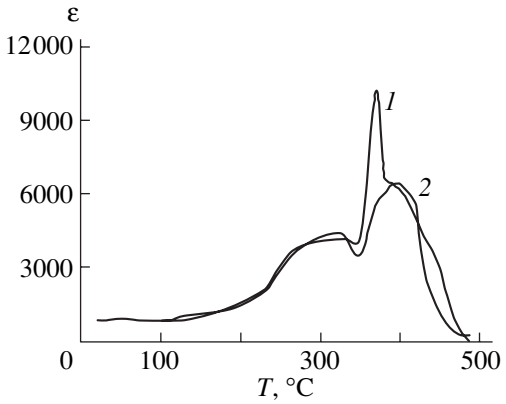

Fig. 2. Temperature dependences of the permittivity of the $PbWO_4$ compound measured during (*1*) heating and (*2*) cooling.

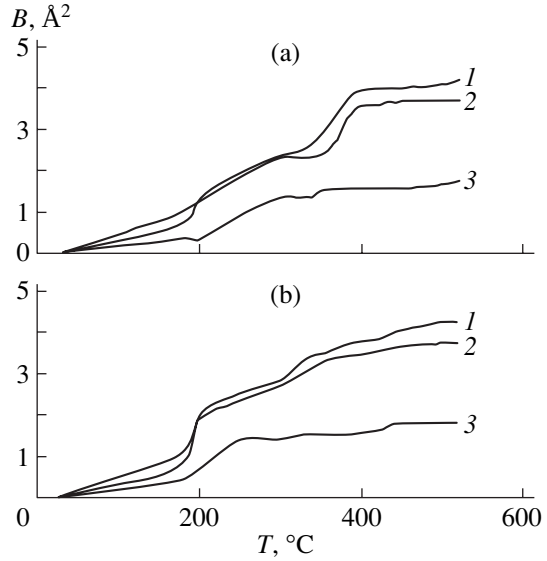

Fig. 3. Temperature dependences of the Debye–Waller factors for (*1*) lead, (*2*) tungsten, and (*3*) oxygen atoms upon (a) heating and (b) cooling.

parameters) correlate well with the temperature dependences of the permittivity $\varepsilon(T)$.

The results obtained can be interpreted as follows. The large parameters B_j for heavy atoms of lead and tungsten (the root-mean-square displacements are of the order of 0.2 Å) can be explained by the fact that, apart from the root-mean-square displacements $\langle u_t \rangle$ of these atoms due to thermal vibrations in the crystal structure, there appear local random displacements $\langle u_{\text{disp}} \rangle$ (similar to those observed in oxide relaxor ferroelectrics [16–18]). Within this model of the structure, the parameter B_{eff} is determined by a superposition of the displacements $\langle u_t \rangle$ and $\langle u_{\text{disp}} \rangle$. The separation of the contributions to the parameter B_{eff} from the root-mean-square amplitudes of thermal atomic vibrations and the local random displacements of heavy lead and tungsten atoms requires more comprehensive and precise x-ray diffraction studies of $PbWO_4$ single crystals.

The character of the anomalies revealed in the temperature dependences of the parameters B(Pb), B(W), and B(O) in the vicinity of 370°C suggests that, at these temperatures, there can occur an isostructural phase transition of the local order–disorder type. From this viewpoint, the observed anomalies in the permittivity (Fig. 2) can be explained by the fact that the change in the local chemical bonds Pb–O and W–O gives rise to spatial charges, which, in the measuring alternating electric field, behave like relaxing electric dipoles [13].

Further experimental investigation into the interrelations between the structural states of $PbWO_4$ and the phase transitions, as well as elucidation of the correlations with the observed physical properties, will make it possible to verify the validity of the physical models of the studied phases [19].

ACKNOWLEDGMENTS

We would like to thank Yu.M. Gufan and E.S. Larin for their participation in discussions of the results and helpful remarks.

This work was supported by the Russian Foundation for Basic Research, project no. 04-03-32039.

REFERENCES

1. J. N. Shpinkov, I. A. Kamenskikh, M. Kirm, V. N. Kolobanov, V. V. Mikhailin, A. N. Vasilev, and G. Zimmer, Phys. Status Solidi A **170**, 167 (1998).
2. N. Senguttuvan, P. Mohan, B. S. Moothy, and P. Ramasamy, J. Cryst. Growth **191**, 130 (1998).
3. M. Springs, V. Tale, and I. Tale, J. Lumin. **72–74**, 784 (1997).
4. M. Nilk and P. Fabeni, Chem. Phys. Lett. **291**, 300 (1998).
5. G. V. Plakhov, E. A. Pobedimskaya, M. A. Simonov, and N. V. Belov, Kristallografiya **15** (5), 1067 (1970) [Sov. Phys. Crystallogr. **15**, 928 (1970)].
6. L. N. Dem'yanets, V. V. Ilyukhin, A. V. Chichagov, and N. V. Belov, Neorg. Mater. **3** (12), 2221 (1967).
7. P. W. Richter, C. J. Kruger, and C. W. F. T. Pistorius, Acta Crystallogr. **32**, 928 (1976).
8. A. V. Bazhenov, V. K. Egorov, L. V. Gasparov, N. V. Klassen, S. F. Kondakov, V. M. Prokopenko, B. S. Red'kin, I. B. Savchenko, J. M. Shmit'ko, S. Z. Shmurak, and A. V. Soloviev, in *Abstracts of the 7th European Conference on Defects in Insulating Materials* (Lyon, France, 1994), p. 311.
9. G. A. Smolenskiĭ, V. A. Bokov, V. A. Isupov, N. N. Kraĭnik, R. E. Pasynkov, and M. S. Shur, *Ferroelectrics and Antiferroelectrics* (Nauka, Leningrad, 1971) [in Russian].
10. J. B. Goodenough and J. M. Longo, in *Landolt–Börstein Numerical Data and Functional Relationships in Science and Technology: New Series*, Ed. by K.-H. Hellwege (Springer, Berlin, 1970), Group III, Vol. 4a, p. 207.
11. H. D. Megaw, Acta Crystallogr. **7**, 187 (1954).
12. E. G. Fesenko, *Perovskite Family and Ferroelectricity* (Atomizdat, Moscow, 1972) [in Russian].
13. O. Bidault, P. Goux, M. Kchikech, M. Belkaoumi, and M. Maglione, Phys. Rev. B **49** (12), 7868 (1994).
14. Yu. V. Kabirov, M. V. Kupriyanov, Ya. Dets, and P. Wawzala, Fiz. Tverd. Tela (St. Petersburg) **42** (7), 1291 (2000) [Phys. Solid State **42**, 1329 (2000)].
15. W. Krause and G. Nolze, J. Appl. Crystallogr. **29**, 301 (1996).
16. S. B. Vakhrushev, J. M. Kiat, and B. Dkhil, Solid State Commun. **103** (8), 477 (1977).
17. R. Kolesova and M. Kupriyanov, Phase Transit. **45**, 271 (1993).
18. A. R. Lebedinskaya and M. F. Kupriyanov, Phase Transit. **75**, 283 (2002).
19. S. Li, R. Ahuja, Y. Wang, and B. Jonansson, High Press. Res. **23** (3), 343 (2003).

Translated by I. Volkov

Physics of the Solid State, Vol. 46, No. 10, 2004, pp. 1917–1921. Translated from Fizika Tverdogo Tela, Vol. 46, No. 10, 2004, pp. 1852–1855.

MAGNETISM AND FERROELECTRICITY

Chromium- and Manganese-Doped $TlInS_2$—A New Relaxor Ferroelectric

R. M. Sardarly, O. A. Samedov, and I. Sh. Sadykhov

Institute for Radiation Problems, Academy of Sciences of Azerbaijan, Baku, 370143 Azerbaijan

e-mail: sardarli@yahoo.com

Received February 16, 2004

Abstract—The dielectric, pyroelectric, and polarization properties of $TlInS_2$ crystals doped with 0.1 mol % Cr and Mn are investigated. It is shown that $TlInS_2$ compounds doped with chromium and manganese can be assigned to the class of relaxor ferroelectric materials. The temperature range of existence of the stable relaxor (nanodomain) state and the temperature of the phase transition from this state to the ferroelectric (macrodomain) state are determined. The temperature dependence of the pyroelectric current is characterized by an anomaly in the range of the phase transition. *© 2004 MAIK "Nauka/Interperiodica".*

1. INTRODUCTION

Ferroelectrics with smeared phase transitions (which are also referred to as relaxors) have been studied intensively in recent years. These materials are characterized by the following features: (i) the temperature dependence of the permittivity $\varepsilon(T)$ exhibits a diffuse maximum; (ii) an increase in the frequency of the measuring field leads to a shift in the maximum of the dependence $\varepsilon(T)$ toward the high-temperature range; (iii) the ferroelectric hysteresis loop has a narrow prolate shape in a limited temperature range; (iv) the temperature dependence of the pyroelectric current exhibits a jump at the temperature of the phase transition from the relaxor state to the ferroelectric state; (v) the relationship $(\varepsilon)^{-1/2} = A + B(T - T_0)$ is satisfied at temperatures above T_m, where T_m is the temperature of the maximum in the dependence $\varepsilon(T)$; and (vi) the frequency dispersion of the temperature of the maximum in the dependence $\varepsilon(T)$ is adequately described by the Vogel–Fulcher relationship [1–9]. Among the compounds which are characterized by the aforementioned features and which, for this reason, are assigned to the class of relaxors, the best known compounds are $Pb(Mg_{1/3}Nb_{2/3})O_3$, $Pb_{1-y}La_y(Zr_{1-x}Ti_x)O_3$, and a number of other ferroelectrics that have been extensively used in industry [1–10]. Compounds that can be classified as relaxors according to the characteristic features listed above are disordered systems. However, analysis of the materials belonging to this class has demonstrated that only systems with a charge disorder rather than with a pure structural disorder exhibit properties inherent in relaxor ferroelectrics.

Although relaxors have been studied for a long time, there has been no unified theory elaborated to provide a satisfactory explanation of the specific features observed in the properties of these materials. To date, several approaches have been proposed for describing the mechanisms responsible for the behavior of ferroelectric relaxors. The first approach is based on the assumption that the studied system is divided into nanodomains under the action of random fields [11]. Within the second approach, relaxors are treated as objects that exhibit a behavior typical of glasses, by analogy with spin glasses in ferromagnetic materials [7, 8, 10, 12]. The third approach is based on the inclusion of localized charges that generate local electric fields, which, in turn, induce polarization in the vicinity of the phase transition [4, 5]. Within the third approach, it is also assumed that the ferroelectric transition is preceded by the formation of an incommensurate phase. According to Mamin [13], it is in this temperature range of the first-order transition from the incommensurate phase to the commensurate phase that thermal filling of the traps initiates the branching sequence of phase transitions responsible for the specific features in the behavior of relaxors.

The considerable interest recently expressed by researchers in relaxors stems from the fact that these materials are very promising for use in optical data-storage systems. Moreover, owing to the presence of embedded domains of nanometer size, relaxors are convenient model objects for various applications in nanotechnology.

The $TlInS_2$ compound is a semiconductor with a layered structure. As was shown in [14, 15], the $TlInS_2$ semiconductor compound is characterized by high x-ray sensitivity and photosensitivity. Moreover, Guseĭnov *et al.* [15] revealed that crystals of this class have a capacity for intercalation and exhibit effects of electrical memory.

On the other hand, the $TlInS_2$ semiconductor is a compound in which the temperature instability of the crystal lattice leads to ferroelectric ordering [16–20]. At present, it has been established with confidence that the

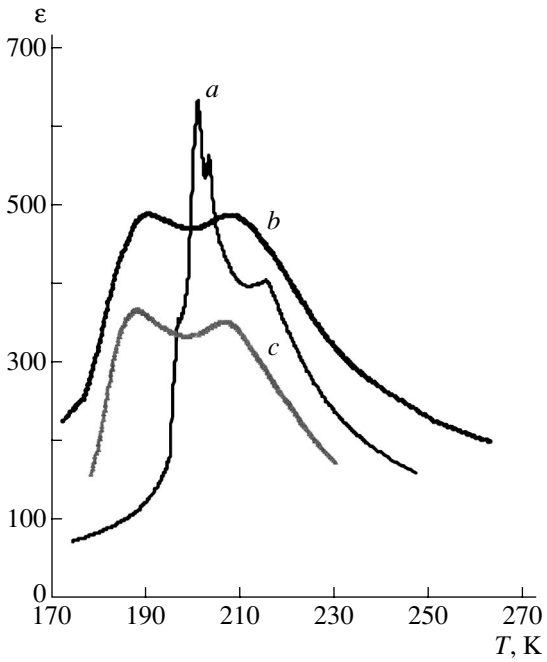

Fig. 1. Temperature dependences of the permittivity $\varepsilon(T)$ for (*a*) $TlInS_2$, (*b*) $TlInS_2\langle Mn\rangle$, and (*c*) $TlInS_2\langle Cr\rangle$ crystals.

$TlInS_2$ compound of stoichiometric composition is an improper ferroelectric with an intermediate incommensurate phase. This means in particular that, as the temperature decreases, the $TlInS_2$ compound undergoes the following sequence of phase transitions: (i) the transition from the initial paraelectric phase with C_{2h}^6 symmetry to the incommensurate phase characterized by the wave vector $k_i = (\delta, \delta, 0.25)$ (where δ is the incommensurability parameter) is observed at a temperature of 216 K, and (ii) the transition from the incommensurate phase to the polar ferroelectric phase occurs at a temperature of ~200 K.

Investigations into the polarization properties of undoped $TlInS_2$ crystals at temperatures below 196 K have revealed dielectric hysteresis loops with spontaneous polarization $P_S = 1.8 \times 10^{-7}$ C/cm^2. These findings indicate that undoped $TlInS_2$ crystals undergo smeared phase transitions [6]. The diffuse character of the phase transitions in this compound is associated with the fact that $TlInS_2$ belongs to the class of berthollides, i.e., compounds characterized by a redistribution of composition during crystal growth [16]. However, these variations in the composition occur in the homogeneity region and the temperature dependence of the permittivity $\varepsilon(T)$ does not change in character. The temperature dependences of the permittivity $\varepsilon(T)$ and the spontaneous polarization $P_S(T)$ for $TlInS_2$ crystal samples corresponding in composition to the singular point in the phase diagram are typical of improper ferroelectric phase transitions [6]. As was shown in our recent work [17], the introduction of 0.1 mol % Mn and Cr into the $TlInS_2$ compound leads to the appearance of diffuse maxima in the temperature dependence of the permittivity $\varepsilon(T)$.

This paper reports on the results of investigations into the temperature dependences of the permittivity $\varepsilon(T)$, the spontaneous polarization $P_S(T)$, and the pyroelectric coefficient $\gamma(T)$ for the $TlInS_2$ crystals doped with 0.1 mol % Mn and Cr.

2. SAMPLE PREPARATION AND EXPERIMENTAL TECHNIQUE

Single crystals of $TlInS_2\langle Mn\rangle$ and $TlInS_2\langle Cr\rangle$ were grown from a melt through oriented crystallization. No anisotropy of the dielectric properties in the plane of the layer was observed. The measurements were performed at crystal facets cut out perpendicular to the polar axis. The crystal facets were ground, polished, and coated with a silver paste. The permittivity ε was measured on E7-8, E7-12, R5058, and Tesla BM560 alternating-current bridges in the temperature range 150–250 K at frequencies varying from 1 kHz to 1 MHz. The rate of change in the temperature was equal to 0.1 K/min. The dielectric hysteresis loops were examined according to a modified Sawyer–Tower scheme at a frequency of 50 Hz. The pyroelectric effect was measured using the quasi-static method on a V7-30 universal voltmeter.

3. RESULTS AND DISCUSSION

The temperature dependences of the permittivity $\varepsilon(T)$ for $TlInS_2$, $TlInS_2\langle Mn\rangle$, and $TlInS_2\langle Cr\rangle$ crystals are shown in Fig. 1. All the curves were measured during cooling of the samples. As can be seen from Fig. 1, the $TlInS_2$ crystals undergo a sequence of phase transitions [20]. In the temperature range 216–270 K, the dependence $\varepsilon(T)$ obeys the Curie–Weiss law with the Curie constant $C^+ = 5.3 \times 10^3$ K. An anomaly manifests itself at a temperature of 196 K only upon cooling, and all the peaks are well pronounced without even insignificant indications of smearing. For Mn- and Cr-doped $TlInS_2$ crystals, the dependence $\varepsilon(T)$ is substantially smeared. In the low-temperature range, the maxima in the curves $\varepsilon(T)$ for $TlInS_2\langle Cr\rangle$ and $TlInS_2\langle Mn\rangle$ crystals are shifted by 8 and 6 K, respectively.

As is known [6, 11, 17, 21], the smearing of phase transitions and, consequently, the relaxor behavior can be caused by composition fluctuations, defects, and impurities. However, for $TlInS_2$ crystals, composition fluctuations (within the homogeneity region) [16] do not lead to a manifestation of the relaxor properties. Earlier investigations into the dielectric properties of $TlInS_2$ crystals doped with impurity cations [17] demonstrated that only the dopant impurities substituting for indium ions in lattice sites bring about the smearing of phase transitions and their shift toward the low-temperature range. At the same time, the introduction of

impurity cations that occupy octahedral holes due to their physicochemical properties (ionic radius, coordination number) leads to a shift in the temperature of phase transitions toward the high-temperature range and does not affect the behavior of the dependence $\varepsilon(T)$; i.e., in this case, the phase transitions are not smeared.

An important feature of the ferroelectrics with smeared phase transitions is that the temperature behavior of the permittivity varies as $\varepsilon^{-1/2}(T)$ rather than according to the Curie–Weiss law. In the case when the temperature decreases from the range of existence of the high-temperature phase, the curve $\varepsilon^{-1/2}(T)$ intersects the abscissa axis at $T = 174$ K for $TlInS_2\langle Mn\rangle$ crystals and at $T = 168$ K for $TlInS_2\langle Cr\rangle$ crystals. It is worth noting that these temperatures coincide with the low-temperature maxima in the temperature dependence of the pyroelectric coefficient (Fig. 2).

Figure 2 depicts the temperature dependences of the pyroelectric coefficient $\gamma(T)$ for pure $TlInS_2$, Mn-doped $TlInS_2$, and Cr-doped $TlInS_2$ crystals. The pyroelectric measurements were performed by the quasi-static method. The pyroelectric coefficient γ was calculated from the following relationship: $\gamma = J/A_0 dT/dt$, where J is the pyroelectric current intensity, A_0 is the surface area of the electrodes, and dT/dt is the heating rate. For these measurements, the samples were preliminarily polarized in an external electric field. It is clearly seen from Fig. 2 that, for the pure $TlInS_2$ crystal at a temperature of 196 K, the pyroelectric coefficient γ reaches a maximum value of 1.6×10^{-7} C/(K cm^2). For doped $TlInS_2$ samples, the dependence $\gamma(T)$ exhibits two anomalies: at $T_m = 188$ K and $T_f = 168$ K for Cr-doped $TlInS_2$ crystals and at $T_m = 190$ K and $T_f = 174$ K for Mn-doped $TlInS_2$ crystals (where T_f is the Vogel–Fulcher temperature).

Examination of the polarization properties of the $TlInS_2\langle Cr\rangle$ and $TlInS_2\langle Mn\rangle$ crystals has revealed dielectric hysteresis loops at temperatures below 168 and 174 K, respectively. The maximum spontaneous polarization observed in these cases reaches $P_S = 0.76 \times 10^{-7}$ C/cm^2 for samples doped with chromium and $P_S = 0.4 \times 10^{-7}$ C/cm^2 for samples doped with manganese. For undoped $TlInS_2$ crystals, we obtained the spontaneous polarization $P_S = 1.8 \times 10^{-7}$ C/cm^2. In the temperature range 180–210 K, the dielectric hysteresis loops are narrow and prolate in shape, which is characteristic of relaxor ferroelectrics. At temperatures below 150 K, the hysteresis loops for the $TlInS_2\langle Cr\rangle$ and $TlInS_2\langle Mn\rangle$ crystals have a shape typical of conventional ferroelectrics.

The frequency dispersion was investigated at four frequencies of the measuring field: $f = 1$, 10, and 100 kHz and 1 MHz. It turned out that an increase in the frequency f does not affect the location of the maxima observed at the temperature T_m in the curve $\varepsilon(T)$ for the $TlInS_2$ crystal, whereas the smeared maxima in the

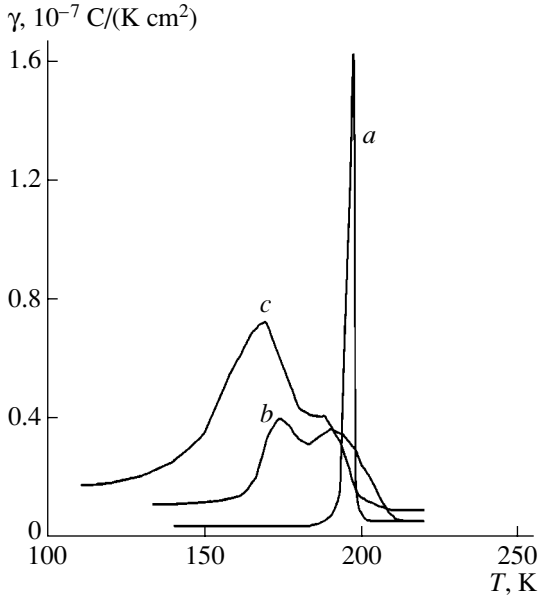

Fig. 2. Temperature dependences of the pyroelectric coefficient $\gamma(T)$ for (*a*) $TlInS_2$, (*b*) $TlInS_2\langle Mn\rangle$, and (*c*) $TlInS_2\langle Cr\rangle$ crystals.

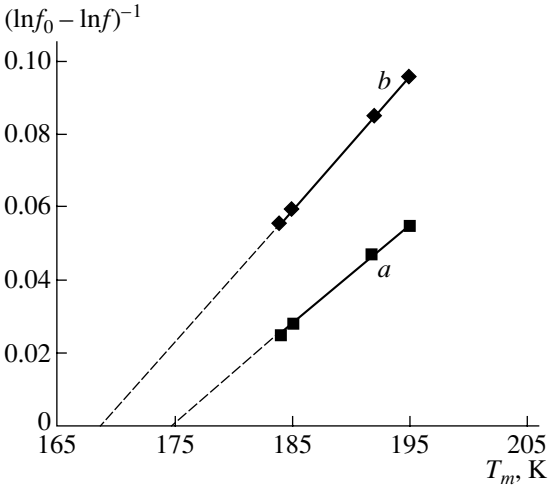

Fig. 3. Dependences of $(\ln f_0 - \ln f)^{-1}$ on the temperature T_m: illustration of the Vogel–Fulcher law for (*a*) $TlInS_2\langle Mn\rangle$ and (*b*) $TlInS_2\langle Cr\rangle$ crystals.

dependence $\varepsilon(T)$ for the $TlInS_2\langle Cr\rangle$ and $TlInS_2\langle Mn\rangle$ crystals are shifted significantly. The observed increase in the temperature of the maximum T_m in the dependence $\varepsilon(T)$ with an increase in the frequency f of the measuring field (Fig. 3) can be adequately described by the Vogel–Fulcher relationship

$$f = f_0 \exp\left[-\frac{E}{k(T_m - T_f)}\right],$$

where f_0 is the frequency at which the probability of surmounting the potential barrier E has a minimum value, k is the Boltzmann constant, and T_f is the Vogel–Fulcher temperature. The Vogel–Fulcher temperature is the temperature of "freezing" of electric dipoles or the phase transition to the dipole-glass state [6, 9]. For the crystals studied, the frequency f_0 is approximately equal to 10^{12} Hz, which is somewhat higher than the values obtained for oxide relaxor ferroelectrics. In the Vogel–Fulcher relationship, the activation energy is calculated to be $E = 0.03 \pm 0.01$ eV for both crystals.

An analysis of the curves shown in Figs. 1–3 demonstrates that the $TlInS_2\langle Cr\rangle$ and $TlInS_2\langle Mn\rangle$ crystals exhibit all the aforementioned features inherent in relaxor ferroelectrics.

The considerable dielectric dispersion and the specific features observed in the ferroelectric properties of $TlInS_2\langle Cr\rangle$ and $TlInS_2\langle Mn\rangle$ crystals are undeniably associated with the structural disordering, which, in turn, brings about local distortions of crystal symmetry and the generation of internal electric fields over a wide temperature range. In our opinion, the substitution of chromium and manganese ions for indium in InS_4 tetrahedra [17] leads to the relaxor behavior and suggests that the soft mode responsible for the ferroelectric phase transition is related to thermal vibrations of indium atoms in InS_4 tetrahedra. It should be noted that, in the $TlInS_2$ crystal lattice, indium occurs in the trivalent state with a coordination number of 4 (InS_4 tetrahedron). In this state, the ionic radius of indium is equal to 0.76 Å. Hence, indium ions can be substituted for by chromium and manganese ions whose radii are equal to 0.55 and 0.53 Å, respectively, and whose coordination number is 4 [22]. However, under these conditions, the valence of both chromium and manganese ions is equal to 4. In this situation, according to Glinchuk *et al.* [11], the electric dipoles that are associated with chromium and manganese impurity ions and are randomly arranged in the crystal lattice tend to order the system through indirect dipole–dipole interactions with the soft mode of the initial phase, whereas other sources of random fields tend to disorder this system. In the case when both these forces are in equilibrium, there can appear dipoles aligned in the same direction.

It should also be noted that, although the phase transitions in $TlInS_2$ crystals have long since been studied, no satisfactory explanations have been offered for their mechanisms. In our opinion, this circumstance can be explained by the fact that all these investigations of the phase transitions in $TlInS_2$ compounds were performed without due regard for their semiconductor properties. This is especially true for $TlInS_2$ crystals doped with impurity cations. In our case, doping of $TlInS_2$ crystals with chromium and manganese should lead to the formation of attachment levels (traps) in the vicinity of the conduction band bottom. Moreover, as was shown by Mamin and Blinc [4, 5, 13], thermal filling of the traps gives rise to a branching sequence of phase transitions and can be responsible for the formation of an unstable intermediate state between the incommensurate and commensurate phases.

4. CONCLUSIONS

Thus, doping of $TlInS_2$ crystals with chromium and manganese leads to the formation of a stable nanodomain relaxor state in the temperature range under investigation. The phase transition from the nanodomain relaxor state to the macrodomain ferroelectric state occurs at a temperature of 168 K for $TlInS_2\langle Cr\rangle$ single crystals and at 174 K for $TlInS_2\langle Mn\rangle$ single crystals. These temperatures correspond to jumps in the temperature dependence of the pyroelectric coefficient $\gamma(T)$, which also coincide with the temperature of freezing of nanopolar domains (the Vogel–Fulcher temperature).

REFERENCES

1. R. Blinc, J. Dolinsek, A. Grigorovich, B. Zalar, Z. Kutnjak, C. Filipic, A. Levstik, and R. Pirc, Phys. Rev. Lett. **83**, 424 (1999).
2. A. E. Glazounov and A. K. Tagantsev, Phys. Rev. Lett. **85**, 2192 (2000).
3. E. V. Colla, E. Yu. Koroleva, N. M. Okuneva, and S. B. Vakhrushev, Ferroelectrics **184**, 209 (1996).
4. R. F. Mamin, Fiz. Tverd. Tela (St. Petersburg) **43** (7), 1262 (2001) [Phys. Solid State **43**, 1314 (2001)].
5. R. F. Mamin and R. Blinc, Fiz. Tverd. Tela (St. Petersburg) **45** (5), 896 (2003) [Phys. Solid State **45**, 942 (2003)].
6. L. E. Cross, Ferroelectrics **151**, 305 (1994).
7. I. P. Raevskiĭ, V. V. Eremkin, V. G. Smotrakov, E. S. Gagarina, and M. A. Malitskaya, Fiz. Tverd. Tela (St. Petersburg) **42** (1), 154 (2000) [Phys. Solid State **42**, 161 (2000)].
8. E. V. Colla, T. Yu. Koroleva, N. M. Okuneva, and S. B. Vakhrushev, Phys. Rev. Lett. **74** (9), 1681 (1995).
9. D. Viehland, S. J. Jang, L. E. Cross, and M. Wuttig, J. Appl. Phys. **68** (6), 2916 (1990).
10. S. B. Vakhrushev and S. M. Shapiro, Phys. Rev. B **66**, 214 101 (2002).
11. M. D. Glinchuk, E. A. Eliseev, V. A. Stephanovich, and B. Hilczer, Fiz. Tverd. Tela (St. Petersburg) **43** (7), 1247 (2001) [Phys. Solid State **43**, 1299 (2001)].
12. F. Chu, I. M. Reaney, and N. Setter, Ferroelectrics **151**, 343 (1994).
13. R. F. Mamin, Pis'ma Zh. Éksp. Teor. Fiz. **58** (7), 534 (1993) [JETP Lett. **58**, 538 (1993)].
14. S. A. Mustafaeva, M. M. Asadov, and V. A. Ramazanzade, Fiz. Tverd. Tela (St. Petersburg) **38** (1), 14 (1996) [Phys. Solid State **38**, 7 (1996)].
15. G. D. Guseĭnov, R. G. Guseĭnova, É. F. Bagirzade, and S. N. Mustafaeva, Izv. Akad. Nauk SSSR, Neorg. Mater. **24** (4), 686 (1988).

16. R. M. Sardarly, O. A. Samedov, I. Sh. Sadykhov, A. I. Nadzhafov, N. A. Éyubova, and T. S. Mamedov, Neorg. Mater. **39** (4), 406 (2003).
17. R. M. Sardarly, O. A. Samedov, A. I. Nadzhafov, and I. Sh. Sadykhov, Fiz. Tverd. Tela (St. Petersburg) **45** (6), 1085 (2003) [Phys. Solid State **45**, 1137 (2003)].
18. A. A. Volkov, Yu. G. Goncharov, G. V. Kozlov, K. R. Allakhvrediev, and R. M. Sardarly, Fiz. Tverd. Tela (Leningrad) **25** (12), 3583 (1983) [Sov. Phys. Solid State **25**, 2061 (1983)].
19. S. B. Vakhrushev, V. V. Zhdanova, B. E. Kvyatkovskiĭ, N. M. Okuneva, K. R. Allakhverdiev, R. A. Aliev, and R. M. Sardarly, Pis'ma Zh. Éksp. Teor. Fiz. **39** (6), 245 (1984) [JETP Lett. **39**, 291 (1984)].
20. R. A. Aliev, K. R. Allakhverdiev, A. I. Baranov, I. R. Ivanov, and R. M. Sardarly, Fiz. Tverd. Tela (Leningrad) **26** (5), 1271 (1984) [Sov. Phys. Solid State **26**, 775 (1984)].
21. R. M. Sardarly, O. A. Samedov, I. Sh. Sadykhov, and V. A. Aliev, Fiz. Tverd. Tela (St. Petersburg) **45** (6), 1067 (2003) [Phys. Solid State **45**, 1118 (2003)].
22. *Modern Crystallography*, Vol. 2: *Structure of Crystals*, Ed. by B. K. Vaĭnshteĭn, V. M. Fridkin, and V. L. Indenbom (Nauka, Moscow, 1979; Springer, Berlin, 1982).

Translated by O. Borovik-Romanova

Physics of the Solid State, Vol. 46, No. 10, 2004, pp. 1922–1926. Translated from Fizika Tverdogo Tela, Vol. 46, No. 10, 2004, pp. 1856–1860.

LATTICE DYNAMICS AND PHASE TRANSITIONS

Phase Transitions in Manganese-Containing Perovskites

A. G. Rudskaya, N. B. Kofanova, L. E. Pustovaya, B. S. Kul'buzhev, and M. F. Kupriyanov

Rostov State University, pr. Stachki 194, Rostov-on-Don, 344090 Russia

e-mail: kupri@phys.rsu.ru

Received February 11, 2004

Abstract—Solid solutions with a perovskite structure of the general formula $A'_{1-x}A''_x MnO_3$ (including the previously unknown compounds with A' = La or Pr and A'' = Cd or Bi) are studied. It is found that the structure of the orthorhombic phases formed from rhombohedral phases with a decrease in the temperature is characterized by strong anisotropy of the Mn–O bond lengths. This anisotropy drastically decreases at lower temperatures.

1. INTRODUCTION

Over many years, compounds with a structure of the oxygen-octahedral type (perovskites, pyrochlores, potassium–tungsten bronzes, ilmenites, layered structures, Aurvillius phases, etc.) have been attracting considerable research attention owing to the great variety of their physical properties. In particular, these materials exhibit properties of great practical importance, such as ferroelectric properties, high-temperature superconductivity, and colossal (or even giant) magnetoresistance. Analysis of the data available in the literature on the characteristics of the compounds under consideration shows that the structures of ferroelectrics and high-temperature superconductors have been studied in sufficient detail, whereas information regarding materials with a colossal magnetoresistive effect is very scarce and, in part, contradictory. This can be explained by the following factors.

First, the structural states of perovskite-type oxides are very sensitive to the quality and amount of different-type defects, including deviations from stoichiometry and variations in nanometer sizes of crystallites. This implies that variations in the structural order and disorder on the microscopic, mesoscopic, and macroscopic levels (i.e., on scales of a unit cell, a crystallite (crystal block), or a crystal, respectively) bring about considerable changes in the physical properties of the studied objects.

It is evident that the manifestation of a colossal magnetoresistive effect due to the specific features in the charge, orbital, and magnetic (spin) ordering [1, 2] substantially depends on the parameters of structural order and disorder in the materials under investigation.

A distinguishing feature of manganese-containing perovskites of the general formula $A'_{1-x}A''_x MnO_3$ is that, in these compounds, manganese can exist in the form of Mn^{4+} ($t_{2g}^3 e_g^0$) or Mn^{3+} ($t_{2g}^3 e_g^1$) cations depending on the charge state of the A' (A' = La^{3+}, etc.) and A'' (A'' = Ca^{2+}, etc.) cations. Under these conditions, there can occur ferromagnetic or antiferromagnetic interactions and magnetic ordering of different types that depend on the arrangement of Mn–O bonds in the perovskite structure. The physical model of colossal magnetoresistance within this approximation allows only for double exchange. More recent interpretation of the charge-transfer effect is based on the assumption that manganese-containing perovskites involve polarons whose energy correlates with lattice distortions. In this case, the electron–lattice interaction is associated with the fact that the e_g monolayer is present in Mn^{3+} and absent in Mn^{4+}. The degeneracy of the e_g monolayer is removed by the reduction in the symmetry of a regular oxygen octahedron through small distortions (Jahn–Teller effect). In the perovskite structure, Mn^{4+} cations do not contribute to lattice distortions. Therefore, Jahn–Teller distortions provide coupling of charge carriers in local regions, thus generating small polarons [3].

Second, perovskite structures have been repeatedly discussed in the literature in terms of the problem of small strains arising upon phase transitions and differing in origin from ferroelectric spontaneous strains. Similar phase transformations were referred to earlier by Isupov [4] as "compressive" phase transitions. More recently, these transformations were termed rotational phase transitions, because, in original publications [5–7], the strains observed in perovskite-type structures were considered to arise from rotations of undistorted oxygen octahedra due to freezing of the M_3 and R_{25} normal modes.

In this work, we experimentally revealed the specific features of the structural transformations in manganese-containing perovskites over a wide temperature range, including ranges of high-temperature phase transitions. For this purpose, we studied the changes in symmetry, unit cell parameters, interatomic bond

lengths, and Debye–Waller factors for individual atoms of the crystal lattice in the isotropic harmonic approximation.

Solid solutions in the well-known system $La_{1-x}Ca_xMnO_3$ (x = 0, 0.125, 0.30, 0.50) and a number of previously unknown compounds, namely, $La_{0.7}Bi_{0.3}MnO_3$, $La_{0.7}Cd_{0.3}MnO_3$, $Pr_{0.7}Bi_{0.3}MnO_3$, and $Pr_{0.7}Cd_{0.3}MnO_3$, were chosen as the objects of our investigation.

2. SAMPLE PREPARATION AND EXPERIMENTAL TECHNIQUE

Samples of solid solutions were prepared according to the standard procedure of solid-phase synthesis from stoichiometric mixtures of La_2O_3 (special-purity grade), Pr_2O_3 (special-purity grade), MnO_2 (special-purity grade), CdO (special-purity grade), CaO (analytical grade), and Bi_2O_3 (high-purity grade) upon sequential annealing in air at different temperatures in the range from 600 to 1000°C for 1 h. The $LaMnO_3$ compound was synthesized immediately in a temperature chamber mounted on an x-ray diffractometer. This

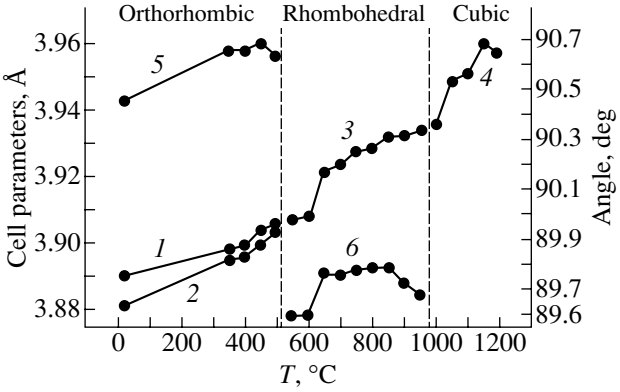

Fig. 1. Temperature dependences of the parameters of the reduced perovskite subcell for the orthorhombic, rhombohedral, and cubic phases of the $LaMnO_3$ compound: (*1*) $a_p = c_p$, (*2*) b_p, (*3*) a_R, (*4*) a_c, (*5*) β_p, and (*6*) α_R.

Table 1. Structural parameters of $A'_{1-x}A''_xMnO_3$ (A' = La, Pr; A'' = Ca, Cd, Bi) solid solutions at room temperature (the accuracy in determining the structural parameters is identical for all compositions)

Parameter	$La_{1-x}Ca_xMnO_3$				A'_{1-x}/A''_x (x = 0.3)		
	x = 0	x = 0.125	x = 0.3	x = 0.5	Pr/Cd	Pr/Bi	La/Bi
	Pnma	*Pnma*	*Pnma*	*Pnma*	*Pnma*	*Pnma*	*R*-3*c*
A_O, A_H, Å	5.4793(3)	5.4811	5.4613	5.4504	5.4370	5.4717	5.5211
B_O, Å	7.7634(4)	7.7595	7.7243	7.6905	7.7069	7.7181	
C_O, C_H, Å	5.5229(3)	5.5179	5.4858	5.4415	5.4852	5.4954	13.4571
A'/A'' x	0.480(1)	0.480	0.481	0.480	0.480	0.455	
z	0.506(1)	0.506	0.497	0.498	0.506	0.513	
$B(A'/A'')$, Å^2	1.06(2)	0.90	0.69	0.32	1.07	0.99	1.80
B(Mn), Å^2	0.71(2)	0.19	0.10	0.17	0.71	0.09	0.30
O(1), O x	0.009(1)	0.009	0.008	0.018	0.009	0.095	0.440
z	0.438(1)	0.437	0.559	0.569	0.437	0.440	
B(O(1), O), Å^2	1.35(2)	1.36	0.21	0.46	1.36	0.11	0.04
O(2) x	0.228(1)	0.229	0.221	0.196	0.229	0.208	
y	0.033(1)	0.043	0.033	0.031	0.033	0.063	
z	0.771(1)	0.771	0.778	0.725	0.771	0.778	
B(O(2)), Å^2	1.09(2)	1.10	2.36	0.15	1.09	0.50	
$\bar{B}_O$, Å^2	0.50(2)	1.58	0.71	2.91	1.50	3.42	1.98
R_p, %	9.55	6.34	9.25	8.83	7.11	11.61	10.16
$a_p = c_p$, a_R, Å	3.8899(3)	3.8888	3.8704	3.8509	3.8616	3.8775	3.8976
b_p, Å	3.8817(3)	3.8777	3.8622	3.8453	3.8535	3.8591	
β_p, α_R, deg	90.45(2)	90.39	90.26	90.09	90.51	90.25	89.91
V_p, Å^3	58.73(2)	58.63	57.85	57.02	57.46	58.02	59.21

Note: In Tables 1 and 2, the unit cell parameters A_O, B_O, and C_O of the orthorhombic phase, the x coordinate of the O(1) oxygen atom, and the parameters $a_p = c_p$ and b_p of the corresponding perovskite subcells are determined in the space group of symmetry *Pnma* and the unit cell parameters A_H and C_H of the rhombohedral phase, the x coordinate of the O oxygen atom, and the parameters a_R and α_R of the corresponding perovskite subcells are determined in the space group of symmetry *R*-3*c*.

Table 2. Structural parameters of the $La_{0.5}Ca_{0.5}MnO_3$ solid solution at different temperatures (the accuracy in determining the structural parameters is identical for all temperatures)

Parameter		*T*, °C				
		600	650		800	1000
		Pnma	*Pnma*	*R*-3*c*	*Pnma*	*Pm*-3*m*
A_O, A_H, Å		5.4740(3)	5.4718	5.4923	5.4912	
B_O, Å		7.7431(4)	7.7731		7.7877	
C_O, C_H, Å		5.4883(3)	5.4876	13.3740	5.5126	
Fraction, %		100	54	46	100	100
La/Ca	*x*	0.498(1)	0.497		0.498	
	z	0.498(1)	0.497		0.498	
B(La, Ca), Å^2		1.97(2)	0.62	1.76	1.33	2.00
B(Mn), Å^2		1.41(2)	0.27	1.00	0.47	0.50
O(1), O	*x*	0.198(1)	0.018	0.490	0.038	
	z	0.512(1)	0.569		0.569	
B(O(1), O), Å^2		0.55(2)	0.56	0.76	1.06	3.00
O(2)	*x*	0.276(1)	0.199		0.202	
	y	0.002(1)	0.031		0.031	
	z	0.745(1)	0.725		0.725	
B(O(2)), Å^2		0.36(2)	0.45		1.05	
$\bar{B}_O$, Å^2		1.01(2)	1.35	5.69	1.07	1.49
R_p, %		9.26	9.46		9.56	9.58
$a_p = c_p$, a_R, a_c, Å		3.8758(3)	3.8747	3.8760	3.8905	3.8971
b_p, Å		3.8716(3)	3.8866		3.8939	
β_p, α_R, deg		90.15(2)	90.17	89.74	90.22	
V_p, Å^3		58.16(2)	58.35	58.23	58.94	59.19

Note: The parameter a_c of the perovskite subcells is determined in the space group of symmetry *Pm*-3*m* (see also note to Table 1).

made it possible to observe the structure formation under specified temperature–time conditions. Ceramic samples were prepared by sintering at temperatures ranging from 1100 to 1250°C for 1 h.

The temperature dependences of the electrical conductivity were measured using samples with silver electrodes on a digital instrument in the temperature range 100–300 K.

X-ray diffraction analysis was performed in the Bragg–Brentano geometry on a DRON-3M diffractometer (CuK_α radiation; Ni filter; 2θ range $20° \le 2\theta \le 75°$; scan step, 0.08°; exposure time per frame, 1 s). The x-ray diffraction patterns were processed with the Powder Cell 2.3 program [8]. The accuracy in determining the structural parameters was as follows: ±0.0004 Å for unit cell parameters, ±0.02 Å for interatomic bond lengths, and ±0.2 Å^2 for Debye–Waller factors.

3. RESULTS AND DISCUSSION

Table 1 presents structural parameters of synthesized samples at room temperature, namely, unit cell parameters of the orthorhombic (A_O, B_O, C_O) and rhombohedral (A_H, C_H) phases, parameters of the corresponding perovskite subcells ($a_p = c_p$, b_p, β_p, a_R, α_R) and their volumes (V_p), positional parameters of atoms (*x*, *y*, *z*), isotropic Debye–Waller factors [*B*(*A*′/*A*″), *B*(Mn), *B*(O)] and generalized Debye–Waller factors ($\bar{B}_O$) for atoms in the structures, and discrepancy factors (R_p).

We compared our results obtained at room temperature with the data available in the literature for the compositions studied in the $La_{1-x}Ca_xMnO_3$ system [9–14]. It turned out that the structural parameters of the compounds synthesized are in good agreement with available data for stoichiometric (with respect to oxygen) compositions. Therefore, our compositions can also be considered to be stoichiometric. Note that direct deter-

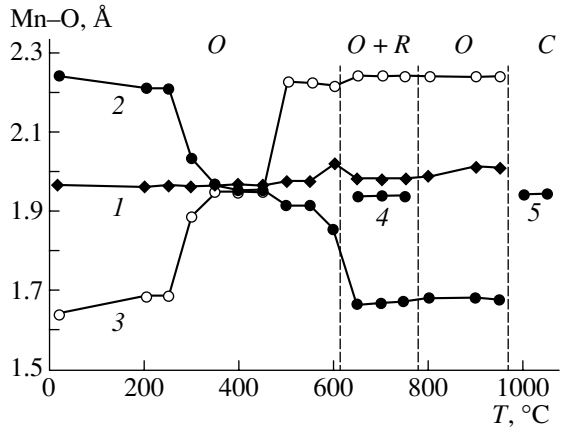

Fig. 2. Temperature dependences of the Mn–O bond lengths in the $La_{0.5}Ca_{0.5}MnO_3$ compound: (*1*) Mn–O(1); (*2*) Mn–O(2) (1); (*3*) Mn–O(2) (2), orthorhombic (*O*) phase; (*4*) Mn–O, rhombohedral (*R*) phase; and (*5*) Mn–O, cubic (*C*) phase.

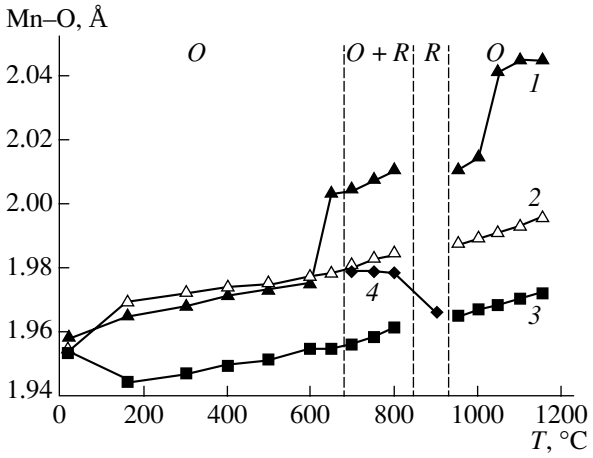

Fig. 3. Temperature dependences of the Mn–O bond lengths in the $Pr_{0.7}Cd_{0.3}MnO_3$ compound: (*1*) Mn–O(1); (*2*) Mn–O(2) (1); (*3*) Mn–O(2) (2), orthorhombic (*O*) phase; and (*4*) Mn–O, rhombohedral (*R*) phase.

mination of the manganese valence is a very complicated problem [15].

The temperature dependences of the parameters of the perovskite subcells for the orthorhombic (*Pnma*), rhombohedral (*R*-3*c*), and cubic (*Pm*-3*m*) phases of the $LaMnO_3$ compound are depicted in Fig. 1. According to the results obtained by Rodriguez-Carvajal *et al.* [10], this compound has a pseudocubic phase in the temperature range from $T_1 = 477$°C to $T_2 = 737$°C. However, our investigations revealed a direct transition from the orthorhombic phase to the rhombohedral phase at $T_1 = 525$°C and a transition from the rhombohedral phase to the cubic phase at $T_2 = 975$°C. This difference in the results obtained in [10] and in this work can be explained by both the different structural qualities of the samples studied and the different accuracies in processing the experimental data.

The results of the structure refinement for the $La_{0.5}Ca_{0.5}MnO_3$ solid solution at several temperatures in the vicinity of high-temperature phase transitions are presented in Table 2. Note that these results were obtained for eighteen temperatures in 50-degree intervals ($\Delta T = 50$°C).

It can be seen from Table 2 that the $La_{0.5}Ca_{0.5}MnO_3$ compound is characterized by an unusual sequence of phase transformations. As the temperature decreases, the $La_{0.5}Ca_{0.5}MnO_3$ compound at temperature $T_1 = 975$°C undergoes a transition from the cubic phase to

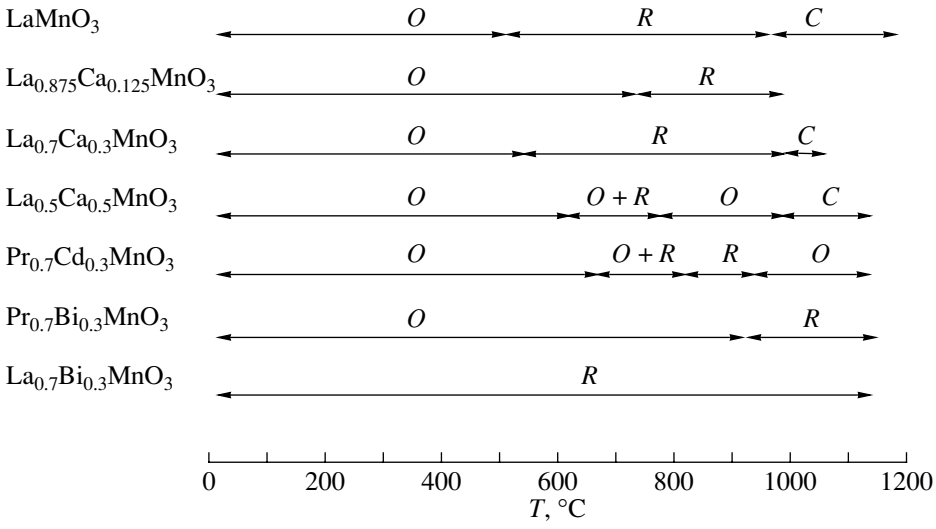

Fig. 4. Schematic diagram illustrating the regions of existence of the orthorhombic (*O*), rhombohedral (*R*), and cubic (*C*) phases of compositions $A'_{1-x}A''_xMnO_3$ (*A*' = La, Pr; *A*" = Ca, Cd, Bi) in the temperature range from 20 to 1180°C.

the orthorhombic phase, which, at $T_2 = 775°C$, partially transforms into the rhombohedral phase. At temperatures below $T_3 = 625°C$, the sample contains only the orthorhombic phase. The temperature dependences of the Mn–O bond lengths in the $La_{0.5}Ca_{0.5}MnO_3$ compound upon the above phase transformations are shown in Fig. 2. A similar sequence of phase transformations with a decrease in the temperature is observed for the $Pr_{0.7}Cd_{0.3}MnO_3$ compound (Fig. 3).

The distinguishing features of the orthorhombic phase are as follows: as the temperature increases in the range below 300°C, the shortened Mn–O bond becomes longer, whereas the lengthened Mn–O bond becomes shorter; as a result, both bond lengths approach a mean value. This indicates that the oxygen octahedra have a nearly perfect shape. As the temperature increases in the range above 450°C, the Mn–O bond, which is shortened at low temperatures, transforms into a lengthened Mn–O bond and the lengthened Mn–O bond transforms into a shortened Mn–O bond. The mean Mn–O bond length only slightly changes over the entire temperature range and is close to the Mn–O bond length in the rhombohedral and cubic phases.

Therefore, it can be assumed that the anisotropy revealed in the Mn–O bond lengths in the orthorhombic phase is associated with a specific strain order parameter. It is worth noting that this order parameter is related to neither the Jahn–Teller effect nor the freezing of the M_3 and R_{25} normal modes.

The schematic diagram illustrating the regions of existence of the orthorhombic, rhombohedral, and cubic phases for the studied compositions of manganese-containing perovskites is given in Fig. 4.

It should be noted that the $La_{0.7}Bi_{0.3}MnO_3$ solid solution is characterized by an interesting feature: in this compound, the rhombohedral phase exists over the entire temperature range under investigation. For a similar compound, namely, $Pr_{0.7}Bi_{0.3}MnO_3$, the rhombohedral phase is observed only at temperatures above 925°C. Our results obtained for solid solutions in the $La_{1-x}Ca_xMnO_3$ ($x = 0$, 0.125, 0.30, 0.50) system in the high-temperature range complement the data reported recently by Naish [16]. In particular, we revealed the high-temperature orthorhombic phase of the $La_{0.5}Ca_{0.5}MnO_3$ compound for the first time. This phase directly transforms into the cubic phase at higher temperatures and into the rhombohedral phase at lower temperatures.

4. CONCLUSIONS

Thus, the above analysis of the structural data on the phase states in the solid solutions studied in the present work demonstrated that these compounds are characterized not only by the parameters of charge, orbital, and spin ordering and disordering (at low temperatures) but also by other order parameters (at high temperatures).

ACKNOWLEDGMENTS

We would like to thank V.P. Sakhnenko and Yu.M. Gufan for their participation in discussions of the results and helpful remarks.

This work was supported by the Russian Foundation for Basic Research, project no. 04-03-32039.

REFERENCES

1. J. B. Goodenough and J. M. Longo, in *Landolt–Börnstein Numerical Data and Functional Relationships in Science and Technology: New Series*, Ed. by K.-H. Hellwege (Springer, Berlin, 1970), Group III, Vol. 4a, p. 207.
2. M. B. Salamon and M. Jaime, Rev. Mod. Phys. **73**, 583 (2001).
3. C. P. Adams, J. W. Lynn, Y. M. Mukovskii, A. A. Arsenov, and D. A. Shulyatev, Phys. Rev. Lett. **85** (18), 3954 (2000).
4. V. A. Isupov, Kristallografiya **4** (4), 603 (1959) [Sov. Phys. Crystallogr. **4**, 564 (1959)].
5. A. M. Glaser, Acta Crystallogr. A **31** (6), 756 (1975).
6. A. M. Glaser, Acta Crystallogr. B **28** (2), 338 (1972).
7. K. S. Aleksandrov, A. T. Anistratov, B. V. Beznosikov, and N. V. Fedoseeva, *Phase Transitions in Crystals of Halide Compounds ABX_3* (Nauka, Novosibirsk, 1981) [in Russian].
8. W. Krause and G. Nolze, J. Appl. Crystallogr. **29**, 301 (1996).
9. Q. Huang, A. Santoro, J. W. Lynn, R. W. Erwin, J. A. Borchers, J. L. Peng, and R. L. Greene, Phys. Rev. B **55** (22), 14 987 (1997).
10. J. Rodriguez-Carvajal, M. Hennion, F. Moussa, A. H. Moudolen, L. Pinsard, and A. Revcolevschi, Phys. Rev. B **57** (6), R3189 (1998).
11. J. He, R. Wang, J. Gui, and C. Dong, Phys. Status Solidi B **229** (3), 1145 (2002).
12. P. G. Radaelli, D. E. Cox, M. Marezio, and S.-W. Cheong, Phys. Rev. B **55** (5), 3015 (1997).
13. S. J. L. Billinge, Th. Proffen, V. Petkov, J. L. Sarrao, and S. Kycia, Phys. Rev. B **62** (2), 1203 (2000).
14. C. H. Booth, F. Bridges, G. H. Kwei, J. M. Lawrence, A. L. Cornelius, and J. J. Neumeier, Phys. Rev. B **57** (17), 10 440 (1998).
15. Z. L. Wang, J. S. Yin, and Y. D. Jiang, Appl. Phys. Lett. **70** (25), 3362 (1997).
16. V. E. Naish, Phys. Met. Metallogr. **92** (5), 437 (2001).

Translated by O. Borovik-Romanova

Physics of the Solid State, Vol. 46, No. 10, 2004, pp. 1927–1932. Translated from Fizika Tverdogo Tela, Vol. 46, No. 10, 2004, pp. 1861–1865.

LOW-DIMENSIONAL SYSTEMS AND SURFACE PHYSICS

Coulomb Instability of Charged Clusters

E. V. Vasyutin and V. V. Pogosov

Zaporozh'e National Technical University, Zaporozh'e, 69063 Ukraine

e-mail: vasutin@zntu.edu.ua

Received February 17, 2004

Abstract—A model different from the Rayleigh model for Coulomb instability of charged metallic clusters is proposed. The two-component model of a metallic cluster in the quasi-classical approximation offers different critical charges depending on the type of charged particles. For small-sized parallelepiped clusters, the quantization of the electronic spectrum is taken into account. The critical sizes of Ag_N^{2-} and Ag_N^{3-} clusters are calculated in the framework of the proposed model. The results of calculations are in good agreement with experimental data. The Coulomb explosion of positively charged clusters Na_N^{n+} at $3 \le n \le 5$ is explained qualitatively.

1. INTRODUCTION

Since the work by Sattler *et al.* [1], mass spectrometric investigations of the charging in cluster beams have clearly demonstrated that the size effect is characteristic of Coulomb instability of charged metallic clusters with a finite number of atoms [2–4].

The problem of finding the stability criterion for a charged spherical droplet was solved by Rayleigh. The instability arises at an excess charge Q such that a sphere stretches into a spheroid and then collapses. Within this approach, the spherical shape corresponds to an extremum of the sum of the electrostatic energy $Q^2/2C$ and the surface energy τA, where C is the electrical capacitance of the droplet, $A = 4\pi R^2$ is the surface area of the droplet, and τ is the surface tension. The critical charge is determined from the condition $X = 1$, where X is the ratio of the electrostatic energy to the doubled surface energy. In their recent work, Duft *et al.* [5] for the first time experimentally confirmed the validity of this criterion ($X = 1$) for micrometer-sized droplets of ethylene glycol.

The Rayleigh expression for the excess charge has the following form [6]:

$$Q_R = \pm\sqrt{16\pi R^3 \tau}. \qquad (1)$$

The particle type determining the charge sign is immaterial in this formula. For example, a metallic droplet can contain an excess number of electrons $\Delta N_R^e = |Q_R|/e$ or ions $\Delta N_R^i = |Q_R|/Ze$, where Z is the valence and e is the elementary positive charge. However, such a problem should be considered within a two-component cluster model in which electrons and ions are treated on equal terms [7–9]. The solution of this problem results in a different size dependence of the excess number of particles $\Delta N_{i,e} \propto R$ (as compared to $\Delta N_R \propto R^{3/2}$).

In the present work, we constructed a simple analytical theory of size-dependent Coulomb instability for charged metallic clusters. For a cluster having the shape of a parallelepiped, the quantization of the electronic spectrum was taken into account. The model makes it possible to elucidate the physical origin of the instability and to explain the critical sizes of silver, gold, and sodium clusters without resorting to complex self-consistent calculations of clusters with different symmetries (see [2, 4] and references therein).

2. THE QUASI-CLASSICAL APPROXIMATION

Let us assume that a neutral cluster contains $N_e/Z = N_i = N$ atoms. The energy of a charged cluster that has an excess number of electrons $|\Delta N_e| \ll N_e$ can be written in the form

$$E_{N_e+\Delta N_e} = E_{N_e} + \mu_e \Delta N_e + \frac{(-e\Delta N_e)^2}{2C}, \qquad (2)$$

where μ_e is the chemical potential of electrons. The cluster will retain the ΔN_e excess electrons if its state with the number of electrons $N_e + \Delta N_e - 1$ is characterized by a higher total energy. The number of electrons ΔN_e^* will be referred to as the critical number when the reaction

$$M_{N_i}^{(\Delta N_e^*)^-} \rightleftharpoons M_{N_i}^{(\Delta N_e^* - 1)^-} + e^-$$

becomes reversible and the following condition is satisfied:

$$\Delta E(\Delta N_e^*) = E_{N_e+\Delta N_e^*-1} - E_{N_e+\Delta N_e^*} \equiv IP^* \longrightarrow 0, \qquad (3)$$

This means that the ionization potential $IP^* > 0$ of this cluster is close to zero. It should be noted that one more excess electron can occur only in the cluster in a metastable state, because the sticking energy of this electron satisfies the inequality

$$\begin{aligned} EA^* &= E_{N_e+\Delta N_e^*} - E_{N_e+\Delta N_e^*+1} \\ &= -\mu_e - \frac{e^2}{2C}(2\Delta N_e + 1) < 0. \end{aligned} \tag{4}$$

In this case, the relationship

$$IP^* - EA^* = \frac{e^2}{C}$$

always holds true. At $\Delta N_e > \Delta N_e^*$, the cluster is overcharged. The electrons in the cluster are separated from free states by a barrier and can be bound for a time. The lifetime of each electron is governed by specific conditions in a nonequilibrium system.

From relationships (2) and (3), we obtain the expression for the critical excess electron charge:

$$\Delta N_e^* = \frac{W_{e0}C - \mu_{e1}}{e^2} + \frac{1}{2}, \tag{5}$$

where $W_{e0} = -\mu_{e0}$ is the work function of the flat surface, $\mu_e = \mu_{e0} + \mu_{e1}/R$, μ_{e1}/R is the first correction for the curvature of the chemical potential of the degenerate electron liquid in the case of a sphere with the radius $R = N^{1/3}r_0$, and r_0 is the mean interionic distance.

It is interesting to note that the critical charge even for particles containing more than a thousand atoms does not exceed several units. This is associated with the fact that the excess electron charge is distributed over the cluster surface. As a consequence, a strong Coulomb repulsion (self-interaction) arises between individual parts of the charge. This is not the case when negative ions are formed by individual atoms and molecules in which excess electrons are not collectivized.

Now, we consider a positively charged cluster that is formed by metal atoms and contains $N_e = ZN_i$ electrons and $N_i + \Delta N_i$ ions. This situation is similar to that for a droplet involving N_i ions and $\Delta N_e < 0$ electrons (deficit). In this case, $|\Delta N_e|$ should be a multiple of Z.

The energy $E_{N_i+\Delta N_i}$ of the charged cluster can be expressed through the total energy of the neutral cluster as follows:

$$E_{N_i+\Delta N_i} = E_{N_i} + \mu_i \Delta N_i + \frac{(+eZ\Delta N_i)^2}{2C}. \tag{6}$$

As in relationship (2), the main contribution to the dependence on R is made by the term $+eZ\Delta N_i$ describing the repulsion of the excess charge. In actual fact, ions have a low mobility and the repulsion of the positive charge is provided by the redistribution of the mobile electronic subsystem.

The change in the energy due to the removal of one ion can be represented in the form

$$\begin{aligned} \Delta E(\Delta N_i) &= E_{N_i+\Delta N_i-1} - E_{N_i+\Delta N_i} \\ &= -\mu_i - \frac{e^2Z^2}{2C}(2\Delta N_i - 1). \end{aligned} \tag{7}$$

The cluster with charge $+eZ\Delta N_i$ is stable under the condition $\Delta E(\Delta N_i) > 0$. The reaction

$$M_{N_i+\Delta N_i^*}^{Z(\Delta N_i^*)+} \rightleftharpoons M_{N_i+\Delta N_i^*-1}^{Z(\Delta N_i^*-1)+} + M_1^{Z+}$$

becomes reversible when the number of ions reaches the critical value ΔN_i^*. Then, we have

$$\Delta N_i^* = \frac{W_{i0}C - \mu_{i1}}{(Ze)^2} + \frac{1}{2}, \tag{8}$$

where $W_{i0} = -\mu_{i0}$ is the ion work function of the flat surface. For a sphere of radius $R = (N_i + \Delta N_i)^{1/3}r_0$, we use the sum rule [8] and write

$$\mu_{i1} = \frac{2\sigma_0}{\bar{n}} - \mu_{e1}, \tag{9}$$

where σ_0 is the specific surface energy and $\bar{n} = 3Z/4\pi r_0^3$ is the electron density. For the metals under investigation, we have $\mu_{e1} \simeq 1.9\ \text{eV} \times a_0$ [8].

For $\Delta N_i > \Delta N_i^*$, the cluster releases a surplus ion and transforms into a state with a lower energy. This approach is equivalent to considering a droplet as a two-component electron–ion system with the corresponding chemical potentials.

The ion work function can be expressed with the use of the Born cycle through the ionization potentials $IP(\zeta)$ of one atom, the cohesive energy $\varepsilon_{\text{coh}0}$, and the electron work function W_{e0} as follows:

$$W_{i0} = \varepsilon_{\text{coh}0} + \sum_{\zeta} IP(\zeta) - \zeta W_{e0}, \tag{10}$$

where ζ is the degree of ionization of an atom ($\zeta \le Z$). At $\varepsilon_{\text{coh}0} = 15$ eV, $W_{e0} = 4.0$ eV, and $IP(1) = 7.4$ eV for lead, we obtain $W_{i0} = 4.9$ eV. At $R = 12a_0$, the critical charge turns out to be equal to $+2.7e$. This agrees well with the experimental data obtained in [1] and the results of complex self-consistent calculations [2].

Within the above approach, it is assumed that the charging of the cluster does not lead to a change in the cluster shape. Expressions (5) for ΔN_e^* and (8) for ΔN_i^* include and differentiate the emission (sticking) of electrons or ions. This is associated with the necessity of expending energy on introducing a particle of a

particular type into the cluster and redistributing the particle charge over the surface. Such a mechanism of explosion of the charged atomic cluster can be treated as an alternative to the Rayleigh mechanism. The estimates show that the inequality $\Delta N_R > \Delta N_i > \Delta N_e^*$ should be satisfied. This implies that the charging should predominantly result in one-particle emission rather than in Rayleigh instability. For small-sized clusters, the quantization of the electronic spectrum plays an important role.

3. QUANTIZATION OF THE ELECTRONIC SPECTRUM

Only in rare cases is a real cluster shaped like a sphere. In this respect, for convenience (see, for example, [10]), the electronic spectrum will be determined for a cluster in the form of a parallelepiped of volume $\Omega = abc$. The potential field inside the cluster $L \equiv a \times b \times c$ in size can be represented as a rectangular potential well with depth $U_0 < 0$:

$$-U_0 = W_{e0} + \varepsilon_F^0. \quad (11)$$

Here, $\varepsilon_F^0 = \hbar^2(3\pi^2\bar{n})^{2/3}/2m$ is the Fermi energy of a degenerate electron liquid and m is the electron mass. The potential outside the well is equal to zero. Relationship (11) describes the position of the conduction band bottom for a semi-infinite metal. The size dependence of the position of the well bottom is ignored [11].

The allowed levels (kinetic energies of electrons) form a discrete spectrum: $\varepsilon_j = \varepsilon_{n_x} + \varepsilon_{n_y} + \varepsilon_{n_z}$. The wave vector components are determined from the equations

$$k_n L = n\pi - 2\arcsin(k_n/k_0), \quad (12)$$

where $n \equiv n_x, n_y$, and n_z are integers and $\hbar k_0 = \sqrt{-2mU_0}$. In order to separate real levels from virtual levels, we introduce the criterion

$$k_n/k_0 < 1. \quad (13)$$

For the parallelepiped cluster with sides a, b, and c and the potential profile with infinitely high walls, the spectrum is given by the expression

$$\varepsilon_j^\infty = \frac{\hbar^2\pi^2}{2m}\left(\frac{n_x^2}{a^2} + \frac{n_y^2}{b^2} + \frac{n_z^2}{c^2}\right),$$

where j is the number of the state.

The solutions of Eqs. (12) can be reduced to the solution for an infinitely deep well within the perturbation theory [12]. For this purpose, we can write

$$k_{n_x} = k_{n_x}^\infty + \Delta k_{n_x}, \quad \xi \equiv \left|\Delta k_{n_x}/k_{n_x}^\infty\right| \ll 1, \quad (14)$$

where $k_{n_x}^\infty = \pi n_x/a$ is the solution corresponding to $k_0 \longrightarrow \infty$. By substituting relationships (14) into Eqs. (12), we find that, to a first approximation, $\xi = -2/ak_0$ for a cube and the spectrum can be represented in the following form:

$$\varepsilon_j = \frac{\hbar^2\pi^2}{2ma^2}[1 + 2\xi + O(\xi^2)](n_x^2 + n_y^2 + n_z^2). \quad (15)$$

The alternative expression directly follows from Eqs. (12) with criterion (13); that is,

$$\varepsilon_j \simeq \frac{\hbar^2\pi^2}{2m}\left(\frac{k_0}{2 + ak_0}\right)^2(n_x^2 + n_y^2 + n_z^2). \quad (16)$$

The number N_e of electrons in a neutral cube is specified, on the one hand, and is determined by the sum $2\sum_j \delta(\varepsilon - \varepsilon_j)$ over all the filled states with due regard for the double spin degeneracy, on the other hand. By distributing electrons over the levels, we find the energy of the highest occupied state $\varepsilon^{HO} < 0$ (reckoned from the vacuum level). The ionization potential IP for the cubic cluster can be determined from the formula

$$IP = -\varepsilon^{HO} + \frac{e^2}{2C}, \quad (17)$$

with the use of the capacitance of an equivalent sphere.

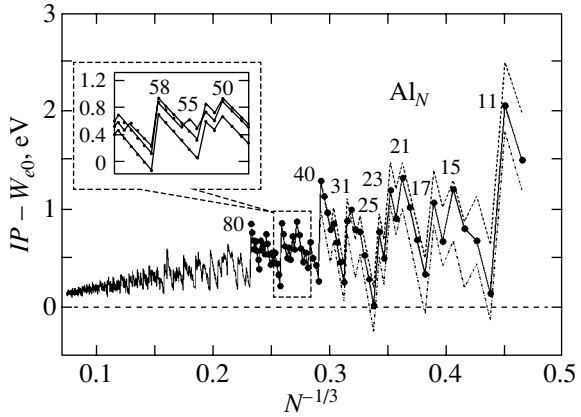

Fig. 1. Size dependences of the first ionization potential (17) calculated for Al_N clusters according to solutions (12) (solid line), (15) (dashed line), and (16) (dot-dashed line). Numbers at the top correspond to the numbers of atoms in the cluster.

4. RESULTS AND DISCUSSION

Initially, we analyze the analytical approximation derived in the preceding section as applied to aluminum clusters ($W_{e0} = 4.25$ eV, $r_0 = 2.99a_0$). The calculated size dependences of the ionization potential (17) for Al_N cubic clusters are plotted in Fig. 1. The dependences were obtained using the spectra calculated from formulas (12), (15), and (16). The results of the calculations carried out in the range $N = (10, 3000)$ demonstrate that the spectrum quantization plays an important role even

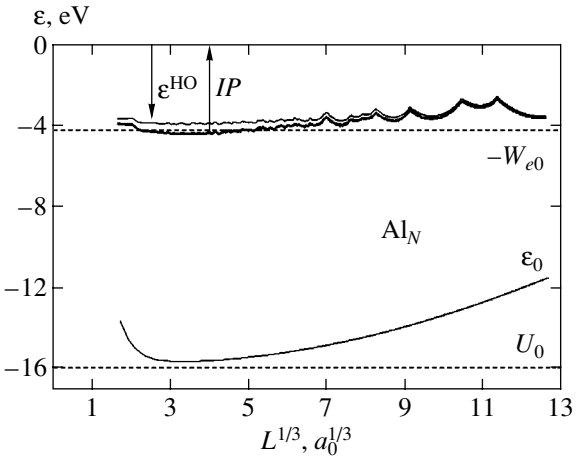

Fig. 2. Evolution in the size dependence of the first ionization potential (17) for an Al_N parallelepiped cluster with a change in the cluster shape from a plate to a wire.

for very large clusters. The obtained magic numbers are close to those observed in experiments [13].

Already for a hundred atoms, the calculations of the spectrum from approximate formulas (15) and (16) lead to quite reasonable results. However, their inaccuracy results in the level system differing from that determined from Eqs. (12). As an illustration, the differences in the spectra for N close to $N = 58$ are shown in the inset to Fig. 1.

It should be noted that the calculations of the spectra from formulas (12) are characterized by specific features. The resulting term is a combination of the solutions of the one-dimensional problem, and it is necessary to determine combinations such that they correspond to the minimum energies of this term.

Now, we examine the dependence of the ionization potential for the cluster on the cluster shape. It is assumed that the cluster shape can change from a strongly flattened parallelepiped to a strongly elongated parallelepiped, so that we have initially a monoatomic plate of thickness L and then a monoatomic wire of length L. The volume in the course of this evolution remains constant, namely, $\Omega = 4$ nm^3.

The interval L is divided into 1000 portions, and the spectrum is determined by solving Eqs. (12) for each geometry. In the ionization potential (17), the capacitance of an equivalent spheroid is used as the capacitance of the parallelepiped. The size dependence of this capacitance exhibits a minimum for a sphere. In the limiting cases, the capacitances of the plate and the wire are approximately two and seven times larger, respectively.

The calculated dependences for aluminum clusters are depicted in Fig. 2. The dotted lines indicate the bottom U_0 and the electron work function W_{e0} of the flat surface. The inequality $-\varepsilon^{HO} \equiv W_e < W_{e0}$ is satisfied over the entire interval L. The minimum in the dependence $\varepsilon_0(L)$ corresponds to a cubic shape of the cluster. Moreover, there are sizes L for which the quite unexpected inequality $IP < W_0$ is satisfied.

Seemingly, the inequality $IP < W_0$ is inconsistent with the well-known empirical fact that the work function W_0 of alkali metals is approximately equal to half the ionization potential IP of an atom [14]. In this respect, it is commonly believed that the ionization potential IP of an arbitrary atomic cluster (irrespective of the shape of the cluster surface) varies in the range $W_0 < IP(N) < IP(1)$. However, the competition between the size component in $W(L)$ and the term $e^2/2C$ in relationship (17) can lead to the opposite inequality.

In their recent work, Yannouleas *et al.* [4] analyzed the spectrometric data and determined the minimum numbers of atoms at which charged gold clusters Au_N^{2-} ($N > 27$) and Au_N^{3-} ($N > 58$) and charged silver clusters Ag_N^{2-} ($N > 27$) containing two or three excess electrons remain stable. This problem is the inverse of the problem considered above. Indeed, in this case, the critical number of electrons ΔN_e^* is specified and it is necessary to determine the corresponding value of R (or N).

In our subsequent calculations, we will use the following empirical data: $W_{e0} = 4.23$ (5.15), 4.23, and 2.75 eV; $r_0 = 3.01a_0$, $3.02a_0$, and $3.99a_0$; and $\tau = 1134$, 780, and 191 erg/cm^2 for Au, Ag, and Na, respectively (here, for simplicity, we assume that the specific surface energy and the surface tension are equal to each other; however, these quantities can differ substantially [15]).

According to the Rayleigh formula (1), the critical numbers of atoms in clusters are approximately four or five times smaller: $N \approx 9$ and 6 for Au_N^{3-} and Ag_N^{2-} clusters, respectively. In our model, the solution of this problem consists in seeking the root of the equation

$$IP^*(\Delta N_e^*, N) = -\varepsilon^{HO}(\Delta N_e^*, N) - \frac{e^2}{2C_{\text{eff}}(N)}(2\Delta N_e^* - 1) = 0. \quad (18)$$

When interpreting experimental data on the charging of clusters, it is expedient to use the effective capacitance $C_{\text{eff}} = R + \delta$. The introduction of a small quantity δ is associated with the increase in the radius of the electron charge cloud. The quantity δ was first determined in calculations of the polarizability [16] and the ionization potential [17]. By calculating the coordinates of the image plane positions (within the stabilized jellium model) for different crystallographic surfaces [18], it is possible to construct the averaged dependence $\delta(r_0) = 1.617 + 0.199(r_0/Z^{1/3} - 2.07)[a_0]$.

It should be noted that the introduction of the quantity δ into relationships (18) and (17) is not a rigorous procedure. Formally, this corresponds to the inclusion

only of the Hartree part δ/R^2 of the next size correction of the energy expansion in $1/R$. However, the solution of Eq. (18) is sensitive to this quantity and is not very sensitive to the self-compression of clusters [8].

Expression (3) with the aforementioned modification of the ionization potential IP ($\Delta N_e < 0$) describes well successive photoionization events of large-sized Al_N clusters over a wide range of N = (2000, 32 000) [19]. The introduction of $C_{\text{eff}} = R + \delta$ only slightly weakens the size dependence $IP(N)$ in Fig. 1.

The size dependences $IP^*(\Delta N_e^*, N)$ calculated from relationships (18) and (5) are shown in Fig. 3. The intersection points of these dependences with the horizontal axis indicate the sought values of N. It can be seen from Fig. 3 that the quasi-classical dependence (5) and the inclusion of the level quantization in expression (18) lead to better agreement with the experimental data as compared to the Rayleigh formula. Note that the work function W_{e0} = 5.15 eV recommended by Michaelson [20] was used for Au_N^{3-} clusters. The Au_N^{2-} clusters are stable at $N > 20$. However, with the work function W_{e0} = 4.3 eV, the solution of Eq. (18) corresponds to the Au_{27}^{2-} and Au_{110}^{3-} clusters. The specific features in the energy properties of gold clusters were noted even by Garron [21].

Finally, we apply our computational procedure to positively charged clusters Na_N^{n+}. Näher *et al.* [3] experimentally determined the critical numbers N = 64, 123, and 208 for clusters with n = 3, 4, and 5, respectively. In our model, we have $N \equiv N_i + \Delta N_i^*$ and $n \equiv \Delta N_i^*$. The critical sizes are calculated from formulas (8)–(10) in which we make the change $W_{e0} \longrightarrow \varepsilon^{HO}$ and eliminate μ_{e1}. For Na, the parameters ε_{coh} = 1.13 eV and $IP(1)$ = 5.14 eV are used in the calculations.

The results of the calculations for Na clusters are presented in Fig. 4. For small-sized clusters, the situation can be described by the Rayleigh formula according to which $|Q_R| \propto N^{1/2}$. The quasi-classical instability leads to the relationship $eZ\Delta N_i^* \propto N^{1/3}$. The calculated critical sizes of clusters are overestimated as compared to the experimental critical sizes. Judging from the data presented in Fig. 2, we can assume that charged cubic clusters are predominantly distorted to parallelepipeds. This leads to the change in the dimension of the electron gas. In this case, the change in the spectrum of their highest occupied states ε^{HO} is less significant than that in the term associated with the charging due to an increase in the capacitance. Moreover, the elongation of clusters is accompanied by a change in the cohesive energy. This is confirmed by the experimental data on the deformation of point contacts: a decrease in the dimension results in a considerable increase in the contact strength [22]. These factors can be responsible for the difference between the calculated and experimental dependences $\Delta N_i^*(N)$.

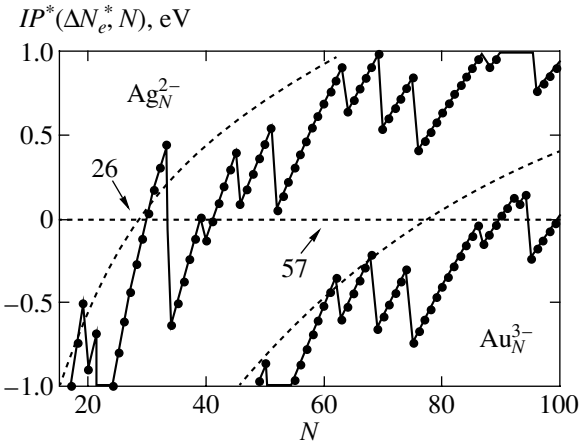

Fig. 3. Size dependences of the ionization potential (18) for Au_N^{3-} and Ag_N^{2-} clusters (solid lines). Dashed lines represent the quasi-classical dependences IP (5). Arrows indicate the experimental critical numbers N.

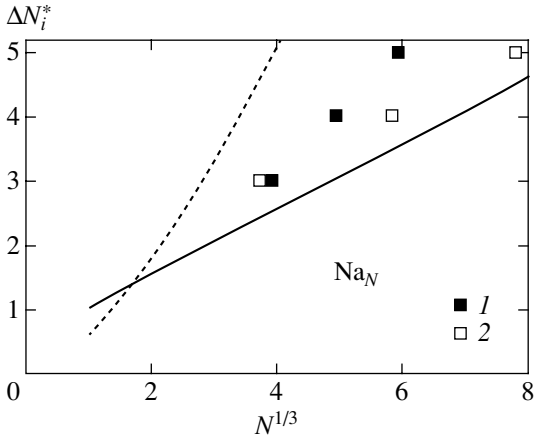

Fig. 4. (*1*) Experimental and (*2*) calculated critical sizes of positively charged clusters Na_N. The solid line indicates the quasi-classical dependence (8), and the dotted line is the Rayleigh dependence.

ACKNOWLEDGMENTS

This work was supported by the Ministry of Education and Science of Ukraine, project no. 06113.

REFERENCES

1. K. Sattler, O. Mühlbach, and E. Recknagel, Phys. Rev. Lett. **47** (3), 160 (1981).
2. U. Näher, S. Bjornholm, S. Frauendorf, F. Garcias, and C. Guet, Phys. Rep. **285**, 245 (1997).

3. U. Näher, H. Göhlich, T. Lange, and T. P. Martin, Phys. Rev. Lett. **68** (23), 3416 (1992).
4. C. Yannouleas, U. Landman, A. Herlert, and L. Schweikhard, Phys. Rev. Lett. **86** (14), 2996 (2001).
5. D. Duft, H. Lebius, B. A. Huber, C. Guet, and T. Leisner, Phys. Rev. Lett. **89** (8), 084503 (2002).
6. V. V. Batygin and I. N. Toptygin, *Modern Electrodynamics*, Part 1: *The Microscopic Theory* (Inst. Komp'yut. Issled., Moscow, 2003) [in Russian].
7. I. T. Iakubov, A. G. Khrapak, L. I. Podlubny, and V. V. Pogosov, Solid State Commun. **53** (4), 427 (1985).
8. V. V. Pogosov, Fiz. Tverd. Tela (St. Petersburg) **37** (9), 2807 (1995) [Phys. Solid State **37**, 1547 (1995)].
9. A. Kiejna and V. V. Pogosov, J. Phys.: Condens. Matter **8** (23), 4345 (1996).
10. D. M. Wood and N. W. Ashcroft, Phys. Rev. B **25** (10), 6255 (1982).
11. V. P. Kurbatskiĭ and V. V. Pogosov, Fiz. Tverd. Tela (St. Petersburg) **46** (3), 526 (2004) [Phys. Solid State **46**, 543 (2004)].
12. A. Kawabata and R. Kubo, J. Phys. Soc. Jpn. **21** (1), 17 (1966).
13. W. A. de Heer, Rev. Mod. Phys. **65** (3), 611 (1993).
14. K. Wong, S. Vongehr, and V. V. Kresin, Phys. Rev. B **67** (3), 035 406 (2003).
15. V. V. Pogosov and V. P. Kurbatsky, Zh. Éksp. Teor. Fiz. **119** (2), 350 (2001) [JETP **92**, 304 (2001)].
16. D. R. Snider and R. S. Sorbello, Phys. Rev. B **28** (10), 5702 (1983).
17. J. P. Perdew, Phys. Rev. B **37** (11), 6175 (1988).
18. A. Kiejna and K. F. Wojciechowski, *Metal Surface Electron Physics* (Pergamon, Oxford, 1996).
19. M. A. Hoffmann, G. Wrigge, and B. von Issendorff, Phys. Rev. B **66** (4), 014 404 (2002).
20. H. B. Michaelson, J. Appl. Phys. **48** (11), 4729 (1977).
21. R. Garron, Ann. Phys. **10** (9/10), 595 (1965).
22. N. Agraït, A. L. Yeyati, and J. M. van Ruitenbeek, Phys. Rep. **377**, 81 (2003).

Translated by O. Borovik-Romanova

Physics of the Solid State, Vol. 46, No. 10, 2004, pp. 1933–1934. Translated from Fizika Tverdogo Tela, Vol. 46, No. 10, 2004, pp. 1866–1867.

LOW-DIMENSIONAL SYSTEMS AND SURFACE PHYSICS

Specific Heat of Quasi-One-Dimensional Superionic $LiCuVO_4$

I. A. Smirnov*, D. Wlosewicz, A. V. Prokof'ev***, and W. Assmus*****

**Ioffe Physicotechnical Institute, Russian Academy of Sciences, Politekhnicheskaya ul. 26, St. Petersburg, 194021 Russia*
e-mail: igor.smirnov@pop.ioffe.rssi.ru

***Institute of Low-Temperature and Structural Research, Polish Academy of Sciences, Wroclaw, 50-950 Poland*

****Institute of Physics, Goethe University, Frankfurt am Main, 60054 Germany*

Received February 24, 2004

Abstract—The specific heat at constant pressure of polycrystalline $LiCuVO_4$ has been measured at temperatures of 80 to 310 K. The data obtained corroborate the earlier conclusion that this material is a superionic.

Measurements of the temperature behavior of thermal conductivity κ^a (in the range 5–300 K), electrical conductivity σ^a (at 300–500 K), and permittivity ε^a (in the interval 300–390 K) were reported in [1, 2] for $LiCuVO_4$ single crystals[1] crystallizing in an orthorhombically distorted inverse spinel structure, in which the nonmagnetic V^{5+} ions occupy tetrahedral cavities, while the nonmagnetic Li^+ and magnetic Cu^{2+} ($S = 1/2$) ions are ordered in octahedral cavities of the anion sublattice [3]. The CuO_6 and LiO_6 octahedra make up magnetic and nonmagnetic chains, respectively, aligned with the *b* and *a* directions in $LiCuVO_4$.

The data from [1, 2] led to the conclusion that $LiCuVO_4$ is a quasi-one-dimensional superionic.

The temperature dependence of the thermal conductivity of $LiCuVO_4$ measured along nonmagnetic lithium chains [1] revealed a growth of κ^a at $T > 150$ K (in place of the expected drop in the lattice thermal conductivity), which we attributed, by analogy with the data presented in [4], to the presence of superionic conduction in this compound.

A study of the thermal conductivity and heat capacity of a number of superionics, including the quasi-one-dimensional superionic $Li_2B_4O_7$, was reported in [4].

$Li_2B_4O_7$ at $T > 250$ K, as well as $LiCuVO_4$ at $T > 150$ K, revealed an additional contribution to thermal conductivity, which was assigned in [4] to the existence of a linear growth of the specific heat at constant pressure, C_p, in this compound.

We did not succeed in carrying out a similar comparison of the behavior of $\kappa^a(T)$ and $C_p(T)$ for $LiCuVO_4$ at high temperatures because of the absence of data on $C_p(T)$ in this temperature range in the literature. The heat capacity of $LiCuVO_4$ has been studied at low temperatures only ($T \le 100$ K) [5, 6].

Therefore, the purpose of this work was (1) to measure $C_p(T)$ of $LiCuVO_4$ within a broader temperature range (80–300 K) and (2) compare the data obtained on $C_p(T)$ and $\kappa^a(T)$ of $LiCuVO_4$ with analogous data from [4] for a related material, the quasi-one-dimensional superionic $Li_2B_4O_7$.

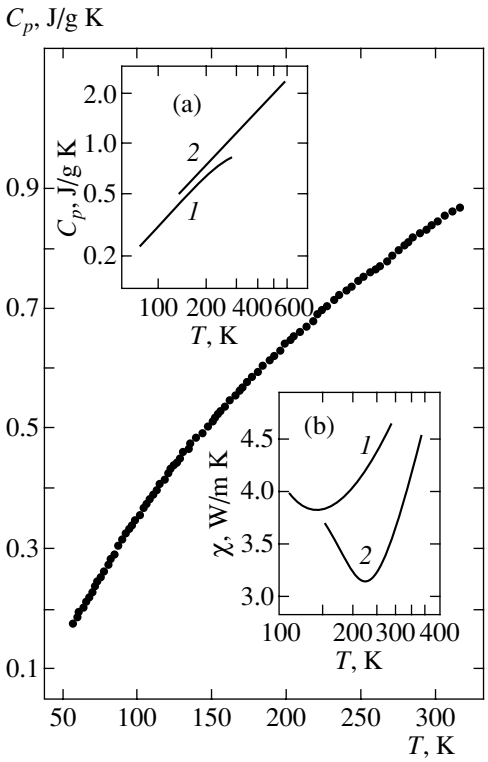

Temperature dependence of the specific heat $C_p(T)$ of $LiCuVO_4$. Insets compare (a) data on $C_p(T)$ for (*1*) $LiCuVO_4$ (this work) and (*2*) $Li_2B_4O_7$ [4] and (b) data on thermal conductivity: (*1*) $\kappa^a(T)$ of $LiCuVO_4$ [1] and (*2*) $\kappa(T)$ of $Li_2B_4O_7$ [4].

[1] The superscript *a* indicates that the measurements on $LiCuVO_4$ were performed along the *a* crystallographic direction.

The specific heat $C_p(T)$ was measured in a setup similar to the one used in [7] on a polycrystalline sample pressed into a pellet $8 \times 8 \times 2$ mm in size. The powder sample was prepared by solid-state technology from Li_2CO_3 (99.9%), CuO (99.99%), and V_2O_5 (99.5%) powders taken in a stoichiometric ratio. The reaction was run in air at a temperature of 530°C in an Al_2O_3 crucible. The reaction and subsequent annealing were performed over ten days with seven intermediate grindings and pressings. The diffraction pattern of the final product did not reveal reflections due to any foreign phases. In terms of its composition, unit cell parameters, and other properties, the material thus obtained can be classed, according to the terminology accepted in [1], among "high-temperature" $LiCuVO_4$ crystals.[2]

The figure displays the experimental data obtained for $C_p(T)$ of $LiCuVO_4$, and insets (a) and (b) compare the results on the specific heat and thermal conductivity of $LiCuVO_4$ and $Li_2B_4O_7$ [4].

As seen from the figure, $C_p(T)$ and $\kappa(T)$ of these compounds follow the same pattern. One may therefore conclude that the additional contribution to thermal conductivity from $LiCuVO_4$ observed for $T > 150$ K, just as in $Li_2B_4O_7$ at $T > 230$ K, derives from the increase in heat capacity in the temperature region specified and that $LiCuVO_4$ is a fairly good superionic.

[2] According to the chemical analysis of a large set of high-temperature $LiCuVO_4$ crystals performed in [1], their average composition is $Li_{0.92}Cu_{1.03}VO_4$; i.e., they deviate from stoichiometry in both lithium and copper. The main type of defects in them, however, are vacancies on the lithium sublattice.

ACKNOWLEDGMENTS

This study was supported by the Russian Foundation for Basic Research (project no. 02-02-17657) as part of bilateral agreements between the Russian Academy of Sciences, Deutsche Forschungsgemeinschaft, and the Polish Academy of Sciences.

REFERENCES

1. L. S. Parfen'eva, A. I. Shelykh, I. A. Smirnov, A. V. Prokof'ev, W. Assmus, H. Misiorek, J. Mucha, A. Jezowski, and I. G. Vasil'eva, Fiz. Tverd. Tela (St. Petersburg) **45** (11), 1991 (2003) [Phys. Solid State **45**, 2093 (2003)].
2. L. S. Parfen'eva, A. I. Shelykh, I. A. Smirnov, A. V. Prokof'ev, and W. Assmus, Fiz. Tverd. Tela (St. Petersburg) **46** (6), 998 (2004) [Phys. Solid State **46**, 1027 (2004)].
3. M. A. Lafontaine, M. Leblanc, and G. Ferey, Acta Crystallogr. C **45**, 1205 (1989).
4. A. É. Aliev, V. F. Krivorotov, and P. K. Khabibulaev, Fiz. Tverd. Tela (St. Petersburg) **39** (9), 1548 (1997) [Phys. Solid State **39**, 1378 (1997)].
5. M. Yamaguchi, T. Furuta, and M. Ishikawa, J. Phys. Soc. Jpn. **65** (9), 2998 (1966).
6. R. K. Kremer, A. Prokofiev, C. Gross, and W. Assmus, *Physikertagung der DPG. Program and Abstracts* (Hamburg, 2001), p. 398.
7. D. Wlosewicz, T. Plackowski, and K. Rogacki, Cryogenics **32** (3), 265 (1992).

Translated by G. Skrebtsov

Physics of the Solid State, Vol. 46, No. 10, 2004, pp. 1935–1939. Translated from Fizika Tverdogo Tela, Vol. 46, No. 10, 2004, pp. 1868–1872.

LOW-DIMENSIONAL SYSTEMS AND SURFACE PHYSICS

Properties of an Al_2O_3/Si Interface

A. S. Shulakov, A. P. Braĭko, S. V. Bukin, and V. E. Drozd

Institute of Physics, St. Petersburg State University, ul. Ul'yanovskaya 1, St. Petersburg, 198904 Russia

e-mail: shulak@paloma.spbu.ru

Received December 24, 2003

Abstract—The phase chemical composition of an Al_2O_3/Si interface formed upon molecular deposition of a 100-nm-thick Al_2O_3 layer on the Si(100) (*c*-Si) surface is investigated by depth-resolved ultrasoft x-ray emission spectroscopy. Analysis is performed using Al and Si $L_{2,3}$ emission bands. It is found that the thickness of the interface separating the *c*-Si substrate and the Al_2O_3 layer is approximately equal to 60 nm and the interface has a complex structure. The upper layer of the interface contains Al_2O_3 molecules and Al atoms, whose coordination is characteristic of metallic aluminum (most likely, these atoms form sufficiently large-sized Al clusters). The shape of the Si bands indicates that the interface layer (no more than 10-nm thick) adjacent to the substrate involves Si atoms in an unusual chemical state. This state is not typical of amorphous Si, *c*-Si, SiO_2, or SiO_x (it is assumed that these Si atoms form small-sized Si clusters). It is revealed that SiO_2 is contained in the vicinity of the substrate. The properties of thicker coatings are similar to those of the 100-nm-thick Al_2O_3 layer and differ significantly from the properties of the interfaces of Al_2O_3 thin layers. © *2004 MAIK "Nauka/Interperiodica".*

1. INTRODUCTION

The present work is a continuation of our investigations into the properties of Al_2O_3/Si interfaces formed upon molecular deposition of aluminum oxide on the surface of silicon single crystals (*c*-Si) [1]. The Al_2O_3/Si composite belongs to materials with a high permittivity (high-*k* materials) and holds promise for use in modern microelectronics and nanoelectronics. The main objective of this work was to determine the phase chemical composition and the thickness of the interface. The investigation was performed by nondestructive depth-resolved ultrasoft x-ray emission spectroscopy [2]. Compared to our earlier work [1], in the present work, we studied deeper interfaces (thicker coatings) in a sample with a 100-nm-thick Al_2O_3 layer. Thicker layers have a similar interface structure.

2. SAMPLE PREPARATION AND EXPERIMENTAL TECHNIQUE

Molecular deposition was carried out under the conditions described in our previous work [1]. Vapors of trimethylaluminum $Al(CH_3)_3$ and water served as precursors. The samples prepared by molecular deposition were not annealed. The experimental conditions for the measurement of x-ray emission spectra were identical to those used in [1].

3. RESULTS AND DISCUSSION

Investigations of thin coatings (up to several tens of nanometers in thickness) revealed that the Al_2O_3 surface layer contains silicon dioxide SiO_2, whose concentration increases as the silicon substrate surface is approached. Moreover, the SiO_2 content is rather high even at the sample surface. An Al_2O_3–SiO_2 layer of variable composition rather than an Al_2O_3/Si interface is formed on the *c*-Si substrate. The formation of such a structure of thin films can be associated with the interdiffusion of oxygen deep into the sample and silicon to the surface along grain boundaries [3]. Neither the formation of a metallic aluminum layer on the interface nor aluminum diffusion deep into the substrate was revealed. Thicker coatings have a more complex structure.

Let us initially consider the x-ray emission bands of the pure compounds, which can be used to analyze the shape of experimental spectra. These bands are shown in Fig. 1. Examination of thick coatings is complicated by the necessity of allowing for the absorption of x-ray radiation that passes through the Al_2O_3 layer (self-absorption effect). The shape of the Al bands should remain identical to that for the pure compounds, because these bands lie in the energy range below the Al and Si $L_{2,3}$ absorption edges, i.e., in the range in which the spectral dependence of the absorption coefficient, as a rule, is weak and smooth. A different situation arises with the Si spectra. It can be seen from Fig. 1 that the Si spectra lie in the spectral range corresponding to a fine structure of the Al absorption spectra above the $L_{2,3}$ absorption edge. Figure 1 depicts the absorption spectrum of Al_2O_3 according to the data taken from [4]. The Si $L_{2,3}$ spectra of the *c*-Si and SiO_2 compounds after passing radiation through a 100-nm-thick Al_2O_3

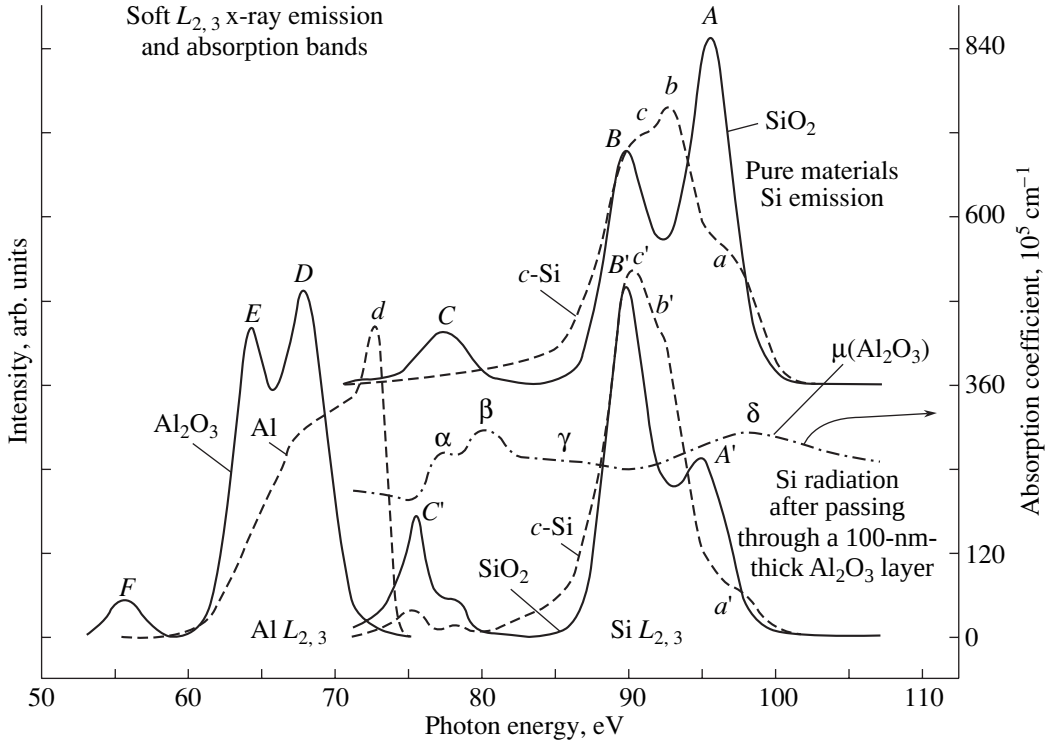

Fig. 1. $L_{2,3}$ x-ray emission bands used for analyzing the spectra of the studied sample: the Al $L_{2,3}$ bands for metallic aluminum and Al_2O_3 and the Si $L_{2,3}$ bands for *c*-Si and SiO_2 after passing radiation through a 100-nm-thick Al_2O_3 layer. The dot-dashed line indicates the absorption spectrum of Al_2O_3 [4]. For comparison, the bands for the *c*-Si and SiO_2 pure compounds are shown in the upper part.

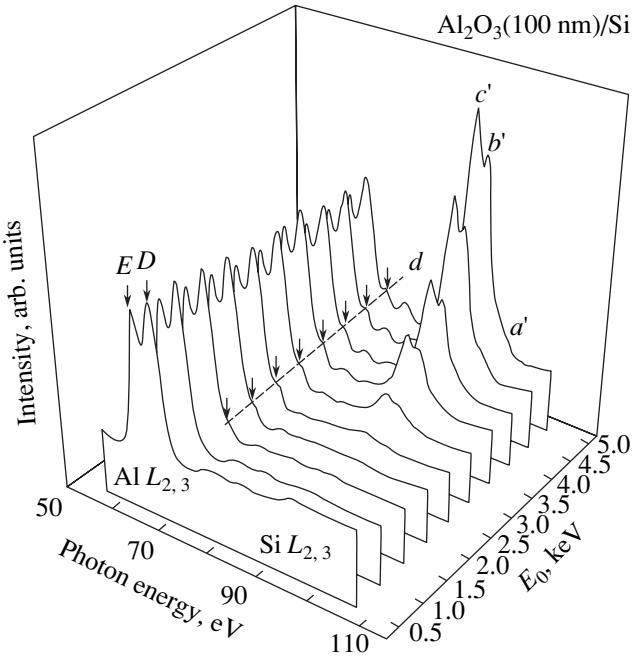

Fig. 2. Dependence of the shape of the x-ray emission spectra on the energy E_0 of primary electrons for the Al_2O_3(100 nm)/Si sample. The intensity of the Al bands is normalized. Designations of the maxima are the same as in Fig. 1.

absorber are shown in the lower part of Fig. 1. Above these spectra, similar spectra of the pure compounds are given for comparison. It is easy to see that, although the fine structure of the absorption spectrum is poorly resolved, distortions introduced by the self-absorption effect lead to a radical change in the shape of the Si spectra. It is evident that the spectra of the Al_2O_3(100 nm)/Si samples cannot be correctly analyzed without accounting for these distortions.

A number of emission spectra of the sample under investigation in the range of the Al and Si $L_{2,3}$ x-ray emission bands at different energies E_0 of primary electrons are depicted in Fig. 2. An increase in the energy E_0 results in a shift of the lower boundary of the emitting layer (the region in which characteristic x-ray radiation is excited) deep into the sample. It can be seen from Fig. 2 that, at $E_0 < 1.4$ keV, the spectrum contains only the Al $L_{2,3}$ emission band of the Al_2O_3 compound (with maxima *E*, *D*). At $E_0 = 1.4$ keV, in the Al x-ray emission spectrum, there arises a maximum *d*, which coincides in energy position with the main maximum of the $L_{2,3}$ band for metallic aluminum. This maximum is observed in all the spectra obtained at $E_0 \geq 1.4$ keV. An increase in the energy E_0 to 2.5 keV leads to the appearance of a weak feature in the range of the Si $L_{2,3}$ band. A further increase in the energy E_0 results in a rapid

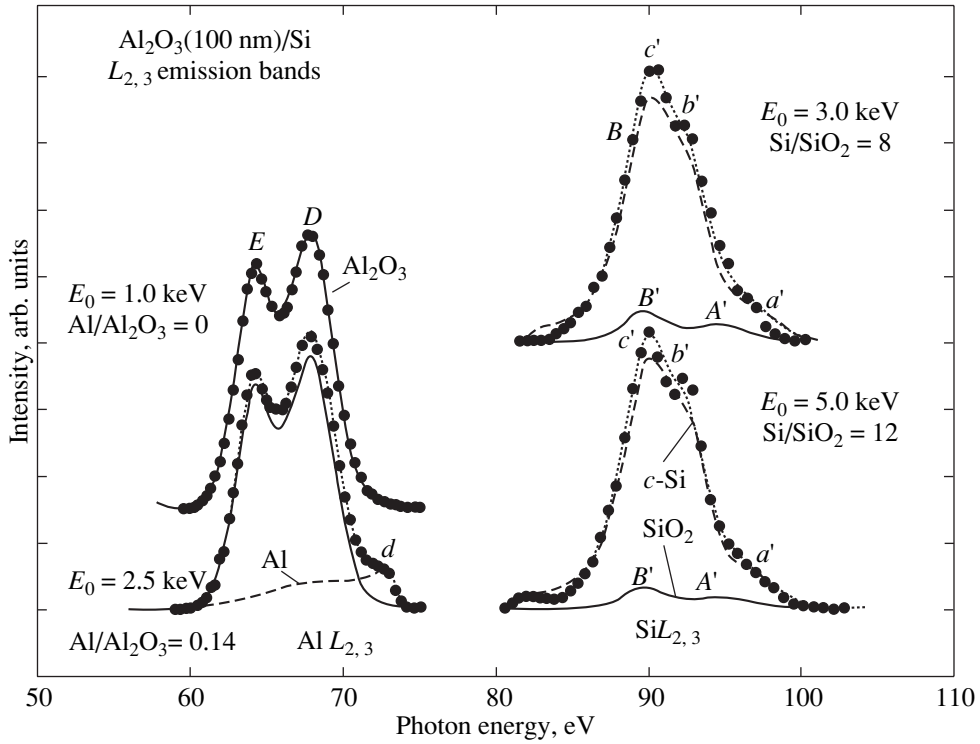

Fig. 3. Decomposition of the experimental Al and Si x-ray emission spectra of the Al_2O_3(100 nm)/Si sample into components: the Al $L_{2,3}$ bands for Al_2O_3 and metallic aluminum and the Si $L_{2,3}$ bands for *c*-Si and SiO_2. The Si $L_{2,3}$ bands are distorted upon passing radiation through a 100-nm-thick Al_2O_3 layer (see Fig. 1). Dashed lines indicate the spectra of metallic aluminum and *c*-Si. Solid lines correspond to the spectra of Al_2O_3 and SiO_2. Dotted lines represent the total spectra. Closed circles are the experimental data.

increase in the intensity of this feature, which becomes dominant in the emission spectrum. Moreover, the shape of this band turns out to be similar to the shape of the band that corresponds to the *c*-Si compound and is modified by the absorption in the Al_2O_3 layer (maxima *a*', *b*', *c*' in Fig. 1). Changes in the spectral intensity clearly observed between maxima *d* and *c*' with an increase in the energy E_0 correlate well with the fine structure of the absorption spectrum (maxima α, β, and γ in Fig. 1) and, hence, are associated with the self-absorption effect.

In general, the interpretation of the evolution of the spectral structure does not involve considerable problems. Similar changes can be expected under the assumption that the synthesized coating has a complex structure. The upper layer is formed by Al_2O_3 oxide. The deeper layer contains Al atoms whose coordination is characteristic of metallic aluminum. Finally, the layer located below contains Si atoms. Let us try to refine this structure by examining more closely the evolution of the spectrum shape.

The Al and Si $L_{2,3}$ bands measured at different energies E_0 were decomposed into components (Fig. 3). It turned out that all the Al spectra obtained at E_0 > 1.0 keV are actually represented by a superposition of the $L_{2,3}$ bands of metallic aluminum and Al_2O_3. However, our data are not sufficient to answer in which the form the metal-like aluminum occurs in the coating. This can be a continuous thin metal layer or clusters that are distributed over the depth and whose size is large enough for the electronic structure of the metal to be formed (no less than several tens of atoms).

The spectra of silicon at E_0 > 2.5 keV can be represented as a superposition of the $L_{2,3}$ bands of the *c*-Si and SiO_2 compounds with due regard for distortions introduced by the self-absorption effect. Note that the contribution from the band of SiO_2 is insignificant and decreases with an increase in the energy E_0. This circumstance indicates that SiO_2 molecules are predominantly located in a thin layer in the vicinity of the boundary of the *c*-Si substrate. It should be noted that the quality of the decomposition of the experimental Si spectra into components is considerably lower than the quality achieved for thin layers [1]. One of the reasons for the deterioration in quality could be errors in the determination of the spectrum shape and the magnitudes of the absorption coefficients for Al_2O_3 oxide [4]. This can be judged from the following fact: at the maximum energy E_0 = 5.0 keV, when the contribution from the $L_{2,3}$ band of the *c*-Si substrate becomes dominant, the spectrum shape does not agree well with the shape of this band after passing radiation through the 100-nm-

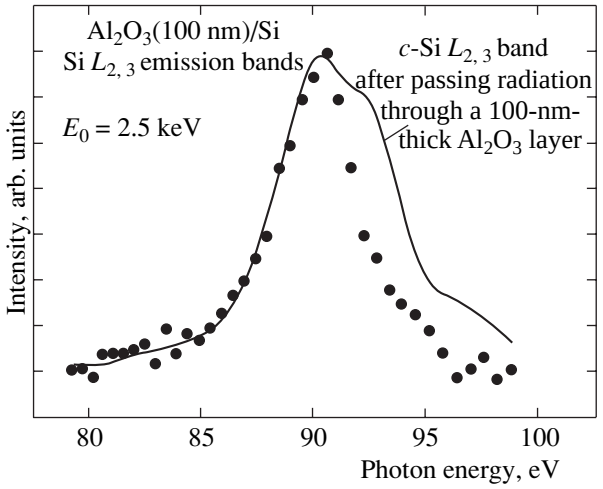

Fig. 4. Si $L_{2,3}$ x-ray emission bands excited by electrons with energy E_0 = 2.5 keV. The solid line indicates the *c*-Si band (distorted as a result of the self-absorption effect).

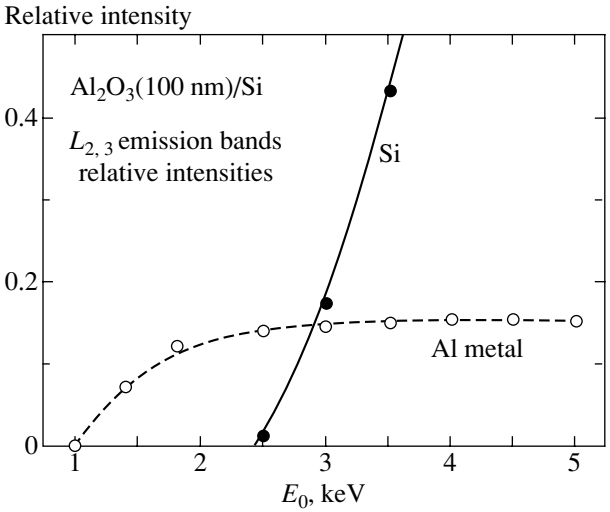

Fig. 5. Dependences of the relative integrated intensities of the $L_{2,3}$ bands on the energy E_0 for metallic aluminum and silicon. The intensities are normalized to the intensity of the spectrum of Al_2O_3 oxide.

thick Al_2O_3 layer. In particular, any attempts to reproduce the minimum observed in the experimental spectrum between the maxima *b*' and *c*' (Figs. 2, 3) have not met with success. In our analysis of the self-absorption effect, we disregard the possible influence of the found metal-like aluminum layer on the absorption. This also can introduce errors.

As can be seen from Fig. 2, the intensity in the range of the Si $L_{2,3}$ band begins to increase at E_0 = 2.5 keV. In order to separate the characteristic radiation, the spectrum obtained at E_0 = 1.8 keV was used as the background spectrum. The result of this separation is presented in Fig. 4. This figure also depicts the $L_{2,3}$ band of the *c*-Si compound that is distorted by the self-absorption effect. It can be seen from Fig. 4 that the shapes of the bands differ substantially: the separated band is almost 2 eV narrower than the band of the *c*-Si compound. The spectrum of the sample cannot be decomposed into the components represented by the bands of the *c*-Si and SiO_2 compounds. Such a drastic difference cannot be explained by the errors in the determination of the spectral dependence of the absorption coefficient because the difference between the spectrum shapes becomes considerably smaller (Fig. 3) with an increase in the energy E_0 by only 0.5 keV (to 3.0 keV).

We can assume that, in the vicinity of the boundary with the substrate, the state of silicon atoms incorporated into the Al_2O_3 layer (possibly, containing metal-like aluminum clusters) is not characteristic of SiO_2 or *c*-Si. Apparently, the spectrum under consideration does not coincide with the spectrum of amorphous silicon (*a*-Si), which appears to be broader than the $L_{2,3}$ band of *c*-Si [5]. It is reasonable to assume that this Si $L_{2,3}$ band is associated with the nonstoichiometric oxide SiO_x. However, this last assumption is inconsistent with the data obtained by Wiech *et al.* [5], according to which, up to x = 0.83, the Si band has a pronounced double-humped shape and the band shape in general is well approximated by a weighted superposition of the spectra of Si and SiO_2. Therefore, our spectrum cannot belong to the family of Si spectra for nonstoichiometric oxides. Possibly, this spectrum corresponds to small-sized clusters that consist of several Si atoms and in which the electronic structure characteristic of bulk silicon is not formed. It is clear that further investigations are needed to elucidate the nature of the unusual Si $L_{2,3}$ band.

Let us now analyze the dependence of the relative intensities of the bands on the energy E_0. The dependences of the relative integrated intensities of the $L_{2,3}$ bands for metallic aluminum and silicon (without decomposition into components) on the energy E_0 are plotted in Fig. 5. The intensities are normalized to the intensity of the Al $L_{2,3}$ band for the Al_2O_3 oxide. The dependence for silicon is observed beginning from E_0 = 2.5 keV. The intensity of the Si spectrum rapidly increases, even though it becomes equal to the intensity of the Al spectrum only at $E_0 \approx 3$ keV. The increase in the intensity is explained by the increase in the contribution from the band of the *c*-Si substrate. The dependence of the intensity of the Al band associated with metal-like aluminum (observed beginning from E_0 = 1 keV) rapidly flattens out with an increase in the energy E_0 at $E_0 \approx 2.5$ keV. According to the results of the analysis performed in our earlier work [1], such a behavior of the dependence suggests that aluminum is

located in a thin layer in the vicinity of the boundary with the substrate.

Furthermore, it is possible to estimate the layer thicknesses. It is assumed that the dependence of the depth of the Al $L_{2,3}$ emission from Al_2O_3 (like the Si $L_{2,3}$ emission from SiO_2 [6]) on the energy E_0 exhibits a linear behavior. Since an Al_2O_3 layer thickness of 100 nm is specified with a high accuracy by the number of molecular deposition cycles, the depth scale can be determined from the appearance of the substrate emission. Most likely, this occurs when the energy E_0 is in the range 2.5 keV < E_0 < 3.0 keV. If this energy is taken to be equal to 2.75 keV, we find that the radiation of metal-like aluminum, which arises at E_0 = 1 keV, escapes from a depth of ~40 nm. Since the silicon emission is observed beginning from E_0 = 2.5 keV, the thickness of the layer that is adjacent to the boundary with the substrate and contains Al_2O_3, silicon atoms in the unusual chemical state, and the stoichiometric oxide SiO_2 does not exceed 10 nm. Note that the silicon atoms in the unusual chemical state are located in the vicinity of the upper boundary of this layer and the oxide molecules are positioned more closely to the boundary with the substrate.

4. CONCLUSIONS

Thus, unlike the Al_2O_3/Si thin coatings in which an Al_2O_3–SiO_2 layer of variable composition rather than Al_2O_3/Si interface is formed on the substrate, thick coatings involve a transition layer between the Al_2O_3 coating and the *c*-Si substrate and this layer can be treated as the Al_2O_3/Si interface. In the 100-nm-thick coating synthesized in the present work, the thickness of this interface is approximately equal to 60 nm. The interface has a complex structure. The upper layer contains the synthesized Al_2O_3 oxide and also metal-like aluminum (the thickness of this layer can be less than or equal to the interface thickness). The layers containing silicon atoms in an unusual state and the stoichiometric oxide SiO_2 are located more deeply (the thickness of the last two layers does not exceed 10 nm).

It is evident that the formation of Al_2O_3/Si thick coatings (whose thickness is larger than several tens of nanometers) is accompanied by complex processes of diffusion and chemical reactions at the interface. As a result, the structure of the interface turns out to be more complex than that formed upon synthesis of thin coatings.

ACKNOWLEDGMENTS

This work was supported by the Russian Foundation for Basic Research, project no. 01-03-32771.

REFERENCES

1. A. S. Shulakov, A. P. Braĭko, S. V. Bukin, and V. E. Drozd, Fiz. Tverd. Tela (St. Petersburg) **46** (6), 1111 (2004) [Phys. Solid State **46**, 1145 (2004)].
2. A. V. Zimina, A. S. Shulakov, S. Eisebitt, and W. Eberhardt, Surf. Sci. Lett. **9** (1), 461 (2002).
3. S. Jakschik, U. Schroeder, T. Hecht, D. Krueger, G. Dollinger, A. Bergmayer, C. Luhmann, and J. W. Bartha, Appl. Surf. Sci. **211**, 352 (2003).
4. V. A. Fomichev, Fiz. Tverd. Tela (Leningrad) **8** (10), 2892 (1966) [Sov. Phys. Solid State **8**, 2312 (1966)].
5. G. Wiech, H.-O. Feldhuetter, and A. Shimunek, Phys. Rev. B **47** (12), 6981 (1993).
6. A. S. Shulakov, A. P. Braĭko, N. V. Moroz, and V. A. Fomichev, Fiz. Tverd. Tela (St. Petersburg) **40** (10), 1932 (1998) [Phys. Solid State **40**, 1754 (1998)].

Translated by O. Borovik-Romanova

Physics of the Solid State, Vol. 46, No. 10, 2004, pp. 1940–1948. Translated from Fizika Tverdogo Tela, Vol. 46, No. 10, 2004, pp. 1873–1880.

LOW-DIMENSIONAL SYSTEMS AND SURFACE PHYSICS

Structure and Electronic Properties of Antimony Films on the Mo(110) Surface

D. A. Gorodetsky†, Yu. P. Mel'nik, D. P. Proskurin, and V. A. Usenko

Shevchenko National University, Vladimirskaya ul. 64, Kiev, 03022 Ukraine

e-mail: pdp@univ.kiev.ua

Received February 10, 2004

Abstract—The structure and electronic properties of antimony on the Mo(110) surface are investigated over a wide range of coverages. In the submonolayer range, $p(2\times1)$, $p(1\times1)$, (1×3), and (1×2) adsorbate structures matched to the substrate are formed at room temperature. For coverages larger than a monolayer, three-dimensional antimony crystals whose orientation is determined by the substrate grow on the surface. Annealing of the system at temperatures higher than 1000 K leads to the formation of structures that are not observed upon condensation. The results of analyzing the electron energy-loss spectra jointly with the work function of the surface suggest the formation of surface molybdenum–antimony alloys. © *2004 MAIK "Nauka/Interperiodica".*

1. INTRODUCTION

The considerable interest expressed by researchers in the adsorption of Group V elements on semiconductors and metals is explained by several factors. First, these elements passivate semiconductor surfaces. Upon condensation on Si, Ge, InP, etc. [1, 2], these elements saturate dangling bonds of surface atoms and suppress the occurrence of further chemical reactions. Second, recently, it has been demonstrated that the layer-by-layer epitaxial growth of metal films on metal surfaces can be induced by surfactants, such as Sb, In, and O_2 [3–6]. In particular, van der Vegt *et al.* [3] studied the homoepitaxial growth of Ag on the Ag(111) surface in the presence of antimony and observed the layer-by-layer growth of films with a thickness of 20 monolayers (ML). The subsequent evaporation of a new portion of Sb again led to the layer-by-layer growth. Therefore, it was assumed that the surfactant properties of antimony are associated with its strong tendency to segregation. However, at present, the mechanisms of dissolution and segregation of Sb on the surface of different metals are not clearly understood.

It is obvious that the surface activity of Sb adatoms depends on their concentration and location on a substrate. A prerequisite for elucidating this dependence is provided by the data on the atomic structure of the surface. However, there are only a few works concerned with investigating the structure of submonolayer Sb films on clean metal surfaces [7–14]. In the present work, we studied the geometry and electronic properties of Sb films on the Mo(110) surface. The data on the film structure were obtained using low-energy electron diffraction. The evolution in the electronic structure of the surface was examined by electron energy-loss spectroscopy. The work function of the surface was evaluated from a change in the contact potential difference.

2. SAMPLE PREPARATION AND EXPERIMENTAL TECHNIQUE

The measurements were performed on two instruments. The electron energy-loss spectra were measured in a USU-4 metal chamber with a four-grid quasi-spherical retarding-field analyzer. The use of primary electrons with low energies (~40 eV) made it possible to increase the sensitivity of the method to the condition of the surface and to resolve a fine structure of the spectrum. The electron diffraction patterns could also be recorded in the same chamber. However, more bright and clear-cut patterns were obtained in a glass tube with a two-grid retarding-field analyzer. The change in the work function $\Delta\varphi$ in these instruments was determined from the change in the voltage across an electron gun cathode and the studied sample. In this case, the current in a sample circuit was maintained constant and the operating voltage corresponded to almost total reflection of the primary beam (determination of the contact potential difference according to the Anderson technique). The work function was determined accurate to within $\Delta\varphi \sim 0.005$ eV. The residual pressure in measurements was maintained at 2×10^{-10} Torr.

The molybdenum surface under investigation was oriented accurate to within ~10′ with respect to the (110) plane. The sample was purified from carbon according to the standard procedure: heat treatment at 1200 K in an oxygen atmosphere (10^{-7} Torr) with periodic removal of oxides by flashing at 2200 K. A platinum tube filled with metallic antimony served as a Sb source. Depending on the tube temperature, antimony

† Deceased.

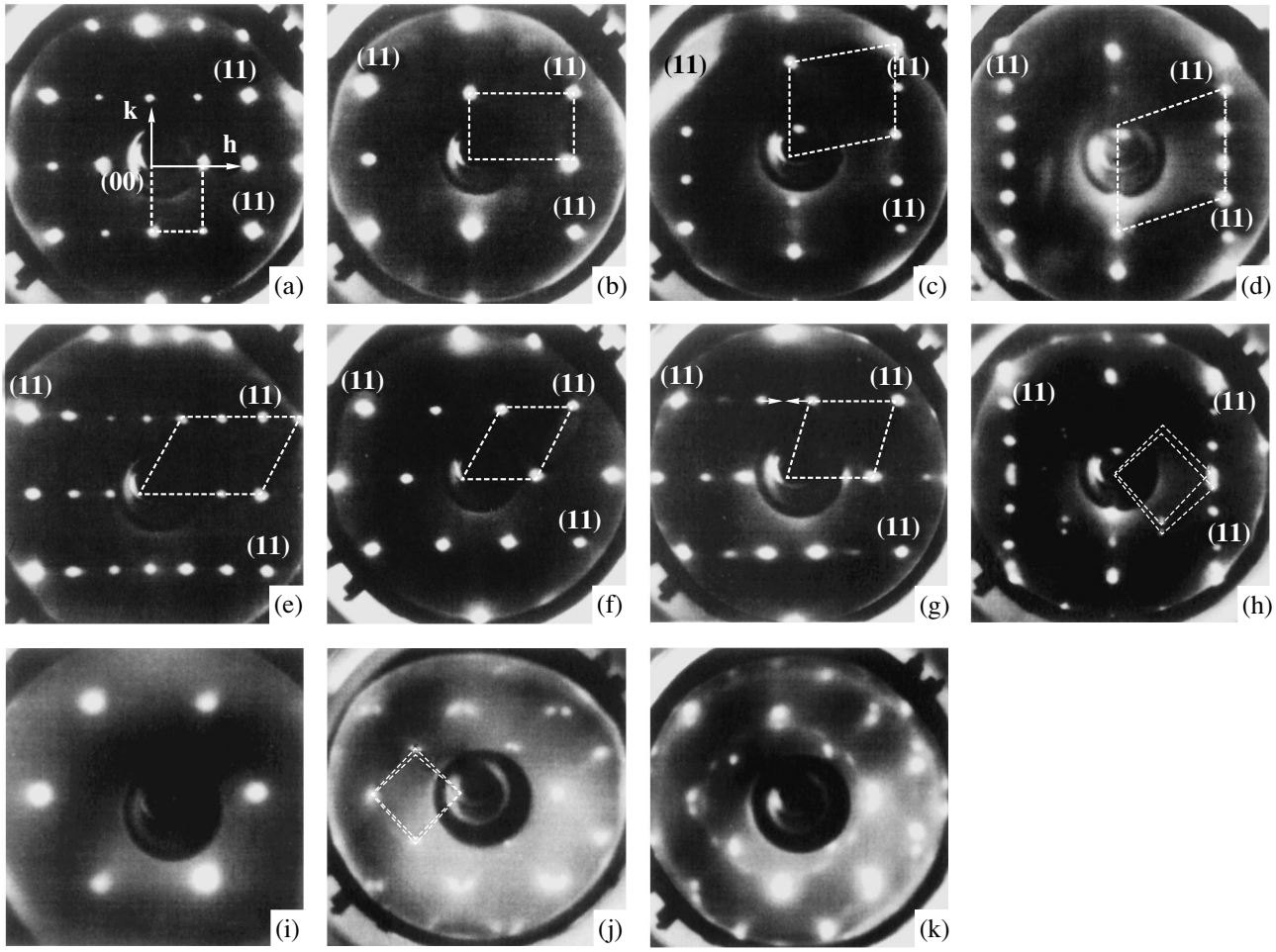

Fig. 1. Diffraction patterns of films formed upon Sb adsorption on the Mo(110) surface. (a–d) Patterns obtained upon condensation at $T = 300$ K: (a) $p(2 \times 1)$ at $\vartheta = 0.25$, (b) $p(1 \times 1)$ at $\vartheta = 0.5$, (c) $c(1 \times 3)$ at $\vartheta = 0.67$, and (d) $p(1 \times 2)$ at $\vartheta = 0.75$. (e–g) Patterns recorded after annealing of the monolayer film at different temperatures: (e) $p(3 \times 1)$ at $T_{ann} = 1220$ K, (f) $c(3 \times 1)$ at $T_{ann} = 1410$ K, and (g) "$c(3 \times 1)$" at $T_{ann} = 1700$ K. (h) Pattern of Sb crystals against the diffraction pattern of the first layer, patterns of (i) Sb(100) and (j) Sb(111) faces, and (k) pattern of a powder structure.

evaporates in the form of Sb_4 clusters ($T \leq 800$ K) or Sb_2 dimers ($T > 800$ K) [15].

The amount of deposited antimony was evaluated using the data obtained by all the used methods. The coverage ϑ in the submonolayer range was determined with respect to the concentration of surface atoms on the Mo(110) face. The relative coverage in a multilayer film was estimated from the condensation time.

3. RESULTS AND DISCUSSION

3.1. Antimony Submonolayer Films on Mo(110)

3.1.1. Structure of Sb films on Mo(110) at $T = 300$ K. The diffraction patterns reflecting the structure of the adsorbed Sb layer on the Mo(110) surface are depicted in Fig. 1. The diffraction patterns in Figs. 1a–1d were recorded during the condensation of Sb on the substrate at room temperature. The patterns of the annealed films are shown in Figs. 1e–1g, and the patterns of three-dimensional crystals are displayed in Figs. 1h–1k. The designations of the patterns are dictated by the choice of the centered rectangular unit cell $c(1 \times 1)$ (Fig. 2a) as the unit cell of surface Mo atoms (the corresponding vectors **h** and **k** of the reciprocal lattice are given in Fig. 1a). The designations of the diffraction patterns do not necessarily reflect the symmetry and periodicity of the lattice in the real space correctly due to the presence of additional reflections associated with multiple electron scattering. In this respect, unit cells that are proposed with due regard for additional data and, in our opinion, correspond to real structures are depicted in the diffraction patterns.

The $p(2 \times 1)$ diffraction pattern (Fig. 1a), which initially appears on the screen of the electron diffractometer in the course of condensation, is determined by the formation of an ordered layer of adsorbed atoms. With an increase in the Sb concentration, the intensity of the

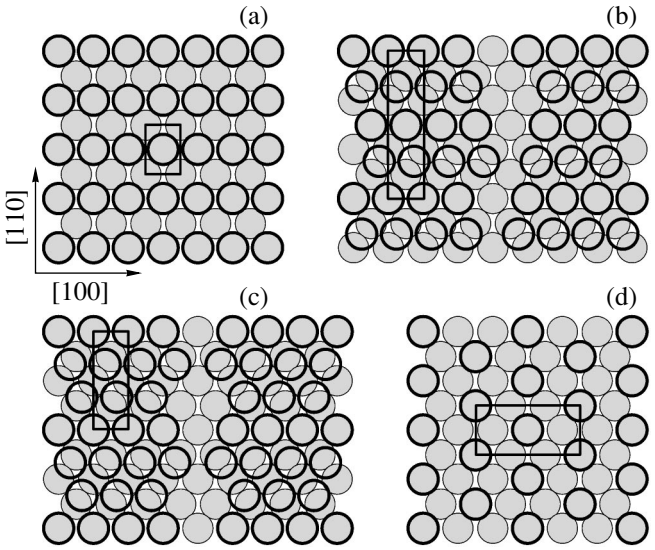

Fig. 2. Atomic arrangement in the (a) $p(1 \times 1)$, (b) (1×3), (c) (1×2), and (d) $c(3 \times 1)$ structures.

$(h + 1/2, k)$ reflections decreases and the $p(2 \times 1)$ diffraction pattern transforms into the $p(1 \times 1)$ pattern (Fig. 1b). As the density of adatoms increases, reflections of the $c(1 \times 3)$ pattern appear against the background of the $p(1 \times 1)$ pattern (Fig. 1c). The intensity of these reflections increases, whereas the intensity of the reflections of the $p(1 \times 1)$ pattern gradually decreases. The transformation into the next structure is attended by a gradual shift of the $(h, k + 1/3)$ reflections along the **k** direction with the formation of the $p(1 \times 2)$ pattern (Fig. 1d). This corresponds to completion of the formation of the first layer. Further condensation leads to the appearance of diffraction patterns attributed to three-dimensional Sb crystals.

The first two low-energy electron diffraction patterns are associated with the formation of rectangular atomic lattices that are matched to the substrate and have the coverages $\vartheta = 0.25$ and 0.5, respectively. In both structures, all atoms occupy equivalent positions on the substrate. Their arrangement in the $p(1 \times 1)$ structure corresponding to the diffraction pattern in Fig. 1b is shown schematically in Fig. 2a. Since adatoms have small dipole moments, the dipole–dipole interaction in the film cannot lead to the formation of isotropic hexagonal unit cells of the adsorbate, as is the case with adsorption of cesium or barium on similar substrates [16, 17]. The film geometry is governed, to a considerable extent, by the strong effect of the potential surface relief, which is determined by the covalent interaction between adatoms and substrate atoms and also the lateral interaction inside the film. It should be noted that the arrangement of Sb atoms with respect to Mo atoms in Fig. 2a is arbitrary, because the low-energy electron diffraction patterns allow us to determine only the ratio between the unit cell parameters of the substrate and the adsorbed layer.

After forming the $p(1 \times 1)$ structure, further condensation cannot proceed on adsorption centers equivalent to previous centers (the atomic radius of antimony is larger than that of molybdenum). Qualitatively new transformations are observed in the film. The incorporation of new atoms into the film leads to the displacement of adsorbed atoms from their positions. As a result, the density of the film increases, part of the bonds originally saturated with substrate atoms become free, and adatoms can be involved in a direct exchange interaction. The competition between the lateral covalent interaction of adatoms in the adsorbed layer and their directional interaction with substrate atoms results in a distortion of the unit cell of the film lattice and the formation of the (1×3) structure (Fig. 2b) corresponding to the $c(1 \times 3)$ pattern at $\vartheta = 0.67$. This structure arises in the form of islands of a new denser phase, and the reflections of both structures $p(1 \times 1)$ and (1×3) are observed in the diffraction pattern. After completing the transition, the entire surface appears to be covered with the film having the (1×3) structure. Further densification of the film occurs through the contraction along the [110] direction up to the formation of the (1×2) structure at $\vartheta = 0.75$ (Fig. 2c). The corresponding diffraction pattern is shown in Fig. 1d. The primitive unit cell of this lattice has the shape of a rhombus with sides equal to the lattice constant of molybdenum (3.16 Å).

At this stage, the filling of the monolayer with $\vartheta = 0.75$ is completed and further condensation proceeds in the second and subsequent layers. The times of reaching the maximum intensities of the $p(2 \times 1)$, $p(1 \times 1)$, $c(1 \times 3)$, and $p(1 \times 2)$ patterns agree well with the coverages of the corresponding structures ($\vartheta = 0.25$, 0.5, 0.67, 0.75). This enables us to replace the condensation time scale by the coverage scale.

3.1.2. Structure of Sb films on Mo(110) at $T = 77$ K. Temperature as a measure of the kinetic energy of adatoms has an effect on their mobility and does not affect the interaction of adatoms with the substrate and each other. For the Cs or Ba adsorbates, the condensation on the substrate cooled to 77 K results in earlier crystallization of a film and the appearance of structures [16, 17] that cannot be formed at room temperature due to an insufficient energy of bonding (as compared to the kinetic energy) between adatoms or with adjacent substrate atoms. The opposite situation is observed upon condensation of antimony on a substrate cooled by liquid nitrogen: the reflections of all the diffraction patterns become diffuse and there arises a high background. This implies that the degree of film ordering is low. The $p(1 \times 1)$ pattern rather than the $p(2 \times 1)$ pattern (as in the case of deposition at room temperature) initially appears on the screen. Apparently, this can be explained by the low mobility of adatoms at $T = 77$ K and the lateral interaction alone is insufficient for displacing and ordering adatoms to form the $p(2 \times 1)$ structure. Therefore, at the first stage, there appears a structure whose formation is predominantly governed by the influence of bonds between adatoms and the sub-

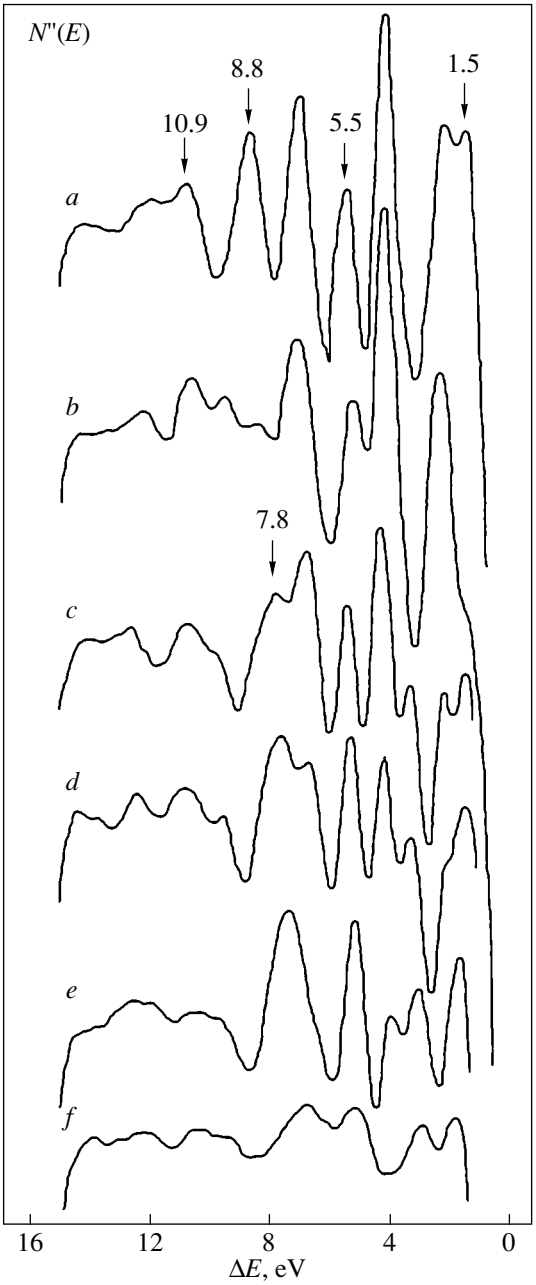

Fig. 3. Evolution of the electron energy-loss spectra in the course of antimony adsorption. ϑ = (*a*) 0, (*b*) 0.2, (*c*) 0.6, (*d*) 0.67, and (*e*) 0.75. (*f*) Spectrum of a three-layer film.

strate. With an increase in the coverage, this phase undergoes a first-order phase transition to the phase with the (1×3) structure. However, this process is not completed. It seems likely that, at $\vartheta > 0.5$, the formation of the first layer is accompanied by growth of the second adsorbate layer, whose atoms cannot be incorporated into the submonoatomic film due to a low mobility. At coverages of the order of two monolayers, the diffraction patterns exhibit only a background, which indicates a completely disordered surface.

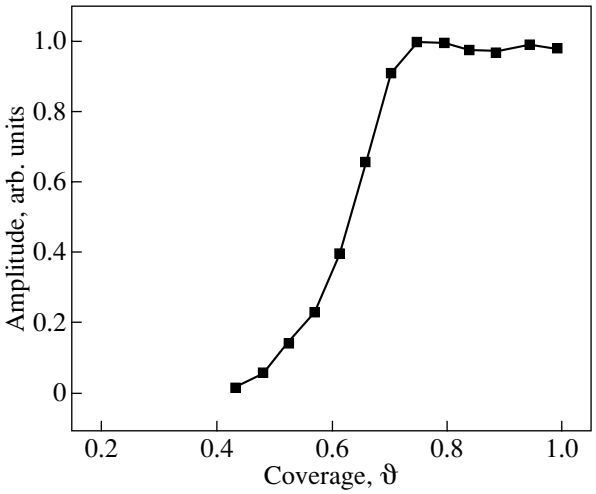

Fig. 4. Dependence of the intensity of the antimony peak at 7.8 eV on the coverage.

3.1.3. Electron energy-loss spectra. As is known, electron energy-loss spectroscopy provides a way of investigating both one-particle and collective processes in a surface layer. Figure 3 shows the electron energy-loss spectra measured at different adsorbate coverages. Spectrum *a* corresponds to a clean Mo(110) face. The specific features of this spectrum were discussed in detail in our earlier work [16] and, hence, are not considered in the present work.

The antimony condensation is attended by a rapid decrease in the intensity of the peaks at 1.5, 5.5, and 8.8 eV (Fig. 3, curves *a*, *b*). These peaks are associated with the one-particle transitions to the surface states of molybdenum (1.5, 5.5 eV) and the excitation of surface plasmons in the *s* electron subsystem of the metal (8.8 eV). At the coverage $\vartheta = 0.5$, there arises a new peak at 7.8 eV (Fig. 3, curve *c*), whose intensity initially increases with an increase in the coverage. The dependence of the intensity of this peak on the coverage is depicted in Fig. 4. The fact that the intensity of the peak increases up to the formation of a monolayer of Sb adatoms and then remains virtually constant suggests a surface character of the corresponding loss. A similar peak was observed for Sb films on (100) surfaces of GaAs, GaSb, and InSb by Ludeke [18], who explained this peak as resulting from the transition from filled surface states to empty states of dangling bonds. Ma and Slavin [8] observed a peak at 7.4 eV in the electron energy-loss spectra of polycrystalline antimony and assigned it to the $Sb(O_1)$ ionization line. On the basis of our data, we can interpret the origin of this peak in the following way. The appearance of the peak at 7.8 eV in the spectrum coincides with the beginning of the transition from the $p(1 \times 1)$ phase to the (1×3) phase. The transition leads to the formation of a new denser structure in which covalent bonds are formed between adatoms. A system of single atoms that interact through long-range lateral forces transforms into a system in

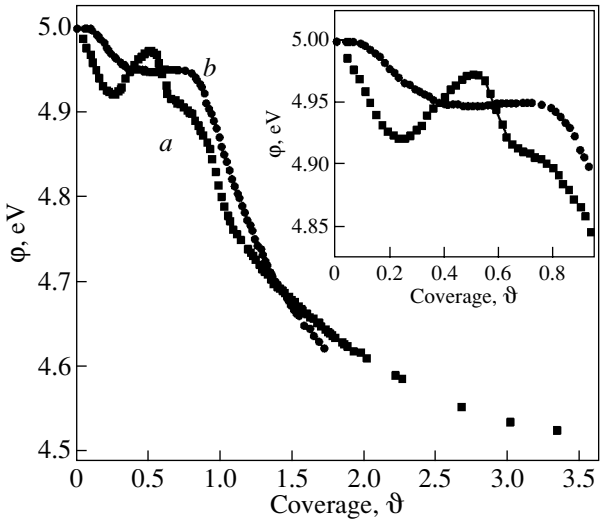

Fig. 5. Dependences of the work function on the coverage in the course of Sb condensation on Mo(110) at T = (*a*) 300 and (*b*) 77 K.

which film electrons are collectivized. The appearance of the new peak can be attributed to the excitation of collective processes (surface plasmons) in the adsorbed layer. The excitation energy of plasmons in the Sb film can be qualitatively estimated within the free-electron approximation. Under the assumption that all valence electrons are excited in the Sb film, the excitation energies of bulk and surface plasmons are estimated at 13.7 and 9.7 eV, respectively. These energies are close to those obtained in experiments.

3.1.4. Work function. Figure 5 depicts the dependences of the work function $\varphi(\vartheta)$ on the Sb coverage at substrate temperatures of 300 (curve *a*) and 77 K (curve *b*). The specific features of the dependences correlate well with the structural transformations in the film. Although the electronegativity of antimony (1.9) is larger than that of molybdenum (1.8), the work function φ decreases at the initial stage of condensation (Fig. 5, curve *a*). This decrease is caused by the redistribution of the electron density of the adatom–substrate system due to an increase in the roughness of the surface layer (the Smoluchowski effect). A decrease in the work function is accompanied by the formation of the $p(2 \times 1)$ structure, whose diffraction pattern has a maximum intensity when the work function φ is minimum. Further densification of the film leads to the formation of the $p(1 \times 1)$ structure. As the surface area of this structure increases, the work function increases as a result of a larger electronegativity of antimony and reaches a maximum at the end of this process.

The next structure is formed in the course of a phase transition, which is attended by a linear decrease in the work function. Making allowance for our assumption regarding the electron collectivization in the (1×3) structure, the change in the work function can be explained by the transformation of the system of single isolated Sb atoms into a surface layer with its own band structure. Islands of a new phase acquire the properties of antimony, whose work function is smaller than that of Mo(110). An increase in their surface area results in a decrease in the total work function.

The next linear portion in the dependence $\varphi(\vartheta)$ corresponds to contraction of the film up to the formation of a closely packed monolayer with the $p(1 \times 2)$ structure.

At both temperatures T = 300 and 77 K, the growth of the second and subsequent layers ($\vartheta > 0.75$) leads to a considerable decrease in the work function, which gradually reaches a value of ~4.5 eV.

At liquid-nitrogen temperature, the work function φ initially decreases to a lesser extent and its dependence does not exhibit a minimum (Fig. 5, curve *b*). This is associated with two factors. First, most likely, not all Sb dimers at 77 K dissociate, thus decreasing the surface roughness. Second, no homogeneous $p(1 \times 1)$ structure is formed over the entire surface due to a poor ordering of the film.

3.1.5. Annealing of monolayer and submonolayer films. The annealing of the monolayer Sb film on the Mo(110) surface up to temperatures of 300–610 K does not lead to structural transformations of the surface and results only in an increase in the degree of ordering. In the diffraction patterns, the background intensity decreases and the reflections become more pronounced. At higher temperatures of 800–1070 K, annealing is attended by the process responsible for the decrease in the antimony concentration due to a partial desorption of the adsorbate from the surface. The (1×2) structure gradually transforms into the (1×3) structure (T_{ann} = 800–980 K), which, in turn, undergoes a phase transition to the $p(1 \times 1)$ structure (T_{ann} = 1020–1070 K). However, the last structure in this situation is not realized in a pure form.

At higher temperatures, there appear patterns that are not observed in the course of Sb condensation at room temperature. The $p(3 \times 1)$ pattern (Fig. 1e) arises at 1220 K after several complex intermediate patterns. A further increase in the annealing temperature leads to a complex displacement of reflections in the [100] direction and the $c(3 \times 1)$ pattern (Fig. 1f) is observed on the screen at T_{ann} = 1410 K.

Upon annealings at temperatures in the range 1470–1700 K, the (h – 1/3, 1) and (h + 1/3, 1) reflections are shifted along the **h** direction (Fig. 1g) and form a pattern that will be conventionally referred to as the "$c(3 \times 1)$" pattern. This process proceeds against the background of a decrease in the intensity of additional reflections, and the pattern of the clean Mo(110) face remains on the screen at T_{ann} = 1820 K.

Identification of the patterns is complicated by the impossibility of accurately determining the concentration of Sb atoms on the surface. First, the structures characterized by the $c(3 \times 1)$ and "$c(3 \times 1)$" patterns

involve islands. After condensing an additional portion of antimony on these structures, there appear reflections of the $p(2 \times 1)$ pattern, which can be observed only upon condensation on the clean Mo surface. Second, in this case, the use of Auger electron spectroscopy does not permit us to estimate the adsorbate concentration, because the change in the intensity of an Auger signal can be associated with the change in the amount of the adsorbate on the surface and with the incorporation of Sb atoms into the substrate. This phenomenon has been observed in the Cu(111)–Sb [11] and Ag(111)–Sb [9] systems even at room temperature and in the Au(111)–Sb system [8] after mild annealing.

The new high-temperature structures turn out to be stable to condensation of additional portions of the adsorbate at room temperature. However, annealing of the system with an additional portion of the adsorbate makes it possible to transform a higher temperature phase into a lower temperature phase. In particular, the "$c(3 \times 1)$" structure after additional condensation of ~0.2 ML and annealing to 1410 K transforms into the $c(3 \times 1)$ structure. Similarly, the $c(3 \times 1)$ structure after condensation of ~0.3 ML and annealing to 1220 K transforms into the $p(3 \times 1)$ structure. One more condensation and annealing lead to the formation of the $p(1 \times 1)$ structure. Thereafter, the evolution of the film geometry in the course of condensation becomes identical to that observed at room temperature. Therefore, the sequence of the diffraction patterns observed upon annealing reflects the formation of structures on the surface in which the total coverage decreases with an increase in the annealing temperature.

Similar to annealing of a monolayer film, annealing of submonolayer films at temperatures of 300–610 K leads only to an increase in the degree of ordering in the film. At higher annealing temperatures, the result depends on the initial coverage ϑ_{in}.

At $\vartheta_{in} \in [0.5, 0.75]$, the transformation of the diffraction patterns with an increase in the annealing temperature is identical to that upon annealing of the monolayer film. However, the $p(3 \times 1)$ pattern appears at temperatures lower than that for the monolayer film (<1220 K).

For initial coverages of 0.33–0.5, only the $c(3 \times 1)$ and "$c(3 \times 1)$" high-temperature structures are formed upon annealing. At coverages $\vartheta_{in} < 0.33$, the $c(3 \times 1)$ pattern cannot be obtained and the "$c(3 \times 1)$" pattern arises only at a temperature of 1550 K.

Therefore, we can draw the following inferences.

(1) The structure with the $p(3 \times 1)$ diffraction pattern is formed upon annealing of the film whose coverage lies in the range 0.5–0.67.

(2) In the structure with the $c(3 \times 1)$ pattern, the total coverage falls in the range 0.33–0.5.

(3) In higher temperature structures ["$c(3 \times 1)$"], the total coverage is less than 0.33.

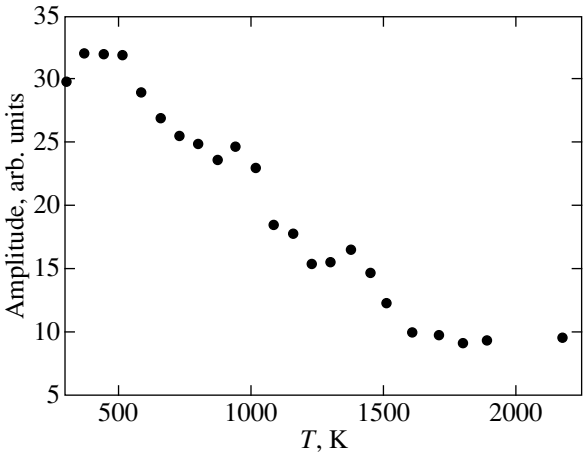

Fig. 6. Dependence of the amplitude of the Sb Auger signal (454 eV) on the annealing temperature.

The above inferences allow us to construct the unit cells of the reciprocal lattices for the high-temperature phases. This cell for the $p(3 \times 1)$ structure is depicted in Fig. 1e and corresponds to the coverage $\vartheta = 0.5$. All the other variants lead to coverages that are either smaller than 0.5 or larger than 0.67. The unit cell of the reciprocal lattice for the $c(3 \times 1)$ structure can be represented by the cell shown in Fig. 1f. This cell corresponds to the coverage $\vartheta = 0.33$. However, for this choice of the unit cell, there arise problems with the identification of the "$c(3 \times 1)$" structure. The formation of this structure is accompanied by a shift of additional reflections (Fig. 1g), so that the area of the unit cell of the reciprocal lattice and, hence, the density of adatoms increase despite an increase in the temperature and a partial desorption of the adsorbate.

This contradiction can be resolved taking into account that Sb atoms incorporated into the substrate can segregate on the surface. The variation in the amplitude of the Sb $M_4N_{45}N_{45}$ Auger signal (454 eV) upon annealing of the Sb monolayer film is shown in Fig. 6. The annealing at temperatures in the range 1270–1470 K corresponding to the formation of the $c(3 \times 1)$ structure results in an increase in the amplitude of the Auger signal. This can be associated with an increase in the number of adatoms on the surface.

The dependences of the work function $\varphi(T_{ann})$ upon annealing of the films with different initial coverages are plotted in Fig. 7. Irrespective of the initial coverage, annealing to $T_{ann} \sim 520$ K does not lead to noticeable changes in the work function φ (or the film structure). At higher annealing temperatures, the behavior of the system depends on the initial coverage.

The work function of the monolayer film at $\vartheta = 0.75$ (Fig. 7, curve *a*) with an increase in the temperature in the range 800–1020 K varies according to a partial desorption of the adsorbate and a transformation into looser structures: $(1 \times 2) \longrightarrow (1 \times 3) \longrightarrow p(1 \times 1)$. The

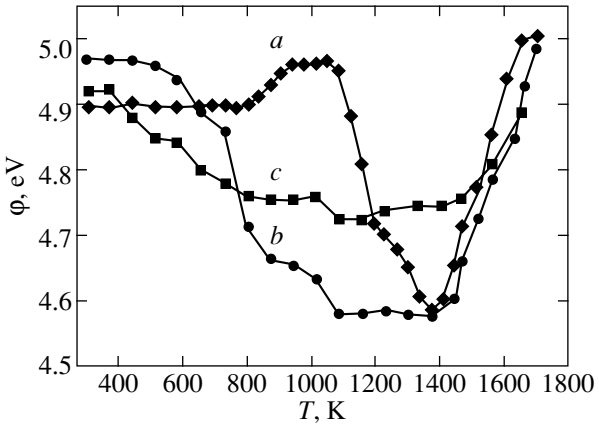

Fig. 7. Dependences of the work function on the annealing temperature for the Mo(110)/Sb system at the initial coverages ϑ_{in} = (*a*) 0.75, (*b*) 0.6, and (*c*) 0.25.

formation of the high-temperature phases above 1070 K is accompanied by a drastic decrease in the work function φ. The dependence $\varphi(T_{ann})$ exhibits a shoulder at $T_{ann} \sim 1200$–1250 K, i.e., upon formation of the $p(3 \times 1)$ structure, and a minimum (4.5–4.6 eV) at $T_{ann} \sim 1410$ K, i.e., upon formation of the $c(3 \times 1)$ structure. As the annealing temperature increases from 1410 to 1820 K, the work function φ progressively increases to the work function of the clean Mo(110) face.

Upon annealing of the submonolayer film with ϑ_{in} = 0.6 (Fig. 7, curve *b*), the dependence $\varphi(T_{ann})$ is qualitatively similar to the preceding dependence. However, the work function starts to decrease at lower temperatures, which correspond to the beginning of the formation of the $p(3 \times 1)$ structure. The dependence obtained upon annealing of the film with ϑ_{in} = 0.25 is represented by curve *c* in Fig. 7. In this case, an increase in the annealing temperature results in the formation of the "$c(3 \times 1)$" island structure on the surface and the dependence $\varphi(T_{ann})$ lies above the previous dependences owing to the influence of an open surface with a larger work function.

Changes in the electron energy-loss spectra (Fig. 8) in the course of sequential annealing of the monolayer film to 1070 K are caused by the partial desorption of the adsorbate. In particular, a decrease in the density of adatoms leads to a decrease in the intensity of the peak at 7.8 eV. Plasmons are completely damped when the (1×3) structure transforms into a "$p(1 \times 1)$" pseudostructure. Then, at the temperature T = 1410 K corresponding to the formation of the $c(3 \times 1)$ structure, a new peak at 3.3 eV appears in the spectrum (Fig. 8, curve *b*). With an increase in the temperature, this peak is retained until the surface has the $c(3 \times 1)$ structure and disappears upon transformation into the "$c(3 \times 1)$" structure (Fig. 8, curve *c*).

The main results obtained upon annealing of the Mo(110)–Sb system can be summarized as follows.

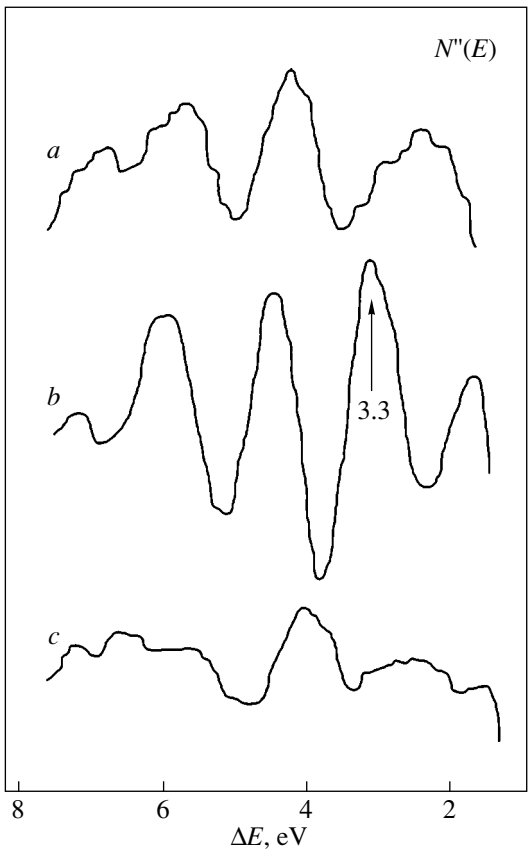

Fig. 8. Electron energy-loss spectra of the Mo(110)/Sb system after annealing to (*a*) 1350, (*b*) 1410, and (*c*) 1470 K.

First, annealing leads to the formation of structures that are not observed at room temperature. Second, these structures are stable to condensation of new portions of the adsorbate. Third, the formation of these structure results in a decrease in the work function. Fourth, the electron energy-loss spectrum contains a peak at 3.3 eV, which is observed only when the surface has the $c(3 \times 1)$ structure.

We can assume that a new chemical compound or alloy is formed on the surface. It is known that annealing of 1/3 ML of Sb on an Ag(111) face leads to surface reconstruction with the formation of a $(\sqrt{3} \times \sqrt{3})R30°$–Sb structure [19]. A similar reconstruction occurs on a Cu(111) surface but at a higher temperature (725 K). In both structures, Sb atoms are incorporated into the substrate, substitute for adsorbent atoms, and form surface alloys.

With due regard for our data on the work function and the evolution in the electron energy-loss spectra upon annealing of the Mo(110)/Sb system, it is assumed that similar alloys are also formed on the Mo surface. The surface reconstruction and the incorporation of Sb atoms into the substrate permit us to explain the sharp decrease in the work function upon formation

of the $p(3 \times 1)$ and $c(3 \times 1)$ structures and also the appearance of the new peak in the electron energy-loss spectrum. The difference between our system and the aforementioned systems lies in a considerably higher temperature of alloy formation. This can be associated with the larger surface tension σ of the Mo(110) surface ($\sigma_{Ag(111)}$ = 1.250 kJ/mol, $\sigma_{Cu(111)}$ = 1.825 kJ/mol, $\sigma_{Mo(110)}$ = 3.000 kJ/mol [20]).

3.2. Multilayer Films and Crystals

The condensation of Sb atoms in the second and subsequent layers results in the formation of different Sb crystals. In nature, α antimony has a rhombohedral structure with a lattice constant of 4.475 Å and an angle of 56°54′ [21]. This structure can also be described by an NaCl-type lattice with a lattice constant of 6.32 Å and an angle of 87°42′, in which atoms located at midpoints of edges are displaced along the cube diagonal. In this respect, hereafter, the designations corresponding to an NaCl-type lattice will be used for convenience.

The condensation of the adsorbate on the monolayer film leads to the appearance of new reflections (associated with the Sb crystals) against the background of the $p(1 \times 2)$ diffraction pattern (Fig. 1h). The crystal film consists of mirror domains, which make an angle of ~9°30′ with each other. Since the diffraction patterns contain reflections of the monolayer and the crystals and reflections corresponding to double scattering are not observed, the crystal growth proceeds through the Stranski–Krastanov mechanism (crystals on a monolayer film). Only the reflections of the crystals are retained at a total coverage of ~4 ML. As can be seen from Fig. 1h, the lattice of the crystals is virtually matched to that of the substrate along the Mo[100] direction. This enables us to determine the lattice parameters with a high accuracy. The Sb crystals grow so that their (100) face [in the (110) rhombohedral lattice] is parallel to the substrate surface. The crystals are somewhat distorted: the lattice constants of the (100) face are equal to 4.24 and 4.63 Å rather than to 4.26 and 4.47 Å for natural antimony, and the angle between the vectors is approximately equal to 90° instead of 87°. The lattice constant of the crystals along the Mo[100] direction is approximately equal to 6.28 Å. This value is very close to twice the lattice constant of the substrate along the same direction (6.315 Å).

Crystals with a different orientation can be grown by annealing (T_{ann} ~ 600 K) of a film deposited on the $p(3 \times 1)$ or $c(3 \times 1)$ structure when more than one monolayer of the adsorbate is additionally condensed on the substrate. The (100) face of these crystals is also parallel to the substrate surface. However, unlike the above case, the reflections of domains are symmetric with respect to the Mo[110] direction (the diffraction pattern of these crystals is shown in Fig. 1i). If the film deposited on the $p(3 \times 1)$ and $c(3 \times 1)$ structures is not annealed, the film undergoes spontaneous crystallization at $\vartheta \sim 7$. In this case, the Sb(111) face is observed on the surface (Fig. 1j).

As was shown above, the condensation of more than one monolayer of Sb at T = 77 K results in the formation of the disordered surface layer. The annealing of this layer to 370 K leads to structuring of the film. As a result, in the diffraction pattern, there arises a ring and reflections of the (111) faces of Sb crystals are observed against the background of this ring (Fig. 1k). A poorly ordered lower adsorbate layer cannot orient these crystals along particular azimuthal directions, and a large number of randomly oriented crystals (powder structure) are formed on the surface. Moreover, the diffraction pattern contains the reflections of the Sb(100) face.

4. CONCLUSIONS

Thus, the antimony films adsorbed on a Mo(110) surface at different temperatures were investigated over a wide range of coverages. It was demonstrated that the condensation at room temperature leads to the formation of structures matched to the substrate. The geometry of these structures is determined by covalent bonds formed between adatoms and the substrate or inside the film.

The annealing of the system at the initial stage results in a decrease in the adsorbate concentration on the surface and the formation of structures in the order opposite to that observed upon condensation. However, upon annealing at a specific temperature dependent on the initial coverage, new structures that are not observed during deposition are formed on the surface. It was assumed that these structures are associated with the formation of a surface molybdenum–antimony alloy. This hypothesis is confirmed by the drastic changes in the work function of the system upon transition and the appearance of a new peak (at 3.3 eV) in the electron energy-loss spectrum. This peak is observed only until the surface has the $c(3 \times 1)$ structure.

At coverages larger than one monolayer, rhombohedral α-antimony crystals somewhat distorted by the substrate grow on the surface. The orientation of the crystals depends on the initial conditions of adsorbate condensation (the structure of the first layer) and the heat treatment temperature (the annealing temperature of the system).

REFERENCES

1. Y. Huttel, P. Soukissian, P. S. Mangat, and Z. Hurych, Surf. Sci. **352–354**, 845 (1996).
2. D.-A. Luh, M. T. Seiger, T. Miller, and T.-C. Chiang, Surf. Sci. **374**, 345 (1997).
3. H. A. van der Vegt, H. M. van Pinxteren, M. Lohmeier, and E. Vlieg, Phys. Rev. Lett. **68** (22), 3335 (1992).
4. H. A. van der Vegt, J. Alvarez, X. Torrelles, S. Ferrer, and E. Vlieg, Phys. Rev. B **52** (24), 17443 (1995).

5. W. F. Egelhoff, Jr. and D. A. Steigerwald, J. Vac. Sci. Technol. A **7** (3), 2167 (1989).
6. S. Esch, M. Hohage, T. Michely, and G. Comsa, Phys. Rev. Lett. **72**, 518 (1994).
7. D. A. Gorodetskiĭ and A. A. Yas'ko, Fiz. Tverd. Tela (Leningrad) **13** (5), 1298 (1971) [Sov. Phys. Solid State **13**, 1085 (1971)].
8. R. Ma and A. J. Slavin, J. Vac. Sci. Technol. A **11** (4), 2003 (1993).
9. S. A. de Vries, W. J. Huisman, P. Goedtkindt, M. J. Zwanenburg, S. L. Bennet, I. K. Robinson, and E. Vlieg, Surf. Sci. **414**, 159 (1998).
10. I. Meunier, J.-M. Gay, L. Lapena, B. Aufray, H. Oughaddow, E. Landemark, G. Falkenberg, L. Lottermoser, and R. L. Johnson, Surf. Sci. **422**, 42 (1999).
11. P. Bailey, Y. C. Q. Noakes, and D. P. Woodruff, Surf. Sci. **426**, 358 (1999).
12. B. Aufray, H. Giordano, and D. N. Seidman, Surf. Sci. **447**, 180 (2000).
13. P. D. Quinn, D. Brown, D. P. Woodruff, P. Bailey, and T. C. Q. Noakes, Surf. Sci. **511** (1–3), 43 (2002).
14. B. Stagemann, T. M. Berngardt, B. Kaiser, and K. Rademann, Surf. Sci. **511** (1–3), 153 (2002).
15. Y. W. Mo, Phys. Rev. Lett. **71** (18), 2923 (1993).
16. D. A. Gorodetsky, Yu. P. Melnik, V. A. Usenko, A. A. Yasko, and V. I. Yarigin, Surf. Sci. **315**, 51 (1994).
17. D. A. Gorodetsky, Yu. P. Melnik, D. P. Proskurin, V. A. Usenko, and A. A. Yasko, Surf. Sci. **416**, 255 (1998).
18. R. Ludeke, Phys. Rev. Lett. **39** (16), 1042 (1977).
19. J. Vrijmoeth, H. A. van der Vegt, J. A. Meyer, E. Vlieg, and R. J. Behm, Phys. Rev. Lett. **72** (24), 3843 (1994).
20. L. Vitos, A. V. Ruban, H. L. Skriver, and J. Kolla'r, Surf. Sci. **411**, 186 (1998).
21. B. F. Ormont, *Structures of Inorganic Materials* (GITTL, Leningrad, 1950) [in Russian].

Translated by O. Borovik-Romanova

Physics of the Solid State, Vol. 46, No. 10, 2004, pp. 1949–1953. Translated from Fizika Tverdogo Tela, Vol. 46, No. 10, 2004, pp. 1881–1885.

LOW-DIMENSIONAL SYSTEMS AND SURFACE PHYSICS

Low-Temperature Method of Cleaning *p*-GaN(0001) Surfaces for Photoemitters with Effective Negative Electron Affinity

O. E. Tereshchenko[1, 2], G. É. Shaĭbler[1, 2], A. S. Yaroshevich[1, 2], S. V. Shevelev[1, 2], A. S. Terekhov[1, 2], V. V. Lundin[3], E. E. Zavarin[3], and A. I. Besyul'kin[3]

[1] *Institute of Semiconductor Physics, Siberian Division, Russian Academy of Sciences, pr. Akademika Lavrent'eva 13, Novosibirsk, 630090 Russia*

[2] *Novosibirsk State University, ul. Pirogova 2, Novosibirsk, 630090 Russia*

e-mail: teresh@thermo.isp.nsc.ru

[3] *Ioffe Physicotechnical Institute, Russian Academy of Sciences, Politekhnicheskaya ul. 26, St. Petersburg, 194021 Russia*

Received December 4, 2003; in final form, March 25, 2004

Abstract—The changes in the chemical composition, atomic structure, and electronic properties of the *p*-GaN(0001) surface upon chemical treatment in an HCl–isopropanol solution and vacuum annealing are investigated by x-ray photoelectron spectroscopy, high-resolution electron energy-loss spectroscopy, and low-energy electron diffraction. It is demonstrated that a considerable part of the surface gallium oxide is removed upon chemical treatment of the GaN surface. Subsequent annealing of the surface under vacuum at temperatures of 400–450°C leads to a decrease in the residual carbon and oxygen contamination to 3–5% of the monolayer. The preparation of a clean *p*-GaN(0001) surface with a (1×1) structure identical to that of the bulk unit cells is confirmed by the low-energy electron diffraction data. The cesium adsorption on the clean *p*-GaN surface results in a decrease in the work function by ~2.5 eV and the appearance of an effective negative electron affinity on the surface. The quantum efficiency of the GaN photocathode at a wavelength of 250 nm is equal to 26%.

1. INTRODUCTION

Over the last decade, the particular attention focused on the problem associated with the cleaning of surfaces of III–N semiconductor compounds has been dictated by the necessity of producing high-quality ohmic contacts, Schottky barriers, and surfaces with an effective negative electron affinity [1–6]. The possibility of manufacturing GaN and $Al_xGa_{1-x}N$ compounds with an effective negative electron affinity on the surface permits one to use these materials in photoreceivers and as emitters in electronic devices with cold cathodes [7, 8]. It is well known [8–10] that, for semiconductor photocathodes serving as electron sources, an atomically clean initial surface prior to deposition of cesium and oxygen atoms is a necessary condition for achieving a high quantum efficiency. Apart from the cleanness of the surface, it is significant that the initial surface of a semiconductor should have a specific atomic structure. In this respect, investigations into physicochemical processes for producing an atomically clean and structurally ordered GaN surface are of considerable scientific and practical interest.

The simplest way to clean a semiconductor surface is to perform heat treatment under vacuum. As is known, the removal of gallium oxide from an initial GaN surface without preliminary treatment requires annealing at temperatures above 600°C [11, 12]. However, residual carbon and oxygen contaminations are not removed even after annealing at a temperature of 900°C [11], when the surface is depleted in nitrogen atoms and the surface morphology is deteriorated [13, 14]. Preliminary chemical treatment makes it possible to remove gallium oxide from the initial surface or to produce a passivating layer from a "controlled" oxide for its subsequent thermal desorption under vacuum. Most frequently, gallium oxide has been removed upon chemical treatment with aqueous solutions of HCl [12, 13] and HF [11, 15] acids and also aqua regia (HNO_3 : HCl = 1 : 3) [16]. The chemical treatment in these acids and subsequent vacuum annealing allow one to prepare surfaces with the lowest content of oxygen and carbon; however, these contaminations cannot be completely desorbed even at an annealing temperature of 900°C [11]. The content of residual contaminations after these treatments is no less than 5% of the monolayer (ML). A lower content of oxygen and carbon at the surface can be achieved only through ion bombardment [1]. However, this is accompanied by a strong depletion of surfaces in nitrogen atoms, surface faceting [17], and a considerable degradation of the electronic properties of these surfaces [18]. Both the ion bombardment and high-temperature annealing lead to the formation of a large number of defects in the surface region of the semiconductor. This circumstance limits the use of the above methods for fabricating highly efficient photoemitters with an effective negative electron affinity [8].

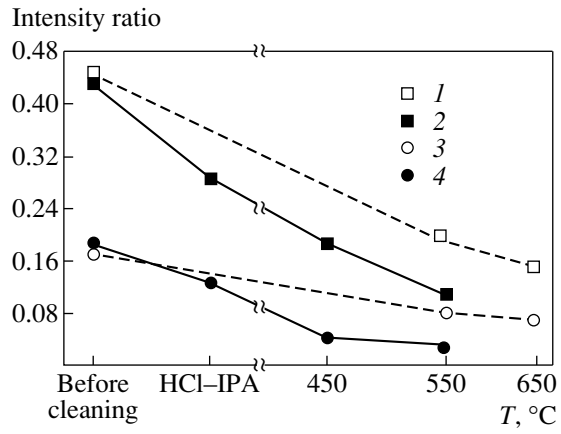

Fig. 1. Dependences of the intensity ratios for (*1*, *2*) O 1*s* and Ga 2*p* lines and (*3*, *4*) C 1*s* and Ga 2*p* lines in the x-ray photoelectron spectrum of the GaN surface on the conditions of vacuum annealing of the surface (*1*, *3*) before and (*2*, *4*) after preliminary treatment in an HCl–isopropanol solution.

The purpose of the present work was to prepare a clean GaN(0001) surface upon low-temperature annealing under ultrahigh vacuum and to activate this surface with cesium and oxygen in order to fabricate a highly efficient photoemitter with an effective negative electron affinity.

2. SAMPLE PREPARATION AND EXPERIMENTAL TECHNIQUE

For experiments, *p*-GaN films doped at a level of $\sim 1 \times 10^{17}$ cm^{-3} were grown through metaloorganic vapor-phase epitaxy on a sapphire substrate. The thickness of a GaN active layer was equal to 3 μm. The treatment was performed in a hermetically sealed box in a dry-nitrogen atmosphere. In order to prevent uncontrollable surface contamination, the samples treated in an HCl–isopropanol solution were transferred in a hermetically sealed transport vessel with a nitrogen atmosphere to an ADES-500 ultrahigh-vacuum spectrometer. The technique of chemical treatment in HCl–isopropanol solutions was described in detail in our earlier works [19, 20]. The samples were annealed in a preparation chamber with an initial pressure of 1×10^{-10} mbar. The measurements were carried out in an analysis chamber with an initial pressure of 4×10^{-11} mbar. The surface composition was determined by x-ray photoelectron spectroscopy and high-resolution electron energy-loss spectroscopy. The electron energy-loss spectra with a total energy resolution of no worse than 100 meV were measured in the specular reflection geometry. The kinetic energy of incident electrons was 15 eV, and the angle of incidence with the respect to the normal to the surface was approximately equal to 55°. The surface structure was studied by low-energy electron diffraction. Changes in the work function due to the cesium adsorption were measured by the retarding-potential method on a low-energy electron diffractometer.

3. RESULTS AND DISCUSSION

3.1. Composition of the GaN(0001) Surface

Figure 1 depicts the dependences of the intensity ratios for the O 1*s* and Ga 2*p* lines and also the C 1*s* and Ga 2*p* lines in the x-ray photoelectron spectrum of the gallium nitride surface on the conditions of vacuum annealing of the surface before and after preliminary treatment in an HCl–isopropanol solution. These dependences reflect the change in the contamination content on the surface. It can be seen from Fig. 1 that the treatment of the surface in the HCl–isopropanol solution leads to an almost twofold decrease in the intensity ratio of the oxygen and gallium lines and only in an insignificant decrease in the intensity ratio of the C 1*s* and Ga 2*p* lines. The annealing of GaN at T = 450°C results in a decrease in the intensity ratio of the carbon and gallium lines by a factor of 4. As will be shown below, this temperature corresponds to the desorption temperature of hydrocarbon molecules. With a further increase in the annealing temperature, the intensity ratio of the C 1*s* and Ga 2*p* lines remains unchanged, whereas the intensity ratio of the O 1*s* and Ga 2*p* lines continues to decrease. It can also be seen from Fig. 1 that, upon vacuum annealing of a gallium nitride surface that is not chemically treated, the content of residual carbon and oxygen is twice as high as their content on a surface treated in an HCl–isopropanol solution. The estimates made according to the procedure proposed in [21] indicate that the residual carbon and oxygen content on the GaN surface chemically treated and annealed at T = 450°C does not exceed 3–5% of a monolayer.

The removal of gallium oxide was confirmed by high-resolution electron energy-loss spectroscopy. Figure 2 shows the electron energy-loss spectra of the GaN surface before (spectrum *a*) and after treatment in the HCl–isopropanol solution (spectrum *b*). These spectra are due to interband transitions of valence electrons to the conduction band. As can be seen from these spectra, the energy losses associated with the interband transitions for the initial surface are observed beginning with an energy of 4.0 eV, whereas the energy losses for the surface treated in the HCl–isopropanol solution appear at an energy of 3.4 eV, which corresponds to the band gap of the GaN compound. The losses for the initial surface at energies higher than 4 eV are caused by the gallium oxide layer that has a band gap of 4.4 eV [22], is located on the surface, and masks the losses in GaN. Therefore, the treatment of the initial GaN surface in the HCl–isopropanol solution leads to the removal of a considerable part of the surface gallium oxide and the transfer of the samples in the hermetically sealed vessel enables us to avoid uncontrollable contamination of the gallium nitride surface after chemical treatment.

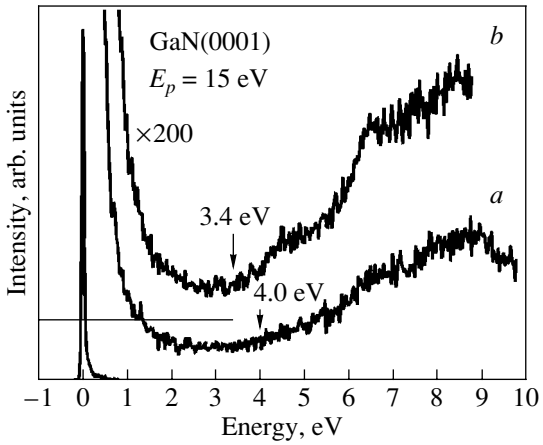

Fig. 2. Electron energy-loss spectra of the GaN surface (*a*) before and (*b*) after chemical treatment in an HCl–isopropanol solution in the range of interband transitions of valence electrons to the conduction band.

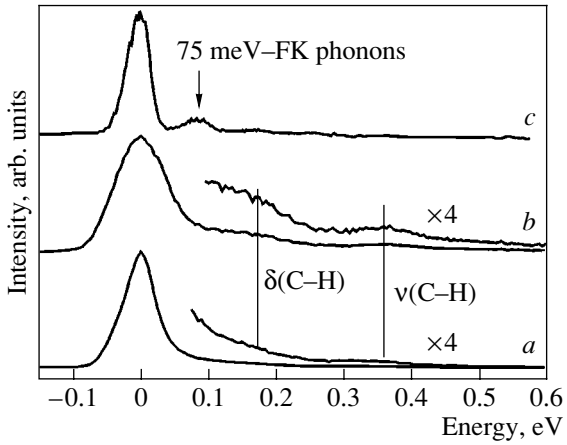

Fig. 3. Electron energy-loss spectra of the GaN surface (*a*) before and (*b*) after chemical treatment in an HCl–isopropanol solution and (*c*) after subsequent annealing at T = 450°C.

In addition to oxygen, carbon compounds are among the contaminations that are the most difficult to remove. High-resolution electron energy-loss spectroscopy is the most sensitive method for revealing hydrocarbon compounds on a surface [23]. Figure 3 depicts the electron energy-loss spectra in the vicinity of the elastic peak for the GaN surface before (spectrum *a*) and after chemical treatment in the HCl–isopropanol solution (spectrum *b*) and also after subsequent annealing at T = 450°C (spectrum *c*). For the initial surface, the energy losses are observed at 170 and 360 meV. These losses increase insignificantly after chemical treatment. The losses at energies of 170 and 360 meV are assigned to the excitation of flexural and longitudinal vibrational modes of C–H bonds in hydrocarbon molecules on the GaN surface. The excitation of similar modes was previously observed on a GaAs surface [19, 24]. It should be noted that the relative content of hydrocarbon compounds on the GaN surface after treatment in the HCl–isopropanol solution is lower than the corresponding content on the GaAs surface after a similar treatment by several factors [19]. Probably, this is associated with the lower reactivity of the gallium nitride surface and, as a consequence, with the smaller coefficient of sticking of hydrocarbon compounds to the surface during chemical treatment and subsequent transfer as compared to the GaAs surface, which contains an As amorphous layer. The annealing of the GaN surface at T = 450°C after chemical treatment results in the disappearance of the losses associated with the excitation of hydrocarbon molecules (Fig. 3, spectrum *c*) and the appearance of the losses at an energy of ~75 meV. The losses at an energy of ~75 meV were previously observed for a clean GaN surface and were assigned to the excitation of surface optical phonons (the so-called Fuchs–Kliewer surface phonons) [17]. The possibility of observing the phonon losses suggests that the GaN surface layer has a perfect crystal structure. Note that the data on desorption of hydrocarbon molecules are inconsistent with the results obtained in [11], according to which bonds between hydrocarbon molecules and the GaN surface treated in an HCl aqueous solution are stable up to temperatures of 650–900°C. The possible reason for this disagreement is the difference in the interaction of aqueous and alcohol solutions of HCl with a GaN surface containing a thin gallium oxide overlayer. Upon treatment in the alcohol solution, residual carbon contaminations on the GaN surface are large-sized hydrocarbon molecules, which have saturated carbon bonds and, hence, are weakly bonded to surface atoms. On the other hand, upon treatment in the HCl aqueous solution, the surface can adsorb fragments of hydrocarbon molecules, such as CH, CH_2, and CH_3, which are more strongly bonded to surface atoms. The difference in the energy of bonding between hydrocarbon molecules and the GaN surface explains the difference in the desorption temperature of hydrocarbon molecules. A residual carbon and oxygen content of 3–5% of a monolayer on the GaN surface is determined by the fact that bonds of the corresponding compounds to surface atoms in GaN are stronger than those in other III–V compounds.

3.2. Structure of the GaN(0001) Surface

The low-energy electron diffraction pattern of the initial GaN surface exhibits a uniform background of diffusely scattered electrons. A specific diffraction pattern of this surface arises only after annealing at temperatures above 650°C and energies of primary electrons $E_P > 180$ eV and contains integral reflections with intensities only slightly higher than the intensity of the average background of the diffraction pattern. Chemical treatment of the surface in the HCl–isopropanol solution results in the appearance of diffraction reflections that correspond to a (1 × 1) unit cell and are

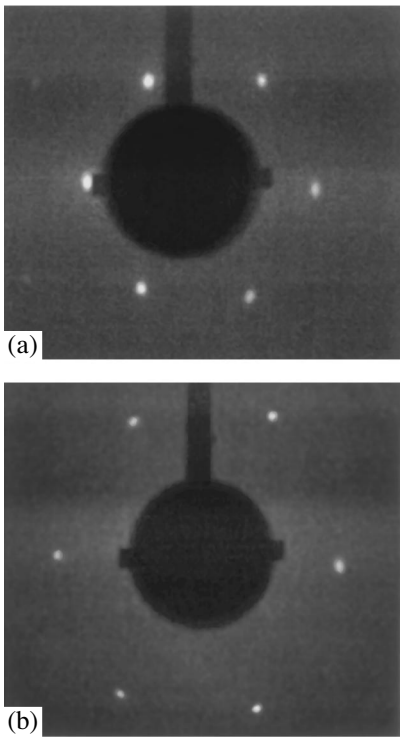

Fig. 4. Low-energy electron diffraction patterns of the GaN(0001) surface prepared through chemical treatment in an HCl–isopropanol solution and subsequent annealing at $T = 450$°C. The measurements were performed at room temperature and primary-electron energies of (a) 147 and (b) 73 eV.

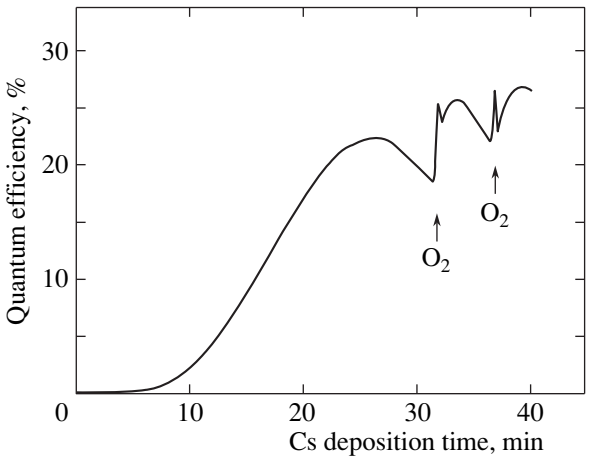

Fig. 5. Dependence of the quantum efficiency on the time of cesium deposition on the GaN surface.

observed at energies of primary electrons $E_P \geq 140$ eV. The low-energy electron diffraction patterns of the GaN surface after treatment in the HCl–isopropanol solution and vacuum annealing at $T = 450$°C for energies of primary electrons $E_P = 147$ and 73 eV are shown in Figs. 4a and 4b, respectively. It can be seen from the diffraction patterns that the GaN surface is not reconstructed and has a (1×1) structure; i.e., surface unit cells are identical to bulk unit cells. In [2, 8], it was demonstrated that, in order to prepare an ordered surface with the (1×1) structure, it is necessary to use considerably higher temperatures (~700–900°C), at which the surface is depleted in nitrogen atoms and defects are formed. The decrease in the annealing temperature required for forming the ordered GaN surface makes it possible to prepare a more stoichiometric surface with a lower concentration of thermal defects.

3.3. Activation of the GaN Surface with Cesium and Oxygen

The GaN surface was activated according to the standard procedure for activating GaAs photocathodes [9]. The dependence of the quantum yield of photoelectrons from GaN on the time of cesium deposition on the gallium nitride surface upon excitation of electrons with light at a wavelength of 250 nm is plotted in Fig. 5. The arrows indicate the instants of oxygen inflow. The first photoemission maximum is observed when the adsorbed cesium coverage is approximately equal to 0.5 ML (according to x-ray photoelectron spectroscopic data), as is the case with the activation of the GaAs surface. Unlike GaAs, for GaN, the addition of oxygen to cesium leads to an increase in the photocurrent by no more than 15%.

It is of interest to note that, as for the GaAs(100)-$(4 \times 2)/c(8 \times 2)$ surface, the surface structure of gallium nitride does not change upon adsorption of 0.5 ML Cs. As follows from our measurements, the work function upon adsorption of 0.5 ML Cs decreases by 2.5 eV. This is in agreement with the data obtained in [25, 26]. The effective negative electron affinity on the GaN–(Cs, O) activated surface was approximately equal to 1.8 eV, and the maximum quantum efficiency of the GaN photocathode at a light wavelength of 250 nm was as high as 26% [27].

4. CONCLUSIONS

Thus, an atomically pure structurally ordered surface of gallium nitride with a (1×1) structure was prepared through the chemical removal of gallium oxide from the GaN surface in an HCl–isopropanol solution, the transfer of samples in a nitrogen atmosphere (with the aim of preventing surface reoxidation), and annealing at 450°C. After removing hydrocarbon compounds from the surface, the high-resolution electron energy-loss spectra exhibited losses associated with the excitation of surface optical phonons in GaN. A decrease in the temperature necessary for forming the clean ordered GaN surface made it possible to prepare the surface with a lower concentration of defects. This is an important advantage in the manufacture of photoemitters with an effective negative electron affinity.

The activation of the *p*-GaN(0001) surface with cesium and oxygen resulted in the appearance of an effective negative electron affinity at the gallium nitride surface. The quantum efficiency of the fabricated GaN photocathode at a wavelength of 250 nm was equal to 26%.

ACKNOWLEDGMENTS

This work was supported by the Russian Foundation for Basic Research (project no. 04-02-16639), the Foundation for Assistance to Domestic Science, and the Grant Council of the President of the Russian Federation.

REFERENCES

1. R. W. Hunt, L. Vanzetti, T. Castro, K. M. Chen, L. Sobra, P. I. Cohen, W. Gladfelter, J. M. von Hove, J. N. Kuznia, M. A. Khan, and A. Franciosi, Physica B (Amsterdam) **185**, 415 (1993).
2. J. Ma, B. Garni, N. Perkins, W. L. O'Brien, T. F. Kuech, and M. G. Lagally, Appl. Phys. Lett. **69**, 3351 (1996).
3. M. A. Khan, J. N. Kuznia, D. T. Olson, and R. Kaplan, J. Appl. Phys. **73**, 3108 (1993).
4. V. M. Bermudes, M. A. Khan, R. Kaplan, and J. N. Kuznia, Phys. Rev. B **48**, 2436 (1993).
5. V. M. Bermudes, T. M. Jung, K. Doverspike, and A. E. Wickenden, J. Appl. Phys. **79**, 110 (1996).
6. S. Nakamura, M. Senoh, S. Nagahama, N. Iwasa, T. Yamada, T. Matsushita, H. Kiyoku, and Y. Sugimoto, Appl. Phys. Lett. **68**, 3269 (1996).
7. F. Machuca, Y. Sun, Z. Liu, K. Ioakeimidi, P. Pianetta, and R. F. W. Pease, J. Vac. Sci. Technol. B **18**, 3042 (2000).
8. F. Machuca, Z. Liu, Y. Sun, P. Pianetta, W. E. Spicer, and R. F. W. Pease, J. Vac. Sci. Technol. A **20**, 1784 (2002).
9. S. Pastuszka, A. S. Terekhov, and A. Wolf, Appl. Surf. Sci. **99**, 361 (1996).
10. R. Holton and P. M. Gundry, Surf. Sci. **63**, 263 (1977).
11. S. W. King, J. P. Barnak, M. D. Bremser, K. M. Tracy, C. Ronning, R. F. Davis, and R. J. Nemanich, J. Appl. Phys. **84**, 5248 (1998).
12. I. Waki, H. Fujioka, K. Ono, M. Oshima, H. Miki, and A. Fukizava, Jpn. J. Appl. Phys. **39**, 4451 (2000).
13. S. Tripathy, S. J. Chua, and A. Ramam, J. Phys.: Condens. Matter **14**, 4461 (2002).
14. G. V. Benemanskaya, A. I. Besyul'kin, M. S. Dunaevskiĭ, A. K. Kryzhanovskiĭ, and N. M. Shmidt, Fiz. Tverd. Tela (St. Petersburg) **45**, 980 (2003) [Phys. Solid State **45**, 1026 (2003)].
15. Z. M. Zhao, R. L. Jiang, P. Chen, D. J. Xi, B. Shen, R. Zhang, and Y. D. Zheng, J. Vac. Sci. Technol. B **19**, 286 (2001).
16. J.-L. Lee, M. Weber, J. K. Kim, J. W. Lee, Y. J. Park, T. Kim, and K. Lynn, Appl. Phys. Lett. **74**, 2289 (1999).
17. V. J. Belitto, B. D. Thoms, D. D. Koleske, A. E. Wickenden, and R. L. Henry, Surf. Sci. **430**, 80 (1999).
18. H. Ishikawa, S. Kobayashi, Y. Koide, S. Yamasaki, S. Nagai, J. Umezaki, M. Koike, and M. Murakami, J. Appl. Phys. **81**, 1315 (1997).
19. O. E. Tereshchenko, S. I. Chikichev, and A. S. Terekhov, J. Vac. Sci. Technol. A **17**, 2655 (1999).
20. O. E. Tereshchenko, D. Paget, P. Chiaradia, J. E. Bonnet, F. Wiame, and A. Taleb-Ibrahimi, Appl. Phys. Lett. **82**, 4280 (2003).
21. *Practical Surface Analysis by Auger and X-ray Photoelectron Spectroscopy*, Ed. by D. Briggs and M. Seah (Wiley, New York, 1983; Mir, Moscow, 1987).
22. T. Tsuruoka, M. Kawasaki, S. Ushida, R. Franchy, Y. Naoi, T. Sugahara, S. Sakai, and Y. Shintani, Surf. Sci. **427–428**, 257 (1998).
23. A. Degiovanni, J. L. Guyaux, P. A. Thiry, and R. Caudano, Surf. Sci. **251/252**, 238 (1991).
24. A. A. Aquino and T. S. Jones, Appl. Surf. Sci. **104/105**, 304 (1996).
25. C. I. Wu and A. Kahn, Appl. Surf. Sci. **162/163**, 250 (2000).
26. T. U. Kampen, M. Eyckeler, and W. Mönch, Appl. Surf. Sci. **123/124**, 28 (1998).
27. O. E. Tereshchenko, A. A. Pakhnevich, H. E. Scheibler, A. S. Jaroshevich, S. V. Shevelev, and A. S. Terekhov, in *Book of Abstracts of the Workshop on Polarized Sources and Target, PST2003* (Novosibirsk, 2003), p. 26.

Translated by O. Borovik-Romanova

Physics of the Solid State, Vol. 46, No. 10, 2004, pp. 1954–1960. Translated from Fizika Tverdogo Tela, Vol. 46, No. 10, 2004, pp. 1886–1892.

LOW-DIMENSIONAL SYSTEMS AND SURFACE PHYSICS

Dispersion and Attenuation of Surface Shear Acoustic Waves with Horizontal Polarization on the Free Statistically Rough Surface of the Hexagonal Crystal

V. V. Kosachev, Yu. N. Gandurin, and K. V. Barsukov

Engineering Physics Institute, Kashirskoe sh. 31, Moscow, 115409 Russia

e-mail: kosachev@theor.mephi.ru

Received December 16, 2003

Abstract—Expressions for dispersion of the phase velocity and inverse damping depth of surface acoustic waves with shear horizontal polarization are derived in an analytical form within perturbation theory using the modified mean-field method for the *Z*-cut hexagonal crystal with a free statically rough surface. Both two- and one-dimensionally rough surfaces are considered. The one-dimensionally rough surface is considered as a special case of the two-dimensionally rough surface. It is shown that shear surface waves with horizontal polarization cannot exist on the flat surface of the *Z*-cut hexagonal crystal. The derived expressions are studied analytically and numerically in the entire frequency range accessible in perturbation theory. The long-wavelength limit (most interesting from the experimental point of view) is considered, where the wavelength is much longer than the roughness correlation radius. The conditions for the existence of SH-polarized waves are determined for both roughness types. It is shown that dispersion and attenuation of SH polarized waves are qualitatively similar in character to those we considered previously for an isotropic medium. *© 2004 MAIK "Nauka/Interperiodica".*

1. INTRODUCTION

It is known that, in addition to Rayleigh waves, shear surface acoustic waves (SAWs) with horizontal polarization (SH polarization) can propagate along a rough surface of an isotropic solid under certain conditions (but cannot propagate along a flat surface of an isotropic solid [1]). Conditions for their existence can be created due to the following factors: inhomogeneities in the properties of an elastic medium near the surface caused by applying a thin layer onto a substrate (the case of the Love wave [2] and weak surface inhomogeneity [3]), piezoelectricity (the Gulyaev–Bleustein wave [4, 5]), ferromagnetism (magnetoelastic waves [6–8]), anharmonicity of lattice vibrations [9], and surface roughnesses.

As for the surface roughness studied in this paper, both two- and one-dimensionally (2D, 1D) rough surfaces have been considered in the literature. The dispersion relation for SH-polarized waves propagating along a 2D rough surface of an isotropic solid was derived for the first time in [10]. Most studies devoted to SH-polarized waves on a 1D rough surface [11–13] limit the analysis to the case of waves incident perpendicular to random grooves of a grating. A dispersion relation for SH-polarized waves propagating along grooves of a random grating was derived in [14]; a similar result (but for a periodic roughness) was obtained in [15]. A dispersion relation for SH-polarized waves propagating perpendicular to grooves of periodic roughness was derived in [16]. A dispersion relation for SH-polarized waves incident at an arbitrary angle on random grooves of a grating in the case of 2D and 1D roughness was derived in [17]. We note that, in the papers cited above, the medium was considered isotropic for SH-polarized SAWs on a rough surface. Furthermore, the problem of the existence of SH-polarized SAW on a flat (not rough) crystal surface remains open.

In this study, a dispersion relation is derived for SH-polarized waves on a slightly rough surface of a hexagonal crystal. In particular, SH-polarized waves propagating in an arbitrary direction along the basal plane of a free statistically rough surface of a hexagonal crystal (*Z*-cut) are considered.

2. STATEMENT OF THE PROBLEM

A hexagonal crystal with a hexad axis parallel to the x_3 axis (considered in the elastic continuum approximation) is bounded by a free statistically rough surface and is placed in the half-space $x_3 > \zeta(\mathbf{x}_\parallel)$, where $\zeta(\mathbf{x}_\parallel)$ is the rough-surface profile function and $\mathbf{x}_\parallel = (x_1, x_2, 0)$. The hexagonal crystal is characterized by the mass density ρ and the tensor of elastic moduli $C_{\alpha\beta\mu\nu}$. An SH-polarized SAW propagates along the statistically rough surface of the hexagonal crystal. We will determine the phase velocity dispersion and inverse wave damping depth caused by surface roughness.

1063-7834/04/4610-1954$26.00 © 2004 MAIK "Nauka/Interperiodica"

It is assumed that the function $\zeta(\mathbf{x}_\parallel)$ has the following statistical properties:

$$\langle \zeta(\mathbf{x}_\parallel)\rangle = 0, \tag{1}$$

$$\langle \zeta(\mathbf{x}_\parallel)\zeta(\mathbf{x}'_\parallel)\rangle = \delta^2 W(|\mathbf{x}_\parallel - \mathbf{x}'_\parallel|), \tag{2}$$

where $\delta = \sqrt{\langle \zeta^2\rangle}$ is the root-mean-square roughness amplitude. Introducing the Fourier representation

$$\zeta(\mathbf{x}_\parallel) = \int \frac{d^2\mathbf{k}_\parallel}{(2\pi)^2}\zeta(\mathbf{k}_\parallel)\exp(i\mathbf{k}_\parallel x_\parallel), \quad \mathbf{k}_\parallel = (k_1, k_2, 0), \tag{3}$$

we get

$$\langle \zeta(\mathbf{k}_\parallel)\zeta(\mathbf{q}_\parallel)\rangle = \delta^2 g(|\mathbf{k}_\parallel|)(2\pi)^2\delta(\mathbf{k}_\parallel + \mathbf{q}_\parallel). \tag{4}$$

The correlation function $g(|k_\parallel|)$ is taken in the Gaussian form

$$g(|\mathbf{k}_\parallel|) = \pi a^2 \exp\left(-\frac{k_\parallel^2 a^2}{4}\right), \tag{5}$$

where a is the roughness correlation length (characterizing the average distance between sequential hills or valleys on the surface). The surface roughness is considered weak; i.e., characteristic heights δ of roughnesses are assumed to be small in comparison to the wavelength λ under consideration ($\delta \ll \lambda$). The time dependence of the displacement field is assumed to be harmonic:

$$\mathbf{u}(\mathbf{x}, t) = \mathbf{u}(\mathbf{x}, \omega)\exp(-i\omega t). \tag{6}$$

3. DISPERSION RELATION FOR SH-POLARIZED WAVES ON THE 2D ROUGH SURFACE

The problem of determining the dispersion relation of SH polarized SAWs is solved using the modified mean-field method described in [17], where it was shown that effective boundary conditions can be used to reduce this problem to considering free vibrations of an elastic medium localized near the $x_3 = 0$ plane. The effective boundary conditions are defined in [17] for a medium with arbitrary symmetry and, therefore, are also valid for a hexagonal crystal. By introducing the Green's function satisfying the equations of motion of a semi-infinite medium and boundary conditions at the $x_3 = 0$ plane and infinity, we can pass from differential equations with effective boundary conditions to integral equations using the Green's integral theorem. Passing to the Fourier representation and combining the integral equations with effective boundary conditions, we derive a set of homogeneous integral equations for the displacement field components $\langle F_\alpha(\mathbf{k}_\parallel, \omega|x_3)\rangle$ to the second order in ζ. After averaging over an ensemble of realizations of surface profile functions, we obtain a homogeneous set of algebraic equations for the components of the average displacement field, which can be written in the general form as

$$\langle F_\alpha(\mathbf{k}_\parallel, \omega|0)\rangle = \delta^2 A_{\alpha\beta}(\mathbf{k}_\parallel, \omega)\langle F_\beta(\mathbf{k}_\parallel, \omega|0)\rangle. \tag{7}$$

For the case of the hexagonal crystal (Z cut), set (7) was derived in [18, Eq. (18)]. It turns out that, in the case of the Z-cut hexagonal crystal, as well as for the isotropic medium [17], the components $\langle F_1(\mathbf{k}_\parallel, \omega|0)\rangle$ and $\langle F_3(\mathbf{k}_\parallel, \omega|0)\rangle$ (corresponding to Rayleigh waves [18]) can be separated from the equation for $\langle F_2(\mathbf{k}_\parallel, \omega|0)\rangle$ corresponding to SH-polarized waves (see [18, Eqs.(18), (19)]). This separation can be performed in virtue of the isotropy of the Z-cut hexagonal crystal. The equation for the component $\langle F_2(\mathbf{k}_\parallel, \omega|0)\rangle$ has the form

$$\langle F_2(\mathbf{k}_\parallel, \omega|0)\rangle = \delta^2\int \frac{d^2 q_\parallel}{(2\pi)^2} g(|\mathbf{k}_\parallel - \mathbf{q}_\parallel|) \times (d_{22}X_{21}^2\tilde{d}_{11} + d_{22}X_{22}^2\tilde{d}_{22})\langle F_2(\mathbf{k}_\parallel, \omega|0)\rangle, \tag{8}$$

where $d_{\alpha\beta} \equiv d_{\alpha\beta}(k_\parallel|\omega)$, $\tilde{d}_{\alpha\beta} \equiv d_{\alpha\beta}(q_\parallel|\omega)$ (the surface Green's function for the hexagonal crystal with a free surface parallel to the basal plane [19]), and $X_{\alpha\beta} \equiv X_{\alpha\beta}(q_\parallel, k_\parallel|\omega)$. From the solvability condition for Eq. (8), after simple algebra, we find a dispersion relation for SH-polarized surface waves,

$$\frac{\alpha_t(k_\parallel, \omega)}{k_\parallel\sqrt{h}} = \left(\frac{\delta}{a}\right)^2 r(\xi), \tag{9}$$

where

$$r(\xi) = \xi^4\frac{h}{8}\exp\left(-\frac{\xi^2}{4}\right)(A(\xi) + B(\xi) + E(\xi)), \tag{10}$$

and $\xi = k_\parallel a$; the functions $\alpha_t(k_\parallel, \omega)$, $A(\xi)$, $B(\xi)$, and $E(\xi)$ and the coefficient h depend only on the components of the elastic moduli tensor (see Appendix 1). The function $\alpha_t(k_\parallel, \omega)$ defines damping of the Fourier components of the displacements

$$u_\alpha(k_\parallel, \omega|x_3) \sim \exp(-\alpha_t(k_\parallel, \omega)x_3). \tag{11}$$

Let us write the solution to dispersion relation (9) in the form

$$\omega = \omega_{SH} + \Delta\omega, \tag{12}$$

where $\omega_{SH} = k_\parallel\sqrt{hc_{44}/\rho}$ corresponds to the solution to Eq. (9) for a flat surface ($\delta = 0$); however, ω_{SH} is a nonphysical solution, since $\alpha_t(k_\parallel, \omega) = 0$ does not correspond to waves localized near the surface. The solution to Eq. (9), in combination with Eq. (12), can be written as

$$\frac{\Delta\omega(\xi)}{\omega_{SH}} = -\frac{\delta^4}{a^4}\frac{r(\xi)^2}{2}. \tag{13}$$

Since $r(\xi)$ is a complex quantity, it is convenient to write it as

$$r(\xi) = r_1(\xi) + ir_2(\xi), \quad (14)$$

so Eq. (13) takes on the form

$$\frac{\Delta\omega(\xi)}{\omega_{SH}} = -\frac{\delta^4}{a^4}\frac{r_1(\xi)^2 - r_2(\xi)^2}{2} - i\frac{\delta^4}{a^4}r_1(\xi)r_2(\xi). \quad (15)$$

Since the wave should damp into the medium depth ($x_3 > 0$), it follows from Eq. (11) that $\mathrm{Re}\,\alpha_t > 0$, which corresponds to the condition

$$r_1(\xi) > 0. \quad (16)$$

In order to prevent an increase in the wave amplitude in the course of propagation along the rough surface, the condition $\mathrm{Im}\,\Delta\omega \le 0$ should be met; then it follows from Eq. (15) that

$$r_2(\xi) \ge 0. \quad (17)$$

Conditions (16) and (17) define the domain of existence of SH-polarized waves.

In the case of an isotropic medium, dispersion relation (13) reduces to Eq. (5.20) from [17].

In the long-wavelength limit, where $\xi \ll 1$ ($\lambda \gg \alpha$), the expressions for $r_1(\xi)$ and $r_2(\xi)$ take on the form

$$r_1(\xi) = \xi\frac{h\sqrt{\pi}}{2}\left(\frac{\sqrt{h}}{a_1}(\sqrt{a_2 + b_2} + \sqrt{a_2 - b_2}) + 1\right), \quad (18)$$

$$r_2(\xi) = \xi^4\frac{h}{8}\left(\frac{10}{3} + \pi\frac{\tilde{\alpha}_p\left(\frac{1}{\varepsilon}\right)\left(1 + \frac{h}{\varepsilon}\right)\varepsilon(1-\varepsilon)\left(\frac{c_{11}}{c_{44}} - \varepsilon\right)}{\left(2a_1 - \frac{c_{11}}{c_{44}} + 1\right)\varepsilon^2 - \varepsilon a_1\left(\frac{c_{11}}{c_{44}} + 3\right) + 2a_1\frac{c_{11}}{c_{44}}} - h\,\mathrm{Im}\int_0^1 dx\frac{\tilde{\alpha}_p(x)\sqrt{x-1}(1+hx)}{\sqrt{x-1}(1-a_1x) + \tilde{\alpha}_m(x)}\right), \quad (19)$$

where

$$a_2 = \frac{a_1}{2} - \frac{c_{13}}{c_{33}}, \quad b_2 = \sqrt{a_2^2 - \frac{c_{11}}{c_{33}}}.$$

It follows from Eqs. (18) and (19) that

$$\mathrm{Re}\,\Delta\omega \sim \zeta^3, \quad \mathrm{Im}\,\Delta\omega \sim \zeta^6. \quad (20)$$

4. THE CASE OF A 1D ROUGH SURFACE

In this case, the statement of the problem differs only in that the surface roughness profile is given by grating grooves with a random distance between them; i.e., the surface profile function $\zeta(x_\parallel) = \zeta(x_2)$ depends only on a single coordinate. It is assumed that a wave propagating along the surface strikes randomly arranged grating grooves at an angle ψ to the normal to the grooves. By analogy with [20], let us consider a 1D roughness as a special case of the 2D roughness. Then, in all above relevant expressions, it is sufficient to make the replacement

$$g(|\mathbf{k}_\parallel|) \longrightarrow g(|\mathbf{k}_\parallel|) = (2\pi)\delta(k_2)g(|k_1|), \quad (21)$$

where $\delta(k_2)$ is the Dirac delta function. As a result, for SH-polarized waves on the 1D rough surface, we obtain dispersion relation (13), in which $\Delta\omega(\xi)$ and $r(\xi)$depend on the angle of incidence ψ:

$$r(\xi, \psi) = \xi^3\frac{h}{2\sqrt{\pi}}(A(\xi, \psi) + B(\xi, \psi) + E(\xi, \psi)). \quad (22)$$

Expressions for $A(\xi, \psi)$, $B(\xi, \psi)$, and $E(\xi, \psi)$ are given in Appendix 2. In this case, the existence conditions (16) and (17) for SH-polarized waves are imposed on $r(\xi, \psi)$ given by Eq. (22).

In the long-wavelength limit $\xi \ll 1$, we have

$$r_1(\xi, \psi) = \xi\frac{2h}{\sqrt{\pi}}\left(\cos^2 2\psi + \frac{\sqrt{h}}{a_1}(\sqrt{a_2 + b_2} + \sqrt{a_2 - b_2})\sin^2 2\psi\right), \quad (23)$$

$$r_2(\xi, \psi) = \xi^3\frac{h}{2\sqrt{\pi}}\left[\frac{\pi}{16}(6 + 5\cos 2\psi - 2\cos 4\psi + \cos 6\psi(15 - 16\sin\psi)) - iE(\xi, \psi) - \int_0^{\max(h - \sin^2\psi, 0)} d\eta\,\mathrm{Im}\left(\frac{\tilde{\alpha}_p(x)\sqrt{x-1}}{\sqrt{x-1}(1-a_1x) + \tilde{\alpha}_m(x)}\right)_{x = \frac{\eta^2 + \sin^2\psi}{h}} \times (\Phi_2(\eta, \psi) + \Phi_2(-\eta, \psi))_{\xi = 0}\right]. \quad (24)$$

Taking into account Eqs. (23) and (24), we obtain from Eq. (15) that

$$\mathrm{Re}\,\Delta\omega \sim \xi^3, \quad \mathrm{Im}\,\Delta\omega \sim \xi^5. \quad (25)$$

5. NUMERICAL CALCULATION

To perform numerical calculations, it is convenient to write $\Delta\omega$ in terms of the real and imaginary parts of the dimensionless function $\omega_{12} = \omega_1 - i\omega_2$ as

$$\frac{\Delta\omega}{\omega_{SH}} = \frac{\delta^4}{a^4}(\omega_1 - i\omega_2). \quad (26)$$

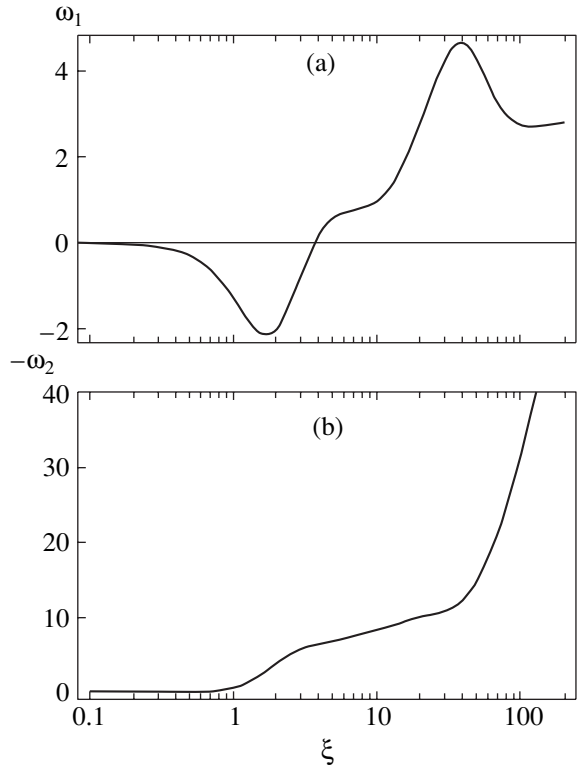

Fig. 1. Dependence of (a) the real, ω_1 and (b) imaginary, ω_2, parts of the complex frequency shift on the dimensionless variable ξ for SH-polarized waves on the 2D rough surface of the ZnO crystal.

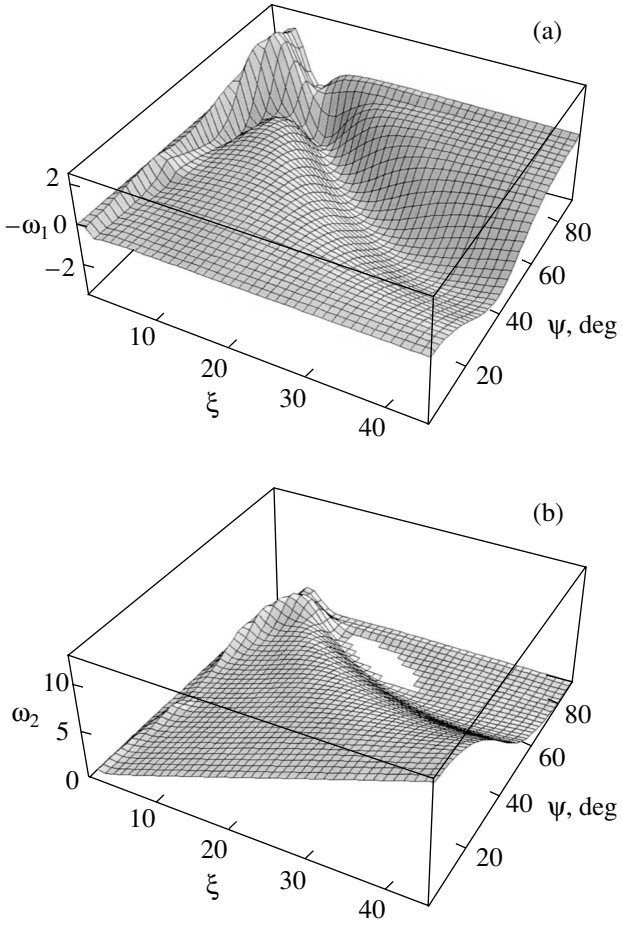

Fig. 2. Dependences of (a) the real, ω_1, and (b) imaginary, ω_2, parts of the complex frequency shift on the dimensionless variable ξ and the angle of incidence ψ for SH-polarized waves on the 1D rough surface of the ZnO crystal.

From Eq. (15), we can obtain expressions for ω_1 and ω_2. In this case, ω_1 defines the relative change in the phase velocity of SH-polarized waves,

$$\frac{\Delta c}{c_{SH}} = \frac{\delta^4}{a^4}\omega_1 \tag{27}$$

(where $c_{SH} = \omega_{SH}/k_\parallel$) and ω_2 defines the inverse damping depth,

$$\frac{1}{L} = \frac{\delta^4}{a^5}\xi 2\omega_2. \tag{28}$$

The functions ω_1 and ω_2 are calculated numerically for most of the known hexagonal crystals. It turned out that the graphs of these functions are qualitatively similar to each other and to the corresponding graphs for the case of an isotropic medium, differing only quantitatively. This conclusion is true for both 2D and 1D rough surfaces. Therefore, we present the results of numerical calculations for one of the best known hexagonal crystals, ZnO (the elastic moduli are taken from [21]).

Let us consider the 2D rough surface. In this case, $r_1(\xi) > 0$ and $r_2(\xi) > 0$ for all values of ξ; therefore, the SH-polarized SAW exists for all ξ. The functions $\omega_1(\xi)$ and $\omega_2(\xi)$ are shown in Figs. 1a and 1b, respectively. In particular, we can see from Fig. 1b that the wave exhibits virtually no damping at $\xi \lesssim 1$; strong damping begins at $\xi > 50$.

For the 1D rough surface (random grating grooves), taking into account the symmetry of the problem, it is sufficient to carry out calculations only for $\psi \in [0°, 90°]$. Calculations show that $r_2(\xi) > 0$ for all ξ; hence (see Eq. (15)), the domain of existence of SH-polarized waves is defined by the condition $\omega_2(\xi, \psi) \geq 0$. The functions $\omega_1(\xi, \psi)$ and $\omega_2(\xi, \psi)$ are shown in Figs. 2a and 2b, respectively. It follows from Fig. 2b that the SH-polarized wave does not exist in the unshaded oval region of $\xi \approx [10, 30]$ and $\psi \approx [65°, 85°]$, where $\omega_2(\xi, \psi) < 0$.

In the long-wavelength limit ($\xi \ll 1$) for the 2D rough surface, we can write [see Eqs. (15), (18), (19)]

$$\omega_1(\xi) = -\xi^2\Phi \quad \left(\frac{\Delta c}{c_{SH}} \sim \frac{\delta^4}{a^2}\omega^2\right), \tag{29}$$

Numerical values of Φ, Λ, and c_{SH} for a two-dimensionally rough surface for a number of hexagonal crystals

Medium	*T*, K	ρ, g/cm^3	c_{SH}, km/s	Φ	Λ
Be	293	1.816	8.297	1.671	2.617
CdS	293	4.825	1.827	1.124	1.706
Co	298	8.836	2.835	0.8794	1.334
Ice	257	0.960	1.950	1.316	2.013
	248	0.960	1.923	1.368	2.093
	263	0.960	1.896	1.375	2.105
	268	0.960	1.882	1.332	2.037
Mg	0	1.799	3.233	1.169	1.790
SiO_2	873	2.517	4.444	2.525	4.005
	873	2.533	4.441	2.533	4.025
ZnO	293	5.676	2.792	1.087	1.650
Y	4	4.472	2.464	1.193	1.835
	75	4.472	2.450	1.187	1.827
	200	4.472	3.393	1.182	1.817
	300	4.472	2.350	1.193	1.833
	400	4.472	2.314	1.211	1.860

Note: The components of the elastic moduli tensor, appearing in c_{SH}, Φ, and Λ, are taken from [18].

$$\omega_2(\xi) = \xi^5\frac{\Lambda}{2} \quad \left(\frac{1}{L} \sim \delta^4 a\omega^6\right), \tag{30}$$

where Φ and Λ are constants that are dependent only on the components of the elastic moduli tensor. The numerical values of Φ and Λ are close to unity and are listed in the table for most of the known hexagonal crystals.

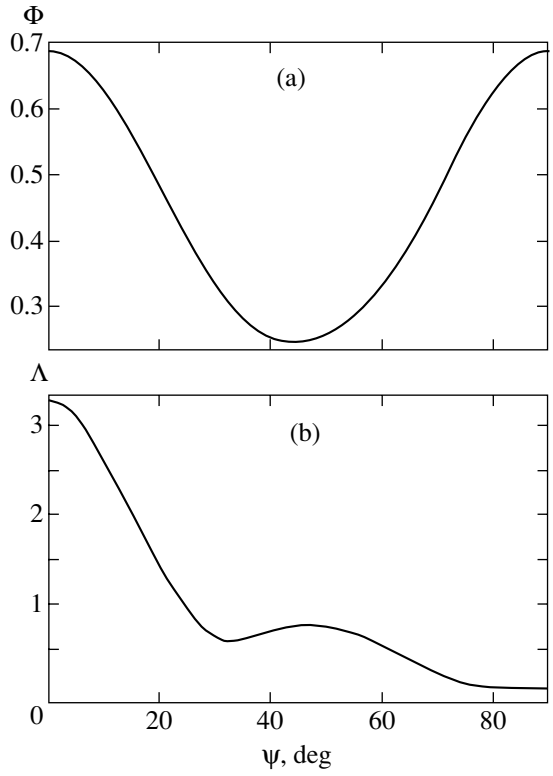

Fig. 3. Dependences of the functions (a) Φ and (b) Λ on the angle of incidence ψ for the 1D rough surface of the ZnO crystal in the long-wavelength limit ($\xi \ll 1$).

In the long-wavelength limit for the 1D rough surface, we can write

$$\omega_1(\xi, \psi) = -\xi^2\Phi(\psi) \quad \left(\frac{\Delta c}{c_{SH}} \sim \frac{\delta^4}{a^2}\omega^2\Phi(\psi)\right), \tag{31}$$

$$\omega_2(\xi, \psi) = \xi^4\frac{\Lambda(\psi)}{2} \quad \left(\frac{1}{L} \sim \delta^4\Lambda(\psi)\omega^5\right). \tag{32}$$

The functions $\Phi(\psi)$ and $\Lambda(\psi)$ for ZnO are shown in Figs. 3a and 3b, respectively. We can see from Fig. 3a that the dispersion of SH-polarized waves is largest at an angle of incidence of 45°. As follows from Fig. 3b, the wave damps much more weakly at large angles of incidence than at normal incidence onto grating grooves.

6. CONCLUSIONS

Thus, using perturbation theory, we have derived analytical expressions for dispersion of the phase velocity and the inverse damping depth of SH-polarized SAWs propagating in a random direction along a 2D or 1D statistically rough free surface of a hexagonal crystal (*Z* cut).

The expressions for the 2D rough surface were derived using a modified mean-field method [17], and the expressions for the 1D rough surface were obtained by considering it as a special case of the 2D rough surface. In the case of an isotropic medium, dispersion relation (13) reduces to formula (5.20) from [17]. The

conditions for the existence of SH-polarized waves were determined for both types of surface roughness of the *Z*-cut hexagonal crystal. It was shown that the SH-polarized SAW cannot propagate along a flat surface of the hexagonal crystal (*Z* cut). In this case, as for an isotropic medium, this wave degenerates into a bulk transverse wave sliding along the surface.

The phase velocity dispersion and damping depth of SH-polarized waves were calculated numerically for most of the known hexagonal crystals for an arbitrary angle of incidence in the entire frequency range accessible to perturbation theory. The corresponding curves are qualitatively similar to each other and to the curve for an isotropic medium, differing only quantitatively. The qualitative similarity to the case of isotropic media is due to the isotropy of the *Z*-cut hexagonal crystal.

Expressions for the dispersion and attenuation of SH-polarized SAWs have been derived in the long-wavelength limit, where the wavelength is much longer than the roughness correlation radius. It was shown that the inverse damping depth is proportional to the sixth and the fifth power of the frequency for 2D and 1D rough surfaces, respectively. The relative change in the phase velocity is proportional to the square of the frequency for both types of surface roughness.

Finally, we note that the modified mean-field method allowed determination of the dispersion and attenuation of the Rayleigh SAW [18] and SH polarization on both 2D and 1D rough surfaces of the *Z*-cut hexagonal crystal. This method also makes it possible to derive the dispersion relation for SAWs of both polarizations for other cuts of various crystals. The necessary condition for such calculations is knowledge of the Green's function on a flat (not rough) surface of the cut at hand, the determination of which is an independent and rather complex problem.

APPENDIX 1

$$\alpha_t(k_\parallel, \omega) = \begin{cases} \sqrt{hk_\parallel^2 - \frac{\rho\omega^2}{c_{44}}}, & hk_\parallel^2 - \frac{\rho\omega^2}{c_{44}} > 0 \\ -i\sqrt{\frac{\rho\omega^2}{c_{44}} - hk_\parallel^2}, & hk_\parallel^2 - \frac{\rho\omega^2}{c_{44}} > 0, \end{cases} \quad \text{(A1.1)}$$

$$A(\xi) = \int_0^\infty dt \exp\left(-\frac{\xi^2 t}{4}\right) \frac{\Phi_2\left(t, \frac{\xi^2\sqrt{t}}{2}\right)}{\tilde{\alpha}_{tt}(t)}, \quad \text{(A1.2)}$$

$$B(\xi) = -hP\int_0^\infty dx \exp\left(-\frac{\xi^2 hx}{4}\right) \times \frac{\tilde{\alpha}_p(x)\sqrt{x-1}}{\sqrt{x-1}(1-a_1x) + \tilde{\alpha}_m(x)} \Phi_1\left(hx, \frac{\xi^2\sqrt{hx}}{2}\right), \quad \text{(A1.3)}$$

$$E(\xi) = i\pi\exp\left(-\frac{\xi^2 h}{4\varepsilon}\right) \times \frac{\tilde{\alpha}_p\left(\frac{1}{\varepsilon}\right)\Phi_1\left(\frac{h}{\varepsilon}, \frac{\xi^2}{2}\sqrt{\frac{h}{\varepsilon}}\right)\varepsilon(1-\varepsilon)\left(\frac{c_{11}}{c_{44}} - \varepsilon\right)}{\left(2a_1 - \frac{c_{11}}{c_{44}} + 1\right)\varepsilon^2 - \varepsilon a_1\left(\frac{c_{11}}{c_{44}} + 3\right) + 2a_1\frac{c_{11}}{c_{44}}}, \quad \text{(A1.4)}$$

$$\Phi_1(t, z) = (1+t)I_0(z) - 2\sqrt{t}I_1(z) - I_2(z) + 2\sqrt{t}I_3(z) - tI_4(z), \quad \text{(A1.5)}$$

$$\Phi_2(t, z) = (1+t)I_0(z) - 2\sqrt{t}I_1(z) + I_2(z) - 2\sqrt{t}I_3(z) + tI_4(z), \quad \text{(A1.6)}$$

where I_n is the modified Bessel function of order n.

In Eqs. (A1.2)–(A1.4), the following notation is used:

$$\tilde{\alpha}_p(x) = \tilde{\alpha}_{t1} + \tilde{\alpha}_{t2}, \quad \tilde{\alpha}_m(x) = \frac{\tilde{\alpha}_{t1}\tilde{\alpha}_{t2}}{\sqrt{x-1}},$$

$$\tilde{\alpha}_{t1}^2 = \frac{1}{2}(z + \sqrt{z^2 - 4y_2}), \quad \tilde{\alpha}_{t2}^2 = \frac{1}{2}(z - \sqrt{z^2 - 4y_2}),$$

$$\mathrm{Re}\,\tilde{\alpha}_{t1,t2} > 0, \quad \mathrm{Im}\,\tilde{\alpha}_{t1,t2} < 0,$$

$$y_2 = \frac{c_{11}}{c_{33}}(x-1)\left(x - \frac{c_{44}}{c_{11}}\right),$$

$$z = \left(a_1 - 2\frac{c_{13}}{c_{33}}\right)x - \left(1 + \frac{c_{44}}{c_{33}}\right),$$

$$\tilde{\alpha}_{tt}(x) = \begin{cases} \sqrt{x-1}, & x-1 \geq 0 \\ -i\sqrt{1-x}, & x-1 < 0, \end{cases}$$

$$a_1 = \frac{c_{11}c_{33} - c_{13}^2}{c_{33}c_{44}}, \quad h = \frac{c_{11} - c_{12}}{2c_{44}},$$

$$\begin{cases} \left(1 - \frac{c_{44}}{c_{33}}\right)\varepsilon^3 + \left(\frac{c_{11}}{c_{33}} - 1 - 2a_1\right)\varepsilon^2 \\ + a_1(2 + a_1)\varepsilon - a_1^2 = 0, \\ 0 < \varepsilon < \min(1, a_1). \end{cases}$$

In expression (A1.3), the symbol P means the Cauchy principal value of the integral and the pole is at the point $x_0 = 1/\varepsilon$.

APPENDIX 2

$$A(\xi, \psi) = \int_0^\infty d\eta \frac{\Phi_1(\eta, \psi) + \Phi_1(-\eta, \psi)}{\tilde{\alpha}_{tt}(\eta^2 + \sin^2\psi)}, \quad \text{(A2.1)}$$

$$B(\xi, \psi) = -P\int_0^\infty d\eta \left(\frac{\tilde{\alpha}_p(x)\sqrt{x-1}}{\sqrt{x-1}(1-a_1 x) + \tilde{\alpha}_m(x)} \right)_{x = \frac{\eta^2 + \sin^2\psi}{h}} \times (\Phi_2(\eta, \psi) + \Phi_2(-\eta, \psi)), \quad \text{(A2.2)}$$

$$E(\xi, \psi) = i\pi \frac{h}{2\sqrt{\frac{h}{\varepsilon} - \sin^2\psi}\, a_1 + \frac{c_{44}}{c_{33}} \frac{\varepsilon^3 (c_{11}/c_{44} - 1)}{2(1-\varepsilon)^2 (a_1 - \varepsilon)}} \times \left(\Phi_2\left(\sqrt{\frac{h}{\varepsilon} - \sin^2\psi}, \psi \right) + \Phi_2\left(-\sqrt{\frac{h}{\varepsilon} - \sin^2\psi}, \psi \right) \right), \quad \text{(A2.3)}$$

$$\Phi_1(\eta, \psi) = \exp\left(-\frac{\xi^2}{4}(\eta - \cos\psi)^2 \right) \times (\cos\theta(\eta, \psi) - \sqrt{\eta^2 + \sin^2\psi}\cos 2\theta(\eta, \psi))^2, \quad \text{(A2.4)}$$

$$\Phi_2(\eta, \psi) = \exp\left(-\frac{\xi^2}{4}(\eta - \cos\psi)^2 \right) \times (\sin\theta(\eta, \psi) - \sqrt{\eta^2 + \sin^2\psi}\sin 2\theta(\eta, \psi))^2, \quad \text{(A2.5)}$$

$$\cos\theta(\eta, \psi) = \frac{\eta\cos\psi + \sin^2\psi}{\sqrt{\eta^2 + \sin^2\psi}}, \quad \sin\theta(\eta, \psi) = \frac{\sin\psi\cos\psi - \eta\sin\psi}{\sqrt{\eta^2 + \sin^2\psi}}. \quad \text{(A2.6)}$$

The quantities $\tilde{\alpha}_{t1}(x)$ $\tilde{\alpha}_{t2}(x)$, $\tilde{\alpha}_p(x)$, $\tilde{\alpha}_m(x)$, $\tilde{\alpha}_{tt}(x)$, h, ε, and a_1 are defined in Appendix 1.

In Eq. (A2.2), the symbol P means the Cauchy principal value of the integral and the pole is at the point $\eta_0 = \sqrt{\frac{h}{\varepsilon} - \sin^2\psi}$.

REFERENCES

1. A. A. Maradudin, in *Nonequilibrium Phonon Dynamics*, Ed. by W. E. Bronn (Plenum, New York, 1985), p. 406.
2. A. E. H. Love, *Some Problems of Geodynamics* (Cambridge Univ. Press, London, 1911).
3. I. A. Viktorov, in *Proceedings of X All-Union Conference on Quantum Electronics* (Fan, Tashkent, 1978), p. 101.
4. J. L. Bleustein, Appl. Phys. Lett. **13**, 412 (1968).
5. Yu. V. Gulyaev, Pis'ma Zh. Éksp. Teor. Fiz. **9**, 37 (1969) [JETP Lett. **9**, 21 (1969)].
6. R. E. Camley and R. Q. Scott, Phys. Rev. B **17**, 4327 (1978).
7. M. Matthews and H. van de Vaart, Appl. Phys. Lett. **15**, 373 (1969).
8. J. P. Parekh, Electron. Lett. **5**, 323 (1969).
9. V. G. Mozhaev, Phys. Lett. A **139**, 333 (1989).
10. O. H. Duparc and A. A. Maradudin, J. Electron Spectrosc. Relat. Phenom. **30**, 145 (1983).
11. A. A. Bulgakov and S. I. Khankina, Solid State Commun. **44** (1), 55 (1982).
12. X. Huang and A. A. Maradudin, Phys. Rev. B **36** (15), 7827 (1987).
13. S. Z. Dunin and G. A. Maksimov, Preprint No. 032-88, MIFI (Moscow Inst. of Engineering Physics, Moscow, 1988).
14. A. A. Maradudin, X. Huang, and A. P. Mayer, J. Appl. Phys. **70** (1), 53 (1991).
15. A. P. Mayer, W. Zierau, and A. A. Maradudin, J. Appl. Phys. **69** (4), 1942 (1991).
16. B. Djafari-Rouhani and A. A. Maradudin, J. Appl. Phys. **65** (11), 4245 (1989).
17. V. V. Kosachev and A. V. Shchegrov, Ann. Phys. (N.Y.) **240** (2), 225 (1995).
18. V. V. Kosachev and Yu. N. Gandurin, Fiz. Tverd. Tela (St. Petersburg) **45** (2), 369 (2003) [Phys. Solid State **45**, 391 (2003)].
19. L. Dobrzynski and A. A. Maradudin, Phys. Rev. B **14** (6), 2200 (1976); **15** (4), 2432(E) (1977).
20. V. V. Kosachev and Yu. N. Gandurin, Fiz. Tverd. Tela (St. Petersburg) **45** (9), 1722 (2003) [Phys. Solid State **45**, 1808 (2003)].
21. O. L. Anderson, in *Physical Acoustics: Principles and Methods*, Ed. by W. P. Mason (Academic, New York, 1965; Mir, Moscow, 1968), Vol. 3, Part B, p. 80.

Translated by A. Kazantsev

Physics of the Solid State, Vol. 46, No. 10, 2004, pp. 1961–1968. Translated from Fizika Tverdogo Tela, Vol. 46, No. 10, 2004, pp. 1893–1900.

FULLERENES AND ATOMIC CLUSTERS

Thermal Conductivity of NaCl Loaded in Regular Arrays of Nanovoids in a Synthetic Opal Single Crystal

V. N. Bogomolov*, N. F. Kartenko*, D. A. Kurdyukov*, L. S. Parfen'eva*, I. A. Smirnov*, N. V. Sharenkova*, H. Misiorek, J. Mucha**, and A. Jezowski****

**Ioffe Physicotechnical Institute, Russian Academy of Sciences, Politekhnicheskaya ul. 26, St. Petersburg, 194021 Russia*
e-mail: igor.smirnov@pop.ioffe.rssi.ru

***Institute of Low-Temperature and Structural Research, Polish Academy of Sciences, Wroclaw, 50-950 Poland*

Received February 4, 2004

Abstract—Samples of opal + NaCl nanocomposites with 100 and 80% filling of first-order opal voids by sodium chloride have been prepared. Their effective thermal conductivities, κ_{eff}, were measured in the temperature interval 5–300 K. The lattice thermal conductivity of NaCl loaded in the opal voids, κ_{ph}^{op}, was calculated from the measured $\kappa_{eff}(T)$. The value of κ_{ph}^{op} was found to be considerably smaller than the lattice thermal conductivity of bulk NaCl throughout the temperature interval studied. For $T > 20$ K, this behavior of $\kappa_{ph}^{op}(T)$ is accounted for by the presence of specific defects that form in NaCl loaded in opal voids. For $T < 20$ K, $\kappa_{ph}^{op}(T)$ is governed by boundary phonon scattering from bottlenecks in horn-shaped channels interconnecting the octahedral and tetrahedral first-order opal voids filled by sodium chloride. It was found that the value of $\kappa_{ph}^{op}(T)$ in this temperature region depends substantially on the dimensions of the bottlenecks, whose thicknesses are related to the amount of the cristobalite forming in a near-surface layer of the amorphous SiO_2 opal spheres in the course of preparation of the opal + NaCl nanocomposite. © *2004 MAIK "Nauka/Interperiodica".*

1. FORMULATION OF THE PROBLEM

This publication reports on the continuation of an investigation we began in 1995 into the thermal conductivity κ of single crystals of synthetic opals and related nanocomposites (opal + PbSe, opal + HgSe, opal + epoxy resin) carried out in the temperature range 5–300 K.[1]

New papers have recently appeared in the literature, among them an experimental study on the thermal conductivity of opals and of opal + $LiIO_3$ nanocomposites in the temperature interval from 290 to 410 K [2] and several theoretical publications on the thermal conductivity of opals [3, 4].

Opals are unique objects for physical studies. Their crystal structure is fairly unusual [1, 5, 6]; indeed, opals are made up of closely packed spheres of amorphous SiO_2 of various diameters. The opals used in our experiments consist of spheres 2000–2500 Å in diameter (first-order spheres). These spheres contain an array of close-packed spheres of a smaller size, ~300–400 Å (second-order spheres), which are formed, in turn, of close-packed spherical particles ~100 Å in size (third-order spheres).

The close-packed sphere array has octahedral and tetrahedral voids interconnected by horn-shaped channels. These voids are also classed as voids of the first, second, and third order, according to the actual order of the amorphous SiO_2 spheres they separate.

To make the picture more revealing, the octahedral and tetrahedral voids are usually approximated by spheres interconnected by cylindrical channels [2]. The diameters of the octahedral and tetrahedral voids and the average diameters of the cylindrical channels[2] for first-order voids in the opal under study were 800, 400, and 300 Å, respectively [6].

The total theoretical opal porosity, which includes voids of the first, second, and third order, is 59%. The first-order voids, which are studied here, make up 26%. Note that the real total porosity of the synthetic opal single crystals grown by us constituted (because of partial sintering of the second- and third-order amorphous SiO_2 spheres) ~46–50% rather than 59% [8], but the volume of the first-order voids always remained ~26%.

The amorphous SiO_2 spheres and first-order voids in opals make up close-packed face-centered cubic lattices. The parameters of these lattices (a) for the opals under study here were ~3000–4000 Å.

[1] References to these studies can be found in [1].

[2] We may recall that the voids in opals are in actual fact interconnected by horn-shaped rather than cylindrical channels (with the smallest cross sections (bottlenecks) being ~100 Å) [7], which, as we shall show later, is of crucial importance for interpreting the experimental data on the thermal conductivity of opal + NaCl nanocomposites reported here.

First-order opal voids can be loaded by metals, semiconductors, and insulators using a variety of techniques (chemical, pressure injection of the melt, or impregnation of the sample by the filler material). In this way (under 100% filling of these voids), regular three-dimensional composites can be produced with a cubic filler lattice with $a \sim 3000$–4000 Å.

Thus, an opal-based nanocomposite with 100% filling of first-order voids with a filler can be considered a system made up of nested unique regular lattices (an opal and a filler lattice) with giant parameters and giant "atomic" masses. The individual properties of these unusual lattices may be manifested in the behavior of the lattice thermal conductivity κ_{ph} only at ultralow temperatures (several millikelvins).

Within the temperature interval 5–300 K, the thermal conductivity of synthetic opal single crystals is determined primarily by the quality of contacts between the amorphous SiO_2 spheres (i.e., it is governed by the contact thermal resistances among these spheres). The more perfect the opal crystal structure (when the contacts between all spheres are strictly the same and approach point type), the lower the opal thermal conductivity [9].

When measuring the thermal conductivity of a nanocomposite with 100% filling (or close to it) of the first-order opal voids by a filler, the heat flux in the nanocomposite will pass through two parallel channels, namely, over the spheres of amorphous SiO_2 making up the opal and over the specific chains of the filler material, e.g., successively through a tetrahedral (octahedral) filled void, filled horn-shaped channel, tetrahedral (octahedral) filled void, filled horn-shaped channel, and so on [6, 7] (see the schematic of the opal crystal lattice given in [6]).

One may conceive of several versions of the behavior of the nanocomposite thermal conductivity.

(a) $\kappa_1 \gg \kappa_2$ (κ_1 is the thermal conductivity of the filler, and κ_2 is that of the matrix (opal)). In these conditions, in nanocomposite thermal conductivity measurements, the heat flux will propagate primarily over the filler material chains. As shown by us for an opal + 100% HgSe nanocomposite, which satisfies the above condition, the thermal conductivity of HgSe loaded in opal voids is determined at low temperatures (5–10 K) by boundary scattering of phonons from the bottlenecks of the horn-shaped channels connecting filled octahedral (tetrahedral) opal voids [7]. Throughout the temperature interval studied in [7] (5–300 K), the filler material can be considered to consist of nanoparticles of material arranged regularly (an essential point) in the regular voids of the matrix.

(b) $\kappa_1 \ll \kappa_2$. In this case, in measuring the nanocomposite thermal conductivity, the heat flux will propagate primarily over the matrix spheres (amorphous SiO_2); the thermal conductivity of the nanocomposite will be close to that of the opal and depend on the quality of the contact between the amorphous SiO_2 spheres. We observed this pattern when measuring the thermal conductivity of an opal + 100% epoxy resin nanocomposite for $T > 100$ K [1].

(c) $\kappa_1 \approx \kappa_2$. In this case, the nanocomposite can be treated at high temperatures as a material characterized by a single thermal conductivity,[3] while at low temperatures Kapitsa's heat resistance may appear [10] at the interfaces between the filler and amorphous SiO_2 spheres.

The present communication reports on a study (in the temperature interval 5–300 K) of the thermal conductivity of opal + x% NaCl nanocomposites (for x = 100% and similar compositions) for which the first of the above conditions is satisfied: $\kappa_1 \gg \kappa_2$.

Our goals were (i) to confirm (or refute) the conclusions drawn in [7] concerning the low-temperature behavior of thermal conductivity of opal-based nanocomposites and (ii) to make a critical analysis of our earlier results [11] on the thermal conductivity of an opal + 100% NaCl nanocomposite.

The interpretation of the results obtained in the study of the thermal conductivity of the opal + 100% NaCl nanocomposite [11] was complicated by the fact that the technique chosen to fill the first-order opal voids by sodium chloride brought about the formation of a thin film of cristobalite in thenear-surface layers of amorphous SiO_2 spheres. In this study, we somewhat modified the technique of loading the opal with NaCl (for more details, see Section 2), in which the percentage of the cristobalite film formed in the course of loading was reduced to a minimum. We prepared opal + 100% NaCl (sample 2) and opal + 80% NaCl (sample 3) nanocomposites. Thermal conductivity measurements of these samples and of the opal + 100% NaCl nanocomposite from [11] (sample 1) were performed on an experimental setup similar to the one employed in [12]. Opal + NaCl nanocomposites are insulators; therefore, their effective thermal conductivity κ_{eff} measured experimentally is actually the lattice thermal conductivity κ_{eff}^{ph}.

Figure 1 displays the results obtained in the study of $\kappa_{eff}^{ph}(T)$ of opal + 100% NaCl nanocomposites (sample 1 from [11] and sample 2 prepared in the present investigation). We can see that the values of $\kappa_{eff}^{ph}(T)$ for these samples differ substantially (particularly in the low-temperature region, $T < 60$ K).

Figure 2 presents data for $\kappa_{eff}^{ph}(T)$ for samples 1 [11], 2, and 3.

[3] In such a nanocomposite, however, defects may form at the matrix–filler interface, which can affect high-temperature thermal conductivity measurements.

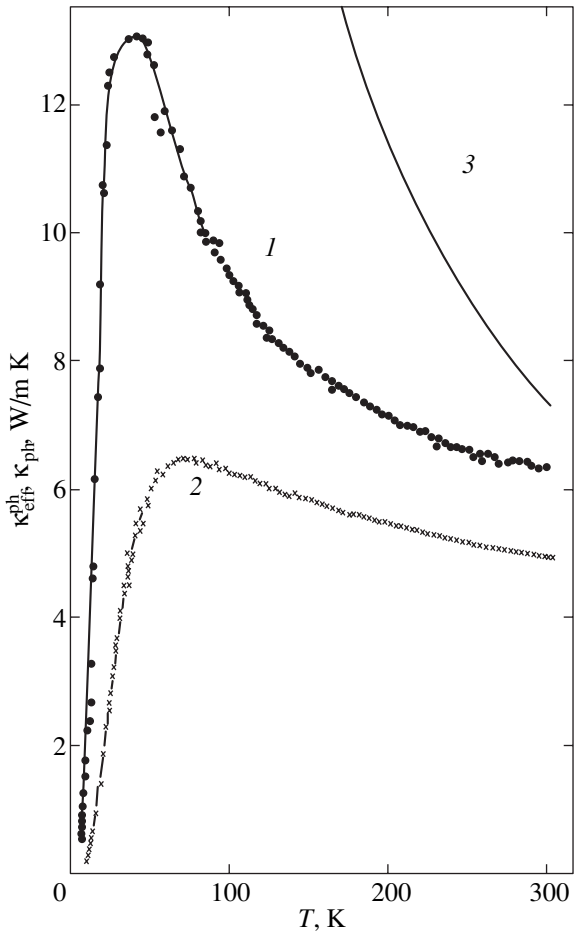

Fig. 1. Temperature dependences (*1*, *2*) of the experimental effective thermal conductivity $\kappa_{eff}^{ph}(T)$ for (*1*) sample 1 [11] and (*2*) sample 2 of opal + 100% NaCl nanocomposites (100% filling of first-order opal voids by NaCl) and (*3*) of the lattice thermal conductivity κ_{ph} of a NaCl single crystal [13].

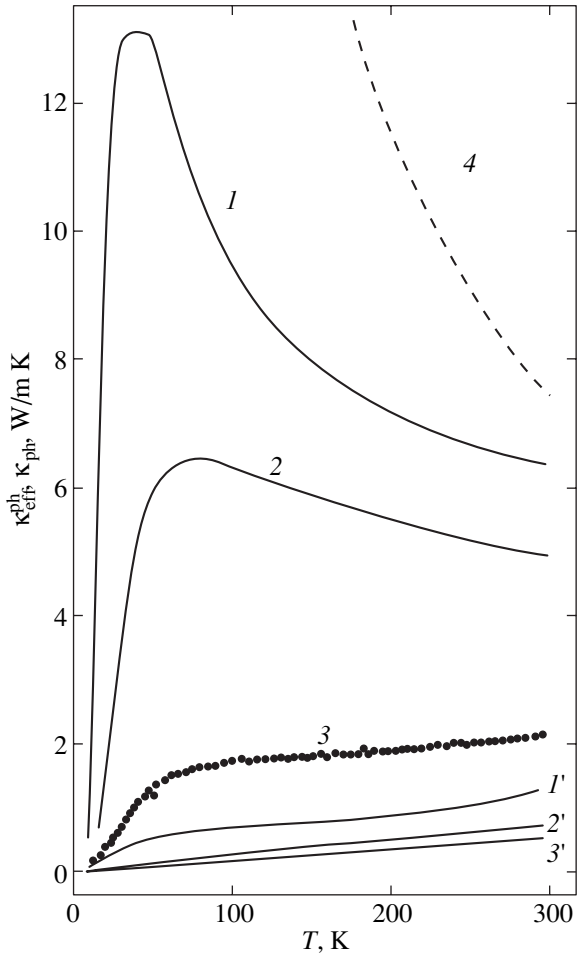

Fig. 2. Temperature dependences (*1–3*) of the thermal conductivity κ_{eff}^{ph} of opal + *x*NaCl nanocomposites (*x* is the percentage of opal first-order void filling) for (*1, 2*) *x* = 100% in (*1*) sample 1 [11] and (*2*) sample 2 and (*3*) *x* = 80% in sample 3; (*1*'–*3*') of the thermal conductivity of opal matrices obtained from the nanocomposites of samples 1 [11], *2*, and *3*, respectively, after washing out of NaCl; and (*4*) of the thermal conductivity κ_{ph} of single-crystal NaCl [13] (for comparison).

It was found that $\kappa_{eff}^{ph}(T)$ for sample 3 is still smaller than that for sample 2.

What could be the explanation for such a strange behavior of the thermal conductivity of these samples? A question may arise as to whether this behavior is associated with the specifics of sample preparation.

2. PREPARATION OF SAMPLES AND THEIR CHARACTERIZATION

Opal + NaCl nanocomposites (samples 1–3) were fabricated by the technique employed in [11], which consisted in saturating single-crystal opal samples with sodium chloride by placing them in a NaCl melt (at $T \sim$ 900°C). The only difference in the sample preparation technique consisted in the length of time that a sample of the original opal was kept (saturated) in the NaCl melt. The saturation time decreased from sample 1 to sample 3. The percentage of filling of opal first-order voids by NaCl was determined by measuring the density of the samples thus obtained.

Figures 3 and 4 show x-ray diffraction intensities for the nanocomposite samples studied. The measurements were conducted on a DRON-2 setup (CuK_α radiation). The data presented in Fig. 3 suggest that (i) the sodium chloride loaded in the voids of all three opal + NaCl nanocomposite samples has a regular (110)-patterned lattice with a = 5.640–5.643 Å (for bulk NaCl crystals, a = 5.640 Å) and (ii) in samples 1 [11] and 2 contact between the opal and the NaCl melt gives rise to partial crystallization of amorphous SiO_2 opal spheres with the formation of a thin cristobalite film on their near-sur-

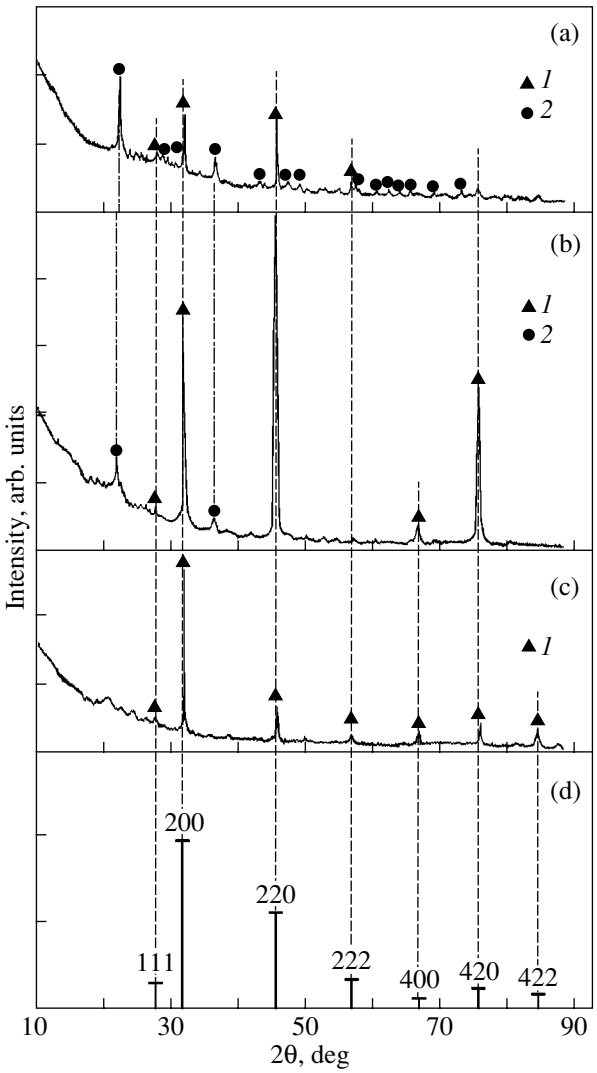

Fig. 3. X-ray diffraction intensities for opal + *x*NaCl nanocomposites with (a, b) $x = 100\%$ for (a) sample 1 [11] and (b) sample 2 and (c) $x = 80\%$ for sample 3 and (d) for bulk NaCl crystal. (*1*) Reflections characteristic of NaCl, and (*2*) reflections typical of cristobalite. For sample 1, the reflections with interplanar distances 4.04 and 2.48 Å correspond to the (101) and (200) reflections of α cristobalite (tetragonal symmetry, $a = 4.9732(4)$ Å, $c = 6.9236(8)$ Å).

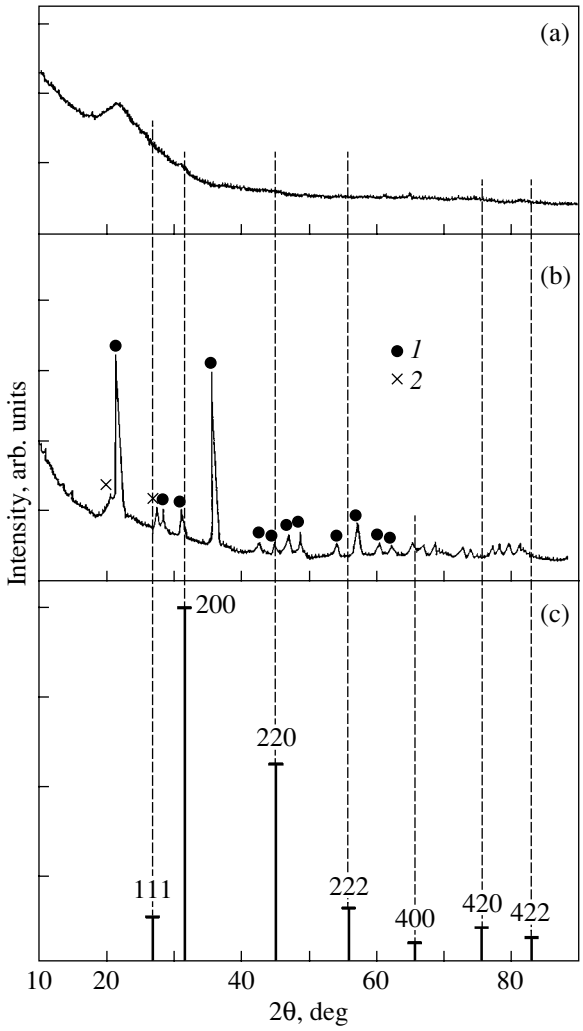

Fig. 4. X-ray diffraction intensities for samples (a) 3' and (b) 1' obtained after NaCl was washed out of nanocomposite samples 3 and 1 and (c) for a bulk NaCl crystal. (*1, 2*) Reflections characteristic of cristobalite and tridymite, respectively.

face layer.[4] Note that, in this particular case, the film forms in the bulk of the SiO_2 spheres themselves rather than on their surface, as was the case, for instance, in opal under molecular layer-by-layer deposition of TiO_2 [14] and the formation of the opal–erbium composite [15].

After the thermal conductivity measurements were taken for samples 1–3 of opal + NaCl nanocomposites (Fig. 2), NaCl was washed out of them, the thermal conductivity was measured again (curves *1'–3'* in Fig. 2), and x-ray diffraction studies were performed (Fig. 4). We now denote samples 1–3 with NaCl removed from them as 1'–3', respectively.

For illustration, Fig. 4 shows the x-ray diffraction intensities obtained for two extreme cases, namely, for opal samples 1' and 3'. An analysis of these data yields interesting information on the "washed" nanocomposite samples.

(1) After the removal of NaCl from sample 1, the x-ray diffraction pattern for sample 1' fully corresponds to α cristobalite with an enhanced (200) reflection, which may be assigned to a weak texture. A small impurity of α tridymite is seen in this diffractogram.

Comparison of the reflection intensities of α cristobalite in sample 1' and of an artificial mixture of amorphous opal with α cristobalite allowed us to obtain an estimate of the content of the cristobalite in sample 1'. It was found to be ~5%.

[4] The NaCl melt initiates cristobalite formation at points where it contacts with the amorphous SiO_2. In pure opal, cristobalite generally does not form at these temperatures.

(2) No sign of cristobalite was detected in the opal sample 3'. The x-ray diffractogram of sample 3' coincided with that of pure opal [16, 17].

(3) Samples 1' and 3' did not contain NaCl traces either. This indicates that, in nanocomposite samples 1 and 3, NaCl-filled voids are interconnected with open (but also filled by NaCl) channels and that there are no closed voids filled by NaCl, which could have formed in the nanocomposites during high-temperature synthesis.

Thus, the above x-ray diffraction data on samples 1–3 of opal + NaCl nanocomposites allow us to conclude that the difference in thermal conductivity observed by us between these samples (which is particularly large at low temperatures) correlates with the presence of a cristobalite film in them in a near-surface layer of the opal amorphous SiO_2 spheres. The larger the content of the cristobalite phase in the samples, the higher their thermal conductivity.

It still remains unclear, however, what physical processes associated with the presence of a cristobalite film in the nanocomposites are responsible for the detected effect.

We will try to find an answer to this question in the next section after analyzing the experimental data obtained.

3. DISCUSSION OF THE EXPERIMENTAL RESULTS

Figures 1 and 2 present the experimental data on the effective thermal conductivity κ_{eff}^{ph} of the opal + NaCl nanocomposites (samples 1–3) and on the thermal conductivity of the corresponding opal matrices κ_{ph} (samples 1'–3'). The thermal conductivities of samples 1' and 2' are larger than that of pure opal [16, 17], because the former contain cristobalite (~5% in sample 1' and a smaller amount in sample 2'). The thermal conductivity of sample 3' with no cristobalite impurity is close to that obtained for pure opal.

As already mentioned, the thermal conductivity of opal is determined primarily by the quality of thermal contacts between the spheres of amorphous SiO_2 [9]. In pure opal, the contacts approach point type, which has a low thermal conductivity (just as in the case of sample 3'). The formation of a cristobalite film in samples 1' and 2' increases the contact area, and the thermal conductivity of these samples may increase, which is exactly what is observed experimentally (Fig. 2).

It should be pointed out, however, that the enhanced thermal conductivity of the opals (samples 1' and 2') does not invalidate condition (a) from the preceding section for the nanocomposites (samples 1 and 2), because the thermal conductivity of the filler is considerably higher than that for the matrix (opal).

To analyze the behavior of the thermal conductivity of NaCl loaded in the regularly arranged voids of an opal single crystal, κ_{ph}^{op}, one has to isolate κ_{ph}^{op} from the measured thermal conductivity $\kappa_{eff}^{ph}(T)$ of the nanocomposite. To do this, one has to choose an appropriate theoretical relation describing the behavior of the thermal conductivity of the composites. There are numerous such relations in the literature [4, 18–22]. While they provide mostly a good qualitative approximation to the $\kappa_{eff}(T)$ behavior, quantitative calculations made with them are not always in agreement.

In view of the need to compare the behavior of the thermal conductivities of various fillers in opal-based nanocomposites, we chose the relation of Litovskiĭ [22], which gives sufficiently accurate results for a large number of standard composites. We used this relation earlier in treating the data on the thermal conductivity of pure opal [16] (to take its porosity into account) and of opal + PbSe [17] and opal + HgSe [7] nanocomposites.

According to [22], we have

$$\kappa_{eff}/\kappa_{mat} = (1-P)(1-P)^{1/2} + P^{1/4}\nu, \qquad (1)$$

where κ_{eff} and κ_{mat} are the thermal conductivities of the composite and the matrix, respectively; P is the porosity of the material; and

$$\nu = \kappa_{por}/\kappa_{mat}. \qquad (2)$$

In our case, κ_{por} and P denote the thermal conductivity of NaCl loaded in first-order opal matrix voids and the amount of NaCl in the matrix, respectively; $P = 0.26$ for samples 1 and 2 and 0.208 for sample 3. The matrices in our opal + x% NaCl nanocomposites are the amorphous spheres with a cristobalite film (samples 1', 2'; Fig. 2) and those without it (sample 3; Fig. 2), with due account of the fact that first-order voids of the opal samples are filled completely (in samples 1, 2) or partially (in sample 3) by sodium chloride [22].

Figure 5 plots the data on $\kappa_{por} = \kappa_{ph}^{op}$ for NaCl filling of the opal voids, which were derived using Eqs. (1) and (2). A cursory examination of this figure shows that the values of $\kappa_{ph}^{op}(T)$ for samples 1–3 differ strongly, as before (as was observed for $\kappa_{eff}^{ph}(T)$ for the same samples).

We may thus conclude that the presence of cristobalite in the matrices does not have a significant effect on the magnitude and temperature behavior of $\kappa_{ph}^{op}(T)$ calculated from Eqs. (1) and (2) (compare $\kappa_{eff}^{ph}(T)$ in Fig. 2 with $\kappa_{ph}^{op}(T)$ in Fig. 5 for samples 1–3). This should possibly be ascribed to the fact that heat flux in the nanocomposites under study propagates primarily over the filler material (NaCl), while the contribution from the matrix thermal conductivity to $\kappa_{eff}(T)$ is small.

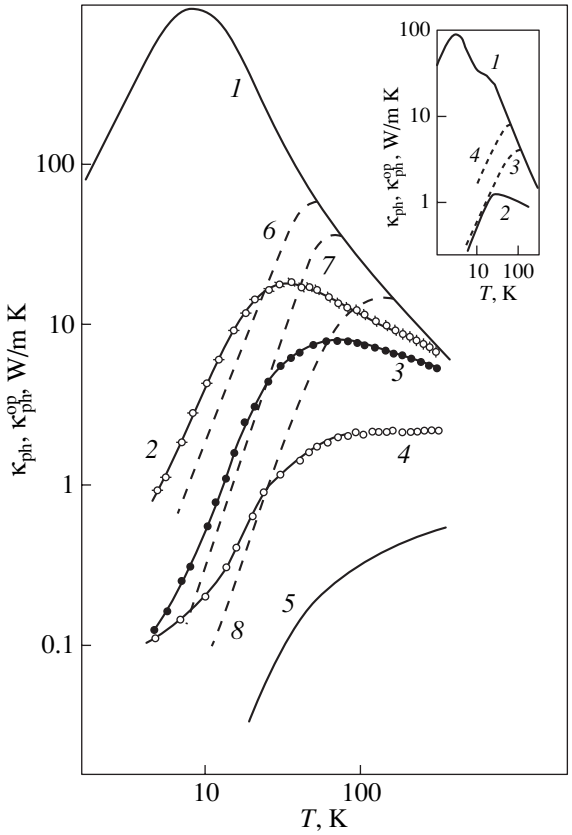

Fig. 5. Temperature dependences of thermal conductivity. (*1*) κ_{ph} of single-crystal NaCl [13]; (*2–4*) κ_{ph}^{op} of samples *1–3*, respectively; (*5*) the minimum thermal conductivity for bulk NaCl crystals [23]; and (*6–8*) thermal conductivities of bulk NaCl calculated for average sound velocity $\bar{v} \sim$ const and phonon mean free path l equal to 800, 400, and 100 Å, respectively (see text for calculation of curves *6–8*). Inset shows the data for the opal + HgSe nanocomposite from [7]: (*1*) temperature dependence of the thermal conductivity of a bulk HgSe sample and (*2*) $\kappa_{ph}^{op}(T)$ of HgSe loaded in an opal first-order void array; dashed curves represent the thermal conductivity of bulk HgSe calculated for $\bar{v} \sim$ const and l equal to (*3*) 100 and (*4*) 300 Å.

If we continue to assume, however, that the difference in the values of $\kappa_{ph}^{op}(T)$ (and $\kappa_{eff}^{ph}(T)$ as well) between samples 1–3 originates from the presence of a cristobalite film in near-surface layers of amorphous SiO_2 spheres of the opal matrix, then some other physical mechanism has to be put forward that is capable of accounting for the experimental data obtained.

Let us consider the behavior of $\kappa_{ph}^{op}(T)$ for the samples under study (Fig. 5) in more detail.

In the $\kappa_{ph}^{op}(T)$ curves for samples 1–3 presented in Fig. 5, we can distinguish three temperature regions: low temperatures (5–20 K), high temperatures (~50–300 K), and an intermediate region (~20–50 K).

We are going to analyze the $\kappa(T)$ dependences in the first two regions. We start with the low-temperature range (5–20 K).

As already mentioned, in an opal + HgSe nanocomposite [7] with 100% filling of first-order voids by the mercury selenide, the low-temperature ($T < 20$ K) thermal conductivity of HgSe in opal, $\kappa_{ph}^{op}(T)$, was dominated by boundary scattering of phonons from bottlenecks (~100 Å in diameter) of horn-shaped channels interconnecting HgSe-filled octahedral and tetrahedral opal voids (curve *2* in the inset to Fig. 5). The phonon mean free path l for $T < 20$ K was larger than the diameter of the horn-shaped channel bottleneck.

By analogy with the opal + HgSe nanocomposite, one can apparently expect the opal + NaCl nanocomposite to exhibit the same behavior of $\kappa_{ph}^{op}(T)$ at low temperatures.

Therefore, one could try to relate the difference in $\kappa_{ph}^{op}(T)$ between samples 1–3 for the opal + NaCl nanocomposite for $T < 20$ K to the presence of channels (and bottlenecks) of different diameters in them, which can form because of the appearance of cristobalite films that differ in thickness (d_1) in the near-surface layers of amorphous opal SiO_2 spheres. The diameter of the new bottlenecks d in samples 1–3 would depend on the concentration of the cristobalite in them, $d = d_1 + d_2$, where d_2 is the diameter of the bottleneck in a NaCl-filled opal channel. We assume, by analogy with [7], that $d_2 \approx$ 100 Å and is the same in samples 1–3. The value of d_1 should be larger for sample 1 than for sample 2 and should be zero for sample 3 (Fig. 3).

The possibility that new "enlarged" channels will form in samples 1 and 2 for the opal + NaCl nanocomposite is borne out by the samples of bulk NaCl, cristobalite, and crystalline quartz having similar thermal conductivities[5] (Fig. 6).

The total thermal conductivity of the new channel (NaCl + cristobalite) in samples 1 and 2 and the thermal conductivity of NaCl in the channel of sample 3 are larger than that of the matrices (curves *1*'–*3*' in Fig. 2); thus, the heat flux in samples 1–3 should propagate primarily over these channels rather than over the matrix material.

Let us make at least a rough guess at the diameter of the bottlenecks in samples 1–3. For this purpose, we invoke the standard relation for the thermal conductivity of solids:

$$l = 3\kappa/C_V\bar{v}, \qquad (3)$$

[5] Unfortunately, we were unable to find any literature data on the thermal conductivity of cristobalite over a broad temperature range. Its thermal conductivity at room temperature [24] does not differ much from that of crystalline quartz (Fig. 6). There are therefore grounds to hope that the thermal conductivities of crystalline quartz and cristobalite do not differ greatly over a broad temperature region as well.

where C_V is the specific heat at constant volume; $\bar{v} = (2v_\perp + v_\parallel)/3$ is the average sound velocity; $v_\perp$ and $v_\parallel$ are the transverse and longitudinal sound velocities, respectively; and κ is the thermal conductivity.

For the calculation, we used the data on $l(T)$ reported in [11] for NaCl (see [11, Fig. 5]).

At certain temperatures, the length l may become comparable to the diameter d of bottlenecks in samples 1–3. As the temperature is lowered still further, the mean free path can be considered constant ($l = d$). Because $\bar{v}$ depends on temperature only weakly, κ in Eq. (3) (in our case, $\kappa = \kappa_{ph}^{op}$) should decrease with decreasing temperature as $C_V(T)$.

The dashed lines in Fig. 5 plot the $\kappa_{ph}^{op}(T)$ dependences for the cases l = const = 800, 400, and 100 Å obtained using the above scheme. The best fit to these curves is provided by the $\kappa_{ph}^{op}(T)$ relations obtained experimentally for samples 1–3, respectively. This result supports the trend for the $\kappa_{ph}^{op}(T)$ relation to grow with increasing bottleneck diameter in the samples, which was pointed out earlier.

We cannot justify judging the accurate bottleneck diameter from the data presented in Fig. 5, because the values of the thermal conductivity $\kappa_{ph} = \kappa_{ph}^{op}$ for low temperatures were calculated using a simplified relation. Instead, it would be appropriate to suggest qualitative agreement between the experiment and calculations.

A question may arise as to whether the difference in the values of $\kappa_{ph}^{op}(T)$ (and $\kappa_{eff}^{ph}(T)$) between samples 1–3 studied by us could be assigned to the contribution of the second phase (cristobalite) to the thermal conductivity in samples 1 and 2. Estimates made using Eqs. (1)–(3) showed this contribution to be very small indeed. Indeed, if we assume the filler (a NaCl + cristobalite film with similar thermal conductivities) to occupy 31% of the opal (5% cristobalite is the highest concentration in sample 1), then κ_{ph}^{op} in sample 1 at 10 K will be 4.07 W/m K (for 26% filling of opal voids by NaCl; κ_{ph}^{op} in this sample at 10 K is 4.21 W/m K). This estimate is one more argument for the difference in thermal conductivity $\kappa_{ph}^{op}(T)$ of samples 1–3 being related primarily to boundary scattering of phonons from the bottlenecks of horn-shaped channels with different dimensions, which form in these samples in the course of their preparation.

Consider now the behavior of $\kappa_{ph}^{op}(T)$ in samples 1–3 of the opal + NaCl nanocomposites in the high-temperature region (~50–300 K).

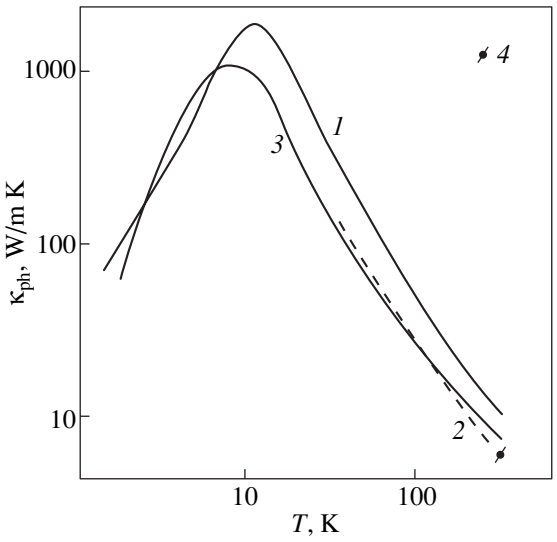

Fig. 6. Temperature dependences of the thermal conductivity (*1*, *2*) of single-crystal quartz lattice (*1*) along and (*2*) perpendicular to the *c* axis [13], (*3*) of a NaCl single crystal [13], and (*4*) of polycrystalline cristobalite [24].

In this temperature region, the length l is considerably smaller than the diameter of the bottlenecks of horn-shaped channels loaded by NaCl in sample 3 and of the new combined bottlenecks in samples 1 and 2, while $\kappa_{ph}^{op}(T)$ of all three samples is smaller than the thermal conductivity of bulk NaCl. We observed the same pattern [7] for HgSe loaded in opal voids.

For $T > 50$ K, the thermal conductivity of NaCl in opal in samples 1 and 2 behaves nearly as it does in bulk NaCl with defects. In sample 3 (and partially in samples 1, 2), there can also exist specific defects (absent in bulk samples), such as vacancies (i.e., breaks in the filler array), surface defects, and defects caused by strains in the filler matrix.

4. CONCLUSIONS

The above study can be summarized to yield the following main conclusions on the behavior of the thermal conductivity of NaCl loaded in regularly arranged first-order voids of single-crystal opal (opal + 80–100% NaCl nanocomposite):

(1) The lattice thermal conductivity of NaCl loaded in opal voids (κ_{ph}^{op}) was found to be substantially smaller than that of bulk NaCl throughout the temperature interval studied (5–300 K).

(2) For $T > 50$ K, this behavior of $\kappa_{ph}^{op}(T)$ can be assigned to the presence of conventional and specific defects forming in NaCl loaded in opal voids.

(3) For $T < 20$ K, $\kappa_{ph}^{op}(T)$ is dominated by boundary scattering of phonons from bottlenecks of horn-shaped

channels connecting the octahedral and tetrahedral first-order voids in opal. The magnitude of κ_{ph}^{op} in this temperature interval depends substantially on the actual size of the bottlenecks present in a sample, whose diameters are related to the amount of the cristobalite forming in near-surface layers of amorphous SiO_2 spheres of opal in the course of preparation of the opal + NaCl nanocomposite. This behavior of $\kappa_{ph}^{op}(T)$ can be accounted for only if the bottlenecks are arranged regularly in the sample volume, the situation typical of the filler array in a nanocomposite based on single-crystal opal.

It should be stressed that the interpretation of the results obtained in the present study of the thermal conductivity of the opal + NaCl nanocomposite differs somewhat from that suggested for this nanocomposite in [11]. As already mentioned [1], as new experimental findings appear in studies of the thermal conductivity of opals and opal-based nanocomposites, it sometimes feels necessary to abandon the conclusions and schemes espoused earlier in favor of another interpretation of the experimental data, which seems fully justified in view of the complexity of the unconventional objects involved.

ACKNOWLEDGMENTS

This study was carried out within the framework of a bilateral agreement between the Russian Academy of Sciences and the Polish Academy of Sciences and was supported by the Russian Foundation for Basic Research (project no. 02-02-17657) and the Polish State Committee on Research (KBN) (project no. 3 T08A 054 26).

REFERENCES

1. V. N. Bogomolov, N. F. Kartenko, D. A. Kurdyukov, L. S. Parfen'eva, I. A. Smirnov, N. V. Sharenkova, H. Misiorek, and A. Jezowski, Fiz. Tverd. Tela (St. Petersburg) **45** (5), 911 (2003) [Phys. Solid State **45**, 957 (2003)].
2. A. É. Aliev, N. Kh. Akhmedzhanova, V. F. Krivorotov, I. N. Kholmanov, and A. A. Fridman, Fiz. Tverd. Tela (St. Petersburg) **45** (1), 60 (2003) [Phys. Solid State **45**, 61 (2003)].
3. J. O. Sofo and G. D. Mahan, Phys. Rev. B **62** (4), 2780 (2000).
4. J. D. Albrecht, P. A. Knipp, and T. L. Reinecke, Phys. Rev. B **63**, 134303 (2001).
5. V. G. Balakirev, V. N. Bogomolov, V. V. Zhuravlev, Yu. A. Kumzerov, V. P. Petranovskiĭ, S. G. Romanov, and L. A. Samolovich, Kristallografiya **38** (3), 111 (1993) [Crystallogr. Rep. **38**, 348 (1993)].
6. V. N. Bogomolov and T. M. Pavlova, Fiz. Tekh. Poluprovodn. (St. Petersburg) **29** (5–6), 826 (1995) [Semiconductors **29**, 428 (1995)].
7. V. N. Bogomolov, N. F. Kartenko, D. A. Kurdyukov, L. S. Parfen'eva, V. V. Popov, L. M. Sorokin, I. A. Smirnov, H. Misiorek, A. Jezowski, and J. Hutchison, Fiz. Tverd. Tela (St. Petersburg) **45** (3), 535 (2003) [Phys. Solid State **45**, 566 (2003)].
8. V. V. Ratnikov, Fiz. Tverd. Tela (St. Petersburg) **39** (5), 956 (1997) [Phys. Solid State **39**, 856 (1997)].
9. V. N. Bogomolov, L. S. Parfen'eva, I. A. Smirnov, H. Misiorek, and A. Jezowski, Fiz. Tverd. Tela (St. Petersburg) **44** (1), 175 (2002) [Phys. Solid State **44**, 181 (2002)].
10. C. Schmidt, Cryogenics **15**, 17 (1975).
11. V. N. Bogomolov, N. F. Kartenko, D. A. Kurdyukov, L. S. Parfen'eva, A. A. Sysoeva, N. V. Sharenkova, I. A. Smirnov, H. Misiorek, J. Mucha, and A. Jezowski, Fiz. Tverd. Tela (St. Petersburg) **41** (2), 348 (1999) [Phys. Solid State **41**, 313 (1999)].
12. A. Jezowski, J. Mucha, and G. Pompe, J. Phys. D: Appl. Phys. **20**, 1500 (1987).
13. *Thermal Conductivity of Solids: Handbook*, Ed. by A. S. Okhotin (Énergoatomizdat, Moscow, 1984) [in Russian].
14. S. G. Romanov, A. V. Fokin, and K. Kh. Bamamuratov, Pis'ma Zh. Éksp. Teor. Fiz. **58** (11), 883 (1993) [JETP Lett. **58**, 824 (1993)].
15. G. N. Aliev, V. G. Golubev, A. A. Dukin, D. A. Kurdyukov, A. V. Medvedev, A. B. Pevtsov, L. M. Sorokin, and J. Hutchison, Fiz. Tverd. Tela (St. Petersburg) **44** (12), 2124 (2002) [Phys. Solid State **44**, 2224 (2002)].
16. V. N. Bogomolov, D. A. Kurdyukov, L. S. Parfen'eva, A. V. Prokof'ev, S. M. Samoĭlovich, I. M. Smirnov, J. Mucha, and H. Misiorek, Fiz. Tverd. Tela (St. Petersburg) **39** (2), 392 (1997) [Phys. Solid State **39**, 341 (1997)].
17. L. I. Arutyunyan, V. N. Bogomolov, N. F. Kartenko, D. A. Kurdyukov, V. V. Popov, A. V. Prokof'ev, I. A. Smirnov, and N. V. Sharenkova, Fiz. Tverd. Tela (St. Petersburg) **39** (3), 586 (1997) [Phys. Solid State **39**, 510 (1997)].
18. G. N. Dul'nev and Yu. P. Zarichnyak, *Thermal Conductivity of Mixtures and Composition Materials* (Énergiya, Leningrad, 1974) [in Russian].
19. K. W. Garrett and H. M. Rosenberg, J. Phys. D: Appl. Phys. **7**, 1247 (1974).
20. R. E. Meredith and C. W. Tobias, J. Appl. Phys. **31**, 1270 (1960).
21. J. C. Maxwell, *A Treatise on Electricity and Magnetism* (Dover, New York, 1954), p. 435.
22. E. Ya. Litovskiĭ, Izv. Akad. Nauk SSSR, Neorg. Mater. **16** (3), 559 (1980).
23. D. G. Cahill, S. K. Watson, and R. O. Pohl, Phys. Rev. B **46** (10), 6131 (1992).
24. M. Kunugi, N. Soda, H. Sawa, and A. Konishi, J. Am. Ceram. Soc. **55** (11), 580 (1972).

Translated by G. Skrebtsov

Physics of the Solid State, Vol. 46, No. 10, 2004, pp. 1969–1983. Translated from Fizika Tverdogo Tela, Vol. 46, No. 10, 2004, pp. 1901–1915.

FULLERENES AND ATOMIC CLUSTERS

The Role of Carbon and Metal in Self-Assembly of the Iron–Carbon System at Various Component Ratios

G. A. Domrachev*, A. I. Lazarev*, B. S. Kaverin*, A. N. Egorochkin*, A. M. Ob"edkov*, E. G. Domracheva*, L. G. Domracheva, G. V. Markin*, E. Huipe Nava***, A. A. Sorokin*, O. N. Suvorova*, V. L. Karnatsevich*, A. I. Kirillov*, and A. A. Zakurazhnov***

**Razuvaev Institute of Organometallic Chemistry, Russian Academy of Sciences, ul. Tropinina 49, Nizhni Novgorod, 603950 Russia*

e-mail: domrachev@imoc.sinn.ru

***Universidad Michoacana de San Nicolas de Hidalgo, Morelia, Mich., Mexico*

****Technological Institute, Morelia, Mich., Mexico*

Received March 10, 2004

Abstract—The problem of self-assembly in a metal–carbon system under dynamic conditions (equilibrium and nonequilibrium) is considered using the iron–carbon system as an example. It is proved theoretically and experimentally that the ratio of the components of the system affects the possibility of carbon self-assembly with the formation of fractal iron structures and of metal self-assembly with the participation of polyhapto derivatives of iron and the formation of fullerene-like carbon structures. © *2004 MAIK "Nauka/Interperiodica".*

1. INTRODUCTION

For many years, various authors have studied the decomposition of organometallic compounds under nonequilibrium conditions with deposition of inorganic solids from the vapor phase (MOCVD) [1, 2]. Such processes demonstrated the formation of different types of structures of the metal–carbon system with a varying *M*/C ratio and its gradient and various solid morphologies, for example, layers of nanospheres, amorphous and crystalline filaments, amorphous particles of spherical and complex shape, anomalous void distribution, layered or columnar structures, fractal and nonlinear structures, and structures of uniform composition including single crystals. These phenomena indicate that MOCVD is an essentially nonequilibrium dynamic process. Recently, we confirmed that fractal-ordered and nanosize solids can form: amorphous, multiphase polycrystalline or block single-crystal, and dendritic single-crystal metals (germanium or iron) [3, 4]. Components of the metal–carbon system (an organometallic compound, its mixtures with organic compounds, a metal impurity in the bulk or at the surface of amorphous or crystalline carbon) are self-assembled at elevated temperatures. Self-assembly occurs because of the difference between the mobilities of metal and carbon atoms, which is related to the origin of the system (free carbon or chemically bonded carbon, e.g., with hydrogen or metal) and to physical conditions (temperature, pressure, material flow velocities, etc.) [1, 2]. The probability of these phenomena was analyzed in [5, 6], and the conclusion was made that, under nonequilibrium conditions of formation of an *M*–C system (for example, during MOCVD), this process can occur for metals and semiconductors that cannot form stable carbides (Zn, Cd, Hg, Ga, In, Tl, Ge, Sn, Pb, Sb, Bi, Te). The metals for which carbides do not form from free carbon and metal at $T < 1000$ K (Cu, Ag, Au, Fe, Co, Ni), as well as the metals of the Pt group dissolving carbon upon fusion and evolving it after cooling (Ru, Os, Rh, Ir, Pd, Pt), can participate in self-assembly.

The methods of preparation of *M*–C nonequilibrium systems are well known: fast cooling of melts of the *M*–C system, MOCVD, various irradiation methods, and plasma chemical and mechanochemical methods. All these treatments result in the appearance of fractal order in the solids obtained [7] and in the void system. The outer surfaces can serve as sites of nucleation of fullerene-like forms of carbon in the process of self-assembly of solid amorphous (according to x-ray diffraction data) carbon. This process is accompanied by decomposition of the carbon–metal system and surface recombination and segregation of carbon impurities.

Simulation of fractal-ordered solids (in the absence of translation invariance) has shown that "stable fractal forms" appear at a certain stage of fractal development [7]. These forms are self-similar, and their number in one generation is finite. They can be arbitrarily filled with building blocks a finite number of times, although the basic fractal skeleton is filled regularly and uniquely. This property is typical of fractal-ordered quasicrystalline systems and is analogous to the properties of void filling in solids [7].

1063-7834/04/4610-1969$26.00 © 2004 MAIK "Nauka/Interperiodica"

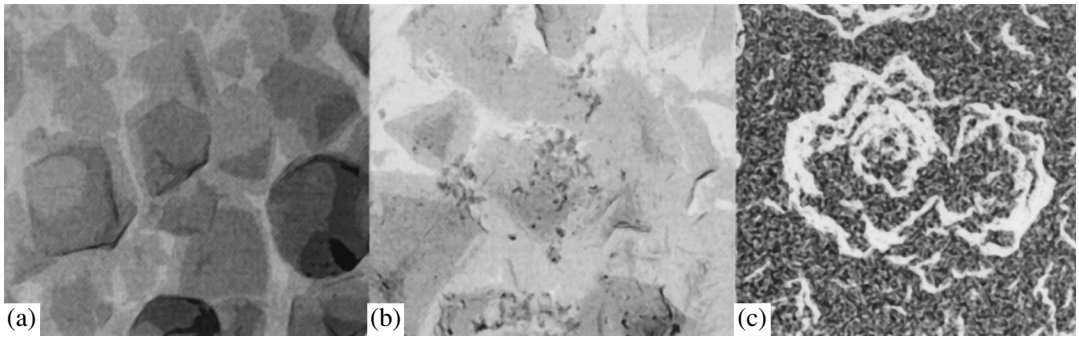

Fig. 1. Morphological forms of iron–carbon coverings obtained by thermal (250–300°C) decomposition of iron pentacarbonyl in a flow in vacuum with addition of organic bromides. (a) In the presence of 1,2-dibromoethane, a "brush" of iron single crystals is formed that exhibits no corrosion in air for a year. (b) In the presence of 1,2-dibromoethane at a limited flow rate of the products of decomposition of iron pentacarbonyl (carbon oxide) and 1,2-dibromoethane (ethylene), iron single crystals form with spherical defect inclusions. (c) In the presence of bromallylene, hierarchies of fractal x-ray amorphous formations arise in the form of "rose-like flowers" containing iron and carbon.

We have shown that transport in solids of this type is assisted by void surface diffusion and that crystallization of metal or carbide phases can occur inside voids with fractal configuration. In this case, the separation of an (M + C) composition into the metal (or metal carbide) and any carbon form occurs at the gas (or vacuum)/solid interface [1, 2].

The experience accumulated to date in preparing numerous fullerene-like structures by catalysis with iron or its organometallic derivatives confirms that self-assembly of carbon on iron is induced by varying the ratio of the elements in the carbon–metal system (with increasing carbon content). However, at a low carbon content in the metal–carbon system, self-assembly of the metal on carbon can be observed. The metals of the iron subgroup and carbide-forming metals most easily undergo self-assembly of metal on carbon, which accounts for the variety of structures of metals with carbon impurities.

For metals that do not form carbides, we found earlier [2, 3] that carbon cages were spontaneously formed on the surface of growing germanium crystals when the x-ray amorphous quasicrystalline (Ge MOCVD–fabricated) Ge–C system was crystallized. Segregation of carbon impurity on the void surface or of stable fractal forms inside solids prepared under nonequilibrium conditions is also possible. Using this process, one can fabricate continuous carbon films having the form of voids or particle cages of various shape (spherical or complex).

2. SELF-ASSEMBLY OF IRON ON CARBON

The study of the deposition of the iron–carbon system controlled by organic additives upon thermal decomposition of iron pentacarbonyl provides unambiguous proof of the self-assembly of iron on carbon. The decomposition of iron pentacarbonyl is accompanied by the appearance of many morphological formations, the oolitic structure of powders, etc. It would be interesting to determine the conditions for deposition either of single-crystal iron or of fractal-ordered nanosize amorphous (aperiodic) morphological formations of the iron–carbon system consisting mainly of iron with carbon impurity (up to 5–10 at. %). Thus there is reason to believe the self-assembly of iron on carbon can be confirmed.

We experimentally studied the effect of two organic haloid derivatives as additives during the deposition of iron. Based on theoretical arguments and extensive previous experience [1, 2], we chose organic bromides that were not very different from each other: 1,2-dibromoethane (DBE) and 1-bromo-propene-2 [bromallylene (BA)]. DBE thermally dissociates in the presence of organometallic compounds with emission of gaseous ethylene and bromine, and BA forms numerous cluster derivatives with strong iron–carbon bonds because of the great affinity of the allyl radical to iron. Heterogeneous decomposition of iron pentacarbonyl on glass-ceramic substrates in a vacuum flow reactor with addition of 10–20 vol % of DBE or BA at a temperature of 250–300°C resulted in the formation of two substantially different types of structures. In DBE vapors, a dense "brush" of iron single crystallites 1–2 mm in size oriented along the flow and having mirror brilliant faces was formed on the substrate (Fig. 1a). With increasing pressure, corresponding to an excess in the products of decomposition of iron pentacarbonyl (carbon oxide) and DBE (ethylene), a brilliant film containing iron single crystals was formed; however, grey spherical inclusions also appeared (Fig. 1b). In BA vapors, a grey x-ray amorphous covering was formed consisting of spherical particles of the same (micron) size, which covered the entire surface of the substrate and consisted of "petals." Above them, fractal "flowers" like roses were formed, which were two or three orders of magnitude larger and also consisted of petals formed by spherical particles similar to those described above (Fig. 1c). It is known that, in contrast to bromallylene, 1,2-dibromoethane does not induce the formation of

carbon during MOCVD. From these experiments, the conclusion was drawn that it is possible to chemically control the self-assembly of the iron–carbon system during its growth. It is possible to induce either the self-assembly during the single-crystal growth (at low carbon content) or the fractal growth of aperiodic structures with self-assembly of iron on carbon. The iron single crystals obtained demonstrate extraordinary stability to corrosion (over one year in the atmosphere of a chemical laboratory), apparently due to the presence of a thin continuous carbon film formed on the surface of iron crystals, while fractal-ordered x-ray amorphous samples, in the form of a nanosize material, transformed into iron oxide within several days.

We simulated the interaction of an allyl radical with several iron atoms belonging to an iron single-layer plate. Optimization of the geometry and calculation of the iron plate parameters were carried out using the method of molecular mechanics (MM+) and the semiempirical PM3 method. The plate consisted of iron atoms forming adjacent squares of four iron atoms. An allyl radical was attached to the iron atoms by three carbon atoms at the center of the plate. The results of the calculation revealed the existence of strong distortion of the geometry of the entire system. After optimization of the geometry, the initially flat plate became a bent surface with a complicated shape with the allyl radical surrounded by iron atoms (Fig. 2). This confirms our statement that the bonding of the allyl radical to the surface of the iron plate generates interaction that gives rise to distortions of the geometry of the flat iron plate and to the disappearance of the periodic structure (translation invariance) in an initially periodic iron configuration.

Thus, the results of experiment and simulation demonstrate the possibility of self-assembly of iron on carbon at low carbon contents as compared to the iron content.

3. SELF-ASSEMBLY OF CARBON ON IRON

It is well known that the equilibrium ground state of carbon is graphite having a layered structure. By using different chemical and physical methods of preparation of solid carbon (CVD, MOCVD, plasma chemical, laser and electron beam sputtering, vacuum thermal sputtering, and other methods), which are nonequilibrium processes, graphite can be formed only at very high temperatures, since the mobility of carbon atoms is very low at moderate temperatures. This is shown by the formation of fullerenes, i.e., the highest energy states of carbon (molecular states), in such processes, whereas all other stable states are polymeric.

It is widely known that atomic and molecular structures with hexagonal and trigonal symmetry, as well as the structures having second- and fourth-order axes or a symmetry plane, can be ordered in the crystalline (periodic) state.

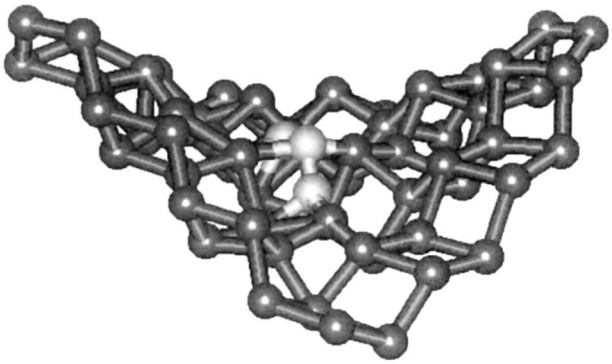

Fig. 2. Simulation of the interaction of a flat periodic iron plate with an allyl radical attached at its center, resulting in the disappearance of translation invariance of iron due to the plate bending (self-assembly of iron on carbon).

Lazarev and Domrachev have shown [7–9] that, by analogy with two-dimensional structures with rotational symmetry C_5, these structures can form aperiodic two-dimensional fractal-ordered quasicrystalline systems having rotational symmetry C_n of the sixth, fourth, third, second, and first orders (n = 6, 4, 3, 2, 1). In contrast to crystalline systems having the same rotational symmetry C_n, these systems are not periodic, since they have no translation invariance, like the aperiodic Penrose mosaics having fifth-order symmetry [7–9]. Such systems are often obtained in the form of x-ray amorphous solids in nonequilibrium processes of solid phase growth from different phases, especially from the gas phase. The formation of such fractal-ordered solids was detected during organometallic chemical vapor-phase deposition (MOCVD) [1, 2], in plasma- or laser-activated processes of PE and LE MOCVD [2], and also in the process of CVD of pyrocarbon by pyrolysis of hydrocarbons and during physical vapor deposition (PVD) of carbon, metals, or inorganic compounds under nonequilibrium conditions [10]. These processes are nonequilibrium and irreversible because of the very high melting temperatures of carbon or other inorganic materials and low deposition temperature and also because of the high rate of solid carbon layer deposition and, hence, of the extremely low mobility of carbon or metal atoms on the growing surface.

The method of plasma-arc sputtering of carbon applied to synthesize a fullerene soot [11] containing fullerenes and carbon nanotubes is also a nonequilibrium process, which is expected to produce fractal-ordered quasicrystalline solid carbon film structures.

Such conditions facilitate the formation of nanostructures (such as fullerenes and nanotubes), noncrystalline aperiodic fractal-ordered materials (such as carbon–metal systems) [12], in which the generation of shift deformations is difficult because of the aperiodicity of the material. Therefore, such materials should conserve kinetic energy under dynamic load, have shape memory, and possess improved mechanical, anti-

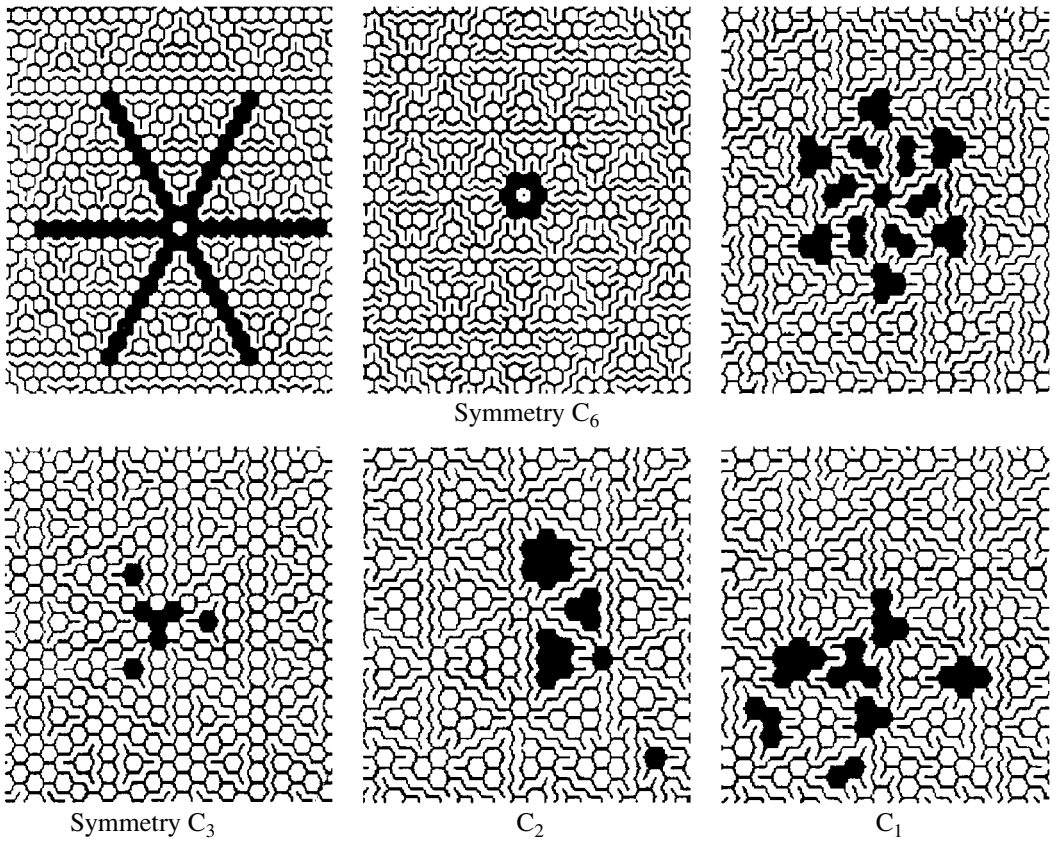

Fig. 3. Selected forms of 2D-quasicrystalline carbon with different rotational symmetries (C_6, C_3, C_2, C_1) and the characteristic elementary structures formed in each case.

corrosion, and other properties. This situation is typical for molecular materials such as fullerenes, as well as for amorphous metal–carbon and other inorganic nanosystems.

Lazarev and Domrachev have developed an approach to the construction of two-dimensional fractal-ordered quasicrystalline systems [12, 13]; using this approach, we can generally consider the structural classification of carbon systems having 2D-quasicrystalline ordering and rotational symmetry in the absence of translation-invariant ordering. Structures are constructed from short pieces (small diagonals of elementary rhombuses), forming quasicrystalline networks with elements similar to those of the models of polycyclic and ramified structures of chemical molecules, such as hydrocarbons, obtained by pyrolysis of oil or gaseous hydrocarbons [10].

These structures are similar to carbon skeletons of benzene, toluene, ethylbenzene, 1,3,5-trimethylbenzene, naphthalene, tri-(ortho-phenylene), coronene ("hexa-benzobenzene"), fluorene, acenaphthelene, fluoranthene, corannulene [14], polycenes, polyphenes, radicals of cyclopentadienyl, indenyl, perinaphthenyl, fluorenyl, and other substituted polycycles, including macrocyclic and infinite polymeric chains. There exists a variety of structures: filaments, bent filaments bonded to cycles, ribbons consisting of cycles, and several ribbons connected via cycles. Most of the cycles in these structures are six-membered rings, which are the most stable carbon rings forming the basis of a graphite network. However, five-membered carbon cycles are often encountered among six-membered cycles. Some of these structures can also arise in the gas phase during CVD of amorphous pyrocarbon from propane: indene, fluorene, acenaphthylene, fluoranthene, benzofluorene, benzofluorantene, and others [10]. Obviously, many analogous structures with a greater carbon content should be present in solid amorphous pyrocarbon. The main structural defects of a graphite network are five-membered rings (i.e., a vacancy of a carbon atom filled with a C–C bond due to recombination of two neighboring carbon atoms separated by a vacancy). The presence of a small number of such defects does not distort the plane of the carbon network appreciably, especially if it lies on other, lower layers of the quasicrystalline network that are arbitrarily oriented and do not reproduce the top network considered.

Lazarev and Domrachev have performed a general analysis of all 2D fractal-ordered quasicrystalline carbon structures possessing rotational symmetry of order 6, 4, 3, 2, or 1 (Fig. 3). Their analysis confirmed the high probability of formation of various types of quasi-

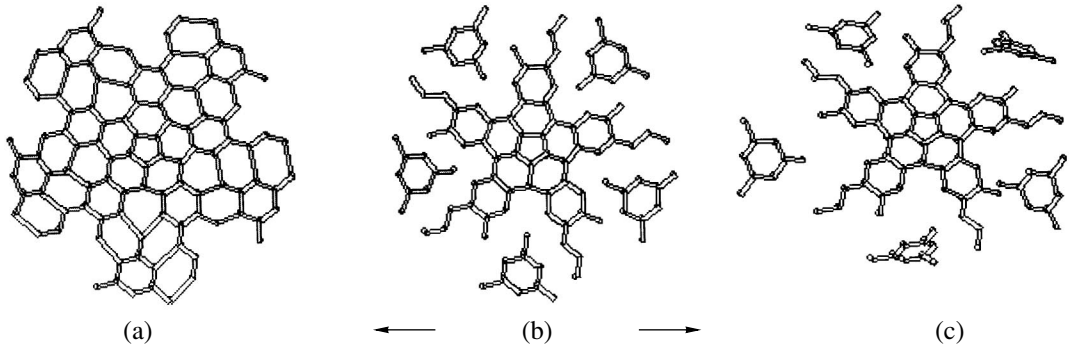

Fig. 4. (b) Self-assembly of two-dimensional quasicrystalline carbon containing a cyclo-C_5 defect at the center and nonbonded carbon fragments analogous to substituted single-nucleus aromatic hydrocarbons. The self-assembly can occur in two ways. In the first way (b ⟶ a), fragments are bonded to the central polycyclic corannulene structure and to condensed polycene ribbons, which results in the formation of "graphite" containing a central cyclo-C_5 defect. Due to this defect, a flat-slope cone forms. The second way (b ⟶ c) is the removal of nonbonded fragments with the formation of small fullerenes (the central block of the quasicrystalline C_{60} structure whose self-assembly is shown in Fig. 5).

crystalline carbon structures (including fifth-order structures). They are formed through CVD under irreversible carbon deposition conditions. X-ray amorphous pyrocarbon is obtained by pyrolysis of saturated or nonsaturated hydrocarbons, individual aromatic and oil hydrocarbons, and, of course, benzene [10].

The main feature of the 2D fractal–ordered quasicrystalline carbon structures (quasicrystalline carbon monolayers) having ordering with rotational symmetry (C_n) is the existence of an aperiodic carbon network having fragments with a graphite structure. Such fragments include polycyclic structures consisting of C_6 rings condensed into ribbons or into large polycyclic structures, as well as chains bonded to them and isolated fragments of hydrocarbons without hydrogen atoms. These structures are unstable and give rise to surface activity of quasicrystalline carbon, similar to activated coal.

Such structures should be formed in the presence of a carbon atom flow from a source and be determined by the geometry of the source and the substrate and by their relative positions (nonequilibrium carbon sputtering conditions). In real pyrolitic structures, there is certainly some amount of hydrogen atoms [10], which partially stabilize the structures and cab be removed only at very high temperatures exceeding 1000°C [10].

The centers of polycondensed ring systems with six-membered cycles are the most stable parts of these structures. The main structural defects of quasicrystalline carbon structures are five-membered rings codeposited with six-membered cyclic systems or structures of the ribbon type (polycycles, polycenes, polyfenes, and others).

Quasicrystalline carbon is also characterized by the presence of fragments (nonbonded in the layer plane), which can be bonded with multimember polycyclic systems located in the layer, thereby forming a graphite-like network (Figs. 3, 4a), or be removed from the layer by heating (Fig. 4b), resulting in self-assembly of fullerene-like structures during recombination of polycene ribbons. This network can also have C_5 defects and facilitate the further formation of bonds between polycene ribbons with a subsequent growth of carbon nanotubes, fullerenes, and fullerene-like or cone-shaped structures (with a C_5 ring at the top of the corannulene basis) (Fig. 4b).

The process of spontaneous formation of fullerene-like structures of quasicrystalline carbon or its fragments should be controlled by thermal fluctuations and the motion of fragments of the original structure, which is intensified as the temperature increases and the energy of formation of new C–C bonds is released upon recombination.

The formation of fullerene-like structures is a thermodynamically allowed process with respect to metastable quasicrystalline carbon; however, this process is kinetically difficult due to the low mobility of carbon atoms and carbon structures, the randomness of vibrations of the carbon network, and the necessity of eliminating possible nonbonded low-molecular fragments.

With respect to the basic carbon modification (graphite), metastable quasicrystalline carbon is thermodynamically even more unstable than fullerenes and nanotubes, but the formation of graphite is kinetically difficult for the same reasons (randomness of vibrations); the situation is still more serious, since it is necessary to form a perfect crystalline structure of graphite in the presence of practically random vibrations and motions of the structure and its fragments.

The processes with kinetic restrictions are expected to be slow; this is especially true for gas phase processes of recombination and growth of fullerene-like structures and graphite. Therefore, these processes require high temperatures, where the mobility of carbon atoms increases to an experimentally detectable value. Indeed, in the case of pyrolysis of hydrocarbons,

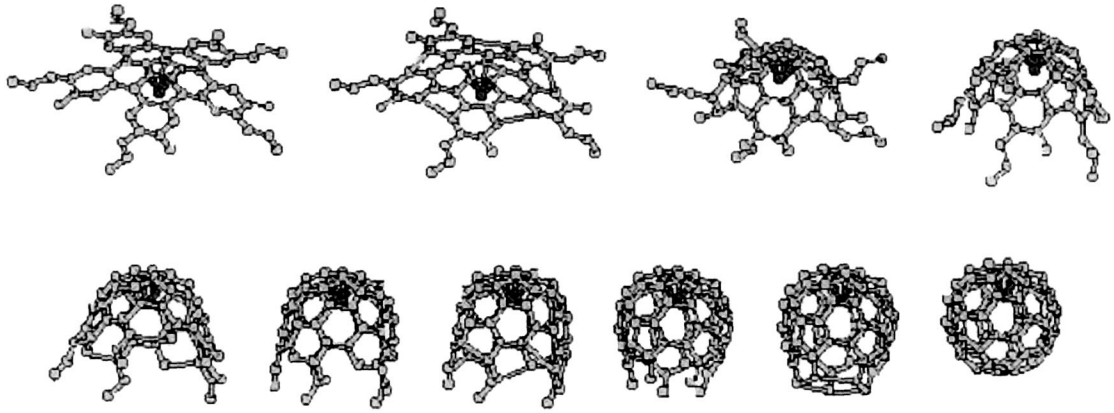

Fig. 5. Self-assembly of carbon fragments with an iron atom into the C_{60} fullerene. The QC symmetry is C_5.

the maximum yield of more complex fullerenes is shifted to 2000–2500 K and to higher pressures (from 1 Pa to atmospheric pressure) [15].

Hence, the probability of self-assembly of isolated fragments of quasicrystalline carbon under the conditions of thermal reactions is low due to kinetic restrictions, randomness of vibrations (especially for end nonbonded fragments), and the necessity of releasing the energy of bond creation during recombination.

4. A POSSIBLE MECHANISM OF GROWTH OF CARBON NANOTUBES AND FULLERENES UPON SELF-ASSEMBLY OF QUASICRYSTALLINE CARBON IN CATALYTIC PROCESSES INVOLVING A METAL

The recently discovered "metallocene" (M = Fe, Co, Ni) and metal-"catalyzed" (with the same metals) methods of obtaining carbon nanotubes [16] provide new insights into the mechanisms and new results in the chemistry of carbon. It is interesting to consider and theoretically study the role of a metal in the catalytic formation of fullerene-like structures.

For a long time, the mechanisms of the MOCVD process [1, 2] and the direct synthesis of organometallic compounds with atomic metals at low temperatures [17, 18] were studied at the Razuvaev Institute of Organometallic Chemistry, Russian Academy of Sciences. A nonequilibrium heterogeneous mechanism of formation of inorganic or organometallic compounds or phases has been suggested [12]; this mechanism involves quasicrystalline and fractal-ordered solids formed during these processes under nonequilibrium conditions related to the presence of mass and energy flows.

It seems reasonable to apply such an approach to nonequilibrium processes of carbon deposition. Plasma (Hafman–Krätschmer arc method) and pyrolytic methods are applied to prepare fullerenes and carbon nanotubes. We suggest a mechanism of growth of fullerenes and carbon nanotubes that can operate under the conditions of self-assembly of fragments or a film of quasicrystalline carbon (QC) [12] and that is thermodynamically allowed. The process is accelerated by the catalytic action of complex formation between some QC structures and transition metal atoms (or clusters) or metallocene fragments (Fe, Co, Ni).

As a model for molecular mechanics (MM+) and dynamics (MD) simulation, we choose isolated ("gas"-phase) structures of layers of two-dimensional quasicrystalline carbon with carbon fragments (without hydrogen), which are similar to tri-(ortho-phenylene) (D_{3h}), coronene ("hexabenzobenzene") (D_{6h}), or corannulene (D_{5h} or C_{5v}) with polycene chains condensed at the sides of benzo-groups of these elements in the QC structures. The formation of such structures of fractal-ordered carbon is illustrated in Fig. 5, This process was demonstrated both in simulation by analyzing all possible structures of quasicrystalline carbon [12, 13] and experimentally by analyzing the hydrocarbonic structures formed during preparation of x-ray amorphous pyrocarbon through pyrolysis of propane [10] and by studying the mechanisms of carbon formation through pyrolysis of hydrocarbons [10].

These two-dimensional carbon forms are solid formations (like condensed hydrocarbons, which also have flat molecules and are solids) and, in addition to nucleation centers of fragments of graphite-like structures, contain active particles with nonsaturated valences, bonded or nonbonded with these fragments ("hydrocarbon molecules without hydrogen"). Such particles determine the reaction and adsorption ability of "activated coal" and quasicrystalline carbon, the latter being a fractal-ordered structure having large areas with rotational symmetry of the 6th, 5th, 4th, 3rd, 2nd, and 1st orders in 2D layers of the solid in the absence of translation invariance ("infinite periodicity") [8].

5. ISOLATED QUASICRYSTALLINE CARBON + Fe ATOM SYSTEM

Let us add a Fe atom at the center of symmetry of the system considered. The symmetry becomes lower (C_{3v}, C_{6v}, C_{5v}), and the Fe atom forms covalent bonds, as in ferrocene. The optimum position for bonding of the iron atom is the center of symmetry, since multicenter multielectron bonds of an iron atom (or another transition metal) with carbon atoms of QC structures can form. These bonds are more stable than those formed with a smaller number of centers and electrons (Fig. 5). Even if, for statistical reasons, a metal atom occupies a position with lower symmetry in a QC (especially, in the C_1 case), the lowering of the symmetry of the neighboring high-symmetry fragments and migration of the metal atom to the central position will be especially favorable; indeed, due to this reduction in symmetry, various interactions are no longer forbidden and energy is gained. This is the reason for the choice of the above models. The existence of real particles corresponding to such models was proved in the experimental studies carried out by Byszewski [19, 20]. Spectroscopic data indicate that such particles exist in space [21].

Optimization of the geometry (MM+) and heating from 0 to 1500 K (MD) result in the η^6- or η^5-type interaction of an iron atom with a C_6 or C_5 fragment of the central ring, in raising the carbon ring above the iron atom, and in bending and raising the carbon structure and the polycene ribbons codeposited with it. This bending causes the C…C distances between the unbonded fractions of polycene structures to decrease to values that are much smaller than the sum of the Van der Waals radii of carbon atoms. Covalent bonding appears between the polycene ribbons located around the upper Fe-containing center bent in the form of an inverted part of the sphere with release of the energy of bond formation. This bonding produces further bending of the subsequent elements of the polycene structures and further bonding of ribbons due to their straightening as a cylindrical surface is formed and so on, until a closed fullerene structure (Fig. 5) or an open-ended structure of a carbon nanotube (Fig. 6) is formed.

Intensive carbon evaporation and recombination favors permanent construction of polycene chains and growth of carbon nanotubes during self-assembly of the QC fragments; however, slow carbon supply during evaporation (PE PVD) and recombination result in closing of growing carbon forms with the formation of fullerenes. Both processes are controlled by the rates of carbon evaporation and formation of quasicrystalline carbon. During self-assembly, nanotubes or higher cylindrical fullerenes are formed from long QC fragments (at high QC formation rates); the small QC fragments, including short polycene, starlike fragments, sometimes with short side chains of linear C_n "substitutes" (n = 1–3), produce lower fullerenes during self-assembly of QC (at low QC formation rates).

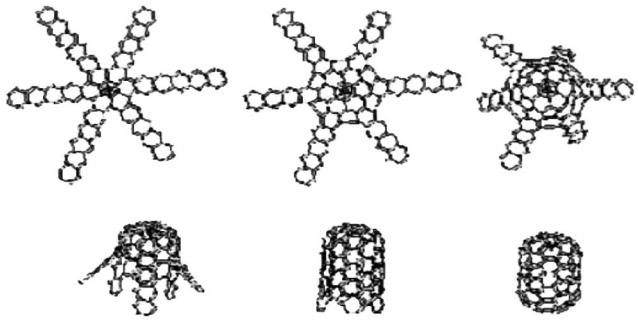

Fig. 6. Self-assembly of fragments of quasicrystalline carbon with an iron atom into a nanotube or a C_{132} fullerene (isolated system, "gas phase"). The nanotube formed (at the center of the lower line) and the C_{132} fullerene (at the right lower corner) have top caps of centro-η^6-coronene with an endo-Fe atom. The QC symmetry is C_6.

Very high carbon sputtering rates should result in the formation of nanosize multilayer amorphous oolitic structures, since the rate of nucleation of small spherical fullerene-like particles is high due to recombination at elementary carbon clusters.

Higher temperatures enhance the process of growth of carbon nanotubes and fullerenes because of the increase in the frequency of collisions of carbon atoms of polycene chains; therefore, the efficiency of formation of fullerene-like structures increases. For a thermodynamically allowed process, the kinetic restrictions are relaxed, similarly to heterogeneous decomposition of organometallics and cryogenic synthesis of these compounds with atomic metals [2, 18]. However, when long carbon nanotubes form, the loose ends of polycene chains recombine less effectively with each other at low temperatures due to the remoteness of the iron atom that organizes the structure (assisted only by the effect of straightening of polycene structures, which are flat in the ground state).

It is interesting that, in the temperature range 800–1300 K, simulation by using the method of molecular dynamics often shows a jump of an iron atom bonded to a carbon (six- or five-membered) cycle of the cap or hat of the initial part of the fullerene structure; the iron atom jumps to the opposite side of the cycle plane (exo–endo-isomerization of metal in the structure). This jump occurs because of the statistical coincidence of the phases of C–C stretching vibrations of all carbon atoms of the cycle with the phase of asymmetric stretching vibrations of the metal–ring fragment of the quasicrystalline carbon structure. Therefore, an iron atom can appear at the top of the initial portion of growing carbon nanotubes or fullerenes (when passing from the endo-position to the exo-position). This phenomenon can be responsible for multilayered growth of nanotubes under conditions of continuous carbon evaporation and the formation of QC fragments on the growing QC surface.

An increase in local temperature (>1000–1500 K) of the lid of a growing nanotube containing an endo-bonded iron atom can result in a reversible jump of the iron atom on both sides of the lid; this further increases the probability of growth of the multilayer tubes or multilayer fullerenes due to migration of the catalytic metal atom to the outer surface.

We have considered the possible self-assembly of an isolated large surface area of one layer of quasicrystalline carbon (with rotational symmetry C_6) on which several iron atoms have randomly fallen. Here, two cases are possible.

First, the iron atoms are fixed at the surface after the energy of created iron–ring polyhapto bonds is released; near each of the iron atoms, the carbon quasicrystalline structure is self-assembled (the structure rises and bends) with the formation of nucleation centers of nanotubes with vertices containing a bonded iron atom each. If the QC layer is in a free state (in an isolated state, not on the surface of other layers) and iron atoms are located at distances of 15–25 Å and are isolated from each other by the matrix [18], then self-assembly of QC occurs with nucleation of nanotubes on both sides of the QC plane.

Second, if the distance between the iron atoms is smaller than that corresponding to matrix isolation at a certain temperature for the given metal and if the quasicrystalline carbon contains large areas with a graphite-like surface, then migration of metal atoms along the most stable surface and their aggregation into clusters can occur. Analogous phenomena were observed experimentally for the migration of atoms and clusters of transition metals or gold over long distances (up to 2500 Å at 77 K) on stable faces (with low *hkl* indices) of benzene molecular crystals. The metal cluster formation either results in metal crystallization (self-assembly of the metal on a molecularly smooth surface) [18], which transforms the reaction into a heterogeneous reaction on the metal phase, or induces self-assembly of quasicrystalline carbon around the metal clusters with the formation of metal clusters and nanocrystals encapsulated in fullerene-like carbon cages [3].

In both cases, the self-assembly of the structures induced by the formation of bonds with iron atoms results in catalytic acceleration of the formation of fullerene-like structures, the transition to which from the state of quasicrystalline carbon is thermodynamically allowed. Thus, we can assert that there exists a catalytic effect of iron atoms on the formation of fullerene-like structures.

For generality, we consider the self-assembly of a graphite plate (one graphite sheet) as an η^6 ligand of an iron-organic compound. The ratio of the number of iron atoms to that of carbon is assumed to be $N \ll 1$

Using the MM+ method, together with the procedure for optimizing the geometry, we studied the self-assembly of a system consisting of a graphite plate and iron atoms bonded according to the η^6 type. We found that the molecular structure of the optimized systems depends on the density of iron atoms on the plate surface. If there is one iron atom per six-membered fragment of the plate on one side of the sheet, then simulation shows that the graphite sheet is bent such that metal atoms appear to lie on the outer side of a formed tube 7.5–7.7 Å in diameter (with respect to the nuclei of carbon atoms). As a result, the Fe–Fe distances parallel to the tube axis equal to 2.57 Å appear to be smaller than the other distances, which are equal to 3.01 Å.

If the density of iron atoms on the surface is not very high and the atoms are separated by six-membered fragments from each another, then the graphite sheet is rolled into a tube 8.8–8.9 Å in diameter, with metal atoms located inside the tube. In this case, the Fe–Fe distances that are parallel to the tube axis and equal to 4.4 Å appear to be greater than the other distances, which are equal to 3.2 Å.

We may conclude that, if iron atoms are bonded to a graphite sheet, the molecular structure is self-assembled from a flat state to a tube because of repulsion between the iron atoms in the first case and attraction in the second.

The catalytic effect of iron atoms on the growth of carbon nanotubes and fullerenes was described above in the approximation of a free iron atom and an isolated fragment with a single-layered structure of quasicrystalline carbon or graphite. A metal can be formed under homogeneous conditions in the gas phase in the case of thermal or plasma chemical activation [1, 2]. However, although multiparticle reactions (multiple collisions) are thermodynamically allowed in the gas phase, they are less probable than heterogeneous gas–solid reactions (due to kinetic restrictions), as has been established for MOCVD processes [1, 2, 17] and for direct vacuum cryogenic synthesis of organometallic compounds from atomic metal and from the condensed phase of an organic compound or a frozen inorganic gas [17, 18]. Therefore, consideration of heterogeneous gas–solid reactions also seems reasonable.

6. HETEROGENEOUS QUASICRYSTALLINE CARBON + Fe_{solid} SYSTEM

To simulate the above heterogeneous reactions, we constructed a solid iron plate consisting of 128 ($8 \times 8 \times 2$) metal atoms. An additional, 129th iron atom (adatom) was placed at the center of the plate surface; this atom was bonded with an arbitrarily chosen iron atom in the central part of the top surface of the plate. After optimization of the geometry (by using the MM+ method), this iron plate had an almost cubic structure with Fe–Fe distances that were close to those of cubic metal iron. Some deviations of the distances (towards greater values) were observed on the lateral surfaces of the plate because of the effect of the boundary conditions. A fragment of quasicrystalline carbon was placed on the surface of this iron plate with the Fe adatom. The

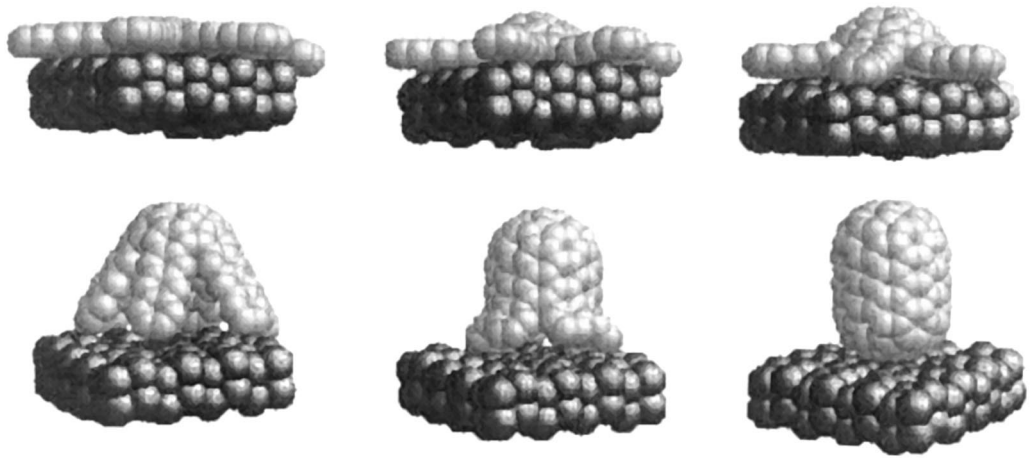

Fig. 7. Self-assembly of fragments of quasicrystalline C_{132} carbon into a nanotube (at the center of the lower line) or into the C_{132} fullerene (at the right lower corner) with an iron adatom on the surface of a two-layer iron plate (consisting of $8 \times 8 \times 2 = 128$ iron atoms). The reaction is heterogeneous. The symmetry of the system is C_6 (or C_{6v}).

QC fragments were chosen to be the same as in the case with the above-mentioned atomic iron. The center of symmetry of the QC layer was located above the Fe adatom. The MM+ optimization of the geometry for the (QC + Fe)–$Fe_{128(solid)}$ system was performed with a step-by-step fixation of any change in the structure. The behavior of the (QC + Fe)–$Fe_{128(solid)}$ system appeared to be similar to the behavior in the gas phase with atomic iron. However, specific features were observed (Fig. 7).

First of all, the process of bending of the quasicrystalline carbon structure quickly becomes an ordered motion of the system bonded with the Fe adatom in the direction perpendicular to the surface of the solid iron plate. In this case, the length of the ($Fe_{ad–cycle}$) bond was shortened, whereas the Fe_{ad}–Fe_{surf} distance was increased more than the distances in solid iron. The Fe_{surf}–Fe_{solid} distances were also increased, and the plate was slightly bent in the direction of the Fe_{solid}–Fe_{surf}–Fe_{ad} axis at the center of the cycle. The first of the Fe–Fe distances to become twice as long as the Fe–Fe distance in solid iron was the Fe_{ad}–Fe_{surf} distance. This case corresponds to separation of the iron adatom from the surface of the iron plate and its conservation at the top of the growing fullerene-like system in the polyhapto-bonded endo-position. The recombination of polycene ribbons occurred simultaneously with bending of the structure and elongation of the Fe_{ad}–Fe_{surf} distance, as well as with evaporation of the low-molecular fragments not bonded in the QC structure. However, these processes were very strongly accelerated because of the decisive and directing action of the iron plate surface and of the Van der Waals interaction (repulsion) of polycene ribbons and the iron plate surface, which ensured sliding of polycene fragments along the iron surface.

Obviously, the role played by the iron surface during the self-assembly of quasicrystalline carbon into carbon nanotubes and fullerenes is behind the fast formation of these structures. The dependence of these processes on the rate of sputtering (and, hence, evaporation) of carbon and on the rate of transformation of sputtered carbon into quasicrystalline carbon layers with various structures can be seen through the example of QC structures.

The QC structures that are centrally ordered in the course of condensation of six- or five-membered carbon rings with polycene ribbon structures are most suitable for forming carbon nanotubes. The large length of these ribbons favors the formation of higher fullerenes or long nanotubes. These QC forms are the most ordered and close to graphite; however, their structures have no translation invariance and are aperiodic. They can be generated under the conditions of high mobility of QC fragments, which, most likely, occurs at high temperatures and high carbon flows supplying the system with high energy and a high carbon concentration because of the carbon condensation into the ribbons and solid phase. The opposite conditions cannot ensure the growth of long polycene ribbons or, hence, the growth of long nanotubes. In this case, centrally ordered short polycene structures can produce small fullerenes. Their size depends on the carbon evaporation rate and on the recombination-induced growth rate of polycene structures. If the temperature of the QC surface is low and, hence, the mobility of carbon atoms and carbon structures is low, QC structures contain chainlike or needle forms. The formation of fullerenes or nanotubes from QC structures of this type is unfavorable.

As an iron heterogeneous catalyst, we chose a single-layered surface of iron atoms with a separate surface iron adatom or a similar surface of limited area

without an iron adatom but with fragments of quasicrystalline carbon deposited on the surface and having a much larger monolayer area (compared to the area of the iron "base"). Then, during the self-assembly of the entire system studied by optimizing the geometry or using the molecular-dynamics method (with increasing temperature), we observed strong interaction of the iron base with the carbon system and retraction of a significant part of the surface iron atoms into the deformable carbon system. This effect can account for the formation of catalyst metal clusters retracted into the carbon cage or covered by it.

If the metal affinity to carbon varies under different conditions, then the formation of complex morphological metal forms covered with carbon or of single crystal metal sediments with only traces of carbon occurs. Such a phenomenon is described above for MOCVD upon thermal decomposition of iron pentacarbonyl vapors in the presence of 1,2-dibromoethane or bromallylene vapors. In the former case, the formation of ethylene and a small amount of carbon ensures the formation of well-faceted α-iron single crystals. The presence of bromallylene, which has a high affinity to iron carbonyl and forms allyl iron carbonyls, results in very complex morphological iron formations (multipetal flowers), produced by strong bonding of iron atoms to the remains of the allyl fragments (fractal structures) [4].

To eliminate the effect of retraction of more than one iron atom into the carbon structure formed, we considered a model two-layer iron plate with an iron adatom at the center (the Fe_{ad}–$Fe_{64\times 2}$ system).

In the case where the center of the condensed carbon structure contains an iron adatom located on the upper surface of a two-layer iron plate, simulation of self-assembly by using the molecular-dynamics method shows extremely fast spontaneous formation of nanotubes or fullerenes with increasing temperature; the bond of the iron adatom with iron plate surface atoms is broken and a recombination of polycene ribbons occurs with the formation of nanotube walls or fullerenes. The condensed carbon structure, located at a distance equal to the sum of the Van der Waals radii of iron and carbon, easily and quickly slides off from the surface of the iron plate. At the same time, a fullerene-like formation not closed at the bottom rises in the direction perpendicular to the plate.

This effect demonstrates strong interaction of the QC system with an iron system (atom, cluster, surface), thus indicating the formation of stable complexes between them.

It is known that the rate of nanotube formation is almost always high and incomparable to gas phase reaction rates, as is the growth rate of filamentary crystals [2] or the rate of migration of metal clusters and particles along the surface of a molecular crystal (e.g., benzene during cryochemical synthesis of organometallic compounds with atomic metals [18]) or along the graphite surface [22].

Estimations of the interactions between an iron atom and fragments of quasicrystalline carbon and fullerene structures, their mutual transformations, and the relation between their structure and ferrocene-like structures are performed in the next section by using the methods of quantum chemistry, molecular mechanics, and molecular dynamics.

7. MOLECULAR AND ELECTRONIC STRUCTURE OF COMPLEXES OF EXO- AND ENDO-IRON WITH FULLERENES CONTAINING COVALENT POLYHAPTO BONDS

The stability and thermal and plasma-chemical decomposition of ferrocene and its derivatives [1, 2], as well as the structures of the solid products of decomposition, have been studied for a number of years at the Razuvaev Institute of Organometallic Chemistry (Russian Academy of Sciences). Such structures usually consist of a polymeric amorphous solid with an elemental composition close to that of ferrocene without hydrogen. In addition, solid germanium covered with a carbon shell like carbon nanotubes was established to form during thermal decomposition of germanium organic compounds [16]. Recent studies aimed at developing a metallocene-involving method [16] for synthesizing carbon nanotubes [23] and exo-fullerene (Fln) transition-metal derivatives [24] confirm our assumption on the possible existence of endo- and exo-complexes, such as Fe@Fln and Fln@Fe.

In this section, we discuss the molecular and electronic structure of various types of iron complexes with a number of fullerenes having different types of Fe–Fln bonding, possible ways they are formed, and their transformations and stability.

We chose the C_{20}, C_{60}, C_{80}, C_{180}, C_{240}, and C_{540} fullerenes with parallel five-membered rings (belonging to the D_{5d} point group) and the C_{70} fullerene with parallel five-membered rings (belonging to the D_{5h} point group), as well as the elongated C_{132} fullerene with two coronene caps (hats) (belonging to the D_{6h} point group).

The formation of complexes of these fullerenes with exo- or endo-Fe atoms was studied using the MM+ and MD methods, as well as using a modification of the semiempirical quantum-chemical INDO method. To calculate the weight factors for the σ–σ and π–π overlap, we optimized the INDO method for finding the enthalpies of formation of ferrocene compounds from atoms. The error in calculating the atomization enthalpies was less than 0.5% of the value measured for ferrocene. Simultaneously, we self-consistently minimized the energy and effective charges on the atoms for the entire molecule [25].

First, we performed calculations for structures with an isolated exo-Fe atom attached to a fullerene via η^5- and η^6-type interaction or an isolated endo-Fe atom attached to a fullerene via η^5- and η^6-type interaction

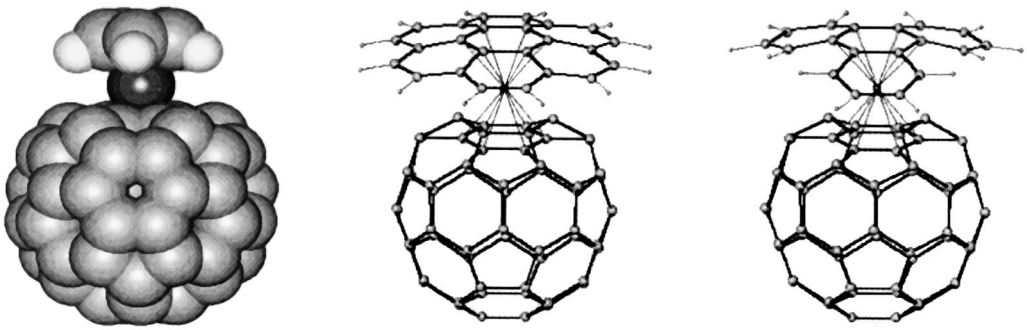

(a) (b) (c)

Fig. 8. Possible molecular structure of (a) (η^5-cyclopentadienele) (η^5-[60]fullerene)–exo-iron, (b) (centro-η^6-coronene) (η^6-[60]fullerene)–exo-iron, and (c) (centro-η^6-tri-ortho-phenylene)(η^6-[60] fullerene)–exo-iron simulated using molecular mechanics and quantum chemistry.

from the internal side of the fullerene. In both cases, the Fe atom can form strong polyhapto bonds with a fullerene and can coordinate additional ligands to the same iron atom, such as η^5-cyclopentadienyl (Cp), η^6-benzene, and η^5- or η^6-fullerene (Fln) (the latter in the case of exo-Fe). Iron derivatives with fullerenes and organic polyhapto ligands, more specifically, $(\eta^5\text{-Fln})_2\text{Fe}$, $(\eta^5\text{-Fln})(\eta^6\text{-Fln})\text{Fe}$, $(\eta^6\text{-Fln})_2\text{Fe}$, $(\eta^5\text{-Fln})\text{Fe}(\eta^5\text{-Cp})$, $(\eta^6\text{-Fln})\text{Fe}$(centro-$\eta^6$-coronene), and $(\eta^6\text{-Fln})\text{Fe}$[centro-$\eta^6$-tri(ortho-phenylene)], were studied using the MD method. They have high thermodynamic and kinetic stability (Fig. 8).

The η^5-FlnFe(η^5-Cp) compound (Fig. 8), as well as similar compounds with radical ligands like η^5-FlnFe(η^5-indenyl) and η^5-FlnFe(η^5-fluorenyl), can be in the paramagnetic state, since the number of hydrogen atoms in the ligand is odd (providing an odd number of electrons in the entire system). These compounds have high stability, although the unpaired electron occupies a high nonbonding level. The HOMO–LUMO interval for these compounds is very narrow, and they can be interesting as solid metal-like materials.

The η^5-FlnFe(η^5-Cp) compound has a large negative enthalpy of formation from atoms (about –9000 cal/mol). The dependence of the enthalpy of formation of fullerenes and their iron derivatives on the number of carbon atoms is almost linear.

The η^6-FlnFe(η^5-Cp) and similar mixed η^n-Fln compounds with the above-mentioned radical ligands have the same high stability and almost the same electronic structure as the symmetric (η^5–η^5) derivatives. They have slightly different Fe–C distances and a somewhat different character of violation of the symmetry of the fullerene structure in the region where the fullerene is bonded with an iron atom (more than *n* carbon atoms participate in η^n-Fln bonding with iron because of partial bond conjugation in the carbon skeleton upon its deformation).

We also considered a series of η^n-FlnFe(η^m-ligand) derivatives with an iron exo-atom, where *m* is an even number of atomic orbitals involved in *m* hapto-bonds and filled with an even number of electrons. The ligands are chosen from the series of polycyclic condensed aromatic hydrocarbons: η^6-benzene and substituted derivatives, η^6-naphthalene, η^6- and η^5-acenaphtylene (Fig. 8), η^6-anthracene, η^6-phenanthrene, centro-η^6-tri-ortho-phenylene, centro-η^6-coronene (Fig. 8), and centro-η^5-corannulene. These η^5 and η^6 fullerene derivatives with η^m-arenes (even with five-membered rings of the nonradical type) having an even number of C–H bonds form exo-iron derivatives in a singlet multielectron state, although the energy difference between the zero singlet and the first triplet state is small.

All compounds in this series with mixed aromatic and fullerene ligands have a large negative enthalpy of formation from atoms, like the above-mentioned radical derivatives.

The structures of the compounds with Fln–Fe bonds and η^n-ligands are very similar to ferrocene structures. The simplest, $(\eta^5\text{-Fln})\text{Fe}(\eta^5\text{-Cp})$ compound has a structure of the Cp-ligand similar to that of ferrocene: hydrogen atoms are shifted towards iron, and the Cp-ligand is not flat. Large condensed ligands, such as fluorenyl, acenaphthylene, anthracene, centro-η^6-tri-ortho-phenylene, and centro-η^6-coronene, are bent towards iron under the effect of the Fe–ligand bond, and the outer parts of the ligand lie around the iron atom and the fullerene bonded to it.

We also considered a series of exohedral-fullerene derivatives of iron represented by bis-(fullerene)iron(0). Possible polyhapto isomers of these compounds are $(\eta^5\text{-Fln})_2\text{Fe}$, $\eta^5\text{-Fln})(\eta^6\text{-Fln})\text{Fe}$, and $(\eta^6\text{-Fln})_2\text{Fe}$. All compounds are singlets in the ground state, and their molecular orbitals, energy levels, and molecular structures are similar. The only distinction in their molecular structures is that the (η^6-Fln)–Fe dis-

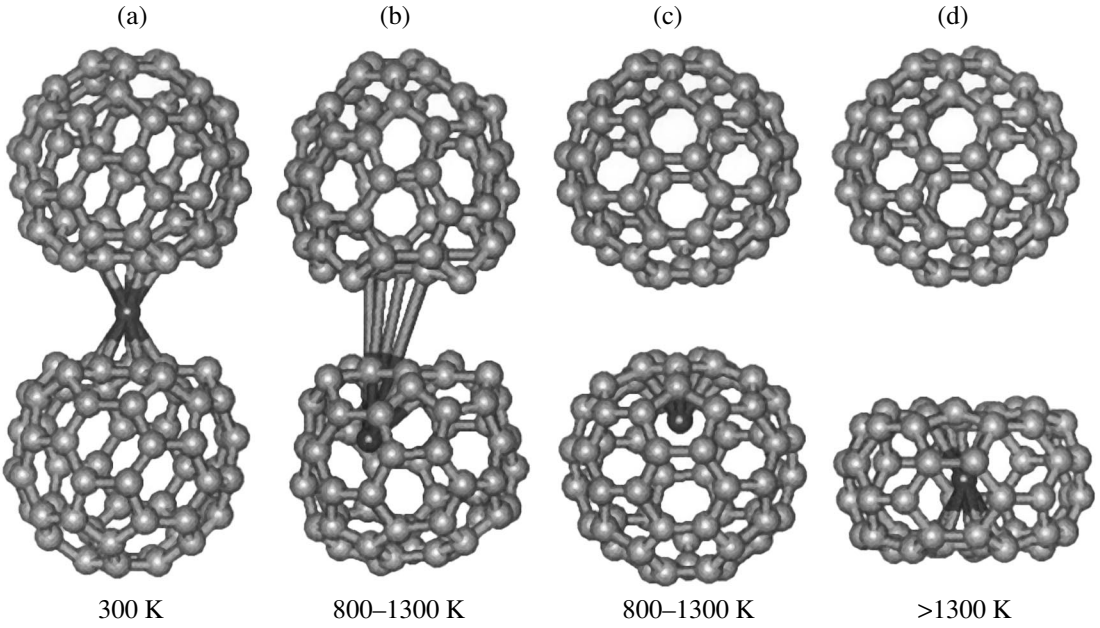

Fig. 9. Thermal decomposition of bis-(η^5-[60]fullerene)–exo-iron (molecular dynamics). (a) bis-(η^5-[60] fullerene)–exo-iron, (b) reversible isomerization with a jump of an iron atom, (c) irreversible isomerization reaction completed with decomposition into an endo-η^5-iron–[60]fullerene and a free [60]fullerene, (d) and a jump at temperatures far exceeding 1300 K with capture of the opposite fullerene wall and formation of Fe@C_{60}-η^{10} and C_{60}.

tances are somewhat greater than the (η^5Fln)–Fe distances. Various types of distortion of the fullerene structure in the region of Fe bonding with the fullerene are also similar to the above-mentioned distortion of the flat structure of aromatic ligands (Fig. 9a).

The analysis of compounds with fullerene–exo-iron–ligand bonds (the ligand can also be a fullerene) leads to the conclusion that the fullerene is a ligand and can form a stable multicenter multielectron bond with a transition metal (which is confirmed experimentally [24]). This bond is not a typical polyhapto bond, but the fullerene acts as a ligand with arbitrary and large polyhapto possibilities, whose realization is determined by the metal or metal–ligand fragments attached to the fullerene. Unfortunately, the modern quantum-chemistry methods cannot determine the strength of the polyhapto-fullerene bond with a metal (in particular, iron) and thermochemical experimental determination of the enthalpy of formation of these bonds presents some difficulties, since such complexes are almost entirely unavailable in sufficient quantities for research.

Exo-compounds of iron with fullerene ligands are stable up to 800–1300 K (as determined in molecular-dynamics studies). However, they decompose statistically at a given temperature through transformation into endo-derivatives Fe@(Fln-η^n) (n = 5, 6) with a jump of an iron atom across the ring to which it is bonded in the fullerene; at the same time, the bond with the fullerene is broken (Figs. 9b, 9c). This jump of the Fe atom from an exo-position of the initial bis-(fullerene)iron(0) to an endo-position inside one of the fullerene molecules occurs statistically in both the direct and reverse directions, and the frequency and amplitude of these jumps increase with temperature. This process depends on the intensity and phases of iron–ring stretching vibrations localized at the center of the fullerene ring bonded to the Fe atom. The jump is favored by the coincidence of the phases of vibrations of one of the rings [which is in the state where the phases of most of the C–C stretching modes in the ring are equal (extension)] with the phase of an asymmetric stretching mode in the Fe–ring system (compression). The statistical nature of this process was confirmed by observing a reversible jump and an irreversible jump, which are accompanied by decomposition of the Fln–Fe–Fln structure into Fln and Fe@Fln-η^n (n = 5, 6) in picoseconds. It is interesting that this effect apparently has a resonance character, since it is observed (according to molecular-dynamics simulations of the system) only at certain multiples of "thermal quanta." In the case of interaction between bending vibrations (with variations in the Fln–Fe–Fln bond angle) and asymmetric vibrations of this bond, the structure is destroyed with elimination of the Fe atom from both fullerene molecules and with the formation of C_{60} molecules not containing iron. Apparently, we experimentally observed a similar reaction in the thermal decomposition of metallocenes (Ni, Co) into pure metal phases in the presence of fullerene, since in the presence of carbon metallocenes never form metals [26].

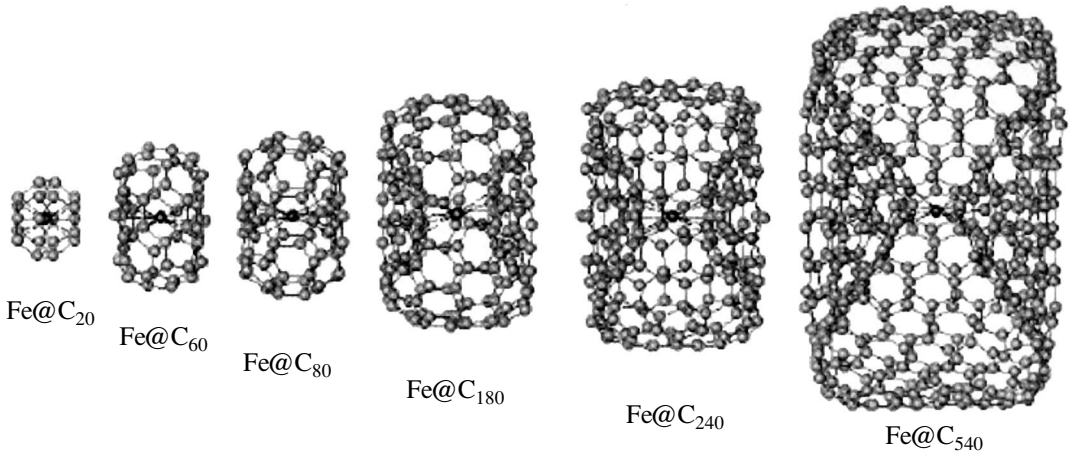

Fig. 10. Optimized molecular structures of Fe@C_n-η^{10} complexes of endo-iron with fullerenes with symmetry D_{5d} for n = 20, 60, 80, 180, 240, and 540.

From vibration spectroscopy studies, it is known that a heavy atom bonded to light ligands has a barrier effect; namely, vibrations of light ligands separated by a heavy metal atom interact only weakly and are virtually independent, which makes vibrations of light ligands highly characteristic [27]. In other words, the ligand vibration frequencies do not depend on the number of ligands and are determined by the ligand itself. The integrated intensity of the vibration spectrum is additive with respect to the number of ligands. Such an effect is observed, for example, in the vibration spectrum of tetraethyl lead.

In complexes of the type of bis-fullerene-iron(0), the main features of the vibrations differ radically from those in the case of light ligands. Since each of the two fullerene ligands has a very heavy mass, the iron atom plays the role of alight atom. In stretching vibrations (both symmetric and asymmetric) of the Fln–Fe–Fln system, a fullerene molecule cannot vibrate with a substantial amplitude as a single unit. Therefore, in this system, we may expect only asymmetric stretching and bending vibrations. The main movements will be localized near the iron atom and the nearest carbon atoms of rings to which it is bonded. Symmetric stretching vibrations related to simultaneous stretching and compression of Fln–Fe–Fln bonds should have a very low intensity due to the small probability of simultaneous displacement of the two huge ligands in opposite directions. Apparently, for the same reason, the melting temperatures of fullerenes are very high (because of the practical absence of translations of huge fullerene molecules in a fullerene molecular crystal), in contrast to the majority of molecular crystals, whose melting temperatures are low (for C_{60}, the melting temperature is estimated to be 1400 K) [28].

During a jump, the Fe atom bonded to two fullerene molecules gives a maximum contribution to the stretching vibrations of Fln–Fe–Fln; indeed, the fullerene molecules participate in stretching vibrations to an insignificant extent, since collective modes have extremely low frequencies and intensities because of the large number of carbon atoms in the fullerenes (60 or more). This circumstance is the main reason for the jump of the Fe atom, since the intensity of stretching vibrations of a single Fe atom at the corresponding temperatures is high. All this and mainly the active participation of the Fe atom in asymmetric stretching vibrations results in its incorporation into one of the fullerene molecules (Figs. 9b, 9c). After the Fe atom has penetrated into the fullerene, the Fe–C distances for the carbon atoms of the fullerene containing the Fe atom are close to 2.0–3.0 Å (in the temperature range 800–1300 K) and the Fe–C distances for the carbon atoms of the fullerene not containing the Fe atom exceed 5.5–6.5 Å. The latter values indicate that the Fe–C bonds are broken for the fullerene not containing the Fe atom. After energy relaxation and optimization of the Fe–C_{60}-η^n distance (n = 5, 6), the Fe–C distances in this compound become the same as those in ferrocene (2.06 Å).

When the energy and amplitude of asymmetric stretching vibrations are high (at $T \gg 1300$ K), the Fe atom has a fairly high amplitude during its jump, in contrast to both heavy fullerene ligands. Therefore, the Fe atom breaks away from the outer surface of the fullerene and becomes bonded to the part of the inner surface of the other fullerene through which the Fe atom has jumped. If the Fe atom has sufficient inertia, it can approach the opposite part of the inner surface of the fullerene. If the distance is such that strong interaction appears between the Fe atom and the opposite part of the fullerene wall, then η^n-endo-bonds of iron can be formed (n = 10–12). As a result, decomposition of Fln–Fe–Fln occurs into a free fullerene and Fe@Fln-η^n (n = 10, 11, 12) (Fig. 9d).

We studied endo-Fe complexes of the fullerene with many hapto-orbitals, for example, the Fe@Fln-η^n complexes (n = 10, 11, 12) (Fig. 10). After optimizing the geometry, all complexes of this type become stable structures similar to "car or tractor wheels" depending on the size of the fullerene. The most stable structure is Fe@C_{60}-η^n (n = 10, 11, 12). The stability of this type of Fe@Fln compounds formed by the above-mentioned higher fullerenes depends on the small stress caused by deformation of the skeleton of the higher fullerenes C_{80}, C_{180}, C_{240}, and C_{540}, as well as the C_{70}-η^{10} or the C_{132}-η^{12} cylinder with two η^6-coronene caps) because of their high elasticity as compared to that of smaller fullerenes.

Calculations for the first several terms in the Fe@-fullerene series were performed using a modified INDO method (up to n = 180) for the entire molecule (Fig. 7) with the parameters optimized for ferrocene derivatives; the error in calculating the enthalpy of formation was 2 cal/mol [25]. The stability of Fe@C_{20}-η^{10} was found to be higher than the stability of the free C_{20} fullerene, although for other higher terms of the fullerene series the stability is somewhat lower than that of a free C_n fullerene.

For higher fullerenes C_{180}, C_{240}, and C_{540}, calculations were performed using the molecular dynamics method. In Fe@-fullerenes, the effect of the number of carbon atoms n in the C_n fullerene on the stress arising in the structure depends on the value of n only weakly (starting from C_{80}) and is small, especially for the last terms of the series.

The majority of metal and fullerene derivatives have a large number of electrons and a large number of very closely spaced molecular orbitals occupied by electron pairs; the highest occupied molecular orbitals are weakly bonding or nonbonding metal orbitals, just as in the case of metallocenes and bis(arene)metals, which creates preconditions for low ionization potentials. Therefore, such derivatives can be "fullerene metals" in the solid state. To define the energy barrier for the metal atom jump, additional studies are needed.

The above studies into the possible molecular and electronic structure of exo- and endo-iron derivatives of various fullerenes demonstrate close analogy with polyalkylated ferrocene derivatives [29, 30], which have low ionization potentials, the ability to form electron-transfer complexes and ionic derivatives, similar molecular structure of the environment of the iron atom, and, hence, high thermodynamic and kinetic stability. The occurrence of jumps of iron atoms in the structure at high temperatures (exo $\rightleftharpoons$ endo-isomerization), found during molecular-dynamics simulations, opens new possibilities for understanding the catalytic effect of forming complexes with iron and, hence, the possibility of forming multilayer structures (fullerenes and carbon nanotubes).

Various parts of this study were presented at the international workshops "Fullerenes and Atomic Clusters" (1995, 1997, 1999, 2001), St. Petersburg.

ACKNOWLEDGMENTS

The study was supported by The International Science and Technology Center (ISTC, grant no. 2511), a grant (no. NSh-1652.2003.3) from the President of the Russian Federation for Support of Leading Scientific Schools, the Russian Foundation for Basic Research (project no. 03-02-16338), the program of the Ministry of Industry, Science, and Technology of the Russian Federation "Research and Design in Priority Lines of Development of Science and Technology for 2002–2006," the programs of the Presidium of the Russian Academy of Sciences "Fundamental Problems in the Physics and Chemistry of Nanosize Systems and Materials" and "Directed Synthesis of Materials with Predetermined Properties and Creation of Functional Materials on Their Basis, and the program of the division of chemistry and materials science of the Russian Academy of Sciences "Theoretical and Experimental Study of the Nature of Chemical Bonding and Mechanisms of important Chemical Reactions and Processes."

REFERENCES

1. G. A. Razuvaev, B. G. Gribov, G. A. Domrachev, and B. A. Salamatin, *Metal–Organic Compounds in Electronics* (Nauka, Moscow, 1972) [in Russian].
2. B. G. Gribov, G. A. Domrachev, B. V. Zhuk, B. S. Kaverin, B. I. Kozyrkin, V. V. Mel'nikov, and O. N. Suvorova, *Deposition of Films and Covers by Decomposition of Metal–Organic Compounds* (Nauka, Moscow, 1981) [in Russian].
3. P. I. Gromov, G. A. Domrachev, E. G. Domracheva, and B. S. Kaverin, Mol. Mater. **8** (1–2), 5 (1996).
4. G. A. Domrachev, E. Huipe Nava, A. I. Lazarev, A. A. Zakurazhnov, B. S. Kaverin, V. A. Kostenkov, and E. G. Domracheva, in *Memoria. XVI Simposio Nacional de Siderurgia "Ingeneriade Procesos"* (Inst. Technologico de Morelia, Mexico, 1994), p. 33.1.
5. G. A. Domrachev, B. S. Kaverin, A. I. Lazarev, and E. G. Domracheva, in *Abstracts of Invited Lectures and Contributed Papers of 3rd International Workshop in Russia on Fullerenes and Atomic Clusters, IWFAC'97* (St. Petersburg, 1997), pp. 0.3, 58.
6. G. A. Domrachev, E. G. Domracheva, E. Huipe Nava, B. S. Kaverin, A. I. Lazarev, E. V. Spivak, and A. A. Zakurazhnov, in *Book of Abstracts of XI International Symposium on Organosilicon Chemistry* (Univ. Montpellier II, France, 1996), OC18.
7. A. I. Lazarev, A. Yu. Sukhanov, and G. A. Domrachev, Kristallografiya **41** (3), 798 (1996) [Crystallogr. Rep. **41**, 756 (1996)].
8. A. I. Lazarev, in *Abstracts of Bulletin of Czech and Slovak Crystallographic Association* (1998), Vol. 5, Special Issue B (ECM-18), p. 277.
9. A. I. Lazarev and G. A. Domrachev, Kristallografiya **39** (5), 811 (1994) [Crystallogr. Rep. **39**, 733 (1994)].

10. O. Feron, F. Langlais, and R. Naslain, Chem. Vap. Deposition **5** (1), 37 (1999).
11. W. Kraetschmer and D. R. Huffman, Philos. Trans. R. Soc. London, Ser. A **343** (1667), 33 (1993).
12. G. A. Domrachev and A. I. Lazarev, Fiz. Tverd. Tela (St. Petersburg) **41** (5), 799 (1999) [Phys. Solid State **41**, 720 (1999)].
13. A. I. Lazarev and G. A. Domrachev, in *Book of Abstracts of 4th Biennial International Workshop in Russia on Fullerenes and Atomic Clusters, IWFAC'99* (St. Petersburg, 1999), pp. 243, 317.
14. A. L. Chistyakov and I. V. Stankevich, Izv. Ross. Akad. Nauk, Ser. Khim., No. 9, 1649 (1999).
15. C. Vahlas, A. Kacheva, M. L. Hitchman, and P. Rocabois, J. Electrochem. Soc. **146** (7), 2752 (1999).
16. R. Sen, A. Govindaraj, and C. N. R. Rao, Chem. Phys. Lett. **267** (3–4), 367 (1997).
17. G. A. Domrachev, L. N. Zakharov, and Yu. A. Shevelev, Usp. Khim. **54** (8), 1260 (1985).
18. G. A. Domrachev, Yu. A. Shevelev, B. S. Kaverin, V. L. Karnatsevich, and I. G. Andreev, in *Low-Temperature Chemistry and Cryochemical Technology* (Mosk. Gos. Univ., Moscow, 1987), p. 87 [in Russian].
19. E. Kowalska, Z. Kucharski, and P. Byszewski, Carbon **37**, 877 (1999).
20. E. Kowalska, P. Byszewski, P. Dluzewski, R. Diduszko, and Z. Kucharski, J. Alloys Compd. **286**, 297 (1999).
21. A. Klotz, P. Marty, P. Boissel, D. de Caro, G. Serra, J. Mascetti, P. de Parseval, J. Derouault, J.-P. Daudey, and B. Claudret, Planet Space Sci. **44** (9), 957 (1996).
22. E. P. Smirnov, in *Directed Synthesis of Solid Materials* (Leningr. Gos. Univ., Leningrad, 1982), Vol. 1, p. 51 [in Russian].
23. L. Matija and D. Koruga, Adv. Mater. Proc. **282** (2), 115 (1998).
24. P. Byszewski, R. Diduszko, and E. Kowalska, in *Proceedings of the Twelfth International Symposium on Recent Advances in the Chemistry and Physics of Fullerenes and Related Materials*, Ed. by P. V. Kamat, D. M. Guldi, and K. M. Kadash (Electrochemical Society, Pennington, N.J., 1999), Vol. 7, p. 1392.
25. L. G. Domracheva, N. V. Karyakin, L. G. Bochkarev, G. A. Domrachev, and E. G. Domracheva, in *Topical Problems in Reformation of Chemical and Pedagogical Education: Proceedings of VI All-Russian Coordination Meeting* (Nizhegor. Pedagog. Inst., Nizhni Novgorod, 1998), pp. 185–187 [in Russian].
26. G. A. Domrachev, B. S. Kaverin, V. L. Karnatsevich, A. I. Kirillov, Yu. A. Kurskii, M. A. Lopatin, A. P. Matveev, S. N. Titova, K. K. Fukin, L. N. Zakharov, S. B. Zhuk, and B. V. Zhuk, in *Abstracts of Invited and Contributed Papers of 3rd International Workshop in Russia on Fullerenes and Atomic Clusters, IWFAC'97* (St. Petersburg, Russia, 1997), pp. 14.5, 252.
27. A. D. Petrov, Yu. P. Egorov, V. F. Mironov, G. N. Nikishin, and A. A. Bugorkova, Izv. Akad. Nauk SSSR, Otd. Khim. Nauk 50 (1956).
28. V. I. Zubov, N. P. Tretiakov, J. N. Teixeira Rabelo, *et al.*, Phys. Lett. A **194**, 223 (1994).
29. A. L. Chistyakov and I. V. Stankevich, Izv. Ross. Akad. Nauk, Ser. Khim., No. 5, 770 (2002).
30. M. Sawamura, Y. Kuninobu, M. Toganoh, Y. Matsuo, M. Yamanaka, and E. Nakamura, J. Am. Chem. Soc. **124**, 9354 (2002).

Translated by I. Zvyagin